Microstructures in Theranostic Microbubbles

Simone A.G. Langeveld

ISBN: 978-94-6421-705-6
Cover design and illustrations: Peter Tenkof
Layout: Simone Langeveld
Printed by: Ipskamp Printing

A digital version of this thesis is available at http://repub.eur.nl

Microstructures in Theranostic Microbubbles

Microstructuren in theranostische microbellen

Thesis

to obtain the degree of Doctor from the
Erasmus University Rotterdam
by command of the
rector magnificus

Prof. dr. A.L. Bredenoord

and in accordance with the decision of the Doctorate Board.

The public defence shall be held on
Wednesday May 11th 2022 at 13:00 hrs
by

Simone Adriana Gertrude Langeveld

born in Haarlem, the Netherlands

Erasmus University Rotterdam

Doctoral Committee:

Promotors	Prof. dr. ir. N. de Jong Prof. dr. ir. A.F.W. van der Steen
Other members	Prof. dr. A.B. Houtsmuller Prof. dr. C.T.W. Moonen Prof. dr. E.P.J. Stride
Co-promotor	Dr. K. Kooiman

Phospholipid Research Center

This work was funded in part by the Phospholipid Research Center in Heidelberg, Germany, grant number KKO-2017-057/1-1, and in part by the Thorax Center of Erasmus University Medical Center in Rotterdam. Additional financial support for the printing of this thesis was kindly provided by the Phospholipid Research Center and Erasmus University Rotterdam.

Financial support by the Dutch Heart Foundation for the publication of this thesis is gratefully acknowledged.

This work was performed in the framework of the Medical Delta UltraHB program. Medical Delta is gratefully acknowledged for financial support for the printing costs of this thesis.

The research described in this thesis was carried out at the Department of Biomedical Engineering, Thoraxcenter, Erasmus University Medical Center, Rotterdam.

Voor Opa

Contents

1

Introduction

1

1.1 Microbubbles

Bubbles are everywhere. From the large soap bubbles made by kids with a bubble blower, to the fluffy milk foam on top of a cappuccino. Even the tap water that we drink contains microscopically small air bubbles. Bubble dynamics have fascinated scientists for over a century, starting with work published by Lord Rayleigh in 1917 [1]. He was interested in bubble cavitation causing the erosion of ships' propellers and his mathematical equations are still widely used today [2, 3]. It was not until the late 1960's that small bubbles were discovered as useful contrast agents for ultrasound imaging [4]. Several generations of microbubbles later, they have evolved into a multifaceted platform used for a plethora of applications: from diagnosis [5] to enhanced drug delivery [6], and from cardiovascular diseases [7] to bacterial infections [8].

With this wide range of applications comes a large variety of microbubbles, sometimes referred to as ultrasound contrast agents [9] or ultrasound-responsive cavitation nuclei [10]. A microbubble consists of a gas core, which can be stabilized with different types of coating. As the name says a microbubble is microscopically small, for biomedical applications typically between 1 and 10 μm in diameter [11]. This means that microbubbles are small enough to travel through the vasculature yet too large to extravasate, making them an excellent blood pool marker [12]. Over the years, the uncoated air bubbles used by Gramiak and Shah [4] were improved by using different gases with a high molecular weight and low solubility in blood, such as C_4F_{10} and SF_6, to enhance *in vivo* stability. The gas core was further stabilized with a coating made of proteins [13], polymers [14], or phospholipids [15]. Protein-coated microbubbles have a thicker shell than phospholipid-coated microbubbles, making them stiffer and less echogenic [16, 17]. Polymer-coated microbubbles have the thickest shell and behave differently in response to ultrasound than phospholipid-coated microbubbles, making them less favorable as ultrasound contrast agent [18]. Hence, this thesis is focused on phospholipid-coated microbubbles.

Phospholipids are versatile molecules consisting of a hydrophilic headgroup and two hydrophobic tails. This ambivalence leads to the formation of different types of particles when phospholipids are dispersed in water, such as micelles and liposomes [19]. A liposome is a small spherical vesicle consisting of two or more layers of phospholipids with an aqueous core, organized so that only the headgroups are in contact with the surrounding water and the tails are all shielded from it [20]. A key difference between liposomes and microbubbles is the core. Microbubbles are filled with gas and coated with just one layer of phospholipids, a monolayer, with the hydrophilic headgroups on the outside in contact with the surrounding

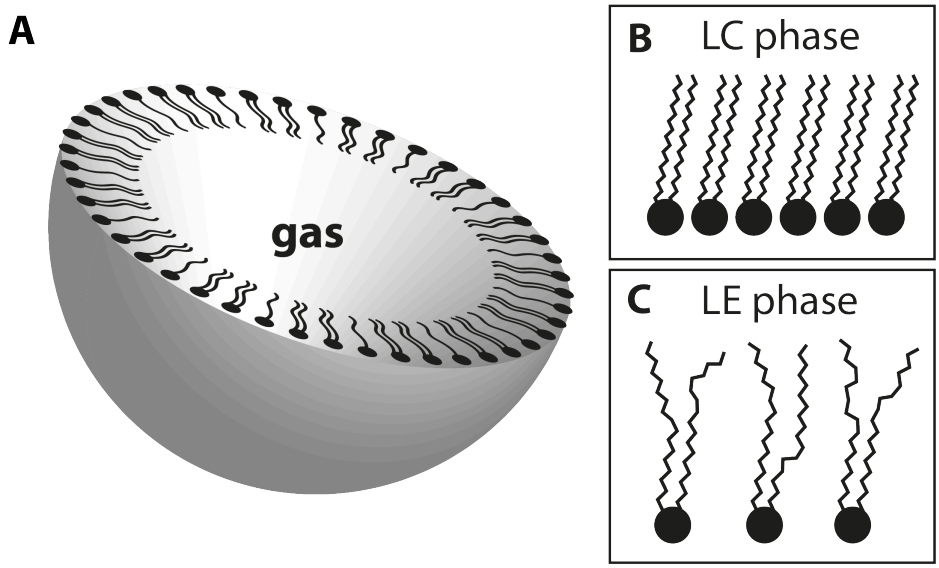

Figure 1.1 Schematic illustration of (**A**) microbubble with gas core and phospholipid coating (not drawn to scale) and phospholipids in (**B**) liquid condensed (LC) phase and (**C**) liquid expanded (LE) phase. Phospholipids are drawn with black circles as the hydrophilic headgroup and black lines as the hydrophobic tails.

water and the hydrophobic tails pointing inside to the gas core of the microbubble (Figure 1.1A) [21, 22].

A phospholipid-coated microbubble generally contains at least two components: a main lipid component and an emulsifier [11]. As main lipid both 1,2-dipalmitoyl-*sn*-glycero-3-phosphocholine (DPPC) [23] and 1,2-distearoyl-*sn*-glycero-3-phosphocholine (DSPC) [24] are popular, and PEG40-stearate as well as DSPE-PEG2000 are popular emulsifiers [25]. The molecules in a monolayer at the gas-water interface, that is the coating of a gas core, can be in two different liquid phases: the liquid condensed (LC, Figure 1.1B) or the liquid expanded (LE, Figure 1.1C) phase [26]. The state of the individual molecules varies per phospholipid type and depends on temperature and area per molecule: as a monolayer is compressed and the area per molecule decreases, some phospholipids shift from LE to LC phase. In addition, mixtures of two or more components behave differently from monolayers consisting of a pure phospholipid [25]. DSPC is always in LC phase, while PEG40-stearate is always in LE phase [27] and DPPC as well as DSPE-PEG2000 can shift from LE to LC phase when compressed [28, 29]. The separation of components into LC and LE phase generates intricate microstructures in the microbubble coating [30] (Figure 1.2).

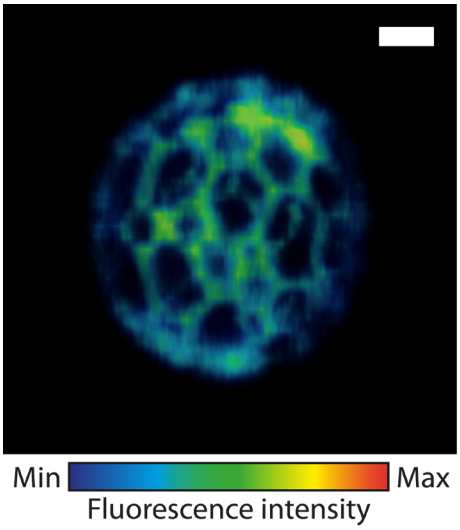

Figure 1.2 Lipid phase distribution of DPPC-based microbubble with microstructure. Selected view of 4Pi confocal microscopy y-stack of microbubble (diameter = 4.7 µm) with ternary coating composition of DPPC/DSPE-PEG2000/PEG40-stearate (84.8/7.0/8.2 mol%) with C_4F_{10} gas core. Scale bare is 1 µm. The coating components are phase separated into dark LC phase domains and a fluorescent network of LE phase.

Besides the low-soluble gas and phospholipid monolayer, the microbubble coating is also stabilized by incorporation of polyethylene glycol (PEG) tails, or a polymer, on the outside of the microbubble. These PEG tails are attached to the emulsifying component such as stearate or DSPE and form a dense layer around the microbubble surface. Depending on the density of the PEGylated molecules in the microbubble coating and the size of the polymer, the PEG tails are in a brush or mushroom regime [31]. This protective layer around the microbubble surface has two functions. First, it provides stability during storage by preventing coalescence, which is when two microbubbles fuse and become one larger microbubble [32]. Second, it increases the *in vivo* circulation time by shielding microbubbles from the immune system and by reducing nonspecific binding [33].

1.2 Acoustics

The most well-known application of ultrasound in modern medicine is prenatal ultrasound imaging [34]. In order to use ultrasound for imaging, an ultrasound wave or pulse is produced by a transducer and subsequently the returning echo is received [35]. This technique is an elegant option for diagnostic imaging, since it is non-invasive, portable, requires no ionizing radiation, and is inexpensive compared to other techniques such as magnetic resonance imaging (MRI) [36]. The discovery of gas bubbles as contrast agents for ultrasound imaging [4] paved the way for new applications such as cardiovascular disease and cancer, where imaging of the blood flow can provide relevant diagnostic information [37].

How microbubbles are activated by ultrasound can be easily demonstrated with a small experiment at home. All you need is a balloon and a speaker or, even better, a musical instrument. Blow up the balloon and hold it in your hands while playing music. If the music is loud enough with a proper bass, you can feel the balloon vibrating between the palms of your hands. This is essentially what happens when a microbubble responds to ultrasound. Ultrasound is a pressure wave, similar to audible music but at higher frequencies. The microbubble gas core responds to this pressure wave, just like the air inside a balloon responds to sound, by compression and expansion (Figure 1.3), also known as microbubble oscillation. The wavelength of an audible bass sound is between 60 to 250 Hz, corresponding to a wavelength of 1.36 to 5.67 m which is much larger than the size of a balloon. Similarly, the wavelength of an ultrasound pulse must be larger than the microbubble size to result in microbubble oscillation [38]. The acoustic response of microbubbles generates an echo or signal that can be differentiated from the surrounding tissue, thus creating contrast [39].

Microbubbles respond to ultrasound with different regimes, depending on the pressure and frequency of the ultrasound pulse. A linear response refers to the oscillation of microbubbles at low pressures at the fundamental frequency, which is the same frequency at which the sound waves leave the transducer. In this regime the oscillation amplitude has a linear relationship with the applied acoustic pressure [40]. Additionally, microbubbles can have a non-linear response, for example where oscillation occurs at half the fundamental frequency, *i.e.* subharmonics, or

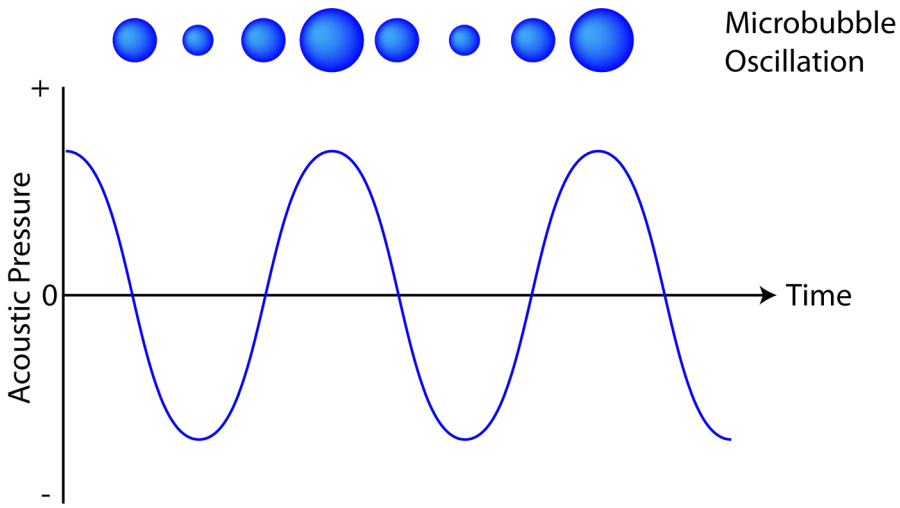

Figure 1.3 Schematic illustration of stable cavitation with an acoustic wave propagating longitudinally, causing microbubble compression and expansion.

multiples of the fundamental frequency, *i.e.* harmonics [3]. Besides linear and non-linear responses during stable cavitation, microbubbles can also undergo inertial cavitation [41]. In this case the ultrasound pulse has such a high pressure that the microbubbles burst, generating jet streaming which can impact the surrounding vessel wall and tissue [42].

The acoustic response of a microbubble is influenced by the coating. When a microbubble is compressed below a critical area, the phospholipid monolayer forms outward buckles. When a microbubble surface expands beyond a critical area, the monolayer ruptures. In between these two states, the microbubble coating behaves as elastic material in the elastic state [43]. Different models have been developed and tested in order to characterize and predict the acoustic behavior of microbubbles, such as the harmonic oscillator model and Rayleigh-Plesset equation [44]. The relation between the microbubble coating and acoustic behavior is captured by two parameters: shell elasticity and shell viscosity.

As with any object that resonates, microbubbles respond with a higher oscillation amplitude to a specific frequency, *i.e.* the resonance frequency. This behavior is size-dependent: larger-sized microbubbles tend to have a lower resonance frequency [45]. The resonance frequency is dependent on the shell elasticity and viscosity. However, even microbubbles of the same size have been found to respond to ultrasound in a heterogeneous way [46]. Since phospholipid-coated microbubbles are complex multi-molecular structures, perhaps simplifying the structure will lead to a more predictable and controllable acoustic response. This thesis is therefore focused on developing a new microbubble formulation where all phospholipid components are miscible and in the same lipid phase.

1.3 Ultrasound molecular imaging and therapeutic applications

Phospholipid-coated microbubbles can be functionalized with a ligand on the outside of the coating, targeting to a specific biomarker [47]. There are different strategies to attach such a ligand to the microbubble coating, for example by streptavidin-biotin bridging [48]. Targeted microbubbles can bind to specific biomarkers or receptors under flow and remain attached whereas non-targeted and non-bound microbubbles remain in the circulation [49]. In ultrasound molecular imaging, the acoustic signal from bound microbubbles must be distinguished from non-bound microbubbles, for example by using a destructive ultrasound pulse and subtracting the post-destruction signal from the pre-destruction signal [47, 50].

Ultrasound molecular imaging can be used to obtain specific information that ultrasound imaging with non-targeted microbubbles is unable to provide. This can be used for diagnosis, for example in oncology [51], and to monitor the response to therapy, for example anti-angiogenic therapy [52].

Microbubble oscillation can induce an array of biological effects when applied *in vivo*, which can be harnessed to enhance delivery of drugs that would normally be restricted to the vasculature. A classic example of this therapeutic application is chemotherapy: administered systemically it causes profuse adverse effects, yet with locally enhanced extravasation the systemic dosage may be reduced, thereby limiting the adverse effects [53]. Another application is to open the blood brain barrier (BBB), a highly specialized area of the vasculature designed to prevent even small molecules from penetrating the brain tissue [54]. Thirdly, there is increasing interest in the development of therapeutic antibodies and larger particles such as liposomes and exosomes, although efficient delivery of these drugs poses a major challenge [55]. Microbubble-mediated drug delivery can be a fitting solution to this problem, with or without targeting to a specific biomarker. Finally, ultrasound molecular imaging and therapy can be combined using one targeted microbubble formulation for image-guided therapy, which is then referred to as a theranostic agent [56, 57].

Ultrasound molecular imaging and therapeutic applications both require a uniform response to ultrasound for different reasons. When targeted microbubbles are used for ultrasound molecular imaging *in vivo*, a limited number of microbubbles attaches to the target biomarker while the bulk of microbubbles remains in the circulation until clearance [47]. When detecting the presence of single microbubbles bound to biomarkers or tumor cells, the more uniform the microbubble responds to ultrasound, the more reliable the diagnosis. For therapeutic applications, both *in vitro* [58, 59] and *in vivo* studies [60, 61] demonstrated a delicate balance between reversible cellular effects, for example pore formation (sonoporation), and permanent damage leading to cell death and inflammatory responses. The microbubble oscillation amplitude can tip this balance, and therefore must be uniform and controlled. Clinically approved microbubble formulations have been developed specifically for diagnostic applications and respond to ultrasound with good non-linear signal, however, their oscillation amplitude is heterogeneous and thus unpredictable [45]. A new microbubble formulation with all components miscible and in the same lipid phase may have a more uniform and controllable response to ultrasound, making it more suitable for ultrasound molecular imaging and therapeutic applications.

1.4 Thesis Outline

This thesis is based on the hypothesis that microstructures in the microbubble coating, caused by phase separation of the phospholipid components, contribute to an unpredictable response to ultrasound. **Chapter 2** provides an overview of therapy and drug delivery applications of microbubbles and other ultrasound-responsive cavitation nuclei. The aim of **Chapter 3** was to elucidate the lipid phase behavior in the microbubble coating of widely used formulations with high-resolution fluorescence microscopy and Langmuir trough studies on phospholipid monolayers. Furthermore, this chapter investigated how the lipid phase distribution in the microbubble coating can be influenced by changing the lipid handling prior to microbubble production. The next step was to develop a novel formulation with all components miscible and in the same lipid phase. **Chapter 4** depicts the lipid phase distribution and acoustic response of microbubbles with a new main lipid component: DSPE.

To show if microbubbles with a homogeneous lipid phase distribution have a more uniform response to ultrasound than microbubbles with microstructures in their coating, we must be able to look at the acoustic response of individual microbubbles while simultaneously observing the lipid phase distribution. **Chapter 5** describes the technical advancement making this possible: coupling of a confocal microscope to the one-of-a-kind Brandaris 128 ultra-high-speed camera, which can record microbubble oscillations with up to 25 million frames per second [62]. Using this combined system, the acoustic behavior of a new microbubble formulation with cholesterol could be unraveled, as detailed in **Chapter 6**. The aim of **Chapter 6** was to relate the effects of lipid handling and phase distribution to the acoustic behavior of phospholipid-coated microbubbles.

After going in-depth into the fundamental qualities that determine a microbubbles' response to ultrasound, the acquired knowledge was applied to the application of vascular drug delivery. **Chapter 7** focused on the microbubble-cell configuration *in vitro* using the combined confocal and Brandaris 128 system with human umbilical vein endothelial cells (HUVECs), detailing the influence of microbubble engulfment on the drug delivery potential by studying membrane perforation upon microbubble oscillation. In **Chapter 8**, the binding efficacy of targeted microbubbles with a homogeneous or a heterogeneous ligand distribution was compared. The binding efficacy of these microbubble types, first characterized in **Chapter 3**, was evaluated *in vitro* using HUVECs with and without flow, and *in vivo* using the chorioallantoic membrane of chicken embryos.

Moving on from research focused on better understanding of underlying mechanisms, **Chapter 9** describes the development and proof-of-principle of a novel theranostic agent: vancomycin-decorated microbubbles. First, vancomycin was conjugated to a PEGylated phospholipid. Next, targeted microbubbles were produced and the binding under flow to bacterial biofilms was investigated. Finally, the targeted microbubbles were evaluated as theranostic agents for ultrasound molecular imaging and sonobactericide, *i.e.* killing of bacteria with microbubbles and ultrasound.

Chapter 10 gives an overview of new developments in the field of targeted microbubbles for ultrasound molecular imaging and therapy. New microbubble targeting strategies are described, as well as pre-clinical studies on ultrasound molecular imaging and therapy using targeted microbubbles. Finally, in **Chapter 11** the scientific contributions from this thesis are discussed including implications for future research.

2

Ultrasound-responsive cavitation nuclei for therapy and drug delivery

Klazina Kooiman, Silke Roovers, **Simone A.G. Langeveld**, Robert T. Kleven, Heleen Dewitte, Meaghan A. O'Reilly, Jean-Michel Escoffre, Ayache Bouakaz, Martin D. Verweij, Kullervo Hynynen, Ine Lentacker, Eleanor Stride, Christy K. Holland

Based on:
Ultrasound in Medicine & Biology, Vol. 46, No. 6, pp. 1296-1325, 2020 [426].

Abstract

Therapeutic ultrasound strategies are actively under development to harness the mechanical activity of cavitation nuclei for beneficial tissue bioeffects. The mechanical oscillations of circulating microbubbles, the most widely investigated cavitation nuclei, which may also encapsulate or shield a therapeutic agent in the bloodstream, trigger and promote localized uptake. Oscillating microbubbles can create stresses either on nearby tissue or in surrounding fluid to enhance drug penetration and efficacy in the brain, spinal cord, vasculature, immune system, biofilm, or tumors. This review summarizes recent investigations that have elucidated interactions of ultrasound and cavitation nuclei with cells, the treatment of tumors, immunotherapy, the blood brain barrier and blood spinal cord barrier, sonothrombolysis, cardiovascular drug delivery, and sonobactericide. In particular, an overview of salient ultrasound features, drug delivery vehicles, therapeutic transport routes, and preclinical and clinical studies is provided. Successful implementation of ultrasound and cavitation nuclei-mediated drug delivery has the potential to change the way drugs are administered systemically, resulting in more effective therapeutics and less-invasive treatments.

Keywords—Ultrasound; Cavitation nuclei; Therapy; Drug delivery; Bubble-cell interaction; Sonoporation; Sonothrombolysis; Blood-brain barrier opening; Sonobactericide; Tumor

2.1 Introduction

Around the start of the European Symposium on Ultrasound Contrast Agents (ESUCI), ultrasound-responsive cavitation nuclei were reported to have therapeutic potential. Thrombolysis was shown to be accelerated *in vitro* [63] and cultured cells were transfected with plasmid DNA [64]. Since then, many research groups have investigated the use of cavitation nuclei for multiple forms of therapy, including both tissue ablation and drug and gene delivery. In the early years, the most widely investigated cavitation nuclei were gas microbubbles, ~1-10 μm in diameter and coated with a stabilizing shell, whereas nowadays both solid and liquid nuclei are also investigated that can be as small as a few hundred nm. Drugs can be co-administered with the cavitation nuclei or loaded in or on them [65, 66]. The diseases that can be treated with ultrasound-responsive cavitation nuclei include but are not limited to cardiovascular disease and cancer [67, 68], the current leading causes of death worldwide according to the World Health Organization [69]. This review focuses on the latest insights into cavitation nuclei for therapy and drug delivery from the physical and biological mechanisms of bubble-cell interaction to

preclinical (both *in vitro* and *in vivo*) and clinical studies (timespan 2014-2019), with particular emphasis on the key clinical applications. The applications covered in this review are the treatment of tumors, immunotherapy, the blood brain barrier and blood spinal cord barrier, dissolution of clots, cardiovascular drug delivery, and the treatment of bacterial infections.

2.2 Cavitation nuclei for therapy

The most widely used cavitation nuclei are phospholipid-coated microbubbles with a gas core. For the 128 preclinical studies included in the treatment sections of this review, the commercially available and clinically approved Definity (Luminity in Europe; octafluoropropane gas core, phospholipid coating) [23, 70] microbubbles were used the most (in 22 studies). Definity was used for studies on all applications discussed here and the most for opening the blood brain barrier (BBB) (12 studies). SonoVue (Lumason in the USA) is commercially available and clinically approved as well (sulfur hexafluoride gas core, phospholipid coating) [24, 70] and was used in a total of 14 studies for the treatment of non-brain tumors (for example Xing et al. [71]), BBB opening (for example Goutal et al. [72]), and sonobactericide (for example Hu et al. [73]). Other commercially available microbubbles were used that are not clinically approved, such as BR38 [74] in the study by Wang et al. [75] and MicroMarker [76] in the study by Theek et al. [77]. Custom-made microbubbles are as diverse as their applications, with special characteristics tailored to enhance different therapeutic strategies. Different types of gasses were used as the core such as air (for example Eggen et al. [78]), nitrogen (for example Dixon et al. [79]), oxygen (for example Fix et al. [80]), octafluoropropane (for example Pandit et al. [81]), perfluorobutane (for example Dewitte et al. [82]), sulfur hexafluoride [83, 84] or a mixture of gases such as nitric oxide and octafluoropropane [85] or sulfur hexafluoride and oxygen [86]. While fluorinated gases improve the stability of phospholipid-coated microbubbles [87], other gases can be loaded for therapeutic applications, such as oxygen to treat tumors [80, 86, 88] and nitric oxide [85, 89] or hydrogen gas [90] for treatment of cardiovascular disease. The main phospholipid component of custom-made microbubbles is usually a phosphatidylcholine such as 1,2-dipalmitoyl-*sn*-glycero-3-phosphocholine (DPPC), used in 13 studies, for example Dewitte et al. [82], Bae et al. [84], Chen et al. [91], Fu et al. [92], or 1,2-distearoyl-*sn*-glycero-3-phosphocholine (DSPC), used in 18 studies, for example Kilroy et al. [93], Bioley et al. [94], Dong et al. [95], Goyal et al [96], Pandit et al. [81]. These phospholipids are popular because they are also the main component in Definity [23] and SonoVue/Lumason [24], respectively. Another key component of the microbubble coating is a PEGylated emulsifier such as polyoxyethylene (40) stearate (PEG40-stearate; for example Kilroy et al. [93]) or

the most often used 1,2-distearoyl-*sn*-glycero-3-phosphoethanolamine-N-carboxy (poly-ethyleneglycol) (DSPE-PEG2000; for example Belcik et al. [97]), which is added to inhibit coalescence and to increase the *in vivo* half-life [21]. In general two methods are used to produce custom-made microbubbles: mechanical agitation (for example Ho et al. [98]) or probe sonication (for example Belcik et al. [99]). Both these methods produce a population of microbubbles that is polydisperse in size. Monodispersed microbubbles produced by microfluidics have recently been developed, and are starting to gain attention for pre-clinical therapeutic studies. Dixon et al. [79] used monodisperse microbubbles to treat ischemic stroke.

Various therapeutic applications have inspired the development of novel cavitation nuclei, which is discussed in depth in the companion review by Stride et al. [100]. To improve drug delivery, therapeutics can be either co-administered with or loaded onto the microbubbles. One strategy for loading is to create microbubbles stabilized by drug-containing polymeric nanoparticles around a gas core [101]. Another strategy is to attach therapeutic molecules or liposomes to the outside of microbubbles, for example by biotin-avidin coupling [82, 88, 102]. Echogenic liposomes can be loaded with different therapeutics or gases and have been studied for vascular drug delivery [85], treatment of tumors [103], and sonothrombolysis [104]. Acoustic Cluster Therapy (ACT) combines Sonazoid microbubbles with droplets that can be loaded with therapeutics for treatment of tumors [105]. The cationic microbubbles utilized in the treatment sections of this review were used mostly for vascular drug delivery, with genetic material loaded on the microbubble surface by charge-coupling (for example Cao et al. [106]). Besides phospholipids and nanoparticles, microbubbles can also be coated with denatured proteins such as albumin. Optison [107] is a commercially available and clinically approved ultrasound contrast agent that is coated with human albumin and used in studies on treatment of non-brain tumors [108], BBB opening [60, 109], and immunotherapy [110]. Nano-sized particles cited in this review have been used as cavitation nuclei for treatment of tumors, such as nanodroplets (for example Cao et al. [111]) and nanocups [112], for BBB opening (nanodroplets, Wu et al. [113]), and for sonobactericide (nanodroplets, Guo et al. [114]).

2.3 Bubble-cell interaction

Physics

The physics of the interaction between bubbles or droplets and cells are described as these are the main cavitation nuclei used for drug delivery and therapy.

Physics of microbubble-cell interaction

Being filled with gas and/or vapor makes bubbles highly responsive to changes in pressure and hence exposure to ultrasound can cause rapid and dramatic changes in their volume. These volume changes in turn give rise to an array of mechanical, thermal, and chemical phenomena that can significantly influence the bubbles' immediate environment and mediate therapeutic effects. For the sake of simplicity, these phenomena will be discussed in the context of a single bubble. It is important to note, however, that biological effects are typically produced by a population of bubbles and the influence of inter bubble interactions should not be neglected.

Mechanical effects

A bubble in a liquid is subject to multiple competing influences: the driving pressure of the imposed ultrasound field, the hydrostatic pressure imposed by the surrounding liquid, the pressure of the gas and/or vapor inside the bubble, surface tension and the influence of any coating material, the inertia of the surrounding fluid, and damping due to the viscosity of the surrounding fluid and/or coating, thermal conduction, and/or acoustic radiation.

The motion of the bubble is primarily determined by the competition between the liquid inertia and the internal gas pressure. This competition can be characterized by using the Rayleigh-Plesset equation for bubble dynamics to compare the relative contributions of the terms describing inertia and pressure to the acceleration of the bubble wall [115]:

$$\ddot{R} = -\left(\frac{3}{2}\frac{\dot{R}^2}{R}\right) + \left(\frac{p_G(R) + p_\infty(t) - \frac{2\sigma}{R}}{\rho_L R}\right) = IF + PF \qquad \textit{(eq. 2.1)}$$

where R is the time dependent bubble radius with initial value R_0, p_G is the pressure of the gas inside the bubble, p_∞ is the combined hydrostatic and time varying pressure in the liquid, σ is the surface tension at the gas liquid interface, and ρ_L is the liquid density.

Flynn [115, 116] identified two scenarios: if the pressure factor (PF) is dominant when the bubble approaches its minimum size, then the bubble will undergo sustained volume oscillations. If the inertia term is dominant (IF), then the bubble will undergo inertial collapse, similar to an empty cavity, after which it may rebound or it may disintegrate. Which of these scenarios occurs is dependent upon the bubble expansion ratio: R_{max}/R_0, and hence the bubble size and the amplitude and frequency of the applied ultrasound field.

Both inertial and non-inertial bubble oscillations can give rise to multiple phenomena that impact the bubble's immediate environment and hence are important for therapy. These include:

1. Direct impingement – even at moderate amplitudes of oscillation, the acceleration of the bubble wall may be sufficient to impose significant forces upon nearby surfaces, easily deforming fragile structures such as a biological cell membranes [117, 118] or blood vessel walls [119].

2. Ballistic motion – in addition to oscillating, the bubble may undergo translation as a result of the pressure gradient in the fluid generated by a propagating ultrasound wave (primary radiation force). Due to their high compressibility, bubbles may travel at significant velocities, sufficient to push them toward targets for improved local deposition of a drug [120] or penetrate biological tissue [121-123].

3. Microstreaming – when a structure oscillates in a viscous fluid there will be a transfer of momentum due to interfacial friction. Any asymmetry in the oscillation will result in a net motion of that fluid in the immediate vicinity of the structure known as microstreaming [124]. This motion will in turn impose shear stresses upon any nearby surfaces as well as increasing convection within the fluid. Due to the inherently non-linear nature of bubble oscillations (equation 1), both non-inertial and inertial cavitation can produce significant microstreaming, resulting in fluid velocities on the order of 1 mm/s [125]. If the bubble is close to a surface then it will also exhibit non-spherical oscillations which increases the asymmetry and hence the microstreaming even further [126, 127].

4. Microjetting – another phenomenon associated with non-spherical bubble oscillations near a surface is the generation of a liquid jet during bubble collapse. If there is sufficient asymmetry in the acceleration of the fluid on either side of the collapsing bubble, then the more rapidly moving fluid may deform the bubble into a toroidal shape causing a high velocity jet to be emitted on the opposite side. Microjetting has been shown to be capable of producing pitting even in highly resilient materials such as steel [128, 129]. However, as both the direction and velocity of the jet are determined by the elastic properties of the nearby surface, its effects in biological tissue are more difficult to predict [130]. Nevertheless, as shown by Chen et al. [119], in many cases a bubble will be sufficiently confined that microjetting will impact surrounding structures regardless of jet direction.

5. Shockwaves – an inertially collapsing cavity that results in supersonic bubble wall velocities creates a significant discontinuity in the pressure in the surrounding liquid leading to the emission of a shockwave, which may impose significant stresses on nearby structures.
6. Secondary radiation force – at smaller amplitudes of oscillation a bubble will also generate a pressure wave in the surrounding fluid. If the bubble is adjacent to a surface, interaction between this wave and its reflection from the surface leads to a pressure gradient in the liquid and a secondary radiation force on the bubble. As with microjetting, the elastic properties of the boundary will determine the phase difference between the radiated and reflected waves and hence whether the bubbles move towards or away from the surface. Motion towards the surface may amplify the effects of 1, 3, and 6.

Thermal effects

As described above, an oscillating microbubble will reradiate energy from the incident ultrasound field in the form of a spherical pressure wave. In addition, the nonlinear character of the microbubble oscillations will lead to energy being reradiated over a range of frequencies. At moderate driving pressures the bubble spectrum will contain integer multiples (harmonics) of the driving frequency; and at higher pressures also fractional components (sub and ultraharmonics). In biological tissue, absorption of ultrasound increases with frequency and this nonlinear behavior thus also increases the rate of heating [131, 132]. Bubbles will also dissipate energy as a result of viscous friction in the liquid and thermal conduction from the gas core, the temperature of which increases during compression. Which mechanism is dominant depends on the size of the bubble, the driving conditions and the viscosity of the medium. Thermal damping is however typically negligible in biomedical applications of ultrasound as the time constant associated with heat transfer is much longer than the period of the microbubble oscillations [133].

Chemical effects

The temperature rise produced in the surrounding tissue will be negligible compared with that occurring inside the bubble, especially during inertial collapse when it may reach several thousand Kelvin [134]. The gas pressure similarly increases significantly. While only sustained for a very brief period, these extreme conditions can produce highly reactive chemical species, in particular reactive oxygen species (ROS), as well as the emission of electromagnetic radiation (sonoluminescence). ROS have been shown to play a significant role in multiple biological processes [135] and both ROS and sonoluminescence may affect drug activity [136-138].

Physics of droplets-cell interaction

Droplets consist of an encapsulated quantity of a volatile liquid, such as perfluorobutane (boiling point -1.7°C) or perfluoropentane (boiling point 29°C), which is in a superheated state at body temperature. Superheated state means that although the volatile liquids have a boiling point below 37°C, these droplets remain in the liquid phase and do not show spontaneous vaporization after injection. Vaporization can be achieved instead by exposure to ultrasound of significant amplitude via a process known as acoustic droplet vaporization (ADV) [139]. Before vaporization, the droplets are typically one order of magnitude smaller than the emerging bubbles, and the perfluorocarbon is inert and biocompatible [140]. These properties enable a range of therapeutic possibilities [141, 142]. For example, unlike microbubbles, small droplets may extravasate from the leaky vessels into tumor tissue due to the enhanced permeability and retention (EPR) effect [143-145], and then be turned into bubbles by ADV [146, 147]. Loading the droplets with a drug enables local delivery [147] by way of ADV. The mechanism behind this is that the emerging bubbles give rise to similar radiation forces and microstreaming as described in the physics of the microbubble – cell interaction above. It should be noted that oxygen is taken up during bubble growth [148], which could lead to hypoxia.

The physics of the droplet – cell interaction is largely governed by the ADV. In general, it has been observed that ADV is promoted by the following factors: large peak negative pressures [139], usually obtained by strong focusing of the generated beam, high frequency of the emitted wave, and a relatively long distance between the transducer and the droplet. Another observation that has been made with micrometer-sized droplets is that vaporization often starts at a well-defined nucleation spot near the side of the droplet where the acoustic wave impinges [149]. These facts can be explained by considering the two mechanisms that play a role in achieving a large peak negative pressure inside the droplet: acoustic focusing and nonlinear ultrasound propagation [150]. In the following, lengths and sizes are related to the wavelength, *i.e.* the distance traveled by a wave in one oscillation (*e.g.*, a 1 MHz ultrasound wave that is traveling in water with a wave speed, *c*, of 1500 m/s has a wavelength, *w* (m), of

$\frac{c}{f} = \frac{1500}{10^6} = 0.0015,$ *i.e.* 1.5 mm).

Acoustic focusing

Because the speed of sound in perfluorocarbon liquids is significantly lower than in water or tissue, refraction of the incident wave will occur at the interface between these fluids, and the spherical shape of the droplet will give rise to focusing. The

assessment of this focusing effect is not straightforward because the traditional way of describing these phenomena with rays that propagate along straight lines (the ray approach) only holds for objects that are much larger than the applied wavelength. In the current case, the frequency of a typical ultrasound wave used for insonification is in the order of 1-5 MHz, yielding wavelengths in the order of 1500-300 μm, while a droplet will be smaller by 2-4 orders of magnitude. Beside this, using the ray approach, the lower speed of sound in perfluorocarbon would yield a focal spot near the backside of the droplet, which is in contradiction to observations. The correct way to treat the focusing effect is to solve the full diffraction problem by decomposing the incident wave, the wave reflected by the droplet, and the wave transmitted into the droplet into a series of spherical waves. For each spherical wave, the spherical reflection and transmission coefficients can be derived. Superposition of all the spherical waves yields the pressure inside the droplet. Nevertheless, when this approach is only applied to an incident wave with the frequency that is emitted by the transducer, this will lead neither to the right nucleation spot nor to sufficient negative pressure for vaporization. Nanoscale droplets may be too small to make effective use of the focusing mechanism and ADV is therefore less dependent on the frequency.

Nonlinear ultrasound propagation

High pressure amplitudes, high frequencies, and long propagation distances all promote nonlinear propagation of an acoustic wave [151]. In the time domain, nonlinear propagation manifests itself as an increasing deformation of the shape of the ultrasound wave with distance traveled. In the frequency domain, this translates to increasing harmonic content, *i.e.* frequencies that are multiples of the driving frequency. The total incident acoustic pressure p(t) at the position of a nanodroplet can therefore be written as

$$p(t) = \sum_{n=1}^{\infty} a_n \cos(n\omega t + \phi_n) \qquad \textit{(eq. 2.2)}$$

where n is the number of a harmonic, a_n and ϕ_n are the amplitude and phase of this harmonic, and ω is the angular frequency of the emitted wave. The wavelength of a harmonic wave is a fraction of the emitted wavelength.

The above effects are both important in case of ADV and should therefore be combined. This implies that first the amplitudes and phases of the incident nonlinear ultrasound wave at the droplet location should be computed. Next, for each harmonic, the diffraction problem should be solved in terms of spherical harmonics. Adding the diffracted waves inside the droplet with the proper amplitude and phase will then yield the total pressure in the droplet. Figure 2.1 shows that the combined effects of nonlinear propagation and diffraction can cause a dramatic amplification of

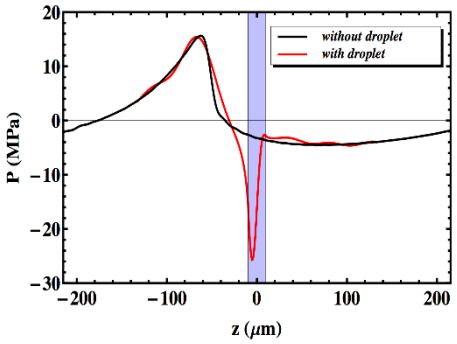

Figure 2.1 Combined effect of nonlinear propagation and focusing of the harmonics in a perfluoropentane micrometer-sized droplet. The emitted ultrasound wave has a frequency of 3.5 MHz and a focus at 3.81 cm, and the radius of the droplet is 10 μm for ease of observation. The pressures are given on the axis of the droplet along the propagating direction of the ultrasound wave, and the shaded area indicates the location of the droplet (reprinted with permission from Sphak et al. [149]).

the peak negative pressure in the micrometer-sized droplet, sufficient for triggering droplet vaporization [149]. Moreover, the location of the negative pressure peak also agrees with the observed nucleation spot.

After vaporization has started, the growth of the emerging bubble is limited by inertia and heat transfer. In the absence of the heat transfer limitation, the inertia of the fluid that surrounds the bubble limits the rate of bubble growth, which is linearly proportional to time and inversely proportional to the square root of the density of the surrounding fluid. When inertia is neglected, thermal diffusion is the limiting factor in the transport of heat to drive the endothermic vaporization process of perfluorocarbon, causing the radius of the bubble to increase with the square root of time. In reality, both processes occur simultaneously, where the inertia effect is dominant at the early stage and the diffusion effect is dominant at the later stage of bubble growth. The final size that is reached by a bubble depends on the time that a bubble can expand, *i.e.* on the duration of the negative cycle of the insonifying pressure wave. It is therefore expected that lower insonification frequencies give rise to larger maximum bubble size. Thus, irrespective of their influence on triggering ADV, lower frequencies would lead to more violent inertial cavitation effects and cause more biological damage, as experimentally observed for droplets with a radius in the order of 100 nm [152].

Biological mechanisms and bioeffects of ultrasound-activated cavitation nuclei

The biological phenomena of sonoporation (*i.e.* membrane pore formation), stimulated endocytosis, and opening of cell-cell contacts and the bioeffects of intracellular calcium transients, reactive oxygen species generation, cell membrane potential change, and cytoskeleton changes have been observed for several years [66, 67, 153, 154]. However, other bioeffects induced by ultrasound-activated cavitation nuclei have recently been discovered. These include membrane blebbing as a recovery mechanism for reversible sonoporation (both for ultrasound-

activated microbubbles [155] and upon ADV [156]), extracellular vesicle formation [157], suppression of efflux transporters P-glycoprotein [158, 159] and BBB (Blood Brain Barrier) transporter genes [160]. At the same time, more insight has been gained in the origin of the bioeffects, largely through the use of live cell microscopy. For sonoporation, real time membrane pore opening and closure dynamics were revealed with pores <30 μm^2 closing within 1 min, while pores >100 μm^2 did not reseal [161] as well as immediate rupture of filamentary actin at the pore location [162] and correlation of intracellular reactive oxygen species levels with the degree of sonoporation [163]. Real-time sonoporation and opening of cell-cell contacts in the same endothelial cells has been demonstrated as well for a single example [164]. The applied acoustic pressure was shown to determine uptake of model drugs via sonoporation or endocytosis in another study [165]. Electron microscopy revealed formation of transient membrane disruptions and permanent membrane structures, *i.e.* caveolar endocytic vesicles, upon ultrasound and microbubble-treatment [166]. A study by Fekri et al. [167] revealed that enhanced clathrin-mediated endocytosis and fluid-phase endocytosis occur through distinct signaling mechanisms upon ultrasound and microbubble treatment. The majority of these bioeffects have been observed in *in vitro* models using largely non-endothelial cells and may therefore not be directly relevant to *in vivo* tissue, where intravascular micron-sized cavitation nuclei will only have contact with endothelial cells and circulating blood cells. On the other hand, the mechanistic studies by Belcik et al. [97, 99] and Yu et al. [168] do show translation from *in vitro* to *in vivo*. In these studies, ultrasound-activated microbubbles were shown to induce a shear-dependent increase in intravascular adenosine triphosphate (ATP) from both endothelial cells and erythrocytes, an increase in intramuscular nitric oxide, and downstream signaling through both nitric oxide and prostaglandins which resulted in augmentation of muscle blood flow. Ultrasound settings were similar, namely 1.3 MHz, *MI* 1.3 for Belcik et al. [97, 99] and 1 MHz, *MI* 1.5 for Yu et al. [168], with *MI* defined as $MI = P\_ / \sqrt{f}$ where $P\_$ is the peak negative pressure of the ultrasound wave (in MPa) and f the center frequency of the ultrasound wave (in MHz).

Whether or not there is a direct relationship between the type of microbubble oscillation and specific bioeffects remains to be elucidated, although more insight has been gained through ultra-high-speed imaging of the microbubble behavior in conjunction with live cell microscopy. For example, there seems to be a microbubble excursion threshold above which sonoporation occurs [164]. Van Rooij et al. [169] further showed that displacement of targeted microbubbles enhanced reversible sonoporation and preserved cell viability whilst microbubbles that did not displace were identified as the main contributors to cell death.

All of the aforementioned biological observations, mechanisms, and effects relate to eukaryotic cells. Study of the biological effects of cavitation on for example bacteria is in its infancy, but studies suggest that sonoporation can be achieved in Gram– bacteria, with dextran uptake and gene transfection being reported in *Fusobacterium nucleatum* [170]. More recent studies have investigated the effect of microbubbles and ultrasound on gene expression [95, 171, 172]. The findings are conflicting because although they all show a reduction in expression of genes involved in biofilm formation and resistance to antibiotics, an increase in expression of genes involved with dispersion and detachment of biofilms was also found [95]. This cavitation-mediated bioeffect needs further investigation.

Modelling microbubble–cell–drug interaction

Whilst there have been significant efforts to model the dynamics of ultrasound driven microbubbles [173, 174], less attention has been paid to the interactions between microbubbles and cells or their impact upon drug transport. Currently there are no models that describe the interactions between microbubbles, cells, and drug molecules. Several models have been proposed for the microbubble – cell interaction in sonoporation focusing on different aspects: the cell expansion and microbubble jet velocity [175], the shear stress exerted on the cell membrane [176-180], microstreaming [178], shear stress exerted on the cell membrane in combination with microstreaming [181], or other flow phenomena [182, 183] generated by an oscillating microbubble. In contrast to the other models, Man et al. [184] propose that the microbubble-generated shear stress does not induce pore formation, but that this is instead due to microbubble fusion with the membrane and subsequent "pull out" of cell membrane lipid molecules by the oscillating microbubble. Models for pore formation (for example Koshiyama and Wada [185]) and resealing [186] in cell membranes have also been developed, but these models neglect the mechanism by which the pore is created. There is just one sonoporation dynamics model, developed by Fan et al. [187], that relates the uptake of the model drug propidium iodide (PI) to the size of the created membrane pore and the pore resealing time for a single cell in an *in vitro* setting. The model describes the intracellular fluorescence intensity of PI as a function of time, $F(t)$, by:

$$F(t) = \alpha \cdot \pi D C_0 \cdot r_0 \cdot \frac{1}{\beta}\left(1 - e^{-\beta t}\right) \qquad \textit{(eq. 2.3)}$$

where α is the coefficient that relates the amount of PI molecules to the fluorescence intensity of PI-DNA and PI-RNA, D is the diffusion coefficient of PI, C_0 is the extracellular PI concentration, r_0 is the initial radius of the pore, β is the pore resealing coefficient, and t is time. The coefficient α is determined by the sensitivity of the fluorescence imaging system, and if unknown the equation can still be used because it is the

pore size coefficient, $\alpha \cdot \pi D C_0 \cdot r_0$, that determines the initial slope of the PI uptake pattern and is the scaling factor for the exponential increase. A cell with a large pore will have a steep initial slope of PI uptake and the maximum PI intensity quickly reaches the plateau value. A limitation of this model is that equation 3 is based on two-dimensional free diffusion models, which holds for PI-RNA but not for PI-DNA because this is confined to the nucleus. The model is independent of cell type, as Fan et al. have demonstrated agreement with experimental results in both kidney [187] and endothelial cells [188]. Other researchers have also used this model for endothelial cell studies and also classified the distribution of both the pore size and pore resealing coefficients using Principal Component Analysis to determine whether cells were reversibly or irreversibly sonoporated. In the context of blood brain barrier (BBB) opening, Hosseinkhah et al. [189] have modeled the microbubble-generated shear and circumferential wall stress for 5 μm microvessels upon microbubble oscillation at a fixed mechanical index (MI) of 0.134 for a range of frequencies (0.5, 1, and 1.5 MHz). The wall stresses were dependent upon microbubble size (range investigated 2-18 μm in diameter) and ultrasound frequency. Wiedemair et al. [190] have also modelled the wall shear stress generated by microbubble (2 μm diameter) destruction at 3 MHz for larger microvessels (200 μm diameter). The presence of red blood cells was included in the model and was found to cause confinement of pressure and shear gradients to the vicinity of the microbubble. Advances in methods for imaging microbubble-cell interactions will facilitate the development of more sophisticated mechanistic models.

2.4 Treatment of tumors (non-brain)

The structure of tumor tissue varies significantly from that of healthy tissue which has important implications for its treatment. To support the continuous expansion of neoplastic cells, the formation of new vessels (*i.e.* angiogenesis) is needed [191]. As such, a rapidly-developed, poorly-organized vasculature with enlarged vascular openings arises. In between these vessels, large avascular regions exist, which are characterized by a dense extracellular matrix, high interstitial pressure, low pH, and hypoxia. Moreover, a local immunosuppressive environment is formed, preventing possible anti-tumor activity by the immune system.

Notwithstanding the growing knowledge of the pathophysiology of tumors, treatment remains challenging. Chemotherapeutic drugs are typically administered to abolish the rapidly-dividing cancer cells. Yet, their cytotoxic effects are not limited to cancer cells, causing dose-limiting off-target effects. To overcome this hurdle, chemotherapeutics are often encapsulated in nano-sized carriers, *i.e.* nanoparticles, that are designed to specifically diffuse through the large openings

of tumor vasculature, while being excluded from healthy tissue by normal blood vessels [143, 144]. Despite being highly promising in pre-clinical studies, drug-containing nanoparticles have shown limited clinical success due to the vast heterogeneity in tumor vasculature [75, 143, 192]. In addition, drug penetration into the deeper layers of the tumor can be constrained due to high interstitial pressure and a dense extracellular matrix in the tumor. Furthermore, acidic and hypoxic regions limit the efficacy of radiation- and chemotherapy-based treatments due to biochemical effects [80, 86, 193]. Ultrasound-triggered microbubbles are able to alter the tumor environment locally, thereby improving drug delivery to tumors. These alterations are schematically represented in Figure 2.2 and include: improving vascular permeability, modifying the tumor perfusion, reducing local hypoxia, and overcoming the high interstitial pressure.

Several studies have found that ultrasound-driven microbubbles improved delivery of chemotherapeutic agents in tumors, which resulted in increased anti-tumor effects [75, 101, 194]. Moreover, several gene products could be effectively delivered to tumor cells via ultrasound-driven microbubbles, resulting in a downregulation of tumor-specific pathways and an inhibition in tumor growth [195, 196]. Theek et al. [77] furthermore confirmed that nanoparticle accumulation can be achieved in tumors with low EPR effect. Drug transport and distribution through the dense tumor matrix and into regions with elevated interstitial pressure is often the limiting factor in peripheral tumors. As a result, several reports have indicated that drug

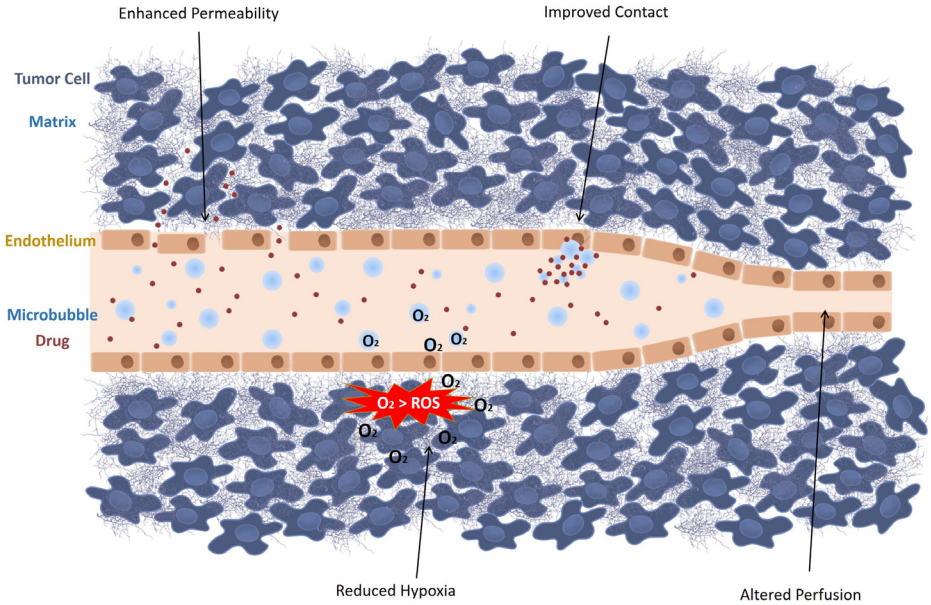

Figure 2.2 Ultrasound-activated microbubbles can locally alter the tumor microenvironment through four mechanisms: enhanced permeability, improved contact, reduced hypoxia, and altered perfusion.

penetration into the tumor remained limited after sonoporation, which may impede the eradication of the entire tumor tissue [75, 78, 197]. Alternatively, microbubble cavitation can affect tumor perfusion, as vasoconstriction and even temporary vascular shut-down have been reported *ex vivo* [198] and *in vivo* [199-201]. These effects were seen at higher ultrasound intensities (>1.5 MPa) and are believed to result from inertial cavitation leading to violent microbubble collapses. As blood supply is needed to maintain tumor growth, vascular disruption might form a different approach to cease tumor development. Microbubble-induced microvascular damage was able to complement the direct effects of chemotherapeutics and anti-vascular drugs by secondary ischemia-mediated cytotoxicity, which led to tumor growth inhibition [98, 202, 203]. In addition, a synergistic effect between radiation therapy and ultrasound-stimulated microbubble treatment was observed, as radiation therapy also induces secondary cell death by endothelial apoptosis and vascular damage [204, 205]. Nevertheless, several adverse effects have been reported due to excessive vascular disruption, including hemorrhage, tissue necrosis, and the formation of thrombi [75, 101, 199].

Furthermore, oxygen-containing microbubbles can provide a local oxygen supply to hypoxic areas, rendering oxygen-dependent treatments more effective. This is of interest for sonodynamic therapy, which is based on the production of cytotoxic reactive oxygen species (ROS) by a sonosensitizing agent upon activation by ultrasound in the presence of oxygen [86, 88, 102]. As ultrasound can be used to stimulate the release of oxygen from oxygen-carrying microbubbles while simultaneously activating a sonosensitizer, this approach has shown to be particularly useful for the treatment of hypoxic tumor types [86, 88]. Additionally, low oxygenation promotes resistance to radiotherapy, which can be circumvented by a momentary supply of oxygen. Based on this notion, oxygen-carrying microbubbles were used to improve the outcome of radiotherapy in a rat fibrosarcoma model [80].

Finally, ultrasound-activated microbubbles promote convection and induce acoustic radiation forces. As such, closer contact with the tumor endothelial and an extended contact time can be obtained [93]. Furthermore, these forces may counteract the elevated interstitial pressure present in tumors [78, 108, 206].

Apart from their ability to improve the tumor uptake, microbubbles can be used as ultrasound-responsive drug carriers to reduce the off-target effects of chemotherapeutics. By loading the drugs or drug-containing nanoparticles directly in or onto the microbubbles, a spatial and temporal control of drug release can be obtained, thereby reducing exposure to other parts of the body [101, 207]. Moreover, several studies have shown improved anti-cancer effects from treatment with drug-coupled microbubbles, compared to a co-administration approach [101,

208]. Additionally, tumor neovasculature expresses specific surface receptors that can be targeted by specific ligands. Adding such targeting moieties to the surface of (drug-loaded) microbubbles improves site-targeted delivery and has shown to potentiate this effect further [71, 84, 209].

Phase-shifting droplets and gas-stabilizing solid agents (e.g. nanocups) have the unique ability to benefit from both EPR-mediated accumulation in the 'leaky' parts of the tumor vasculature due to their small sizes, as well as from ultrasound-induced permeabilization of the tissue structure [112, 194, 210, 211]. Several research groups have reported tumor regression after treatment with acoustically-active droplets [111, 210, 212, 213] or gas-stabilizing solid particles [112, 214]. A different approach to the use of droplets for tumor treatment, is Acoustic Cluster Therapy (ACT), which is based on microbubble-droplet clusters that upon ultrasound exposure, undergo a phase shift to create large bubbles that can transiently block capillaries [215]. While the mechanism behind the technique is not yet fully understood, studies have shown improved delivery and efficacy of paclitaxel and Abraxane in xenograft prostate tumor models [105, 212]. Another use of droplets for tumor treatment is enhanced high-intensity focused ultrasound (HIFU)-mediated heating of tumors [216].

Although microbubble-based drug delivery to solid tumors shows great promise, it also faces important challenges. The ultrasound parameters used in *in vivo* studies highly vary between research groups and no consensus was found on the oscillation regime that is believed to be responsible for the observed effects [75, 101]. Moreover, longer ultrasound pulses and increased exposure times are usually applied in comparison to *in vitro* reports [53]. This could promote additional effects such as microbubble clustering and microbubble translation, which could cause local damage to the surrounding tissue as well [217]. To elucidate these effects further, fundamental *in vitro* research remains important. Therefore, novel *in vitro* models that more accurately mimic the complexity of the *in vivo* tumor environment are currently being explored. Park et al. [218] engineered a perfusable vessel-on-a-chip system and reported successful doxorubicin delivery to the endothelial cells lining this microvascular network. While such microfluidic chips could be extremely useful to study the interactions of microbubbles with the endothelial cell barrier, special care to the material of the chambers should be taken to avoid ultrasound reflections and standing waves [219]. Alternatively, 3D tumor spheroids have been used to study the effects of ultrasound and microbubble-assisted drug delivery on penetration and therapeutic effect in a multicellular tumor model [220]. Apart from expanding the knowledge on microbubble-tissue interactions in detailed parametric studies *in vitro*, it will be crucial to obtain improved control over the microbubble behavior *in vivo*, and link this to the therapeutic effects. To this end, passive cavitation detection (PCD) to monitor microbubble cavitation behavior in real-time is currently under

development, and could provide better insights in the future [103, 221, 222]. Efforts are being committed to constructing custom-built delivery systems, which can be equipped with multiple transducers allowing drug delivery guided by ultrasound imaging and/or PCD [103, 223-225].

Clinical studies

Pancreatic cancer

The safety and therapeutic potential of improved chemotherapeutic drug delivery using microbubbles and ultrasound was first investigated for the treatment of inoperable pancreatic ductal adenocarcinoma at Haukeland University Hospital, Norway [226, 227]. In this clinical trial, gemcitabine was administrated by intravenous injection over 30 min. During the last 10 min of chemotherapy, an abdominal echography was performed to locate the position of pancreatic tumor. At the end of chemotherapy, 0.5 mL of SonoVue microbubbles followed by 5 mL saline were intravenously injected every 3.5 min to ensure their presence throughout the whole sonoporation treatment. Pancreatic tumors were exposed to ultrasound (1.9 MHz, MI 0.2, 1% DC) using a 4C curvilinear probe (GE Healthcare) connected to an LOGIQ 9 clinical ultrasound scanner. The cumulative ultrasound exposure was only 18.9 s. All clinical data showed that microbubble-mediated gemcitabine delivery did not induce any serious adverse events in comparison to chemotherapy alone. At the same time, tumor size and development were characterized according to the Response Evaluation Criteria in Solid Tumors (RECIST) criteria. In addition, Eastern Cooperative Oncology Group (ECOG) performance status was used to monitor the therapeutic efficacy of the microbubble-mediated gemcitabine delivery. All ten patients tolerated an increased number of gemcitabine cycles compared to treatment with chemotherapy alone from historical controls (8.3 ± 6 *vs* 13.8 ± 5.6 cycles; $p < 0.008$), thus reflecting an improved physical state. After 12 treatment cycles, one patient's tumor showed a 2-fold decrease in tumor size. This patient was excluded from this clinical trial to be treated with radiotherapy and then with pancreatectomy. In five out of ten patients, the maximum tumor diameter was partially decreased from the first to last therapeutic treatment. Subsequently, a consolidative radiotherapy or a FOLFIRINOX treatment, a bolus and infusion of 5-fluorouracil, leucovorin, irinotecan, and oxaliplatin, was offered to them. The median survival was significantly increased from 8.9 months to 17.6 months ($p = 0.0001$). Altogether, these results show that the drug delivery using clinically-approved microbubbles, chemotherapeutics, and ultrasound is feasible and compatible with respect to clinical procedures. Nevertheless, the authors did not provide any evidence that the improved therapeutic efficacy of gemcitabine was related to an increase in intratumoral bioavailability of the drug. In addition, the effects of microbubble-

assisted ultrasound treatment alone on the tumor growth were not investigated while recent publications describe that according to the ultrasound parameters, such treatment could induce a significant decrease in tumor volume through a reduction in tumor perfusion as described above.

Hepatic metastases from digestive system

A safety study of chemotherapeutic delivery using microbubble-assisted ultrasound for the treatment of liver metastases from gastrointestinal tumors and pancreatic carcinoma was conducted at Beijing Cancer Hospital, China [228]. Thirty minutes after intravenous infusion of chemotherapy (for both monotherapy and combination therapy), 1 mL of SonoVue microbubbles was intravenously administrated which was repeated another five times in 20 min. An ultrasound probe (C1-5 abdominal convex probe; GE Healthcare, USA) was positioned on the tumor lesion which was exposed to ultrasound at different MIs (0.4 to 1) in contrast mode using a LogiQ E9 scanner (GE Healthcare, USA). The primary aims of this clinical trial were to evaluate the safety of this therapeutic procedure and to explore the largest MI and ultrasound treatment time which cancer patients can tolerate. According to the clinical safety evaluation, all twelve patients showed no serious adverse events. The authors reported that the microbubble mediated-chemotherapy led to fever in two patients. However, there is no clear evidence this related to the microbubble and ultrasound treatment. Indeed, in the absence of direct comparison of these results with a historical group of patients receiving the chemotherapy on its own, one cannot rule out a direct link between the fever and the chemotherapy alone. All the adverse side effects were resolved with symptomatic medication. In addition, the severity of side effects did not worsen with increases in MI, suggesting that microbubble-mediated chemotherapy is a safe procedure. The secondary aims were to assess the efficacy of this therapeutic protocol using contrast-enhanced CT and MRI. Thus, tumor size and development were characterized according to the RECIST criteria. Half of the patients had stable disease and one patient obtained a partial response after the first treatment cycle. The median progression-free survival was 91 days. However, making any comparison and interpretation of results is very difficult because none of the patients were treated with the same chemotherapeutics, MI, and/or number of treatment cycles. The results of safety and efficacy evaluations should be compared to patients receiving the chemotherapy on its own in order to clearly identify the therapeutic benefit of combining with ultrasound-driven microbubbles. Similar to the pancreatic clinical study, no direct evidence of enhanced therapeutic bioavailability of the chemotherapeutic drug after the treatment was provided. This investigation is all the more important as the ultrasound and microbubble treatment was applied 30 min after intravenous chemotherapy (for both monotherapy and combination therapy) independently of drug pharmacokinetics and metabolism.

Ongoing and upcoming clinical trials

Currently, two clinical trials are ongoing: (i) Prof. F. Kiessling (RWTH Aachen University, Germany) proposes to examine whether the exposure of early primary breast cancer to microbubble-assisted ultrasound during neoadjuvant chemotherapy results in increased tumor regression in comparison to ultrasound treatment alone (NCT03385200); (ii) Dr. J. Eisenbrey (Sidney Kimmel Cancer Center, Thomas Jefferson University, USA) is investigating the therapeutic potential of perflutren protein-type A microspheres in combination with microbubble-assisted ultrasound in radioembolization therapy of liver cancer (NCT03199274).

A proof of concept study (NCT03458975) has been set in Tours Hospital, France for treating non-resectable liver metastases. The aim of this trial is to perform a feasibility study with the development of a dedicated ultrasound imaging and delivery probe with a therapy protocol optimized for patients with hepatic metastases of colorectal cancer and who are eligible for monoclonal antibodies in combination with chemotherapy. A dedicated 1.5D ultrasound probe has been developed and interconnected to a modified Aixplorer imaging platform (Supersonic imagine, Aix-en-Provence, France). The primary objective of the study is to determine the rate of objective response at two months for lesions receiving optimized and targeted delivery of systemic chemotherapy combining bevacizumab and FOLFIRI compared with those treated with only systemic chemotherapy regimen. The secondary objective is to determine the safety and tolerability of this local approach of optimized intratumoral drug delivery during the three months of follow-up, by assessing tumor necrosis, tumor vascularity and pharmacokinetics of bevacizumab and by profiling cytokine expression spatially.

2.5 Immunotherapy

Cancer immunotherapy is considered to be one of the most promising strategies to eradicate cancer as it makes use of the patient's own immune system to selectively attack and destroy tumor cells. It is a common name that refers to a variety of strategies that aim to unleash the power of the immune system by either boosting antitumoral immune responses or flagging tumor cells to make them more visible to the immune system. The principle is based on the fact that tumors express specific tumor antigens which are not, or to a much lesser extent, expressed by normal somatic cells and hence can be used to initiate a cancer-specific immune response. In this section we aim to give insight into how microbubbles and ultrasound have been applied as useful tools to initiate or sustain different types of cancer immunotherapy as illustrated in Figure 2.3.

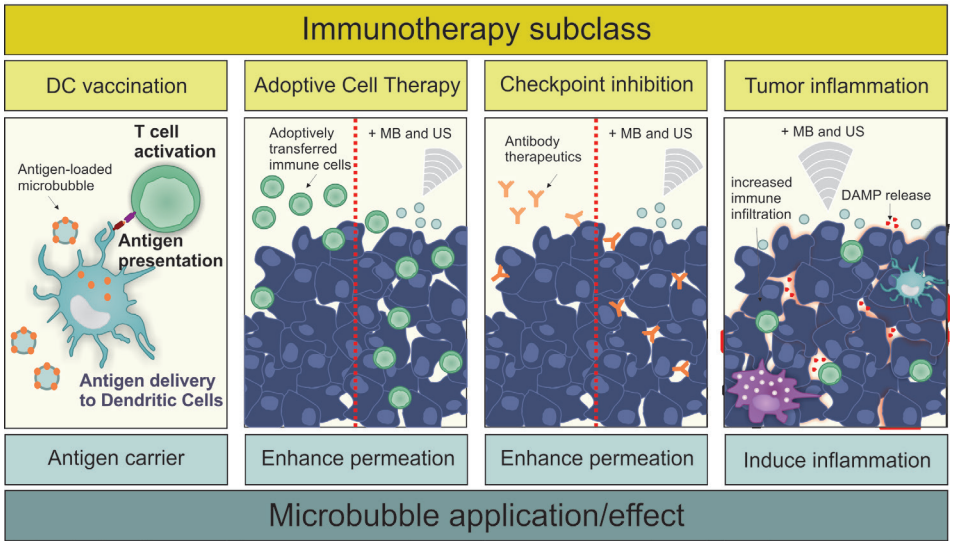

Figure 2.3 Schematic overview of how microbubbles and ultrasound have been shown to contribute to cancer immunotherapy. From left to right: microbubbles can be used as antigen carriers to stimulate antigen uptake by dendritic cells. Microbubbles and ultrasound can alter the permeability of tumors thereby increasing the intratumoral penetration of adoptively transferred immune cells or checkpoint inhibitors. Finally, exposing tissues to cavitating microbubbles can induce sterile inflammation by the local release of DAMPS.

When Ralph Steinman [229] discovered the dendritic cell (DC) in 1973, its central role in the initiation of immunity made it an attractive target to evoke specific antitumoral immune responses. Indeed, these cells very efficiently capture antigens and present them to T-lymphocytes in major histocompatibility complexes (MHCs), thereby bridging the innate and adaptive immune system. More specifically, exogenous antigens engulfed via the endolysosomal pathway are largely presented to $CD4^+$ T cells *via* MHC-II, whereas endogenous, cytoplasmic proteins are shuttled to MHC-I molecules for presentation to $CD8^+$ cells. As such, either $CD4^+$ helper T cells or $CD8^+$ cytotoxic T cell responses are induced. The understanding of this pivotal role played by DCs formed the basis for DC-based vaccination, where a patient's DCs are isolated, modified *ex vivo* to present tumor antigens and re-administered as a cellular vaccine. DC-based therapeutics, however, suffer from a number of challenges, of which the expensive and lengthy *ex vivo* procedure for antigen-loading and activation of DCs is the most prominent [230]. In this regard, microbubbles have been investigated for direct delivery of tumor antigens to immune cells *in vivo*. Bioley et al. [94] showed that intact microbubbles are rapidly phagocytosed by both murine and human DCs, resulting in rapid and efficient uptake of surface-coupled antigens without the use of ultrasound. Subcutaneous injection of microbubbles loaded with the model antigen ovalbumin (OVA) resulted in the activation of both $CD8^+$ and $CD4^+$ T cells. Effectively, these T-cell responses could partially protect vaccinated mice against

an OVA-expressing Listeria infection. Dewitte et al. [231] investigated a different approach, making use of messenger RNA (mRNA) loaded microbubbles combined with ultrasound to transfect DCs. As such, they were able to deliver mRNA encoding both tumor antigens as well as immunomodulating molecules directly to the cytoplasm of the DCs. As a result, preferential presentation of antigen fragments in MHC-I complexes was ensured, favoring the induction of $CD8^+$ cytotoxic T cells. In a therapeutic vaccination study in mice bearing OVA-expressing tumors, injection of mRNA-sonoporated DCs caused a pronounced slowdown of tumor growth and induced complete tumor regression in 30% of the vaccinated animals. Interestingly, in humans, intradermally injected microbubbles have been used as sentinel lymph node detectors as they can easily drain from peripheral sites to the afferent lymph nodes [232, 233]. Since lymph nodes are the primary sites of immune induction, the interaction of microbubbles with intranodal DCs, could be of high value. To this end, Dewitte et al. [82] showed that mRNA-loaded microbubbles were able to rapidly and efficiently migrate to the afferent lymph nodes after intradermal injection in healthy dogs. Unfortunately, further translation of this concept to an *in vivo* setting is not straightforward, as it prompts the use of less accessible large animal models (e.g., pigs, dogs). Indeed, conversely to what has been reported in humans, lymphatic drainage of subcutaneously injected microbubbles is very limited in the small animal models typically used in preclinical research (mice and rats), which is the result of substantial difference in lymphatic physiology.

Another strategy in cancer immunotherapy is adoptive cell therapy, where *ex vivo* manipulated immune effector cells, mainly T cells and NK (natural killer) cells, are employed to generate a robust and selective anticancer immune response [234, 235]. These strategies have mainly led to successes in hematological malignancies, not only because of the availability of selective target antigens, but also because of the accessibility of the malignant cells [235, 236]. By contrast, in solid tumors, and especially in brain cancers, inadequate homing of cytotoxic T cells or NK cells to the tumor proved to be one of the main reasons for the low success rates, making the degree of tumor infiltration an important factor in disease prognosis [235, 237, 238]. To address this, focused ultrasound and microbubbles have been used to make tumors more accessible to cellular therapies. The first demonstration of this concept was provided by Alkins et al. [239] who used a xenograft HER-2-expressing breast cancer brain metastasis model to determine whether ultrasound and microbubbles could allow intravenously infused NK cells to cross the blood-brain barrier (BBB). By loading the NK cells with superparamagnetic iron oxide (SPIO) nanoparticles, the accumulation of NK cells in the brain could be tracked and quantified via MRI. An enhanced accumulation of NK cells was found when the cells were injected immediately prior to BBB disruption. Importantly NK cells retained

their activity and ultrasound treatment resulted in a sufficient NK to tumor cell ratio to allow effective tumor cell killing [240]. In contrast, very few NK cells reached the tumor site when BBB disruption was absent or performed before NK cell infusion. Although it is not known for certain why timing had such a significant impact on NK extravasation, it is likely that the most effective transfer to the tissue occurs at the time of insonification, and that the barrier is most open during this time [241]. Possible other explanations include the difference in size of the temporal BBB openings or a possible alternation in the expression of specific leukocyte adhesion molecules by the BBB disruption, thus facilitating the translocation of NK cells. Also for tumors where BBB crossing is not an issue, ultrasound has been used to improve delivery of cellular therapeutics. Sta Maria et al. [242] demonstrated enhanced tumor infiltration of adoptively transferred NK cells after treatment with microbubbles and low dose focused ultrasound. This result was confirmed by Yang et al. [243] in a more recent publication where the homing of NK cells was more than doubled after microbubble injection and ultrasound treatment of an ovarian tumor. Despite the enhanced accumulation, however, the authors did not observe an improved therapeutic effect, which might be due to the limited number of treatments that were applied, or the immunosuppressive tumor microenvironment that counteracts the cytotoxic action of the NK cells.

There is growing interest in exploring the effect of microbubbles and ultrasound on the tumor microenvironment, as recent work has shown that BBB disruption with microbubbles and ultrasound may induce sterile inflammation. Although a strong inflammatory response may be detrimental in the case of drug delivery across the BBB, it might be interesting to further study this inflammatory response in solid tumors as it might induce the release of damage-associated molecular patterns (DAMPS) such as heat-shock proteins and inflammatory cytokines. This could shift the balance towards a more inflammatory microenvironment that could promote immunotherapeutic approaches. As reported by Liu et al. [244] exposure of a CT26 colon carcinoma xenograft to microbubbles and low pressure pulsed ultrasound increased cytokine release and triggered lymphocyte infiltration. Similar data have been reported by Hunt et al. [245]. In their study, ultrasound treatment caused a complete shut-down of tumor vasculature followed by the expression of HIF-1α (hypoxia-inducible factor 1α), a marker of tumor ischemia and tumor necrosis, as well as increased infiltration of T cells. Similar responses have been reported following thermal and mechanical HIFU treatments of solid tumors [246, 247]. A detailed review of ablative ultrasound therapies is however out of the scope of this review.

At present, the most successful form of immunotherapy is the administration of monoclonal antibodies to inhibit regulatory immune checkpoints that block T cell action. Examples are CTLA-4 (cytotoxic T lymphocyte-associated protein-4) and PD-1 (programmed cell death-1), which act as brakes on the immune system. Blocking the effect of these brakes can revive and support the function of immune effector cells. Despite the numerous successes achieved with checkpoint inhibitors, responses have been quite heterogeneous as the success of checkpoint inhibition therapy largely depends on the presence of intratumoral effector T cells [248]. This motivated Bulner et al. [249] to explore the synergy of microbubble and ultrasound treatment with PD-L1 checkpoint inhibition therapy in mice. Tumors in the treatment group that received the combination of microbubble and ultrasound treatment with checkpoint inhibition were significantly smaller than tumors in the monotherapy groups. One mouse showed complete tumor regression and remained tumor free upon rechallenge, indicative of an adaptive immune response.

Overall, the number of studies that investigate the impact of microbubble and ultrasound treatment on immunotherapy is limited, making this a rather unexplored research area. It is obvious that more in-depth research is warranted to improve our understanding on how (various types of) immunotherapy might benefit from (various types of) ultrasound treatment.

2.6 BBB and Blood Spinal Cord Barrier opening

The barriers of the central nervous system (CNS), the BBB and Blood-Spinal Cord Barrier (BSCB), greatly limit drug-based treatment of CNS disorders. These barriers help to regulate the specialized CNS environment by limiting the passage of most therapeutically relevant molecules [250]. Although several methods have been proposed to circumvent the BBB and BSCB, including chemical disruption and the development of molecules engineered to capitalize on receptor-mediated transport (so-called Trojan Horse molecules), the use of ultrasound in combination with microbubbles [54] or droplets [113] to transiently modulate these barriers has come to the forefront in recent years due to the targeted nature of this approach and its ability to facilitate delivery of a wide range of currently available therapeutics. First demonstrated in 2001 [54], ultrasound-mediated BBB opening has been the topic of several hundred original research articles in the last two decades, and in recent years has made headlines for ground-breaking clinical trials targeting brain tumors and Alzheimer's disease as described below in the clinical studies section.

Mechanisms, bioeffects, and safety

Ultrasound in combination with microbubbles can produce permeability changes in the BBB via both enhanced paracellular and transcellular transport [251, 252]. Reduction and reorganization of tight junction proteins [253] and upregulation of active transport protein Caveolin-1 [254] have been reported. Although the exact physical mechanisms driving these changes are not known, there are several factors that are hypothesized to contribute to these effects, including direct tensile stresses due to the expansion and contraction of the bubbles in the lumen, as well as shear stresses at the vessel wall arising from acoustic microstreaming. Recent studies have also investigated the suppression of efflux transporters following ultrasound exposure with microbubbles. A reduction in P-glycoprotein expression [158, 159] and BBB transporter gene expression [160] has been observed by multiple groups. One study showed that P-glycoprotein expression was suppressed for over 48 h following treatment with ultrasound and microbubbles [159]. However, the degree of inhibition of efflux transporters as a result of ultrasound with microbubbles may be insufficient to prevent efflux of some therapeutics [72], and thus this mechanism requires further study.

Many studies have documented enhanced CNS tumor response following ultrasound and microbubble-mediated delivery of drugs across the Blood-Tumor-Barrier in rodent models. Improved survival has been shown in both primary [255, 256] and metastatic tumor models [240, 257].

Beyond simply enhancing drug accumulation in the CNS, several positive bioeffects of ultrasound and microbubble induced BBB opening have been reported. In rodent models of Alzheimer's disease, numerous positive effects have been discovered in the absence of exogenous therapeutics. These effects include a reduction in amyloid-β plaque load [258-261], reduction in tau pathology [81], and improvements in spatial memory [259, 260]. Two-photon microscopy has shown that amyloid-β plaque size is reduced in transgenic mice for up to two weeks post ultrasound and microbubble treatment [261]. Opening of the BBB in both transgenic and wild-type mice has also revealed enhanced neurogenesis [259, 262, 263] in the treated tissue.

Gene delivery to the CNS using ultrasound and microbubbles is another area that is increasingly being investigated. Viral [264, 265] and non-viral [266] delivery methods have been investigated. While early studies demonstrated the feasibility of gene delivery using reporter genes (for example Thevenot et al. [267], Alonso et al. [265]), there have been promising results delivering therapeutic genes. In particular, advances have been made in Parkinson's disease models, where therapeutic genes have been tested [268, 269], and where long lasting functional improvements have

been reported in response to therapy [268]. It is expected that research into this highly promising technique will expand to a range of therapeutic applications.

Despite excellent safety profiles in non-human primate studies investigating repeat opening of the BBB [270, 271], there has been recent controversy due to reports of a sterile inflammatory response observed in rats [60, 272, 273]. The inflammatory response is proportional to the magnitude of BBB opening and is therefore strongly influenced by experimental conditions such as microbubble dose and acoustic settings. However, McMahon and Hynynen [61] showed that when clinical microbubble doses are used, and treatment exposures are actively controlled to avoid over treating, the inflammatory response is acute and mild. They note that while chronic inflammation is undesirable, acute inflammation may actually contribute to some of the positive bioeffects that have been observed. For example, the clearance of amyloid-β following ultrasound and microbubble treatment is thought to be mediated in part by microglial activation [258]. These findings reiterate the need for carefully controlled treatment exposures to select for desired bioeffects.

Cavitation monitoring and control

It is generally accepted that the behavior of the microbubbles in the ultrasound field is predictive, to an extent, of the observed bioeffects. In the seminal study on the association between cavitation and BBB opening, McDannold et al. [274] observed an increase in second harmonic emissions in cases of successful opening, compared to exposures that lead to no observable changes in permeability as measured by contrast enhanced MRI. Further, they noted that successful opening could be achieved in the absence of inertial cavitation, which was also reported by another group [275]. These general guidelines have been central to the development of active treatment control schemes that have been developed to date—all with the common goal of promoting stable bubble oscillations, while avoiding violent bubble collapse that can lead to tissue damage. These methods are based either on detection of sub or ultraharmonic [276-278], harmonic bubble emissions [279, 280] or a combination thereof [281]. An approach based on the sub- or ultraharmonic controller developed by O'Reilly and Hynynen [276] has been employed in early clinical testing [282, 283].

Control methods presented to date have generally been developed using single receiver elements, which simplifies data processing but does not allow signals to be localized. Focused receivers are spatially selective but can miss off-target events, while planar receivers may generate false positives based on signals originating outside the treatment volume. The solution to this is to use an array of receivers

and passive beamforming methods, combined with phase correction methods to compensate for the skull bone [284, 285] to generate maps of bubble activity. In the brain this has been achieved with linear arrays [286, 287], which suffer from poor axial resolution when using passive imaging methods, as well as large-scale sparse hemispherical or large aperture receiver arrays [288-292] that optimize spatial resolution for a given frequency. Recently, this has extended beyond just imaging the bubble activity to incorporate real-time, active feedback control based on both the spectral and spatial information obtained from the bubble maps [289] (Figure 2.4). Robust control methods building on these works will be essential for widespread adoption of this technology to ensure safe and consistent treatments.

BSCB opening

Despite the similarities between the BBB and BSCB, and the great potential benefit for patients, there has been limited work investigating translation of this technology to the spinal cord. Opening of the BSCB in rats was first reported by Wachsmuth et al. [293], and was followed by studies from Weber-Adrien et al. [294], Payne et al. [109], and O'Reilly et al. [295] in rats (Figure 2.5) and from Montero et al. [296] in rabbits, the latter performed through a laminectomy window. In 2018, O'Reilly et al. [295] presented the first evidence of a therapeutic benefit in a disease model, showing improved tumor control in a rat model of leptomeningeal metastases.

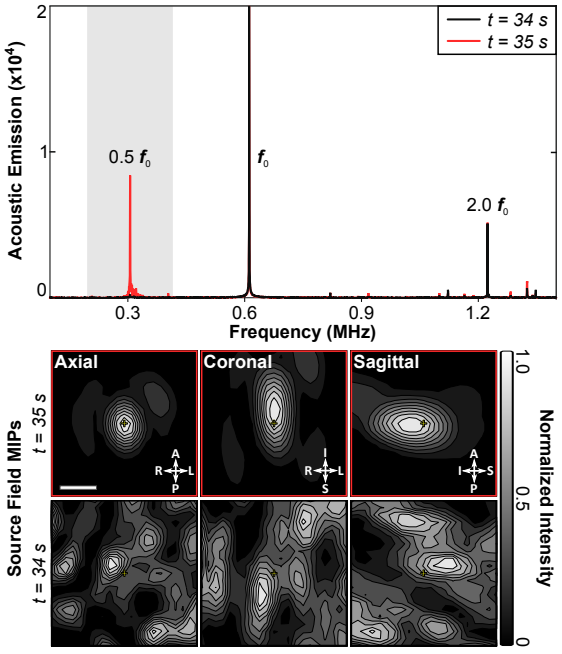

Figure 2.4 3D transcranial subharmonic microbubble imaging and treatment control *in vivo* in rabbit brain during BBB opening. Spectral information (top) shows the appearance of subharmonic activity at t = 35 s into the treatment. Passive mapping of the subharmonic band localizes this activity to the target region. Scale bar indicates 2.5 mm (reprinted (adapted) with permission from Jones et al. [289]).

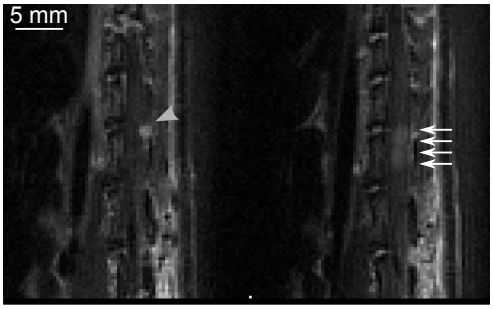

Figure 2.5 T1 weighted sagittal MR images showing leptomeningeal tumors in rat spinal cord (grey arrowheads) before ultrasound and microbubble treatment (left column), and the enhancement of the cord indicating BSCB opening (white arrows) post-ultrasound and microbubble treatment (right column) (reprinted (adapted) with permission from O'Reilly et al. [295]).

Although promising, there remains significant work to be done to advance BSCB opening to clinical studies. A more thorough characterization of the bioeffects in the spinal cord and how, if at all, they differ from the brain is necessary to ensure safe translation. Additionally, methods and devices capable of delivering controlled therapy to the spinal cord at clinical scale are needed. While laminectomy and implantation of an ultrasound device [296] might be an appropriate approach for some focal indications, treating multifocal or diffuse disease will require the ultrasound to be delivered through the intact bone to the narrow spinal canal. Fletcher and O'Reilly [297] have presented a method to suppress standing waves in the human vertebral canal. Combined with devices suited to the spinal geometry, such as that presented by Xu and O'Reilly [298], these methods will help to advance clinical translation.

Clinical studies

The feasibility of enhancing BBB permeability in and around brain tumors using ultrasound and microbubbles has now been demonstrated in two clinical trials. In the study conducted at Assistance Publique–Hôpitaux de Paris in Paris, France, an unfocused 1 MHz ultrasound transducer (SonoCloud) was surgically placed over the tumor-resection area and permanently fixed into the hole in the skull bone. The skin was placed over the transducer and after healing, treatments were conducted by inserting a needle probe through the skin to provide the driving signal to the transducer. Monthly treatments were then conducted while infusing a chemotherapeutic agent into the blood stream (carboplatin). The sonication was executed during infusion of SonoVue microbubbles. A constant pulsed sonication was applied during each treatment followed by a contrast enhanced MRI to estimate BBB permeability. The power was escalated for each monthly treatment until enhancement was detected in MRI. This study demonstrated feasibility and safety [299] and a follow up study may indicate increase in survival [300].

The second brain tumor study was conducted at Sunnybrook Health Sciences Centre in Toronto, Canada, which used the InSightec Exablate 220 kHz device and through-skull MRI–guided sonications of brain tumors prior to the surgical resection. It also showed the feasibility of inducing highly localized BBB permeability enhancement, safety, and that chemotherapeutic concentration in the sonicated peritumor tissue was higher than in the unsonicated tissue [282].

Another study conducted in Alzheimer's disease patients with the Exablate device demonstrated safe BBB permeability enhancement and that the treatment could be repeated one month later without any imaging or behavior indications of adverse events [283]. A third study with the same device investigated the feasibility of using functional MRI to target motor cortex in Amyotrophic Lateral Sclerosis (ALS) patients again showing precisely targeted BBB permeability enhancement without adverse effects in this delicate structure [301]. All of these studies were conducted using Definity microbubbles. These studies have led to the current ongoing brain tumor trial with six monthly treatments of the brain tissue surrounding the resection cavity during the maintenance phase of the treatment with temozolomide. This study sponsored by InSightec is being conducted in multiple institutions. Similarly, a phase II trial in Alzheimer's disease sonicating the hippocampus with the goal of investigating the safety and potential benefits from repeated (three treatments with two-week interval) BBB permeability enhancement alone is ongoing. This study is also being conducted in several institutions that have the device.

2.7 Sonothrombolysis

Occlusion of blood flow through diseased vasculature is caused by thrombi, blood clots which form in the body. Due to limitations in thrombolytic efficacy and speed, sonothrombolysis, ultrasound which accelerates thrombus breakdown alone, or in combination with thrombolytic drugs and/or cavitation nuclei, has been under extensive investigation in the last two decades [302]. Sonothrombolysis promotes thrombus dissolution for the treatment of stroke [303-306], myocardial infarction [307-309], acute peripheral arterial occlusion [310], deep vein thrombosis [311], and pulmonary embolism [312-314].

Mechanisms, agents, and approaches

Ultrasound improves recombinant tissue plasminogen activator (rt-PA) diffusion into thrombi and augments lysis primarily via acoustic radiation force and streaming [315-317]. Additionally, ultrasound increases rt-PA and plasminogen penetration into the thrombus surface and enhances removal of fibrin degradation products via ultrasonic bubble activity, or acoustic cavitation, that induces microstreaming [67,

315, 318]. Two types of cavitation are correlated with enhanced thrombolysis: stable cavitation, with highly nonlinear bubble motion resulting in acoustic emissions at the subharmonic and ultraharmonics of the fundamental frequency [319-321], and inertial cavitation, with substantial radial bubble growth and rapid collapse generating broadband acoustic emissions [322, 323].

Specialized contrast agents and tailored ultrasound schemes have been investigated with the aim of optimizing sonothrombolysis. Petit et al. [317] observed a greater degree of rt-PA lysis with BR38 microbubbles exposed to 1 MHz pulsed ultrasound at an amplitude causing inertial cavitation (1.3 MPa peak rarefactional pressure) than at a lower amplitude causing stable cavitation (0.35 MPa peak rarefactional pressure). Goyal et al. [96] also measured a higher degree of thrombolysis with 1 MHz pulsed ultrasound at 1.0 MPa peak rarefactional pressure with inertial cavitation than at 0.23 MPa peak rarefactional pressure with stable cavitation in an *in vitro* model of microvascular obstruction using perfluorobutane-filled, lipid shelled microbubbles [324] as a nucleation agent. However, Kleven et al. [325] observed more than 60% fractional clot width loss for highly retracted human whole blood clots exposed to rt-PA, Definity and 220 kHz pulsed or continuous wave (CW) ultrasound at an acoustic output with sustained stable cavitation throughout the insonification periods (0.22 MPa peak rarefactional pressure) (Figure 2.6).

Echogenic liposomes loaded with rt-PA enhanced lysis compared to rt-PA alone at concentrations of 1.58 and 3.15 mg/mL [104], suggesting that encapsulation of rt-PA could reduce the rt-PA dose by a factor of two with equivalent lytic activity. Subsequently it has been demonstrated that these liposomes protect rt-PA

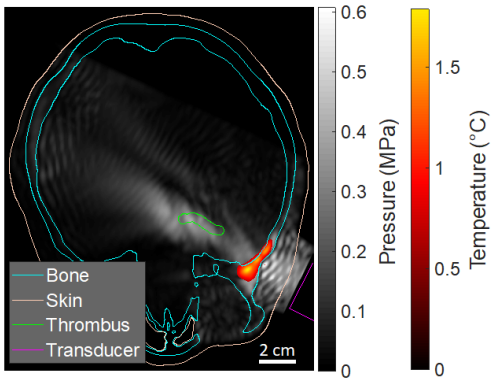

Figure 2.6 Simulated acoustic pressure and temperature in a representative subject exposed to pulsed 220 kHz ultrasound with a 33.3% duty cycle. The absolute peak-to-peak pressure maximum for the simulations is displayed in gray scale. Temperature is displayed using a heat map with a minimum color priority write threshold of 1 °C. Computed tomography features such as bone (cyan), skin and internal epithelium (beige), and clot (green), are plotted using contour lines. The transducer is outlined in magenta. Constructive interference is prominent in the soft tissue between the temporal bone and the transducer. Some constructive interference is also present in the brain tissue close to the contralateral temporal bone, however, the pressure in this region did not exceed the pressure in the M1 section of the middle cerebral artery. Temperature rise was prominent in the ipsilateral bone along the transducer axis. Computational model is described in Kleven et al. [325].

against degradation by plasminogen activator inhibitor-1 (PAI-1), while achieving equivalent thrombolytic efficacy relative to rt-PA, Definity, and intermittent 220 kHz CW ultrasound [326]. Promising agents, including a nanoscale (< 100 nm) contrast agent [327] and magnetically targeted microbubbles [328], have also demonstrated enhanced rt-PA thrombolysis *in vitro*. All of these investigators noted that in the absence of rt-PA, the combination of ultrasound and microbubbles did not degrade the fibrin network.

Several minimally invasive techniques have also been explored, with or without the inclusion of rt-PA or exogenous cavitation nuclei. In the clinical management of stroke, rapid treatments are needed because of the neurologist's adage "time is brain". Thus, treatment options that promote fast clot removal, reduce edema and intracerebral bleeding, and improve patient outcomes are of immense value. Magnetic resonance image-guided high intensity focused ultrasound has been investigated for the treatment of both ischemic [329] and hemorrhagic [330] stroke, and Zafar et al. [331] have provided an excellent review of the literature for this approach. Histotripsy, a form of high intensity focused ultrasound that relies on the mechanical action of microbubble clouds to ablate thrombi with and without rt-PA [122, 332-334] is under development to treat deep vein thrombosis. Additionally, ultrasound-accelerated catheter-directed thrombolysis using the EKOS system (EKOS/BTG, Bothell, WA, USA) combines 2 MHz low-intensity pulsed ultrasound and rt-PA without cavitation nuclei to improve lytic efficiency to treat deep vein thrombosis [311] and pulmonary embolism [335].

Cavitation monitoring

Acoustic cavitation has been shown to mediate direct fibrinolysis [336] and accelerated rt-PA lysis [315, 316, 337, 338]. Passive and active cavitation detection techniques have been developed to monitor acoustic cavitation [122, 339, 340]. Passive cavitation imaging, or passive acoustic mapping, employs a transducer array that listens passively (*i.e.*, no transmit) to emissions from acoustically activated microbubbles [222, 341, 342]. Vignon et al. [343] developed a prototype array enabling spectral analysis of bubble activity for sonothrombolysis applications. Superharmonic Doppler effects have also been utilized to monitor bubble activity from 500 kHz pulsed therapeutic ultrasound [344]. Both a linear array [286, 345, 346] and a sparse hemispherical array [347] have been integrated into a clinical magnetic resonance image-guided high intensity focused ultrasound system to assess microbubble dynamics during sonothrombolysis in the brain.

Preclinical studies

Information gathered from animal studies can help inform human clinical trials, despite a strong species dependence of clot rt-PA lytic susceptibility [348-350]. A comprehensive systematic evaluation of 16 *in vivo* preclinical sonothrombolysis studies was carried out by Auboire et al. [351] summarizing treatment efficacy and safety outcomes in models of ischemic stroke. Since that review was published, the efficacy of sonothrombolysis using nitrogen microbubbles stabilized with a non-crosslinked shell delivered intra-arterially through a catheter and rt-PA delivered intravenously has been demonstrated in a rat model of ischemic stroke [79].

Clinical studies

A rich literature exists of clinical trials exploring the safety and efficacy of sonothrombolysis. Two recent meta-analyses of seven randomized controlled trials [306, 331] attempt to determine whether the administration of rt-PA and ultrasound improve outcomes in acute ischemic stroke. Both analyses conclude that sonothrombolysis significantly enhances complete or partial recanalization, with improved neurologic function (assessed via the National Institutes of Health Stroke Scale, NIHSS). An ongoing clinical trial (TRUST; NCT03519737) will determine whether large vessel occlusions can be recanalized with sonothrombolysis (Cerevast Medical, Inc., Bothell, WA, USA) and rt-PA, tenecteplase or alteplase, [352] while patients are transferred to a stroke center for mechanical thrombectomy [353].

Several clinical trials have shown that high MI pulsed diagnostic ultrasound exposure of Definity before and after percutaneous coronary intervention for ST elevation myocardial infarction can prevent microvascular obstruction and improve functional outcomes [307-309]. A systematic review of 16 catheter-directed sonothrombolysis clinical trials comprised mostly of retrospective case series using the EKOS system without microbubble infusions determined that this treatment modality is safe and promising for the treatment of deep vein thrombosis, DVT [311]. However, a large-sample randomized prospective clinical trial is needed to improve the clinical evidence for use as a front-line therapy for DVT. In retrospective studies in patients with pulmonary embolism Lee et al. [314] conclude that catheter directed sonothrombolysis is safe and decreases right-sided heart strain, but Schissler et al. [354] conclude that this therapy is not associated with a reduction in mortality nor increased resolution of right ventricular dysfunction. And finally, an ongoing trial in a small cohort of 20 patients with acute peripheral arterial occlusions [310] will determine whether Luminity (marketed in the US as Definity) and 1.8 MHz

transdermal diagnostic ultrasound with intermittent high MI (1.08) and low MI (0.11) for visualization of the microbubbles and flow will improve recanalization. In summary, sonothrombolysis has demonstrated clinical benefit in the treatment of acute and chronic thrombotic disease. Ultrasound-assisted thrombolysis has a potential role as an emerging viable and therapeutic option for future management of stroke and cardiovascular disease.

2.8 Cardiovascular drug delivery and therapy

In cardiovascular drug delivery, cavitation nuclei are co-administered or loaded with different therapeutics for the treatment of various diseases. For atherosclerosis treatment in an ApoE-deficient mouse model, intercellular adhesion molecule-1 targeted microbubbles carrying angiogenesis inhibitor Endostar were used [355]. Upon intermittent insonification over the abdominal and thoracic cavity with 1 MHz ultrasound (2 W/cm^2 intensity, 50% duty cycle) for 30 s with two repeats and another treatment 48 h later, plaque area and intraplaque neovascularization were significantly reduced two weeks after treatment. Percutaneous coronary intervention is often used to restore blood flow in atherosclerotic arteries. The treatment of coronary microembolization, a complication of percutaneous coronary intervention, was demonstrated in pigs treated with ultrasound (1 MHz, 2.0 W/cm^2 intensity, 10 s on and 10 s off, 20 min duration) and microRNA-21-loaded microbubbles four days before coronary microembolization [356]. This resulted in an improved cardiac dysfunction. Although not a therapeutic study, Liu et al. [357] did show that plasmid transfection to the myocardium was significantly larger when the microbubbles were administered into the coronary artery compared to intravenously via the ear vein in pigs even though the intracoronary microbubble dose was half of the intravenous dose (1 MHz ultrasound, 2 W/cm^2, 50% duty cycle, 20 min duration). Percutaneous coronary intervention can also result in neointimal formation which induces restenosis. Sirolimus-loaded microbubbles were shown to reduce neointimal formation in coronary arteries by 50% in pigs, see Figure 2.7, 28 days after angioplasty in combination with a mechanically rotating intravascular ultrasound catheter (5 MHz, 500 cycles, 50% duty cycle, 0.6 MPa peak negative pressure) [358]. Another research group showed that paclitaxel-loaded microbubbles and ultrasound (1 MHz, 1.5 MPa for 10 s) can also significantly inhibit neointimal formation in the iliac artery in rabbits one week after percutaneous coronary intervention [359].

In diabetic cardiomyopathy, microbubble-mediated delivery of fibroblast growth factor has shown therapeutic effects. Zhao et al [360] could prevent diabetic cardiomyopathy in rats by treating the heart with ultrasound (14 MHz, 7.1 MPa for 10 s, three repeats with off interval of 1 s) and microbubbles co-administered with

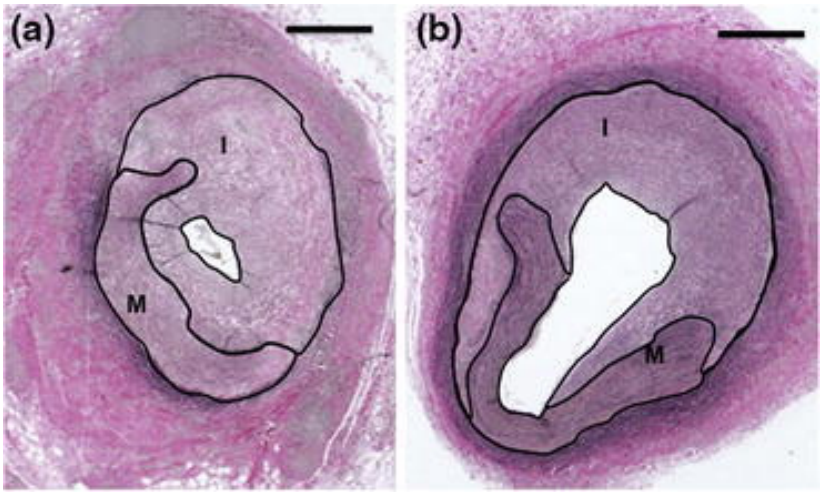

Figure 2.7 Histological sections of a coronary artery of a pig 28 days after angioplasty. Pigs were treated with sirolimus-loaded microbubbles only (**a**) or sirolimus-loaded microbubbles and ultrasound (**b**) using a mechanically rotating intravascular ultrasound catheter (5 MHz, 500 cycles, 50% duty cycle, 0.6 MPa peak negative pressure). Treatment with ultrasound and sirolimus-loaded microbubbles reduced neointimal formation by 50%. In both sections the intima (I) and media (M) are outlined; scale bar is 500 µm (Reprinted by permission from Springer Nature: Springer, Annals of Biomedical Engineering, Reducing Neointima Formation in a Swine Model with IVUS and Sirolimus Microbubbles, Kilroy JP, Dhanaliwala AH, Klibanov AL, Bowles DK, Wamhoff BR, Hossack JA, COPYRIGHT [358]).

acidic fibroblast growth factor nanoparticles twice weekly for 12 consecutive weeks. In already established diabetic cardiomyopathy in rats, the same investigators co-administered basic fibroblast growth factor-containing nanoparticles with microbubbles with the same ultrasound treatment, albeit that it was given three times with one day in between treatments. At four weeks after treatment, this resulted in restored cardiac functions as a result of structural remodeling of the cardiac tissue [361]. Microbubbles loaded with acidic fibroblast growth factor in combination with ultrasound (14 MHz, 7.1 MPa for 10 s, three repeats with off interval of 1 s) also showed significantly improved cardiac function in a rat model of diabetic cardiomyopathy. Treatment was performed twice weekly for 12 consecutive weeks [362]. For doxorubicin induced cardiomyopathy, repeated co-administration of microbubbles and nanoparticles containing acidic fibroblast growth factor in combination with ultrasound (14 MHz, 7.1 MPa for 10 s, three repeats with off interval of 1 s) applied at the heart successfully prevented doxorubicin induced cardiomyopathy in rats [363]. Once doxorubicin induced cardiomyopathy had occurred, microbubble-mediated reversal of cardiomyopathy was shown by the delivery of survivin plasmid to cardiomyocytes and endothelial cells [364] or glucagon-like peptide-1 (GLP-1) to cardiomyocytes, endothelial cells, vascular muscle cells, and mesenchymal cells [365] in rats. The ultrasound settings were 5 MHz (120 V power, pulsing interval

of 10 cardiac cycles at end-systole) for a 5 min treatment [364] or not specified [365]. The microbubble-mediated gene therapy study by Chen et al. [91] showed that ANGPTL8 gene therapy does not need to be done in the heart to reverse doxorubicin induced cardiomyopathy in rats as their microbubble and ultrasound (1.3 MHz, 1.4 MPa peak negative pressure, four bursts triggered to every fourth end-systole using a delay of 45-70 ms of the peak of the R wave) therapy was done in the liver (90 s treatment). This resulted in overexpression of ANGPTL8 in liver cells and blood which stimulated cardiac progenitor cells in the epicardium.

A few dozen articles have been published on treating myocardial infarction with microbubble and ultrasound-mediated gene delivery *in vivo*, in mouse, rat, rabbit, and dog models. These are reviewed by Qian et al. [366]. Amongst these are a few targeted microbubble studies which all show that the targeted microbubbles induced higher degrees of gene transfection, increased myocardial vascular density, and improved cardiac function in comparison to non-targeted microbubbles. This improvement occurred independent of the type of ligand on the microbubble, the gene that was transfected, or the animal model: matrix metalloproteinase 2 target with Timp3 gene in rats [367], intracellular adhesion molecule-1 target with Ang-1 gene in rabbits [368], P-selectin target with hVEGF165 gene in rats [369]. Ultrasound settings for these studies were similar at 1.6 MHz (1.6 MPa peak negative pressure, pulsing interval of four cardiac cycles) for 20 min during infusion of the plasmid-loaded microbubbles (both Yan et al. [367] and Shentu et al. [369]), or 1.7 MHz (1.7 MPa peak negative pressure, pulsing interval every four to eight cardiac cycles) for 5 min after bolus injection of the plasmid-loaded microbubbles [368].

Other gene therapy studies for vascular disease include stimulating angiogenesis for the treatment of chronic hindlimb ischemia in rats using miR-126-3p-loaded microbubbles and ultrasound (1.3 MHz, 2.1 MPa peak negative acoustic pressure, pulsing interval 5 s). The treatment lasted for 20 min of which microbubbles were infused for 10 min and resulted in improved perfusion, vessel density, arteriolar formation, and neovessel maturation [106]. Recently, successful gene therapy was demonstrated in baboons where Vascular Endothelial Growth Factor (VEGF)-plasmid loaded microbubbles were infused and ultrasound (2-6 MHz, MI 1.9, repeated 5 s burst pulses with three bursts per minute) was applied for 10 min on days 25, 35, 45, and 55 of gestation with the transducer placed over the placental basal plate [370]. This was a mechanistic study elucidating the role of VEGF in uterine artery remodeling.

The gas core of the cavitation nuclei can also be the therapeutic. Sutton et al. [85] have shown that ultrasound-mediated (1 MHz, 0.34 MPa acoustic pressure, 30 cycle pulse, 50 s treatment) nitric oxide gas delivery from echogenic liposomes

to *ex vivo* perfused porcine carotid arteries induces potent vasorelaxation. The vasodialative effect of nitric oxide-loaded echogenic liposomes upon insonification (5.7 MHz, 0.36 MPa peak negative pressure, 30 s treatment) was also shown in ex vivo perfused rabbit carotid arteries with arterial wall penetration of nitric oxide confirmed by fluorescence microscopy [89]. In addition to this, vasodialative effects were demonstrated in carotid arteries *in vivo* in rats with vasospasms following subarachnoid hemorrhage using 1 MHz ultrasound with 0.3 MPa peak-to-peak pressure, 50% duty cycle for a duration of 40 min with constant infusion of the echogenic liposomes. This resulted in improved neurological function (limb placement, beam and grid walking) [89]. Ultrasound-activation of the antioxidant hydrogen gas encapsulated in microbubbles was shown to prevent myocardial ischemia-reperfusion injury in rats when administered before reperfusion [90]. There was a dose-dependent effect as 2×10^{10} microbubbles resulted in a more significant reduction in infarct size (70%) than 4×10^{9} microbubbles (39%) compared to vehicle-treated rats. Furthermore, treatment with the high dose hydrogen-microbubbles prevented changes in left ventricular end-diastolic and left ventricular end-systolic dimension as well as minimal reductions in ejection fraction and fractional shortening. Histological and ELISA analysis showed a reduced degree of myocardial necrosis, apoptosis, hemorrhaging, inflammation, and oxidant damage. At the same time that cardiovascular drug delivery and therapy using microbubbles and ultrasound is moving forward to large animal and clinical studies, sophisticated *in vitro* models are being used and/or developed for mechanistic studies, such as flow chambers (μSlides, Ibidi) [371] and perfused 3D microvascular networks [372] in which human umbilical vein endothelial cells are grown.

Clinical study

Microbubbles and ultrasound were clinically investigated to augment muscle blood flow in 12 patients with stable sickle cell disease in the absence of a drug at the Oregon Health & Science University, Portland, Oregon, USA [97]. Perfusion increased ~2-fold in the forearm flexor muscles upon Definity infusion and insonification at 1.3 MHz (MI 1.3). Ultrasound was applied 3 times for 3 min with ~5 min intervals. The change in perfusion was determined from contrast enhanced ultrasound imaging and extended well beyond the region where ultrasound was applied. This study showed that the therapeutic ultrasound settings directly translate from mouse to man for superficial muscles, as the same investigators demonstrated augmented blood flow in ischemic and non-ischemic hindlimb muscles in mice in the same study and an earlier publication [99]. However, for the preclinical studies custom-made microbubbles were used instead of Definity.

2.9 Sonobactericide

Sonobactericide has been defined as the use of ultrasound in the presence of cavitation nuclei for the enhancement of bactericidal action [8]. This topic has recently gained attention with 17 papers being published in the last five years. Research on ultrasound-mediated enhancement of antimicrobials has focused on several sources of infections including general medical devices [73, 92, 95, 373, 374], acne [375], chronic bacterial prostatitis [376], infective endocarditis [8], pneumonia [377], prosthetic joint infections [114, 171, 172, 378], or urinary tract infections [83]. However, there was no specific disease aim in two studies [379, 380]. One group targeted membrane biofouling for water and wastewater industries [381]. Direct bacterial killing, biofilm degradation and dispersal, and increased or synergistic therapeutic effectiveness of antimicrobials have been reported as the therapeutic effects of sonobactericide. These studies show that sonobactericide can be applied to treat Gram+ or Gram– bacteria, when they are planktonic, associated with a surface and embedded in biofilm, or intracellular. The majority of these studies were carried out *in vitro*. However, seven were performed *in vivo* in either mice [171, 172, 375, 377], rats [376], or rabbits [373, 378]. Sonobactericide was mostly performed with co-administration of antimicrobials. Investigators also employed an antimicrobial encapsulated in liposomes that were conjugated to the microbubbles [83], or the antimicrobial lysozyme was a microbubble coating [375], or did not use antimicrobials altogether [376, 380, 381]. An extensive review of sonobactericide has been published recently by Lattwein et al. [382]. Although sonobactericide is an emerging strategy to treat bacterial infections with intriguing potential, the mechanism and the safety of the treatment should be explored, particularly regarding biofilm degradation and dispersal. Future studies should also focus on maximizing the efficacy of sonobactericide *in situ*.

2.10 Future perspectives and conclusions

Therapeutic ultrasound technology is experiencing a paradigm shift in terms of both technical developments and clinical applications. In addition to its inherent advantages for imaging (e.g., real time nature, portability and low cost), ultrasound in combination with cavitation nuclei is under exploration as a drug delivery modality. The results from several preclinical studies have already demonstrated the potential of ultrasound-responsive cavitation nuclei to deliver multiple types of drugs (including model drugs, anticancer, therapeutic antibodies, genes, nanoparticles, etc.) efficiently in various tumor models, including both ectopic and orthotopic models, for immunotherapy, brain disease, to promote the dissolution of clots, and in the treatment of cardiovascular disease and bacterial infections.

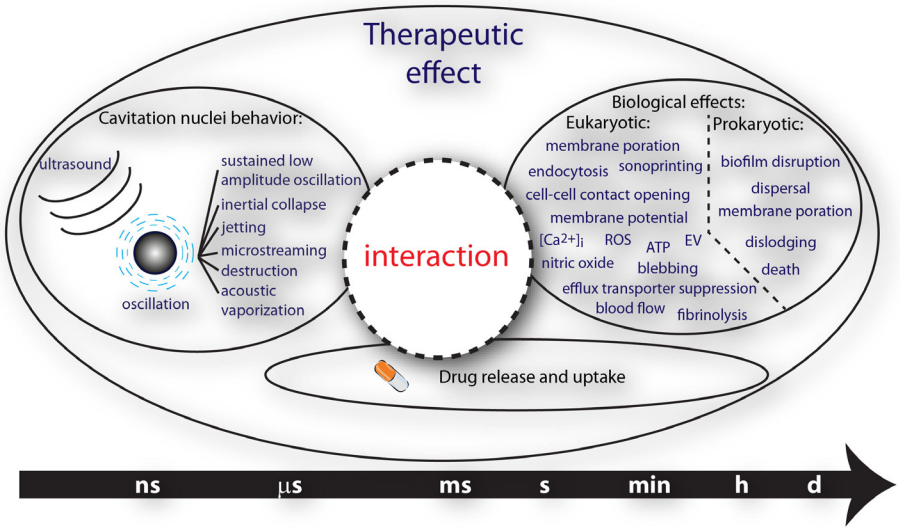

Figure 2.8 Different time scales of the therapeutic effects of ultrasound and cavitation nuclei treatment. $[Ca^{2+}]_i$ = intracellular calcium; ROS = reactive oxygen species; ATP = adenosine triphosphate; EV = extracellular vesicles (reprinted (adapted) with permission from Lattwein et al. [382]).

Based on these encouraging preclinical data, several clinical trials have been initiated and others are planned. However, whilst animal studies provide proof of concept, and impetus for clinical studies, careful attention must be given to their relevance in human disease; in particular, the applicability of therapeutic protocols, and appropriate ultrasound settings. Otherwise we risk underestimating the therapeutic effects and potential deleterious side effects. The elucidation of all of the interactions between cavitation nuclei – cells and drugs will help to address this need. The biggest challenges lie in the large differences in timescales between the cavitation nuclei, drug release and uptake, and the biological response (Figure 2.8). A multidisciplinary approach is needed to tackle these challenges integrating expertise in physics, biophysics, biology, chemistry, and pharmacology.

Custom-made microbubbles which serve as cavitation nuclei are often used for ultrasound-mediated drug delivery studies. An advantage is full control over the payload, as well as the disease target. At the same time, full acoustical characterization and sterility of the microbubbles must be considered during translation to human studies, which often requires approval from the United States Food and Drug Administration (FDA) or other similar federal agencies in Europe and Asia. As an example, for gene therapy, will each different type of genetic material loaded onto microbubbles need such approval, or will a class of cationic microbubbles be approved regardless of the specific gene? The former path would hinder fast clinical translation. For now, co-administration of drugs with FDA-approved ultrasound

contrast agents is being explored in clinical trials. Apart from applications in the brain, ongoing clinical studies evaluating microbubble-mediated drug delivery are based on standard clinical ultrasound scanners operating mostly in Doppler mode. In order to promote the progress of this emerging technology, it is very important to design and implement specific therapeutic ultrasound pulse sequences that might be vastly different from clinical diagnostic imaging output. Clinical scanners can indeed be modified to be able to generate drug delivery protocols. In a similar way that elastography requires long ultrasound pulses to generate the push sequences [383] , ultrasound scanners can be modified to be able to transmit drug delivery ultrasound sequences with tailored and optimized parameters (pulse duration, duty cycle, and center frequency).

Ultimately, ultrasound image-guided drug delivery and the monitoring of treatment response could be feasible with the same equipment. Additionally, with recent developments in ultrasound imaging technology, ultrasound-mediated therapy could be planned, applied and monitored in a rapid sequence with high spatial and temporal resolution. The use of a single imaging and therapy device would alleviate the need for co-registration, because the imaging equipment would also be used to induce localized therapy ensuring a perfect co-location. Nonetheless, a compromise between efficacy and safety remains a major challenge for successful clinical applications of this dual methodology, which combines real-time image guidance of therapeutic delivery.

In conclusion, ultrasound-responsive microbubbles which serve as cavitation nuclei are being used to treat a wide variety of diseases and show great potential preclinically and clinically. The elucidation of the cavitation nuclei–cell–interaction and the implementation of drug delivery ultrasound sequences on clinical ultrasound scanners are expected to invigorate clinical studies.

Acknowledgments—Financial support from the European Research Council (ERC) under the European Union's Horizon 2020 research and innovation programme (grant agreement No 805308; PI: KK), Phospholipid Research Center in Heidelberg, Germany (PhD grant; PI: KK), FWO Vlaanderen (grant 12E3916N), U.S. Department of Health and Human Services, National Institutes of Health, National Institute of Neurological Disorders and Stroke grant R01 NS047603 (PI: CKH), Engineering and Physical Sciences Research Council (grants EP/I021795/1 and EP/L024012/1; PI: ES), the Canada Research Chair Program (PI: KH, PI: MAO) is gratefully acknowledged.

3

Ligand distribution and lipid phase behavior in phospholipid-coated microbubbles and monolayers

Simone A.G. Langeveld, Christian Schwieger, Inés Beekers, Jacob Blaffert, Tom van Rooij, Alfred Blume, and Klazina Kooiman

Based on:
Langmuir, Vol. 36, No. 12, pp. 3221-3233, 2020 [428].

Abstract

Phospholipid-coated targeted microbubbles are ultrasound contrast agents that can be used for molecular imaging and enhanced drug delivery. However, a better understanding is needed of their targeting capabilities, and how they relate to microstructures in the microbubble coating. Here we investigated the ligand distribution, lipid phase behavior, and their correlation in targeted microbubbles of clinically relevant sizes, coated with a ternary mixture of 1,2-dipalmitoyl-*sn*-glycero-3-phosphocholine (DPPC) or 1,2-distearoyl-*sn*-glycero-3-phosphocholine (DSPC), with PEG40-stearate and DSPE-PEG2000. To investigate the effect of lipid handling prior to microbubble production in DSPC-based microbubbles, the components were either dispersed in aqueous medium (*direct method*) or first dissolved and mixed in organic solvent (*indirect method*). To determine the lipid phase behavior of all components, experiments were conducted on monolayers at the air/water interface. In comparison to pure DSPC and DPPC, the ternary mixtures had an additional transition plateau around 10-12 mN/m. As confirmed by Infrared Reflection Absorption Spectroscopy (IRRAS), this plateau was due to a transition in the conformation of the PEGylated components (mushroom to brush). While the condensed phase domains had a different morphology in the ternary DPPC and DSPC monolayers on the Langmuir trough, domain morphology was similar in the coating of both ternary DPPC and DSPC microbubbles (1.5–8 μm diameter). The ternary DPPC microbubbles had a homogenous ligand distribution and significantly less LC phase area in their coating than the DSPC-based microbubbles. For ternary DSPC microbubbles, the ligand distribution and LC phase area in the coating depended on the lipid handling. The direct method resulted in a heterogeneous ligand distribution, less LC phase area than the indirect method, and the ligand colocalizing with the LE phase area. The indirect method resulted in a homogenous ligand distribution with the largest LC phase area. In conclusion, lipid handling prior to microbubble production is of importance for a ternary mixture of DSPC, PEG40-stearate, and DSPE-PEG2000.

3.1 Introduction

Microbubbles with a diameter of 1 to 10 μm have been used as ultrasound contrast agents for non-invasive diagnostic imaging of perfusion since they became available for clinical use in the 1990s [384]. When administered intravenously, these microbubbles are too large to extravasate and therefore function as blood pool agents [39]. The gas core of a microbubble compresses and expands in response to ultrasound. This feature not only provides contrast for ultrasound imaging, but

can also induce bioeffects in nearby cells, resulting in locally enhanced drug delivery [53, 66]. The gas core of the microbubble is usually stabilized by a phospholipid, protein, or polymer coating, which prolongs its lifetime by reducing surface tension and gas diffusion. The coating can be functionalized by incorporating a ligand such that these microbubbles can be targeted to specific biomarkers expressed by cells. Novel targeted microbubbles are being developed for ultrasound molecular imaging of cancer and cardiovascular disease, and for therapeutic applications [51, 66, 385, 386]. However, before there can be widespread use of targeted microbubbles in the clinic, a better understanding and control is needed of the acoustic response and targeting, especially the ligand distribution on the microbubble coating.

A common type of coating for clinically approved microbubbles consists of a monolayer of phospholipids and emulsifiers, such as in Definity (Luminity in Europe; coating composition: 1,2-dipalmitoyl-*sn*-glycero-3-phosphocholine (DPPC), 1,2-dihexadecanoyl-*sn*-glycero-3-phosphate (DPPA), and 1,2-dipalmitoyl-*sn*-glycero-3-phosphoethanolamine(polyethylene glycol) (DPPE-PEG5000) [23], and Lumason (SonoVue in Europe; coating composition: 1,2-distearoyl-*sn*-glycero-3-phosphocholine (DSPC), polyethylene glycol (PEG4000), and 1,2-dihexadecanoyl-*sn*-glycero-3-phospho-(1'-rac-glycerol) (DPPG)) [387]. Many experimental microbubbles are in-house produced analogues of these clinically approved microbubbles, consisting of a main phospholipid component such as DPPC (C16 tail) or DSPC (C18 tail), and an emulsifier such as polyoxyethylene(40) stearate (PEG40-stearate) and/or 1,2-distearoyl-*sn*-glycero-3-phosphoethanolamine-N-carboxy(polyethylene glycol) (DSPE-PEG2000) [30, 388-390]. For the production of targeted microbubbles, a ligand is typically coupled to DSPE-PEG2000 by biotin-avidin bridging or an alternative method of chemical coupling [385].

Although it is generally assumed that the ligand, *i.e.* DSPE-PEG2000 lipid, covers the microbubble surface uniformly, heterogeneous ligand distributions have been reported for DSPC-based microbubbles coated with binary and ternary mixtures [389, 392]. One study illustrated that the ligand distribution could be altered from heterogeneous to homogenous in microbubbles coated with DSPC and DSPE-PEG2000 (9:1) by different heating–cooling protocols [389].

We have previously shown that the main phospholipid component influences the ligand distribution, since for DPPC-based microbubbles the ligand distribution in ternary coating mixtures was homogenous in contrast to a heterogeneous distribution in DSPC-based microbubbles [392]. Increased probability of successful binding of a targeted microbubble is expected when the ligand is distributed homogeneously over the microbubble coating. This is especially important in large

vessels where blood flow is high and targeting is more challenging [393]. It therefore remains to be explored if there are other ways to tune the ligand distribution in DSPC-based ternary coated microbubbles.

Next to a homogeneous ligand distribution for optimal targeting, the acoustic response of the microbubble is important for safe and effective use in therapeutic applications [53]. Microbubbles coated with a DPPC-based ternary mixture proved to be less acoustically stable than those coated with a DSPC-based ternary mixture [45]. Both these types of microbubbles show a large variation in their response to ultrasound [45, 394], even when their size distribution is monodisperse [46]. Kim et al. [388] proposed that the acoustical properties of the microbubbles are influenced by microstructures in the coating. Microstructures are formed as a result of the phase behavior and miscibility of the different components [395], and can be influenced by the conformation of the polymer chain for PEGylated components, which can be either in a brush or mushroom state [31]. The degree of phase separation in the microbubble coating was also found to influence the subharmonic response [396].

The phospholipid DPPC can transition from the liquid expanded (LE) to the liquid condensed (LC) phase during monolayer compression[28], whereas the phospholipid DSPC is always in the LC phase at room temperature [27]. In addition, the emulsifier PEG40-stearate is known to be in the LE phase only [30], whereas DSPE-PEG2000 in a binary mixture with DSPC could transition from the LE to LC phase depending on the concentration and surface pressure [29]. Studies using binary lipid mixtures (phospholipid with C18 to C24 tail and PEG40-stearate) demonstrated that microbubble coatings had microstructures with larger domain sizes when they were cooled at a slower rate after production by probe sonication [388]. Another study confirmed LE and LC phase co-existence in binary microbubble coatings (phospholipids with C12 to C24 tail and PEG40-stearate), and domain morphologies varied depending on the cooling rate as well [30].

Next to the lipid phase behavior, microstructures in the microbubble coating are also influenced by the miscibility and conformation (mushroom or brush) of the PEGylated components. The most widely used emulsifiers PEG40-stearate and DSPE-PEG2000 have one and two acyl chains, respectively [390]. When microbubbles coated with a binary mixture of DSPC and PEG40-stearate (9:1) were studied with confocal microscopy, no domains were observed in microbubbles smaller than 5 µm [25], suggesting that there was no phase separation. Lozano and Longo concluded from their phase diagrams of monolayers at an air/water interface that DSPC and DSPE-PEG2000 are immiscible at all relevant pressures since DSPC is always in LC phase, while DPPC and DSPE-PEG2000 were miscible in both the LE and LC phase [29]. Another study focused on the distribution of DSPE-PEG2000, with a fluorescent

ligand attached, in microbubbles (diameter >10 μm) coated with DSPC and DSPE-PEG2000 (9:1). DSPE-PEG2000, *i.e.* the ligand, was heterogeneously distributed and colocalized with the LE phase as reported for a single example, yet no quantification was performed [389]. Up to now, the ligand distribution and lipid phase co-existence in microbubble coatings have not been quantified simultaneously in individual microbubbles.

A major difference between studies that evaluated microbubbles coated with a binary mixture and those coated with a ternary mixture is the handling of phospholipid components during microbubble production. For binary mixtures, the components were generally dissolved and premixed in organic solvent first, then dried to form a lipid film, and dispersed in aqueous medium before microbubbles were produced [25, 30, 389] (*i.e.,* indirect method). For ternary mixtures the components were generally dispersed directly in aqueous medium before microbubble production [392, 397-399] (*i.e.*, direct method). Based on the effect of cooling rate on microstructures in large microbubbles (>10 μm) after microbubble production [30], we hypothesize that the method of handling the lipids prior to microbubble production may also influence the ligand distribution and/or lipid phase in the coating of microbubbles. The ligand distribution, *i.e.* the location of the ligand on the microbubble surface, is important for the binding probability while the lipid phases are expected to affect the elasticity and stiffness of the coating, and thereby influence the acoustical performance.

The main objective of this study was to determine the DSPE-PEG2000 (*i.e.*, ligand) distribution and lipid phase behavior in microbubbles of clinically relevant sizes (diameter 2-8 μm) coated with a ternary mixture of DPPC or DSPC as main component and both PEG40-stearate and DSPE-PEG2000 as emulsifiers. Microbubbles were made by probe sonication after which the ligand distribution and lipid phase behavior in the microbubble coatings were visualized with high axial resolution 4Pi confocal microscopy. In addition, the relationship between the ligand distribution and the lipid phase behavior was investigated by quantifying the co-localization of ligand and LE phase. Previous studies have shown that DSPC-based microbubbles were acoustically more stable than DPPC-based microbubbles [45], but they had a heterogeneous ligand distribution [392]. We therefore also investigated the effect of lipid handling on the ligand distribution in DSPC-based microbubbles. To gain insights into the physicochemical properties of the ternary mixtures, we first focused on characterizing the lipid phase behavior and PEG conformation in monolayers at an air/water interface. Because the phospholipid molecules (1 nm^2) [391] in the microbubble coating are so much smaller than the total surface area (0.3-0.8 $\times 10^8$ nm^2 for microbubbles of 3-5 μm diameter), the coating can be regarded as a flat monolayer, despite the spherical shape of the microbubble. Compression isotherms

were obtained and were used together with fluorescence microscopy to visualize the lipid phase behavior of the ternary mixtures. Infrared Reflection Absorption Spectroscopy (IRRAS) was performed to determine the phase and conformation of the individual components during monolayer compression.

3.2 Materials and methods

Materials

DPPC, DSPE-PEG2000, 1,2-distearoyl-*sn*-glycero-3-phosphoethanolamine-N-biotinyl(polyethylene glycol) (DSPE-PEG2000-biotin), as well as the chain deuterated lipids DPPC-d_{62} and DSPC-d_{70} were purchased from Avanti Polar Lipids (Alabaster, Alabama, USA). DSPC and PEG40-stearate were obtained from Sigma-Aldrich (Zwijndrecht, the Netherlands). Perfluorobutane (C_4F_{10}) was purchased from F2 Chemicals (Preston, UK) and argon gas was purchased from Linde Gas Benelux (Schiedam, the Netherlands). Streptavidin Oregon Green 488 was purchased from BioSynthesis (Louisville, Texas, USA) and Lissamine Rhodamine B 1,2-dihexadecanoyl-*sn*-glycero-3-phosphoethanolamine, triethylammonium salt (Rhodamine-DHPE) was purchased from ThermoFisher (Waltham, Massachusetts, USA).

Monolayer compression isotherms

Monolayer compression isotherms were obtained at 20 °C with a Langmuir trough (sample trough 6.8 × 80 cm^2) purchased from Riegler and Kirstein GmbH (Berlin, Germany) equipped with movable barriers and a Wilhelmy pressure sensor with a filter paper functioning as pressure probe. The pressure sensor was calibrated prior to each experiment to a surface pressure of 0 mN/m in water and 72 mN/m in air. The temperature was maintained constant at 20 °C by a circulation water bath. The complete setup was placed inside a hood to reduce dust deposition and water evaporation. Monolayers of pure DPPC or DSPC, a binary mixture (composition in mol%: DPPC or DSPC 92.4; DSPE-PEG2000 7.6) or ternary mixture (composition in mol%: DPPC or DSPC 84.8; PEG40-stearate 8.2; DSPE-PEG2000 5.9; DSPE-PEG2000-biotin 1.1) were spread on a surface of phosphate-buffered saline (PBS) as the subphase buffer solution. The binary mixture with 7.6 mol% DSPE-PEG2000 was chosen based on previously published work on microbubbles coated with a binary mixture of DPPC or DSPC (92.4 mol%) and DSPE-PEG2000 (7.6 mol%) [400], having the same molar ratio of 12:1 for the main lipid to DSPE-PEG2000 as the ternary mixtures studied. Chloroform:methanol (9:1 vol/vol) was used as the spreading solvent [401], and allowed to evaporate for at least 15 min [402] before starting compression with a speed of 2 $Å^2$ $molecule^{-1}$ min^{-1}. The surface pressure was

recorded during compression with a time resolution of 2 s with RUK trough control software (Riegler and Kirstein GmbH).

Monolayer fluorescence microscopy

To study the lipid organization with fluorescence microscopy, Rhodamine-DHPE (0.01 mol%) was added to the DPPC- and DSPC-based ternary mixtures before spreading the monolayer. Since this dye does not diffuse into the LC phase [403], all dark areas are lipids in the LC phase and all areas with a fluorescent signal are in a more fluid phase, *i.e.* LE phase. The monolayers were spread on a Langmuir trough (sample trough 9.9 × 26 cm^2; Riegler and Kirstein GmbH) and imaged during compression with an Axio Scope A1 Vario epifluorescence microscope (Carl Zeiss MicroImaging, Jena, Germany) equipped with a mercury arc lamp (HXP 120 C) for excitation, a long working distance objective (NEOFLUAR 50×), and a filter/beam splitter set (Zeiss Filter Set 09), which allows excitation between 450-490 nm and detection of emitted light above 515 nm. Images were recorded with an EMCCD Camera (ImageEM, C9100-13, Hamamatsu, Herrsching, Germany) and the surface pressure was recorded as described previously.

IRRAS experiments

On the basis of the isotherms and the fluorescence microscopy images it is not possible to distinguish the phase state of the individual components in the ternary mixtures. To investigate the phase behavior of the individual components, IRRAS experiments were performed. The use of chain-deuterated phospholipids (DPPC-d_{62} or DSPC-d_{70}) in the ternary mixtures allowed us to distinguish the signal from the PEGylated (CH_2 vibrations) and non-PEGylated (CD_2 vibrations) components. The IRRAS measurements were performed using a Bruker Vector 70 FT–IR spectrometer equipped with a nitrogen cooled MCT detector and an A511 reflection unit (Bruker Optics, Ettlingen, Germany), placed over a Langmuir trough setup (Riegler and Kierstein GmbH). The sample trough (6 × 30 cm^2) was set up according to the protocol described above. A circular reference trough (3 cm radius) placed next to the sample trough could be brought into the focus of the IR beam by means of a shuttle. Both troughs were filled with PBS as the subphase buffer solution and lipid mixtures were spread in the sample trough as described above. The filling levels of both troughs were kept equal and constant by means of an automated, laser reflection controlled, pumping system connected to PBS reservoirs. The IR beam was coupled out from the spectrometer and focused by mirrors onto the buffer or film surface at an incidence angle of φ = 60°. A KRS-5 polarizer was used to generate

perpendicular polarized light. The compression of the monolayer was performed at 2 $Å^2$ $molecule^{-1}$ min^{-1}. The compression was stopped at several predefined areas per molecule, as indicated in Figure 3.3B and 3.3D, to record at least three IRRA spectra at constant molecular area before the compression was continued. Spectra were recorded with a spectral resolution of 4 cm^{-1} and 160 kHz scanner velocity. One thousand single interferograms were zero-padded with a factor of two and averaged, followed by fast Fourier transformation, resulting in a nominal spectral resolution of 2 cm^{-1}. IRRA spectra were calculated from the reflectivity on the monolayer covered surface (R) and the bare buffer surface (R_0) according to reflection absorption $RA = -\log_{10}(R/R_0)$. All IRRA spectra were corrected for atmospheric water vapor absorption using OPUS software (Bruker Optics GmbH, Ettlingen, Germany) and set to a common baseline in a spectral range where no absorptions occurred (4500 – 4600 cm^{-1}). The maxima of the CH_2 (2800 – 2950 cm^{-1}) and CD_2 (2020 – 2270 cm^{-1}) stretching vibrational bands were determined using the standard method of the OPUS software. The peak positions were averaged for spectra recorded at the same lipid molecular area and surface pressure, and are presented together with their standard deviation. The presented spectra are averages of all spectra recorded at the same monolayer state. To identify the contribution of the phospholipid headgroups to the transitions, principal component analysis (PCA) [404, 405] was done with the princomp function of MATLAB. PCA was chosen to analyze the variation in the data by computing eigenvectors, which can be used to determine the factor responsible for the largest variance. Corresponding eigenvalues were used to determine how much variance occurred. For the analysis, the spectral regions between 1050 – 1300 cm^{-1} for headgroup vibrations and 2020 – 2270 cm^{-1} for CD_2 stretching vibrations were selected from the IRRA spectra recorded at various surface pressures. From both spectral ranges, a linear baseline was subtracted before they were normalized to a vector norm of unity. Subsequently, both subspectra were combined to a single input vector for the PCA, where the wavenumbers were the variables and the surface pressures the conditions. The first principal components and the respective scores are presented in the Results section. Scores of the higher principal components did not change systematically with film compression.

Microbubble production

Biotinylated lipid-coated microbubbles (composition in mol%: DSPC or DPPC 84.8; PEG40-stearate 8.2; DSPE-PEG2000 5.9; DSPE-PEG2000-biotin 1.1) with a C_4F_{10} gas core were made by probe sonication at 20 kHz with a Sonicator Ultrasonic Processor XL2020 at power setting 10 (HeatSystems, Farmingdale, NY, USA) for 10 s as described previously [397]. The coating components were prepared in two different ways. (1) For the direct method all components were dissolved in PBS with

a final concentration of 2.5 mg/mL DSPC or DPPC, 0.625 mg/mL PEG40-stearate, 0.625 mg/mL DSPE-PEG2000, and 0.125 mg/mL DSPE-PEG2000-biotin. Fluorescent dye Rhodamine-DHPE (0.01 mol%) was added to study the lipid phase organization in the microbubble coating. (2) For the indirect method, DSPC, PEG-40 stearate, DSPE-PEG2000, and DSPE-PEG2000-biotin were dissolved in chloroform:methanol (9:1 vol/vol). The organic solvent was then evaporated with argon gas and the obtained lipid film was dried under vacuum overnight. Finally, the lipid film was dispersed in PBS with a final concentration of 2.5 mg/mL DSPC or DPPC, 0.625 mg/mL PEG40-stearate, 0.625 mg/mL DSPE-PEG2000, and 0.125 mg/mL DSPE-PEG2000-biotin, fluorescent dye Rhodamine-DHPE (0.01 mol%) was added, the solution was placed in a sonicator bath for 10 min, and a probe sonicator was used at a power setting 3 for 5 min. The three types of microbubbles produced are referred to as "direct DPPC", "direct DSPC", or "indirect DSPC" microbubbles.

Microbubble fluorescence imaging

The fluorescent ligand streptavidin Oregon Green 488 was conjugated to the biotinylated microbubbles as described previously by Kooiman et al. [392], allowing us to determine the distribution of DSPE-PEG2000-biotin over the lipid phases in the microbubble coating. Briefly, 0.9 mL microbubble suspension was placed in a 3 mL syringe and topped with 2.1 mL PBS saturated with C_4F_{10} for washing by flotation. The subnatant was drained after 45 min, the microbubbles were re-suspended in 0.3 mL PBS saturated with C_4F_{10}, and collected. Next, 22.5 µL of streptavidin (2 mg/mL) was added to 0.7-1.0 $\times 10^8$ microbubbles. After incubation on ice for 30 min the excess streptavidin was washed by flotation, as described above, and the microbubbles were re-suspended in 0.2 mL PBS saturated with C_4F_{10}.

A Coulter Counter Multisizer 3 (Beckman Coulter, Mijdrecht, the Netherlands) was used to measure the microbubble size distribution and concentration. A 50 µm aperture tube was used for quantification of particles between 1 and 30 µm with a linear spacing between the 256 channels. The size distribution of the samples was evaluated by the span value, which illustrates the width of the distribution, defined as (d90%–d10%)/d50%, where d90%, d10%, and d50% are the microbubble diameters below which 90, 10, and 50% of the cumulative number of microbubbles was found.

After conjugation with streptavidin Oregon Green 488, microbubbles were visualized as described by Kooiman et al [392]. To reduce Brownian motion, microbubbles were placed in 87% glycerol (vol/vol in PBS) and visualized using a Leica TCS 4Pi confocal laser-scanning microscope [406]. The 87% was chosen because this has the same refractive index as the quartz glass and glycerol objective of the 4Pi microscope. This high-resolution imaging system has a matched pair of aligned opposing 100×

glycerol HCX PL APO objective lenses (Numerical aperture 1.35), increasing the axial resolution up to 90 nm. A 488 nm laser was used for excitation of Oregon Green 488 and a 561 nm laser was used for excitation of Rhodamine-DHPE. Image stacks were recorded as y-stacked xz-scans in a green (500-550 nm) and red (580-640 nm) spectral channel. The software AMIRA (Version 2019.1, FEI, Mérignac Cedex, France) was used to volume-render the image stacks with the "voltex" function.

Microbubble data analysis

Custom-developed image analysis software in MATLAB (Mathworks, Natick, MA, USA) was used for quantitative analysis of the 4Pi microscopy data. The ligand distribution was analyzed based on the method described by Kooiman et al [392]. First, a circle was fitted through the fluorescence intensity maxima of the green channel (Oregon Green 488, 500-550 nm) and per *xz*-slice a region of interest (ROI) was defined in a band of 7 pixels around the fitted circle. Only slices with an ROI radius larger than 75% of the radius in the equatorial plane ROI were included in the analysis. Each of the ROIs was divided into 32 angular parts and the mean fluorescence pixel intensity (I_{part}) was calculated for each of those parts. The I_{part} values were plotted per microbubble as a function of the axial plane and the microbubble circumference in 2D color-coded heatmaps (Supplemental Figure 3.1A). On average, 30 *xz*-slices were included per microbubble, resulting in an average of 960 angular parts per microbubble. The median intensity of all the angular parts (I_{median}) was calculated for each microbubble. The image analysis software classified an individual angular part as inhomogeneous when the absolute difference between I_{part} and I_{median} was more than two-third times the value of I_{median} (*i.e.*, $|I_{part} - I_{median}| > 2/3 \times I_{median}$). The percentage of parts classified as inhomogeneous was calculated per microbubble as a measure for the inhomogeneity of the ligand distribution. After this analysis, an adapted version of the software was used to analyze the lipid phase behavior in the red channel (Rhodamine-DHPE, 580-640 nm). The same *xz*-slices and ROIs were used as those obtained during the ligand distribution analysis. Again, the ROIs were divided in 32 angular parts and the mean fluorescence pixel intensity ($I_{part\text{-}Rhod}$) in each part was calculated. From these, the median part intensity ($I_{median\text{-}Rhod}$) was calculated per microbubble and plotted as 2D color-coded heatmaps (Supplemental Figure 3.1B). The software classified an individual angular part as LC phase when the value of $I_{part\text{-}Rhod}$ was less than one-third of $I_{median\text{-}Rhod}$ (*i.e.*, $I_{part\text{-}Rhod} < 1/3 \times I_{median\text{-}Rhod}$) (Supplemental Figure 3.1C). The LC phase surface area was determined per microbubble in μm^2 and presented as percentage of the total analyzed surface area per microbubble. To study if the ligand colocalized with the parts classified as LC areas, the median fluorescence intensity of the green channel (ligand) was calculated for all parts in LC phase and for those not in LC phase

(Supplemental Figure 3.1D, E). The ratio between these two values was defined as the colocalization ratio.

IBM SPSS Statistics 25 was used to perform statistical analysis. The distribution of the data was assessed using a Shapiro-Wilk test. The data on ligand inhomogeneity was not normally distributed ($p < 0.001$) for all microbubble types. The data on the LC phase area was only normally distributed for direct DPPC ($p = 0.228$); not for direct DSPC ($p = 0.002$) and indirect DSPC ($p < 0.001$) microbubbles. The colocalization ratio was normally distributed (DPPC: $p = 0.168$, DSPC direct method: $p = 0.203$, DSPC indirect method: $p = 0.334$). Therefore, the Mann-Whitney U test was used to test if the microbubble types had a significant difference in inhomogeneity of the ligand distribution and LC phase area. For the colocalization ratio a regular t-test was used to analyze the differences between the microbubble types. Differences were regarded as significant at p-value < 0.01.

3.3 Results and discussion

Monolayers

Monolayer compression isotherms

The results of the Langmuir trough experiments are presented in Figure 3.1. All curves are representative of the results from three or more experiments. In accordance with literature [28, 29], there was a clear difference between the isotherms of pure DPPC (Figure 3.1A, black line) and DSPC (Figure 3.1C, black line) as DPPC had a transition from the LE to LC phase at a surface pressure (π) of ~5 mN/m, whereas DSPC did not form an LE phase and therefore underwent a direct gaseous to LC phase transition. The binary mixture with 7.6 mol% DSPE-PEG2000 was chosen based on previously published work on microbubbles coated with a binary mixture of DPPC or DSPC (92.4 mol%) and DSPE-PEG2000 (7.6 mol%) [400]. For DPPC in mixtures with PEGylated compounds we observed two transitions (Figure 3.1A, 3.1B). The transition from the LE to LC phase of DPPC occurred almost at the same surface pressure in the binary mixture (DPPC/DSPE-PEG2000), whereas it was slightly shifted to a lower pressure in the ternary mixture containing PEG40-stearate. This shift to a lower surface pressure is due to the long stearoyl chain of the PEG40-stearate increasing the stability of an LC phase. In the binary mixture, a second transition at ~10 mN/m was observed (Figure 3.1B, orange line). In the ternary mixture with a higher content of PEGylated components the second transition moved to ~12 mN/m (Figure 3.1B, blue line). For DSPC in mixtures with PEGylated lipid components, we observed phase transition plateaus only at ~10 mN/m (Figure 3.1B, blue line, binary mixture) and ~12 mN/m (Figure 3.1D, blue line, ternary mixture), similar to the second transition in DPPC-based mixtures (Figure 3.1C, 3.1D, orange and blue lines). Again, the transition

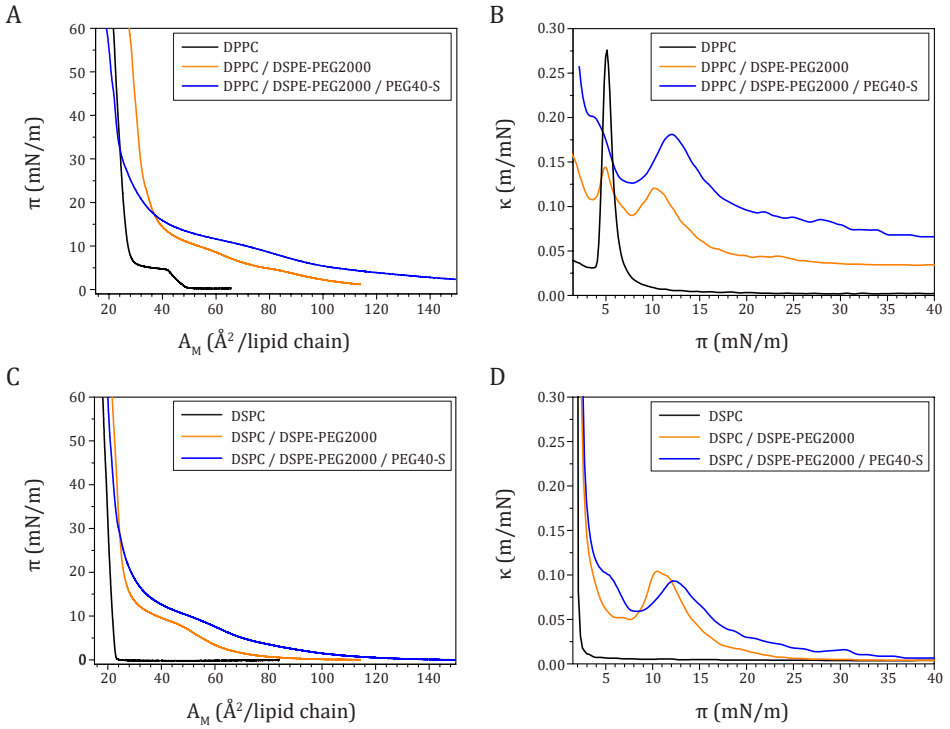

Figure 3.1 Langmuir isotherms of pure, binary (92.4:7.6 mol%), and ternary (84.8:7.0:8.2 mol%) mixtures with (**A**) DPPC or (**C**) DSPC as main lipid components and DSPE-PEG2000 and/or PEG40-stearate (PEG40-S) as additional components. **A,C**) surface pressure (π) as a function of the area per molecule (A_M). **B,D**) derived compressibility (κ) as a function of the surface pressure (π) where the peaks indicate transition plateaus. Representative curves are shown of at least three repeated experiments.

pressure increased with increasing content of PEGylated components. As the transition ≥ 10 mN/m is independent of the type of phospholipid, we assume that it is due to the so-called mushroom to brush transition of the PEG chains attached to the lipid headgroups [407-409]. Theoretical calculations of the mushroom to brush transition [32] for the binary mixture in this study is 45 Å^2 (lipid chain)$^{-1}$ (see Supplemental Figure 3.2) which is in agreement with the experimental findings of 30-60 Å^2 (lipid chain)$^{-1}$. For the ternary mixture, the calculated mushroom to brush transition is 87 Å^2 (lipid chain)$^{-1}$ (see Supplemental Figure 3.2) which is only slightly higher than the experimentally observed 60-80 A_M/Å^2 (lipid chain)$^{-1}$. The difference could be explained by the polydispersity of the PEG40-stearate [410] since a decrease in chain length lowers the Florius radius.

The isotherms of the binary mixtures presented here are in agreement with literature for the same binary mixtures [29, 411]. By contrast, another study on binary mixtures of DSPC with DSPE-PEG2000 or PEG40-stearate (9:1) found that the mixture with

DSPE-PEG2000 had an isotherm similar to that of pure DSPC, while the binary mixture with PEG40-stearate had an extra transition plateau around 35 mN/m [25]. This was attributed to expulsion of material from the monolayer, sometimes referred to as squeeze-out [30]. However, in the present study we observed no squeeze-out plateau in the ternary mixtures that contained PEG40-stearate. This may be explained by the differences in concentration of PEG40-stearate (10 mol% versus 8 mol%) and the addition of DSPE-PEG2000 as third component.

Monolayer fluorescence microscopy

Fluorescent micrographs of monolayers containing ternary mixtures with DSPC or DPPC at different surface pressures during compression are shown in Figure 3.2. The DPPC containing mixture was homogenous with some bright spots at the starting surface pressure (< 1 mN/m). These bright spots could be due to the co-existence of gaseous and LE phases, with the fluorescent lipid dye enriched in the LE phase spots. With increasing surface pressure the bright fluorescent spots disappeared and at 5 mN/m the fluorescent dye was homogenously distributed, indicating that all components were in the same phase, namely the LE phase. Above 5 mN/m dark domains of LC phase lipids appeared and grew larger as the compression of the monolayer advanced. Initially, these dark domains were clustered like flower petals connected to a central point (Figure 3.2, DPPC 10 mN/m). As the surface pressure increased, the LC domains separated and the inter-domain region became brighter, because a fixed amount of fluorescent dye was distributed over a smaller surface area. These micrographs show the same morphology of dark domains as in previously published micrographs on a binary mixture of DPPC and PEG40-stearate (9:1) [30]. Interestingly, the dark LC domains containing mainly DPPC did not form the characteristic bean- or propeller like shapes with defined chirality as observed for pure DPPC [412, 413]. This seems to be an indication that the LC phase is not pure

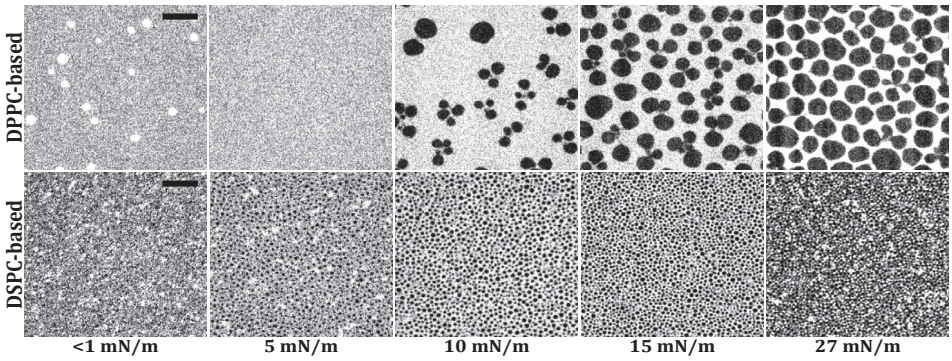

Figure 3.2 Fluorescent micrographs of monolayers of ternary mixtures containing DSPE-PEG2000 (7.0 mol%), PEG40-stearate (8.2 mol%), and either DPPC (84.8 mol%, top row) or DSPC (84.8 mol%, bottom row) at various surface pressures, taken during monolayer compression. Scale bars (black) represent 25 µm and apply to all images.

DPPC but contains some achiral PEG40-stearate or DSPE-PEG2000, thus preventing the formation of chiral domains.

A major difference between DPPC- and DSPC-based mixtures is the presence of LC domains in the DSPC containing monolayer at low surface pressures (<1 mN/m). This is consistent with the isotherms of pure DSPC where a direct transition from the gaseous phase to LC phase is observed. Interestingly, in the DSPC mixture there appeared to be three phases at low surface pressures (<1-5 mN/m). Previous work on bilayers has indeed shown that three-phase co-existence can occur in a ternary mixture of DSPC with 1,2-dioleoyl-*sn*-glycero-3-phosphocholine (DOPC) and cholesterol [414]. With increasing surface pressure the dark LC domains grew larger. However, the size of the LC domains at different surface pressures is much smaller than in the DPPC containing monolayers. The size of LC domains is dependent on the line tension between the LC domains and the surrounding phase and the excess dipole density in the LC domains [412, 415, 416]. The latter effect leads to a repulsion between the domains and prevents the domain growth driven by the line tension. The DSPC containing LC domains probably have a larger excess dipole density with respect to the surrounding gaseous phase, than DPPC containing LC domains with respect to the surrounding LE phase, which prevents further LC domain growth of DSPC. High excess dipole density leading to small LC domains has been reported for DMPC/DSPC monolayers containing 60 mol% DSPC [415] and for DSPC monolayers containing 1-9 mol% DSPE-PEG2000 [417]. The transition around 10 mN/m that was identified in the isotherms was less apparent in the fluorescence micrographs. With increasing surface pressure, the most noticeable change was an increase in the relative surface area of the LC domains, indicating that the surrounding LE phase is being compressed without molecules transitioning into the LC phase. This suggests a transition in the headgroup region occurs instead, namely a mushroom-brush transition of the PEG chains in the aqueous phase.

IRRAS experiments

Figure 3.3 shows the results of the IRRAS experiments we performed to attribute the different transition plateaus of the isotherms to specific phase transitions. The position of the methylene stretching vibrational bands in the IRRA spectra is dependent on the phase state of the respective lipid, with a downshift in their wavenumbers being indicative for an LE to LC transition [418-420]. The stretching vibrations of the CD_2 groups of the deuterated lipids are well separated from the CH_2 stretching vibrations of the PEGylated components and any other vibrational bands, allowing separate analysis of the phase state of the main phospholipid component and the PEGylated components (Figure 3.3A, 3.3C). Isotherms of pure DPPC-d_{62} and DSPC-d_{70} were measured to confirm that deuteration had only little

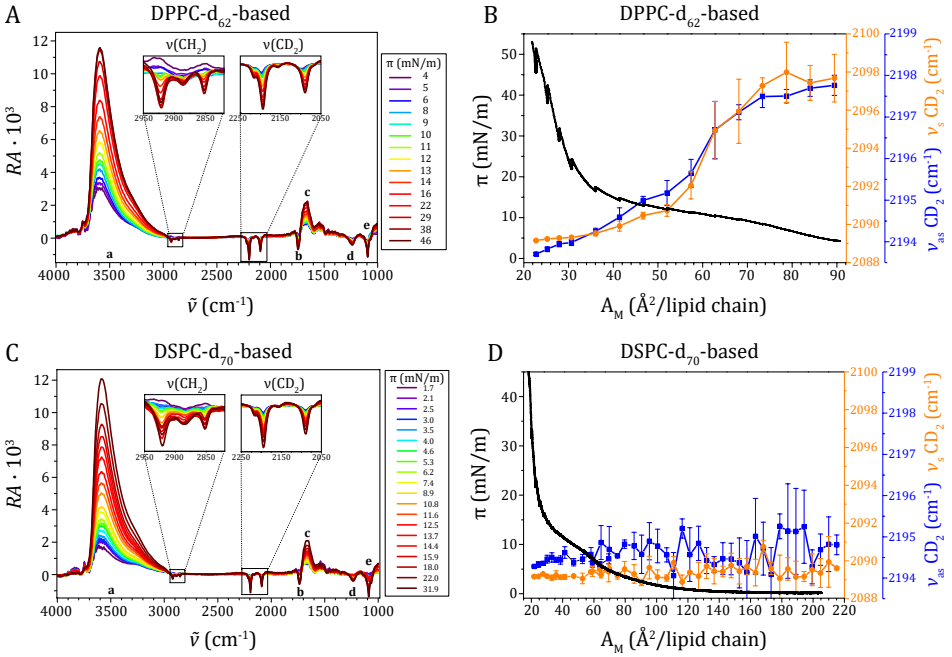

Figure 3.3 Spectra obtained by IRRAS of a monolayer composed of the ternary mixture (**A**) DPPC-d_{62}/DSPE-PEG2000/PEG40-stearate (84.8:7.0/8.2 mol%) and (**C**) DSPC-d_{70}/DSPE-PEG2000/PEG40-stearate (84.8/7.0/8.2 mol%), reflection absorption ($RA = -\log_{10}(R/R_0)$) as a function of wavenumber ($\tilde{\nu}$) for different surface pressures (π). CH_2 and CD_2 stretching bands are zoomed in; other bands are labeled: (a) OH stretching, (b) C=O stretching, (c) OH bending, (d) PO_2 antisymmetric stretching, (e) PO_2 symmetric stretching and C–O stretching. (**B, D**) surface pressure (π) as a function of area per molecule (A_M) (black curve, left *y*-axis); wavenumbers ($\tilde{\nu}$) of symmetric (orange line and symbols, right *y*-axis) and antisymmetric (blue line and symbols, right *y*-axis) CD_2 stretching vibration of the (**B**) DPPC-d_{62}-based or (**D**) DSPC-d_{70}-based ternary mixtures. Note the wider area range in (**D**) as compared to (**B**). Wavenumbers of the CH_2 stretching vibrational bands are given in Supplementary Figure 3.

effect on the lipid phase behavior (Supplemental Figure 3.3, compared to Figure 3.1A and C). However, the LE to LC phase transition of pure DPPC-d_{62} shifted to slightly higher surface pressure, *i.e.* towards the second transition detected for DPPC-based ternary mixtures, resulting in a slight overlap of both transitions. Nevertheless, IRRA spectra of the monolayers of ternary mixtures containing DPPC-d_{62} showed a transition from LE to LC phase concomitant with the plateau (at ~12 mN/m) in the isotherm (Figure 3.3B). In contrast, no DSPC-d_{70} molecules were found in the LE phase, indicating a direct transition from the gaseous to the LC phase (Figure 3.3D, blue and orange line). The position of the CD_2 stretching vibrational bands at low wavenumbers throughout the examined compression range indicates that DSPC-d_{70} is already in the LC phase at high molecular areas. This unambiguously shows that the transition plateau we found around ~10-12 mN/m is not due to a phase transition of DSPC itself and must thus be caused by a reorganization of the PEGylated

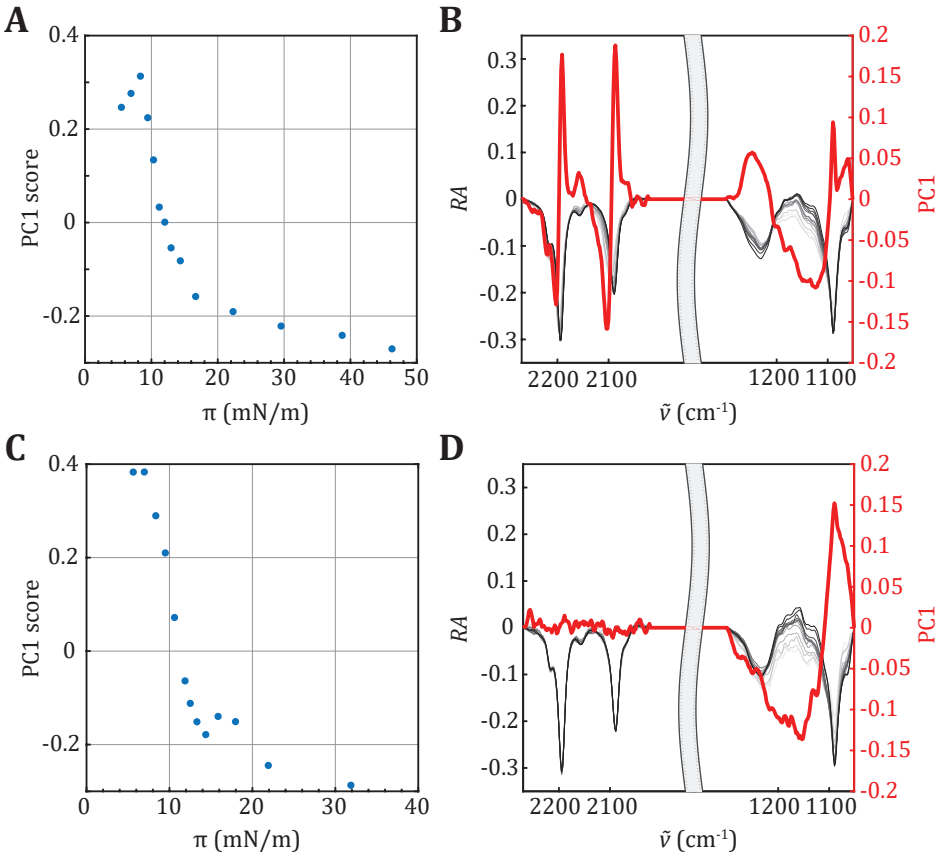

Figure 3.4 Principal component analysis of IRRA spectra recorded during the compression of a PL/DSPE-PEG2000/PEG40-stearate (84.8/7.0/8.2 mol%) mixed monolayer, where PL = DPPC-d_{62} (**A** and **B**) and DSPC-d_{70} (**C** and **D**). IRRA spectra were simultaneously analyzed in the range of the headgroup vibrations (1050–1300 cm^{-1}) and the CD_2 stretching vibrations (2020–2270 cm^{-1}) after separate vector normalization in the two respective ranges (gray lines in **B** and **D**; low surface pressures (light grey) to high surface pressures (dark grey)). **A** and **C** show the scores of the first principal components (PC1) as function of the surface pressure (π). **B** and **D** show the reflection absorption (*RA*, grey lines, left *y*-axis) and PC1 score (red lines, right *y*-axis) as a function of the wavenumbers ($\tilde{\nu}$).

components, probably the mushroom to brush transition of the PEG chains [29]. The CH_2 stretching vibrations of the PEGylated components were analyzed as well (Supplemental Figure 3.4B, D). However, due to low signal we only have data from surface pressures above 12.5 mN/m, so we cannot distinguish the transition that occurs below this surface pressure. The CH_2 vibrational bands arise from the CH_2 groups in the chains and in the headgroups of the PEGylated components, mainly PEG40-stearate, with the majority of the CH_2 groups being located in the PEG groups of PEG40-stearate and DSPE-PEG2000. However, because the conformation of the CH_2 groups in the flexible PEG chains is not well defined, their contribution to the CH_2

stretching vibrational band is broad and the band position is still dominated by the vibrations of the higher ordered lipid acyl chains. The CH_2 vibrational bands of pure DPPC before and after transition can be used as a reference for characteristic LE and LC phase wavenumbers (Supplemental Figure 3.5). The CH_2 bands in the ternary mixtures were observed at a wavenumber characteristic for neither an LC nor an LE phase, but in between; namely at 2852 cm^{-1} (symmetric CH_2-vibration) and at 2922 cm^{-1} (antisymmetric CH_2-vibration) (Supplemental Figure 3.4B, D). This suggests that part of the PEGylated molecules was in the LE phase and part was in the LC phase. When comparing the CH_2 vibrational bands of the PEGylated molecules to the CH_2 vibrational band of pure DPPC during transition, the observed wavenumbers ($\tilde{\nu}$) suggest that the majority (about 60%) of the PEGylated lipids are still in LE phase (Supplemental Figure 3.5). In case of the DSPC-based ternary mixtures, the LE phase is consequently formed only by the PEGylated molecules, whereas in the DPPC-based mixtures the LE phase contains DPPC and/or PEGylated molecules.

To identify the contributions of the lipid headgroups to the transitions, we performed a PCA on the IRRA spectra in the region of the PO_2 and C–O stretching vibrations (symmetric and antisymmetric; Figure 3.3A and C, label d and e), originating from the headgroup attached PEG chains (1050 – 1300 cm^{-1}), and the CD_2 stretching vibrations, originating from the acyl chains (2020 – 2270 cm^{-1}) (Figure 3.4). This type of analysis identifies the main variances in the spectra during compression of the mixed monolayers and attributes them to different spectral regions, influential in the reorganization of different molecular moieties. The extent of these variations is expressed in first principal component (PC1) scores (Figure 3.4A, 3.4C). In the here presented analysis, these scores change systematically with the surface pressure, with a pronounced step at about 10 mN/m. This corroborates our finding that both mixed monolayers show a transition when compressed above this surface pressure. Interestingly, the reason for this transition is different in DPPC-d_{62} containing and DSPC-d_{70} containing monolayers, as can be deduced from the PC1 scores depicted in Figure 3.4B and 3.4D. The DPPC-d_{62} containing monolayer spectra show simultaneous changes in the CD_2 stretching vibrational region and in the region of the headgroup vibrations. This suggests that both the acyl chains and the PEGylated headgroups contributed to the transition. In contrast, for the DSPC-d_{70} containing monolayer, spectral changes corresponding to the transition were only identified in the head group region, because the PC1 score (red line in Figure 3.4D) shows variations in the spectral range of the PO_2 and C–O stretching vibrations but is essentially zero in the range of the CD_2 stretching vibrations. With this finding, the transition in the ternary mixtures containing DSPC can clearly be attributed to reorganizations in the PEGylated headgroups, presumably a PEG mushroom to brush transition.

To verify that the changes in the headgroup region are not only due to the phospholipid phosphate groups but contain contributions of PEG chain reorganization, we repeated the IRRAS compression experiment and PCA with a pure DPPC-d_{62} monolayer (see Supplemental Figure 3.6). Comparison of the first principal components shows lower PC1 scores in the range of the headgroup vibrations for pure DPPC-d_{62}, indicating that only phosphate reorganization would not be sufficient to explain the variations in the above presented spectra. Thus, we conclude that PEG chain conformational changes must be involved in the transitions of the monolayers containing ternary mixtures of DSPE-PEG2000 and PEG40-stearate with DPPC or DSPC.

All experiments described above were performed at the air/buffer interface. However, during microbubble production, C_4F_{10} gas is added to the air and the phospholipids are dispersed in PBS saturated with C_4F_{10} gas. Recently published work demonstrates how the LE to LC transition of DPPC was shifted to higher surface pressures in the presence of C_6F_{14} in the gas phase [421]. Another study showed a shift of the LE to LC transition to higher surface pressures in a binary mixture of DPPC with 5 mol% DSPE-PEG2000, in the presence of C_6F_{14} in the subphase and air in the gasphase [422]. Taking this into consideration, the influence of a fluorinated hydrocarbon in the gas phase on the isotherms cannot be excluded, meaning the isotherms would be slightly shifted to higher transition pressures.

Microbubbles

Figure 3.5 shows the number weighted size distribution of the streptavidin-conjugated microbubbles. The number-weighted mean diameter was 3.6 µm for direct DPPC microbubbles, 4.2 µm for direct DSPC microbubbles, and 5.17-5.22 µm (N = 2 batches) for indirect DSPC microbubbles. The volume-weighted mean diameter was 6.6 µm for direct DPPC microbubbles, 6.4 µm for direct DSPC

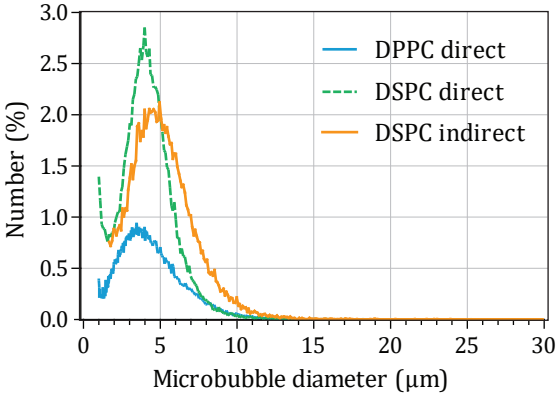

Figure 3.5 Number weighted size distribution of DPPC direct (blue line, N = 1 batch), DSPC direct (green dashed line, N = 1 batch), and DSPC indirect (orange line, representative for N = 2 batches) microbubbles with ternary coating composition containing DSPE-PEG2000 (7.0 mol%) and PEG40-stearate (8.2 mol%) as additional components.

microbubbles, and 7.9-8.4 μm (*N* = 2 batches) for indirect DSPC microbubbles. Direct and indirect DSPC microbubbles had a similar size distribution (span 1.0), while the direct DPPC microbubbles were more polydisperse (span 1.4). The size distributions of the direct microbubbles are in agreement with previously published work [392]. The indirect method resulted in slightly larger DSPC microbubbles than direct DSPC microbubbles, but did not affect the polydispersity.

Ligand distribution in microbubbles

The lipid phase and ligand distribution in the microbubble coating were imaged for direct DPPC (*N* = 50, 2 batches), direct DSPC (*N* = 47, 3 batches), and indirect DSPC microbubbles (*N* = 46, 2 batches) of 1.5-8 μm in diameter. Typical examples of the different types of microbubbles are shown in Figure 3.6. The ligand distribution, representative for the DSPE-PEG2000 distribution, is shown in the left column, the LE phase stained with Rhodamine-DHPE in the middle column, and a composite of both signals is displayed in the right column. The calculated ligand distribution inhomogeneity is shown in Figure 3.7. In concurrence with our previous study [392], the direct DPPC microbubbles had a mostly homogenous ligand distribution (Figure 3.6A, Figure 3.7), while there was a large variability in ligand distribution for the direct DSPC microbubbles ranging from heterogeneous with areas where the ligand was either lacking or enriched (Figure 3.6D), to a more homogenous ligand distribution (Figure 3.6G). Nevertheless, the indirect DSPC microbubbles all had a homogenous ligand distribution (Figure 3.6J, Figure 3.7). No correlation was found between microbubble size and ligand inhomogeneity. A previous study, which focused on phase separation in phospholipid-coated microbubbles processed with different heating-cooling regimes, showed that the ligand was distributed heterogeneously in slowly cooled microbubbles and homogenously in rapidly cooled microbubbles [389]. These microbubbles were coated with a binary mixture of DSPC and DSPE-PEG2000 (9:1) and made by mechanical shaking. In the present study we investigated no heating-cooling regimes, yet we found that a different handling of phospholipids before microbubble production could also result in a more uniform ligand distribution.

Lipid phase distribution in microbubbles

In all types of direct and indirect microbubbles, the lipids were phase-separated resulting in dark domains (*i.e.* LC phase) and bright inter-domain regions (*i.e.* LE phase), when studying the fluorescence of Rhodamine-DHPE (Figure 3.6B, 3.6E, 3.6H, 3.6K). Although the LC domains in the DPPC- and DSPC-based ternary mixture monolayers had different morphologies (Figure 3.2), the LC domains in the microbubble coatings were similar for all types of microbubbles. Fluorescent dyes have been used before to examine domain formation in microbubbles coated with

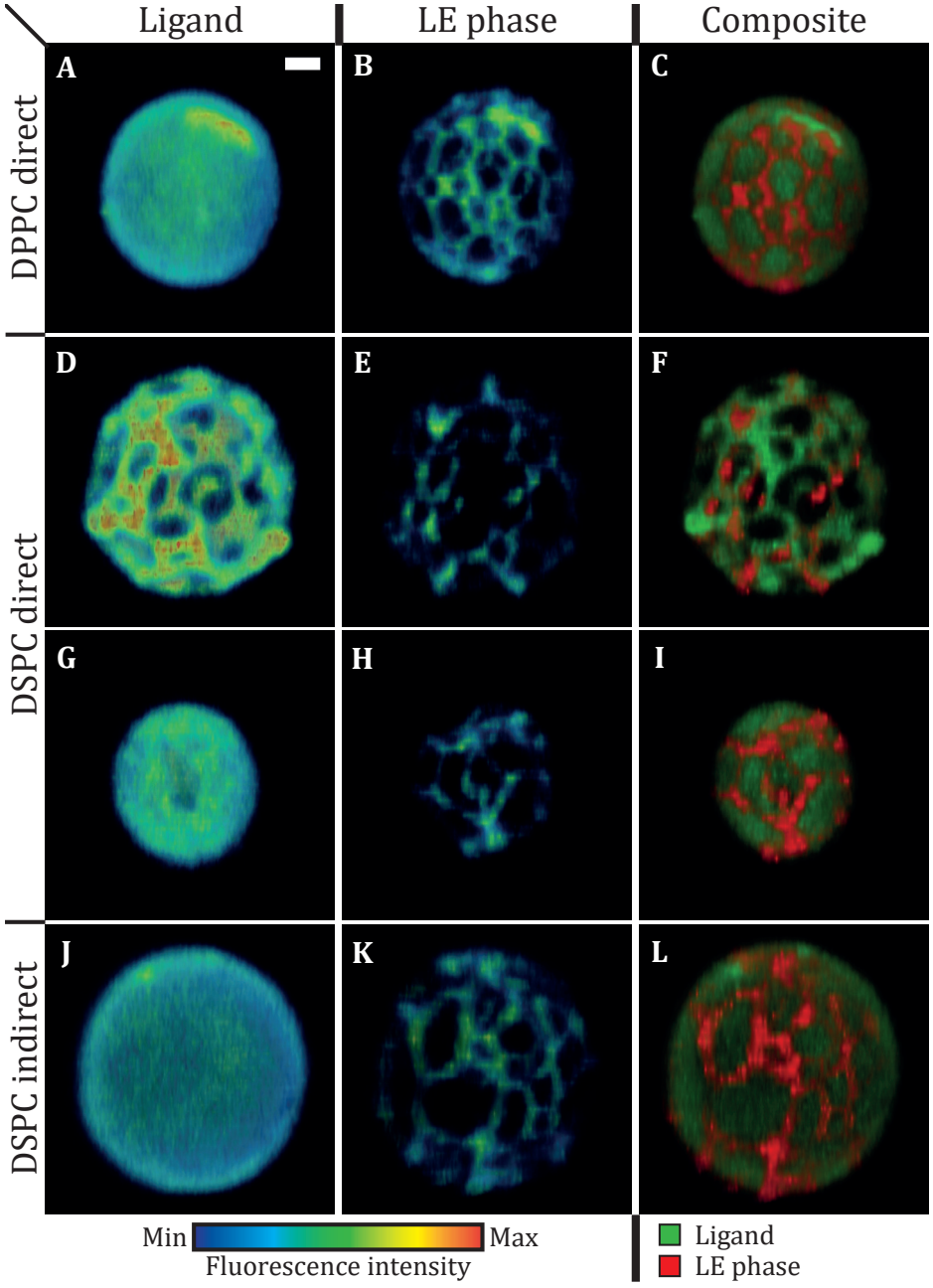

Figure 3.6 Selected views of 4Pi confocal microscopy *y*-stacks of direct DPPC (**A-C**, diameter (*d*) = 4.7 µm), direct DSPC (**D-F**, *d* = 4.9 µm; G-I, *d* = 3.4 µm) and indirect DSPC microbubbles (**J-L**, *d* = 5.3 µm) with ternary coating composition containing DSPE-PEG2000 (7.0 mol%) and PEG40-stearate (8.2 mol%) as additional components. The images show the ligand distribution (**A, D, G, J**; Oregon Green 488), the LE phase (**B, E, H, K**; Rhodamine-DHPE), and the composite view (**C, F, I, L**). Scale bar is 1 µm and applies to all images. Full 3D reconstructions of these examples are provided as Supplemental Videos 3.1-4).

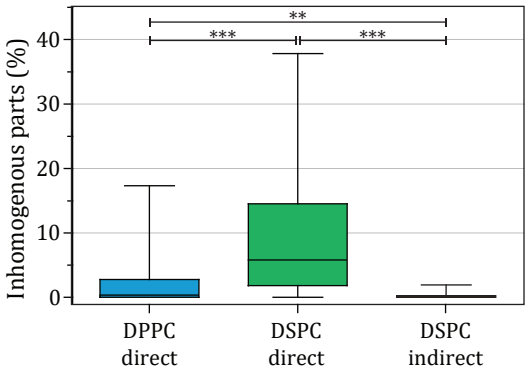

Figure 3.7 Parts classified as inhomogeneous (%) in the ligand distribution of direct DPPC (*N* = 50), direct DSPC (*N* = 47) and indirect DSPC (*N* = 46) microbubbles with ternary coating composition containing DSPE-PEG2000 (7.0 mol%) and PEG40-stearate (8.2 mol%) as additional components. Boxplots show the median, interquartile range, and have whiskers from minimum to maximum. Statistical significance was indicated with $^{**}p<0.01$, $^{***}p<0.001$.

binary mixtures of DPPC and DSPC with PEG40-stearate or DSPE-PEG2000, with a diameter larger than 10 µm [25, 30, 388-390]. In these studies the microstructures in the microbubble coating were tuned by varying the cooling rate after microbubble production, or by varying the pure lipid to PEGylated molecule ratio. To the best of our knowledge, the present study is the first to include microbubbles coated with a ternary mixture and of clinically relevant sizes, namely 1.5-8 µm in diameter.

The domain morphology of microbubbles coated with a ternary mixture presented here resembles that of microbubbles (diameter >5 µm) coated with a binary mixture of DSPC and PEG40-stearate or DSPE-PEG2000 (9:1), despite the use of different fluorescent dyes and microbubble production methods [388, 389]. Others imaged phase separation with epifluorescence or confocal microscopy, in contrast to the high resolution 4Pi confocal microscopy that was used for this study. Previous studies reported that no domain formation was observed in microbubbles with a binary mixture of DSPC and PEG40-stearate (9:1) smaller than 5 µm, even though domains smaller than 5 µm2 were observed in microbubbles larger than 5 µm [25]. However, all microbubbles analyzed for the present study (1.5-8 µm diameter) had condensed domains in the coating. This is likely due to phase separation of the three components: the main lipid component DPPC (in LE/LC phase), or DSPC (in LC phase), PEG40-stearate in LE phase, and DSPE-PEG2000 in LC or LE phase. Microbubbles were mounted in 87% glycerol for 4Pi high-resolution imaging. Monolayer studies at the air/water interface showed that glycerol in the subphase had no effect on the phase behavior below the transition temperature [423]. In our study glycerol was added after microbubble production and the sample was kept at room temperature during imaging experiments. We therefore assume that the glycerol did not have an effect on the molecular structure of the lipid microbubble coating.

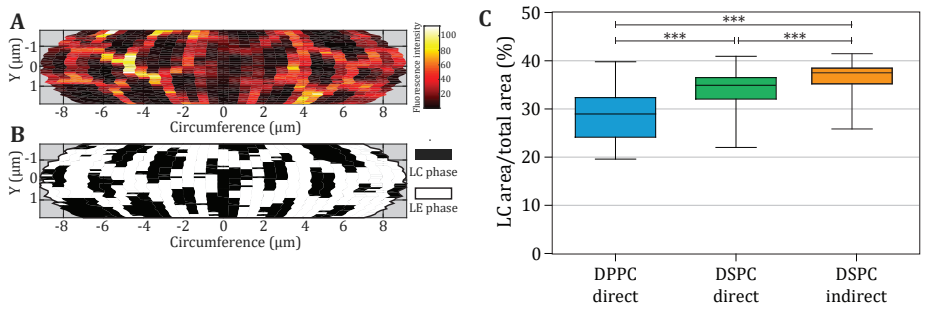

Figure 3.8 A) Example of a heatmap of Rhodamine-DHPE intensity over the analyzed surface area for an indirect DSPC microbubble (d = 5.74 µm). **B**) Thresholded map of (**A**) showing the parts classified as LC area in black. **C**) Size of the LC area (% of total surface area) of DPPC direct (N = 50), DSPC direct (N = 47), and DSPC indirect (N = 46) microbubbles with ternary coating composition containing DSPE-PEG2000 (7.0 mol%) and PEG40-stearate (8.2 mol%) as additional components. Boxplots show the median, interquartile range, and with whiskers from minimum to maximum. Statistical significance was indicated with *** for p<0.001.

The Rhodamine-DHPE fluorescence intensity ($I_{part\text{-}Rhod}$) and the surface area classified as LC phase were plotted as a function of the axial plane and the corresponding circumference (Figure 3.8A, 3.8B). The LC area fraction is presented in Figure 3.8C, as the percentage of the total surface area analyzed per microbubble. The mean percentage of LC area was significantly lower for the direct DPPC microbubbles than for both types of DSPC microbubbles. This was expected since DSPC is always in the LC phase, according to our monolayer results presented above and literature [27]. The direct DSPC microbubbles had a significantly smaller LC phase area than the indirect DSPC microbubbles. Since DSPC is always in the LC phase and the other PEGylated components were the same, there must be a difference in the localization of these PEGylated components causing the differences in LC area between direct and indirect DSPC microbubbles. No correlation was found between microbubble size and LC phase area. These results indicate that the lipid handling affects the phase separation between different components. Previous studies that investigated domain characteristics focused mainly on the effect of cooling rates in microbubbles coated with binary mixtures of DSPC with PEG40-stearate [30, 388], yet the microbubbles in those studies were much larger (diameter >20 µm) than the microbubbles investigated here.

The right column of Figure 3.6 shows composites of the lipid phase and ligand distribution in the microbubble coating. For the direct DPPC and indirect DSPC examples, the green fluorescent ligand is distributed homogenously over the fluorescently stained LE phase and the LC phase (Figure 3.6C, 3.6L). For the direct DSPC microbubbles two examples are shown to illustrate the variability within this group: heterogeneous distribution where the ligand is colocalized with the LE phase (Figure 3.6F), and homogenous ligand distribution similar to the other

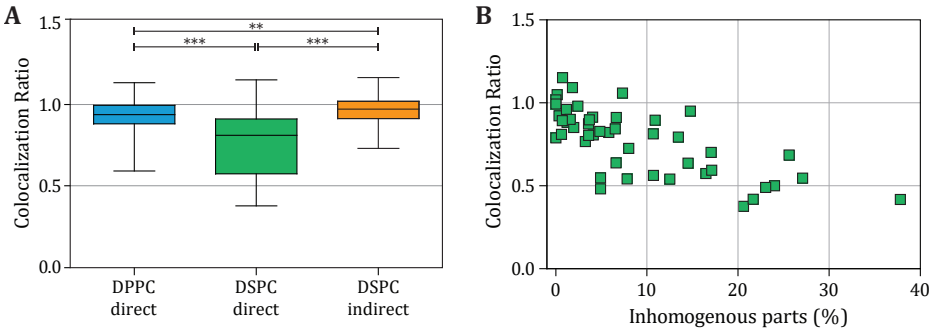

Figure 3.9 A) Colocalization ratio of direct DPPC (*N* = 50), direct DSPC (*N* = 47), and indirect DSPC (*N* = 46) microbubbles with ternary coating composition containing DSPE-PEG2000 (7.0 mol%) and PEG40-stearate (8.2 mol%) as additional components. Boxplots show the median, interquartile range, and with whiskers from minimum to maximum. Statistical significance was indicated with ***p<0.001, **p<0.01. **B**) Colocalization ratio as a function of the parts classified as inhomogeneous (%) ligand distribution for direct DSPC microbubbles (*N* = 47).

types of microbubbles (Figure 3.6I). Co-localization of the DSPE-PEG2000 with the LE phase has been reported before for a single example of a ~20 µm diameter microbubble coated with a binary mixture of DSPC and DSPE-PEG2000 (9:1) without quantification [389]. In our study we quantified the colocalization between the LC phase (no Rhodamine-DHPE fluorescence) and DSPE-PEG2000, the component where the fluorescent ligand Oregon Green 488 is attached to, which is presented in Figure 3.9A. For the direct DPPC and indirect DSPC microbubbles the mean colocalization ratio was approximately 1, indicating that the amount of DSPE-PEG2000 in the LC phase domains was equal to the amount of DSPE-PEG2000 in the inter-domain region. The colocalization ratio was significantly lower for the direct DSPC microbubbles, indicating that there was less DSPE-PEG2000 in the LC phase domains than in the inter-domain regions. For these direct DSPC microbubbles, there was a negative correlation between the percentage of inhomogeneity in the ligand distribution and the colocalization ratio (Figure 3.9B). This suggests that in microbubbles with a heterogeneous ligand distribution, the ligand was depleted in the LC domains.

Based on the difference we found in LC area and ligand distribution between the direct and indirect DSPC microbubbles, we expect that the DSPE-PEG2000 component is either excluded from pre-formed LC domains (for direct method, Figure 3.6D-F, Supplemental Video 3.2) or equally distributed over the LE and LC phase (for indirect method), depending on the phospholipid handling prior to the microbubble production. This is in accordance with the IRRAS results indicating that the PEGylated components were distributed over both the LE and LC phase, whereby we assume that the monolayer at the air/buffer interface was in thermodynamic equilibrium. With the indirect method for microbubble production, all components

were dissolved and mixed in organic solvent. After evaporation of the solvent, the dried film of mixed lipids was dispersed in PBS buffer using a sonicator bath and a probe sonicator at low power. With the direct method, in contrast, the components were each dispersed in PBS buffer without use of sonication, and then mixed together. Therefore, it is likely that the lipids in the precursors of the microbubbles, *i.e.* in the liposomes and micelles [21], were more uniformly mixed with the indirect method, than with the direct method. The lipids spontaneously self-assemble around the newly formed gas microbubbles during probe sonication [11, 22], likely through membrane spreading [424]. In other words, the indirect DSPC microbubbles are more in equilibrium than the direct DSPC microbubbles. This is in contrast to previous studies on monolayers at the air/water interface, which found that DSPC and DSPE-PEG2000 were immiscible at all surface pressures [29].

For a fair comparison, the 4Pi confocal microscopy experiments were performed at room temperature, in accordance with all microscopy studies on lipid and ligand distribution on microbubble coatings. However, when developing microbubbles for *in vivo* applications, experiments at body temperature will be more translatable to human applications. Another important aspect for *in vivo* applications is the ligand distribution, since a more homogenous distribution could result in higher targeting efficiency. While the homogenous ligand distribution makes direct DPPC microbubbles a good candidate for *in vivo* applications, they are acoustically less stable than direct DSPC microbubbles [45]. Our studies now show that homogenous ligand distributions are also possible for DSPC-based microbubbles. Future studies on the acoustical behavior of indirect DSPC microbubbles may give insight on the effect of LC area and ligand homogeneity on the acoustical stability, diversity in response to ultrasound, and efficacy to enhance molecular imaging and local drug delivery in a safe and effective way.

3.4 Conclusions

We investigated the ligand distribution and lipid phase state in microbubbles coated with a ternary phospholipid-based mixture of clinically relevant sizes. For better understanding of the lipid phases, we studied the lipid phase behavior in monolayers at the air/water interface of the same ternary mixtures that coated the microbubbles. Isotherms showed that DPPC had a transition from LE to LC phase during monolayer compression at ~5 mN/m, which shifted to lower surface pressures in mixtures with DSPE-PEG2000 only, or DSPE-PEG2000 and PEG40-stearate. In contrast, DSPC was always in the LC phase, also in the binary and ternary mixtures we studied. All binary and ternary mixtures had a transition plateau around 10-12 mN/m. As confirmed by IRRAS, this plateau was due to a conformational transition (mushroom to brush)

in the PEGylated components. Based on 4Pi high-resolution imaging, direct DPPC microbubbles had a homogenous ligand distribution, with a significantly smaller LC phase area than the DSPC-based microbubbles. The lipid handling prior to microbubble production influenced both the ligand distribution and the LC phase area in the DSPC-based microbubbles. Microbubbles made by the direct method had a heterogeneous ligand distribution, while the ligand colocalized with the LE phase area. Microbubbles made by the indirect method had a significantly larger LC phase area and homogenous ligand distribution. By controlling the ligand distribution and microstructures in the microbubble coating, we can better understand the underlying mechanisms of targeting. This will lead to tailored microbubble formulations for specific clinical applications.

Acknowledgments—The authors are grateful to Prof. A. L. Klibanov from the University of Virginia, Cardiovascular Division, Charlottesville, Virginia, USA for discussions about the microbubble preparation. The authors thank the Erasmus Optical Imaging Centre of Erasmus MC for use of their facilities, and Dr. Gert van Cappellen and Alex Nigg for their help.

Funding

This project was supported in part by the Phospholipid Research Center, Heidelberg, Germany; and the Thoraxcenter of Erasmus MC. CS and AB thank Deutsche Forschungsgemeinschaft (DFG) for financial support through the grant FOR1145.

Supporting information

The Supporting Information is available free of charge at https://pubs.acs.org/doi/10.1021/acs.langmuir.9b03912.

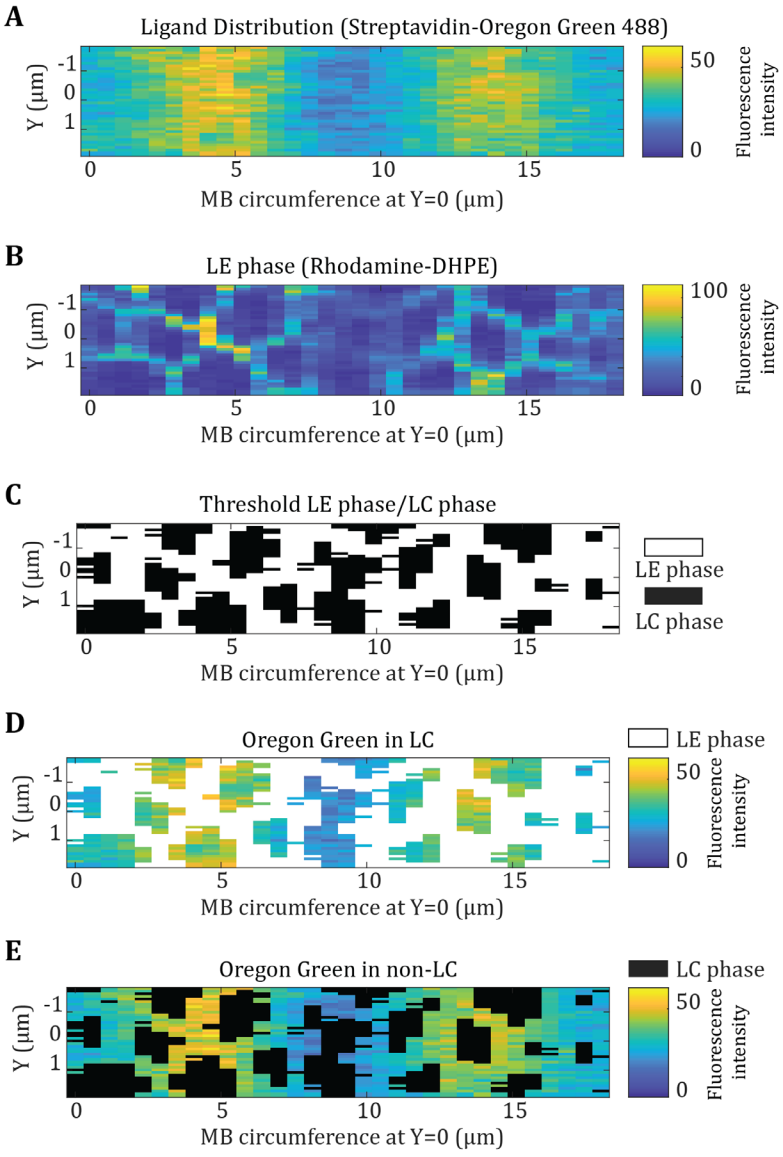

Supplemental Figure 3.1 Typical example of 2D heatmaps of an indirect DSPC microbubble with a diameter of 5.7 µm. Mean fluorescence pixel intensity (I_{part}) of (**A**) the ligand (Streptavidin-Oregon Green 488) and (**B**) the LE phase (Rhodamine-DHPE). **C**) Thresholded image with LC phase area in black and inter-domain region in white. Masked image of ligand fluorescence intensity in (**D**) LC phase area (median 34.26) and (**E**) inter-domain region (median 34.13, colocalization ratio 1.00).

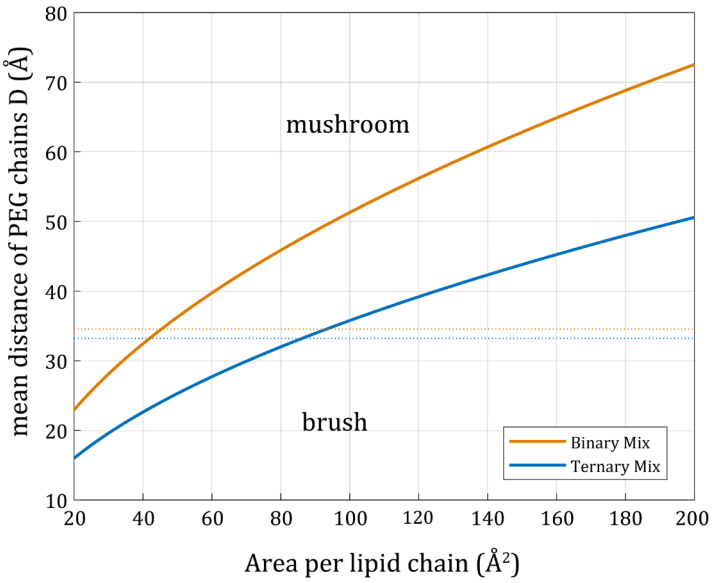

Supplemental Figure 3.2 Theoretical calculation of the mushroom to brush transition for the binary and ternary mixture. The solid lines are the calculations using Equation 2, $D=\sqrt{(A_{lipid}/m)}$ from Abou-Saleh et al. [32], where D is the mean distance between PEG chains, A_{lipid} the area occupied per lipid chain, and *m* the mole fraction of PEG/lipid chain. For the binary mixture (orange solid line), an *m* of 0.038, *i.e.* 7.6 mol% PEG / (2*100) lipid chains, was used while this was 0.0781 for the ternary mixture (15 mol% PEG / (2*85 + 2*7 + 1*8) lipid chains) (blue solid line). The dotted lines show the Flory radius calculated from Equation 1, $R_F=aN^{(3/5)}$ from Abou-Saleh et al [32], where R_F is the Flory radius of the grafted PEG, *a* the size of the monomer (=0.35 nm), and *N* is the number of monomers per chain. For the binary mixture (orange dotted line), an *N* set to 2000 / 44 (mean molecular weight of the Polymer chain / monomer molecular weight), while for the ternary mixture (blue dotted line), which contains PEG chains of slightly different length a weighted average of *N* = 44.24 was used (8/15 * 40 + 7/15*(2000/44)). The mushroom to brush transition is predicted where dotted and solid lines intersect, *i.e.* where the mean PEG chain distance becomes smaller than the Flory radius.

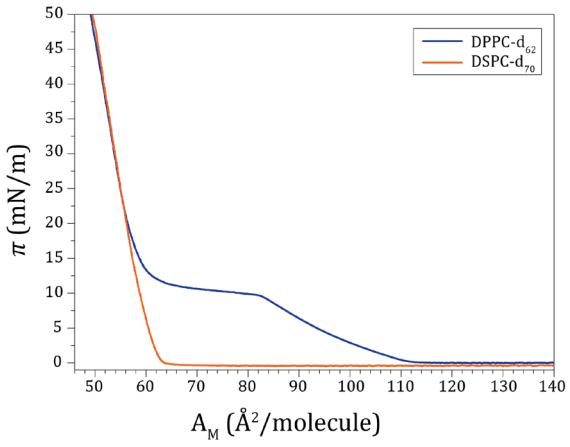

Supplemental Figure 3.3 Compression isotherms of pure DPPC-d_{62} and DSPC-d_{70} at the air/water interface. Graph of surface pressure (π) as a function of the area per molecule (A_M). Experiments performed at 20 °C.

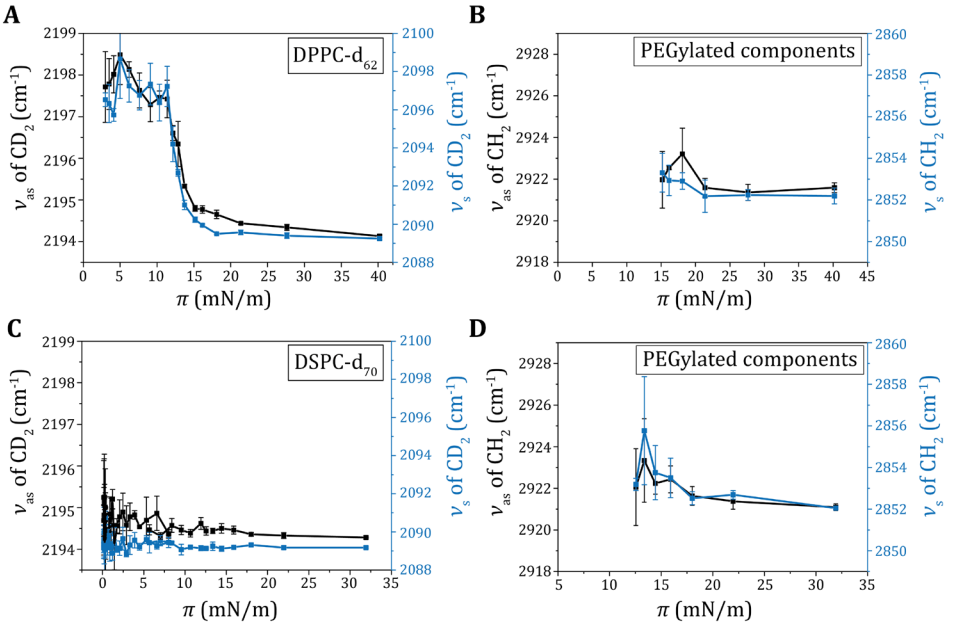

Supplemental Figure 3.4 Wavenumbers ($\tilde{\nu}$) of antisymmetric (ν_{as}) and symmetric (ν_s) CD_2 (**A, C**) and CH_2 (**B, D**) stretching vibration of the ternary mixtures DPPC-d_{62}/DSPE-PEG2000/PEG40-stearate (**A, B**) and DSPC-d_{70}/DSPE-PEG2000/PEG40-stearate (**C, D**) (84.8:7.0:8.2 mol%) as function of the surface pressure (π). Note the difference in *x*-axis of 3A, 3B, 3C, and 3D.

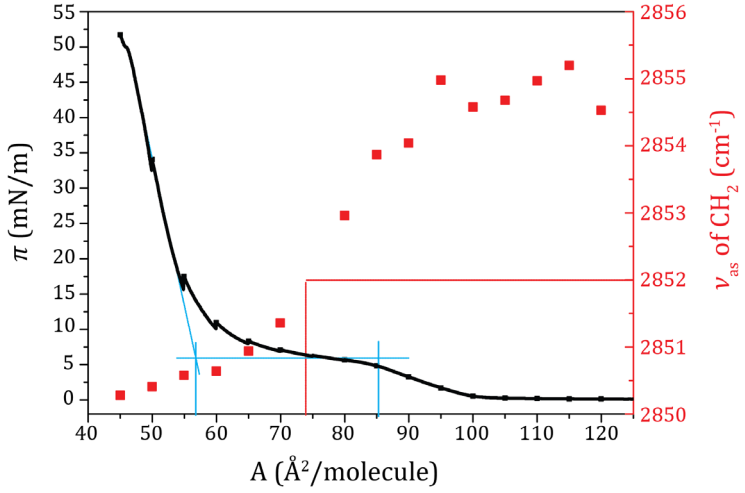

Supplemental Figure 3.5 Compression of a pure DPPC monolayer with simultaneous recording of the compression isotherm (black line, left *y*-axis) and IRRA spectra. Wavenumbers of antisymmetric CH_2 stretching vibrations (ν_{as} of CH_2) are shown as red symbols (right *y*-axis). The blue perpendicular lines indicate the limits of the LE to LC phase transition plateau. The phase transition pressure is marked with a blue horizontal line at ca. 6 mN/m. The position of ν_{as} at 2852 cm^{-1} (marked with a red line) is indicative for a partly ordered monolayer state with LE and LC phase co-existence, where the majority of the lipids is still in the LE state and the minority in the LC state. The LE/LC ratio as estimated from the position in the transition plateau was approximately 1.5 (or 60 % of the lipids are in LE, 40% are in LC).

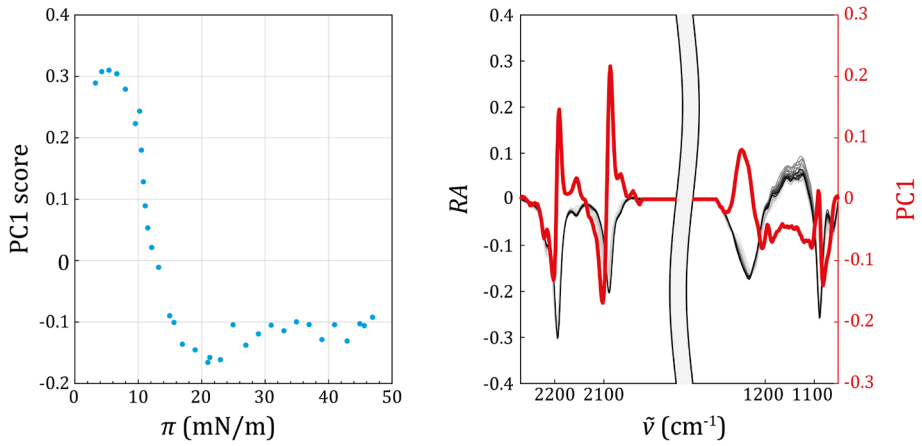

Supplemental Figure 3.6 Principal component analysis of IRRA spectra recorded during the compression of a pure DPPC-d_{62} monolayer. IRRA spectra were simultaneously analyzed in the range of the headgroup vibrations (1050 – 1300 cm^{-1}) and the CD_2 stretching vibrations (2020 – 2270 cm^{-1}) after separate vector normalization in the two respective ranges. The left panel shows the PC1 scores as function of the surface pressure (π). The right panel shows the reflection absorption (*RA*) as a function of the wavenumber (ν) for different surface pressures (low – light grey, to high – dark grey, left *y*-axis), and the PC1 as a function of the wavenumbers ($\tilde{\nu}$) (red line, right *y*-axis).

Supplemental videos

Supplemental video 3.1 3D render of direct DPPC microbubble (diameter = 4.7 µm) coated with DPPC, PEG40-stearate, and DSPE-PEG2000 (84.8:8.2:7.0).

Supplemental video 3.2 3D render of direct DSPC microbubble (diameter = 4.9 µm) coated with DSPC, PEG40-stearate, and DSPE-PEG2000 (84.8:8.2:7.0).

Supplemental video 3.3 3D render of direct DSPC microbubble (diameter = 3.4 µm) coated with DSPC, PEG40-stearate, and DSPE-PEG2000 (84.8:8.2:7.0).

Supplemental video 3.4 3D render of indirect DSPC microbubble (diameter = 5.3 µm) coated with DSPC, PEG40-stearate, and DSPE-PEG2000 (84.8:8.2:7.0).

4

Lipid phase distribution and acoustic response of DSPE-based microbubbles

Simone A.G. Langeveld, Gonzalo Collado-Lara, Gerrit J.W. Wiggers, Antonius F.W. van der Steen, Nico de Jong, Klazina Kooiman

Based on:
2021 IEEE International Ultrasonics Symposium, 2021

Abstract

Microbubbles (MBs) are versatile ultrasound contrast agents that can be used for ultrasound molecular imaging and targeted drug delivery. However, a uniform and controlled response to ultrasound is essential for safe and effective use of targeted MBs in the clinic. It is suggested that the heterogeneous lipid distribution of currently available MB formulations causes variability in acoustic response. Hence, the objective of this study was to develop and characterize a new MB formulation with all coating components miscible and in the same lipid phase. MBs with 1,2-distearoyl-*sn*-glycero-3-phosphoethanolamine (DSPE) as main lipid were produced by probe sonication (MB_{probe}) or by amalgamation, with 10% (MB_{shake}-10) or 30% (MB_{shake}-30) propylene glycol (PG). The lipid phase distribution, shelf-life, and acoustic attenuation were investigated. MB_{probe} and MB_{shake}-30 had a homogeneous lipid distribution, while MB_{shake}-10 had circular condensed phase domains. For all MBs the condensed phase increased over time. The PG concentration also affected the size and concentration: MB_{shake}-30 had the largest mean diameter 20 min after production, while MB_{shake}-10 had a tenfold higher concentration. All types of MBs had a short shelf-life stability, decreasing in size during the first hour post-production. The coating composition had a more significant effect on size and concentration than the production method. The MBs had a size-dependent resonance behavior and MB_{shake}-10 and MB_{shake}-30 had the highest peak attenuation, revealing a stabilizing role for PG in these MB formulations. Even though the *in vivo* applications for the DSPE-based MBs may be limited because of the short shelf-life stability, the newly developed MB formulations are interesting candidates for further studies on the effect of lipid phase distribution on acoustic behavior of MBs.

Keywords—Ultrasound contrast agents; Phospholipid coating; Lipid distribution; Attenuation; Propylene glycol

4.1 Introduction

Phospholipid-coated MBs can be used for numerous applications, including ultrasound molecular imaging and targeted drug delivery [425]. These applications, however, require MBs that respond to ultrasound in a uniform and controlled manner. Studies on the mechanism of sonoporation have demonstrated the delicate balance between reversible pore formation and irreversible effects including non-resealing pores in the membrane, depending on the oscillation amplitude of vibrating MBs [58]. Commercially available MBs are currently tailored for diagnostic use and respond to ultrasound in a non-uniform way [45]. Furthermore, single MBs of the same size have been shown to respond differently to the same ultrasound pulse [426].

All the studies mentioned above have used 1,2-distearoyl-*sn*-glycero-3-phosphocholine (DSPC)-based MBs. In the phospholipid monolayer coating of a MB, DSPC is always in the liquid condensed (LC) phase, whereas PEGylated components are mostly in the liquid expanded (LE) phase. Due to the co-existence of these two immiscible phases, DSPC-based MBs have distinct microstructures in their coating [427]. The MBs acoustic response is dominated by the viscoelastic properties of their coating [428]. Thus, since these microstructures are highly variable between MBs, it is possible they modify the coating viscoelasticity, generating a non-uniform response to ultrasound. Other lipid compositions, which are miscible and in the same lipid phase, could yield a homogeneous coating, resulting in MBs with a predictable response to ultrasound.

Characterizations of monolayers composed of phospholipids with phosphatidylcholine (PC) or phosphatidylethanolamine (PE) headgroups have revealed a different phase behavior for PE than for PC phospholipids [429]. Due to the polar headgroup, PE phospholipids are able to form intermolecular hydrogen bonds, which is desirable to form a stable MB coating. The aim of this study was to investigate the feasibility of using the PE lipid 1,2-distearoyl-*sn*-glycero-3-phosphoethanolamine (DSPE) as main lipid component. MBs coated with a ternary mixture of DSPE, PEG40-stearate, and DSPE-PEG2000 were produced by probe sonication or by amalgamation with 10% or 30% propylene glycol (PG). Lipid phase distribution, shelf-life stability, and acoustic response to ultrasound were investigated.

4.2 Methods

Microbubble production

DSPE (Lipoid GmbH, Ludwigshafen, Germany), PEG40-stearate (Sigma-Aldrich, Zwijndrecht, the Netherlands), and DSPE-PEG2000 (Avanti Polar Lipids, Alabaster, Alabama, USA) were dissolved in chloroform/methanol (9:1 vol/vol) and mixed with a ratio of 84.8/8.2/7.0 mol% (0.5/0.16/0.14 mg/mL). A lipid film was obtained by evaporation of the solvent with argon gas (Linde Gas Benelux, Schiedam, the Netherlands) and freeze drying for two hours. Dried lipid films were rehydrated with C_4F_{10} (F2 Chemicals, Preston, UK) saturated phosphate buffered saline (PBS) solution to a concentration of 3.74 mg/mL for probe sonicator MBs (MB_{probe}) or 0.88 and 1.14 mg/mL for VialMix MBs (MB_{shake}). After addition of 0.01 mol% Lissamine rhodamine B 1,2-dihexadecanoyl-*sn*-glycero-3-phosphoethanolamine (rhodamine-DHPE, Thermo Fisher, Waltham, Massachusetts, USA), lipid solutions were placed in a sonicator bath for 10 min and finally the lipid film was dispersed using a probe sonicator (Sonicator Ultrasounic Processor XL2020, Heat Systems, Farmingdale, NY, USA) for 5 min at low power (setting 3). MB_{probe} were produced as described

previously [426], by probe sonication at high power (setting 10) under constant flow of C_4F_{10} for 1 min. For MB_{shake}, the dispersed lipid solution was divided over glass vials (volume 2.5 mL) with 0.1 mL (MB_{shake}-10PG) or 0.3 mL (MB_{shake}-30PG) PG (Sigma-Aldrich, Zwijndrecht, the Netherlands) to a final volume of 1 mL with lipid concentration 0.8 mg/mL and the headspace was filled with C_4F_{10} gas. MB_{shake} were produced by amalgamation using VialMix (Bristol-Myers Squibb Medical Imaging, Inc., North Billerica, Massachusetts, USA) for 45 seconds. After production, all MBs were stored at 4 °C for at least 15 min. For the acoustic attenuation measurements, DSPC-based MBs were produced by amalgamation as described previously (F-type, [400, 430]), to compare with the new formulations.

Physicochemical characterization

MB_{probe} were first washed by flotation: 3 mL MB suspension was placed in a syringe, after 45 min the subnatant was drained and MB_{probe} were resuspended in 1 mL PBS saturated with C_4F_{10}. To study the lipid phase distribution, MB samples were taken every 30 min up to 2 h post-production (for MB_{shake}) or post-washing (for MB_{probe}), mounted on an object glass in 87 vol% glycerol, and imaged using a custom-built confocal microscope (Nikon Instruments, Amsterdam, the Netherlands [431]). Z-stacks with 0.3 µm steps were acquired using a 60× water immersion (WI) objective with a 561 nm laser exciting rhodamine-DHPE and detecting emitted light in a 595/50 nm channel. MBs were scored manually for presence of LC domains. To study the stability, *i.e.* shelf-life, of MBs in high concentration (*i.e.,* stock solution), the size distribution and concentration were measured over time with a Coulter Counter Multisizer 3 (Beckman Coulter, Mijdrecht, the Netherlands). A 50 µm aperture tube was used to quantify particles between 1 and 30 µm. At each time point one sample was measured 3 times with approximately 1 min in between. Samples were measured every 20 min up to 2 h post-production for MB_{shake}-10PG and MB_{shake}-30PG, while MB_{probe} were measured every 20 min up to 1.5 h post-production, plus once at 24 h post-production.

Acoustical characterization

To characterize the acoustic attenuation of MBs, a poly(methyl methacrylate) (PMMA) water tank with two single-element focused transducers was used [432]. Transducer 1 (3.5 MHz, 80% -6dB bandwidth, V381, Olympus, Tokyo, Japan) was used to generate acoustic waves that were later received by transducer 2 (3.5 MHz, 75% -6dB bandwidth, V380, Olympus, Tokyo, Japan). A sample container (2×2×10 cm) with 20 µm polyester walls was filled with PBS and placed at the acoustic foci (75 mm) of the co-aligned transducers. An arbitrary waveform generator (Tabor ww2571a, Tabor Electronics, Nesher, Israel) was connected to an amplifier (38 dB,

ENI 310L, Electronics and Innovation, New York, USA) and used to drive Transducer 1. Signals from Transducer 2 were recorded with a digital oscilloscope at a 125 MHz sampling rate (15 bits, PicoScope 5443D, Pico Technology, Cambridgeshire, United Kingdom). The acoustic response of MBs was investigated using single-cycle broadband pulses with a center frequency of 3.5 MHz and peak negative pressure (PNP) of 15 kPa. The PNP was calibrated prior to the experiments using a 0.2-mm needle hydrophone (Precision Acoustics, Dorchester, UK). Before adding the MBs to the container, a measurement was taken as a reference for the attenuation. Next, three MB samples with a concentration of 1.0 $\times 10^5$ MBs/mL were measured. All measurements were performed at room temperature within 20 min after Coulter Counter measurements (*i.e.* 60 min post-production for MB_{probe} and 20 min post-production for MB_{shake}).

4.3 Results

Physicochemical characterization

Figure 4.1 shows typical examples of the lipid phase distribution in the coating of MB_{probe}, MB_{shake}-10PG, and MB_{shake}-30PG. At 30 min after washing, 74% of MB_{probe} (N = 34) had a homogeneous lipid phase distribution (Figure 4.1A), however, this number decreased to 11% (N = 9) after 2 h. MB_{probe} with heterogeneous lipid phase distribution had circular LC phase domains which grew in size and number over time. MB_{shake}-10PG had a heterogeneous lipid phase distribution from the first time point on, with circular LC phase domains in black (Figure 4.1B). For the MB_{shake}-30PG, 50% (N = 10) had a fully homogeneous lipid phase distribution (Figure 4.1C) at 30 min post-production, while this number decreased to 30% (N = 10) after 2 h. MB_{shake}-30PG with heterogeneous lipid phase distribution had LC phase domains in different sizes, both smaller and larger than those shown in Figure 4.1B.

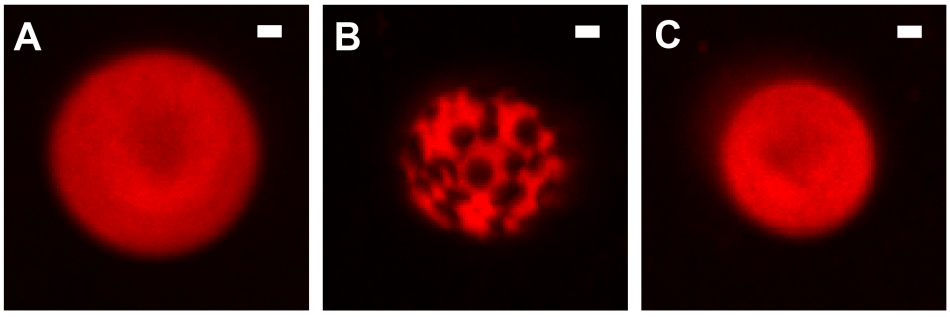

Figure 4.1 Lipid phase distribution in coating of MB_{probe} (**A**), MB_{shake}-10PG (**B**), and MB_{shake}-30PG (**C**), stained with Rhodamine-DHPE (0.01 mol%, red), shown as maximum intensity projection of confocal *Z*-stack. Scale bars are 1 µm. MB samples shown here were taken 30 min post-production for MB_{shake} (10% and 30% PG) and 30 min post-washing for MB_{probe}.

Figure 4.2 presents the size and concentration of DSPE-based MBs over time. MB_{probe} had a mean diameter of 3 µm at the first time point measured after washing, *i.e.* 70 min post-production (Figure 4.2A). The mean size decreased over time and remained stable at 2 µm. MB_{shake}-10PG initially had a smaller mean diameter than MB_{shake}-30PG (Figure 4.2A). At 40 min post-production both types of MB_{shake} decreased in size to approximately 2 µm and remained stable up to 120 min post-production. The mean diameter of MB_{probe} at 70 min post-production was comparable to that of MB_{shake}-10PG at 20 min post-production, for both the first time point measured. MB_{shake}-30PG had a larger mean diameter at the first time point measured. The concentration of MB_{probe} followed the same trend as the size; it decreased until 100 min post-production and then remained stable (Figure 4.1B). The concentration of MB_{shake}-10PG was tenfold higher than the concentration of MB_{shake}-30PG (Figure 4.1B). For both types of MB_{shake} the concentration in stock solution was relatively stable over time, although the standard error of the mean (SEM) was notably larger for MB_{shake}-10PG. The concentration of MB_{shake}-10PG decreased during the three measurements, whereas the concentration of MB_{shake}-30PG remained stable. The concentration of MB_{probe} was slightly higher than the concentration of MB_{shake}-30PG, but MB_{shake}-10PG had a much higher concentration. Additionally, MB_{probe} were measured 24 h post-production to check for overnight stability, however, no measurable amount of MBs was present in the sample at this time point.

Acoustical characterization

The attenuation spectra from 1 to 5 MHz of MB_{probe}, MB_{shake}-10PG, MB_{shake}-30PG, and DSPC-based MB_{shake} are shown in Figure 4.3. MB_{probe} had a peak attenuation at 2.2 MHz (Figure 4.3A) while MB_{shake}-10PG had a peak attenuation at 2.6 MHz (Figure 4.3B). MB_{shake}-30PG had no clear peak attenuation, although the attenuation

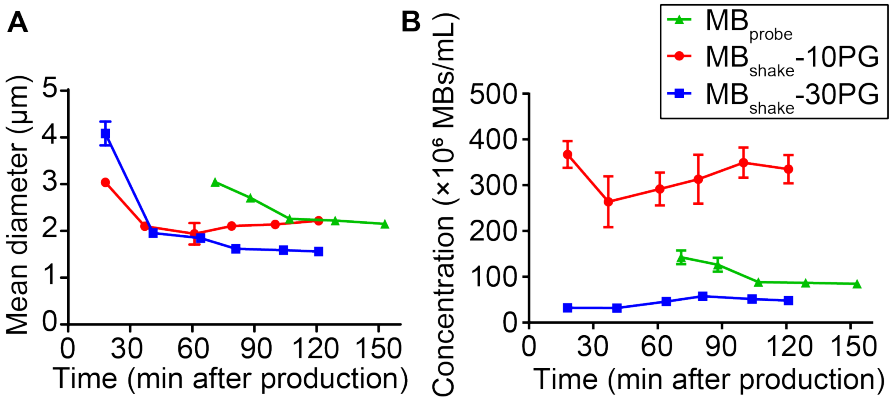

Figure 4.2 Microbubble (MB) shelf-life stability over time. **A**) Size (mean diameter in µm) over time (in min post-production). **B**) Concentration (×10^6 MBs/mL) over time (in min post-production). All datapoints are the mean from *N*=3 shown with the standard error of the mean (SEM).

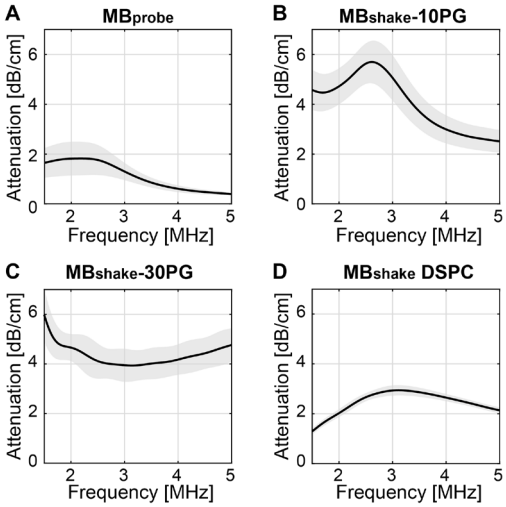

Figure 4.3 Attenuation (dB/cm) of broadband measurements at 3.5 MHz and 15 kPa PNP of MB_{probe} (A), DSPE-based MB_{shake}-10PG (B), DSPE-based MB_{shake}-30PG (C), and DSPC-based MB_{shake} (F-type) (D). The black line represents the average and the grey shaded areas indicate the range of 3 independent measurements.

was increased at frequencies below 2 MHz (Figure 4.3C). DSPC-based MB_{shake} had a peak attenuation at 3.1 MHz (Figure 4.3D). These results show the echogenicity of the presented formulations. Since the acoustic measurements were done within 20 min after the Coulter Counter measurements, the same size distribution can be assumed: MB_{probe} and MB_{shake}-10PG had the same mean diameter of 2.9 µm while MB_{shake}-30PG were larger with 4.4 µm and DSPC-based MB_{shake} were smaller with 2.1 µm.

4.4 Discussion

DSPE-based MBs with a homogeneous lipid phase distribution were successfully produced by probe sonication and by amalgamation. For the MB_{shake} formulations, PG was chosen as co-surfactant because it has been shown to increase MB stability [400] and the amount of lipids incorporated in the MB coating [433]. Interactions between PG and a hydrated phospholipid bilayer have been investigated previously [434]. While the main lipid in that study, 1,2-dipalmitoyl-*sn*-glycero-3-phosphatidylcholine (DPPC), was different from the DSPE lipid used in the present study, the disordering effect on the phospholipid bilayer is in agreement with the lipid phase distributions observed in MBs: with an increasing amount of PG, a decreased LC phase area was observed (Figure 4.1B, C). This indicates that the phospholipid molecules were in a more disordered state with 30% PG. Phospholipid molecules in a more disordered state, that is LE phase, have a larger area per molecule. This may have partly caused the larger size of MB_{shake}-30PG compared to MB_{shake}-10PG at the first time point (Figure 4.2A). A higher viscosity of the solution during amalgamation may have also played a role in the size difference between MB_{shake}-10PG and MB_{shake}-30PG.

Based on phospholipid monolayer studies with pure DSPE, the phospholipid is expected to be in the LC phase [435], which is in contrast with the homogeneous lipid distribution we observed at 30 min post-washing in MB_{probe} and 30 min post-production in MB_{shake}-30PG. This may be influenced by the emulsifiers PEG40-stearate and DSPE-PEG2000, as the addition of either of these emulsifiers resulted in a different compressibility in DSPC-based monolayers [25], suggesting that the addition of these emulsifiers can modify the lipid phase behavior. In all MB types investigated in the present study, the LC phase area increased over time, indicating that the DSPE molecules present in the MB coating were compressed to a smaller surface area. This is in agreement with the observed decrease in size (Figure 4.2A), likely caused by a loss of gas from the MB core.

Previous studies focused on the lipid phase distribution of MBs with main lipid DSPC that were produced by the same probe sonication method and coated with the same ternary mixture, that is main lipid/PEG40-stearate/DSPE-PEG2000 in 84.8/8.2/7.0 molar ratio [427]. These DSPC-based MBs had a heterogeneous lipid phase distribution with distinct LC phase domains. The difference in lipid phase distribution with the MB_{probe} from the current study can only be explained by the difference in main lipid.

The size and concentration measurements indicate that the shelf-life stability was limited, as all MB types decreased in size during the first 60 min (*i.e.* 3 time points) measured. Previous studies comparing the size and concentration of DSPC-based MBs found larger diameters for MBs produced by sonication than those produced by amalgamation [400], in contrast to the comparable size found for MB_{probe} and MB_{shake}-10PG in the current study. Previously, it was suggested that other factors than production method, such as the coating composition and gas core, may affect the MB size. This is confirmed by the results from the present study (MB_{probe}: mean diameter 3 µm, 0.15 $\times 10^9$ MBs/mL), as the only difference with MB type A investigated by Daeichin et al [400, 430] (mean diameter 1.9 µm, 1.9 $\times 10^9$ MBs/mL) was the use of DSPE instead of DSPC as main lipid component, while the size and concentrations differ considerably.

It has been shown that the acoustic behavior of MBs is influenced by the phospholipid packing of the MB coating as the lipid density or phase distribution determines the stiffness and viscosity [43, 436]. Although MB_{probe} and MB_{shake}-10PG had a peak attenuation in the same range of frequencies, the attenuation curve of MB_{probe} was broader (Figure 4.3A,B). These two MB types had a similar size (mean diameter 2.9 µm), while the lipid phase distribution was dramatically different as MB_{probe} had a homogeneous lipid distribution and MB_{shake}-10PG had a heterogeneous lipid distribution. This difference in shell structure could possibly lead to the differences in

the attenuation spectra. MB_{shake}-30PG had a larger mean diameter than all other MB types, leading to an increased attenuation at lower frequencies (Figure 4.3C), which is expected for larger sized MBs [44]. MB_{shake}-10PG and MB_{shake}-30PG had a higher attenuation than MB_{probe}, indicating that PG might play a role in stabilizing the MB formulations. The previously characterized and established DSPC-based MB_{shake} (F-type MB) [400, 430, 437] was included for comparison to the newly developed MB formulations. The DSPC-based MB_{shake} had the smallest mean diameter and lowest peak attenuation at the highest frequency, which is typical size-dependent resonance behavior [44].

There are indications that the variability in lipid distribution between MBs at least partly explains the variability in acoustic response of MBs of the same size [426]. Thus, with the aim of obtaining a uniform response, DSPE-based MB_{probe} and MB_{shake}-30PG are interesting candidates for investigation of the single MB acoustic behavior, as these MBs have a homogeneous lipid distribution. Furthermore, the MB_{shake}-10PG and MB_{shake}-30PG can be compared to investigate the effect of LC phase domains on the acoustic behavior. In practice, however, these are challenging experiments as all three types of MBs change over time with decreasing size and increasing LC phase area in the MB coating, leaving only a short time window to acquire data. Additionally, the lipid phase distribution should be imaged simultaneously with the acoustic response, which can be achieved by using the combined confocal microscope and Brandaris 128 ultra-high-speed camera system [431].

4.5 Conclusion

DSPE-based MBs with a homogeneous lipid distribution were successfully produced by probe sonication and amalgamation with 30% PG. The MB size and concentration were more affected by the coating composition, *i.e.* choice of main lipid and co-surfactant, than by the production method. Although the short shelf-life stability may limit the *in vivo* applications for the newly developed MB formulations, they are interesting candidates for further research on the effect of lipid phase distribution on the acoustic behavior of single MBs.

Acknowledgments—The authors thank R. Beurskens from the Department of Biomedical Engineering, Erasmus MC, Rotterdam, the Netherlands, for technical assistance during the experiments. The authors thank Lipoid GmbH (Ludwigshafen, Germany) for providing a free sample of DSPE phospholipid.

Funding

This research was funded in part by the Phospholipid Research Center in Heidelberg, grant nr KKO-2017-057/1-1, and in part by the Thorax Center of Erasmus University Medical Center in Rotterdam.

5

Combined confocal microscope and Brandaris 128 ultra-high-speed camera

Inés Beekers, Kirby R. Lattwein, Joop J.P. Kouijzer, **Simone A.G. Langeveld**, Merel Vegter, Robert Beurskens, Frits Mastik, Rogier Verduyn Lunel, Emma Verver, Antonius F.W. van der Steen, Nico de Jong, Klazina Kooiman

Based on:
Ultrasound in Medicine & Biology, Vol. 45, No. 9, pp. 2575-2582, 2019 [432].

Abstract

Controlling microbubble-mediated drug delivery requires the underlying biological and physical mechanisms to be unraveled. To image both microbubble oscillation upon ultrasound insonification and the resulting cellular response, we developed an optical imaging system that can achieve the necessary nanosecond temporal and nanometer spatial resolutions. We coupled the Brandaris 128 ultra-high-speed camera (up to 25 million frames per second) to a custom-built Nikon A1R+ confocal microscope. The unique capabilities of this combined system are demonstrated with three experiments showing microbubble oscillation leading to either endothelial drug delivery, bacterial biofilm disruption, or structural changes in the microbubble coating. In con- clusion, using this state-of-the-art optical imaging system, microbubble-mediated drug delivery can be studied with high temporal resolution to resolve microbubble oscillation and high spatial resolution and detector sensitivity to discern cellular response. Combining these two imaging technologies will substantially advance our knowledge on microbubble behavior and its role in drug delivery.

Keywords—Bacteria; Confocal microscopy; Drug delivery; Fluorescence microscopy; High-speed imaging; Lipid coating; Microbubble; Sonoporation; Ultrasound; Ultrasound contrast agents

5.1 Introduction

To successfully treat diseases, administered drugs need to overcome barriers in the human body that hinder efficient delivery. Currently, high dosages are required because only a fraction of the therapeutic actually reaches the target site. This leads to high toxicity levels in healthy tissue, causing undesirable side effects [438, 439]. However, lipid-coated gas microbubbles (1-10 mm) in combination with ultrasound can locally enhance drug delivery, allowing for therapeutics to be delivered efficiently and only to the intended target site. When ultrasound is applied, microbubbles oscillate and thereby permeabilize cell membranes (sonoporation), open intercellular junctions, and stimulate endocytosis [66, 153, 154]. The underlying physical and biological mechanisms enhancing these different pathways are poorly understood. Elucidating the microbubble-cell interaction is fundamentally important for controlling and optimizing drug delivery, and therefore, microbubble oscillation behavior and the cellular response should be studied simultaneously.

To resolve the microbubble oscillation in an ultrasound field of clinically relevant frequencies (MHz), a system with nanosecond temporal resolution is required. Currently, there are two ultra-high-speed cameras that can achieve such high

frame rates, up to 25 million frames per second (Mfps) with sufficient consecutive frames: the Brandaris 128 [62] and the UPMC Cam [440]. Both cameras have been coupled to an upright microscope (BXFM, Olympus, Tokyo, Japan) for brightfield and widefield fluorescence microscopy. This enables the concurrent visualization of microbubble oscillation and cellular response. Although these systems have been used to study vascular drug delivery [117, 164, 441, 442], imaging resolution showing the cellular response was very poor. Microbubble oscillation leading to bacterial biofilm disruption has been observed at a lower temporal resolution using a 3 Mfps camera [380]. With the use of high-speed cameras, it has been possible to study the microbubble-cell interaction; however, the cellular response was still imaged with poor sensitivity and at a low optical and temporal resolution.

Confocal microscopy allows us to better unravel cellular response, as it provides nanometer spatial resolution, 3D imaging with high axial resolution, and good detector sensitivity for different fluorescent cell labeling. Live confocal microscopy imaging of microbubble-mediated drug delivery has revealed a wide-range of cellular effects: pore formation [187] and recovery [161], opening of intercellular junctions [164], endocytosis [165], lipoplex [443] and doxorubicin [444] delivery, changes in reactive oxygen species levels [163], increased bacterial metabolism [73], sonoprinting [445], cytoskeleton disruption [162], and intercalation of model drugs [446]. However, all these studies lack information on the specific microbubble behavior that was responsible for the observed cellular effect, because of the relatively low frame rates of confocal microscopy imaging (<500 fps).

Microbubble response to ultrasound varies a lot, and even equal-sized microbubbles in the same ultrasound field do not respond identically [46, 396, 447]. We need to gain more insight into microbubble behavior to achieve a more predicable response to ultrasound. To understand how the response is affected by microbubble composition, we want to image both the microbubble oscillation behavior and the coating microstructure [448]. In the past, it has only been possible to image coating microstructure in a static setup, without ultrasound, using, for example, 4Pi high-resolution confocal microscopy [392].

To date, the technological gap has made it impossible to image microbubble oscillation (high temporal resolution) and detailed cellular response (high spatial resolution) in the same field of view of a single sample. To overcome this challenge, we developed a novel optical imaging system by coupling an upright custom-built Nikon confocal microscope to the Brandaris 128 ultra-high-speed camera (Figure 5.1), which is described in this technical note.

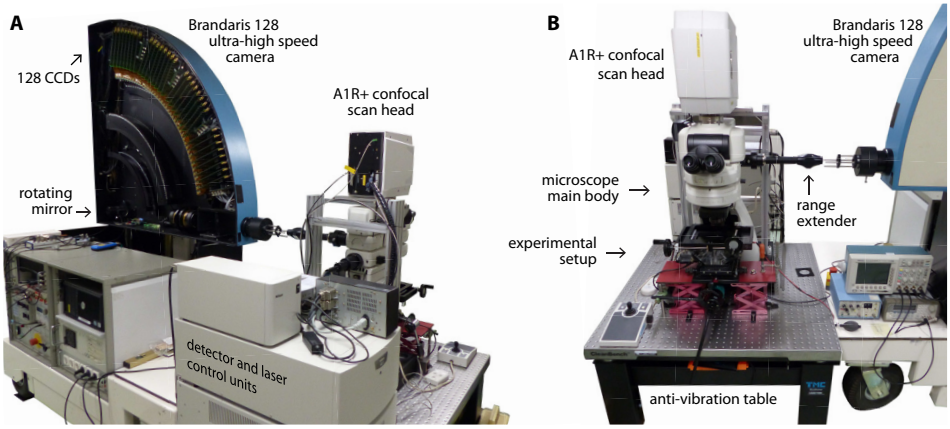

Figure 5.1 Combined confocal microscope and Brandaris 128 ultra-high-speed camera. **A**) From the back of the system, the inside of the Brandaris 128 casing with the rotating mirror and 128 charge-coupled devices (CCDs) is seen. **B**) At the front of the system are the confocal microscope and the experimental setup. The range extender facilitates the coupling of the Brandaris 128 to the confocal microscope.

5.2 Methods

The Brandaris 128 ultra-high-speed camera is a programmable camera with 128 sensitive charge-coupled devices (CCDs) and a fast rotating mirror that sweeps the image over the CCDs, resulting in a minimum interframe time of 40 ns (25 Mfps) [62]. Consecutive 128-frame recordings can be done at an 80 ms interval, with a maximum of 50 consecutive recordings [449]. The brightfield image is 500×292 pixels with 8-bit gray-scale values and a typical resolution of 400 nm [62].

The main body of the confocal microscope is a custom-built upright Eclipse Ni-E microscope (Nikon Instruments, Amsterdam, The Netherlands). By physically removing the conventional base of the main body, the microscope was customized to accommodate the water bath for ultrasound insonification. Microscope modules were chosen to meet our requirements such that the light path (Figure 5.2) could be directed toward the four different output ports: (i) a binocular (NI-TT-E Motorized Quadrocular Tilting Tube, Nikon Instruments), (ii) a color camera (DS-Fi3, Nikon Instruments) for digital acquisition of brightfield and widefield fluorescence images, (iii) the A1R+ confocal scan head, and (iv) the Brandaris 128 ultra-high-speed camera.

Two motorized turret modules (NI-FLT6-E Mot Epi-fluorescent turret, Nikon Instruments) were incorporated to rotate the desired filters or mirrors into the light path. One turret holds a full mirror to direct the light path toward the Brandaris 128 camera (Figure 5.2, turret A). The other turret is used for switching between filter cubes for widefield fluorescence imaging (Figure 5.2, turret B). The four installed filter cubes have the following excitation (Ex), dichroic mirror (DM), and emission (Em) filters: BFP-A with Ex390/18, DM416, and Em460/60; GFP-A with Ex469/35, DM497,

and Em525/39; TRITC-A with Ex542/20, DM570, and Em620/52; and Cy5-4040 C with Ex628/40, DM660, and Em692/40 (center wavelength/bandwidth in nanometers; Semrock Inc., Rochester, NY, USA). Widefield fluorescence is performed with a metal halide light source with motorized shutters and neutral density filters (C-HGFIE, Fiber Illuminator Intensilight, Nikon Instruments). During confocal imaging, excitation is achieved with a laser unit (LU-N4, Nikon Instruments) equipped with four lasers (405, 488, 561, and 640 nm; all 15 mW at the out- put of the fiber tip). The system has a hybrid detector unit (A1-DUG, GaAsP Multi Detector Unit, Nikon Instruments) that includes two gallium arsenide phosphide (GaAsP) photomultiplier tubes (PMTs) and two standard multi-alkali PMTs. The GaAsP PMTs are highly efficient in detecting the 525/50 and 595/50 nm ranges in comparison to the standard multi-alkali PMTs. To create four detection channels, the emitted light is split using three filter cubes. The first filter cube (DM FF495-Di03, Semrock Inc.; Em filter ET450/50 m, Chroma, Bellows Falls, VT, USA) delimits the 450/50 nm channel which is detected by a standard multi-alkali PMT. The second filter cube (DM T560 LPXR, Chroma; Em filter ET525/50 m, Chroma) delimits the 525/50 nm channel, which is detected by a GaAsP PMT. The third filter cube (DM T640 LPXR, Chroma; Em filter ET595/50 m, Chroma; Em ET700/75 m, Chroma) delimits the 595/50 and 700/75 nm channels, which are detected with a GaAsP PMT and a standard multi-alkali PMT, respectively.

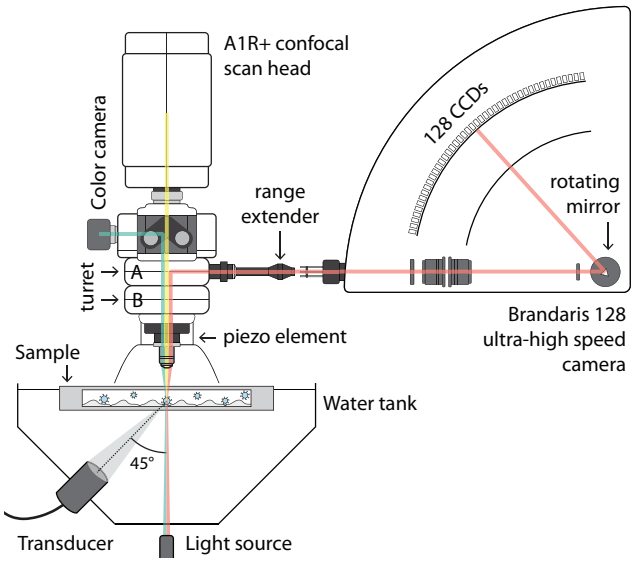

Figure 5.2 Schematic of the light paths to the different imaging output ports (not to scale). The light path goes through the sample, the objective, and the main body of the microscope toward either the color camera (green), the confocal scan head (yellow) or the Brandaris 128 ultra-high-speed camera (red). The light source is used for brightfield and Brandaris 128 imaging. The motorized turret A can place the full mirror in the light path for Brandaris 128 imaging, while turret B can insert the desired filter cubes for widefield fluorescence imaging. The sample can be insonified from below under a 45˚ angle in a water tank, which can be heated to 37 ˚C. CCDs = charge-coupled devices.

For high-precision focusing and 3D *z*-stack imaging, the microscope's main body combines two *z*-scanning devices. First, long ranges (12 mm) can be scanned with the main body's motorized *z* functionality, which was retained despite the customization. Next, with a piezo element (MCL NANO-F200 N, Mad City Labs Inc., Madison, WI, USA), faster and more precise *z*-focusing can be performed in a 200 mm range, resulting in improved *z*-stack imaging. To isolate vibration, the confocal microscope was installed on an active antivibration optical table (74-9090 M Cleanbench top and 12M-424-88 micro-g modular post mount support, Physik Instrumente, Karlsruhe, Germany).

The field of view of the Brandaris 128 camera had to overlap with that of the microscope. Therefore, the Brandaris 128 camera's casing had to be aligned and coupled to the output port of the microscope's main body. This was achieved by fixing a laser pointer on the casing of the Brandaris 128 to project onto a target on the microscope body. Further, to reproduce alignment, the position of both systems with respect to the room was documented using a laser distance measuring tool (GLM 40, Bosch, Stuttgart, Germany). A second requirement was parfocality; that is, the Brandaris 128 and the confocal need to have the same focal plane. To that end, a range extender (XT2 Collimating Emission-Port Adaptor, Photometrics, Tucson, AZ, USA) was inserted in the light path between the output port of the microscope and the Brandaris 128 input port.

When fast switching between confocal imaging and Brandaris 128 acquisition is desired, a Multifunction I/O Device (USB-6000, National Instruments, Austin, TX, USA) can trigger the motorized turret to rotate the full mirror into the light path, temporarily intercepting timelapse confocal imaging to acquire with the Brandaris 128 camera instead. The trigger is given when the rotating mirror in the Brandaris 128 reaches a desired rotation speed. Once the Brandaris 128 acquisition is complete, another trigger is given to remove the mirror from the light path, such that confocal imaging is restored. The confocal recording is intercepted at least for the duration of consecutive Brandaris 128 recordings and the mechanical turret rotation time of 300 ms. The trigger events and turbine speeds are registered in the confocal recording for correct data registration.

The capabilities of the combined Brandaris 128 and confocal microscopy imaging system are demonstrated with three *in vitro* experiments: endothelial drug delivery, bacterial biofilm disruption, and microbubble coating microstructure alterations. The microbubbles used in the experiments were all in-house produced by probe sonication as previously described [392]. Briefly, the main lipid of the coating was 1,2-distearoyl-*sn*-glycero-3-phosphocholine and the microbubbles had a C_4F_{10} gas core. All images were acquired with a 100× objective (CFI Plan 100XC W,

Nikon Instruments) that is chromatic aberration-free infinity (CFI), corrected for field curvature (Plan) and water dipping (W). This objective has a numerical aperture of 1.10; therefore, the resolution achieved with confocal microscopy is 250 nm. The confocal scan speed varies from 0.03 to 1 fps per acquisition channel, depending on the chosen pixel dwell time. By decreasing the field of view, we can image up to 5 fps. From the Brandaris 128 ultra-high-speed recordings, the microbubble radius as function of time was determined using custom-designed image analysis software [44]. During the endothelial drug delivery and biofilm disruption experiments, the sample was inserted in the water tank at 37 ˚C (Figure 5.2) and insonified with a single-element focused transducer (2.25 MHz center frequency, 76.2 mm focal length, -6 dB beam width at 2 MHz of 3 mm; V305, Panametrics-NDT, Olympus, Waltham, MA, USA). When the microbubble coating was studied, the sample was inserted in the water tank at room temperature and insonified with a single-element broadband transducer (1 to 9 MHz bandwidth, 25 mm focal distance, -6 dB beam width at 1 MHz of 1.3 mm; PA275, Precision Acoustics, Dorchester, U.K.).

5.3 Results

In the first experiment, the response of human umbilical vein endothelial cells to $\alpha_v\beta_3$-targeted microbubbles upon ultrasound insonification was imaged. Acquisition started with confocal microscopy time-lapse imaging (0.65 fps, CFI Plan 100× W objective), revealing the initial state of the cells and the location of the microbubble (Figure 5.3A). Next, the light path was automatically switched toward the Brandaris 128 to record micro- bubble oscillation during ultrasound insonification (2 MHz, 250 kPa peak-negative-pressure [PNP], single 10-cycle burst) (Figure 5.3B). This temporarily intercepted confocal microscopy imaging until the Brandaris 128 recording finished and the light path was switched back. Confocal microscopy imaging proceeded for 3.5 min after ultrasound, monitoring the cellular response (Figure 5.3C). Uptake of propidium iodide was observed locally around the microbubble (Figure 5.3C, 00:30-00:44), followed by diffusion throughout the cytoplasm and into the nucleus (Figure 5.3C, 02:25). Moreover, confocal microscopy imaging revealed opening of the intercellular junctions (Figure 5.3C, 02:25-03:50, arrows).

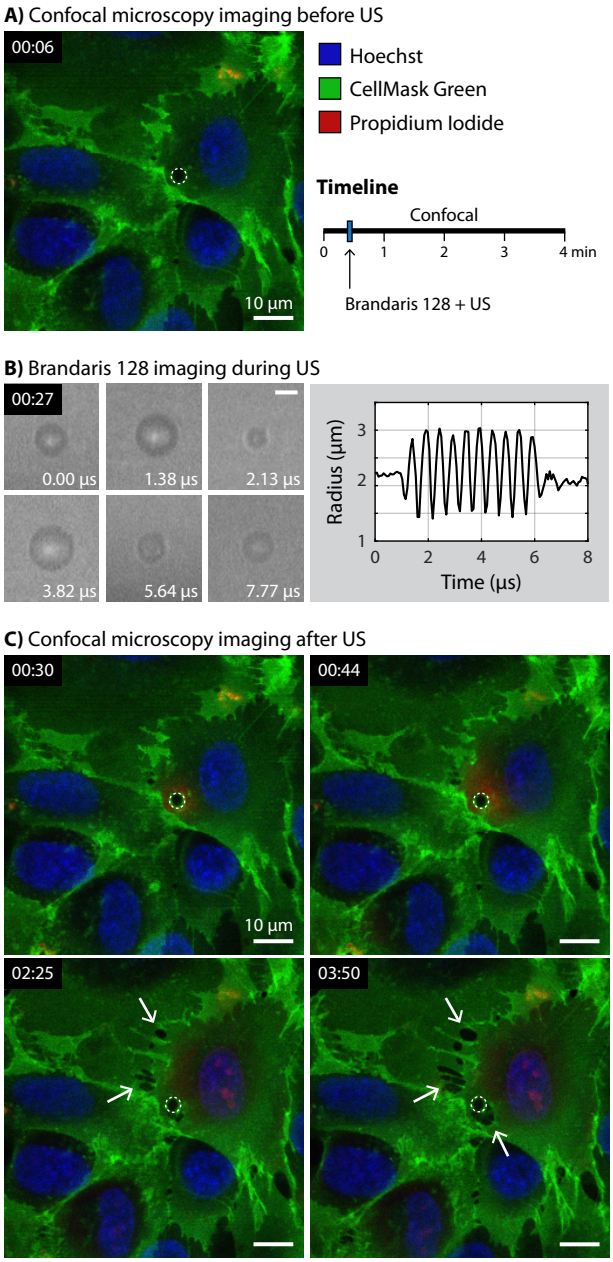

Figure 5.3 Selected frames from time-lapse imaging of microbubble-mediated endothelial drug delivery. Human umbilical vein endothelial cells (Lonza, Verviers, Belgium) were grown in MV medium (PromoCell GmbH, Heidelberg, Germany) to confluency for 2 d in a CLINIcell (50 mm membrane; Mabio, Turcoing, France). The cell nuclei were stained with Hoechst (5 mg/mL; Thermo Fisher Scientific, Waltham, MA, USA), the cell mem- branes with CellMask Green (4 mg/mL; Thermo Fisher Scientific), and sonoporation with propidium iodide (25 mg/mL; Sigma-Aldrich, St. Louis, MO, USA). The dashed line delineates the microbubble. **A**) Confocal microscopy before ultrasound (US) to image the initial cell state. **B**) Microbubble oscillation recorded with the Brandaris 128 ultra-high-speed camera (bar = 3 mm) and the microbubble radius as a function of time determined from this recording. **C**) Confocal microscopy after US to image cellular response. The arrows indicate opening of intercellular junctions.

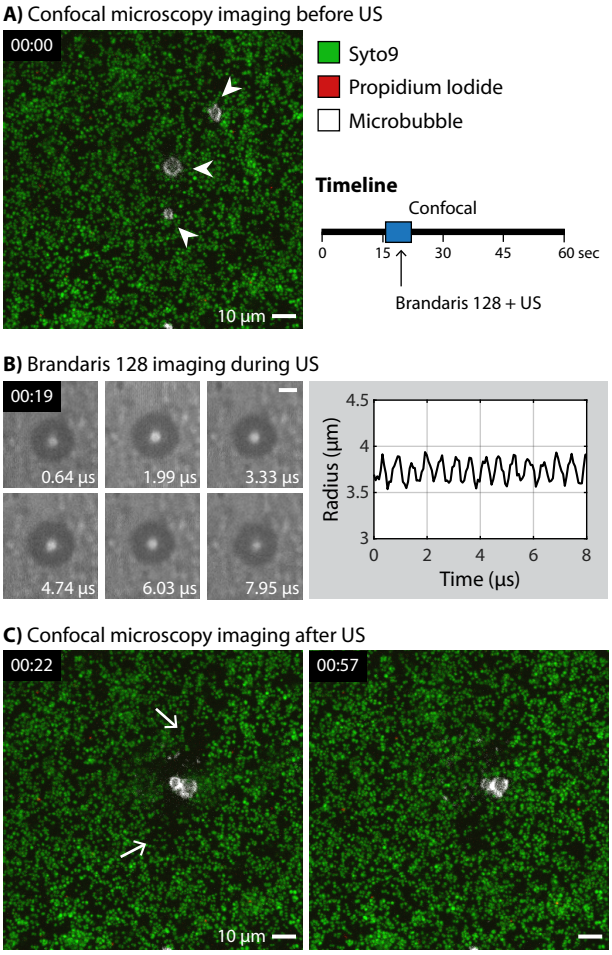

Figure 5.4 Selected frames from time-lapse imaging of microbubble-mediated biofilm disruption. A clinical isolate of *Staphylococcus aureus* (SA25268) was grown in IMDM medium (Thermo Fisher Scientific) for 24 h in an ibiTreat m-slide (0.8 mm channel height; I Luer; Ibidi GmbH, Martinsried, Germany). The live bacteria were stained with SYTO 9 (4 mg/mL; Thermo Fisher Scientific), the dead bacteria with propidium iodide (25 mg/mL; Sigma-Aldrich) and the microbubble shell with DiD (Thermo Fisher Scientific). **A**) Confocal microscopy before ultrasound (US) to image the initial biofilm and microbubbles (arrowheads). **B**) The oscillation of the microbubble located in the center of (**A**) was recorded with the Brandaris 128 ultra-high-speed camera (bar = 3 mm). The microbubble radius as a function of time was extracted from this recording. **C**) Confocal microscopy after US to image biofilm disruption (arrows).

The second experiment started with confocal microscopy time-lapse imaging (0.32 fps, CFI Plan 100× W objective) of a *Staphylococcus aureus* biofilm. This revealed vancomycin-targeted microbubbles adhered to bacteria (Figure 5.4A). Confocal time-lapse imaging was temporarily intercepted to record microbubble oscillation with the Brandaris 128 upon ultrasound insonification (2 MHz, 250 kPa PNP, single 10,000-cycle burst). After the Brandaris 128 recording, the light path was switched back and confocal imaging continued for 40 s. Confocal microscopy imaging after insonification revealed microbubbles had clustered (Figure 5.4C). Moreover, bacteria detached in the area where microbubbles were originally located, revealing microbubble-mediated disruption of the biofilm (Figure 5.4C, 0:22, arrows). Toward the end of the confocal recording, partial redisposition of bacteria was observed (Figure 5.4C, 00:57).

The third experiment aimed to image the microbubble coating microstructures before and after ultrasound insonification. Before ultrasound, a *z*-stack was acquired (0.4 mm step size, 31 slices, CFI Plan 100× W objective) of a microbubble that also contained rhodamine-B-1,2-dihexadecanoyl-*sn*-glycero-3-phosphoethanolamine, triethylammonium salt (rhodamine-DHPE). The 3-D image (Figure 5.5A) revealed that the lipid expanded phase, as stained by the rhodamine-DHPE [403], was distributed in a characteristic honeycomb pattern. Next, Bran- daris 128 ultra-high-speed imaging revealed microbubble oscillation (Figure 5.5B) upon ultrasound

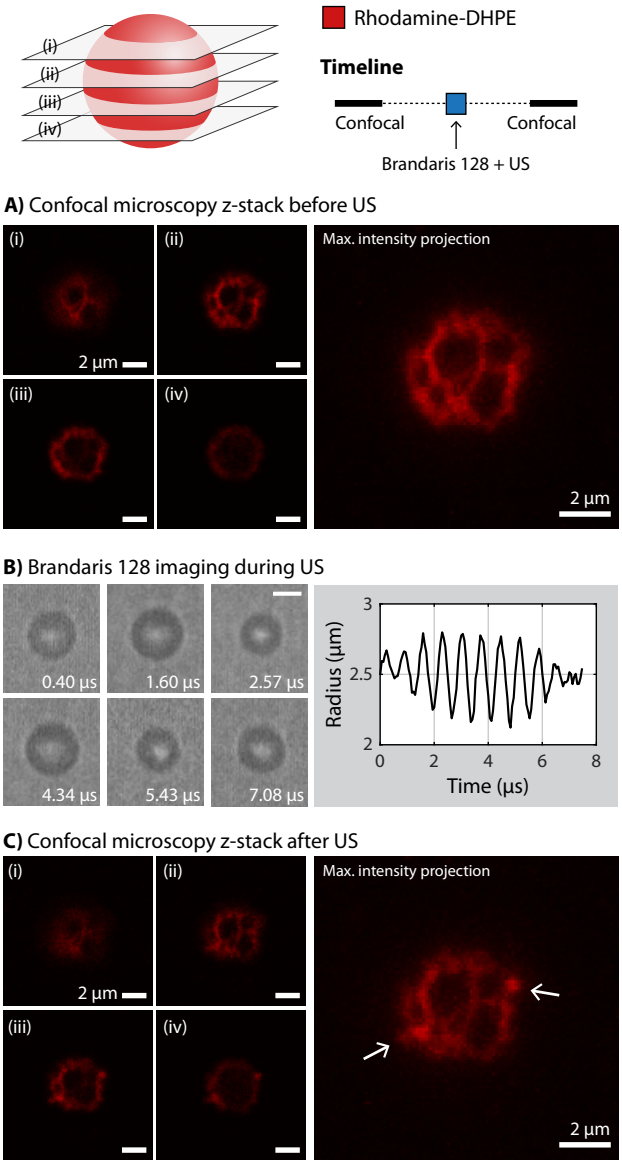

Figure 5.5 Imaging of structural changes in microbubble coating. The lipid-expanded phase was stained with rhodamine-DHPE (0.01 mol%; Thermo Fisher Scientific). Microbubbles were studied in a CLINIcell (50 mm membrane; Mabio). **A**) Selected *z*-slices from 3D confocal microscopy (i-iv) and the maximum intensity projection before ultrasound (US). **B**) Selected frames of the Brandaris 128 ultra-high-speed recording revealing microbubble oscillation (bar = 3 mm) and the resulting microbubble radius as a function of time. **C**) Selected *z*-slices (i-iv) and maximum intensity projection after US. The arrows indicate a focal area of increased fluorescence intensity (*i.e.*, hot spot) suggestive of local microbubble shell buckling.

insonification (1.4 MHz, 50 kPa PNP, single 8-cycle burst). After ultrasound, another *z*-stack was acquired revealing structural changes in the microbubble coating (Figure 5.5C, arrows).

5.4 Discussion

The novel combined confocal microscope and Brandaris 128 ultra-high-speed camera make it possible to study both the cell and microbubble structures with nanometer spatial resolution and the microbubble oscillation with nanosecond temporal resolution, as demonstrated with the three experiments. With this unique device we were able for the first time to relate microbubble oscillation behavior to alterations in cell integrity and microbubble coating microstructures.

Microbubble-mediated endothelial drug delivery (Figure 5.3) monitored with confocal microscopy provides better detector sensitivity and higher frame rates than the widefield microscope originally coupled to the Brandaris 128. As a result, low and fast changes of local propidium iodide uptake caused by sonoporation can now be detected. This is essential when studying safe drug delivery because low uptakes have been associated with reversible sonoporation and cell viability [169]. Moreover, specific fluorescent cell dyes can now be imaged with high resolution, revealing previously concealed cellular responses. For example, we were able to observe the opening of intercellular junctions using a cell membrane dye (Figure 5.3C).

The advantage of high-resolution confocal microscopy is also demonstrated when imaging biofilm disruption by oscillating microbubbles (Figure 5.4). Because of the small size of bacteria (~1 mm in diameter), they cannot be well resolved with widefield microscopy. The added value of this new optical system is that we can now distinguish individual bacteria and observe effects on bio films caused by oscillating microbubbles, while also gaining insight into how microbubbles vibrate nearby a biofilm. Furthermore, the light path switching is quick enough to observe the disruption of the biofilm before redisposition of bacteria occurs (Figure 5.4C). However, this data set also reveals a drawback of the Brandaris 128 ultra-high-speed camera recordings. Because a maximum of 128 frames can be acquired, it is only possible to partially image the 10,000-cycle microbubble oscillation. Therefore, in this Brandaris 128 acquisition, the microbubble clustering was not observed (Figure 5.4B) and could only be inferred from the confocal microscopy after ultrasound (Figure 5.4C).

The developed optical imaging system will be essential not only in understanding ultrasound-mediated drug delivery, but also in designing ultrasound contrast agents. We can finally image how microbubble oscilla- tion behavior affects the structural organization of the coating and vice versa. Although 4Pi microscopy has higher axial resolution and overcomes the signal loss toward the part of the microbubble furthest away from the objective (Figure 5.5, iv), because of the laser diffraction by the microbubble's gas core, we were able to discern the coating microstructures with the confocal microscope (Figure 5.5). To date, lipid shedding and buckling of the phospholipid shell caused by microbubble oscillation has been observed only using widefield fluorescence microscopy, at 150,000 fps [450] or 5 Mfps [451]. However, because of the poor axial resolution of widefield microscopy, structural details of the phospholipid shell could not be resolved.

Simultaneous Brandaris 128 and confocal microscopy imaging is not possible with the combined system. This technical limitation remains as the Brandaris 128 requires 100% of the light path to overcome the CCD detection limits. Automatic switching between confocal and Brandaris 128 imaging minimizes the time during which confocal microscopy imaging is interrupted. It is difficult to precisely predict the start of a Brandaris 128 acquisition, as the acceleration of the turbine is variable. Therefore, confocal microscopy is often interrupted about 2 s before the Brandaris 128 recording starts. During this time no change is expected in the confocal image, because insonification has not taken place yet. As soon as the Brandaris 128 acquisition has completed, during which ultrasound was applied, the full mirror is rotated out of the light path. As a result, the confocal microscope can restore imaging to detect rapid cellular effects with a maximum delay of 300 ms plus the time to scan a confocal frame (which depends on the confocal scan speed chosen). For the endothelial drug delivery example, this corresponded to <1.8 s, and for the biofilm disruption example, this was <3.4 s.

The confocal microscope can image a larger field of view than the Brandaris 128 ultra-high-speed camera. For instance, with the CFI Plan 100× W objective, the field of view of the confocal microscope is 128×128 mm and that of the Brandaris 128 is 45×32 mm. Hence, as seen in Figure 5.4, sometimes microbubbles are observed in the field of view of the confocal microscope, but their oscilla- tion cannot be recorded with the Brandaris 128. Finally, adapting the microscope's main body by removing the conventional base disabled the automatic refocusing capability. Regardless, a desired focus depth can be manually restored because the software is still able to read out the *z*-position of the objective.

5.5 Conclusions

A state-of-the-art optical imaging system was developed by coupling a custom-built confocal microscope to the Brandaris 128 ultra-high-speed camera. Microbubble-mediated drug delivery can now be studied at both high spatial and temporal resolution to evaluate cellular response upon microbubble oscillation. Additionally, changes in microbubble coating structure caused by oscillation behavior can be dis- cerned. With this novel optical imaging system we expect to further elucidate microbubble-mediated drug delivery and advance the development of ultrasound contrast agents.

Acknowledgments—This work was supported in part by the Applied and Engineering Sciences TTW (Veni-Project 13669), a part of NWO; the Erasmus MC Foundation; the Phospholipid Research Center, Heidelberg, Germany; and the Thoraxcenter of Erasmus MC. The authors thank Gert van Cappellen and Adriaan Houtsmuller from the Erasmus MC Optical Imaging Center; Willem J. B. van Wamel from the Department of Medical Microbiology and Infectious Diseases, Erasmus MC; and Alessandra Scarpellini from Nikon Instruments Europe for the fruitful discussions.

6

The impact of lipid handling and phase distribution on the acoustic behavior of microbubbles

Simone A.G. Langeveld, Inés Beekers, Gonzalo Collado-Lara, Antonius F.W. van der Steen, Nico de Jong, Klazina Kooiman

Based on:
Pharmaceutics, Vol. 13, No. 1, pp. 119-140, 2021 [427].

Abstract

Phospholipid-coated microbubbles are ultrasound contrast agents that can be employed for ultrasound molecular imaging and drug delivery. For safe and effective implementation, microbubbles must respond uniformly and predictably to ultrasound. Therefore, we investigated how lipid handling and phase distribution affected the variability in acoustic behavior of microbubbles. Cholesterol was used to modify the lateral molecular packing of 1,2-distearoyl-*sn*-glycero-3-phosphocholine (DSPC)-based microbubbles. To assess the effect of lipid handling, microbubbles were produced by a direct method, i.e. lipids directly dispersed in aqueous medium, or indirect method, *i.e.* lipids first dissolved in organic solvent. The lipid phase and ligand distribution in the microbubble coating were investigated using confocal microscopy and the acoustic response was recorded with the Brandaris 128 ultra-high-speed camera. In microbubbles with 12 mol% cholesterol the lipids were miscible and all in the same phase, which resulted in more buckle formation, lower shell elasticity and higher shell viscosity. Indirect DSPC microbubbles had a more uniform response to ultrasound than direct DSPC and indirect DSPC-cholesterol microbubbles. The difference in lipid handling between direct and indirect DSPC microbubbles significantly affected the acoustic behavior. Indirect DSPC microbubbles are the most promising candidate for ultrasound molecular imaging and drug delivery applications.

Keywords—Ultrasound contrast agents; Phospholipid coating; Ligand distribution; Cholesterol; Acoustic response; Microbubble; Lipid phase

6.1 Introduction

Microbubbles are small gas bubbles (diameter 1–10 μm) that are clinically used as ultrasound contrast agent for non-invasive diagnostic imaging of blood perfusion [37]. Targeted microbubbles are employed for molecular imaging of inflammation, tumors, and cardiovascular disease [50]. Other types of microbubbles are being developed specifically for drug delivery [425]. All of these applications make use of the compression and expansion of the microbubble gas core upon ultrasound insonification. These microbubble vibrations produce a non-linear response, including super- and subharmonic oscillations, which can be differentiated from the surrounding tissue to form a contrast-enhanced image [37]. Additionally, this acoustic response can induce bioeffects on nearby cells – resulting in enhanced uptake or extravasation of drug molecules [66]. Successful translation to clinical use of microbubbles for molecular imaging and enhanced drug delivery is currently challenged, however, by the microbubbles' unpredictable acoustic behavior.

To stabilize the gas core, microbubbles are usually coated with a phospholipid monolayer, proteins, or polymers. For a schematic representation the reader is referred to recent reviews on microbubbles [100, 452]. The coating reduces surface tension and gas diffusion [11]. If phospholipids or polymers are used as microbubble coating, a ligand can be attached for molecular imaging [385] and they can be loaded with a drug for localized delivery [425]. The physicochemical properties of the microbubble coating, such as the shell elasticity and viscosity, are related to the acoustical properties, such as the resonance frequency and the damping coefficient [43, 428]. Therefore, the composition of the microbubble coating can affect the acoustical properties. For instance, the use of a phospholipid molecule with a longer acyl chain length, 1,2-distearoyl-*sn*-glycero-3-phosphocholine (DSPC; C18), resulted in a higher shell elasticity and more acoustic stability than the use of a shorter acyl chain length phospholipid, 1,2-dipalmitoyl-*sn*-glycero-3-phosphocholine (DPPC; C16) [45]. Besides the shell elasticity, acyl chain length has also been shown to affect the half-life of microbubbles, with longer acyl chain length resulting in a more stable size distribution and ultrasound signal over time [453].

Since microbubbles are generally coated with a mixture of phospholipids and a PEGylated emulsifier, the physicochemical properties are determined by the miscibility and lipid phase behavior. Molecules in the microbubble coating can be in the liquid expanded (LE) or liquid condensed (LC) phase, resulting in distinctive microstructures. These microstructures can be altered by using different types of phospholipids [30], changing the ratio between phospholipid and emulsifier, or heating and cooling of the microbubble coating [389]. Microstructures formed by lipid phase separation have been shown to affect the subharmonic response to ultrasound [396]. The effect of lipid phase separation on the subharmonic response to ultrasound has been characterized previously in three types of microbubbles with different levels of lipid phase separation: 20%, 50% or 80% of the microbubbles had LC phase domains. Each microbubble type had a peak subharmonic response at a different microbubble size, suggesting that microstructures in the coating affect the acoustical properties of a microbubble [396]. The microbubble coating can also be altered by the distribution of the phospholipid and PEGylated-emulsifier molecules over the microbubble coating, depending on the lipid handling prior to microbubble production by probe sonication. The use of organic solvent resulted in a more homogeneous ligand distribution than the use of aqueous solutions only [427]. The effect of lipid handling on the acoustic response of microbubbles, however, has not been investigated.

For both ultrasound molecular imaging and drug delivery it is important that all microbubbles respond uniformly and predictably to ultrasound. Currently available microbubbles respond to ultrasound in a heterogeneous way [45, 394], even when

they are the same size [46]. While it is thought this variability in response could be due to the microstructures in the microbubble coating, this is challenging to confirm because it can only be investigated by looking at single microbubbles. Different approaches have been used to record a single microbubble's response to ultrasound, including an ultra-high-speed camera to image the microbubble during insonification [44], recording the acoustic response [396] or optical scattering [454], and photo-acoustic techniques [455]. Until recently however, no techniques were available to image both the lipid phase distribution in 3D and the acoustic response of the same microbubble. In this regard, the challenge lies in the time scale (μs) and optical resolution (μm) needed to record the lipid phase distribution and response to ultrasound of a single microbubble.

The purpose of this study was to relate the effects of lipid handling and phase distribution before microbubble production to the acoustic behavior of phospholipid-coated microbubbles. Cholesterol can modify the lateral molecular packing of phospholipids in a monolayer, resulting in a single liquid phase [456-458]. While microbubbles with cholesterol in their coating have been produced before [459, 460], the effect of cholesterol on the lipid phase separation in microbubbles has not been studied. To determine this effect in the microbubble coating, we made microbubbles by probe sonication with DSPC as main lipid, and varying concentrations of cholesterol. The lipid phase distribution and ligand distribution in the microbubble coating were imaged using high-axial-resolution 4Pi confocal microscopy. To assess the acoustic response and variability in the acoustic behavior, we used a unique system combining a confocal microscope with the Brandaris 128 ultra-high-speed camera. With this system the lipid phase separation (in nanometer resolution) and acoustic response to ultrasound (in nanosecond resolution) were captured at single microbubble level.

6.2 Materials and methods

6.2.1 Materials

DSPC was provided by Lipoid GmbH (Ludwigshafen, Germany). PEG40-stearate and cholesterol were purchased from Sigma-Aldrich (Zwijndrecht, the Netherlands), 1,2-distearoyl-*sn*-glycero-3-phosphoethanolamine-N-carboxy-(polyethylene glycol) (DSPE-PEG2000) was purchased from Iris Biotech GmbH (Marktredwitz, Germany), and 1,2-distearoyl-*sn*-glycero-3-phosphoethanolamine-N-biotinyl(polyethylene glycol) (DSPE-PEG2000-biotin) was purchased from Avanti Polar Lipids (Alabaster, Alabama, USA). Perfluorobutane (C_4F_{10}) was purchased from F2 Chemicals (Preston, UK) and argon gas was purchased from Linde Gas Benelux (Schiedam, the Netherlands). Streptavidin Oregon Green 488 was purchased from BioSynthesis

(Louisville, Texas, USA), and Lissamine rhodamine B 1,2-dihexadecanoyl-*sn*-glycero-3-phosphoethanolamine, triethylammonium salt (rhodamine-DHPE) was purchased from Thermo Fisher (Waltham, Massachusetts, USA).

6.2.2 Microbubble production

Biotinylated lipid-coated microbubbles with a C_4F_{10} gas core were made as described previously [397], by probe sonication at 20 kHz with a Sonicator Ultrasonic Processor XL2020 at power setting 10 (HeatSystems, Farmingdale, NY, USA) for 10 s. Three types of microbubbles were made by altering the production method or adding cholesterol to the microbubble coating. For microbubbles without cholesterol the coating components (84.8 mol% DSPC; 8.2 mol% PEG40-stearate; 5.9 mol% DSPE-PEG2000; 1.1 mol% DSPE-PEG2000-biotin) were prepared with either an indirect or a direct method as described previously [427]. In short, for the indirect method the components were dissolved in chloroform/methanol (9:1 vol/vol), the solvent was evaporated using argon gas, and the obtained lipid film was dried overnight under vacuum. The lipid film was then dispersed in saline solution (0.9% NaCl, saturated with C_4F_{10}) with a final concentration of 2.5 mg/mL DSPC, 0.625 mg/mL PEG40-stearate, 0.625 mg/mL DSPE-PEG2000 and 0.125 mg/mL DSPE-PEG2000-biotin. The fluorescent dye rhodamine-DHPE (0.01 mol%) was added to image the lipid phase separation in the microbubble coating. The solution was placed in a sonicator bath for 10 min, and the probe sonicator was used at power setting 3 for 5 min. For the direct method, the coating components (84.8 mol% DSPC; 8.2 mol% PEG40-stearate; 5.9 mol% DSPE-PEG2000; 1.1 mol% DSPE-PEG2000-biotin) were dispersed directly in C_4F_{10}-saturated saline solution with a final concentration of 2.5 mg/mL DSPC, 0.625 mg/mL PEG40-stearate, 0.625 mg/mL DSPE-PEG2000 and 0.125 mg/mL DSPE-PEG2000-biotin. Fluorescent dye rhodamine-DHPE (0.01 mol%) was added before sonication.

Microbubbles with cholesterol, referred to as DSPC-cholesterol microbubbles, were produced with the indirect method only, since cholesterol is insoluble in aqueous medium and organic solvent was required to mix all microbubble coating components [461]. Cholesterol was added (7, 10, 12, 14, or 32 mol%) to the ternary mixture of coating components: DSPC, PEG40-stearate, DSPE-PEG2000, and DSPE-PEG2000-biotin (molar ratio 84.8/8.2/5.9/1.1) in chloroform/methanol (9:1 vol/vol). The lipids were then dried to form a lipid film and dispersed in saline solution, as described above, with 0.02 mol% rhodamine-DHPE added for fluorescent labeling of the microbubbles. All types of microbubbles were produced by sonicating under constant flow of C_4F_{10}.

6.2.3 Physicochemical characterization

To image the ligand distribution, fluorescent ligand streptavidin Oregon Green 488 was conjugated to the biotinylated microbubbles as described previously [392]. Briefly, microbubbles were first washed by flotation: 0.9 mL microbubble suspension was placed in a 3 mL syringe and topped with 2.1 mL saline solution saturated with C_4F_{10}. After 45 min the subnatant was drained and the microbubbles were resuspended in 0.3 mL saline solution saturated with C_4F_{10}. Then, 22.5 µL of streptavidin-Oregon Green 488 (2 mg/mL) was allowed to incubate with 0.7-1.0 × 10^8 microbubbles for 30 min on ice. The excess of streptavidin was washed away by flotation as described above, with resuspension of the microbubbles in 0.2 mL saline solution.

To measure the microbubble size distribution and concentration, a Coulter Counter Multisizer 3 (Beckman Coulter, Mijdrecht, the Netherlands) was used. To quantify particles between 1 and 30 µm, a 50 µm aperture tube was used. To evaluate the polydispersity of the samples, the span value was calculated, defined as (*d*90-*d*10%)/*d*50%, where *d*90, *d*10 and *d*50% are the microbubble diameters below which 90, 10 and 50% of the cumulative number of microbubbles was found. Samples were measured after the first flotation wash and again after conjugation with streptavidin Oregon Green 488.

The streptavidin-conjugated microbubbles were imaged by microscopy as described by Langeveld et al. [427]. In short, the microbubbles were placed between quartz glass in 87% glycerol (vol/vol in phosphate buffered saline) to reduce Brownian motion, and imaged with a Leica TCS 4Pi confocal laser-scanning microscope [406]. An axial resolution up to 90 nm was achieved with a matched pair of aligned opposing 100× glycerol HCX PL APO objective lenses (Numerical aperture 1.35). For excitation of Oregon Green 488 a 488 nm laser was used and for excitation of rhodamine-DHPE a 561 nm laser was used. Images were recorded in 3D as *y*-stacked *xz*-scans in a green (500–550 nm) and red (580–640 nm) spectral channel. The "voltex" function was used to volume-render the image stacks with AMIRA (Version 2020.2, FEI, Mérignac Cedex, France).

Quantitative analysis was performed on the 4Pi microscopy data using custom-developed image analysis software in MATLAB (Mathworks, Natick, Massachusetts, USA), based on the method described by Langeveld et al. [427]. The microbubble coating was subdivided into 32 parts of which the mean fluorescence pixel intensity (I_{part} for the green channel and $I_{part\text{-}rhod}$ for the red channel) was calculated. The median intensity of all parts (I_{median} for the green channel and $I_{median\text{-}rhod}$ for the red channel) was calculated per microbubble. To evaluate the ligand distribution, parts were classified as inhomogeneous when the absolute difference between Ipart and Imedian was more than two-third times the value of I_{median} (*i.e.*, $|I_{part} - I_{median}| > 2/3 \times I_{median}$), and the

percentage of inhomogeneous parts was calculated per microbubble. To evaluate the lipid phase distribution, parts were classified as LC phase when the value of *I*part-rhod was less than one-third of $I_{median\text{-}rhod}$ (*i.e.*, $I_{part\text{-}rhod} < 1/3 \times I_{median\text{-}rhod}$). The LC phase surface area was first calculated in μm^2 and then as percentage of the total analyzed surface area per microbubble. Before evaluating the ligand distribution or the lipid phase distribution, an additional normalization step was included in the image analysis. This step corrected for a difference in fluorescence intensity between the center and the top or bottom of the microbubbles, likely caused by attenuation of the laser light leading to a lower fluorescence signal at the center of the sample. The normalization factor was calculated based on the median Ipart (for the green channel) or the median $I_{part\text{-}rhod}$ (for the red channel) per angular part from all microbubbles (Supplemental Figure 6.1). To determine the number of microbubbles with buckles, the microbubble coating was manually scored for fluorescent signal outside and attached to the microbubble coating, based on the red channel (rhodamine-DHPE signal). Only bright spots with 1 µm diameter or larger were classified as a buckle.

6.2.4 Acoustical characterization

To study both the acoustical behavior and the lipid phase separation of single microbubbles simultaneously, the combined confocal microscopy and Brandaris 128 ultra-high-speed camera system was used [431]. Microbubble spectroscopy was employed to characterize the acoustic behavior of single microbubbles as described previously [45, 462]. Microbubbles were washed by flotation once and counted using the Coulter Counter Multisizer 3, as described above. An acoustically compatible [462] CLINIcell (MABIO, Tourcoing, France) with 50 µm membranes (25 μm^2) was first blocked with 12 mL of 2% (w/v) bovine serum albumin (BSA) in phosphate buffered saline (PBS) for 1 h, to avoid unspecific microbubble binding to the membranes. The CLINIcell was washed three times with PBS before inserting 12 mL of 10^5 microbubbles/mL in PBS. Next, the CLINIcell was placed under water in the experimental set-up and kept at room temperature for up to 2 hours. To study the lipid phase separation, the custom-built confocal microscope (Nikon Instruments, Amsterdam, The Netherlands) was used with a 561 nm laser to excite rhodamine-DHPE and emitted light was detected in a 595/50 nm channel. *Z*-stacks with 0.4 µm steps were acquired with a CFI Plan 100× W objective of single microbubbles directly before and after insonification. To perform microbubble spectroscopy, each individual microbubble was insonified over a range of transmit frequencies (f_T) from 1 to 4 MHz in steps of 200 kHz. The microbubbles were insonified with 8-cycle Gaussian tapered sine wave bursts either at 50 kPa, or first at 20 kPa and then at 150 kPa external peak negative pressure (PNP), generated by a Tabor

8026 arbitrary waveform generator (AWG, Tabor Electronics, Tel Hanan, Israel). The signal was first attenuated by a 20-dB attenuator (Mini-Circuits, Brooklyn, New York, USA), then amplified by a broadband amplifier (ENI A-500, Electronics & Innovation, Rochester, New York, USA), and finally transmitted to the microbubble sample at a 45° incidence angle with a single-element transducer (1-9 MHz bandwidth, 25 mm focal distance, -6 dB beamwidth at 1 MHz of 1.3 mm, PA275, Precision Acoustics, Dorchester, UK), which was calibrated using a 1-mm needle hydrophone (Precision Acoustics, Dorchester, UK) in water. The Brandaris 128 ultra-high-speed camera [62], coupled to the confocal microscope [431], was used to record the microbubble oscillation behavior at approximately 17 million frames/s. First, a recording was made without ultrasound to establish the initial microbubble size. Next, 16 recordings at 50 kPa PNP, or 16 recordings at 20 kPa PNP and then 16 recordings at 150 kPa PNP, were made of a single microbubble upon ultrasound insonification at the different transmit frequencies with 80 ms in between recordings. To avoid any effects from nearby microbubbles on the oscillation behavior, only microbubbles which were at least 0.7 mm from other microbubbles were investigated.

To quantify microbubble oscillation, custom-developed image analysis software in MATLAB was used to determine the change in microbubble radius as a function of time (R–t curve) [44]. As previously described, the resonance frequency and shell parameters can be obtained from the spectroscopy dataset [44, 45]. Briefly, the relative oscillation amplitude (x_0) of each microbubble was defined as the maximum of the filtered R–t curve (a third-order Butterworth bandpass filter centered at f_T with a 300-kHz bandwidth) and divided by the resting size of the microbubble (R_0; mean size of the first five frames). Next, for each f_T, the x_0 obtained at 50 kPa were fitted to the harmonic oscillator model

$$x_0 = \frac{|P| / \left(4\pi^2 \rho R_0^2\right)}{\sqrt{\left(f_0^2 - f_T^2\right)^2 + (\delta f_T f_0)^2}} \qquad \textit{(eq. 6.1)}$$

with P being the acoustic pressure and $\rho = 10^3$ kg/m^3 being the density of water. The eigenfrequency (f_0) of the microbubble is defined as

$$f_0 = \frac{1}{2\pi}\sqrt{\frac{1}{\rho R_0^2}\left[3\gamma P_0 + \frac{2(3\gamma - 1)\sigma_w}{R_0} + \frac{4\chi}{R_0}\right]} \qquad \textit{(eq. 6.2)}$$

with $\gamma = 1.07$ the ratio of specific heats for C_4F_{10}, $P_0 = 10^5$ Pa the ambient pressure, $\sigma_w = 0.072$ N/m the surface tension in water, and χ the microbubble shell elasticity. The damping coefficient (δ) is given by

$$\delta = \frac{\omega_0 R_0}{c} + 2\frac{4\pi}{R_0^2 \rho \omega_0} + \frac{4\kappa_S}{R_0^3 \rho \omega_0} \qquad \textit{(eq. 6.3)}$$

with $\omega_0 = 2\pi f_0$, c = 1500 m/s the speed of sound in water, $\mu = 10^{-3}$ Pa·s the viscosity of water, and κ_s the microbubble shell viscosity. The resonance frequency is defined by $f_{res} = f_0\sqrt{1-\delta^2/2}$.

The variability in acoustical response of each microbubble type was quantified by determining the interquartile range (IQR) of the relative oscillation amplitude (x_0) at each f_T and in diameter bins of 0.5 µm (N > 3 per bin). Since the microbubbles deflated after insonification, the acoustic stability was evaluated by quantifying the relative diameter decrease upon insonification as $(D_0–D_{end})/D_0$, with D_0 the mean microbubble diameter of all 128 frames of the first recording without ultrasound and Dend the mean microbubble diameter of the last ten frames of the last recording.

The non-linear behavior of microbubbles was assessed by calculating the Fast Fourier Transforms (FFTs) of the *R–t* curves. The noise level of each microbubble was determined by the FFT of the first recording before ultrasound. A microbubble was categorized as exhibiting non-linear behavior when in at least two recordings it showed a detectable peak in the FFT (using the islocalmax function in MATLAB) around $½·f_T$ for the subharmonic or around $2·f_T$ for the second harmonic and the peak's amplitude was at least 6 dB above the noise level. If so, then the amplitude of the non-linear component was defined as the maximum FFT amplitude in a 300-kHz bandwidth around $½·f_T$ for the subharmonic component and around $2·f_T$ for the second harmonic component and normalized to the fundamental at f_T.

Finally, the confocal microscopy recordings were scored manually for the presence of buckles (none, single, multiple, or extensive) before and after ultrasound and for change in the microbubble coating before and after ultrasound (unchanged, buckles formed, coating material shed). Only bright spots with 1 µm diameter or larger were classified as buckle (Supplemental Figure 6.2). Microbubbles between 4.5 and 6.0 µm in diameter were manually scored for the LC domain size as well (mostly large, large and small, undefined). The relationship between these classifications and the acoustical data was evaluated to determine the effect of the lipid phase distribution and buckling in the microbubble coating on the resulting acoustic response. To rule out size dependent differences in oscillation amplitude, only microbubbles with an initial diameter in the range of 4.5-6.0 µm were included in this analysis.

6.2.5 Statistics

Statistical analysis was performed using IBM SPSS Statistics 25 for all 4Pi microscopy image analysis. Statistical analysis for the acoustical characterization was performed using MATLAB. A Shapiro-Wilk test was used to assess the distribution of the data. For data that was normally distributed a regular *t*-test was used to analyze the

differences between groups. For all other data the Mann–Whitney *U* test was used to test the difference between groups. Differences between groups were only tested for $N > 2$. Pearson correlation tests were performed to assess correlation between parameters.

6.3 Results

6.3.1 Physicochemical characterization

Figure 6.1A presents the number weighted size distributions of indirect DSPC-based microbubbles with and without cholesterol. For microbubbles without cholesterol (0 mol%; $N = 5$) and microbubbles with 12 mol% cholesterol ($N = 6$) the size distributions of batches for 4Pi microscopy and for acoustic experiments are both included, and the mean number (%) per diameter is shown with the standard error of the mean (SEM). For microbubbles with 7, 10, and 14 mol% cholesterol a representative curve is shown from 2 batches, as these types of microbubbles were produced for 4Pi microscopy only. The concentration of microbubbles ranged from

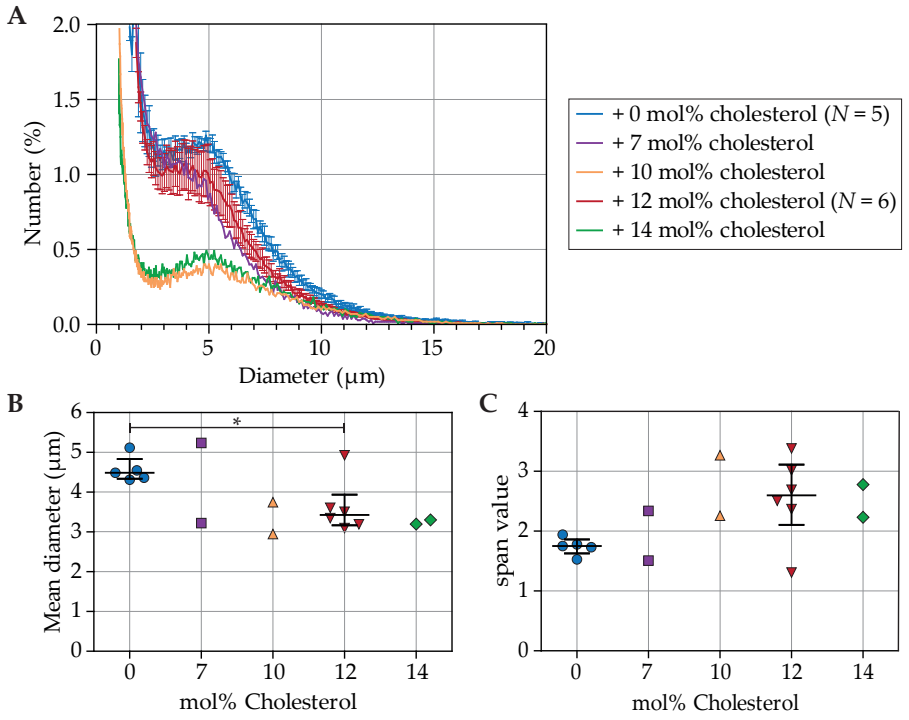

Figure 6.1 A) Number weighted size distribution; **B**) Number weighted mean diameter (µm); and (**C**) span value of indirect DSPC-based microbubbles with cholesterol in a range from 0 to 14 mol%. In (**B**) and (**C**) each symbol represents one batch of microbubbles; jittering was applied to avoid overlapping. The overlaid black lines represent the median and interquartile range. Statistical significance is indicated with $*p<0.05$.

2.78×10^8 to 1.17×10^9 microbubbles per mL (Supplemental Table 6.1). The indirect DSPC-based microbubbles without cholesterol had more particles with diameter >3 µm than all types of microbubbles with cholesterol in the coating. Indirect DSPC-based microbubbles with 32 mol% cholesterol in the coating were highly unstable, with a concentration too low for measurement of the size distribution. Therefore, indirect DSPC-based microbubbles with 32 mol% cholesterol were not investigated further.

Figure 6.1B shows the mean diameter (µm) of indirect DSPC-based microbubbles without cholesterol and with 7, 10, 12, or 14 mol% cholesterol. Microbubbles with 12 mol% cholesterol had a smaller mean diameter than those without cholesterol (p = 0.045). Figure 6.1C shows the width of the size distributions represented as the span value. The size distributions of microbubbles with 12 mol% cholesterol were more polydisperse than those of microbubbles without cholesterol (p = 0.068).

The ligand and lipid phase distribution in the microbubble coating were imaged in indirect DSPC-based microbubbles without cholesterol (N = 58), with 7 mol% cholesterol (N = 34), with 10 mol% cholesterol (N = 40), with 12 mol% cholesterol (N = 61), and with 14 mol% cholesterol (N = 45). Images were recorded of at least two batches of microbubbles for all formulations, with microbubble diameters ranging from 2.2 µm to 8.7 µm. Typical examples of all formulations are presented in Figure 6.2. The ligand distribution is shown in the top row, the LE phase in the middle row, and a composite of both channels in the bottom row. Figure 6.3 shows a quantitative analysis of the 4Pi confocal microscopy images, with the calculated ligand distribution inhomogeneity in Figure 6.3A and the LC phase relative to the total surface area analyzed per microbubble in Figure 6.3B. Indirect DSPC-based microbubbles without cholesterol had a homogeneous ligand distribution (Figure 6.2A, Figure 6.3A). The inhomogeneity of the ligand distribution can be observed in Figure 6.2B, 6.2C, and 6.2E, where the ligand is enriched in some areas of the microbubble surface. All indirect DSPC-cholesterol microbubbles had a significantly more heterogeneous ligand distribution compared to those without cholesterol (Figure 6.2B-E, Figure 6.3A). Microbubbles with 12 mol% cholesterol had a more homogeneous ligand distribution than those with 7 mol% cholesterol (p = 0.070), 10 mol% cholesterol (p = 0.040), and 14 mol% cholesterol (p < 0.001).

The lipids were phase-separated in indirect DSPC-based microbubbles without cholesterol, as shown in Figure 6.2F and quantified in Figure 6.3B. The fluorescent dye rhodamine-DHPE was enriched in bright interdomain regions (*i.e.*, LE phase) and absent in LC domains. In indirect DSPC-cholesterol microbubbles, the LC domains were less pronounced compared to those without cholesterol (Figure 6.2G-J). With increasing concentrations of cholesterol up to 12 mol%, the lipid phase

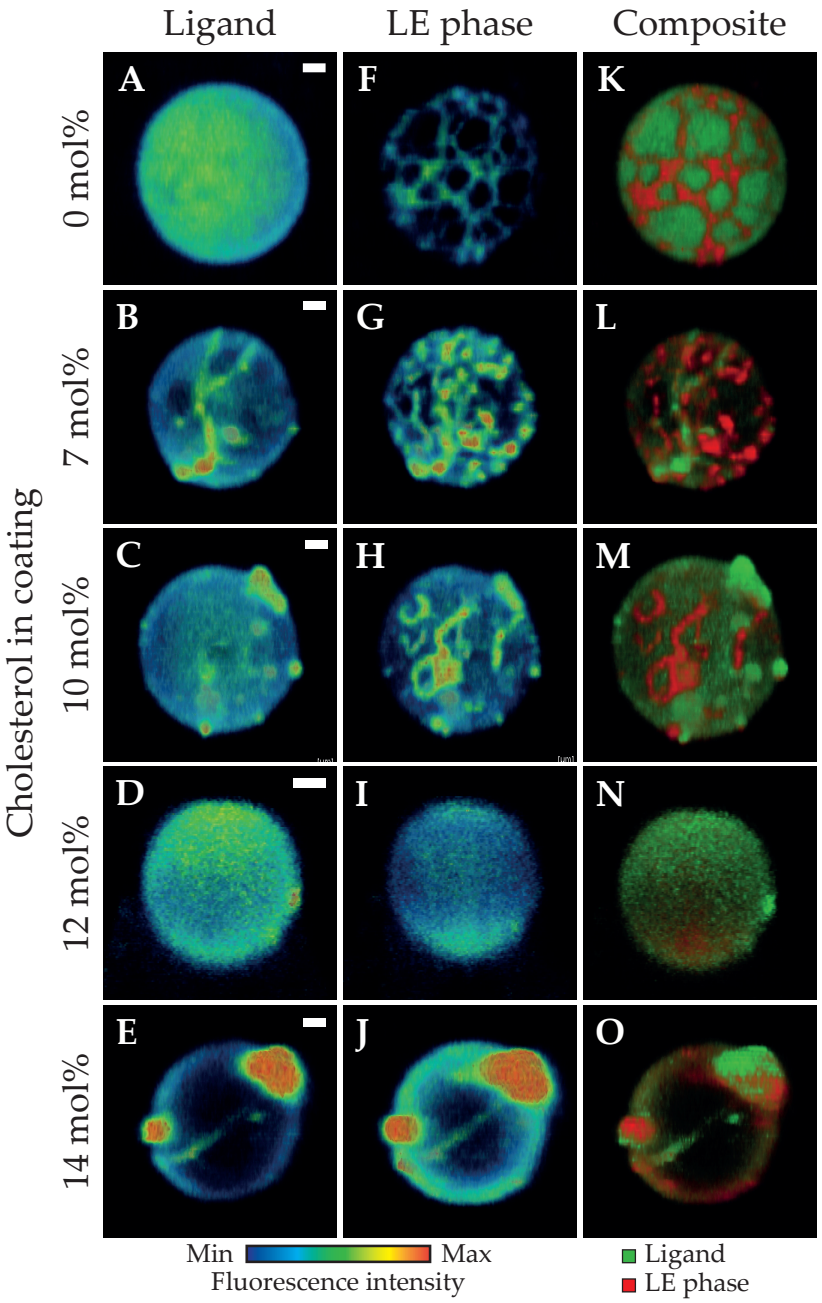

Figure 6.2 Selected views of 4Pi confocal microscopy *y*-stacks of indirect DSPC-based microbubbles without cholesterol (**A**, **F**, **K**, diameter (*d*) = 6.4 µm, LC phase area 35%), with 7 mol% cholesterol (**B**, **G**, **L**, *d* = 5.6 µm, LC phase area 22%), with 10 mol% cholesterol (**C**, **H**, **M**, *d* = 6.1 µm, LC phase area 22%), with 12 mol% cholesterol (**D**, **I**, **N**, *d* = 3.6 µm, LC phase area 7%), and with 14 mol% cholesterol (**E**, **J**, **O**, *d* = 5.8 µm, LC phase area 22%) in the phospholipid coating. Images show the ligand distribution (**A**-**E**; Oregon Green 488), LE phase (**F**-**J**; rhodamine-DHPE), and composite view (**K**-**O**). Scale bars are 1 µm.

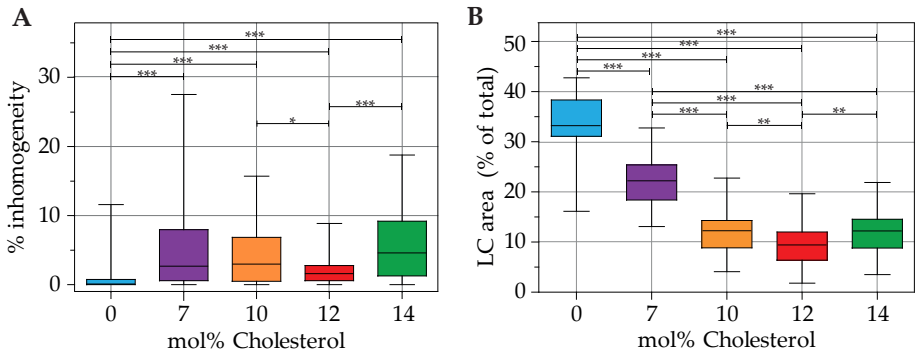

Figure 6.3 A) Parts classified as inhomogeneity (%) in the ligand distribution, and (**B**) size of the LC area (% of total surface area) of indirect DSPC microbubbles without cholesterol (*N* = 58), with 7 mol% (*N* = 34), 10 mol% (*N* = 40), 12 mol% (*N* = 61), and with 14 mol% (*N* = 45) cholesterol in the coating. Boxplots show the median and interquartile range with whiskers from minimum to maximum. Statistical significance is indicated with **p*<0.05, ***p*<0.01, or ****p*<0.001.

distribution was increasingly affected, as reflected by quantification of the LC phase area (Figure 6.3B). Microbubbles without cholesterol had a significantly larger surface area in LC phase than those with cholesterol in their coating. Microbubbles with 7 mol% cholesterol displayed LE phase areas with enriched fluorescent dye (Figure 6.2G) and had a significantly larger surface area in LC phase than those with more cholesterol in their coating. Microbubbles with 10 mol% cholesterol displayed LE phase areas as well (Figure 6.2H). Microbubbles with 12 mol% cholesterol had a homogeneous distribution of the fluorescent dye Rhodamine-DHPE (Figure 6.2I), with the smallest LC phase area per microbubble of all formulations (Figure 6.3B). In microbubbles with 14 mol% cholesterol, Rhodamine-DHPE was not only distributed homogeneously in the coating, but also present in buckles on the outside of the coating (Figure 6.2J). The LC phase area in microbubbles with 14 mol% cholesterol was comparable to the LC phase area in microbubbles with 10 mol% cholesterol (Figure 6.3B).

Figure 6.4 shows the percentage of indirect DSPC-based microbubbles with buckles per batch. An example of a microbubble with buckles is shown in Figure 6.2J, 6.2O. Microbubbles without cholesterol in the coating had the lowest incidence of buckles. Microbubbles with 12 mol% cholesterol in the coating had a higher incidence of buckles (p = 0.050) than those without cholesterol. Furthermore, the variability between batches increased with higher concentrations of cholesterol.

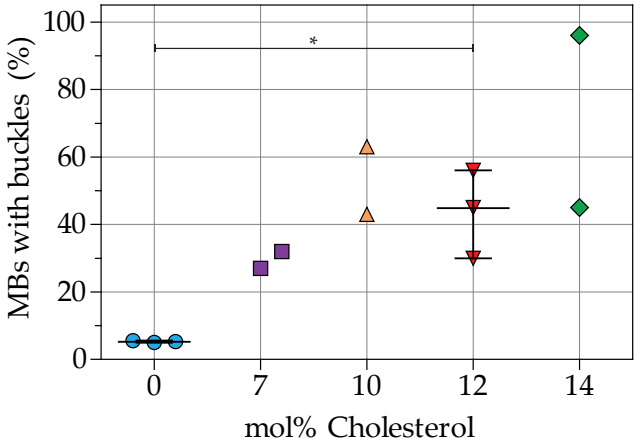

Figure 6.4 Percentage of microbubbles (MBs) with buckles per batch of indirect DSPC-based microbubbles without cholesterol and with 7, 10, 12, or 14 mol% cholesterol. Each symbol represents one batch of microbubbles. Overlaid black lines represent the median and interquartile range. Statistical significance is indicated with $*p<0.05$.

6.3.2 Acoustical characterization

Based on the physicochemical characterization described above, indirect DSPC-based microbubbles with 12 mol% cholesterol were chosen for acoustical characterization because they had the most homogeneous ligand and lipid phase distribution. They were compared to the direct and indirect DSPC-based microbubbles without cholesterol and for each type of microbubble data was acquired from at least two separate batches. Figure 6.5 shows a typical example of a 3D confocal acquisition before and after ultrasound with the corresponding *R–t* curve obtained from the ultra-high-speed recording at 50 kPa PNP for a direct DSPC (top row), indirect DSPC (middle row), and indirect DSPC-cholesterol (bottom row) microbubble. The coating of direct and indirect DSPC microbubbles was phase separated into dark LC domains with a bright interdomain region, while the coating of indirect DSPC-cholesterol microbubbles was in one homogeneous lipid phase. This was in line with the results obtained by 4Pi confocal microscopy. The direct DSPC microbubble shown in Figure 6.5 had one bright spot present in the coating before and after ultrasound, which was classified as a buckle. The coating of the indirect DSPC microbubble in Figure 6.5 had one large and several smaller LC phase domains. For the indirect DSPC-cholesterol microbubble in Figure 6.5, the maximum intensity projection of the confocal *z*-stacks resulted in more brightness near the edge of the microbubble than in the center. However, when looking at the separate *z*-slices the fluorescent signal was homogeneous over the microbubble coating (Supplemental Figure 6.3).

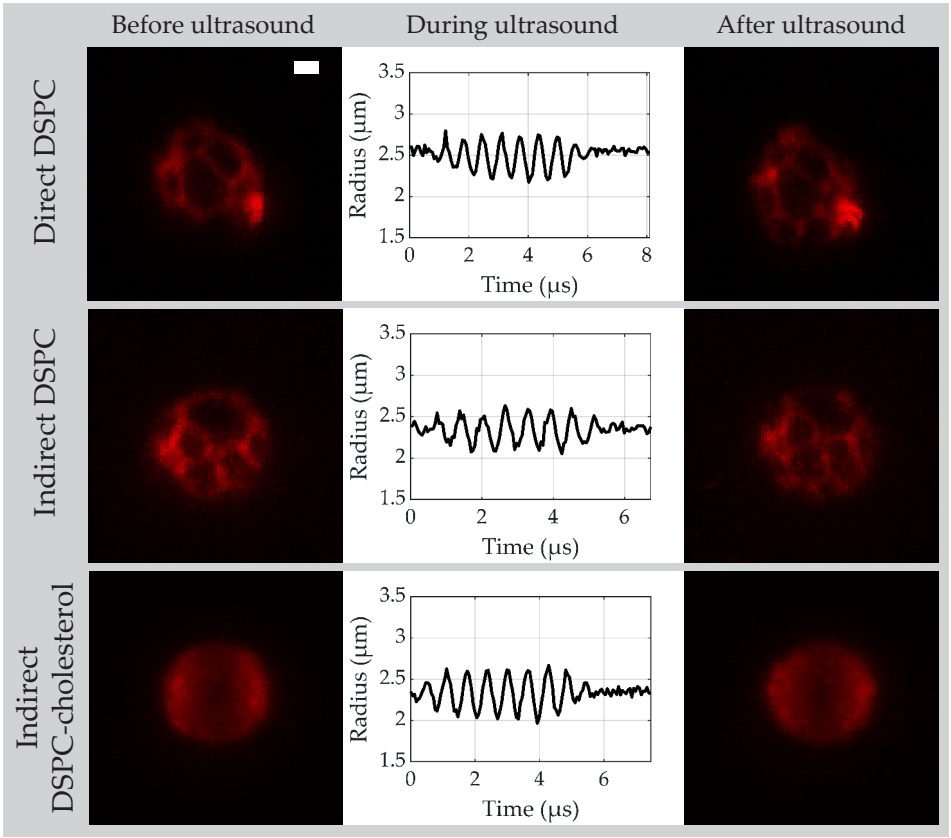

Figure 6.5 Maximum intensity projections of confocal *z*-stack from direct DSPC, indirect DSPC, and indirect DSPC-cholesterol (12 mol%) microbubbles with the LE phase in red, before and after ultrasound, with the microbubble radius as a function of time obtained from the Brandaris 128 ultra-high-speed recordings during ultrasound (50 kPa PNP, 1.6 MHz). Scale bar is 1 μm and applies to all images.

Oscillation amplitudes at frequencies between 1-4 MHz and acoustic pressure of 50 kPa were obtained per microbubble from the *R–t* curves and fitted to the harmonic oscillator model at each f_T (examples at 1.2, 1.6. and 2.0 MHz shown in Supplemental Figure 6.4). Resonance frequencies resulting from the fit to the harmonic oscillator model are presented in Figure 6.6, with the obtained shell elasticity and viscosity parameters listed in Table 6.1. The shell elasticity of direct DSPC microbubbles was the highest, while the shell elasticity of indirect DSPC-cholesterol microbubbles was close to that of an uncoated microbubble. The shell viscosity parameter is related to damping of the oscillation, and was lowest for the direct DSPC microbubbles, which had the highest oscillation amplitudes.

Table 6.1 Microbubble (MB) spectroscopy results at 50 kPa.

MB Type	N	Shell elasticity[1] (N/m)	Shell viscosity[1] ($\times 10^{-8}$ kg/s)	Max IQR of oscillation amplitude (%)	Median IQR of oscillation amplitude (%)
Direct DSPC	44	0.14 (0.12-0.15)	0.43 (0.38-0.61)	8.0	1.5
Indirect DSPC	49	0.03 (0.01-0.06)	0.99 (0.89-1.40)	4.5	0.6
DSPC-cholesterol[2]	50	0.01 (0.01-0.02)	1.39 (0.97-1.55)	10.2	0.7

[1] presented as median (IQR); [2] indirect DSPC-cholesterol microbubbles with 12 mol% cholesterol.

Figure 6.7 illustrates the variability in acoustical response within the three types of microbubbles. The variability was quantified as the interquartile range (IQR) of the oscillation amplitude from different microbubbles of the same size at the same transmit frequency ($N > 3$ per bin). The maximum and median IQR values for each type of microbubble are listed in Table 6.1. Indirect DSPC-cholesterol microbubbles had the highest maximum IQR, while direct DSPC microbubbles had the highest median IQR. Overall, indirect DSPC microbubbles exhibited the lowest variability in acoustical response.

Figure 6.8 shows the deflation of the microbubble, quantified as the diameter decrease relative to the initial diameter, for direct DSPC, indirect DSPC, and indirect DSPC-cholesterol microbubbles. At 50 kPa, direct DSPC microbubbles deflated significantly more than the indirect DSPC and DSPC-cholesterol microbubbles, while no statistically significant difference in deflation was found between the indirect DSPC and DSPC-cholesterol microbubbles. However, at 50 kPa the direct DSPC microbubbles had higher oscillation amplitudes than the other two groups. When comparing the deflation of microbubbles with similar oscillation amplitudes, marked as a grey area in Figure 6.8B, no statistically significant differences were

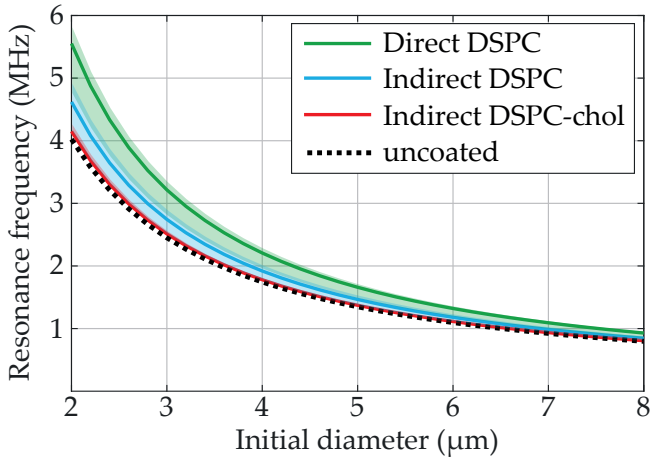

Figure 6.6 Resonance frequency (MHz) per initial diameter (μm) at 50 kPa of direct DSPC (green), indirect DSPC (blue), and indirect DSPC-cholesterol (red, 12 mol%) microbubbles. The dotted line represents the resonance frequency of uncoated microbubbles. The shaded areas indicate the range of individual microbubble resonance frequencies obtained by fitting at each f_T.

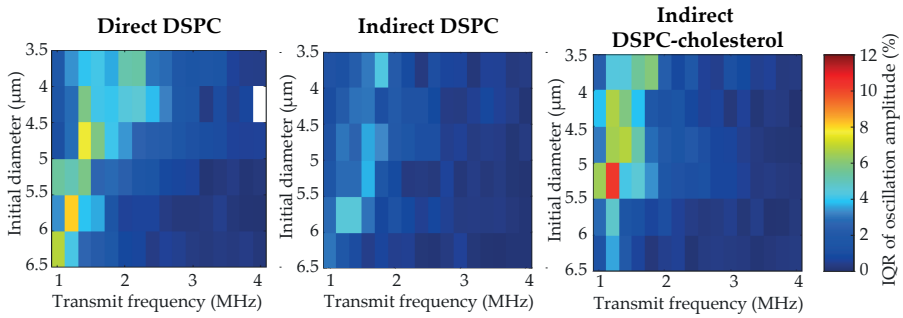

Figure 6.7 Variability in acoustic response represented as the IQR of the oscillation amplitude at 50 kPa of direct DSPC, indirect DSPC, and indirect DSPC-cholesterol (12 mol%) microbubbles of different sizes (3.5-6.5 µm) at different transmit frequencies (1-4 MHz). All bins are based on $N > 3$, bins with $N < 3$ are blank.

found. Therefore, the statistical differences found at 50 kPa can be explained by a difference in oscillation amplitude, not acoustical stability. At 150 kPa, all types of microbubbles deflated significantly more than at 50 kPa. Furthermore, the indirect DSPC microbubbles deflated significantly less than both other groups, also when comparing only microbubbles with similar oscillation amplitudes (Figure 6.8C). No statistically significant difference in deflation was found between direct DSPC and indirect DSPC-cholesterol microbubbles.

The non-linear behavior was studied by looking at the acoustic response at the subharmonic and second harmonic frequencies at 50 and 150 kPa. At subharmonic frequencies, all types of microbubbles had a low response rate and no statistical differences were found between the groups (Supplemental Figure 6.5). The percentages of microbubbles with a response at the second harmonic frequency are presented in Figure 6.9A. At 50 kPa, the direct DSPC microbubbles exhibited

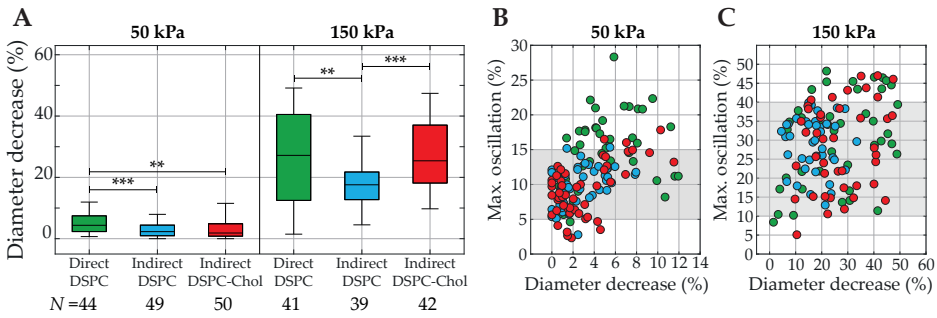

Figure 6.8 A) Diameter decrease (%) for direct DSPC (green), indirect DSPC (blue), and indirect DSPC-cholesterol (red, 12 mol% cholesterol) microbubbles at 50 kPa (left panel) and 150 kPa (right panel). Boxplots represent the median and IQR. $^{**}p<0.01$. $^{***}p<0.001$. **B-C**) Maximum oscillation (%) as a function of diameter decrease (%) for direct DSPC (green), indirect DSPC (blue), and DSPC-cholesterol (red, 12 mol% cholesterol) microbubbles at 50 kPa (**B**) and 150 kPa (**C**). Grey areas indicate the range of maximum oscillation values reached by all three types of microbubbles.

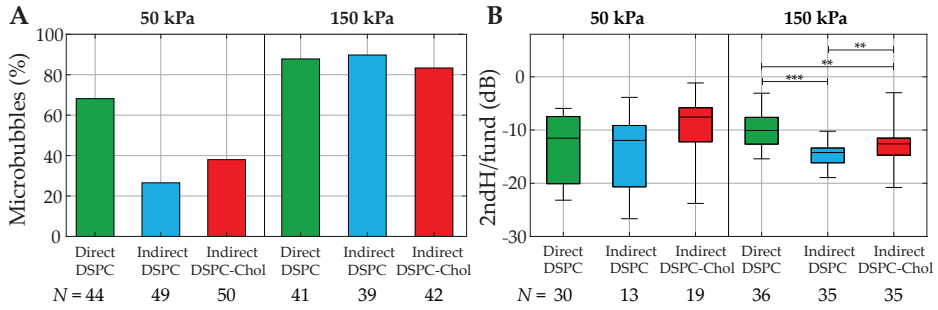

Figure 6.9 A) Percentage of direct DSPC (green), indirect DSPC (blue), and indirect DSPC-cholesterol (red, 12 mol% cholesterol) microbubbles with second harmonic response at 50 kPa (left panel) and 150 kPa (right panel). **B**) Second harmonic amplitude normalized to the fundamental (dB) of direct DSPC (green), indirect DSPC (blue), and indirect DSPC-cholesterol (red, 12 mol% cholesterol) microbubbles at 50 kPa (left panel) and 150 kPa (right panel). Boxplots represent the median and IQR, with whiskers ranging from maximum to minimum. $^{**}p<0.01$. $^{***}p<0.001$.

the highest number of second harmonic responses (68%), while this number was considerably lower for the indirect DSPC (26%) and the indirect DSPC-cholesterol (38%) microbubbles. At 150 kPa, all three types had similar percentages of microbubbles with a second harmonic response, and all occurrences were higher than those at 50 kPa. The second harmonic amplitudes were similar for all microbubble types at 50 kPa (Figure 6.9B). At 150 kPa, however, the direct DSPC microbubbles had significantly higher second harmonic amplitudes than both other microbubble types. Additionally, the indirect DSPC-cholesterol microbubbles had a significantly higher second harmonic amplitude than the indirect DSPC microbubbles.

Confocal *z*-stacks of each microbubble were manually scored for the presence of buckles (none, single, multiple, or extensive with examples provided in Supplemental Figure 6.2), before and after ultrasound insonification (Figure 6.10). Indirect DSPC microbubbles (N = 49 at 50 kPa; N = 39 at 150 kPa) had the lowest occurrence of buckles both before and after ultrasound insonification, which was comparable

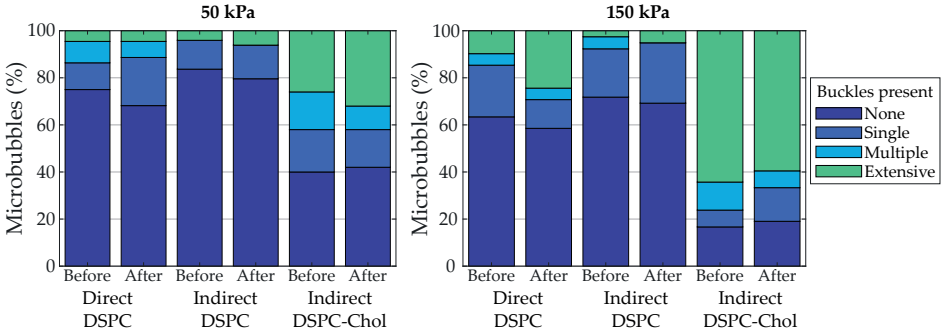

Figure 6.10 Percentage of microbubbles with buckles (none, single, multiple, or extensive) before and after insonification at 50 kPa (left panel) and 150 kPa (right panel). Indirect DSPC-cholesterol microbubbles contained 12 mol% cholesterol.

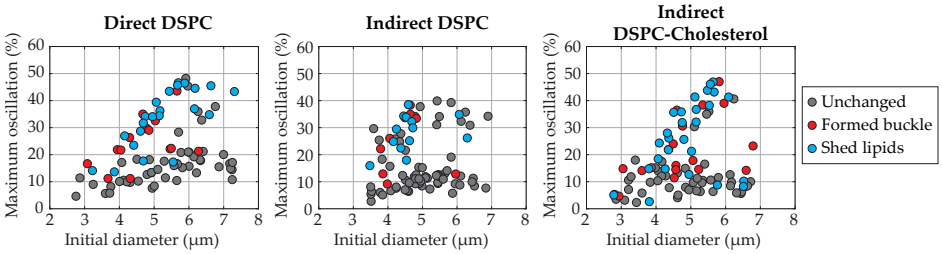

Figure 6.11 Maximum oscillation amplitude (%) of single direct DSPC (left, *N* = 85), indirect DSPC (middle, *N* = 88), and indirect DSPC-cholesterol (right, 12 mol% cholesterol, *N* = 92) microbubbles as a function of the initial microbubble diameter (μm). Microbubbles imaged by confocal microscopy directly before and after insonification (1-4 MHz, 50 or 150 kPa) were compared and scored as unchanged (grey), formed a buckle (red) or shed lipid material (blue).

to that of the direct DSPC microbubbles (*N* = 44 at 50 kPa; *N* = 41 at 150 kPa). Indirect DSPC-cholesterol microbubbles (*N* = 50 at 50 kPa; *N* = 42 at 150 kPa) had a notably higher occurrence of buckles than both other groups at both 50 and 150 kPa. Further analysis did not reveal a direct correlation between the oscillation amplitude and the presence of buckles in the shell before ultrasound insonification (Supplemental Figure 6.6). The maximum oscillation amplitude was compared between microbubbles without buckles, with a single buckle, with multiple buckles, or with extensive buckles in the coating before ultrasound insonification. For all types of microbubbles, at 50 and 150 kPa, no statistically significant differences in oscillation amplitude were found between the groups. Next, the correlation between the change in microbubble coating upon ultrasound insonification and the maximum oscillation amplitude was evaluated as shown in Figure 6.11. The median excursion amplitude of microbubbles that experienced a change, either by forming a buckle or by shedding lipids from the coating, was significantly larger ($p < 0.001$) than the excursion amplitude of unchanged microbubbles for all microbubble types. For direct DSPC microbubbles, the difference between changed and unchanged coatings was the most explicit, with a threshold amplitude of approximately 20% above which most microbubbles were changed after ultrasound insonification. For indirect DSPC microbubbles the threshold amplitude was similar, albeit less pronounced. The indirect DSPC-cholesterol microbubbles also exhibited formation of buckles and shedding of lipid material in microbubbles oscillating with amplitudes <20%.

Finally, the correlation between LC domain size and oscillation amplitude was investigated for a limited size range of microbubbles, ruling out size dependent differences in oscillation (Figure 6.12). Since the indirect DSPC-cholesterol microbubbles were lacking LC domains they could not be scored for their LC domain size. Unscored microbubbles are shown as black dots in Figure 6.12. For the direct and indirect DSPC microbubbles of 4.5-6.0 μm (initial diameter), the lipid phase

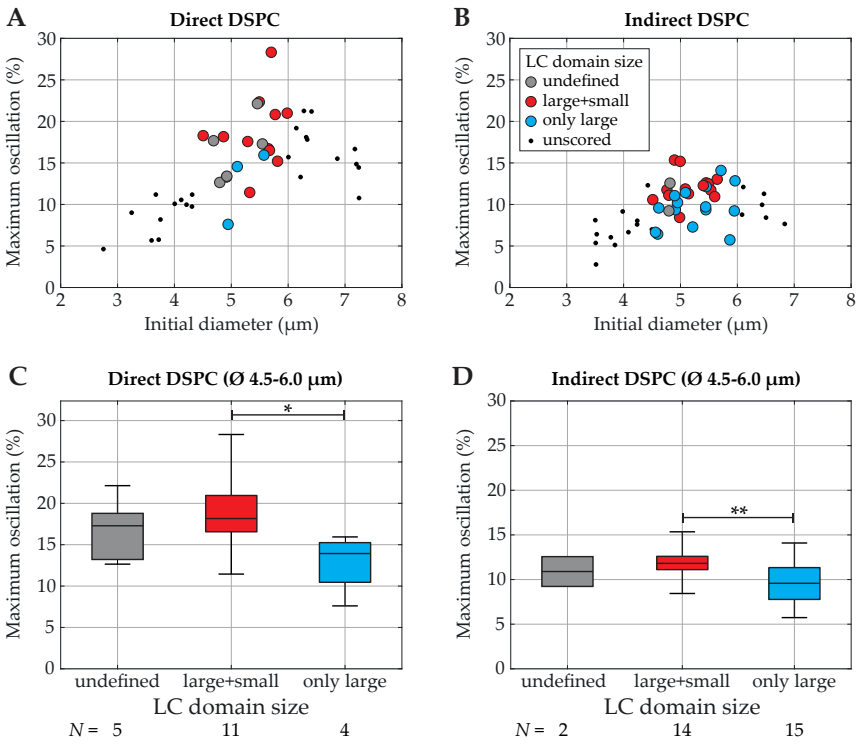

Figure 6.12 Maximum oscillation amplitude (%) at 50 kPa (over 1-4 MHz) as a function of initial diameter (µm) (**A-B**) for single direct DSPC (left) and indirect DSPC (right) microbubbles of 4.5-6.0 µm in diameter with LC domain size score as undefined (grey), large and small (red) or only large LC domains (blue), and as boxplot (**C-D**) representing the median and IQR with whiskers ranging from maximum to minimum. In (**A**) and (**B**) the unscored microbubbles outside the 4.5-6.0 µm range are shown as black dots. *p<0.05. **p<0.01.

distribution was scored as "only large LC domains", "large and small LC domains", or "undefined" (Supplemental Figure 6.7). Both the direct (N = 11) and indirect (N = 14) DSPC microbubbles with large and small LC domains had a significantly higher oscillation amplitude than those with only large LC domains (direct: N = 4, indirect: N = 15).

6.4 Discussion

The results of this study showed that cholesterol significantly affected the ligand and lipid phase distribution in DSPC-based phospholipid-coated microbubbles made by the indirect method. The lipid handling prior to microbubble production also affected the ligand distribution, as shown previously [427]. Both the addition of cholesterol and the lipid handling prior to microbubble production were shown to influence the acoustic behavior of the microbubbles, as reflected in the apparent elasticity

and viscosity values and resonance frequencies. Finally, the variability in acoustic response was enhanced for the microbubbles without lipid phase separation in the coating, namely the indirect DSPC-based microbubbles with 12 mol% cholesterol.

6.4.1 Physiscochemical characterization

The first part of this study revolved around the production and physicochemical characterization of DSPC-based microbubbles with cholesterol. Results indicated that the mean size of the microbubbles decreased with increasing concentrations of cholesterol. In contrast, Kaur et al. found that microbubbles with DSPC and cholesterol (1:1 molar ratio) were not significantly different in size from microbubbles with DSPC only [459]. However, those microbubbles were air-filled and did not contain any emulsifier such as PEG40-stearate or DSPE-PEG2000 like the microbubbles investigated in the present study. In our study, the span value increased with increasing concentrations of cholesterol, indicating that microbubbles with cholesterol were more polydisperse than those without cholesterol. Furthermore, the variability in polydispersity was larger between batches of microbubbles with cholesterol than those without cholesterol.

Addition of cholesterol to the indirect DSPC-based microbubble coating affected both the ligand and the lipid phase distribution. Indirect DSPC microbubbles without cholesterol had a mostly homogeneous ligand distribution as shown by fluorescence microscopy imaging, which is in agreement with results from Langeveld et al. [427]. However, all types of microbubbles with cholesterol had a significantly more heterogeneous and variable ligand distribution than those without cholesterol. While the ligand distribution of microbubbles with 12 mol% cholesterol was the most homogeneous and comparable to that of the indirect DSPC microbubbles without cholesterol, indirect DSPC microbubbles with 14 mol% cholesterol had a more heterogeneous ligand distribution. The increased number of buckles in the coating is likely the reason for this increase in heterogeneity.

The indirect DSPC microbubbles without cholesterol had a lipid phase distribution similar to previous reports, with dark LC domains and a bright interdomain LE region [389, 427]. All types of microbubbles with cholesterol had a significantly smaller LC phase area than those without cholesterol, indicating that cholesterol molecules modified the lateral molecular packing of the microbubble coating. The impact of cholesterol on the lipid phase distribution was most evident in microbubbles with 12 mol% cholesterol, where all components appeared to be miscible and in a single homogeneous phase. With a higher concentration of cholesterol, specifically 14 mol%, the quantified LC phase area was larger than in microbubbles with 12 mol% cholesterol. A previously reported analysis of the lipid phase behavior in

binary monolayers of DPPC or DSPC with cholesterol suggested a three-state phase model [457], where cholesterol either reduced or increased the lateral molecular packing. According to that study, the lateral molecular packing of a lipid monolayer is expected to decrease with low concentrations of cholesterol and increase with higher concentrations of cholesterol. This is in agreement with our results of the lateral molecular packing, quantified here as LC phase area, decreasing up to 12 mol% and then increasing at 14 mol% cholesterol. Other work focused on lipid phase behavior in monolayers includes atomic force microscopy images of monolayers with DPPC and 33 mol% cholesterol, showing a homogeneous phase distribution [456]. While we found microbubbles with 33 mol% cholesterol to be highly unstable, those with 12 mol% had a homogeneous phase distribution. This suggests that the phase behavior of phospholipids in a monolayer cannot be directly translated to the phase behavior of phospholipids in a microbubble coating, which is supported by a direct comparison of lipid phase behavior in monolayers and microbubble coatings with the same ternary mixture of DPPC or DSPC with DSPE-PEG2000 and PEG40-stearate [427].

Interestingly, cholesterol (10-50 mol%) has been used for many years to stabilize liposomes with DPPC or DSPC by increasing the lateral molecular packing [464], emphasizing the difference in lamellar structures, *i.e.* bilayers, of a liposome compared to the phospholipid monolayer coating of a microbubble. DSPC forms lamellar structures when suspended in water at room temperature [21], however, during microbubble production by probe sonication the lamellar structures are disrupted and the molecules self-assemble as a monolayer of phospholipids at the gas-liquid interface [22]. In a model membrane system with monolayer-bilayer junctions, cholesterol was shown to be involved in lipid-driven budding of the membrane, with higher concentrations of cholesterol resulting in increased budding [464]. These findings are in agreement with the increased budding and formation of buckles we found in microbubbles with higher concentrations of cholesterol in the coating. In this context budding refers to formation of lipid bilayer-coated vesicles, while buckle formation refers to bilayers that are still attached to the lipid monolayer coating of the microbubble.

The present study includes a normalization factor in the analysis of the 4Pi microscopy data, to compensate for a difference in fluorescence intensity between the middle and the top or bottom of the microbubbles. The normalization factor did not affect the proper quantification of LC phase area in microbubbles without cholesterol. Since the difference in fluorescence signal between LC and LE phase in those microbubbles was much larger than the difference in signal between the middle and top or bottom of the microbubble, the LC phase area could easily be quantified in microbubbles with clear separation of the lipids into LC and LE phase.

The imaging artefact only became evident during analysis of microbubbles with a homogeneous lipid phase distribution, *i.e.* containing cholesterol. All experiments in this study were performed at a room temperature of 19-21 °C. Since the 4Pi confocal microscope operates at a limited range of temperature, this practice facilitated comparison of the data obtained from the 4Pi confocal microscopy and the acoustic characterization with the combined confocal and Brandaris 128 system, and was in accordance with previous microscopy studies on lipid and ligand distribution in microbubble coatings [389, 427]. Slight fluctuations in the temperature of the sample due to for instance the light or ultrasound are not expected to affect the lipid phase distribution, since the transition temperature for DSPC is 55 °C [465]. Furthermore, it was previously reported that in lipid bilayers of DPPC and cholesterol (10 or 20 mol%) the lipid phase distribution was only affected by temperatures above 40 °C [466]. Processing of lipid films in the sonicator bath and with the probe sonicator at power 3 did not affect the temperature of the samples.

6.4.2 Acoustical characterization

Microbubble spectroscopy was performed on direct DSPC, indirect DSPC, and indirect DSPC-cholesterol (12 mol%) microbubbles to characterize their acoustic behavior. The shell parameters found here can be directly compared to a previous study by van Rooij et al. [45], that used a similar method and included the same direct DSPC microbubbles as the current study. The shell elasticity found in the present study (0.14 (0.12-0.15) N/m) (median (IQR)) was slightly lower and the shell viscosity (0.43 (0.38-0.61) $\times 10^{-8}$ kg/s) slightly higher than previously published (0.26 ± 0.13 N/m, mean ± SD; 1.0 (0.7) $\times 10^{-8}$ kg/s, median (IQR)), however, still within the error margins. The indirect DSPC microbubbles had a shell elasticity approaching that of an uncoated microbubble, similar to the DPPC-based microbubbles studied by van Rooij et al. [45]. As the shell elasticity was lower, the resonance frequency was also lower (Eq. 6.2). Both the indirect DSPC and the indirect DSPC-cholesterol microbubbles had a higher shell viscosity than the direct DSPC microbubbles. This was reflected in the oscillation amplitudes at 50 kPa, which were higher for the direct DSPC microbubbles than for the other groups, indicating lower damping and therefore lower viscosity (Eq. 6.1).

The influence of lipid phase distribution and lipid handling on the variability in acoustic response was assessed by comparing microbubbles with lipid phase separation, *i.e.* indirect DSPC, to those without lipid phase separation, *i.e.* indirect DSPC-cholesterol (12 mol%), and to those made with a different way of lipid handling prior to microbubble production, *i.e.* direct DSPC. While indirect DSPC-cholesterol microbubbles had the highest maximum variability in response, the median variability was highest for the direct DSPC microbubbles. These results suggest that lipid

handling prior to microbubble production can reduce the variability in response and that although the maximum variability was highest in the indirect DSPC-cholesterol microbubbles, the difference in lipid phase separation did not affect the variability in acoustic response overall. Due to their more uniform response, the indirect DSPC microbubbles would be the most suitable candidate for drug delivery applications. Two maxima can be observed in the variability in response of direct and indirect DSPC microbubbles. While this might be explained as a size dependent effect, it is not a distinct trend and perhaps more likely due to the limited sample size. Apart from differences between the microbubble types, all microbubbles exhibited the highest variability in response at the resonance frequency. Thus, to insonify microbubbles at a frequency other than their resonance frequency could be a new strategy to achieve a more uniform response to ultrasound, although monodisperse microbubbles are needed for this strategy to yield a uniform and predictive response of a bulk of microbubbles.

Acoustical stability was studied using the decrease in diameter after ultrasound, *i.e.* deflation. For this analysis, the mean microbubble diameter of 128 frames without ultrasound was regarded as the initial diameter. Since the final diameter was determined based on the last recording of each microbubble, *i.e.* the recording of ultrasound insonification at 4 MHz, only the last 10 frames were used to calculate the mean microbubble diameter. The microbubble size in these last frames was stable and the difference in sample size is therefore not expected to influence the results. At 50 kPa, statistical differences in deflation could be explained by differences in the oscillation amplitude. At 150 kPa, however, the indirect DSPC microbubbles were significantly more stable than the direct DSPC and indirect DSPC-cholesterol microbubbles. Since no statistical differences were found between the direct DSPC and indirect DSPC-cholesterol microbubbles, the difference in acoustical stability was not caused by a difference in coating microstructure, which is in accordance with previous studies [467]. As the composition of direct and indirect DSPC microbubbles was exactly the same, the difference in acoustical stability must have been caused by the difference in lipid handling prior to microbubble production which is known to alter the ligand distribution, synonymous to the distribution of DSPE-PEG2000 [427].

The non-linear behavior of microbubbles is imperative for successful contrast-enhanced ultrasound imaging and ultrasound molecular imaging. At 50 kPa, the direct DSPC microbubbles had a more frequent second harmonic response than the other types of microbubbles. At 150 kPa, the majority of all types of microbubbles had a second harmonic response. The differences in variability in the acoustic response between the types of microbubbles, as presented in Figure 7, are also reflected in the range of the second harmonic response at 150 kPa, presented in

Figure 9B. Indirect DSPC microbubbles had the lowest variability in second harmonic amplitude at 150 kPa, while the response at 50 kPa was comparable to the other types. This could be due to the low amplitudes of the second harmonic response at 50 kPa, which translates to a larger experimental error. The percentage of direct DSPC microbubbles with a non-linear response, subharmonic or second harmonic, at 50 kPa was lower than published before [45]. This may be explained by the different pulse length (8 cycle instead of 10 cycle pulse), or the fact that as a lower amount of light reaches the Brandaris 128 camera in the current imaging system, the noise level is slightly higher. More experiments focused on non-linear behavior are needed for a comprehensive assessment of indirect DSPC microbubbles for ultrasound molecular imaging. However, this lies outside the scope of the present study.

6.4.3 Lipid phase distribution and acoustical behavior

The homogeneous lipid phase distribution in indirect DSPC-cholesterol microbubbles found by 4Pi confocal microscopy was confirmed with confocal microscopy of the microbubbles also analyzed acoustically. Besides the homogeneous lipid phase distribution, indirect DSPC-cholesterol microbubbles had buckles in their coating before insonification more frequently and more extensively than microbubbles without cholesterol, demonstrated by 4Pi confocal microscopy as well. The DSPC-cholesterol microbubbles insonified at 150 kPa had more buckles than those insonified at 50 kPa, underlining the heterogeneity between different indirect DSPC-cholesterol microbubbles from the same batch. The variable buckle incidence may be explained by the low stability of the DSPC-cholesterol coating. Due to the low amount of LC phase area in their coating, indirect DSPC-cholesterol microbubbles are expected to dissolve at a faster rate than those without cholesterol [468]. Different collapse and shedding mechanisms, such as budding, folding, and buckling, have been proposed to explain how the phospholipid monolayer around the gas core responds to spontaneous dissolution of the microbubble [469].

Next, the correlation between maximum oscillation amplitude and change in the microbubble coating was investigated. After combining the data from microbubbles insonified at 50 and 150 kPa, the oscillation amplitude of microbubbles that experienced change due to ultrasound insonification was found to be significantly higher than that of unchanged microbubbles for all microbubble types, with a threshold amplitude of approximately 20%. Other studies investigating the lipid coating behavior in microbubbles during ultrasound insonification found comparable results, namely a threshold oscillation amplitude of 30% [450, 451]. The difference in threshold amplitude may be explained by the microbubble formulation as microbubbles in other studies were coated with DPPC [450] or DSPC [451] and

DSPE-PEG2000, without PEG40-stearate. Another explanation could be a difference in the production method, as the microbubbles for the present study were all made by probe sonication, in contrast to the vial shaker method used for previous studies.

This study is the first to record both the lipid phase distribution and acoustic response in single microbubbles with the combined confocal microscope and Brandaris 128 camera system. Whereas no correlation could be confirmed between the oscillation amplitude and the amount of buckles present before insonification, the LC domain size did correlate with the oscillation amplitude. Microbubbles with small sized LC domains had higher oscillation amplitudes, which is in accordance with previous reports on phospholipid-coated microbubbles with different sized LC domains, where those with smaller LC domains had a lower resistance to deformation [388]. By contrast, another study found no significant differences in the behavior or stability of microbubbles during ultrasound insonification when they related the lateral molecular packing to the acoustic behavior of microbubbles in different formulations, even though the method of production did affect the lipid packing significantly [470]. The reason for this could be the quantification of the lateral molecular packing as this was done by calculating the generalized polarization value for single microbubbles, which does not account for lipid phase separation or microstructures in the coating. Before the DSPC-based microbubbles with and without cholesterol studied here can be used for *in vivo* applications, several differences between the *in vitro* setting and the *in vivo* situation need to be considered. Besides the temperature, these differences also include the blood flow, blood viscosity, and soft boundaries affecting the microbubbles' acoustic behavior. Furthermore, the targeting strategy has to be adapted to avoid an immune response to streptavidin, a foreign protein [471].

6.4.4 Implications of the study

Addition of cholesterol to the indirect DSPC-based microbubble coating increased the variability in ligand distribution, acoustic response, polydispersity, and buckle formation. These effects can be explained by the altered lipid phase distribution as described above, and imply that the indirect DSPC-cholesterol microbubbles are less stable than those without cholesterol. Because the indirect DSPC-cholesterol microbubbles had heterogeneities in the form of buckles, they could not be regarded as microbubbles with a uniform lipid distribution when comparing their acoustic behavior to that of the microbubbles with heterogeneous lipid phase distribution, *i.e.* the direct and indirect DSPC microbubbles. Thus, reduced stability of the microbubble coating is expected when the components are all miscible and in the same LE phase, which will increase the heterogeneity of the microbubble population and thereby increase the variability of the acoustical response. Therefore, a different

approach will be required to achieve a more uniform microbubble response to ultrasound, possibly by tailoring the LC phase domains, as our results suggest that differences in LC domain size can predict the relative oscillation amplitude.

6.5 Conclusions

We produced indirect DSPC-based microbubbles with 7, 10, 12, and 14 mol% cholesterol in the coating. Cholesterol reduced lipid phase separation in the microbubble coating, resulting in a single phase at 12 mol% where all components were miscible. Buckle formation was increased with reduction of the LC phase area, suggesting increased spontaneous dissolution of the microbubbles. As the acoustic behavior of DSPC-based microbubbles made by the direct and indirect method was compared to that of indirect DSPC-based microbubbles with 12 mol% cholesterol, indirect DSPC microbubbles had the most uniform response to ultrasound and were the most stable acoustically. They had a lower shell elasticity and higher shell viscosity than the direct DSPC microbubbles. The modified lateral molecular packing of indirect DSPC-cholesterol microbubbles resulted in the lowest shell elasticity and highest shell viscosity of all microbubble types. Direct DSPC microbubbles displayed more non-linear acoustic behavior than the indirect DSPC and indirect DSPC-cholesterol microbubbles. Based on these results we can conclude that the both the lipid phase separation and lipid handling prior to microbubble production significantly affected the acoustic behavior of microbubbles. The indirect DSPC microbubbles had the most promising results with regard to stability and uniform ultrasound response. These are important traits for an ultrasound molecular imaging agent and for drug delivery applications, as the acoustic behavior of the microbubble must be predictable and controllable.

Acknowledgments—The authors thank F. Mastik and R. Beurskens from the Department of Biomedical Engineering, Erasmus University Medical Center, Rotterdam, the Netherlands, for their technical assistance during the experiments. The authors thank the Erasmus Optical Imaging Centre of Erasmus MC for use of their facilities, and Dr. Gert van Cappellen and Alex Nigg for their help. Finally, the authors thank Lipoid GmbH for providing a free sample of DSPC phospholipid.

Funding
This research was funded in part by the Phospholipid Research Center in Heidelberg, grant number KKO-2017-057/1-1, and in part by the Thorax Center of Erasmus University Medical Center in Rotterdam.

Supporting information

The Supporting Information is available free of charge at
https://doi.org/10.3390/pharmaceutics13010119

Supplemental Table 6.1 Concentration of indirect DSPC microbubbles (MBs)

Cholesterol (mol%)	*N*	Mean concentration ($\times 10^8$ MBs/mL)	SD ($\times 10^8$) or Range (min – max $\times 10^8$)
0	5	4.71	2.14
7	2	5.28	5.01 – 5.55
10	2	9.85	8.04 – 11.7
12	6	5.96	2.60
14	2	7.21	6.01 – 8.40

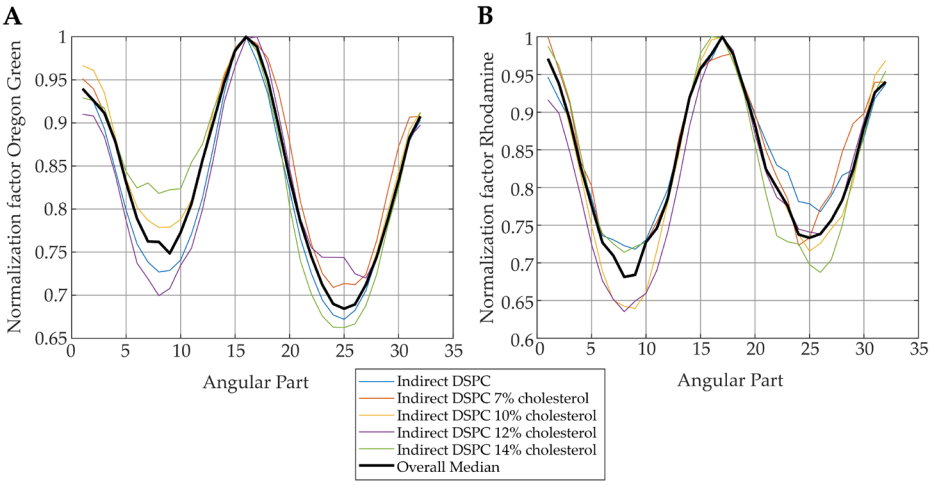

Supplemental Figure 6.1 Normalization factors for quantitative analysis of 4Pi confocal microscopy data. **A**) Normalization factor for Oregon Green (green channel) per angular part. **B**) Normalization factor for Rhodamine (red channel) per angular part. The normalization factor is based on the difference in fluorescence intensity between angular parts in the center (part 5-10 and part 23-28) and the angular parts at the top and bottom of the microbubble (part 15-20, part 1-3, part 30-32). The fluorescence signal from the center of the microbubble is captured by both objectives, while the fluorescence signal from the top and bottom of the microbubble is captured by only one of the objectives. This is caused by attenuation of the signal and because the gas core of the microbubble has a different refraction index than the rest of the sample.

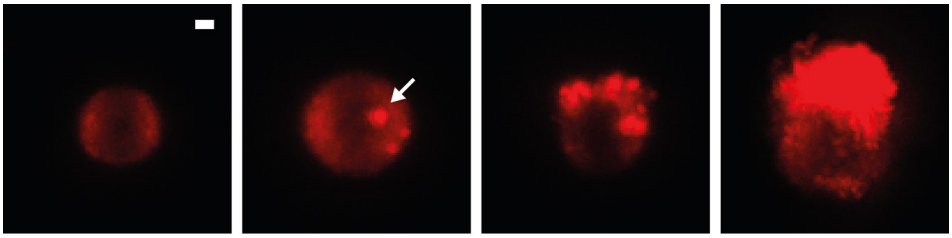

Supplemental Figure 6.2 Confocal maximum intensity projections of *z*-stack from indirect DSPC-cholesterol (12 mol%) microbubbles with LE phase in red. Examples of buckle score: none, single, multiple, extensive. Bright spots with 1 µm diameter or larger were classified as a buckle. Scale bar represents 1 µm and applies to all images. In the single buckle example, the bright spot classified as buckle is indicated with a white arrow.

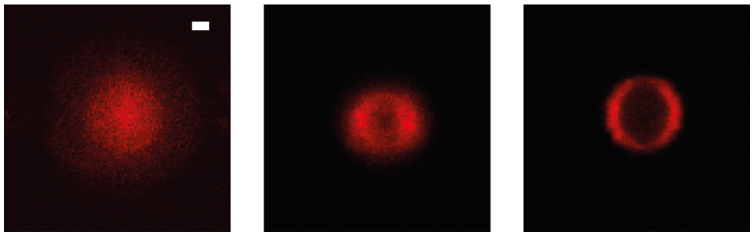

Supplemental Figure 6.3 Confocal slices from *z*-stack acquisition of indirect DSPC-cholesterol (12 mol%) microbubble, presented as maximum intensity projection in Figure 6.5. Scale bar represents 1 µm and applies to all images. Positions of the slices (*z*-axis) are 0, 1.6 µm, 3.6 µm.

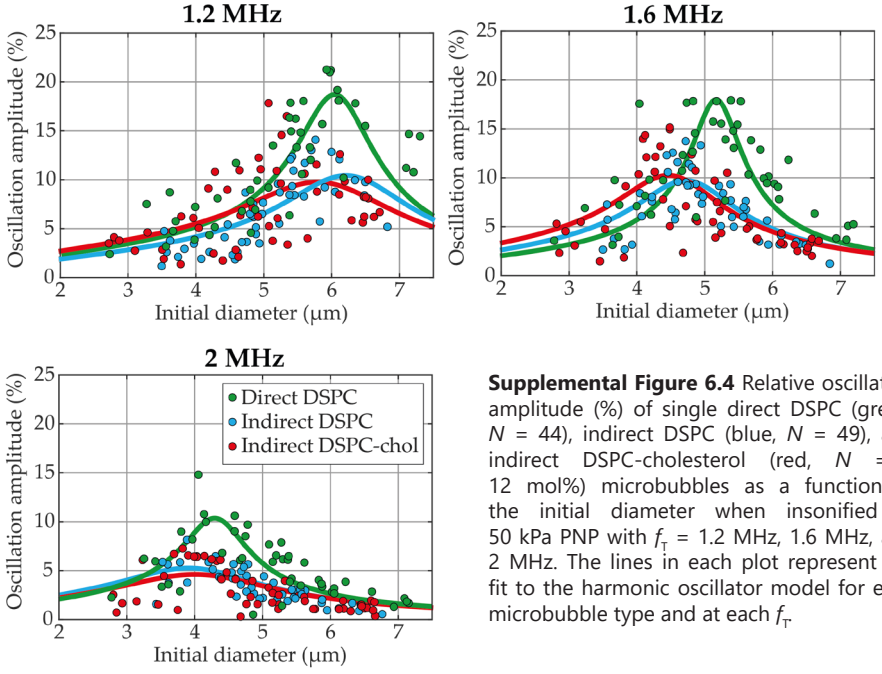

Supplemental Figure 6.4 Relative oscillation amplitude (%) of single direct DSPC (green, N = 44), indirect DSPC (blue, N = 49), and indirect DSPC-cholesterol (red, N =50, 12 mol%) microbubbles as a function of the initial diameter when insonified at 50 kPa PNP with f_T = 1.2 MHz, 1.6 MHz, and 2 MHz. The lines in each plot represent the fit to the harmonic oscillator model for each microbubble type and at each f_T.

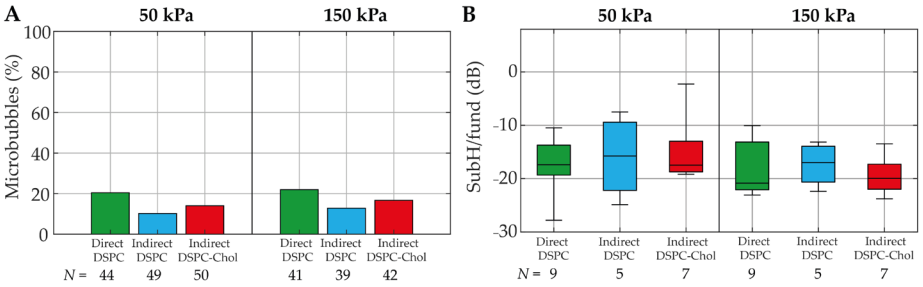

Supplemental Figure 6.5 A) Percentage of direct DSPC (green), indirect DSPC (blue), and indirect DSPC-cholesterol (red, 12 mol%) microbubbles with subharmonic response at 50 kPa (left panel) and 150 kPa (right panel). **B**) Subharmonic amplitude (dB) normalized by the fundamental of direct DSPC (green), indirect DSPC (blue), and DSPC-cholesterol (green) microbubbles at 50 kPa (left panel) and 150 kPa (right panel). Boxplots represent the median and IQR.

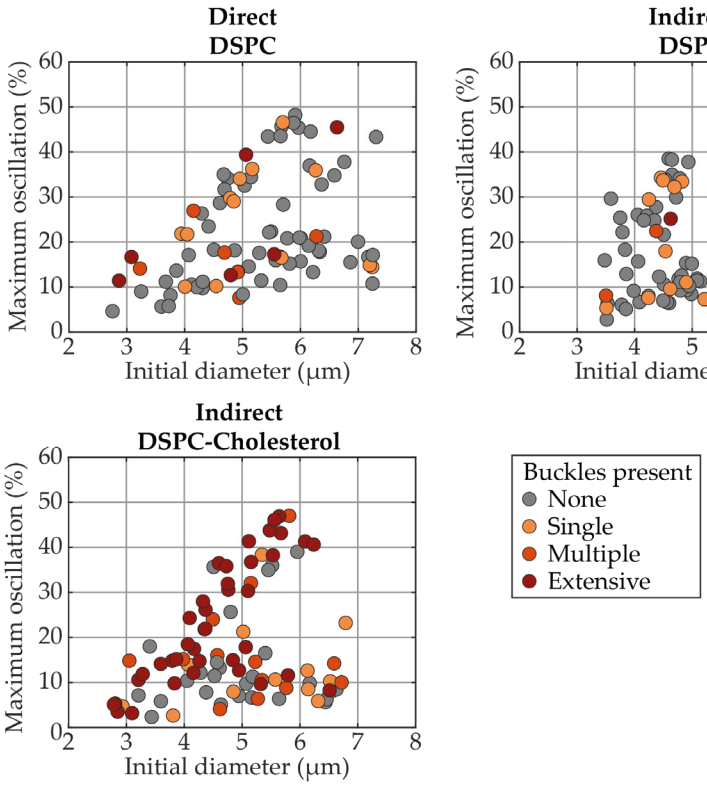

Supplemental Figure 6.6 Shell buckles versus oscillation amplitude. Maximum oscillation amplitude (%) of single direct DSPC (left, *N* = 85), indirect DSPC (middle, *N* = 88), and indirect DSPC-cholesterol (right, *N* = 92, 12 mol%) microbubbles as a function of the initial diameter (μm). Microbubbles were scored for buckles present before insonification (1-4 MHz, 50 or 150 kPa) based on confocal *z*-stacks as none (grey), single (orange), multiple (bright red) or extensive (dark red).

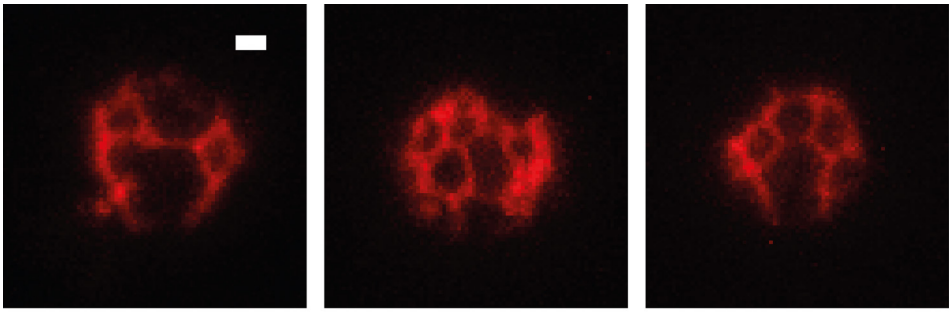

Supplemental Figure 6.7 Confocal maximum intensity projections of *z*-stacks from indirect DSPC microbubbles with LE phase in red. Examples of lipid phase distribution scores: "only large LC domains", "large and small LC domains", or "undefined". Scale bar represents 1 µm and applies to all images.

7

The 3D microbubble-cell dynamics: microbubble internalization and drug delivery by pores and tunnels

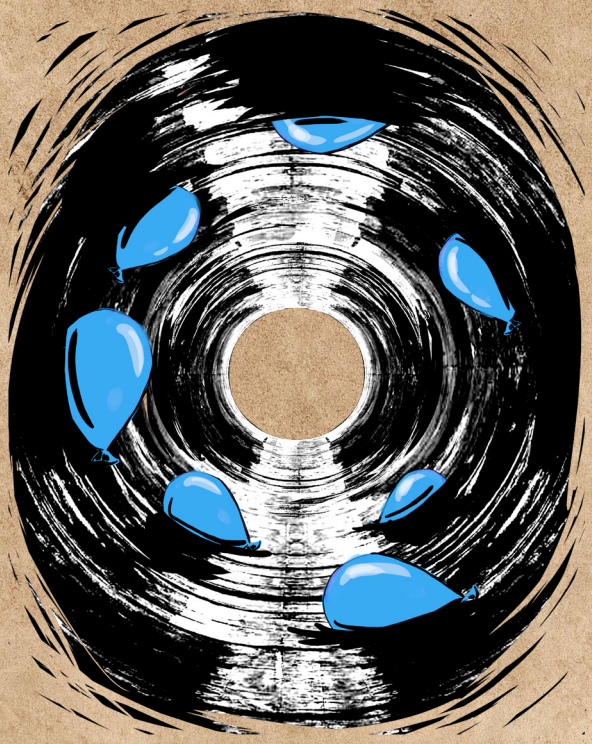

Inés Beekers, **Simone A.G. Langeveld**, Bram Meijlink, Antonius F. W. van der Steen, Nico de Jong, Martin D. Verweij, Klazina Kooiman

Submitted for publication

Abstract

Ultrasound insonification of microbubbles can locally enhance vascular drug delivery by increasing the cell membrane permeability. To aid development of a safe and effective therapeutic microbubble, more insight into the microbubble-cell interaction is needed. In this *in vitro* study we aimed to unravel the initial 3D morphology of a microbubble (*N* = 301) bound to an endothelial cell, determine whether this morphology was affected by the type of ligand on the microbubble, and investigate its influence on microbubble oscillation and the drug delivery outcome. High-resolution 3D confocal microscopy revealed that targeted microbubbles were internalized by endothelial cells, while this was not the case for non-targeted or IgG1-κ control microbubbles. The extent of internalization was ligand-dependent, since $\alpha_v\beta_3$-targeted microbubbles were significantly more internalized than CD31-targeted microbubbles. Ultra-high-speed imaging (~17 Mfps) in combination with high-resolution confocal microscopy (*N* = 246) showed that microbubble internalization resulted in a damped microbubble oscillation upon ultrasound insonification (2 MHz, 200 kPa, 10 cycles). Nevertheless, the cell's susceptibility to sonoporation (*i.e.* PI uptake) was increased for internalized microbubbles. Monitoring cell membrane integrity (*N* = 230) upon sonoporation showed the formation of either a pore, for intracellular delivery, or a tunnel (*i.e.* transcellular perforation), for transcellular delivery. Internalized microbubbles caused fewer transcellular perforations and lead to smaller pore areas. In conclusion, studying microbubble-mediated drug delivery using a state-of-the-art imaging system provided novel insights and revealed receptor-mediated microbubble internalization and its effect on microbubble oscillation and resulting membrane perforation.

Keywords—Microbubbles; Ultrasound; Drug delivery; Sonoporation; Transcellular perforation; Contrast agents

7.1 Introduction

Endothelial cells lining the vessel walls form an excellent barrier against drugs, while they are rarely the intended target as drugs often need to extravasate to reach the underlying diseased tissue. Thus, if extravasation can be locally enhanced, lower dosages of drugs can be administered systemically and therefore lower toxicity will be achieved. Phospholipid-coated microbubbles (1–10 μm in diameter) can do just that: upon ultrasound insonification, microbubbles with a gas core start to oscillate resulting in various mechanical and cellular effects [425]. Microbubbles were developed as ultrasound contrast agents and are widely used in the clinic for diagnostic ultrasound imaging [37]. Drug delivery is enhanced by oscillating microbubbles through different pathways: by perforation of the cell membrane,

referred to as sonoporation, by opening intercellular junctions or cell-cell contacts, and by stimulating endocytosis [53, 66, 153]. While the exact mechanisms are not fully understood [53, 66, 154, 425], it is clear that there exists a delicate balance between stable microbubble oscillation leading to enhanced drug delivery and more violent microbubble oscillation or inertial cavitation causing irreversible damage [3, 66, 472]. More insight in the interaction between microbubbles and endothelial cells is needed to facilitate translation to safe and effective clinical use of phospholipid-coated microbubbles for locally enhanced drug delivery.

Previous work on endothelial cells has mostly focused on establishing the relationship between the microbubbles' acoustic behavior and subsequent cellular effects such as intracellular drug uptake [473], opening of cell-cell contacts [58], and intracellular calcium fluctuations [59]. However, the therapeutic outcome in terms of drug delivery enhancement is expected to also depend on the microbubble-cell morphology prior to ultrasound insonification. This morphology may be affected by phagocytosis or internalization of microbubbles, as has been observed since the first generation of ultrasound contrast agents. Contrast enhanced ultrasound imaging has shown hepatosplenic uptake of microbubbles stabilized by either a polymer shell in Sonovist [474, 475], a surfactant in Levovist [476-478], or a phospholipid shell in BR14 [479] and Sonazoid [478, 480]. A spleen-specific uptake has been shown for SonoVue [482]. The uptake of microbubbles gives a late phase contrast enhancement that is sustained after the typical blood pool phase. The hepatosplenic uptake has been attributed to the phagocytosis by Kupffer cells in particular [478]. Phagocytic ratios differ for various contrast agents, influenced by for instance the charge of the microbubble or the shell composition [33, 478, 482].

Although macrophages and neutrophils are the classic examples of phagocytic cells, endothelial cells can also internalize particles through phagocytosis. Human umbilical vein endothelial cells (HUVECs) have been shown to phagocytose lipid droplets [483], bacteria [484], and micron-sized magnetic beads conjugated to a VEGFR2 antibody [485]. However, up to now the microbubble-cell interaction has been investigated mostly in 2D with a focus on what happens after microbubble oscillation. To incorporate possible phagocytosis into the understanding of sonoporation mechanisms, the microbubble-cell morphology prior to oscillation must be studied in 3D. Furthermore, Helfield et al. [473] have shown how sonoporation of endothelial cells can be transmembrane in nature, indicating that 3D images are also essential for a holistic view of sonoporation after ultrasound.

A recent literature overview on targeted microbubbles for therapeutic applications revealed that all studies reported a better therapeutic outcome with targeted microbubbles than with non-targeted microbubbles [486]. This inspired the idea that

there must be a receptor- or ligand-dependent component influencing the efficacy of enhanced drug delivery by ultrasound-activated microbubbles. A comprehensive study focusing on the microbubble-cell configuration, or morphology of targeting, both prior to and after ultrasound activation, will give valuable insights for future development of targeted microbubbles for therapeutic applications.

The aim of this study was to investigate the 3D morphology of microbubbles on the endothelial cell membrane and the resulting drug delivery response upon ultrasound insonification. The phagocytosis, or internalization, of microbubbles by endothelial cells was evaluated using 3D confocal microscopy for non-targeted, $\alpha_V\beta_3$-targeted, CD31-targeted, and IgG1-κ control microbubbles. Additionally, the oscillatory response of the microbubbles was quantified by ultra-high-speed Brandaris 128 imaging. The influence of microbubble-cell morphology on the drug delivery potential was evaluated by studying propidium iodide (PI) uptake and membrane perforation upon microbubble oscillation for each microbubble type.

7.2 Materials and methods

7.2.1 Microbubble preparation and targeting

The four types phospholipid-coated biotinylated microbubbles (non-targeted, $\alpha_V\beta_3$- and CD31-targeted, and IgG1-κ control) were produced in-house with a C_4F_{10} gas core according to the indirect method as described previously [397, 427]. The coating composition included 1,2-distearoyl-*sn*-glycero-3-phosphocholine (DSPC; 84.8 mol%; Lipoid GmbH, Ludwigshafen, Germany), polyoxyethylene-40-stearate (PEG-40 stearate; 8.2 mol%; Sigma-Aldrich, Zwijndrecht, the Netherlands), 1,2-distearoyl-*sn*-glycero-3-phosphoethanolamine-N-[carboxy(polyethylene glycol)-2000] (DSPE-PEG(2000); 5.9 mol%; Iris Biotech GmbH, Marktredwitz, Germany), and 1,2-distearoyl-*sn*-glycero-3-phosphoethanolamine-N-[biotinyl(polyethylene glycol)-2000] (DSPE-PEG(2000)-biotin; 1.1 mol%; Avanti Polar Lipids, Alabaster, Alabama, USA). In short, all components were dissolved in chloroform:methanol (9:1 vol/vol), which was evaporated with argon gas (Linde Gas Benelux, Schiedam, the Netherlands). The lipid film was first freeze-dried (Alpha 1-2 LD plus; Mertin Christ GmbH, Osterode am Harz, Germany), then dispersed in PBS with lipid dye DiD (1,1'-dioctadecyl-3,3,3',3'-tetramethylindodicarbocyanine perchlorate; Thermo Fisher Scientific, Waltham, MA, USA) to fluorescently label the microbubble coating. The solution was next placed in a sonicator bath for 10 min and then the mixture was further dispersed using low power probe sonication (Sonicator ultrasonic processor XL2020, HeatSystems, Farmingdale, NY, USA) for 5 min. Finally, microbubbles were produced by high power probe sonication for 1 min.

Microbubbles were functionalized to target $\alpha_V\beta_3$ or CD31 using biotin-streptavidin bridging as described previously [47, 58]. Before targeting, microbubbles were first washed three times by centrifugation at 400g for 1 min, then counted with the Coulter Counter Multisizer 3 (50 µm aperture tube, Backman Coulter, Mijdrecht, the Netherlands). Next, 6×10^8 microbubbles were incubated with 60 µg streptavidin (Sigma-Aldrich) for 30 min on ice, washed once, then incubated for 30 min on ice with 6 µg of either biotinylated anti-human CD51/61 antibody (*i.e.* $\alpha_V\beta_3$; BioLegend, San Diego, CA, USA) or biotinylated anti-human CD31 antibody (R&D Systems, Minneapolis, MN, USA). After incubation one final washing step was performed and the targeted microbubbles were counted to determine the final concentration and size distribution. Control microbubbles were functionalized with IgG1-κ, a biotinylated isotype control antibody for both the CD31 and $\alpha_V\beta_3$ antibody (Sony Biotechnology, San Jose, CA, USA). When using non-targeted microbubbles, these were taken from the counted stock after the first three wash steps.

7.2.2 Endothelial cell culture

All experiments were performed with primary human umbilical vein endothelial cells (HUVECs) from pooled donors (C2519A, LOT 437550, Lonza, Verviers, Belgium) with passage number 4 to 8. The HUVECs were cultured with Endothelial Cell Growth Medium (EGM)-2 (Lonza) in T75 flasks and grown at 37 °C and 5% CO_2 in a humidified incubator to full confluency before replating. Before each experiment, the HUVECs were detached with Accutase solution (Sigma-Aldrich) and replated on the bottom membrane of an acoustically compatible CLINIcell [463] (Mabio, Tourcoing, France) with 50 µm membranes (25 μm^2) in 12 mL EGM-2. CLINIcells were incubated for two days at 37 °C and 5% CO_2 to achieve a confluent monolayer [58, 59]. In total, 23 cultured CLINIcells were used for experiments.

7.2.3 Experimental set-up

To investigate the microbubble-cell interaction in 3D, the combined confocal microscopy and Brandaris 128 ultra-high-speed camera system was used as described previously [58, 59, 431]. In short, a CLINIcell was placed into a water tank at 37 °C for simultaneous imaging and ultrasound insonification (Figure 7.1A). At 45° incidence angle, a single element focused transducer (2.25 MHz center frequency; 76.2 mm focal length; −6 dB beam width at 2 MHz of 3 mm; V305, Panametrics-NDT, Olympus, Waltham, MA, USA) was mounted in the water tank after calibration with a needle hydrophone (1-mm diameter, PA2293, Precision Acoustics, Dorchester, UK). After alignment of the ultrasound and optical foci, the cells were insonified with

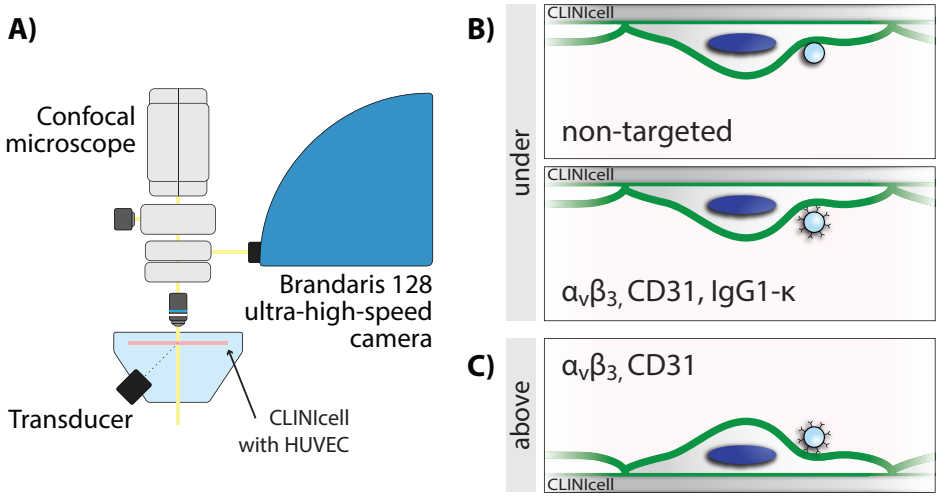

Figure 7.1 Schematic representation of the experimental set-up and sample orientations to study microbubble-cell morphology and drug delivery outcome. **A**) System for simultaneous high-resolution imaging and ultrasound insonification of the CLINIcell with Human Umbilical Vein Endothelial Cells (HUVEC). **B**) Orientation with microbubbles under the cells. **C**) Orientation with microbubbles above the cells.

7

a single 2 MHz and 10-cycle burst by an arbitrary waveform generator (33220A, Agilent, Palo Alto, CA, USA). A peak negative pressure (PNP) of 200 kPa at the focus was generated with a broadband amplifier (ENI A-500, Electornics & Innovation, Rochester, NY, USA).

7.2.4 Live cell experimental protocol

The cell membranes were stained with CellMask Green Plasma Membrane Stain (Thermo Fisher Scientific) by incubating with 4 µg/ml final concentration for 10 min inside the cell incubator. Next, Hoechst 33342 (5 µg/ml final concentration; Thermo Fisher Scientific) was added to stain the cell nuclei, propidium iodide (PI; 25 µg/ml final concentration; Sigma-Aldrich) was added as a marker for sonoporation, and a final concentration of 1×10^5 microbubbles/ml was added. The CLINIcell was incubated during 5 min in the cell incubator while turned upside down (*i.e.*, with the cells on top). This allowed microbubbles to float towards the cells and, in the case of targeted microbubbles, allow them to bind to the cells. This was done for all types of microbubbles to ensure a proper control experiment in the case of non-targeted and IgG1-κ control microbubbles.

Figure 7.1 shows a schematic of the different CLINIcell configurations used for imaging, with either the microbubbles positioned under the cells (Figure 7.1B) or the microbubbles positioned above the cells (Figure 6.1C). For non-targeted and

IgG1-κ microbubbles the configuration with microbubbles above the cells is not experimentally feasible, since the microbubble would float up and away from the cell. From now on we will refer to targeted microbubbles as $\alpha_V\beta_{3\text{-under}}$ and $CD31_{under}$ when positioned under the cells, while $\alpha_V\beta_{3\text{-above}}$ and $CD31_{above}$ will indicate they are positioned above the cells. To image the CLINIcell as depicted in Figure 7.1C, the CLINIcell was turned upright after the last incubation step and the top membrane without cells was cut out from the CLINIcell to enable imaging with an objective with a working distance smaller than the 5 mm spacing between the CLINIcell membranes. A 100× water dipping objective (CFI Plan 100XC W, 2.5 mm working distance, Nikon Instruments, Amsterdam, the Netherlands) was used with four laser channels to image the microbubble-cell interaction: (1) Hoechst excited at 405 nm, detected at 450/50 nm (center wavelength/bandwidth), (2) CellMask Green excited at 488 nm, detected at 525/50 nm, (3) PI excited at 561 nm, detected at 595/50 nm, and (4) DiD excited at 640 nm, detected at 700/75 nm. Channel 1 and 4 were excited and detected simultaneously because there is no spectral overlap between Hoechst and DiD.

To image the microbubble-cell morphology in 3D prior to microbubble oscillation, first a *z*-stack was acquired with 0.33 µm steps and at 0.12 µm/pixel (FOV of 256 × 256 pixels). Next, the microbubble oscillation and cellular response upon ultrasound insonification were imaged in 2D at 0.25 µm/pixel (FOV of 256 × 256 pixels), similarly to as described previously [58, 59]. In short, a time-lapse of 3 min was acquired with 2.6 frames per second (fps). After about 30 s, the light path was automatically switched from the confocal to the Brandaris 128 ultra-high-speed camera to record the microbubble oscillation during ultrasound insonification at ~17 Mfps. Start of ultrasound insonification was defined as t = 0 s. Once completed, the light path was automatically switched back to the confocal to monitor the cellular response for at least 2.5 min. After time-lapse imaging was completed, another *z*-stack was acquired to observe the cellular effect of microbubble oscillation in 3D.

To obtain a control measurement of the cell thickness without a microbubble, *z*-stacks were also taken of FOVs without a microbubble on the cell. To mimic both set-up orientations images were taken of cells when under the CLINIcell membrane (configuration Figure 7.1B, 'under') and when above the CLINIcell membrane (configuration Figure 7.1C, 'above').

7.2.5 Chromatic aberration

The 100× water dipping objective used in this study was not corrected for axial chromatic aberration. Therefore, during confocal microscopy different excitation wavelengths were focused onto different planes and lead to a slight displacement

of the four imaging wavelengths along the focal axis. In this study, we are especially interested in the axial colocalization of the green 488 nm channel (*i.e.* the cell membrane) and the far-red 640 nm channel (*i.e.* the microbubble shell). Therefore, the axial offset between these two channels was quantified by acquiring a confocal microscopy *z*-stack (21 slices with 0.2 μm step size) of the reflection from a glass coverslip [487]. The focal plane for each channel was obtained by fitting a Gaussian to the intensity profile along the *z*-axis, similar to the internalized depth image analysis, as explained below. The focal plane of the far-red channel (640 nm) was found to appear 0.32 μm closer to the objective than the green (488 nm) channel. During the quantification of the axial location of the microbubble, we compensated for this axial offset of 0.32 μm.

7.2.6 Microbubble internalization image analysis

Microbubble internalization by the endothelial cell was quantified using the Cell Mask green and DiD channels of the *z*-stacks before ultrasound by using a custom semi-automated procedure in MATLAB (The Mathworks Inc., Natick, MA, USA). A step-by-step example of the internalized depth analysis is presented in Supplementary Figure 7.1. First of all, to identify the orthogonal planes slicing through the center of the microbubble, in the *xy*-plane with maximum sum of DiD intensity the microbubble was located (*imfindcircles* function). Next, the *xz*- and *yz*-planes intersecting at the center of the microbubble were used to quantify the internalization depth (red lines in Supplementary Figure 7.1A). In the DiD channel of the intersection planes (Supplementary Figure 7.1B), the upper half of the microbubble (closest to the objective) has the highest fluorescent intensity because only the upper half can be imaged without artefacts due to the gas core. Therefore, a circular fit (*circfit*) through the maximum of each *z*-intensity profile in both intersection planes was used to identify the microbubble location (red circle in Supplementary Figure 7.1B). Next, in the CellMask Green channel of the same intersection planes the apical and basal cell membrane were identified. Since the microbubble's gas core may alter the cell membrane's visualization, the membranes were tracked on the side of the microbubble. For each *z*-intensity profile, two Gaussian non-linear least square fits (*gauss1*) were used to identify the apical and the basal membrane (Supplementary Figure 7.1D). This was repeated for all *z*-profiles within 4 μm to the left and right of the microbubble. A linear least-squares fit (*poly2*) through the maximum of the Gaussian fit provided the apical and basal cell membranes at the microbubble (Supplementary Figure 7.1C). Finally, the internalized depth was quantified as the difference between the *z*-plane of the apical cell membrane at the microbubble's center and the *z*-plane of the microbubble closest to the basal membrane (top of microbubble when under the cell and bottom of the microbubble when above the cell). Due to the

limited axial resolution (600 nm with the current 100× objective) [488], the distorted imaging through the gas core of a microbubble, and the common inhomogeneities in the cell membrane staining, the determined *z*-plane of the microbubble did not always intersect with the *z*-plane of the apical cell membrane or lie inside the cell, resulting in a negative internalization depth. Similarly, the microbubble's *z*-plane was sometimes deeper than the *z*-plane of the basal cell membrane, resulting in a relative internalization up 101%.

To quantify how deep a microbubble went into a cell, the cell thickness at the microbubble location was also quantified for all field of views (FOVs) as the difference between the apical and basal cell membranes at the microbubble's center. Since the endothelial cell thickness is known to vary depending on the location on the cell, being thickest around the nucleus and thinning towards the edges, the effect of microbubble location on internalization was also evaluated. The microbubble location on the cell was quantified as the distance from the microbubble to the closest cell edge in the first frame of confocal microscopy time-lapse imaging, as previously described [58].

The occurrence of distinctive cell membrane morphological traits identified in the CellMask Green channel was manually scored for all FOVs with microbubbles. We evaluated for the presence of four different traits at the microbubble location: 1) a circular area of decreased intensity in the *xy*-plane, referred to as 'shadow' (Supplementary Figure 7.2F); 2) a high intensity ring in the *xy*-plane, referred to as 'green ring' (Supplementary Figure 7.2C and D); 3) a protrusion of the cell membrane in the *xz*- and *yz*-plane, referred to as 'dome' (Supplementary Figure 7.2D); and 4) the presence of green signal around the microbubble shell outside the cell, referred to as 'dye-transfer' (Supplementary Figure 7.2F).

7.2.7 Ultra-high-speed imaging analysis

The microbubble radius upon ultrasound insonification as a function of time was quantified from the Brandaris 128 ultra-high-speed recordings using custom-designed image analysis [44]. Microbubble excursion amplitude was defined as the difference between the maximum radius (R_{max}) and the initial radius (R_0, determined from the first 10 frames without ultrasound). The oscillation amplitude thresholds for sonoporation were determined by linear discriminant analysis, as previously described [58, 164].

7.2.8 Drug delivery image analysis

The cellular response after ultrasound was evaluated for sonoporation, identified as a local increase of PI in the cell on which the microbubble was located. This cell was

also delineated using custom-built image analysis software to quantify the amount of PI uptake over time, as previously described [58, 59]. To quantify membrane perforation, a semi-automated custom-built image analysis script in MATLAB was used to automatically track the perforated area in the CellMask Green channel as a function of time after insonification. In the first confocal microscopy frame after ultrasound an initial square region of interest (ROI) was drawn, approximately 6 × 6 µm. Within this initial ROI, the script searched for a local decrease of CellMask green intensity, defined as a connected region (bwconncomp) of more than 3 pixels that have a fluorescent intensity lower than 2/3 of the mean intensity in the ROI (after *imfill* of holes, at 4-pixel connectivity). For each time point, this analysis was repeated in a ROI defined by the bounding box of the previously found perforated area increased by 5 µm in width and height (or the initial square ROI, as long as no perforated area could be identified). Finally, a perforated area was classified as a *pore* when there was still CellMask signal remaining or as a *tunnel* when there was no apparent CellMask fluorescent intensity remaining in the perforated area, hence comparable to the background noise level.

7.2.9 Statistical analysis

Statistical analysis was performed using MATLAB. Data was tested for normality using the Shapiro-Wilk test. For data that was not normally distributed, the Kruskal-Wallis test was performed to evaluate whether groups ($N > 2$) originated from the same distribution. When the Kruskal-Wallis test was rejected at a significance level of $p < 0.05$, follow-up multiple comparison Mann Whitney tests on pairs with a Bonferroni correction were performed to determine which groups were statistically significantly different. To determine the correlation between non-normally distributed parameters, the Spearman's rank-order correlation was evaluated. Categorical data was tested for significant differences among groups using a Fisher's exact test, accounting for possible zero occurrence.

To explore the influence and correlation of the many different parameters involved in microbubble internalization and microbubble-mediated drug delivery, principal component analysis (PCA) was applied. PCA was used since this method reduces the dimensionality of a large dataset, thereby increasing its interpretability, by computing the principal components (*i.e.* eigenvectors) along which the data has the largest variance and quantifying how much variance there is in each direction (*i.e.* the corresponding eigenvalues). The principal components were calculated for the microbubble excursion amplitude, internalized depth, distance from the microbubble to the nearest cell edge, and cell thickness. This was employed to explore the differences between the microbubble types and set-up orientations and drug delivery outcomes.

All graphical representations using boxplots display the median and interquartile range (IQR), using the standard whiskers ranging from the first quartile minus 1.5 times the IQR up to the third quartile plus 1.5 times the IQR, and show outliers outside this range with black dots.

7.3 Results

7.3.1 Microbubble internalization

The position and morphology of a microbubble with respect to a cell was evaluated for 221 FOVs with a microbubble underneath a cell and for 80 FOVs with a microbubble above a cell, with $N \geq 39$ for each microbubble type and orientation. The detailed *N* numbers for each microbubble type can be found in Supplementary Table 1.

In Figure 7.2, typical examples of the 3D microbubble-cell morphology are shown for each microbubble type and set up orientation. Figure 7.2A shows a non-targeted microbubble (diameter (Ø) = 3.5 μm) underneath the cell and without any apparent alteration of the cell membrane (Supplementary Figure 7.2A). By quantifying the distance between the microbubble and the apical membrane, the internalized depth was found to be 0.2 μm. Figure 7.2B shows an IgG1-κ control microbubble (Ø = 3.3 μm) underneath the cell, with an internalized depth of 0.5 μm, and without any apparent alteration of the cell membrane (Supplementary Figure 7.2B). Figure 7.2C shows an $\alpha_V\beta_{3\text{-under}}$ microbubble (Ø = 5.0 μm) that is localized between the two cell membranes, with an internalized depth of 3.9 μm, and with a distinguishable green ring in the cell membrane around the microbubble (Supplementary Figure 7.2C). In Figure 7.2C(ii) and (iii) the apical cell membrane directly below the microbubble is poorly distinguishable because imaging is hampered by the gas core of the microbubble. Figure 7.2D shows an $\alpha_V\beta_{3\text{-above}}$ microbubble (Ø = 3.9 μm) localized inside the cell, with an internalized depth of 3.1 μm, and with both a distinctive green ring and a dome in the cell membrane (Supplementary Figure 7.2D). Figure 7.2E shows a $CD31_{under}$ microbubble (Ø = 3.1 μm) underneath the cell, with an internalized depth of 0.8 μm, and with no distinguishably alteration of the cell membrane (Supplementary Figure 7.2E). Finally, Figure 7.2F shows a $CD31_{above}$ microbubble (Ø = 3.3 μm) above the cell, with an internalized depth of -0.1 μm, and with a distinguishably shadow on the cell membrane and CellMask Green dye-transfer around the microbubble shell (Supplementary Figure 7.2F). In Figure 7.2F(ii) and (iii) the cell membrane is again poorly distinguishable directly below the microbubble.

The $\alpha_V\beta_3$ microbubbles showed significantly ($p < 0.001$) more internalization than any other type of microbubble, with a median (IQR between square brackets) internalized depth of 4.0 μm for $\alpha_V\beta_{3\text{-under}}$ and 3.0 μm for $\alpha_V\beta_{3\text{-above}}$ (Figure 7.3A).

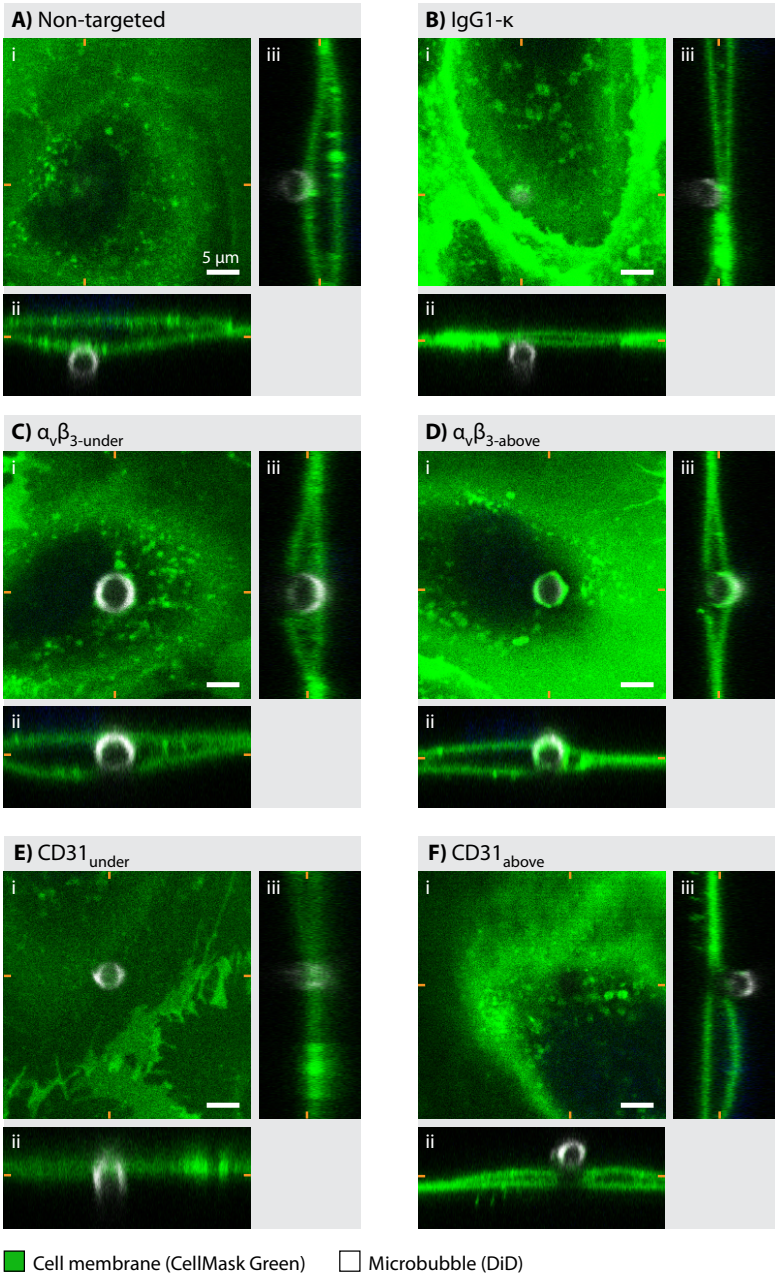

Figure 7.2 Orthogonal views of typical examples of confocal microscopy *z*-stacks showing the 3D morphology of microbubbles and cells: **A**) non-targeted microbubble underneath the cell, (**B**) IgG1-κ control microbubble underneath the cell, (**C**) $\alpha_v\beta_{3\text{-under}}$ targeted microbubble underneath the cell, (**D**) $\alpha_v\beta_{3\text{-above}}$ targeted microbubble above the cell, (**E**) $CD31_{under}$ targeted microbubble underneath the cell, and (**F**) $CD31_{above}$ microbubble above the cell. Side views have the objective imaging from (**ii**) above or (**iii**) the right. Orange markings indicate the cross-section of the orthogonal planes of the side views. See Supplementary Figure 7.2 for only the CellMask Green channel of the same views.

The $CD31_{under}$ microbubbles, with an internalized depth of 0.9 μm, internalized significantly (p < 0.001) more than the $CD31_{above}$ microbubbles (0.1 μm), non-targeted microbubbles (0.1 μm), and IgG1-κ microbubbles (0.1 μm). The orientation of the microbubble with respect to the cell affected the internalized depth when comparing the same microbubble type. When the $\alpha_V\beta_3$ or CD31 microbubble was located underneath the cells the internalized depth was significantly larger (p < 0.001) than when located above the cells.

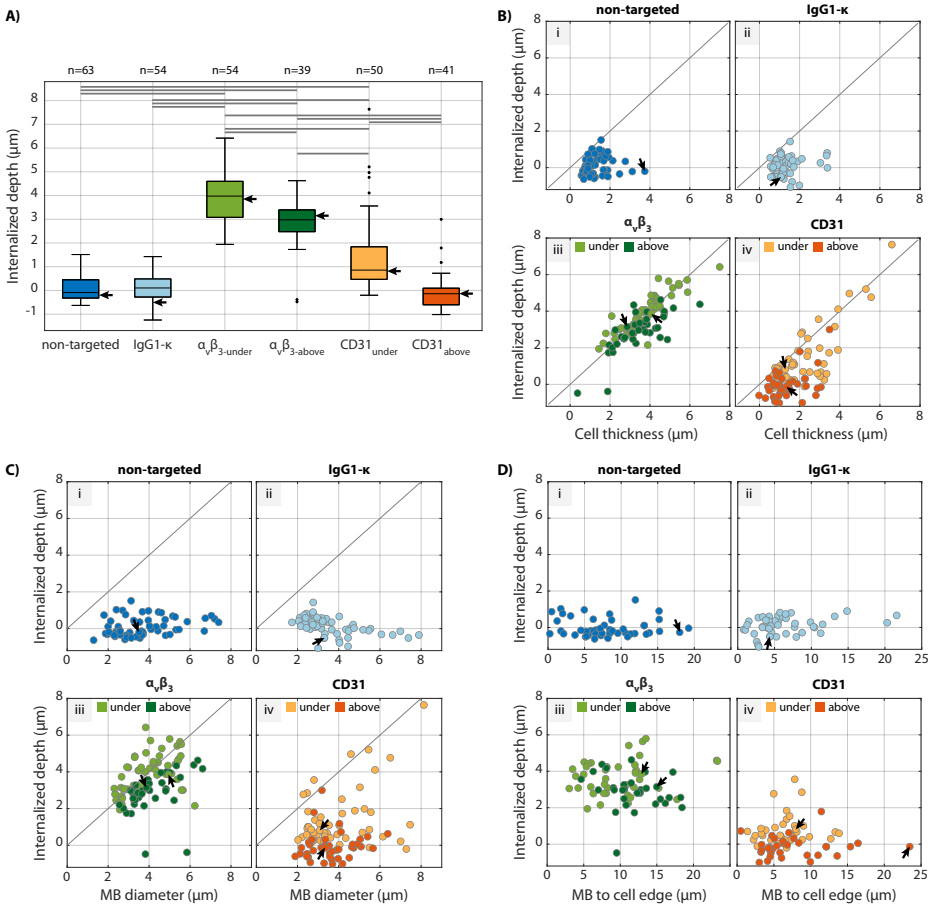

Figure 7.3 Internalized depth of microbubbles into endothelial cells for non-targeted microbubbles (dark blue), IgG1-κ control microbubbles (light blue), $\alpha_V\beta_{3\text{-under}}$ targeted microbubbles (light green), $\alpha_V\beta_{3\text{-above}}$ targeted microbubbles (dark green), $CD31_{under}$ targeted microbubbles (yellow), $CD31_{above}$ targeted microbubbles (orange). **A**) Internalized depth for the distinct microbubble types and experimental set-up orientations; statistically significant differences indicated by horizontal lines (all at p<0.001, *i.e.* p<6.67e-05 after Bonferroni correction). **B**) Internalized depth as a function of cell thickness. **C**) Internalized depth as a function of microbubble (MB) diameter. **D**) Internalized depth as a function of the distance from the microbubble to the nearest cell edge. In all plots the arrows indicate the data points corresponding to the typical examples of Figure 7.2.

In Figure 7.3B the correlation between the internalized depth and cell thickness is shown for each microbubble type and set-up orientation. The internalized depth of $\alpha_V\beta_3$ microbubbles strongly correlated with the cell thickness [Figure 7.3B(iii)], both for $\alpha_V\beta_{3\text{-under}}$ (Spearman's correlation coefficient ρ = 0.89, p < 0.001) and $\alpha_V\beta_{3\text{-above}}$ (ρ = 0.69, p < 0.001). This correlation appeared to weaken for microbubbles types with decreasing internalized depths, showing a moderate correlation for $CD31_{under}$ microbubbles (ρ = 0.57, p < 0.001) [Figure 7.3B(iv)]. A weak correlation was found for the categories that had a median internalized depth ≤ 0.1 μm, which was significant for non-targeted microbubbles (ρ = 0.26, p < 0.05) and non-significant for $CD31_{above}$ (ρ = 0.26, p = 0.1) and IgG1-κ (ρ = 0.11, p = 0.4) microbubbles. An overview of all correlation coefficients between internalized depth and cell thickness is given in Supplementary Table 7.2.

To further investigate internalization, we can compare the scatter plots of $\alpha_V\beta_3$ microbubbles in Figure 7.3B(iii) and of CD31 microbubbles in Figure 7.3B(iv). It becomes apparent that there are more CD31 microbubbles with an internalized depth smaller than the cell thickness (on the right bottom half of the graph), than for $\alpha_V\beta_3$ microbubbles. This indicates that there are more CD31 than $\alpha_V\beta_3$ microbubbles that do not completely fill the cell. If we normalize the internalized depth to the cell thickness, to quantify how much of the cell is filled with the microbubble, this is only 28% for CD31 microbubbles and indeed significantly (p < 0.001) lower than the 101% for $\alpha_V\beta_3$ microbubbles.

The cell thickness (Supplementary Figure 7.3) was also evaluated for cells without a microbubble in both set up orientations, *i.e.* with the cells under (N = 21) or above (N = 12) the CLINIcell membrane. The median cell thickness was 2.3 μm and 2.2 μm, respectively. There was no significant difference in cell thickness between these two orientations when there was no microbubble on the cell. The cell thickness found for $\alpha_V\beta_3$ microbubbles was significantly (p < 0.001) larger than that of any other type of microbubble.

In Figure 7.3C the internalized depth is shown as a function of the microbubble diameter. The internalized depth of $\alpha_V\beta_3$ microbubbles correlated with the microbubble diameter, both for $\alpha_V\beta_{3\text{-under}}$ (Spearman's correlation coefficient ρ = 0.50, p < 0.001) and $\alpha_V\beta_{3\text{-above}}$ (ρ = 0.62, p < 0.001). Despite that this correlation was not significant for CD31 microbubbles, Figure 7.3C(iv) does show that the $CD31_{under}$ microbubbles that are most internalized correspond to those with the largest diameter. An overview of all correlation coefficients between the internalized depth and microbubble diameter is given in Supplementary Table 7.2.

Finally, Figure 7.3D shows the relationship between internalized depth and the microbubble location on the cell, quantified as the distance between the microbubble

and the nearest cell edge. There was no correlation between internalization and microbubble location for any of the microbubble types or set-up orientations, see detailed correlation coefficients in Supplementary Table 7.2.

The overall occurrence of the distinctive cell membrane morphological traits identified and described above (Figure 7.2 and Supplementary Figure 7.2), revealed that a shadow was found significantly ($p < 0.001$) more often for microbubbles above a cell ($\alpha_V\beta_{3\text{-above}}$ and $CD31_{above}$) and for $\alpha_V\beta_{3\text{-under}}$ than for the other microbubble types ($CD31_{under}$, non-targeted, IgG1-κ; Supplementary Figure 7.4A(i)). In 24% of the $CD31_{under}$ microbubbles a shadow was identified, which corresponded to the most internalized microbubbles: the internalized depth of $CD31_{under}$ with a shadow was significantly ($p < 0.001$) larger than those not exhibiting a shadow, as shown in Supplementary Figure 7.4A(ii). Green rings were found significantly ($p < 0.001$) more often for $\alpha_V\beta_3$ and CD31 microbubbles than for IgG1-κ or non-targeted microbubbles (Supplementary Figure 7.4B). Domes were found for 33% of all $\alpha_V\beta_3$ and CD31 microbubbles, but significantly ($p < 0.001$) more often for the $\alpha_V\beta_{3\text{-above}}$ microbubbles (79%) than for any other type or orientation (Supplementary Figure 7.4C). Finally, dye transfer was found significantly ($p < 0.001$) more often for $CD31_{above}$ microbubbles than any other type and orientation (Supplementary Figure 7.4D). When either a dome or dye-transfer was identified in the *xz*- or *yz*-plane, most often also a green ring was identified in the *xy*-plane (striped areas in Supplementary Figure 7.4C and D).

7.3.2 Acoustic behavior

After 3D imaging of the initial microbubble-cell configuration, for 246 of these FOVs the microbubble's excursion upon ultrasound insonification was recorded using the Brandaris 128 ultra-high-speed camera, with $N \geq 32$ per microbubble type. The sample size per microbubble type and set-up orientation can be found in Supplementary Table 7.1. The ultra-high-speed imaging revealed that microbubble excursion amplitude was smaller when microbubbles were internalized (Figure 7.4). In Figure 7.4A, the microbubble excursion amplitude ($R_{max}–R_0$) is shown as a function of initial microbubble radius (R_0), where the scatter markers are color-coded ranging from not internalized in blue to highly internalized in yellow. This color-coded representation reveals the blue scatter points at higher excursion amplitudes than those colored in green/yellow tones, hence showing how a larger internalized depth led to a lower excursion amplitude. This is confirmed by the average excursion of non-internalized microbubbles (internalized depth < 1 μm, blue line) being consistently higher than that of internalized microbubbles (internalized depth ≥ 1 μm, yellow line). Additionally, in Figure 7.4A, the characteristic resonance behavior of microbubbles can be recognized, revealing a resonance radius of approximately

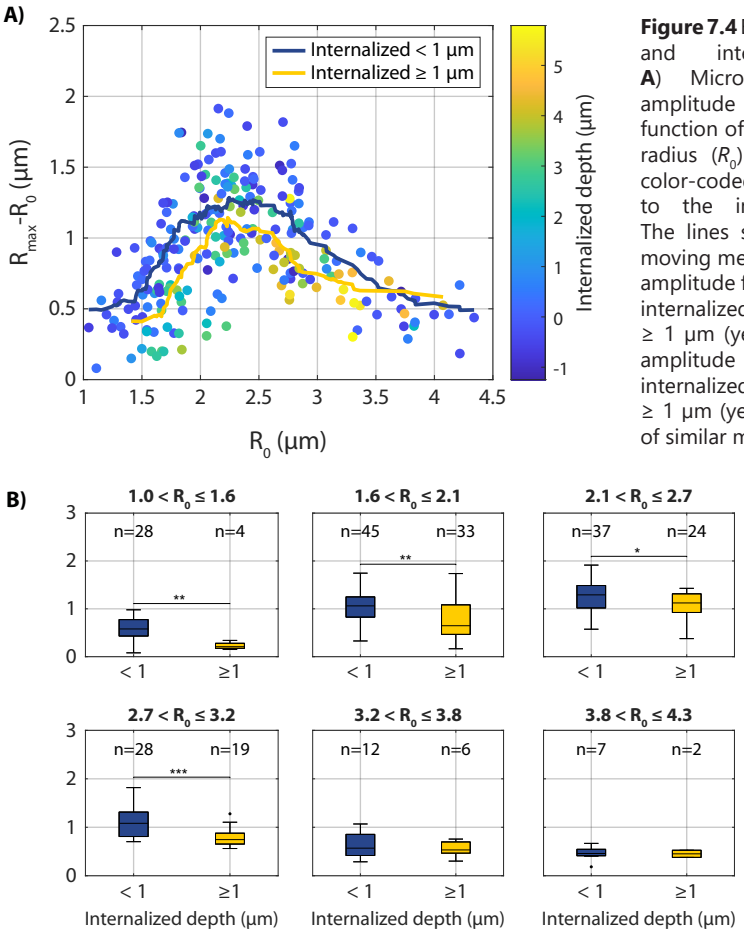

Figure 7.4 Excursion amplitude and internalized depth. **A**) Microbubble excursion amplitude (R_{max}–R_0) as a function of initial microbubble radius (R_0) with scatter dots color-coded corresponding to the internalized depth. The lines show the 20 point moving mean of the excursion amplitude for all microbubbles internalized < 1 µm (blue) or ≥ 1 µm (yellow). **B**) Excursion amplitude of microbubbles internalized < 1 µm (blue) or ≥ 1 µm (yellow) within ranges of similar microbubble size.

2.1 µm at 2 MHz insonification, irrespective of internalized depth. For microbubbles with R_0 up to 3.2 µm, statistical testing confirmed that the excursion amplitude was significantly higher for non-internalized microbubbles (internalized depth < 1 µm), as represented in Figure 7.4B.

7.3.3 Drug delivery by pores or tunnels

After ultra-high-speed imaging of the microbubble oscillation behavior, the cellular response upon microbubble oscillation was evaluated for a total of 230 FOVs using time-lapse confocal microscopy, with $N \geq 31$ per microbubble type and set-up orientation (detailed sample size per category in Supplementary Table 7.1). Typical examples of the cellular responses are presented in Figure 7.5, showing selected frames of confocal microscopy time-lapse imaging, the microbubble excursion, and time profiles of the perforated area and PI and CellMask Green intensity. Before

ultrasound, confocal microscopy showed a single microbubble in each field view and revealed that each cell was viable and had an intact cell membrane (absence of PI).

Figure 7.5A shows a typical example of PI uptake and distinguishable membrane perforation. The corresponding confocal microscopy recording is shown in Video 7.1. After ultrasound, high PI uptake was observed starting at the microbubble location and gradually spreading into the cell over time. Additionally, membrane perforation was identified as an area with decreased CellMask Green intensity, localized next to the microbubble. This perforated area increased to about 30 μm^2 during the first ~30s and then remained stable throughout the rest of the recording. The 3D confocal microscopy image after the time-lapse recording, confirmed that there was still CellMask Green signal in the perforated area (Supplementary Figure 7.5A). This

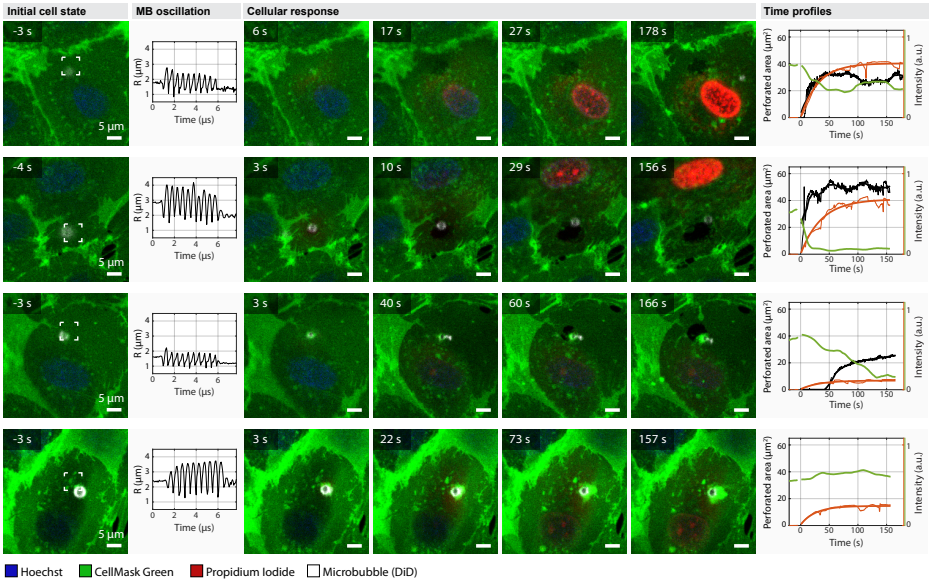

Figure 7.5 Typical examples of microbubble-mediated drug delivery by pores and tunnels. **A**) High PI uptake and a distinguishable membrane perforation identified as a pore caused by an IgG1-κ microbubble (0.7 µm internalized depth). **B**) High PI uptake and distinguishable membrane perforation identified as a tunnel caused by a non-targeted microbubble (-0.1 µm internalized depth). **C**) Low PI uptake and distinguishable membrane perforation identified as a tunnel caused by a $CD31_{under}$ microbubble (1.0 µm internalized depth). **D**) Low PI uptake and no distinguishable membrane perforation caused by an $\alpha_v\beta_3$ under microbubble (3.1 µm internalized depth). For every example the images from left to right show: one confocal microscopy frame showing the initial cell state before ultrasound; the microbubble (MB) radius as a function of time obtained from the Brandaris 128 ultra-high-speed imaging during ultrasound; four selected frames of confocal microscopy time-lapse imaging after ultrasound; and the time profiles (thick line shows moving average) of the perforated area (black), PI fluorescent intensity in the cell (red), and CellMask Green fluorescent intensity within the area indicated by the white corners in the initial cell state (green). See Supplementary Figure 7.5 for the 3D confocal microscopy imaging of these examples before and after time-lapse imaging.

indicates that there was still cell membrane present there, suggesting that only the apical membrane was perforated and that the basal membrane was still intact. This type of perforation will from now on be described as the formation of a *pore*.

In Figure 7.5B another typical example is shown of PI uptake and visibly distinguishable membrane perforation. The corresponding confocal microscopy recording is shown in Video 7.2. After ultrasound insonification, again high PI uptake was observed to gradually fill the cell over time and membrane perforation was identified. The perforated area quickly increased to about 50 μm^2 within the first ~20s and then stabilized. However, in this case the CellMask Green signal seemed to have completely disappeared in the perforated area. This suggests that both the apical and the basal membrane had been perforated. This resulted into a transcellular perforation, as confirmed by the final 3D confocal microscopy (Supplementary Figure 7.5B). This type of perforation will from now on be described as formation of a *tunnel*.

In Figure 7.5C another typical example is shown of PI uptake and tunnel formation. The corresponding confocal microscopy recording is shown in Video 7.3. After ultrasound insonification, PI uptake was observed but in contrast to the previous examples, it stabilized at a low level. About 50 s after ultrasound, a perforated area appeared and gradually increased to about 25 μm^2, with no remaining CellMask Green signal in the perforated area, indicating the formation of a tunnel. This transcellular perforation was again confirmed by the final 3D confocal microscopy (Supplementary Figure 7.5C). The confocal microscopy images and the time profile of the PI intensity in the cell (red curve) indicate noticeably lower PI uptake in Figure 7.5C than that in Figure 7.5A and B, despite that in all three cases the membrane perforation clearly remains and is of similar size (black curve). This suggests that in Figure 7.5C the initial perforation allowing uptake of PI from the extracellular space into the cytoplasm has resealed and only the transcellular perforation remains. The difference between the perforated areas classified as a pore or a tunnel is clearly confirmed by the time profile of the CellMask Green intensity: for a pore (Figure 7.5A) the intensity decreased to 54% of the fluorescent intensity before ultrasound, while for the tunnel it decreased to only 13% (Figure 7.5B) or 20% (Figure 7.5C) of the initial fluorescent intensity.

Finally, in Figure 7.5D a typical example is shown of PI uptake without distinguishable membrane perforation. The corresponding confocal microscopy recording is shown in Video 7.4. After ultrasound, PI uptake was observed to gradually fill the cell while stabilizing at a low level. However, this time no area of decreased CellMask Green intensity could be identified that would indicate membrane perforation (Supplementary Figure 7.5D). This indicates that a pore was formed by the oscillating microbubble, causing PI uptake, but that it resealed too quickly and/or was too

small to be identified with the CellMask Green dye and current imaging resolution.

The uptake of PI and the perforation of the cellular membrane was monitored, revealing four distinct responses: 1) no PI uptake and no distinguishable membrane perforation, 2) PI uptake with a distinguishable membrane perforation identified as a pore (Figure 7.5A), 3) PI uptake with a distinguishable membrane perforation identified as a tunnel (Figure 7.5B and C), and 4) PI uptake without distinguishable membrane perforation (Figure 7.5D).

The occurrence of tunnels upon sonoporation was lower for $\alpha_V\beta_3$ microbubbles (0% of sonoporated cells for $\alpha_V\beta_{3\text{-under}}$ and 11.5% for $\alpha_V\beta_{3\text{-above}}$) than for the other types of microbubbles (25.0% of sonoporated cells for non-targeted, 17.9% for IgG1-κ, 26.1% for $CD31_{under}$, and 34.8% for $CD31_{above}$) (Figure 7.6, blue). Additionally, $\alpha_V\beta_3$ microbubbles resulted in PI uptake with invisible pores upon sonoporation more often (93.3% of sonoporated cells for $\alpha_V\beta_{3\text{-under}}$ and 80.8% for $\alpha_V\beta_{3\text{-above}}$), than for any other type of microbubble (12.5% of sonoporated cells for non-targeted, 28.6% for IgG1-κ, 26.1% for $CD31_{under}$, and 56.5% for $CD31_{above}$) (Figure 7.6, light red).

In Figure 7.7A, the amount of PI uptake is shown as a function of the perforated area, evaluated 120 s after ultrasound insonification. This quantification reveals that for $\alpha_V\beta_3$-targeted microbubbles the perforated area upon PI uptake was small and often not distinguishable [Figure 7.7A(iii)]. High PI uptake took place; however, the membrane disruption could often not be identified (see typical example in Figure 7.5D). For the other types of microbubbles, upon sonoporation with a pore (red) a large perforated area correlated with high PI uptake [Figure 7.7A (i), (ii), and (iv)]. On the other hand, upon sonoporation with a tunnel (blue) a large perforated area did not correlate with the amount of PI uptake (see typical example in Figure 7.5C). This indicates that sometimes PI uptake stabilized early on, suggesting resealing of the membrane, while the transcellular perforation (*i.e.* tunnel) remained

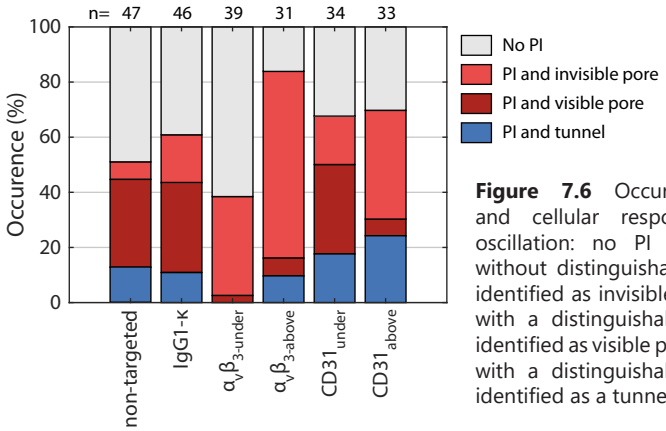

Figure 7.6 Occurrence of drug delivery and cellular responses upon microbubble oscillation: no PI uptake (gray), PI uptake without distinguishable membrane perforation identified as invisible pore (light red), PI uptake with a distinguishable membrane perforation identified as visible pore (dark red), and PI uptake with a distinguishable membrane perforation identified as a tunnel (blue).

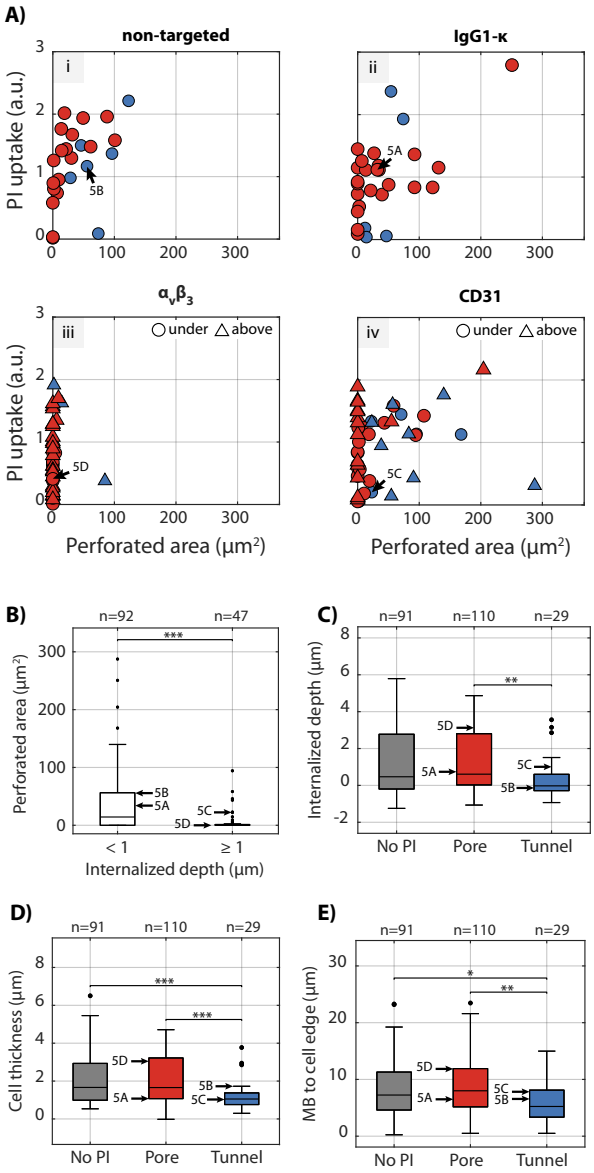

Figure 7.7 Cellular response upon microbubble oscillation either resulting in no propidium iodide (PI) uptake (gray, *N* = 91) or causing PI uptake with pores (red, *N* = 110) or tunnels (blue, *N* = 29). **A**) Amount of propidium iodide (PI) uptake upon sonoporation as a function of the perforated cell membrane area at 120 s after ultrasound for **i**) non-targeted microbubbles, **ii**) IgG1-targeted microbubbles, **iii**) $\alpha_v\beta_3$-targeted microbubbles, and **iv**) CD31-targeted microbubbles, with circles for MB on the bottom of the cell and triangle, above. **B**) Perforated area of sonoporated cells caused by microbubbles with an internalized depth < 1 or ≥ 1 μm. **C**) Internalized depth of microbubbles leading to the various cellular responses. **D**) Cell thickness at the microbubble location for each cellular response. **E**) Distance from the microbubble to the cell edge for each cellular response. The arrows indicate the data points corresponding to the typical examples of Figure 7.5. In Supplementary Figure 7.6 the data in C-E is presented per microbubble type.

open (Figure 7.10B iii). Overall, Figure 7.7B reveals that microbubbles internalized by at least 1 µm, created significantly (p < 0.001) smaller perforated areas upon sonoporation.

The median (IQR between square brackets) internalized depth of microbubbles that caused sonoporation with a tunnel was 0.0 [-0.3 – 0.6] µm and significantly (p < 0.01) smaller than that of microbubbles that caused sonoporation with a pore (0.6 [0.0 – 2.8] µm) (Figure 7.7C). The thickness (1.1 [0.8 – 1.4] µm) of cells in which tunnels were caused was significantly (p<0.001) smaller than that of cells with pores (1.7 [1.1 – 3.2] µm) or without sonoporation (1.7 [1.0 – 2.9] µm) (Figure 7.7D). Additionally, tunnels were caused by microbubbles that were significantly closer to the cell edge than those that caused a pore or no sonoporation (Figure 7.7E). Finally, there was no significant difference between the excursion amplitude of microbubbles that caused pores or tunnels (Supplementary Figure 7.6A), but in both cases the excursion amplitude was significantly (p < 0.001) higher than the amplitude of the microbubbles that caused no sonoporation.

The threshold for sonoporation was lower for $\alpha_V\beta_3$ targeted microbubbles ($R_{max} - R_0$ = 0.7 µm) than for CD31, IgG1-κ, or non-targeted microbubbles ($R_{max} - R_0$ = 0.9 µm) (Figure 7.8). The response appeared more predictable when the $\alpha_V\beta_3$ microbubble was above the cell, since 24 out of 24 microbubbles above the threshold caused sonoporation for $\alpha_V\beta_{3\text{-above}}$, but only 12 out of 20 microbubbles that oscillated above the threshold caused sonoporation for $\alpha_V\beta_{3\text{-under}}$.

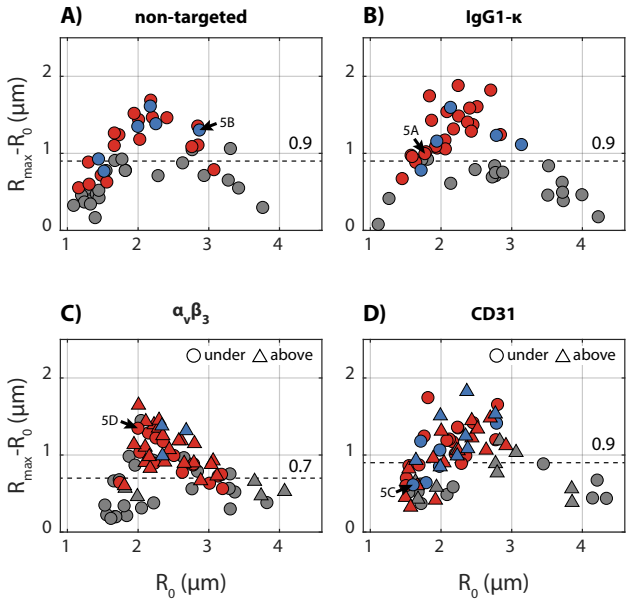

Figure 7.8 Microbubble excursion and drug delivery outcome resulting in no PI uptake (gray), sonoporation with pores (red), or sonoporation with tunnels (blue) for all microbubble types: **A**) non-targeted, **B**) IgG1-κ, **C**) $\alpha_V\beta_{3\text{-under}}$ (circles) and $\alpha_V\beta_{3\text{-above}}$ (triangles), **D**) $CD31_{under}$ (circles) and $CD31_{above}$ (triangles). All plots show microbubble excursion amplitude ($R_{max} - R_0$) as a function of microbubble resting radius (R_0). Sonoporation threshold indicated by the dotted line and the number. The arrows indicate the data points corresponding to the typical examples of Figure 7.5. See Supplementary Figure 7.6A for statistical comparison between drug delivery outcome categories.

7.3.4 Principal component analysis

To explore the influence of the different parameters on microbubble internalization, drug delivery outcome and cellular response, a principal component analysis was performed of which the results are presented in Table 7.1 and Figure 7.9. The first principal component (PC1) is dominated by the microbubble excursion amplitude, cell thickness, and internalized depth. The second principal component (PC2) is dominated by the microbubble excursion amplitude and distance from the microbubble to the nearest cell edge. The loading plot in Figure 7.9A visualizes these components.

In Figure 7.9B, the PCA scoring and loading plot show the distribution of the different microbubble types and set-up orientations. The $\alpha_V\beta_3$ targeted microbubbles (light and dark green) are clearly shifted towards the right of the plot, towards the PC1 > 0. Based on the variable loading (Table 7.1), that means that $\alpha_V\beta_3$ microbubbles exhibit lower microbubble excursion amplitudes, higher internalized depths, larger distances from the cell edge, and higher cell thicknesses than any of the other microbubble types. In Figure 7.9C, the PCA scoring is shown for the different drug delivery outcomes. The occurrence of sonoporation with distinguishable pores (red) is shifted towards both the top and left quadrants of the plot, corresponding to the higher excursion amplitudes. The occurrence of sonoporation with tunnels (blue) is shifted more towards the left (PC1 < 0), corresponding to lower internalized depths, smaller distance from the cell edge, and lower cell thickness.

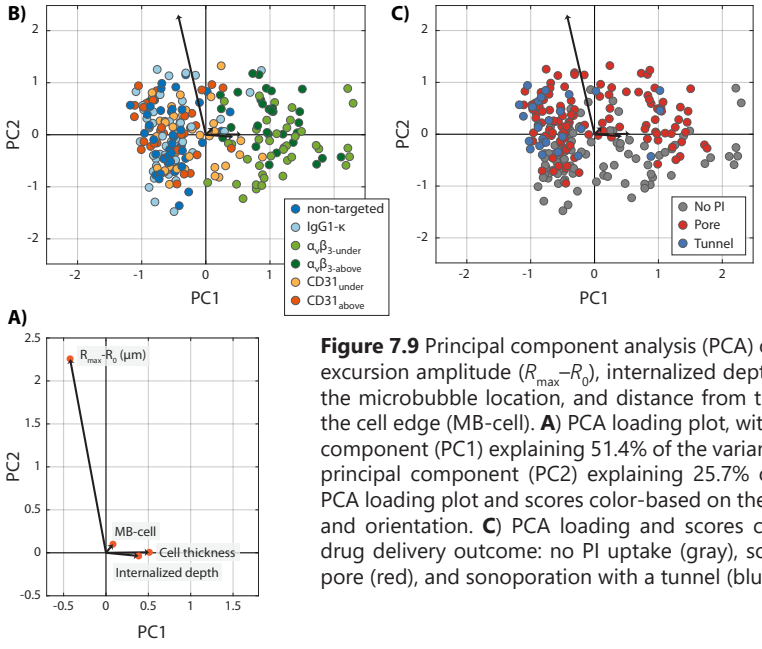

Figure 7.9 Principal component analysis (PCA) of the microbubble excursion amplitude ($R_{max}-R_0$), internalized depth, cell thickness at the microbubble location, and distance from the microbubble to the cell edge (MB-cell). **A**) PCA loading plot, with the first principal component (PC1) explaining 51.4% of the variance and the second principal component (PC2) explaining 25.7% of the variance. **B**) PCA loading plot and scores color-based on the microbubble type and orientation. **C**) PCA loading and scores color-based on the drug delivery outcome: no PI uptake (gray), sonoporation with a pore (red), and sonoporation with a tunnel (blue).

Table 7.1 Scores of principal component analysis of microbubble excursion amplitude (R_{max}–R_0), internalized depth, distance between microbubble and nearest cell edge, and cell thickness.

	PC1	***PC2***
Microbubble excursion	-0.4239	2.2570
Internalized depth	0.3850	-0.0364
Distance to cell edge (MB-cell)	0.0829	0.1005
Cell thickness	0.5119	-0.0062

The scores indicate the weight of each variable in the PCA component.

7.4 Discussion

The 3D morphology of microbubbles on the endothelial cell membrane was evaluated for non-targeted, $\alpha_V\beta_3$-targeted, CD31-targeted, and IgG1-κ control microbubbles. The $\alpha_V\beta_3$ microbubbles were most internalized, with a median internalized depth of 3 µm when above and 4 µm when under the cell, while for CD31 microbubbles internalization was only significant when the microbubble was under the cell (0.9 µm). Since non-targeted and IgG1-κ control microbubbles showed negligible internalized depths (≤ 0.1 µm), internalization appeared to be a receptor-mediated mechanism. Furthermore, the influence of microbubble internalization on the drug delivery outcome and cellular response was investigated by recording the microbubble oscillation at ultra-high temporal resolution and subsequent model drug uptake and membrane perforation at high-spatial resolution in 2D and 3D. Different cellular responses were observed with sonoporation occurring by formation of pores and tunnels. The sonoporation threshold was lower for $\alpha_V\beta_3$ microbubbles than all other microbubble types, signifying that the 3D morphology of the internalized microbubble in the endothelial cell and the resulting microbubble oscillation affected the drug delivery outcome.

7.4.1 Internalized targeted microbubbles

For a better understanding of microbubble internalization, the correlations between internalized depth and other parameters – cell thickness, microbubble size, and microbubble distance to cell edge – were explored in more detail (Figure 7.3). While there was no clear correlation between the microbubble distance to cell edge and the internalized depth, the cell thickness and microbubble size both correlated with the internalized depth, especially for $\alpha_V\beta_3$ microbubbles. Cell thickness was larger when microbubbles were more internalized and when compared to the control cells without microbubbles. Moreover, the larger the microbubble, the higher the internalized depth. Hence, it appears that $\alpha_V\beta_3$ microbubbles were fully internalized into the cell, with the cell membrane covering the internalized microbubbles entirely and resulting in thickening of the cells (Figure 7.10A iii, iv). This can be observed in

the typical examples shown in Figure 7.2C and D (Supplementary Figure 7.2C and D) and often resulted into dome formation (Figure 7.2D) when the cell membrane covered the microbubble but the microbubble was bigger than the cell thickness (Figure 7.10A iv).

The orientation of the set-up, being microbubble under the cell or microbubble above the cell, also affected the internalized depth. Both $\alpha_V\beta_3$ and CD31 microbubbles located above the cells were significantly less internalized than the same type of microbubble located underneath the cell. This can be explained by buoyancy, since despite the fact that the microbubble is internalized when it is located above the cells it tends to float upwards, thereby slightly 'pulling' itself out of the cells causing lower internalized depths (Figure 7.10A iv). In this orientation ($\alpha_V\beta_{3\text{-above}}$) the formation of domes was observed more often, confirming that the cell membrane lined the internalized microbubble. Vice versa, when the microbubble was underneath the cell, it would float upwards, hence favoring a higher internalized depth. By studying microbubbles internalization in two orientations, we were able to properly visualize the basal cellular membrane when the microbubble was located under the cell or properly visualize the apical cellular membrane when the microbubble was above the cell, thereby still providing us with a complete picture of the internalization morphology.

No difference was found between internalized depth measured after about 10 min, *i.e.* the first microscopy imaging time point, compared to after 2 hours after adding the microbubbles to the cells. This indicates that internalization of microbubbles by endothelial cells occurred within 10 min upon targeted microbubbles coming into contact with the receptors on the cells, instead of progressing over a longer time window. This is in agreement with the previously found timescales of internalization (5-15 min) of similarly-sized particles by HUVEC and of microbubbles by leukocytes [489, 490].

Distinct morphological traits in the cell membrane were monitored, being the occurrence of a shadow or green ring at the microbubble location, and dome formation or dye-transfer from the cell membrane to the microbubble coating. When the microbubble was under the cell, observation of a shadow indicated microbubble internalization ($\alpha_V\beta_{3\text{-under}}$ and $CD31_{under}$, Supplementary Figure 7.4). The appearance of a shadow in the endothelial cell membrane was related to the internalized depth of the microbubble. When the microbubble was above the cell ($\alpha_V\beta_{3\text{-above}}$ and $CD31_{above}$), a shadow was found irrespective of internalization, explained by the microbubble's gas core having a different breaking index than the surrounding medium, resulting in a decreased fluorescent signal. In the case of dome formation, it appeared as if the cell membrane fully covered the microbubble, which was noticeably different

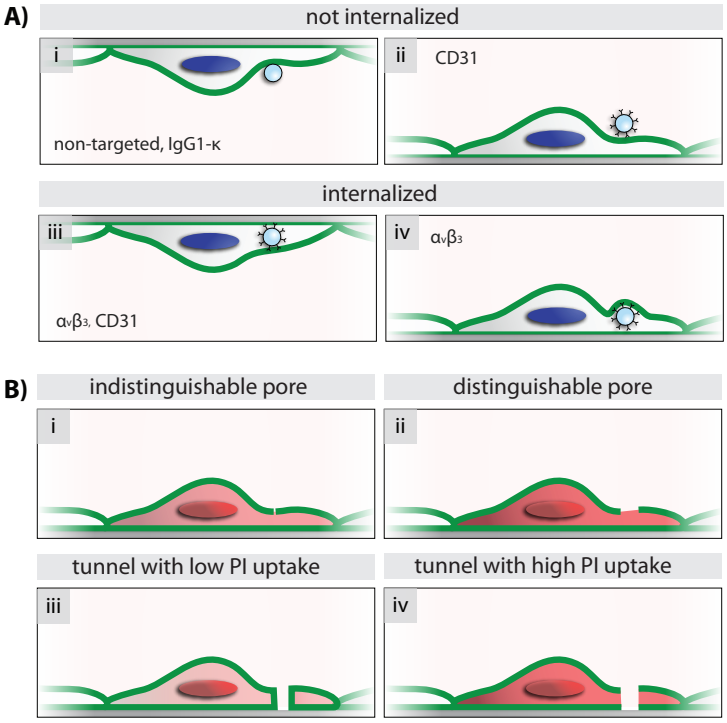

Figure 7.10 Schematic representation of the observed 3D microbubble-endothelial cell dynamics. **A**) Microbubble-cell morphology showing the microbubble (**i**) under or (**ii**) above the cell and a targeted microbubble internalized (**iii**) under or (**iv**) above the cell. **B**) Cellular response and drug delivery outcome resulting in PI uptake by (**i**) an indistinguishable perforation, (**ii**) a distinguishable perforation, (**iii**) a tunnel with low PI uptake due to resealing of the membrane while the tunnel remains open and (**iv**) a tunnel with simultaneous membrane perforation leading to high PI uptake.

from the occurrence of dye-transfer, where only some spots of cell membrane dye were visible on the microbubble shell. Based on our results it is not possible to distinguish between the transfer of dye only, or the transfer of membrane lipids into the microbubble coating bringing the fluorescent dye molecules along. Dye transfer was observed for IgG1-κ control, non-targeted, and CD31 microbubbles, but not for $\alpha_V\beta_3$ microbubbles. This suggests that the process of dye or lipid transfer was not solely receptor-mediated. Since dome formation was often observed for $\alpha_V\beta_3$ microbubbles, perhaps dye transfer was inhibited or obscured by complete internalization of the microbubble by the endothelial cell. Finally, green rings were observed for the majority of $\alpha_V\beta_3$ and CD31 microbubbles, but notably less observed for the non-targeted and IgG1-κ control microbubbles. The occurrence of this highly fluorescent ring might be due to the rearrangement of membrane lipids, which could become more tightly packed around the microbubble location resulting in an increased concentration of dye.

Previous work that focused on internalization of microbubbles by macrophages and endothelial cells showed that while macrophages efficiently internalized polyvinyl-alcohol-coated microbubbles, endothelial cells did not [491]. This is in agreement with the non-targeted and IgG1-κ control groups, which were not internalized in our study. To the best of our knowledge, internalization by endothelial cells of microbubbles targeted to specific receptors has not been investigated before; although the endothelial cell receptors $\alpha_V\beta_3$-integrin and CD31 have been investigated extensively. HUVECs cultured under flow are able to internalize submicron-sized membrane vesicles with a mechanism involving $\alpha_V\beta_3$-integrin [492], which is in line with our observations of $\alpha_V\beta_3$-targeted microbubbles being internalized.

The CD31-targeted microbubbles adhered to the endothelial cells by binding to CD31, also known as PECAM-1. Similar sized particles, such as Plasmodium falciparum-infected erythrocytes, also adhere to PECAM-1, but were suggested to be too large for internalization [493]. Different ligand-dependent pathways have been shown to facilitate internalization of smaller particles (100-300 nm in diameter) by HUVECs through PECAM-1 binding [494]. Since for CD31 microbubbles internalization was only significant when the microbubble was located under the cell and to a lesser extent than for $\alpha_V\beta_3$ microbubbles, it is possible that internalization for CD31 was partly driven by the buoyancy of the microbubble. Although non-targeted and IgG1-κ microbubbles were studied under this same orientation, internalization was not observed. Hence, internalization of $\alpha_V\beta_3$ and CD31 microbubbles appeared to be a combined result of an orientation- and ligand-driven process.

Previous work on the phagocytosis of microbubbles found that non-targeted phospholipid-coated microbubbles were phagocytosed by leukocytes through opsonization of the complement component C3/C3b [489]. However, in the current study non-targeted microbubbles were not internalized by HUVECs, hence it is unlikely that complement factors binding to the microbubble surface or ligand play a role in the internalization of targeted microbubbles by HUVECs.

7.4.2 Drug delivery outcome by pores and tunnels

The acoustic response of individual microbubbles was recorded with ultra-high-speed imaging to determine the effect of acoustic behavior on the drug delivery outcome. The excursion amplitude was lower for internalized microbubbles, while the resonance size appeared to be unaltered by internalization. This suggests an increase in viscous damping, which is in agreement with the decreased oscillation observed by high-speed streak imaging of phagocytosed MP1950 microbubbles in neutrophils [495].

After microbubble oscillation, sonoporation identified by PI uptake and a frequently coincided distinguishable cell membrane perforation were observed (Figure 7.5). In the distinguishable perforated areas, the level of fluorescence signal in the CellMask Green channel was either half of the pre-insonification level or approaching zero. Hence a distinction could be made between pore formation, where only the apical cell membrane was perforated, and tunnel formation, where both the apical and basal cell membranes were perforated. These different cellular effects can lead to either intracellular delivery with or without a distinguishable pore (Figure 7.10B i, ii), transcellular delivery through a tunnel with limited intracellular delivery (Figure 7.10B iii), or both intracellular and transcellular delivery occurring simultaneously (Figure 7.10B iv). The occurrence of tunnels or pores was affected by different factors such as the orientation, internalized depth, cell thickness, microbubble distance to the cell edge, and the excursion amplitude (Figure 7.7 and Figure 7.8). Tunnels occurred more often when the microbubble was closer to the cell edge (Figure 7.7). This could just be a mechanical effect because the cell is thinner there, as confirmed by tunnels occurring more often at thinner cell locations (Figure 7.7). However, it could also be enhanced by a biological underlying mechanism, just like neutrophils are known to migrate towards the cell edge for extravasation [496, 497].

Tunnels upon microbubble oscillation, also known as transcellular or transendothelial perforations or holes, have been previously identified in HUVECs upon insonification of non-targeted DSPC-based microbubbles [473]. This is in agreement with the tunnel formation by non-targeted microbubbles we observed in the current study. In the current study, we additionally found tunnel formation by targeted microbubbles. The range of perforated areas of tunnels found in the current study (2,287 μm^2, at 200 kPa PNP) was comparable to those found previously (39,683 μm^2, at 100-800 kPa PNP) [473]. However, we additionally observed intracellular uptake via pores (perforations of only the apical membrane) or indistinguishable perforations, suggesting that there are multiple potential drug delivery pathways as opposed to only tunnel formation. Additionally, Helfield et al. [473] show membrane resealing to occur, on timescales up to 15 min after ultrasound, indicating that in the current study resealing might be missed due to the limited timescale of up to 2.5 min after ultrasound. The difference in cellular responses observed may be caused by the cell culture chamber: for the present study the acoustically compatible CLINIcell with 50 µm thick membranes was used in contrast to the glass-bottom dishes used in the previous study [473]. This highlights the importance of the *in vitro* model, in this case the surface on which endothelial cells are cultured, and how a model more analogous to the *in vivo* situation may produce more relevant results.

When a CD31-targeted microbubble was located above the cell, the higher occurrence of sonoporation with an indistinguishable perforation may partly be explained by the microbubble orientation, since the gas core of a microbubble above the cell membrane could obscure pore formation. However, for other microbubble types the observed perforated areas were often much larger than the microbubble size, their imaging would therefore not have been fully hampered by the microbubble. Hence, it is more likely that the microbubble orientation influenced the microbubble-cell interaction resulting in smaller perforated areas upon sonoporation. The occurrence of transcellular perforations was the lowest for $\alpha_V\beta_3$-targeted microbubbles, both when under or above the cell. Additionally, the perforated area was smallest, and often even indistinguishable, for internalized microbubbles. This indicates that the microbubble-cell morphology prior to microbubble oscillation, including the internalized depth and dome formation, had a major effect on the cellular response. When pooling all types of microbubbles and orientations together, there was a significant difference in internalized depth, cell thickness, and microbubble location on the cell between pore and tunnel formation. The microbubble excursion amplitude was not significantly different between pore and tunnel outcomes, indicating that while a certain oscillation threshold must be reached to induce PI uptake, causing either pores or tunnels was not oscillation-driven within the studied range of excursion amplitudes. As the $\alpha_V\beta_3$-targeted microbubbles were the most internalized, the excursion amplitudes were lower than for the other groups. However, the threshold for sonoporation was also lower for $\alpha_V\beta_3$-targeted microbubbles than for any other microbubble type, with a value of 0.7 μm in agreement with previous studies [58, 59]. Hence, the different microbubble-cell interaction caused by internalized microbubbles increased the susceptibility to sonoporation.

A principal component analysis was performed to bring all different parameters influencing the drug delivery outcome and cellular response together. Microbubble excursion was an important determinant, which was negatively correlated to the internalized depth and cell thickness. Together with the rest of the data analysis this again indicates that while the microbubble excursion is indeed an important factor in sonoporation, the drug outcome is also determined by the microbubble-cell interaction, including internalized depth, cell thickness, and the microbubble location on the cell. For less internalized microbubbles and located closer to the cell edge, tunnel formation and thus transcellular delivery is more likely to occur. However, the complex interaction between all different parameters ultimately determine which cellular response occurs.

7.4.3 Limitations and future perspectives

All experiments performed for this study were done *in vitro*, raising the question how the results translate to the *in vivo* situation. Human endothelial cells are a proper model for this type of experiments, however, in the current study all cells were cultured in static conditions instead of under flow. This may influence the cellular responses and drug delivery outcome, as previous studies indicated that the susceptibility to sonoporation was significantly lower for HUVECs cultured under flow than for HUVECs cultured statically, while using the same ultrasound settings [498]. In practice, this difference in sonoporation threshold can be easily circumvented by increasing the acoustic pressure when translating to *in vitro* experiments under flow or an *in vivo* situation.

Another consequence of the *in vitro* experimental method is the absence of immune cells, making it impossible to study the role of the immune response in the internalization of targeted microbubbles. Furthermore, if reducing internalization would be desired, that may be achieved by introducing a longer PEG tail to the microbubble formulation to reduce the immune recognition by creating a buried-ligand architecture, as previously described [33].

The microbubble targeting strategy used here is not suitable for *in vivo* applications, as the streptavidin protein may induce an unwanted immune response [471]. However, several studies are ongoing to develop clinically translatable targeting strategies for microbubbles targeted to $\alpha_V\beta_3$ integrin [433, 499, 500]. The use of $\alpha_V\beta_3$-targeted microbubbles has been proposed for ultrasound molecular imaging of angiogenesis [501, 502], however, up to now no studies have investigated the cellular response upon binding of $\alpha_V\beta_3$-microbubbles. Since our results indicate that endothelial cells are able to internalize $\alpha_V\beta_3$-targeted microbubbles *in vitro* under static conditions, it should be further investigated if this also occurs *in vivo*, and if so if this leads to endothelial cell activation and subsequent platelet adhesion as reported for HUVECs cultured under flow after internalization of submicron-sized membrane vesicles [492].

The results presented here reveal that the microbubble-cell interaction stretches beyond a simple ligand-receptor binding, with the internalization of microbubbles playing a substantial role in the acoustic response and drug delivery outcome. We found significant differences in the internalization of microbubbles depending on the ligand, when comparing $\alpha_V\beta_3$ versus CD31-targeted microbubbles. This implicates the importance of investigating internalization by other ligands in the future, before choosing which ligand must be used for the desired outcome, such that the targeted

microbubble formulation can be tailored to specific applications. For ultrasound molecular imaging lower oscillation amplitudes of internalized microbubbles may be undesirable, while for drug delivery applications the internalization of microbubbles might be favorable.

7.5 Conclusions

Investigating the 3D morphology of microbubbles on endothelial cells revealed that microbubbles were internalized into the cell when targeted to $\alpha_V\beta_3$, both when they were orientated under and above the cell, or targeted to CD31, only when under the cell. Hence, microbubble internalization was found to be a receptor mediated and buoyancy-enhanced cellular mechanism and correlated with cell thickness and microbubble size. Although internalized microbubbles exhibited lower excursion amplitudes upon insonification, the oscillation threshold for sonoporation was also lowest thus making cells with internalized microbubbles more susceptible to sonoporation. Evaluating the morphology of membrane perforation revealed that microbubble oscillation either caused a pore, when only the apical cell membrane was perforated resulting in intracellular drug delivery, or a tunnel, when both the apical and basal cell membrane were perforated resulting in intracellular drug delivery and a transcellular perforation. Internalized microbubbles caused less transcellular perforations and lead to the smallest, or even indistinguishable, perforated areas. These novel insights demonstrate the influence of the microbubble-cell morphology on the drug delivery outcome and thereby aid the development of the optimal therapeutic microbubble.

Acknowledgments—The authors would like to thank Robert Beurskens and Frits Mastik from the Department of Biomedical Engineering and Michiel Manten from the Department of Experimental Medical Instrumentation for technical assistance, all from the Erasmus MC University Medical Center Rotterdam, the Netherlands. The authors also thank Ann Seynhaeve from the Laboratory Experimental Oncology, Department of Pathology, Erasmus MC University Medical Center Rotterdam, for the fruitful discussions. This work was funded in part by the Applied and Engineering Sciences TTW (VIDI-project 17543), part of NWO, the Phospholipid Research Center in Heidelberg, grant number KKO-2017-057/1-1, and in part by the Thorax Center of Erasmus MC University Medical Center in Rotterdam.

Video captions

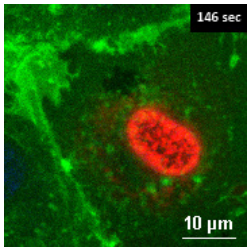

Video 1. Time-lapse confocal microscopy imaging showing sonoporation with high PI uptake and a distinguishable membrane perforation identified as a pore (corresponding to Figure 7.5A). Ultrasound insonification occurred at the 22 s timestamp, during which confocal microscopy was temporarily intercepted for Brandaris 128 ultra-high-speed imaging of microbubble oscillation. The pseudo-colored video shows cell nuclei in blue, cell membranes in green, propidium iodide in red, and microbubble in white and is displayed 20× faster than real time (at 50 frames per second).

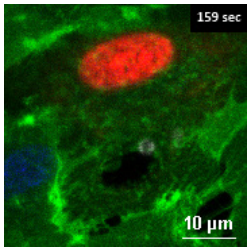

Video 2. Time-lapse confocal microscopy imaging showing sonoporation with high PI uptake and distinguishable membrane perforation identified as a tunnel caused by a non-targeted (corresponding to Figure 7.5B). Ultrasound insonification occurred at the 23 s timestamp, during which confocal microscopy was temporarily intercepted for Brandaris 128 ultra-high-speed imaging of microbubble oscillation. The pseudo-colored video shows cell nuclei in blue, cell membranes in green, propidium iodide in red, and microbubble in white and is displayed 20× faster than real time (at 50 frames per second).

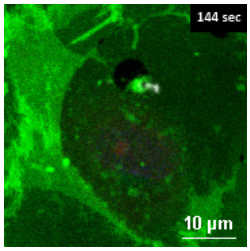

Video 3. Time-lapse confocal microscopy imaging showing sonoporation with low PI uptake and distinguishable membrane perforation identified as a tunnel (corresponding to Figure 7.5C). Ultrasound insonification occurred at the 22 s timestamp, during which confocal microscopy was temporarily intercepted for Brandaris 128 ultra-high-speed imaging of microbubble oscillation. The pseudo-colored video shows cell nuclei in blue, cell membranes in green, propidium iodide in red, and microbubble in white and is displayed 20× faster than real time (at 50 frames per second).

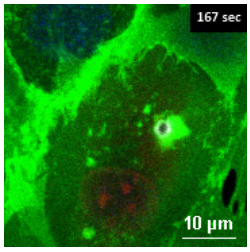

Video 4. Time-lapse confocal microscopy imaging showing sonoporation with low PI uptake and no distinguishable membrane perforation (corresponding to Figure 7.5D). Ultrasound insonification occurred at the 22 s timestamp, during which confocal microscopy was temporarily intercepted for Brandaris 128 ultra-high-speed imaging of microbubble oscillation. The pseudo-colored video shows cell nuclei in blue, cell membranes in green, propidium iodide in red, and microbubble in white and is displayed 20× faster than real time (at 50 frames per second).

Supporting information

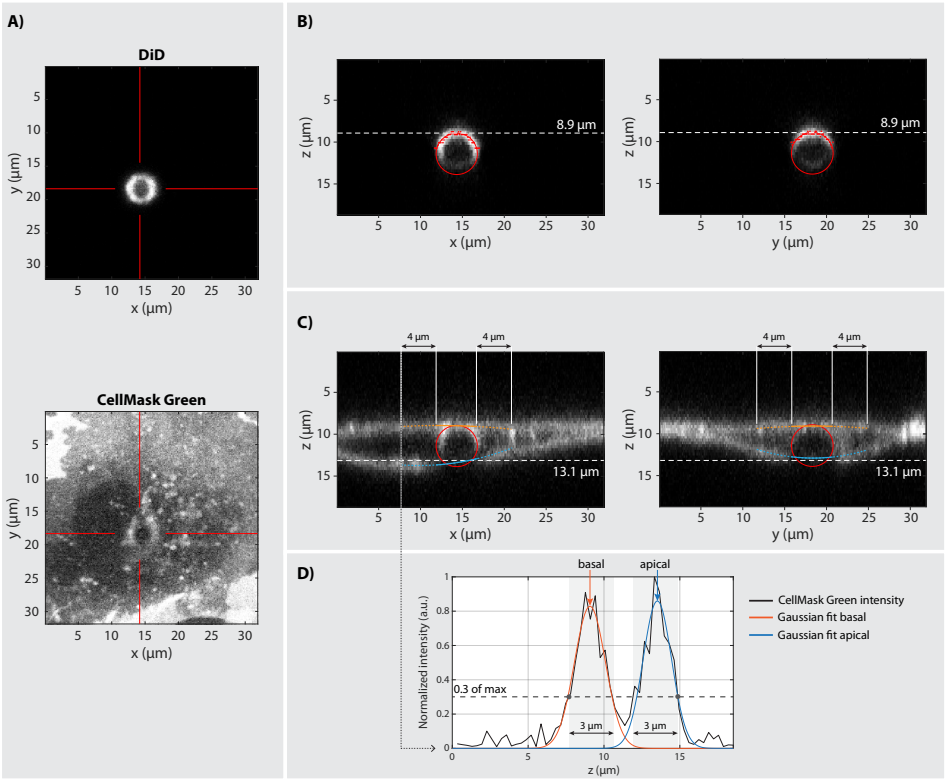

Supplemental Figure 7.1 Step-by-step examples of the image analysis to quantify the internalized depth. The example in the analysis corresponds to Figure 7.2C, *i.e.* $\alpha_V\beta_{3\text{-under}}$. **A**) The *xy*-plane with the highest sum of DiD intensity. The center of the microbubble was found using the *imfindcircles* function. The red lines indicate the orthogonal *xz*- and *yz*- planes that intersect through the center of the microbubble and in which the internalized depth was quantified. **B**) The intersection planes of the DiD channel and the red line showing the circular fit (*circfit*) through the maximum of each *z*-intensity profile (red dots). The top of the microbubble is located at z = 8.9 µm, average of the *xz*- and *yz*-plane. **C**) The intersection planes of the CellMask Green channel with the orange line showing the *poly2* fit through the maxima of the Gaussian fits for the basal membrane and the blue line for the apical membrane. The Gaussian fits were performed for every *z*-intensity profile within 4 µm on both sides of the microbubble (indicated by the black arrows). The apical membrane at the center of the microbubble is located at z = 13.1 µm, average of the *xz*- and *yz*-plane. **D**) For each *z* intensity profile, the basal membrane was found by fitting a Gaussian through the intensities up to 3 µm after the first occurrence of 30% of the maximum intensity; and the apical membrane was found by fitting a Gaussian through the intensities from 3 µm before the last occurrence of 30% of the maximum. Hence, the internalized depth of this example was: [z of the apical membrane] – ([z of the top of the microbubble] + [chromatic aberration correction]) = 13.1 – (8.9 + 0.32) = 3.9 µm.

Supplementary Table 7.1 The sample size (*N* numbers) for each microbubble type.

Dataset sample size	*Non-targeted*	*IgG1-κ*	$\alpha_v\beta_{3\text{-under}}$	$\alpha_v\beta_{3\text{-above}}$	$CD31_{under}$	$CD31_{above}$	*Total*
Internalization	63	54	54	39	50	41	301
Microbubble excursion	50	50	42	32	34	38	246
Drug delivery outcome	47	46	39	31	34	33	230

After imaging microbubble internalization using 3D confocal microscopy, the microbubble excursion upon ultrasound was recorded for a subset of the data, and for a subset of that, the drug delivery outcome was also monitored by time-lapse confocal microscopy. The microbubble excursion and drug delivery outcome data is only available for subsets of the original internalization dataset due to technical challenges, such as poor image quality, focus drift, or system malfunctions.

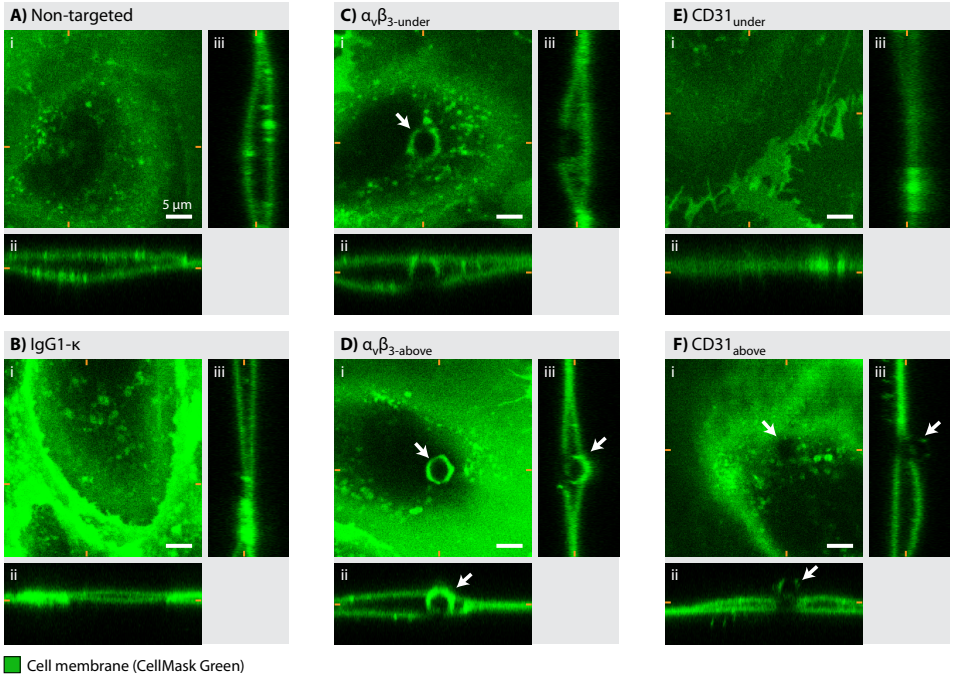

Supplementary Figure 7.2 Typical examples of Figure 2 showing only the CellMask Green channel to visualize the cell membrane. Side views have the objective imaging from (**ii**) above or (**iii**) the right. Orange markings indicate orthogonal planes of the side views. The white arrows in **C**(**i**) and **D**(**i**) indicate a green ring, in **D**(**ii**) and **D**(**iii**) a dome, in **F**(**i**) a shadow, and in **F**(**ii**) and **F**(**iii**) dye-transfer.

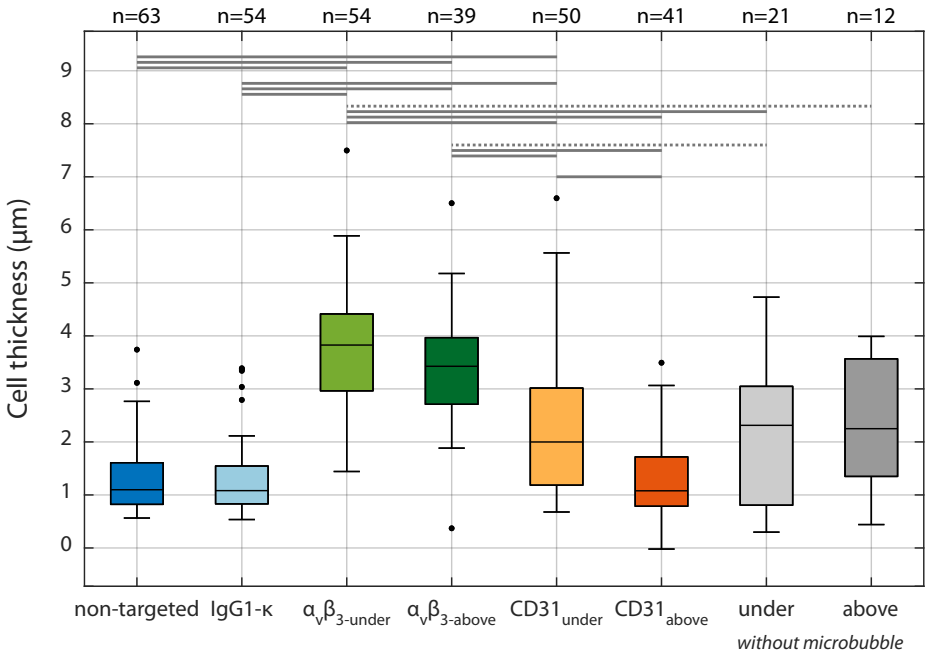

Supplementary Figure 7.3 Cell thickness found at the location of the microbubble for each microbubble type and set-up orientation and for the control images of cells without microbubbles (gray). Statistically significant differences indicated by horizontal lines, using a dotted line when $p < 0.05$ ($p < 0.018$ after Bonferroni correction) and a continuous line when $p < 0.001$ ($p < 3.57e\text{-}05$ after Bonferroni correction).

Supplementary Table 7.2 Spearman correlation coefficient (ρ) and corresponding statistical significance indicated by the p-value between internalized depth and either the cell thickness, the microbubble diameter, or the distance between microbubble (MB) and cell edge.

Spearman correlation between		*Non-targeted*	*IgG1-κ*	$\alpha_v\beta_{3\text{-under}}$	$\alpha_v\beta_{3\text{-above}}$	*CD31 under*	*CD31 above*
Internalized depth vs. cell thickness	*ρ*	0.26	0.11	0.89	0.69	0.57	0.26
	p-*value*	<0.05	0.42	<0.001	<0.001	<0.001	0.11
Internalized depth vs. microbubble diameter	*ρ*	0.34	-0.62	0.50	0.62	0.14	0.22
	p-*value*	<0.01	<0.001	<0.001	<0.001	0.33	0.16
Internalized depth vs. distance between MB and cell edge	*ρ*	-0.01	0.36	0.22	-0.32	0.16	0.16
	p-*value*	0.94	<0.05	0.17	0.08	0.36	0.38

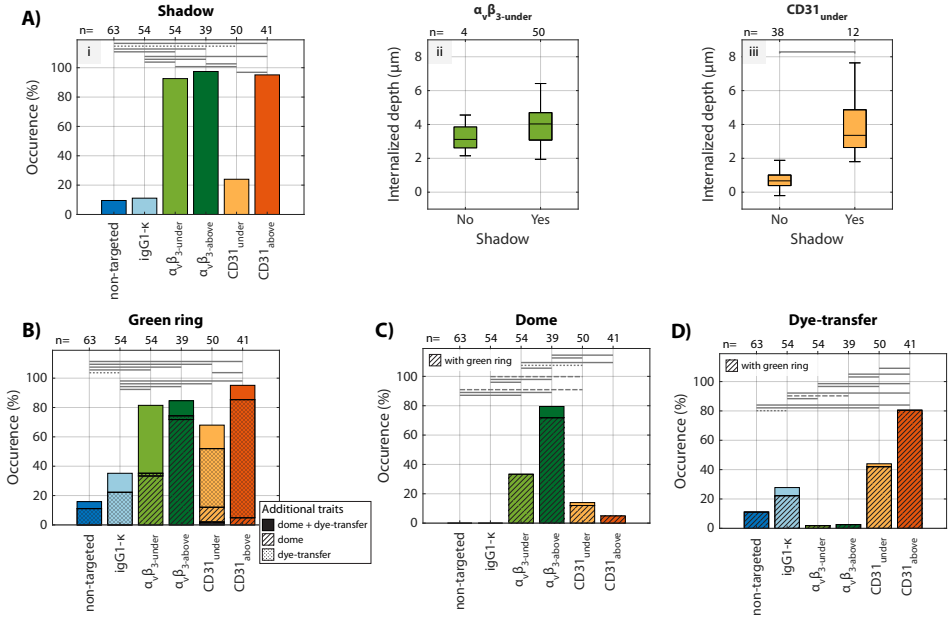

Supplementary Figure 7.4 Distinctive cell membrane morphological traits for the different microbubble types and set-up orientations. **A**) (**i**) Occurrence of shadows and internalized depth of (**ii**) CD31 and (**iii**) $\alpha_v\beta_3$ microbubbles under the cell either showing a shadow on the cell membrane or not. **B**) Occurrence of green rings, with or without a dome and/or dye-transfer. **C**) Occurrence of domes with or without green ring. **D**) Occurrence of dye-transfer with or without green ring. Statistically significant differences indicated by horizontal lines, using a dotted line when $p < 0.05$, a dashed line when $p < 0.01$, and a continuous line when $p < 0.001$.

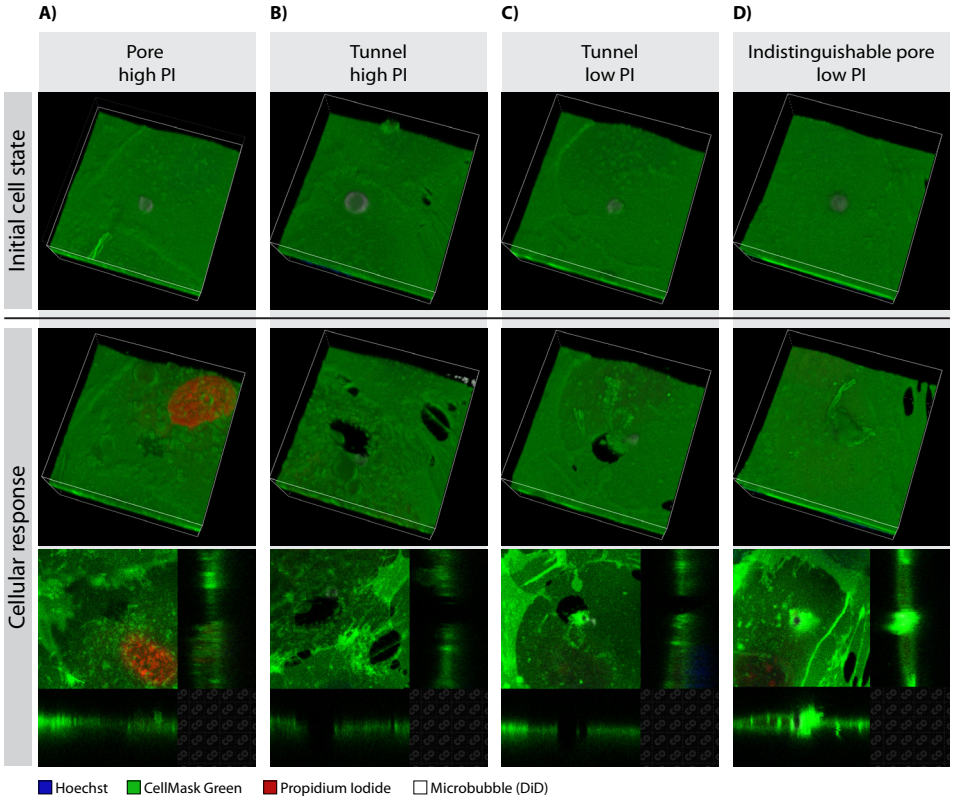

Supplementary Figure 7.5 Typical examples of confocal microscopy 3D imaging of microbubble mediated drug delivery by pores and tunnels, corresponding to the examples presented in Figure 7.5. The first row shows 3D view of the initial cell state approximately 1-2 min before ultrasound insonification, the second and third row show the endothelial cell approximately three minutes after ultrasound insonification, in a 3D view and an orthogonal view, respectively. **A**) High PI uptake and distinguishable membrane perforation identified as a pore, as in Figure 7.5A. **B**) High PI uptake and distinguishable membrane perforation identified as a tunnel, as in Figure 7.5B. **C**) Low PI uptake and distinguishable membrane perforation identified as a tunnel, as in Figure 7.5C. **D**) Low PI uptake and no distinguishable membrane perforation, as in Figure 7.5D.

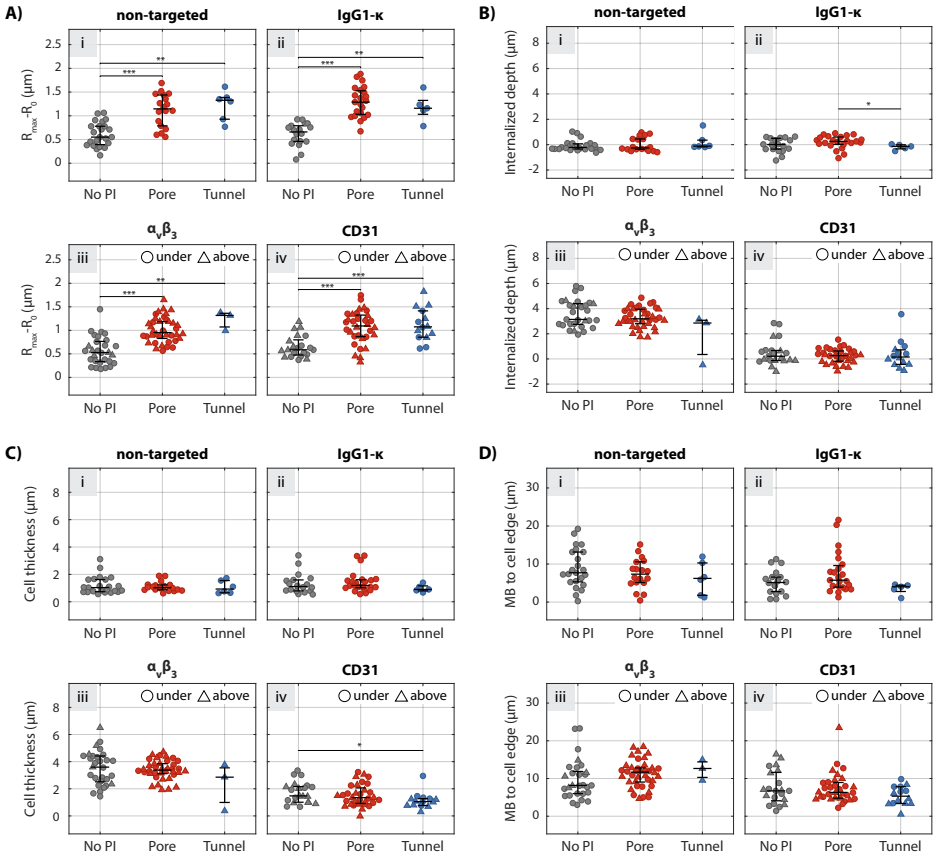

Supplementary Figure 7.6 Drug delivery outcome and microbubble and cell parameters: **A**) Microbubble excursion amplitude (R_{max}- R_0), **B**) internalized depth, **C**) cell thickness at the microbubble location, **D**) distance from the microbubble (MB) to the nearest cell edge. Drug delivery outcome: no PI (gray) and sonoporation with pores (red) or tunnels (blue). Orientation of the set-up indicated with different scatters: under the cell (circles) or above the cell (triangles).

8

Theranostic microbubbles with homogeneous ligand distribution for higher binding efficacy

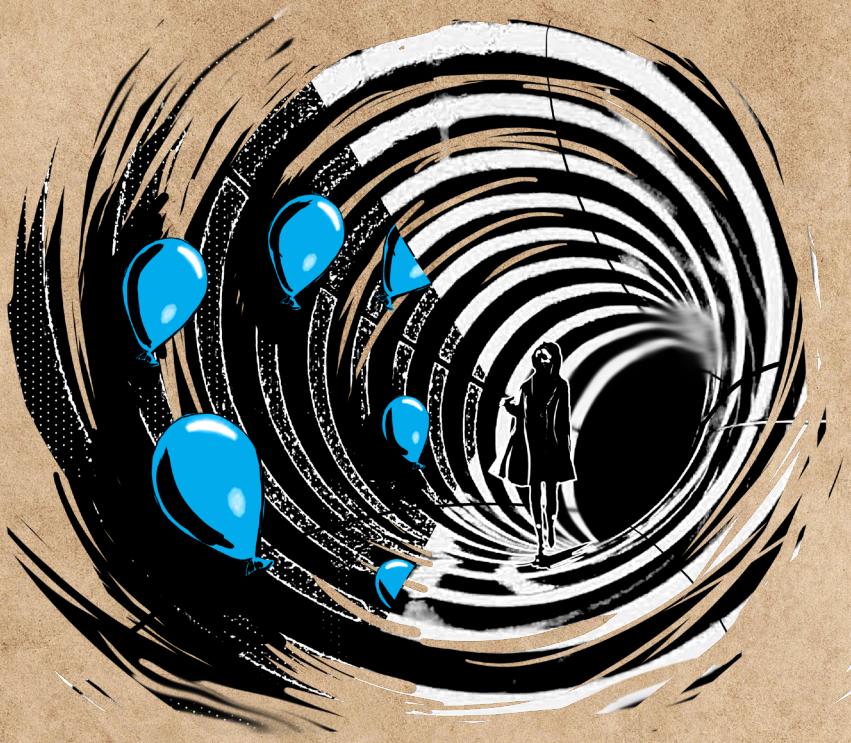

Simone A.G. Langeveld, Bram Meijlink, Inés Beekers, Mark Olthof, Antonius F.W. van der Steen, Nico de Jong, Klazina Kooiman

Based on:
Pharmaceutics, Vol. 14, No. 2, pp. 311-331, 2022.

Abstract

Phospholipid-coated targeted microbubbles are used for ultrasound molecular imaging and locally enhanced drug delivery, with the binding efficacy being an important trait. The use of organic solvent in microbubble production makes the difference between a heterogeneous or homogeneous ligand distribution. This study demonstrates the effect of ligand distribution on the binding efficacy of phospholipid-coated $\alpha_v\beta_3$-targeted microbubbles *in vitro* using a monolayer of human umbilical vein endothelial cells and *in vivo* using chicken embryos. Microbubbles with a homogeneous ligand distribution had a higher binding efficacy than those with a heterogeneous ligand distribution both *in vitro* and *in vivo*. *In vitro*, 1.55× more microbubbles with a homogeneous ligand distribution bound under static conditions, while this was 1.49× more under flow with 1.25 dyn/cm^2, 1.56× more under flow with 2.22 dyn/cm^2, and 1.25× more *in vivo*. The *in vitro* dissociation rate of bound microbubbles with homogeneous ligand distribution was lower at low shear stresses (1-5 dyn/cm^2). The internalized depth of bound microbubbles was influenced by microbubble size, not by ligand distribution. In conclusion, for optimal binding the use of organic solvent in targeted microbubble production is preferable over directly dispersing phospholipids in aqueous medium.

Keywords—Phospholipid-coated microbubbles; Binding efficacy; Ligand distribution; Ultrasound molecular imaging; Targeted drug delivery

8.1 Introduction

Microbubbles are a type of ultrasound contrast agents that consist of a gas core with phospholipid, polymer, or protein coating [11]. With a diameter of 1 to 10 μm, microbubbles are confined to the vasculature and therefore function as a blood pool marker in diagnostic ultrasound imaging [37]. The gas core of a microbubble responds to an ultrasound wave by compressing and expanding, referred to as oscillation. Depending on the ultrasound pressure and frequency, this acoustic response results in stable or inertial cavitation and elicits a non-linear signal that provides contrast to the surrounding tissue [503]. Microbubble oscillation can induce several biological effects, such as sonoporation – *i.e.* pore formation – [117], opening of cell-cell junctions [58], and stimulated endocytosis [167]. Together these effects result in locally enhanced drug uptake, which is particularly useful for targeted delivery of chemotherapeutics [101, 227, 500] and for reversible opening of the blood brain barrier [6, 54].

Phospholipid-coated microbubbles have a thinner shell than polymer- or protein-coated microbubbles, making them less stiff and more echogenic [16-18]. Furthermore, phospholipid-coated microbubbles can be functionalized with the addition of a ligand targeting to a specific biomarker [47, 504]. Targeted microbubbles can be used for ultrasound molecular imaging [386, 505, 506], and when combined with therapeutic agents they function as theranostic agents [56, 57, 507]. A recent review on targeted microbubbles stated that when comparing the therapeutic effects of targeted and non-targeted microbubbles, treatment with targeted microbubbles always resulted in a significantly better therapeutic outcome [486]. Clinical translation is ongoing, with one microbubble formulation targeted to vascular endothelial growth factor receptor 2 (VEGFR2) showing potential for diagnostic imaging in patients with prostate cancer [51] and breast and ovarian lesions [386], both first-in-human studies. Besides clinical use, targeted microbubbles are already being applied in pre-clinical studies as ultrasound molecular imaging agents for studying disease progression [508, 509] and monitoring response to therapy [510-512].

While it is clear that targeted microbubbles are a powerful diagnostic and therapeutic tool, translation from the pre-clinical phase to clinical studies requires extensive safety studies. Furthermore, pre-clinical drug development studies involving targeted microbubbles need standardization of microbubble production methods and ultrasound molecular imaging protocols [50]. An abstract first published by Klibanov et al. [504] is often referred to in papers where phospholipid-coated targeted microbubbles were produced by directly dispersing the coating components in aqueous medium [47, 399, 508, 513, 514] such as phosphate buffered saline (PBS), *i.e.* the direct method [427]. Others reported dissolving the coating components first in organic solvent, then drying to form a lipid film and finally dispersing the lipid film in aqueous medium [515-518], *i.e.* thin-film hydration or the indirect method [427]. Both production methods have been used for *in vitro* [427, 504, 515-517] as well as *in vivo* [47, 399, 508, 513, 514, 518] studies. Our previous study comparing the spatial ligand distribution over the surface of 1,2-distearoyl-*sn*-glycero-3-phosphocholine (DSPC)-based microbubbles functionalized by streptavidin-biotin coupling showed that microbubbles produced by the direct method had a heterogeneous ligand distribution, in contrast to the microbubbles produced by an indirect method which had a homogeneous ligand distribution [427]. However, to the best of our knowledge no studies have been done to directly compare the binding efficacy of microbubbles with the same coating composition with either a homogeneous or heterogeneous ligand distribution. Improved binding efficacy entails higher numbers of bound microbubbles, which is expected to improve the ultrasound molecular imaging signal [397] and, for therapeutic applications, has shown to increase drug uptake [519].

The aim of this study was to determine if a homogeneous ligand distribution in targeted microbubbles results in different binding efficacy than a heterogeneous ligand distribution. Microbubbles produced with a direct method, resulting in heterogeneous ligand distribution, were compared to microbubbles produced with an indirect method, resulting in homogeneous ligand distribution. The binding efficacy was determined *in vitro* by confocal microscopy imaging of $\alpha_V\beta_3$-targeted microbubbles bound to human umbilical vein endothelial cells (HUVECs) cultured under static conditions and under physiologically relevant flow. The chorioallantoic membrane (CAM) vessels of chicken embryos were used to evaluate the binding efficacy of $\alpha_V\beta_3$-targeted microbubbles *in vivo*. A recent study showed that the microbubble-cell interaction upon binding led to microbubble internalization, which affected the drug delivery outcome after ultrasound insonification (*Chapter 7*). Hence the 3D morphology of direct and indirect $\alpha_V\beta_3$-targeted microbubbles bound to HUVECs under static conditions was investigated, to determine the effect of ligand distribution on the internalization of $\alpha_V\beta_3$-targeted microbubbles.

8.2 Materials and methods

8.2.1 Targeted microbubble preparation

Phospholipid-coated microbubbles were produced with a C_4F_{10} gas core as described previously [397, 427]. Two methods were used and the resulting microbubbles will be referred to as direct and indirect microbubbles. For both methods the coating consisted of 84.8 mol% DSPC (Lipoid GmbH, Ludwigshafen, Germany), 8.2 mol% PEG40-stearate (Sigma-Aldrich, Zwijndrecht, the Netherlands), 5.9 mol% DSPE-PEG2000 (Iris Biotech GmbH, Marktredwitz, Germany), and 1.1 mol% DSPE-PEG2000-biotin (Avanti Polar Lipids, Alabaster, AL, USA). For the indirect method all coating components were first dissolved in chloroform/methanol (9:1 vol/vol), the solvent was then evaporated using argon gas (Linde Gas Benelux, Schiedam, the Netherlands) and the lipids were freeze dried (Alpha 1-2 LD plus, Martin Christ GmbH, Osterode am Harz, Germany) for 2 h. The obtained lipid film was rehydrated by adding PBS saturated with C_4F_{10} gas (F2 Chemicals, Preston, UK), fluorescently labelled by adding lipid dye DiD (1,1'-dioctadecyl-3,3,3',3'-tetramethylindodicarbocyanine perchlorate, Thermo Fisher Scientific, Waltham, MA, USA), placed in a sonicator bath for 10 min and subsequent probe sonication with a Sonicator ultrasonic processor XL2020 (HeatSystems, Farmingdale, NY, USA) at power setting 3 for 5 min (20 kHz). For the direct method, all coating components were dispersed directly in PBS saturated with C_4F_{10}, mixed, and lipid dye DiI (1,1'-dioctadecyl-3,3,3',3'-tetramethylindocarbocyanine perchlorate, Thermo Fisher Scientific) was added for fluorescent labeling of the direct microbubbles. For both methods the final concentration was 2.5 mg/mL DSPC, 0.625 mg/mL PEG40-stearate, 0.625 mg/mL DSPE-PEG2000 and 0.125 mg/mL

DSPE-PEG2000-biotin. Microbubbles were then produced by sonication at 20 kHz (power setting 10) at the gas/water interface for 1 min under a constant stream of C_4F_{10} gas.

After production, microbubbles were functionalized to target the $\alpha_V\beta_3$ integrin by biotin-streptavidin coupling, as described previously [47, 442]. In short, microbubbles were first washed three times by centrifugation for 1 min at 400g using PBS saturated with C_4F_{10}. The microbubble concentration was determined using a Coulter Counter Multisizer 3 (50 µm aperture tube, Beckman Coulter, Mijdrecht, the Netherlands) and 6×10^8 microbubbles were incubated with 60 µg of streptavidin (2 mg/mL in PBS, Sigma-Aldrich) for 30 min on ice, followed by washing by centrifugation. Next, the streptavidin-conjugated microbubbles were incubated with 6 µg biotinylated anti-human CD51/61 antibody (*i.e.* anti-$\alpha_V\beta_3$, 304412, BioLegend, San Diego, CA, USA) for 30 min on ice. After incubation the $\alpha_V\beta_3$-targeted microbubbles were washed again, the concentration and size distribution were determined by Coulter Counter, and a mixed sample with a 1:1 ratio of indirect:direct was prepared, from here on referred to as stock sample. A new sample of microbubbles was functionalized for each experimental day, six batches of microbubbles were produced in total, and samples were taken from a batch of microbubbles up to 21 days post-production.

8.2.2 Endothelial cell culture

All *in vitro* experiments were performed using primary human umbilical vein endothelial cells (HUVECs; C2519A, Lonza, Verviers, Belgium) from pooled donors, cultured with Endothelial Cell Growth Medium (EGM)-2 (Lonza) and grown to full confluency at 37 °C with 5% CO_2 in T75 flasks in a humidified incubator. HUVECs were detached before each experiment with Accutase solution (Sigma-Aldrich). HUVECs used for experiments were between passage number 4 and 9. For experiments in static conditions, HUVECs were replated onto the bottom membrane of a CLINIcell (Mabio, Tourcoing, France) with 50 µm membranes (25 cm^2) in 12 mL EGM-2, and incubated for two days at 37 °C with 5% CO_2 to achieve a confluent monolayer. In total eight CLINIcells were used for binding efficacy experiments and four CLINIcells were used for internalization experiments. For experiments under flow, IbiTreat polymer µ-slides (80196, 0.8 mm channel height, Ibidi GmbH, Gräfelfing, Germany) were first pre-coated by incubating with 7.6 µg fibronectin (Roche, Basel, Switserland) in 200 µL PBS at 37 °C with 5% CO_2 for 1 to 2 h as instructed by Ibidi, then washed with 800 µL PBS. After seeding in the µ-slide, the HUVECs were placed in the humidified incubator at 37 °C with 5% CO_2 without flow for 2 h to attach, then connected to and Ibidi fluidic unit and the computer-controlled Ibidi Pump system (Ibidi) with corresponding perfusion sets (Perfusion set Yellow and Green, 10964, Ibidi). For later injection of fluorescent dyes and microbubbles, two Luer injection

ports (Ibidi) were inserted in the perfusion set: one at 3.5 cm downstream from the µ-slide and the other 7 cm upstream from the µ-slide. Laminar flow was started with controlled shear stress at 2.5 dyn/cm^2 for 30 min, then 5.0 dyn/cm^2 for 30 min, and finally 7.5 dyn/cm^2 until at least 48 h post-seeding to obtain a confluent monolayer. In total six µ-slides were used to evaluate binding efficacy under flow, and eight µ-slides were used to evaluate dissociation of bound microbubbles under increasing flow.

8.2.3 CAM model preparation

For *in vivo* experiments, the CAM was prepared as described previously [520]. All animal experiments were conducted in accordance with the Netherlands Experiments on Animals Act and in accordance with the European Council (2010/63/EU) on the protection of animal use for scientific purposes. In short, freshly fertilized eggs (Drost Pluimveebedrijf Loenen BV, Loenen aan de Vecht, the Netherlands) were incubated for 5 days at 37 °C in a humidified incubator. The chicken embryo was taken out of the eggshell and placed into a weighing boat with the embryo and CAM on top. First a mixture of 2 µl Hoechst 33342 (10 mg/mL, Thermo Fisher Scientific) to stain the cell nuclei, 3 µl CellMask Green Plasma Membrane Stain (5 mg/mL, Thermo Fisher Scientific) to stain the cell membrane, and 5 µL targeted microbubbles (indirect and direct 1:1 ratio) was prepared, then 5 µL of this mixture was injected into a CAM vein using a capillary glass needle with a VisualSonics micro injection system (Fujifilm VisualSonics, Toronto, Canada). A CLINIcell (Mabio) was prepared by cutting out the top membrane and filling the frame with a solution of 2% agarose (A9539, Sigma Aldrich) in demi water. The membrane containing the chicken embryo and the CAM was cut out, rinsed with PBS, and pinned down on the prepared CLINIcell for imaging with a confocal microscope. The heart rate was monitored prior to and during the imaging and a total of seven chicken embryos were used for *in vivo* experiments.

8.2.4 Confocal microscopy imaging

For the *in vitro* binding efficacy and dissociation and *in vivo* binding efficacy experiments, fluorescent images were acquired with a custom-built Nikon A1R+ confocal microscope [431] equipped with a 60 × water dipping objective (NIR Apo 1.0W DIC, Nikon Instruments). For the *in vitro* 3D imaging of microbubble internalization, the microscope was equipped with a 100 × water dipping objective (CFI Plan 100XC W, Nikon Instruments). Four channels were used to capture the different fluorescent signals: Hoechst was excited at 405 nm and detected at 450/50 nm (center wavelength/bandwidth), CellMask Green was excited at 488 nm and detected at 525/50 nm, DiI was excited at 561 nm and detected at 595/50, and

DiD was excited at 640 nm and detected at 700/75 nm. All imaging experiments were performed in a custom-made water bath at 37 °C positioned beneath the microscope and completed within 2 h after placing the sample in the confocal set-up.

8.2.5 Binding efficacy *in vitro* static

Statically cultured HUVECs in the CLINIcells were first incubated with CellMask Green Plasma Membrane Stain (4 µg/mL final concentration) for 10 min inside the humidified incubator to stain the cell membranes. Then, to stain the cell nuclei, Hoechst 33342 (5 µg/mL final concentration) was added together with the microbubbles (direct/indirect 1:1 ratio, 1×10^6 microbubbles/mL final concentration) and the CLINIcell was placed with the HUVEC monolayer on top in the incubator for 5 min, to allow the targeted microbubbles to float up and bind to the cells. The CLINIcell top membrane was cut out to image the cells with an objective with a smaller working distance than the 5 mm between the CLINIcell top and bottom membranes [58] and the CLINIcell was then placed in the confocal set-up in a water bath at 37 °C with the HUVEC monolayer on the bottom membrane. Each confocal microscopy field of view (FOV) covered 210 × 210 µm (512×512 pixels) and 25 FOVs were acquired in each CLINIcell. Additionally, to determine the ratio of indirect:direct microbubbles in each stock sample, 25 FOVs were acquired using a control CLINIcell without HUVECs, every experimental day when a new stock sample of targeted microbubbles was prepared. This control CLINIcell was first blocked with 2% (w/v) bovine serum albumin (BSA) for 1 h, to avoid nonspecific microbubble binding to the CLINIcell membranes, then washed three times with PBS and pre-heated to 37 °C before adding the microbubbles (1×10^6 microbubbles/mL final concentration) and placing the CLINIcell in the confocal microscopy imaging set-up.

8.2.6 Binding efficacy *in vitro* under flow

For experiments under flow, the flow on the HUVECs cultured in the µ-slide was stopped for approximately 10 min to transport the µ-slide from the humidified incubator to the experimental set-up. The µ-slide was first inserted into the set-up upright in a water bath at 37 °C, with the HUVEC monolayer on the bottom of the µ-slide. Then, flow was started at a shear stress of 7.5 dyn/cm^2 and a mixture of 1.36 µL Hoechst 33342 (10 mg/mL) and 10.9 µL CellMask Green Plasma Membrane Stain (5 mg/mL) in 200 µL EGM-2 was injected into the upstream Luer injection port with a 1 mL Luer Solo syringe (Omnifix-F, B Braun, Melsungen, Germany) and 19G needle (Sterican, B Braun). The fluorescent dyes were allowed to incubate under flow for 15 min, after which the µ-slide was inverted to have the HUVEC monolayer on the top side of the µ-slide [507]. For the binding efficacy under

flow experiments, different flow conditions were evaluated with a shear stress of 1.25, 2.22, 4.45, 5.0, 6.8, or 7.5 dyn/cm^2. To monitor binding under flow, confocal microscopy time lapse imaging (0.31 fps) was started 15 s prior to injection of the microbubbles (indirect:direct 1:1 ratio, 1 × 10^6 microbubbles/mL final concentration) into the downstream Luer injection port and continued for 7 min. Next, to quantify the number of bound microbubbles under flow, single frame FOVs were acquired at different locations throughout the µ-slide with each FOV covering 210 × 210 µm (512×512 pixels). For 1.25 and 2.22 dyn/cm^2, the flow was kept constant during imaging of 25 FOVs. For 6.8 and 7.5 dyn/cm^2, after acquiring 15 FOVs the flow was adjusted to a shear stress of 4.45 or 5 dyn/cm^2, respectively, and 15 more FOVs were acquired. Additionally, 25 FOVs were acquired in a control µ-slide without HUVECs to determine the ratio of indirect:direct microbubbles on each experimental day. The control µ-slide was connected to the Ibidi pump system and filled with pre-heated EGM-2 to compare to the situation of µ-slides with HUVECs. The microbubbles (1 × 10^6 microbubbles/mL final concentration) were injected downstream at a shear stress of 1.5 dyn/cm^2 to mimic the experimental procedure of the binding efficacy under flow experiment. However, 10 s after injection the flow was turned off to make imaging feasible, since otherwise the non-bound microbubbles would float out of the µ-slide in the absence of HUVECs.

8.2.7 Dissociation *in vitro* under flow

For the dissociation under flow experiments, the µ-slide with HUVECs grown under flow was transported to the confocal set-up and dyes were added as described above in *Section 9.2.6*. After 15 min incubation of the dyes and subsequent inverting of the µ-slide, the flow was adjusted from 7.5 dyn/cm^2 to 1.5 dyn/cm^2. The microbubbles (direct/indirect 1:1 ratio, 1 × 10^6 microbubbles/mL final concentration) were injected downstream and after 10 s the flow was stopped, to allow the microbubbles to flow into the µ-slide and bind to the HUVEC monolayer. After 5 min incubation with microbubbles a confocal microscopy time lapse recording (0.31 fps) was started first without flow, then the flow was started at 1.0 dyn/cm^2 and gradually increased with 0.5 dyn/cm^2 steps every 60 s up to 7.5 dyn/cm^2. The time lapse FOV covered 210 × 210 µm (512×512 pixels) and one time lapse was recorded per µ-slide.

8.2.8 Binding efficacy *in vivo*

For *in vivo* experiments the CAM was prepared and dyes were added as described above in *Section 8.2.3*. The CLINIcell with the CAM was placed in the confocal set-up in a water bath at 37 °C. Each FOV covered 210 × 210 µm (512×512 pixels) and to get a full picture of the blood vessels, *z*-stacks (step-size 0.575 µm) were acquired to include all microbubbles bound at one FOV at different *z*-planes. On average

12 FOVs were imaged per CAM. Additionally, 25 FOVs were acquired of the stock sample in a control CLINIcell without HUVECs as described above, to determine the indirect:direct ratio of the sample on each experimental day.

8.2.9 Internalization of bound microbubbles *in vitro*

To image the microbubble-cell morphology in 3D of microbubbles internalized by HUVECs, as described previously (*Chapter 7*), CLINIcells were prepared and placed in the confocal imaging set-up as described above. *Z*-stacks were acquired with 0.325 µm steps.

8.2.10 Data analysis

All *in vitro* binding efficacy and dissociation under flow results were analyzed with ImageJ software by counting the number of direct and indirect microbubbles in each FOV. The *in vivo* binding efficacy results were analyzed with the NIS-Elements AR Analysis software (version 5.02.00) from Nikon by counting the cumulative number of direct and indirect microbubbles per FOV over all *z*-slices. For the binding efficacy experiments, the median ratio of indirect:direct microbubbles in the control FOVs was calculated per experimental day to correct for any deviations in the stock sample from the desired ratio of 1:1 (indirect:direct). All FOVs with less than five bound direct or indirect microbubbles were excluded from the binding efficacy analysis. The binding efficacy was quantified as the ratio of the number of bound indirect microbubbles divided by the number of bound direct microbubbles (indirect:direct) and corrected for the indirect:direct ratio of the stock sample. The cumulative number of bound microbubbles per µ-slide under flow at 4.45-7.5 dyn/cm^2 was multiplied by 1.67 to correct for the difference in number of FOVs, since for 1.25-2.22 dyn/cm^2 25 FOVs were recorded and for 4.45-7.5 dyn/cm^2 15 FOVs were recorded. The results from 4.25 and 5 dyn/cm^2 were pooled and are presented as 4.7 dyn/cm^2, and the results from 6.8 and 7.5 dyn/cm^2 were pooled and are presented as 7.2 dyn/cm^2.

For the dissociation under flow experiments, for each shear stress the number of bound microbubbles was counted and normalized to the initial number of bound microbubbles, thereby starting at 100% before flow. If the focus was lost for the full 60 s of a shear stress condition during time lapse imaging, the data point at that shear stress was excluded from analysis. A curve was fitted through the data using the restricted cubic spline curve function (5 knots) in GraphPad Prism 9.0.0. Microbubble sizes were measured using the measure Radius tool in the NIS-Elements AR Analysis software (version 5.02.00) from Nikon. Microbubbles were only measured if the gas core was clearly visible inside the circular fluorescent coating. For the *in vitro* binding efficacy, a random sample of 11 FOVs at 1.25 dyn/cm^2 and 11 FOVs at 2.22 dyn/cm^2

were analyzed to obtain a minimum N number of 100 microbubbles per type at each flow condition. For 4.45, 5, 6.8, and 7.5 dyn/cm^2 all FOVs were analyzed. The results from 4.25 and 5 dyn/cm^2 were pooled and are presented as 4.7 dyn/cm^2, and the results from 6.8 and 7.5 dyn/cm^2 were pooled and are presented as 7.2 dyn/cm^2. For the *in vitro* dissociation under flow, microbubbles were measured in the first FOV of a time lapse, before starting flow, and at the last FOV, at the maximum flow of 7.5 dyn/cm^2.

The internalization of bound microbubbles was quantified as described previously (*Chapter 7*), with a custom semi-automated procedure in MATLAB (The Mathworks Inc., Natick, MA, USA). Briefly, the orthogonal planes crossing the center of the microbubble were found based on the *xy*-plane with maximum fluorescence intensity in the DiI (direct microbubble) or DiD (indirect microbubble) channel. These orthogonal planes, *i.e. xz*- and *yz*-planes, were then used to obtain the microbubble location by fitting a circle through the maximum intensity in the DiI or DiD channel. The CellMask Green channel of the same orthogonal planes was then used to identify the apical and basal cell membrane at the location of the microbubble. These planes were used to quantify the cell thickness. Next, the internalized depth was quantified at the center of the microbubble, as the difference between the *z*-plane of the apical cell membrane and the bottom of the microbubble (*i.e., z*-plane closest to the basal cell membrane). Finally, the CellMask Green channel was scored manually for the occurrence of a dome, that is when the top of the microbubble was covered by the cell membrane, and the occurrence of green rings, that is when there was a ring with high fluorescence intensity present at the location of the microbubble.

8.2.11 Statistics

The statistical analysis was done using IBM SPSS Statistics 25. First a Shapiro-Wilk test was used to assess the normality and distribution of the data. As the data was non-parametric, a Mann-Whitney U test or Kruskal-Wallis test was used to test for differences between groups and the exact Wilcoxon Signed-Rank test was used for paired data (microbubble size from Coulter Counter measurement and percentage of bound microbubbles in dissociation under flow experiment). The correlation between parameters was assessed with Pearson's correlation test and differences between groups were only tested for $N > 2$.

8.3 Results

In Figure 8.1 the mean microbubble diameters and size distribution of direct and indirect targeted microbubbles are summarized. There was no significant difference between the mean size of direct and indirect targeted microbubbles (p = 0.209, Figure 8.1A). The size distribution was polydisperse and comparable for both types of microbubbles, as shown in Figure 8.1B.

The binding efficacy of direct and indirect targeted microbubbles was evaluated in three models using confocal imaging of bound microbubbles, as shown in Figure 8.2. HUVECs grown under static conditions (Figure 8.2A) had a typical cobble stone appearance, with high fluorescence intensity at the cell-cell borders. In contrast, the HUVECs grown under flow (shear stress 7.5 dyn/cm^2, Figure 8.2B) were more elongated and covered a larger area per cell. The DiI and DiD channels showing the bound direct and indirect microbubbles in red and white, respectively, are presented in Figure 8.2A2 and 8.2B2. The white stripes in Figure 8.2B2 represent non-bound microbubbles flowing through the µ-channel during imaging. Figure 8.2C shows the volume view of a *z*-stack acquired of a vessel in the *in vivo* CAM model. The curved top side of the vessel is visible with targeted microbubbles (red and white) bound to the endothelial cells in green. Three slices from the *z*-stack are shown in Figure 8.2D-F, with the bound microbubbles in Figure 8.2D2-2F2. In comparison to the HUVEC monolayers, the cell-cell borders were less distinguishable in the CAM model due to the more challenging imaging environment and 3D structure *in vivo*. The mean heart rate was 88 ± 24 beats per minute.

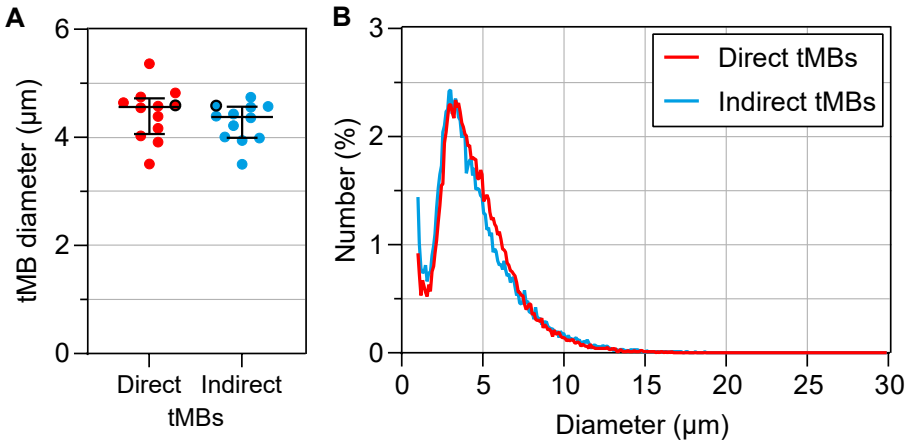

Figure 8.1 (**A**) Number weighted mean diameter (µm) of direct and indirect targeted microbubbles (tMBs). Each circle represents one sample of targeted microbubbles (N = 12) for each experimental day, with the median and interquartile range (IQR) overlaid in black. The size distribution of circles with a black border is shown in (**B**): number weighted size distribution of direct (red) and indirect (blue) targeted microbubbles.

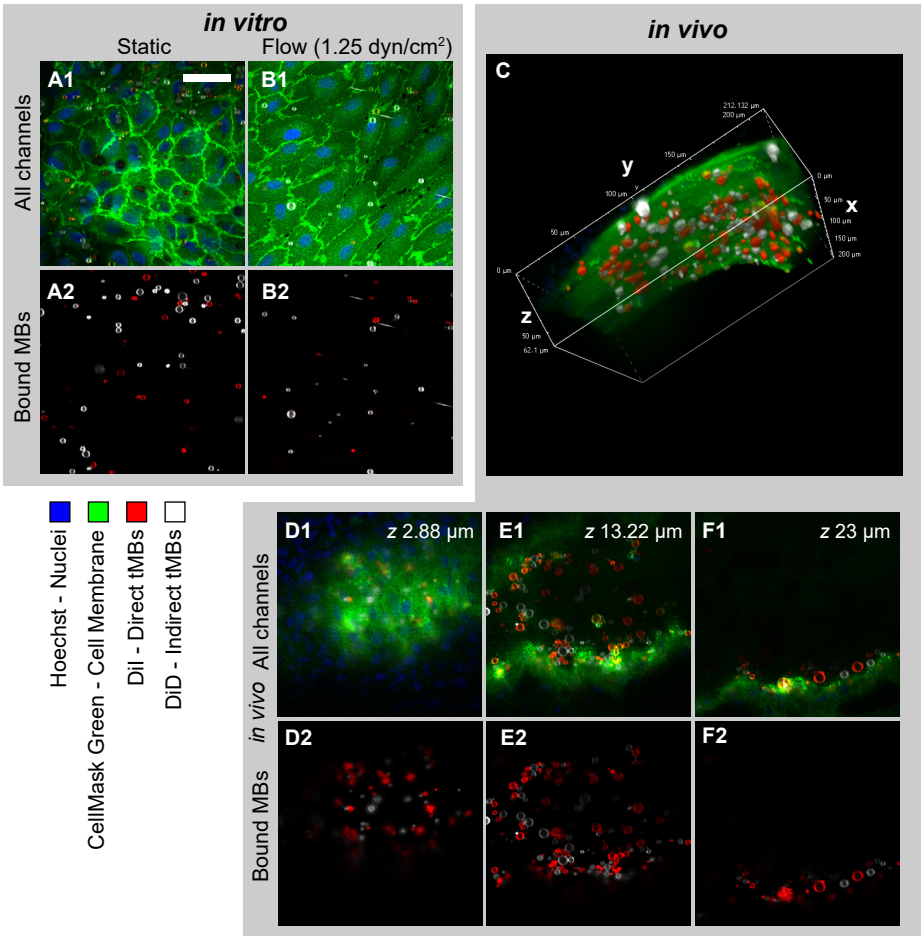

Figure 8.2 Typical examples of targeted microbubbles bound to a monolayer of HUVECs cultured (**A**) statically or (**B**) under flow (cultured at 7.5 dyn/cm^2, imaged at 1.25 dyn/cm^2) showing (**1**) all channels and (**2**) DiI and DiD channels. (**C**) Volume view of targeted microbubbles bound to endothelial cells *in vivo* in the CAM model based on confocal *z*-stack. (**D-F**) 2D view of slices at different *z* positions in *z*-stack shown in (**C**) and imaged from the top, showing (**1**) all channels and (**2**) DiI and DiD channels. Cell membrane shown in green, cell nuclei in blue, direct microbubbles in red (DiI) and indirect microbubbles in white (DiD). Scale bar represents 50 µm and applies to all 2D images. Normalized ratio of indirect/direct bound microbubbles was (**A**) 1.87, (**B**) 3.09, (**C**) 1.14. All experiments were performed in a temperature-controlled water bath at 37 °C.

The binding efficacy was quantified as the normalized ratio of indirect to direct bound microbubbles *in vitro* under static conditions and under flow (1.25 and 2.22 dyn/cm^2), and *in vivo* in the CAM model, as presented in Figure 8.3. Since all ratios based on FOVs with less than five bound microbubbles were excluded, results from higher shear stresses *in vitro* (4.7 to 7.2 dyn/cm^2) are not presented in Figure 8.3. The mean ratio in the stock sample was (0.85 ± 0.25):1 indirect:direct targeted microbubbles (N = 12 experimental days). For the static condition, more

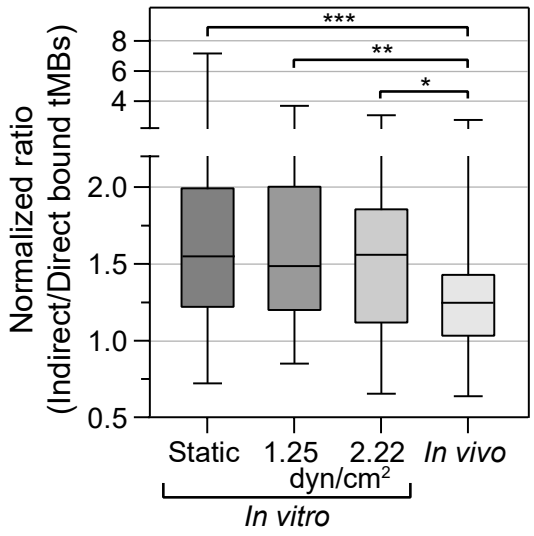

Figure 8.3 Binding efficacy of direct versus indirect targeted microbubbles (tMBs), plotted as the ratio of indirect:direct bound microbubbles per condition, normalized to the median ratio (indirect:direct microbubbles) of the control without cells. Static (N = 186 FOVs), shear stress 1.25 dyn/cm^2 (N = 47 FOVs), shear stress 2.22 dyn/cm^2 (N = 23 FOVs), and in vivo in the CAM model (N = 66 FOVs). Boxplots show the median, IQR and whiskers from minimum to maximum. Statistical significance is indicated with *p < 0.05, **p < 0.01, ***p < 0.001. Only results from FOVs with >5 bound direct and >5 bound indirect microbubbles are included.

indirect than direct microbubbles were bound in 89.2% of the FOVs, with a median of 1.55× more indirect microbubbles bound. There was some variability in the extent of how many more indirect microbubbles were bound, ranging from 0.72 to 7.2× the number of direct bound microbubbles. The cumulative number of microbubbles bound in 25 FOVs, *i.e.* one CLINIcell, ranged from 1000 to 2000. For the flow condition with 1.25 dyn/cm^2, 87.2% of the FOVs had more indirect than direct microbubbles bound, with a median of 1.49× more indirect microbubbles bound, and for the flow condition with 2.22 dyn/cm^2, 82.6% of the FOVs had more indirect than direct microbubbles bound with a median of 1.56× more indirect microbubbles bound. Both *in vitro* flow shear stresses resulted in ratios comparable to the static condition but with a lower maximum and lower standard deviation. Finally, using the *in vivo* CAM model, in 77.3% of the FOVs more indirect than direct microbubbles had bound with a median of 1.25× more indirect microbubbles bound. *In vivo*, most of the microbubbles bound in the vein near the injection site and no bound microbubbles were observed in the arteries. The cumulative number of microbubbles bound per chicken embryo ranged from 150 to 1800. The ratio of indirect:direct bound microbubbles in static conditions was significantly higher than *in vivo* (p < 0.001). Furthermore, the ratios at 1.25 and 2.22 dyn/cm^2 for the *in vitro* flow conditions were significantly higher than *in vivo* (p = 0.001 and p = 0.031, respectively).

Binding efficacy under flow was investigated *in vitro* at shear stresses of 1.25 and 2.22 as shown in Figure 8.3, and also 4.7 and 7.2 dyn/cm^2. With increasing shear stress, the number of microbubbles binding under flow decreased towards zero at 7.2 dyn/cm^2. The cumulative number of bound microbubbles per µ-slide is shown in Figure 8.4A, to incorporate the results from high shear stress conditions

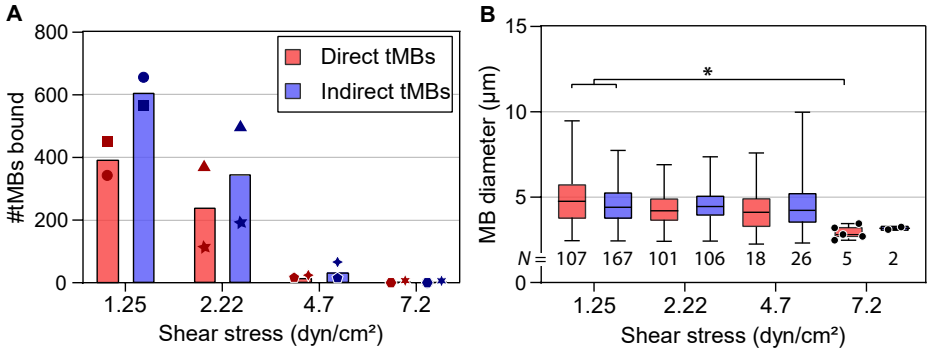

Figure 8.4 Direct and indirect targeted microbubbles (tMBs) bound in vitro at different shear stresses. (**A**) Mean cumulative number of microbubbles counted in a total of 25 FOVs per slide, each symbol represents one slide. Bar represents mean of N = 2 µ-slides. (B) Microbubble diameter as a function of shear stress. N = number of microbubbles measured, in 11 FOVs for 1.25 and 2.22 dyn/cm^2 and all FOVs for 4.7 and 7.2 dyn/cm^2. Boxplots are presented with median, IQR, and whiskers from min to max. For N < 6 individual data points are shown as circles. Statistical significance is indicated with *p < 0.05. Results from 4.25 and 5 dyn/cm^2 were pooled presented as 4.7 dyn/cm^2, results from 6.8 and 7.5 dyn/cm^2 were pooled presented as 7.2 dyn/cm^2.

(> 2.22 dyn/cm^2) in which only a limited number of microbubbles bound under flow. Despite the variability in numbers of bound microbubbles between µ-slides at the same shear stress, the number of bound indirect microbubbles was higher than the number of bound direct microbubbles at all shear stresses except for 7.2 dyn/cm^2. The diameters of bound microbubbles were measured to investigate the influence of shear stress on the size distribution of microbubbles binding under flow (Figure 8.4B). N numbers in Figure 8.4B do not correspond to the cumulative numbers from Figure 8.4A, as not every microbubble had a clearly visible gas core and thus some microbubbles were counted without measuring the diameter. The mean diameter of bound microbubbles was comparable at 1.25 to 4.7 dyn/cm^2, while the diameter of bound direct microbubbles at 7.2 dyn/cm^2 was significantly smaller than the diameter of bound direct (p = 0.011) and indirect (p = 0.023) microbubbles at 1.25 dyn/cm^2. The sample size of bound indirect microbubbles at 7.2 dyn/cm^2 (N = 2) was too small for statistical comparison to the other groups.

The binding dissociation under flow was investigated *in vitro* by allowing targeted microbubbles to bind to a HUVEC monolayer without flow and subsequent exposure to increasing shear stress conditions. The median number of direct microbubbles bound before flow in one FOV was 63 [interquartile range (IQR) 32 – 139] and the median number of indirect microbubbles bound was 49 [IQR 25 – 91]. After correction for the stock sample this corresponded to a ratio of 1.13 ± 0.32 indirect/direct targeted microbubbles (mean ± SD, N = 8). Figure 8.5 shows the percentage of targeted microbubbles, relative to the number of microbubbles bound before

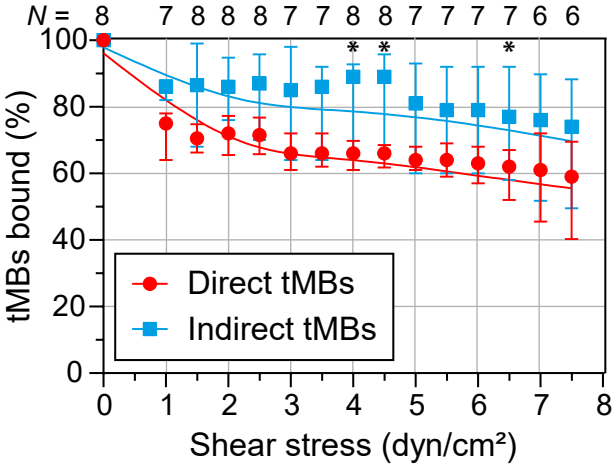

Figure 8.5 Dissociation of bound targeted microbubbles (tMBs) at increasing shear stress in vitro. The median percentage of bound direct (red) and indirect (blue) microbubbles, relative to the number of microbubbles bound before flow, is plotted with the IQR and curve fitting (restricted cubic spline). Statistical significance is indicated with * $p < 0.05$. The number of µ-slides analyzed at each shear stress is shown on top of the graph as *N* number.

flow, remaining bound to the HUVEC monolayer upon increasing shear stress with a spline curve fitted through the data. The median percentage of indirect microbubbles bound was always higher than the median percentage of direct microbubbles, with a significant difference at 4, 4.5, and 6.5 dyn/cm^2. Based on the curve fitting, there was a significant difference in dissociation rate between direct and indirect microbubbles at low shear stresses (1 to 3 dyn/cm^2), with the slope being -7.5 (95% confidence interval: -8.0 – -7.0) for direct microbubbles and -4.7 (95% confidence interval: -5.0 – -4.4) for indirect microbubbles. No differences in microbubble size distribution were found after evaluation of the microbubble sizes before flow and at 7.5 dyn/cm^2 (Supplemental Figure 8.1).

To evaluate the internalization of direct and indirect bound microbubbles, the 3D morphology of targeted microbubbles bound to HUVECs was studied in static conditions with confocal *z*-stacks as shown in Figure 8.6. In Figure 8.6A and B a bright fluorescent ring can be observed in the middle of the image in the CellMask green channel, at the location of the internalized direct and indirect microbubble respectively. Furthermore, the apical cell membrane in green is covering the top of the internalized microbubbles, referred to as a dome. In Figure 8.6C an example is shown of an internalized indirect microbubble where a dome is present, but no green fluorescent ring.

Quantification of the internalized depth is presented in Figure 8.7. The internalized depth of direct targeted microbubbles was significantly larger than that of indirect targeted microbubbles ($p = 0.027$, Figure 8.7A). Moreover, the size of direct microbubbles (median diameter 3.7 µm) was significantly larger ($p < 0.001$) than the size of indirect microbubbles (median diameter 2.8 µm) analyzed for internalized

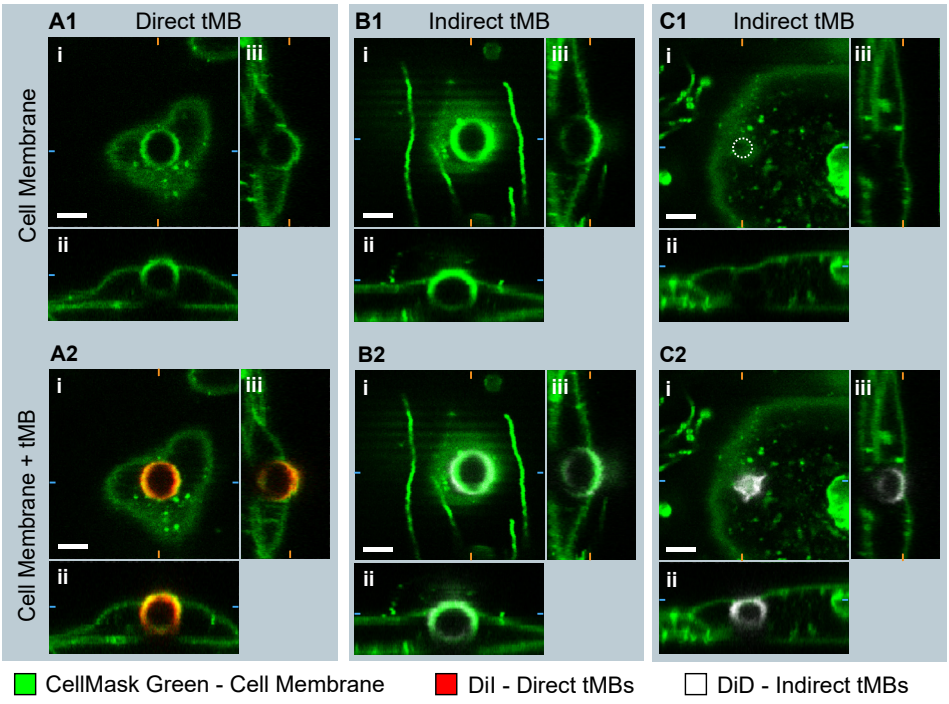

Figure 8.6 Orthogonal views of confocal microscopy *z*-stack of (**A**) bound direct microbubble (diameter 6.0 µm, internalized depth 5.5 µm), (**B**) bound indirect microbubble (diameter 5.8 µm, internalized depth 4.7 µm), and (**C**) bound indirect microbubble (diameter 3.7 µm, internalized depth 4.4 µm) with microbubble location marked with white dotted circle in **C1**. Side views were imaged with the objective from (**ii**) above or (**iii**) the right. Scale bar represents 5 µm, orange and blue markings indicate the cross-section of the orthogonal planes of the side views.

depth. All microbubbles analyzed for internalized depth (N = 61 in total) were also scored for the presence of a dome and a green ring in the cell membrane. The internalized depth of microbubbles with a dome (N = 41) was significantly (p < 0.001, Supplemental Figure 8.2A) larger than that of microbubbles without a dome (N = 20). Furthermore, the internalized depth of microbubbles with a green ring (N = 37) was significantly (p < 0.001, Supplemental Figure 8.2B) larger than that of microbubbles without a green ring (N = 24). Not all microbubbles covered by the apical cell membrane, classified as a dome, also displayed a green ring (N = 4, Figure 8.6C). However, in all cases where a green ring was present in the CellMask Green channel, a dome was also found (N = 37). The influence of ligand distribution on the occurrence of domes and green rings was further investigated by comparing the direct and indirect targeted microbubbles (Figure 8.7B, C). For microbubbles with a dome, the internalized depth of direct microbubbles (N = 22) was significantly higher (p = 0.001) than that of indirect microbubbles (N = 19). For microbubbles with a green ring, the internalized depth of direct microbubbles

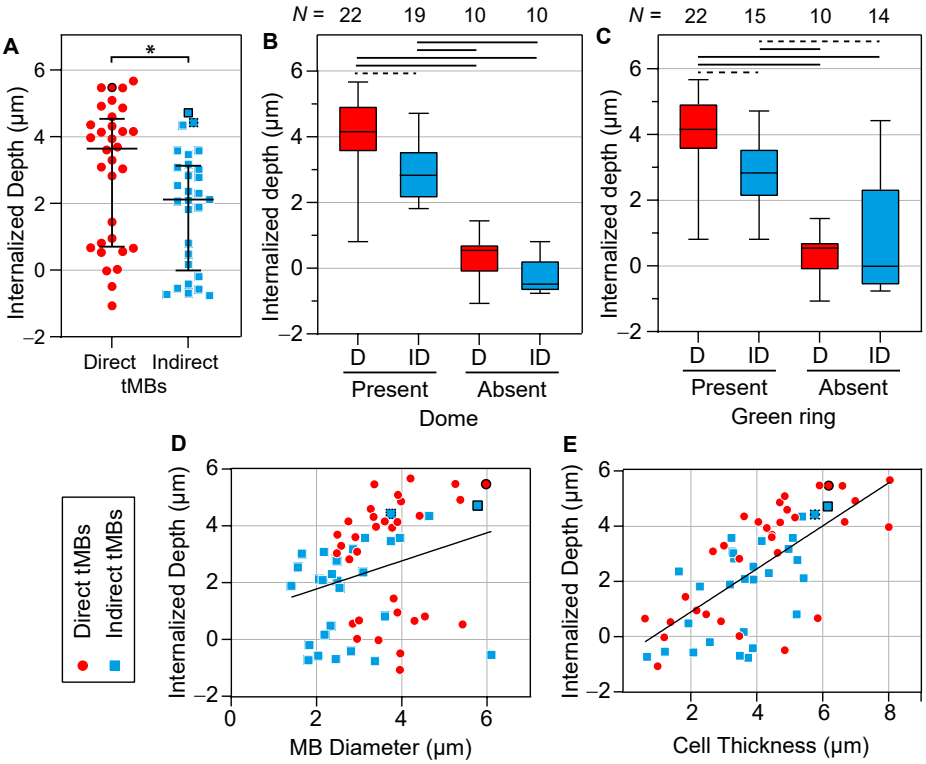

Figure 8.7 Internalization of targeted microbubbles (tMBs) bound to a HUVEC monolayer in static conditions with direct (circles) in red and indirect (squares) in blue. (**A**) Internalized depth (µm) of direct (N = 32) versus indirect (N = 29) targeted microbubbles with median and IQR. Significance is indicated with *p < 0.05. (**B-C**) Internalized depth of direct (D, red) and indirect (ID, blue) bound microbubbles with (**B**) dome or (**C**) green ring present or absent in the CellMask Green channel, shown as boxplot with whiskers from min to max and N numbers listed above the graphs. Statistics are indicated with a solid black line for p < 0.001 and a dashed line for p < 0.01. (**D**) Internalized depth as a function of microbubble diameter. (**E**) Internalized depth as a function of cell thickness. In **A, D**, and **F** the examples from Figure 8.6 are marked with: F6A) black circle, F6B) black square, and F6C) dotted black square.

(N = 22) was significantly higher (p = 0.001) than that of indirect microbubbles (N = 15). There were no significant differences in internalized depth of direct (N = 10) and indirect (N = 10) microbubbles without a dome (p = 0.059) and without a green ring (direct N = 10, indirect N = 14, p = 0.861). The correlation of internalized depth with microbubble size and cell thickness was first analyzed per microbubble type. Based on linear regression no significant differences were found between the slopes and intercepts of the lines for direct and indirect microbubbles, therefore, the data was pooled for correlation analysis. The internalized depth was positively correlated with the microbubble size (Spearman correlation coefficient ρ = 0.278, p = 0.030, Figure 8.7D). Additionally, the internalized depth was positively correlated with the cell thickness (ρ = 0.686, p < 0.001, Figure 8.7E).

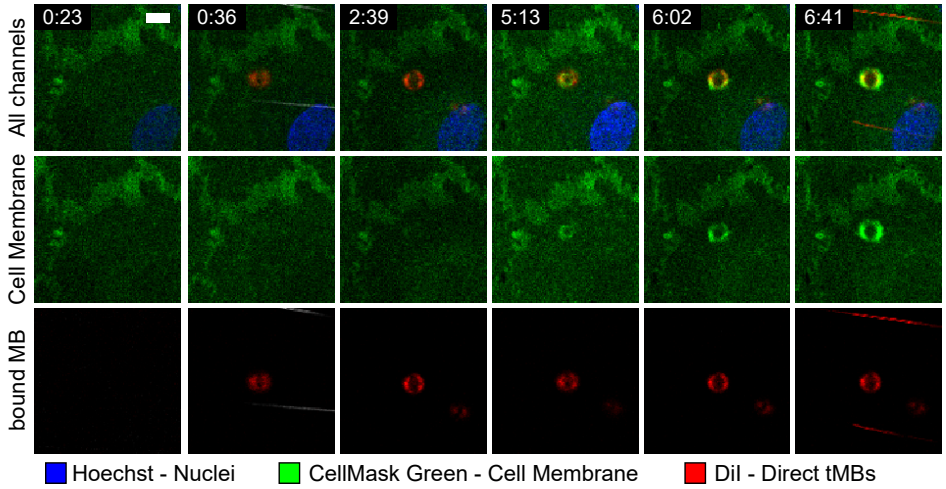

Figure 8.8 Internalization event of targeted direct microbubble (diameter 5.9 µm) over time indicated with min:sec, at a shear stress of 1.25 dyn/cm^2 and with targeted microbubbles added at 0:15. Scale bar represents 10 µm and applies to all images.

With time-lapse imaging of targeted microbubbles binding under flow to a HUVEC monolayer, an internalization event could be tracked over time, as shown in Figure 8.8. At 0:36 a direct targeted microbubble appeared in the field of view and bound to the HUVEC monolayer. Over the next six minutes a bright green ring appeared in the cell membrane at the location of the bound microbubble, indicating that the bound microbubble was being internalized by the HUVEC.

8.4 Discussion

The effect of ligand distribution on the binding efficacy of $\alpha_V\beta_3$-targeted microbubbles was evaluated by comparing direct and indirect targeted DSPC-based microbubbles with heterogeneous and homogeneous ligand distributions, respectively. In the three experimental models used for this study – a HUVEC monolayer under static conditions and under flow with a shear stress of 1.25 to 7.5 dyn/cm^2, and the *in vivo* CAM model – microbubbles with a homogeneous ligand distribution always had a higher binding efficacy than those with a heterogeneous ligand distribution. Furthermore, the dissociation rate of microbubbles with a homogeneous ligand distribution was significantly lower and more microbubbles with a homogeneous ligand distribution remained bound at a shear stress of 1.5 to 7.5 dyn/cm^2. Additionally, the effect of ligand distribution on internalization of $\alpha_V\beta_3$-targeted microbubbles was evaluated by quantifying the internalized depth of bound direct and indirect microbubbles to a HUVEC monolayer in static conditions, and was found to be independent of the ligand distribution.

The ratio of indirect to direct bound microbubbles was calculated as a measure of binding efficacy and found to be > 1, indicating that more indirect targeted microbubbles had bound. Therefore, the indirect microbubbles, with a homogeneous ligand distribution, had a higher binding efficacy than the direct microbubbles, with a heterogeneous ligand distribution. There were no significant differences in microbubble size, therefore any differences in binding efficacy between direct and indirect targeted microbubbles cannot be caused by a difference in size. Although our previous study found a slight difference in size between direct and indirect microbubbles [427], the microbubbles in that study were washed twice whereas the targeted direct and indirect microbubbles in the present study underwent five washing steps before measuring the size distribution. Washing of microbubbles by centrifugation is known to influence the size distribution [521], which may explain why the more size-selected direct and indirect targeted microbubbles in the present study had no significant difference in size. The variability in binding efficacy was the highest without flow, when microbubbles bound to a HUVEC monolayer under static conditions. There was no correlation between the cumulative number of microbubbles bound per CLINIcell, ranging from 1000 to 2000 in 25 FOVs, and the percentage of indirect bound microbubbles, suggesting that the variability in binding efficacy was not due to a difference in total number of bound microbubbles per CLINIcell. In addition, there was no correlation between the percentage of indirect bound microbubbles and the passage number of the HUVECs used. Regardless of the variability in the binding efficacy under static conditions, the normalized ratio of indirect:direct bound microbubbles was > 1 in 89.2% of the FOVs, indicating that microbubbles with a homogeneous ligand distribution had a higher binding efficacy than microbubbles with a heterogeneous ligand distribution in static conditions.

The next step was to evaluate the binding efficacy and dissociation rate of $\alpha_V\beta_3$-targeted microbubbles under flow, in order to mimic more physiologically relevant conditions. Shear stresses of 1 to 7.5 dyn/cm^2 were investigated, comparable to the blood flow in healthy veins [522]. The target $\alpha_V\beta_3$ integrin is expressed during angiogenesis [523] and atherosclerosis [524], and is an established target for molecular imaging of tumors [525] and anti-tumor therapies [526]. Although tumors are known to have a complex microenvironment with highly variable blood flow, shear stresses have been estimated to be as low as 0.5 dyn/cm^2 [527, 528]. The HUVEC monolayers cultured under flow (shear stress 7.5 dyn/cm^2) in this study had a different morphology compared to the HUVEC monolayers cultured under static conditions, indicating that the cells had adapted in response to the shear stress to which they were exposed, in agreement with previous observations [498]. Although this was not investigated in the present work, previous studies reported that the $\alpha_V\beta_3$ integrin expression was upregulated when HUVECs [529] and bovine endothelial cells

[530] were cultured under flow, in contrast to cells cultured under static conditions. Although all experiments were performed at 37 °C and thus can be extrapolated to the *in vivo* situation, different ambient hydrostatic pressures and temperatures were not investigated in relation to microbubble binding characteristics. What is known is that microbubble's acoustic properties change dependent on the ambient hydrostatic pressure, where the subharmonic amplitude decreased with increasing pressure [531], and temperature, where the shell elasticity and viscosity decreased [455, 532] and attenuation either decreased [533] or increased [532, 534] with increasing temperature. In addition, temperature changes may affect microbubble sizes, as decreases [533], increases [534, 535], and no effect [532, 533] in size have been reported. An increase in size will affect microbubble binding efficacy at higher shear rates as shown in our study (Figure 8.4B).

When looking at the cumulative number of bound microbubbles in all 25 FOVs per µ-slide (Figure 8.4), always more indirect microbubbles bound than direct microbubbles. This indicates that $\alpha_V\beta_3$-targeted microbubbles with a homogeneous ligand distribution bound more efficiently under flow than those with a heterogeneous ligand distribution, which was confirmed by the ratio of indirect:direct bound microbubbles (Figure 8.3). At 1.25 dyn/cm^2, the cumulative number of bound microbubbles was comparable to the number of bound microbubbles under static conditions, being approximately 1000 bound microbubbles per 25 FOVs (Figure 8.4A). The number of microbubbles binding under flow decreased with increasing shear stress, which is in agreement with previous studies on $\alpha_V\beta_3$-targeted microbubbles binding to HUVECs under flow (shear stress 0.5-5 dyn/cm^2) [536], and microbubbles targeted to other biomarkers such as P-selectin [49], vascular cell adhesion molecule (VCAM)-1 [537], and intracellular adhesion molecule (ICAM)-1 [324], all using microbubbles functionalized with an antibody through biotin-streptavidin coupling. In our study, the size distribution of bound microbubbles at 1.25 to 4.7 dyn/cm^2 was comparable, suggesting that at a low shear stress the microbubble size has limited influence on the binding rate. In contrast, at 7.2 dyn/cm^2 the microbubble diameter of bound direct microbubbles, median 3.11 µm (IQR 2.77-3.23), was significantly smaller with than at 1.25 dyn/cm^2. While it should be noted that the sample sizes of bound microbubbles at 7.2 dyn/cm^2 were small, this could be an indication that smaller microbubbles have a higher binding rate at a high shear stress. A computational model revealed that a diameter of 2 to 4 µm would be the optimal size for microbubbles targeted to P-selectin and E-selectin [538], and a study on targeted spherical particles (diameter 0.1 to 10 µm) showed that spheres with 2 to 5 µm diameter were optimal for targeting under flow [539]. This may be explained by the increased force encountered by larger particles, as they extend further from the endothelial cell layer to the center of the vessel.

The dissociation under flow was investigated by allowing the microbubbles to bind first and then starting an escalating flow regime with shear stresses from 1 to 7.5 dyn/cm^2. The measured dissociation rate of direct microbubbles was higher than that of indirect microbubbles at low shear stresses (1-5 dyn/cm^2), although above 5 dyn/cm^2 the dissociation rates of direct and indirect microbubbles were similar. The difference between direct and indirect microbubbles in percentage of bound microbubbles was significant at 4, 4.5, and 6.5 dyn/cm^2, however, with a larger sample size a significant difference between direct and indirect microbubbles may also be expected for other shear stresses above 4.5 dyn/cm^2. There were no differences in size distribution of microbubbles bound before flow started and at 7.5 dyn/cm^2, indicating that although the binding rate may be influenced by the microbubble size, the dissociation of bound microbubbles occurred independent of the size. Moreover, the mean size of bound microbubbles was similar to the mean size measured by Coulter Counter. Together, these results confirm that under flow a homogeneous ligand distribution results in a higher binding efficacy than a heterogeneous ligand distribution.

A study on P-selectin-targeted microbubbles reported that microbubble dissociation or detachment under flow was related to the receptor density on the target surface [49], with our results corresponding to the dissociation rate of the highest receptor density tested (109 molecules/μm^2). In our study, the percentage of microbubbles remaining bound at increasing shear stress was several times higher than the percentage reported recently on vancomycin-decorated microbubbles binding to a bacterial biofilm under flow [507]. With the experimental set-up used for the present study, the unbound targeted microbubbles kept on circulating through the μ-slide with the HUVEC monolayer for as long as the flow was on. Hence, it is possible that at low shear stresses new microbubbles bound during the experiment and the results do not only reflect a difference in dissociation rate, but also a difference in binding of microbubbles at low shear stresses. The number of microbubbles remaining bound at shear stresses above 4 dyn/cm^2 was much higher than the number of microbubbles binding under flow at 4.7 and 7.2 dyn/cm^2, which is in concert with previous reports on P-selectin-targeted microbubbles [49]. This indicates that while the binding rate may be low at high shear stress, the microbubbles can remain bound successfully. To improve the binding rate in high shear stress conditions, acoustic radiation forces can be used to reduce the flow speed of targeted microbubbles and displace them towards the target surface [120].

Finally, the binding efficacy of $\alpha_V\beta_3$-targeted microbubbles was evaluated *in vivo* using the CAM model. Although the size of the injected vein and the number of microbubbles injected varied, the number of indirect bound microbubbles was higher than the number of direct bound microbubbles in 77.3% of the FOVs, with a median

of 1.25× more indirect bound microbubbles. Studies have shown that for ultrasound molecular imaging, the acoustic scattering of individual bound microbubbles can be detected [397]. Based on this, using indirect targeted microbubbles – with homogeneous ligand distribution – would result in 25% higher molecular signal *in vivo* compared to the direct targeted microbubbles, with heterogeneous ligand distribution. The experimental set-up limited the view of the CAM hence the injection site could not be imaged in each chicken embryo. Nonetheless, this should have no effect on the ratio of indirect:direct bound microbubbles. A study using intravital microscopy to observe the behavior of targeted microbubbles in the microcirculation of rodents reported that microbubbles predominantly bound in veins and not the arteries or arterioles [540], similar to our observation in the present study. The observed heart rates of the chicken embryos were in agreement with a previous report on chicken embryo experiments involving $\alpha_V\beta_3$-targeted microbubbles, where it was found that the uptake of a model drug was increased when more microbubbles bound to the endothelial cells [519]. In the context of our results, this suggests that the use of targeted microbubbles with homogeneous ligand distribution may result in increased enhancement of drug delivery compared to those with a heterogeneous ligand distribution.

The effect of ligand distribution on the internalization of $\alpha_V\beta_3$-targeted microbubbles was investigated, since a recent study has shown how the drug delivery outcome upon sonoporation is affected by the internalization of targeted microbubbles (*Chapter 7*). While there was a significant difference in internalized depth between direct and indirect microbubbles, the internalized depth was size-dependent and a significant difference was found in the diameters of direct and indirect microbubbles in this data set. Therefore, the difference found in internalized depth is likely due to a difference in microbubble size, as opposed to the difference in ligand distribution. The internalized depth and its correlations with microbubble diameter and cell thickness reported here are all in agreement with the previously published results on indirect microbubbles, although the number of non-internalized indirect microbubbles found here was slightly higher than in the previous study. The dome formation and occurrence of green rings is substantiated by the previous study as well. For both types of microbubbles, two separate groups were observed: those with internalized depth between 2 to 6 μm and those with internalized depth around 0 μm (Figure 8.6A). This separation into two groups was confirmed by the dome formation, based on which the microbubbles could be divided into a non-internalized group without dome and an internalized group of microbubbles with a dome. All cases where a green ring was observed in the cell membrane, the microbubble was internalized, and hence a green ring was a clear marker for internalization. On the other hand, a green ring was not always present when a

microbubble was internalized. It is possible that the occurrence of bright fluorescent rings at the location of the bound microbubbles is caused by rearrangement of the cell membrane lipids and fluorescent dye. The process of internalization appeared to be independent of the ligand distribution, and is instead expected to be receptor-mediated (*Chapter 7*).

A live internalization event was observed with a direct targeted microbubble under flow, based on the emerging green fluorescent ring observed in the cell membrane (Figure 8.7). Since the confocal microscopy imaging of microbubbles binding under flow was all in 2D, it was not possible to quantify the internalized depth. The internalization of the microbubble took approximately 6 minutes, the same time scale found in studies on internalization of 3.2 µm sized silicon micro-particles, which were starting to be encapsulated by the HUVEC cell membrane after 5 minutes of incubation, and fully internalized after 15 minutes [541]. Furthermore, non-targeted phospholipid-coated microbubbles with diameters from 2.8 to 4.1 µm adhered to activated leukocytes after 3 min incubation and were fully phagocytosed, *i.e.* internalized, after 15 min of incubation [489]. These microbubbles were internalized through complement opsonization, however, in our previous study non-targeted microbubbles were not internalized by HUVECs (*Chapter 7*). Therefore, it is unlikely that complement factors binding to the microbubble surface or ligand play a role in the internalization of microbubbles by HUVECs as studied here.

8.5 Conclusions

The effect of the ligand distribution on the binding efficacy of $\alpha_V\beta_3$-targeted microbubbles was evaluated *in vitro* under static conditions and under flow with a shear stress from 1.25 to 7.5 dyn/cm^2, and *in vivo* in the CAM model. Microbubbles with a homogeneous ligand distribution had a higher binding efficacy than those with a heterogeneous ligand distribution. The dissociation rate of bound microbubbles with homogeneous ligand distribution was significantly lower than the dissociation rate of those with heterogeneous ligand distribution at a low shear stress (1 to 5 dyn/cm^2). Although the ligand distribution had no influence on the internalization of $\alpha_V\beta_3$-targeted microbubbles by HUVECs, the internalization depth correlated with the microbubble size and cell thickness. In conclusion, the ligand distribution of targeted microbubbles has a significant effect on the binding efficacy *in vitro* and *in vivo*. For optimal results in ultrasound molecular imaging and drug delivery with targeted microbubbles, the indirect production method of phospholipid-coated microbubbles is preferred, whereby the phospholipid-components are first dissolved in organic solvent to obtain a lipid film before the lipids are dispersed in aqueous medium to achieve a homogeneous ligand distribution.

Acknowledgments—The authors thank R. Beurskens from the Department of Biomedical Engineering, Erasmus University Medical Center, Rotterdam the Netherlands, for technical assistance during the experiments. Furthermore, the authors thank Lipoid GmbH for providing a free sample of DSPC phospholipid.

Funding

This research was funded in part by the Phospholipid Research Center in Heidelberg, Germany, grant number KKO-2017-057/1-1, in part by the Applied and Engineering Sciences TTW grant of NWO, VIDI-project number 17543, and in part by the Thorax Center of Erasmus University Medical Center in Rotterdam.

Supporting information

The Supporting Information is available free of charge at
https://doi.org/10.3390/pharmaceutics14020311

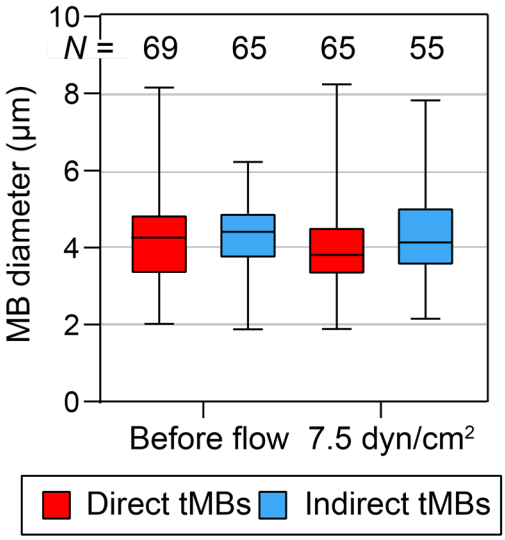

Supplemental Figure 8.1 Diameter (µm) of bound direct and indirect targeted microbubbles (tMBs) from dissociation under flow assay with HUVEC monolayer *in vitro*. Diameters were measured in a frame from the recorded confocal time lapse video before flow was started, and at the end of the assay at 7.5 dyn/cm². Boxplots are shown with median, IQR, and whiskers from min to max.

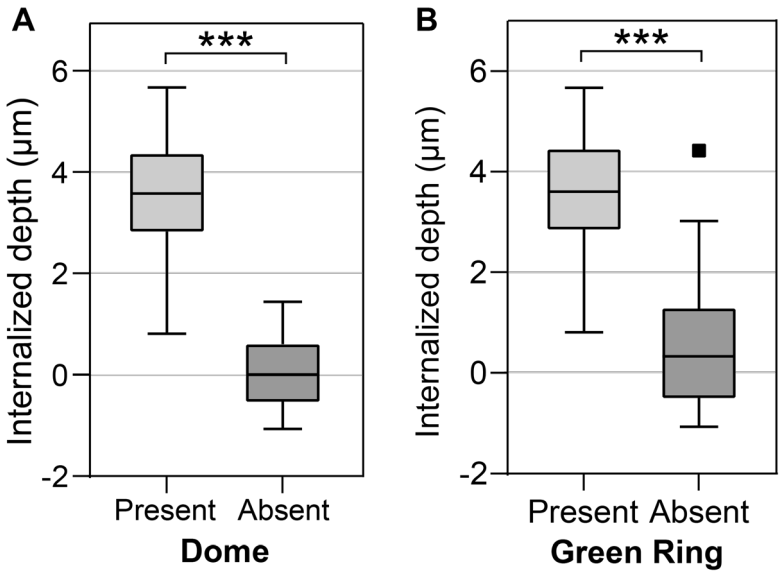

Supplemental Figure 8.2 Internalized depth of (**A**) bound targeted microbubbles with a dome present (N = 41) or absent (N = 20), and (**B**) bound targeted microbubbles with a green ring present (N = 37) or absent (N = 24) in the CellMask Green channel, shown as boxplot with outlier in black (square). Significance is indicated with ***p < 0.001.

9

Vancomycin-decorated microbubbles as a theranostic agent for Staphylococcus aureus biofilms

Joop J.P. Kouijzer, Kirby R. Lattwein, Inés Beekers, **Simone A.G. Langeveld**, Mariël Leon-Grooters, Jean-Marc Strub, Estefania Oliva, Gaëtan L.A. Mislin, Nico de Jong, Antonius F.W. van der Steen, Alexander L. Klibanov, Willem J.B. van Wamel, Klazina Kooiman

Based on:
International Journal of Pharmaceutics, Vol. 609, 2021 [508].

Abstract

Bacterial biofilms are a huge burden on our healthcare systems worldwide. The lack of specificity in diagnostic and treatment possibilities result in difficult-to-treat and persistent infections. The aim of this *in vitro* study was to investigate if microbubbles targeted specifically to bacteria in biofilms could be used both for diagnosis as well for sonobactericide treatment and demonstrate their theranostic potential for biofilm infection management. The antibiotic vancomycin was chemically coupled to the lipid shell of microbubbles and validated using mass spectrometry and high-axial resolution 4Pi confocal microscopy. Theranostic proof-of-principle was investigated by demonstrating the specific binding of vancomycin-decorated microbubbles (vMB) to statically and flow grown *Staphylococcus aureus* (*S. aureus*) biofilms under increasing shear stress flow conditions (0-12 dyn/cm^2), as well as confirmation of microbubble oscillation and biofilm disruption upon ultrasound exposure (2 MHz, 250 kPa, and 5,000 or 10,000 cycles) during flow shear stress of 5 dyn/cm^2 using time-lapse confocal microscopy combined with the Brandaris 128 ultra-high-speed camera. Vancomycin was successfully incorporated into the microbubble lipid shell. vMB bound significantly more often than control microbubbles to biofilms, also in the presence of free vancomycin (up to 1,000 µg/mL) and remained bound under increasing shear stress flow conditions (up to 12 dyn/cm^2). Upon ultrasound insonification biofilm area was reduced of up to 28%, as confirmed by confocal microscopy. Our results confirm the successful production of vMB and support their potential as a new theranostic tool for *S. aureus* biofilm infections by allowing for specific bacterial detection and biofilm disruption.

Keywords—Biofilm; Sonobactericide; Targeted microbubble; Theranostic; Ultrasound; Vancomycin

9.1 Introduction

Approximately 80% of all bacterial infections are associated with biofilms [542], where bacteria encase themselves in a protective matrix hindering antibiotic effectiveness up to 1,000-fold compared to free-floating (*i.e.*, planktonic) bacteria and facilitating development of antibiotic resistance [543, 544]. This increased resistance is largely due to the reduced metabolic activity of biofilm-embedded bacteria and the limited penetration of antibiotics throughout the biofilm [545-547]. These life-threatening infections are challenging to diagnose and treat, and are increasing in prevalence alongside the vulnerable aging population and surging use of implantable life-saving/enhancing technologies that create niches primed for colonization [548, 549]. Furthermore, biofilm infections are difficult to cure, often requiring high-risk, costly, invasive procedures and can still become persistent, necessitating lifelong

antibiotic use and/or repeated medical interventions. Biofilm infections can occur anywhere in all organ systems and can carry a high mortality rate depending on the location and infecting microbe. For example, infective endocarditis is an infection of the heart valves and/or endocardial surface with an in-hospital mortality of 18-47.5% [550, 551] and a 5-year mortality of 40-69% [552-555]. Delayed diagnosis of infective endocarditis is associated with increased mortality and early diagnosis of biofilm infection is therefore critical [552, 556, 557]. Currently there is no theranostic tool available in the clinic which combines the detection of biofilms with treatment possibilities. A novel theranostic agent to detect early biofilm formation with subsequent treatment possibilities would be a major breakthrough.

Microbubbles (1 – 10 μm in diameter) are ultrasound contrast agents that consist of an inert-gas core encapsulated by a protein, phospholipid, or biocompatible polymer shell [66, 400] and used in daily clinical practice for several decades to aid in the ultrasound diagnosis of cardiovascular diseases and cancer [66, 425, 558, 559]. Their therapeutic potential, however, has only begun being substantiated with clinical trials over the past years [226, 227, 282, 283]. Microbubbles respond volumetrically, *i.e.*, oscillate, to the increase and decrease of pressure from ultrasonic waves [66, 400], and it is these ultrasound-activated responses that enable them to be detected as well as induce various bioeffects for potential therapeutic applications. Promising pre-clinical investigations have only recently begun to determine if microbubble-mediated effects can be used to treat bacterial infections, which is referred to as sonobactericide [382]. Until now, biofilms both grown and then treated under flow with sonobactericide have yet to be investigated, which would be physiologically relevant for infections situated in flow environments.

Targeted microbubbles are microbubbles that have a ligand incorporated into their coating so they can specifically bind to biomarkers, and have been extensively studied for their theranostic potential in regards to mammalian cells [50]. Preclinically, targeted microbubble binding under flow conditions has been used for the diagnosis of atherosclerosis [560], while clinical studies have shown the potential of ultrasound molecular imaging of cancer [51, 386]. Treatment of different diseases was more effective with targeted than with non-targeted microbubbles in *in vitro* and *in vivo* studies [385, 425]. To the best of our knowledge, targeted microbubbles for biofilms have been investigated only once before, which was for the detection of *Staphylococcus aureus* (*S. aureus*) biofilms using a monoclonal immunoglobulin antibody to protein A (*S. aureus* bacterial cell wall surface protein) or a *Pseudomonas aeruginosa* lectin [561]. Although these microbubbles successfully bound to the biofilms, the clinical translation is poor because the antibody to protein A must compete with host antibodies that already bind to protein A for immune surveillance/clearance and the *P. aeruginosa* lectin causes red blood cell agglutination [562, 563].

The purpose of this proof-of-principle study was to develop a clinically translatable novel theranostic agent using vancomycin-decorated microbubbles (vMB) for the detection and treatment of clinically relevant bacteria-associated biofilms. The antibiotic vancomycin was chosen as the ligand for its 1) binding ability to the D-Ala-D-Ala moiety (K_D ~1-4 μM) present in most gram-positive bacterial cell walls [564], 2) potential for clinical application, and 3) possibility to covalently couple this compound without losing its functionality (Figure 9.1) [565]. Vancomycin was chemically coupled to the microbubble coating via the functionalized polyethylene-glycol (PEG) conjugated lipid (DSPE-PEG(3400)) and confirmed with matrix-assisted laser desorption/ionization - time-of-flight mass spectrometry (MALDI-TOF MS), thin-layer chromatography (TLC), and 4Pi microscopy imaging. To mimic physiological conditions, a biofilm flow model was grown and treated under physiological shear stress conditions using an Ibidi microchannel flow set-up. We investigated the capability of the vMB to remain bound to bacterial biofilms under static and shear stress conditions and evaluated their theranostic potential using confocal microscopy combined with ultra-high-speed imaging using the Brandaris 128.

9.2 Methods

9.2.1 Conjugation of vancomycin to phospholipid and incorporation in the microbubble shell

9.2.1.1 Vancomycin coupling to lipid DSPE-PEG(3400)-N-hydroxysuccinimide

Thirty milligrams of DSPE-PEG(3400)-*N*-hydroxysuccinimide (DSPE-PEG(3400)-NHS; Sunbright DSPE-034GS; NOF America Corporation, New York, USA or NOF Europe GmbH, Frankfurt am Main, Germany) was dissolved in 1280 μL dimethylsulfoxide (276855; Sigma-Aldrich, Saint. Louis, Missouri, USA) for a final concentration of 23.4 mg/mL. The covalent coupling of vancomycin to DSPE-PEG-NHS was performed as previously described for coupling of the cyclic RGD peptide [433], where the NHS ester of DSPE-PEG reacts with the primary amino group of the peptide. The reaction mixture was made by adding the DSPE-PEG(3400)-NHS solution to a 20% molar excess of vancomycin hydrochloride hydrate (V0045000, Sigma-Aldrich) in dimethylsulfoxide. A 2-fold molar excess of *N,N*-diisopropylethylamine (496219, Sigma-Aldrich) relative to the vancomycin hydrochloride hydrate was also added. The reaction mixture was incubated on a rocker (15 rpm, PTR-35, Grant Instruments Ltd, Shepreth, United Kingdom) overnight at room temperature. N-hydroxy succinimide, unreacted vancomycin, and byproducts were removed by dialysis (Spectra/Por 1 Dialysis Membrane 6-8 kD; Spectrum, New Jersey, USA) in 500 mL 0.9% saline solution (Baxter International Inc., Deerfield, Illinois, USA) at 4 °C for 24 h.

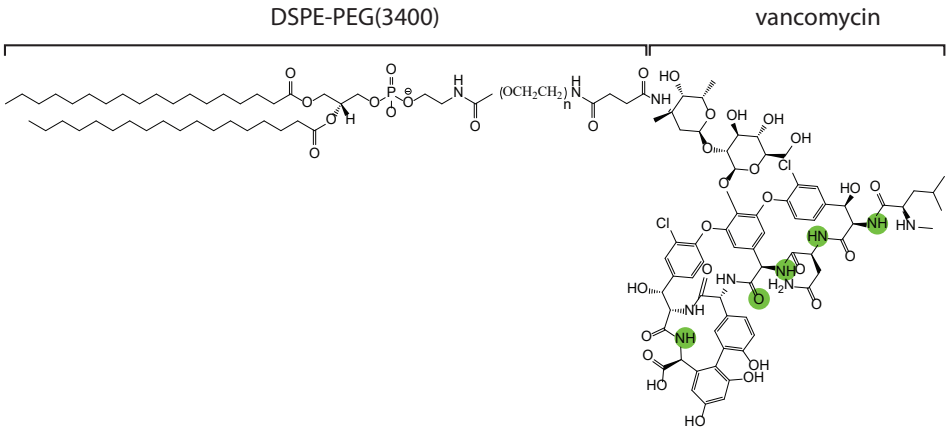

Figure 9.1 Molecular structure of the functionalized polyethylene-glycol (PEG) conjugated lipid (DSPE-PEG(3400)) coupled to the antibiotic molecule vancomycin. Green circles indicate where the vancomycin interacts with the D-Ala-D-Ala moiety present in gram-positive bacterial cell walls [566].

Then the saline solution was replaced with 4 °C demi water every 24 h for two days. On the fourth day of dialysis, the demi water was replaced twice with 4 h in between to reach the microSiemens value (Greisinger GMH 3431, Regenstauf, Germany) of demi water, *i.e.* 1-3 µS. The final product (Figure 9.1) was then freeze-dried (Alpha 1-2 LD plus; Martin Christ GmbH, Osterode am Harz, Germany) and stored at -20 °C. Depending on the supplier of the DSPE-PEG(3400)-NHS, the produced DSPE-PEG(3400)-vancomycin conjugate is referred to as 'lipid conjugate (batch USA)', *i.e.* made from the DSPE-PEG(3400)-NHS obtained from NOF America Corporation or 'lipid conjugate (batch EU)', *i.e.* made from DSPE-PEG(3400)-NHS obtained from NOF Europe.

9.2.1.2 Mass spectrometry

Electrospray ionization mass spectrometry experiments were performed on an Agilent Accurate Mass QToF 6520 quadrupole time-of-flight instrument (Agilent Technologies, Santa Clara, CA, USA) based on mass spectrometry analysis reported for similar compounds [567]. The electrospray ionization source was operated in the positive ionization mode using a capillary voltage of 4500 V and the following conditions: nebulizer nitrogen gas pressure, 10 psig; drying gas flow rate, 5 L/min; and drying temperature, 340 °C. The scan range was m/z 50–3200 at 1 s/scan. Data acquisition was performed using MassHunter Qualitative Analysis software (B.07.00, Agilent). Direct introduction conditions: samples were prepared at a concentration of 1 mg/mL (in chloroform for the DSPE-PEG(3400)-NHS, lipid conjugate (batch USA), and lipid conjugate (batch EU) and in water for vancomycin) and 1 µL was

injected. Injections were done using acetonitrile as the mobile phase with a flow rate of 0.1 mL/min. MALDI-TOF Mass measurements were carried out on an Autoflex MALDI-TOF mass spectrometer (Bruker Daltonics GmbH, Bremen, Germany). This instrument was used at a maximum accelerating potential of 20 kV in positive mode and was operated in linear mode. The delay extraction was fixed at 560 ns and the frequency of the laser (nitrogen 337 nm) was set at 5 Hz. The acquisition mass range was set to 2,000-8,000 m/z with a matrix suppression deflection (cut off) set to 1,500 m/z. The equipment was externally calibrated with the single charge and double ion of insulin. Each raw spectrum was opened with flexAnalysis 2.4 build 11 (Bruker Daltonics GmbH, Bremen, Germany) software and processed using the following parameters: Savitzky-Golay algorithm for smoothing (width 5 and cycles 2), and sum algorithm for peak detection and labelling. The matrix solution was prepared from a saturated solution of α-cyano-4-hydroxycinnamic acid in water/acetonitrile 50/50. The sample (less than 0.1 mg) was suspended in 1 mL of chloroform, and then 1 µL of the sample was added to 10 µL of saturated matrix solution. The mixture (1 µL) was loaded on the target and dried at room temperature.

9.2.1.3 Thin-layer chromatography

TLC sheets (TLC Silica gel 60 F254 Aluminum sheets; EMD Millipore Corporation, Burlington, Massachusetts, USA) were used as a stationary phase. A mixture of chloroform and methanol in a 9:1 vol/vol ratio was used as the mobile phase. DSPE-PEG(3400)-NHS and the lipid conjugate (batch USA and EU), were dissolved in chloroform to a concentration of 25 mg/mL and vancomycin was dissolved in methanol to a concentration of 25 mg/mL. Dissolved compounds were then spotted onto the TLC sheet using glass capillaries. Sheets were inspected for compounds under UV light (VL-6M, Vilber Lourmat, Collégien, France) after exposure to iodine vapors (207772; Thermo Fisher Scientific, Waltham, Massachusetts, USA).

9.2.1.4 Microbubble production

To produce vMB, 1,2-distearoyl-*sn*-glycero-3-phosphocholine (DSPC, 12.5 mg/mL, 86.4 mol%; Sigma-Aldrich), custom-made lipid conjugate (batch USA or EU) (4.35 mg dissolved as 2.9 mg/mL, 5.3 mol%), and PEG-40 stearate (12.5 mg/mL, 8.3 mol%; Sigma-Aldrich) were first dissolved in phosphate buffered saline (PBS; 14200083; Thermo Fisher Scientific) saturated with perfluorobutane (C_4F_{10}; 355-25-9, F2 Chemicals Ltd, Preston, Lancashire, UK) using a sonicator bath for 10 min. To fluorescently label the vMB coating, the lipid dye DiD (1,1'-dioctadecyl-3,3,3',3'-tetramethylindodicarbocyanine perchlorate; D307; Thermo Fisher Scientific) was added and mixed by probe sonication (Sonicator Ultrasonic Processor XL2020, Heat Systems, Farmingdale, New York, USA) at 20 kHz at power level 3 for 3 min. This

was followed by probe sonication for 60 s at power level 8 under continuous C_4F_{10} gas flow [397]. vMB were produced without the addition of lipid dye for ultrasound molecular imaging experiments and determining the vancomycin concentration on vMB. Microbubbles were stored in sealed 30 mL glass vials (DWK Life Sciences GmbH, Mainz, Germany) under C_4F_{10} atmosphere at 4 °C and used within three days. To produce non-targeted control microbubbles (cMB), the custom-made lipid conjugate was substituted for DSPE-PEG(3400) (2142-3400; Nanosoft Polymers, New York, USA). To fluorescently label the cMB coating, the lipid dye DiD or DiI (1,1'-Dioctadecyl-3,3,3',3'-Tetramethylindocarbocyanine Perchlorate; D282; Thermo Fisher Scientific) was added before probe sonication. Before experiments, microbubbles were washed three times with C_4F_{10}-saturated PBS by centrifugation at 400 *g* for 1 min (Heraeus Biofuge Primo, Waltham, Massachusetts, USA). The microbubble size distributions and concentrations were measured using a Coulter Counter Multisizer 3 (Beckman Coulter, Brea, California, USA). Particles (1-30 µm) were quantified using a 50 µm aperture tube. To determine the vancomycin loading efficiency of the vMB, 1970 µL out of a total of 3260 µL washed vMB (batch EU), were sonicated in a water bath for 10 min to destroy the microbubbles. This was followed by freeze-drying (Martin Christ GmbH) which yielded 23.24 mg of destroyed freeze-dried vMB. The destroyed freeze-dried vMB (4.65 and 3.83 mg) and corresponding lipid conjugate (batch EU; 0.79 and 0.48 mg) were dissolved in 50 µL and 350 µL Multi-Assay Manual Diluent (7D82P; Abbott Laboratories, Chicago, Illinois, USA), respectively. The obtained solutions were inserted in the Architect c4000 clinical chemistry analyzer (Abbott Laboratories) in combination with the Multigent vancomycin reagents kit (6E44-21; Abbott Laboratories) to obtain the vancomycin concentration. The vMB loading efficiency was defined by the following formula:

$$\text{Loading efficiency} = \frac{\text{vancomycin in 1 washed vMB batch}}{\text{vancomycin in 4.35 mg lipid conjugate}} \times 100\%$$

The amount of vancomycin molecules per µm^2 of microbubble shell was calculated by dividing the amount of vancomycin on the vMB by the surface of the vMB:

$$4\pi N \sum_{i=1}^{k} x_i r_i^2$$

where x_i is the number fraction, r_i the radius of that fraction, and k the number of bins (as determined with the Coulter Counter).

9.2.1.5 4Pi microscopy imaging

vMB (lipid conjugate batch EU) and DiI-containing cMB were incubated with anti-vancomycin IgG rabbit antibody coupled to a FITC-molecule (1 µg/1×10^8 MBs; LS-C540056; LifeSpan BioSciences, Seattle, Washington, USA) on ice for 30 min. To remove excess antibody, microbubbles were washed with C_4F_{10}-saturated PBS as

described above. Microbubbles were then placed in 87% glycerol (vol/vol in PBS) to reduce Brownian motion. *Y*-stacked *xz*-scans were acquired using a Leica TCS 4Pi confocal laser-scanning microscope with two aligned opposing objectives for high axial resolution (90 nm step size, 100× glycerol HCX PL APO objective lens, numerical aperture 1.35). The FITC antibody was excited using a 488 nm laser and detected at 500-550 nm. For lipid shell visualization, DiI and DiD were excited with a 561 nm laser and detected at 580-640 nm and 647-703 nm, respectively. The 'voltex' function in AMIRA software (Version 2020.1, FEI, Mérignac Cedex, France) was used for rendering volume projections of the acquired *y*-stacked *xz*-scans.

9.2.2 Biofilm formation

9.2.2.1 Static biofilm formation

An infective endocarditis patient-derived *S. aureus* bacterial strain, associated with cardiovascular infections (ST398), was used for this study. This strain was collected by the department of Medical Microbiology and Infectious Diseases, Erasmus MC University Medical Center Rotterdam, the Netherlands, and anonymized and de-identified according to institutional policy. Frozen stock samples were streaked onto tryptic soy agar containing 5% sheep blood (BD, Trypticase, Thermo Fisher Scientific) and allowed to grow overnight at 37 °C. Bacterial colonies were suspended in Iscove's Modified Dulbecco's Media (IMDM; Gibco, Thermo Fisher Scientific) until an optical density of 0.5 (± 0.05) was reached at 600 nm (Ultraspec 10, Amersham Biosciences, Little Chalfont, United Kingdom) corresponding to 1×10^8 colony forming units per mL (CFU/mL). IbiTreat polymer µ-Slides (80196; 0.8 mm channel height; I Luer; Ibidi GmbH, Gräfelfing, Germany) were inoculated with 200 µL of diluted bacterial suspension consisting of 1×10^4 CFU/mL. The IbiTreat µ-Slide in- and outlet-reservoirs were filled with 60 µL of IMDM. Slides were then incubated at 37 °C for 24 h in a humidified incubator under constant agitation (150 rpm; Rotamax 120, Heidolph Instruments, Schwabach, Germany).

9.2.2.2 Biofilm formation under flow

IbiTreat µ-Slides were incubated with 320 µL of type O human plasma (citrate phosphate double dextrose as an anti-coagulant; pooled from five donors to minimize donor variability; Sanquin, Rotterdam, the Netherlands) to aid bacterial attachment under flow. After incubation at 37 °C for 24 h in a humidified incubator, plasma was removed and the slides were rinsed three times with 200 µL 0.9% saline solution (Baxter International). Then, an IMDM diluted *S. aureus* bacterial suspension of 200 µL containing 1×10^6 CFU/mL was pipetted into the slide. Bacteria were allowed to attach to the surface of the µ-Slide for 3 h at 37 °C and then the µ-Slide was

connected to an Ibidi fluidic unit using corresponding perfusion sets (Perfusion set red, 10962; Ibidi) and a computer-controlled air pressure pump (Ibidi pump system; Ibidi). In order to later on inject microbubbles and dyes, an in-line Luer injection port (10820; Ibidi) was placed in the perfusion set 3.5 cm before the µ-Slide inlet. Biofilms were grown under laminar flow at 5 dyn/cm^2 (14.4 mL/min, corresponding to a Reynolds number of 32) for 24 h at 37 °C.

9.2.3 Experimental set-up

The µ-Slides were inserted into a custom-built water tank, that was maintained at 37 °C and situated underneath a custom-built Nikon A1R+ confocal microscope [431] (Nikon Instruments, Amsterdam, the Netherlands) (Figure 9.2A, C). The orientation of the µ-Slide was either upright (Figure 9.2A-B) or flipped 180° (Figure 9.2C-D) depending on the experiment performed. The transducer (2.25 MHz center frequency used at 2 MHz; 76.2 mm focal length; -6 dB beam width of 3 mm at 2 MHz; V305;

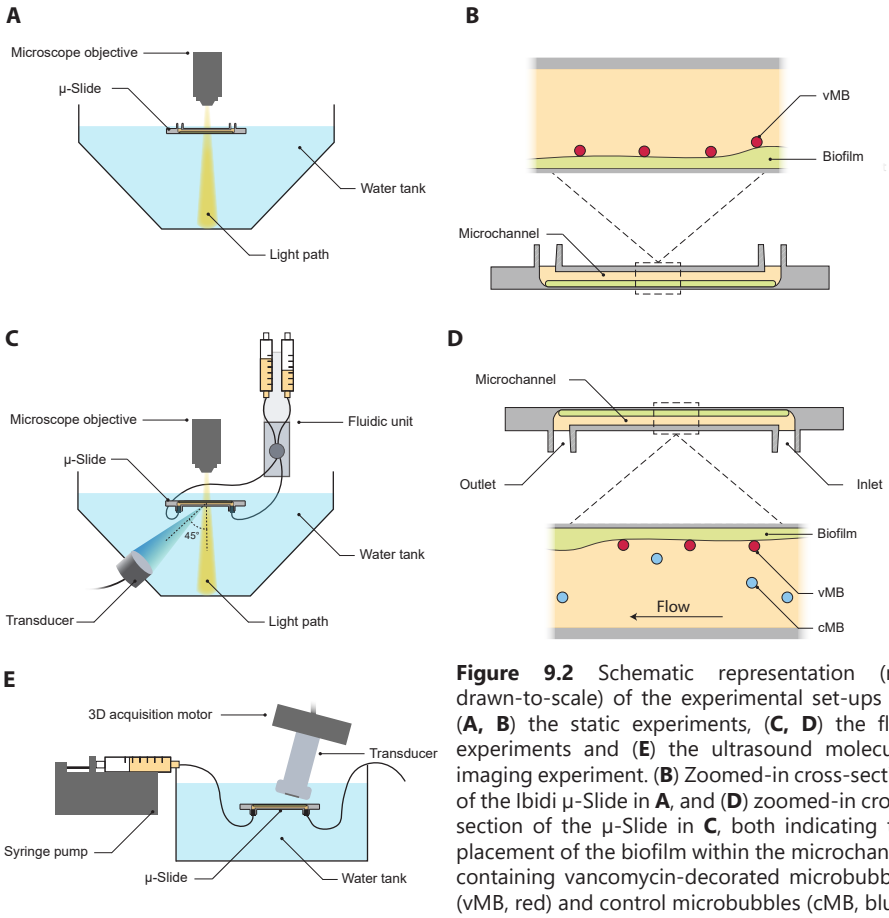

Figure 9.2 Schematic representation (not drawn-to-scale) of the experimental set-ups for (**A, B**) the static experiments, (**C, D**) the flow experiments and (**E**) the ultrasound molecular imaging experiment. (**B**) Zoomed-in cross-section of the Ibidi µ-Slide in **A**, and (**D**) zoomed-in cross-section of the µ-Slide in **C**, both indicating the placement of the biofilm within the microchannel containing vancomycin-decorated microbubbles (vMB, red) and control microbubbles (cMB, blue).

Panametrics-NDT, Olympus, Waltham, MA, USA) was placed underneath the sample at a 45° angle to minimize ultrasound reflection and standing wave formation. Both the optical and ultrasound foci were aligned using a pulse-echo approach and a needle tip located at the optical focal plane [440], hereby the microbubbles and biofilm could both be simultaneously imaged and insonified. An arbitrary waveform generator (33220A; Agilent), in combination with a broadband amplifier (ENI A-500; Electronics & Innovation, Rochester, NY, USA), was connected to the transducer. The transducer output was calibrated in a separate experiment using a needle hydrophone (1 mm diameter; PA2293; Precision Acoustics, Dorchester, UK). As a live/dead staining, SYTO 9 (S34854; Thermo Fisher Scientific) was excited at 488 nm and detected at 525/50 nm (center wavelength/bandwidth) and propidium iodide (PI; P4864-10ML; Sigma-Aldrich) was excited at 561 nm and detected at 595/50 nm. For experiments with DiI incorporated into the cMB, the 561 nm laser with the same detection was also used for optical imaging. A third channel was used for the visualization of DiD incorporated into vMB or cMB with an excitation at 640 nm and fluorescence detected at 700/75 nm.

9.2.4 Binding of targetd microbubbles to bacteria in biofilms

9.2.4.1 Competitive microbubble binding assay

To study the competitive binding of vMB (lipid conjugate batch USA and EU), statically grown biofilms were pre-incubated at room temperature for 5 min with vancomycin concentrations of 0, 10, 20, 100 or 1,000 µg/mL dissolved in IMDM. This includes the maximal recommended clinical blood level concentration of vancomycin, *i.e.* 20 µg/mL [568, 569]. A final vancomycin concentration of 0 or 1,000 µg/mL was used in the µ-Slides for cMB. After this, the dyes (0.4 µL of 5 mM SYTO 9, 5 µL of 1.5 mM PI) and fluorescent DiD microbubbles (7.0×105 vMB or cMB) were added to IMDM containing the same pre-incubation vancomycin concentration to a total of 200 µL, which was then added to the µ-Slide replacing the pre-incubation. Slides were flipped 180° for 5 min to allow the microbubbles to float up towards the biofilm for binding at room temperature and then flipped back to their original position, such that any unbound microbubbles would rise to the top of the channel (Figure 9.2B). For each vancomycin concentration, the binding assay was performed in at least three µ-slide. Slides were systematically imaged with a 100× water-dipping objective (CFI Plan 100XC W, Nikon Instruments) of which each field-of-view consisted of 512 × 512 pixels (128 × 128 µm). Locations within the slide were named 1 to 5 and were equally spaced apart, with 1 representing the field-of view nearest to the inlet and 5 nearest to the outlet. The number of microbubbles attached to bacterial biofilms was manually determined using Fiji software for 20 different fields-of-view

(5 locations distributed over the length of the microchannel, with 4 equally spaced fields-of-view per location) distributed over each µ-Slide.

9.2.4.2 Non-specific microbubble binding assay

For assessment of non-specific binding of microbubbles, µ-Slides with and without statically grown biofilms were treated similarly. µ-Slides without biofilm were filled with 200 µL IMDM and in- and outlet-reservoirs with 60 µL of IMDM. Slides were then incubated at 37 °C for 24 h in a humidified incubator under constant agitation (150 rpm). Before the binding assay, all µ-Slides were first rinsed by adding 200 µL IMDM to the inlet and removing 200 µL IMDM from the outlet. After 5 min, 200 µL IMDM containing the dyes (0.4 µL of 5 mM SYTO 9, 5 µL of 1.5 mM PI), 7.0×10^5 fluorescent microbubbles (vMB lipid conjugate batch EU), and either 0, 0.1, or 1% of bovine serum albumin (BSA; A9418-50G; Sigma-Aldrich) [426, 451] or casein (37582; Thermo Fisher Scientific) [570] was added to the microchannel. µ-Slides were then flipped 180° for 5 min to allow the microbubbles to float up towards the bottom of the microchannel for binding and then flipped back to their original position. Three binding assays were performed for each condition. µ-Slides were systematically imaged with the 100× objective (for specifics see *Section 9.2.4.1*). The number of vMB attached to the bottom and top of the microchannel was manually determined using Fiji software in 40 different field-of-view distributed over the µ-Slide, divided in 20 fields-of-view located at the bottom and 20 fields-of view located at the top of the microchannel. The binding efficiency was defined by the following formula:

$$\text{Binding efficiency} = \frac{\text{Sum amount MBs bottom}}{\text{Total amount MBs bottom and top}} \times 100\%$$

9.2.4.3 Microbubble binding under increasing shear stress

To exclude differences in results due to biofilm heterogeneity and possible variable biofilm erosion under flow conditions, vMB (lipid conjugate batch EU) and DiI-containig cMB were simultaneously added at a ratio of 1:1 to biofilms grown under flow at 5 dyn/cm^2. A solution of 200 µL IMDM containing 0.4 µL of 5 mM SYTO 9 and 1.2×10^7 microbubbles was injected into the in-line Luer injection port with a 1 mL Luer Solo syringe (Omnifix-F, B Braun, Melsungen, Germany) and 19G needle (Sterican, B Braun) while the flow was turned off and the Ibidi µ-Slide was oriented upside down (Figure 9.2D). To introduce microbubbles and SYTO 9 into the microchannel, a shear stress of 1.3 dyn/cm^2 (3.74 mL/min) was applied for 17 s. The vMB and cMB were then incubated with the biofilm for 5 min without flow. Flow was started and increased every 60 s, with an initial shear stress increase of 0.5 dyn/cm^2 (1.43 mL/min), from 1.5 (4.33 mL/min) to 2 dyn/cm^2 (5.76 mL/min),

and then each subsequent step was increased by 1 dyn/cm^2 (~2.87 mL/min) until 12 dyn/cm^2 (34.53 mL/min, Reynolds number: 74.2) was achieved. The number of microbubbles remaining attached to the biofilm while applying increasing flows was monitored with confocal time-lapse microscopy (0.77 frames per second (fps)) using a 60× water-immersion objective (Plan Apo 60XA WI, Nikon Instruments) of which each field-of-view consisted of 512 × 512 pixels (210 × 210 µm). The binding percentage was defined by the following formula:

$$\text{Binding percentage} = \frac{\text{MBs bound after 60 s shear stress}}{\text{Total amount MBs before flow}} \times 100\%$$

9.2.5 Sonobactericide with vancomycin-decorated microbubbles

9.2.5.1 Sonobactericide therapy

To biofilms grown under flow at 5 dyn/cm^2, a solution of 200 µL containing 0.4 µL of 5 mM SYTO 9, 5 µL of 1.5 mM PI and 1.2×10^7 vMB (lipid conjugate batch EU) in IMDM was added into the in-line Luer injection port as described above. After this, a continuous laminar flow of 5 dyn/cm^2 was applied to the biofilm. For sonobactericide therapy, the clinically used transthoracic echocardiography frequency of 2 MHz was chosen [571]. Biofilms were insonified with ultrasound after a minimum of 50 s of continuous flow exposure. A single 5,000- or 10,000-cycle burst at 250 kPa peak negative pressure was given, resulting in a treatment time of 2.5 or 5 ms. For the ultrasound only control, a single 10,000-cycle burst at 250 kPa peak negative pressure was given. The spatial peak intensity (I_{SP}) was calculated by using the formula: $I_{SP} = P^2/2\rho c$ [572, 573] where P denotes the peak pressure, ρ denotes the density and c the speed of sound, resulting in an I_{SP} of 2.06 W/cm^2. All experiments were monitored for bacterial and vMB responses with time-lapse confocal microscopy (0.77 fps) using the 60×objective (for specifics see *Section 9.2.4.3*).

The biofilm reduction was quantified based on the SYTO 9 signal using a custom-built image analysis code in MATLAB (The MathWorks, Natick, MA, USA). The area without biofilm was determined in a frame before and within 15 s after ultrasound insonification, both selected based on minimal signal variability due to focus drift. Images were first converted to binary by thresholding at 300 (image intensity ranging from 0-4095). Next, all connected components were identified through the *bwconncomp* function in MATLAB. All connected components with an area larger than 200 pixels (33.5 µm^2) were classified as areas without biofilm and normalized to the size of the field-of-view (512×512 pixels; 210 × 210 µm). The biofilm reduction was defined as the change in normalized area without biofilm before and after ultrasound insonification.

9.2.5.2 Brandaris 128 ultra-high-speed recordings

To resolve the oscillation behavior of the vMB (lipid conjugate batch EU) while bound to the bacterial biofilm under flow at 5 dyn/cm^2 upon ultrasound exposure, the Brandaris 128 ultra-high-speed camera was used as previously described [431]. Briefly, the Brandaris 128 was coupled to the custom-built Nikon A1R+ confocal microscope, which made it possible to visualize both the microbubble behavior on a microsecond time-scale and sonobactericide treatment effect after ultrasound exposure with high resolution confocal microscopy. Time-lapse confocal imaging using the 100× objective (for specifics see *Section 9.2.4.1*) started during continuous flow (5 dyn/cm^2), capturing first the initial state of the biofilm and bound vMB. For the Brandaris 128 ultra-high-speed camera recording, the light path was automatically switched from the confocal scan head to the Brandaris 128 and was defined as t = 0 s. During ultrasound exposure (2 MHz, 250 kPa, 5,000 cycles), the first ~14 microbubble oscillations were recorded in 128 frames at a framerate of 14.9 million fps. The microbubble diameter as a function of time was subtracted from the Brandaris 128 recording using custom-designed software [44]. After obtaining all 128 frames, the light path was automatically switched back to the original position to continue confocal time-lapse imaging. The biofilm reduction was quantified as described above with the exception that 544 pixels were taken for all connected components with an area larger than 33.5 μm^2 to account for the difference in magnification.

9.2.6 Ultrasound molecular imaging

A high frequency pre-clinical scanner (Vevo 3100, FUJIFILM VisualSonics, Toronto, Canada) was used in combination with an ultra-high frequency linear array transducer (MX250, FUJIFILM VisualSonics) operated at 18 MHz to visualize vMB bound to the biofilm. Biofilms were grown under flow at 5 dyn/cm^2 as described under *Section 9.2.2.2*, with the exception that the perfusion set was modified with the addition of an *y*-style splitter (1.6 mm, 10828; Ibidi) placed 11.5 cm from the inlet of the μ-Slide. To the *y*-style splitter, 20 cm of additional biocompatible silicone tubing (1.6mm; 10828; Ibidi) was attached which was clamped off during biofilm growth using a hose clip (10821; Ibidi). For the experiment, the flow by the Ibidi pump system was stopped and the perfusion set clamped just after the additional *y*-style splitter. Then, the tubing was cut just under the original *y*-style splitters on both sides of the perfusion set, the additional tubing unclamped, and attached to a syringe pump (Pump 11 Elite, Harvard Apparatus, Holliston, Massachusetts, USA) so that injected fluid and vMB passed the biofilm only once (Figure 9.2E). A solution of 200 μL IMDM containing 1.2×10^7 vMB (lipid conjugate batch EU) and 1% BSA was added into the in-line Luer injection port as described under *Section 9.2.4.3*. After

5 min of incubation, a shear stress of 1.5 dyn/cm^2 was applied for 60 s to remove unbound vMB from the biofilm. The transducer was operated in a 7° angle at 10% transmit power, medium beamwidth and 40 dB dynamic range and manipulated using a 3D acquisition motor (FUJIFILM VisualSonics) with a step size of 0.04 mm. Burst mode was used 1, 5 and 10 times to locally destroy vMB. B-mode and non-linear contrast mode were used to acquire images. Vevo LAB software was used to determine the mean contrast power and for rendering volume projections of 6.52 mm non-linear contrast scans.

9.2.7 Statistical analysis

All data were statistically analyzed using IBM SPSS Statistics 27 (IBM Corporation, Armonk, New York, USA), and a *p*-value of < 0.05 was used as the significance level. Data distribution was assessed using the Shapiro-Wilk test. The data on the microbubble size distribution, competitive microbubble binding assay, stability and microbubble binding under increasing shear stress was not normally distributed and was compared by performing a Mann-Whitney U test. To further analyze the competitive microbubble binding assay data, the Spearman's rank-order correlation was evaluated in MATLAB. The sonobactericide therapy data was not normally distributed and the robust test of equality of means showed to be significant, so a Welch's t-test was performed instead. Normally distributed data of the non-specific vMB binding assay was compared using an unpaired t-test or one-way ANOVA with post-hoc Tukey HSD test for multiple groups.

9.3 Results

9.3.1 Conjugation of vancomycin to phospholipid and incorporation in the microbubble shell

The freeze-dried product obtained after dialysis was analyzed by mass spectrometry in order to assess the formation of the expected DSPE-PEG(3400)-vancomycin conjugate. Electrospray experiments were performed on the freeze-dried product containing both the lipid and the expected lipid conjugate. The multiplicity of PEG units in the lipid and the presence of the chlorine isotopes in vancomycin led to intricated spectra where the average molecular weight (MW) determination of the conjugate was not possible. According to MALDI-TOF experiments, the starting lipid was found to have a MW of ~4,260 (Figure 9.3A). The presence of the starting lipid and a second compound with an average MW of 5,691, matching with the expected conjugate of ~5,700, was confirmed for the freeze-dried product (Figure 9.3B). Successful conjugation between the DSPE-PEG(3400)-NHS and vancomycin was further confirmed by TLC (Supplemental Figure 9.1).

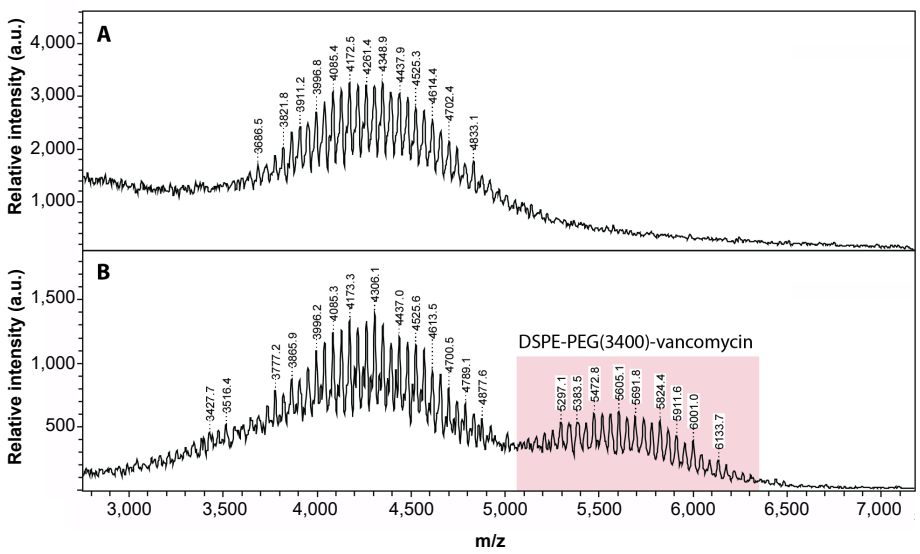

Figure 9.3 Matrix-assisted laser desorption/ionization - time-of-flight mass spectra of (**A**) DSPE-PEG(3400) and (**B**) the freeze-dried product after dialysis with the red shaded region confirming the vancomycin coupled to the polyethylene-glycol (PEG) lipid.

The number weighted mean diameter of the vMB produced with the lipid conjugate batch USA or lipid batch conjugate EU did not show a significant difference between batches (p = 0.737). When comparing the number weighted diameter of vMB (median: 3.97, interquartile range: 0.52) to cMB diameter (median: 3.83, interquartile range: 0.58) (Figure 9.4A), no significant difference was found (p = 0.604). The number weighted diameter of vMB does not indicate changes in microbubble size over the three-day period in which the experiments were performed. Figure 9.4B shows similar polydisperse microbubble size distributions for vMB and cMB.

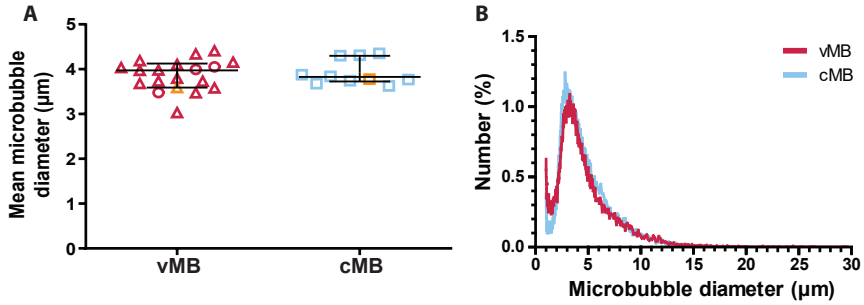

Figure 9.4 Microbubble number-weighted mean diameter and size distribution. (**A**) The mean diameter of vancomycin-decorated microbubbles (vMB, red, N = 19 batches) and control microbubbles (cMB, blue, N = 10 batches) used in all experiments. The vMB were produced with either lipid conjugate batch USA (red circles) or lipid conjugate batch EU (red triangles). The median and interquartile range are overlaid. Orange-colored symbols indicate the MB batches corresponding to those represented in B. (**B**) Representative size distribution of vMB and cMB batches.

Incubation of vMB with a FITC-labeled anti-vancomycin antibody confirmed the presence of vancomycin as a ligand on the phospholipid coating using high-axial resolution 4Pi confocal microscopy. The patch-like FITC-signal within the three-dimensional reconstruction of the vMB, as seen in Figure 9.5A, indicates that vancomycin is heterogeneously distributed over the vMB coating. The corresponding 4Pi confocal microscopy recording is shown in Video 9.1. The absence of any FITC-signal in the cMB (Figure 9.5D) shows that there was no non-specific binding of the FITC-labeled anti-vancomycin antibody to the other phospholipid components. The corresponding 4Pi confocal microscopy recording is shown in Video 9.2. The destroyed freeze-dried vMB samples contained 3.23 and 2.69 µg/mL of vancomycin, corresponding to an average of 0.035 µg of vancomycin per mg of destroyed freeze-dried vMB. The lipid conjugate samples contained 87.46 and 60.43 µg/mL vancomycin, corresponding to an average of 41.41 µg vancomycin per mg of lipid conjugate. The average vancomycin loading efficiency was calculated to be 0.71%. The average number of vancomycin molecules per μm^2 of microbubble shell was calculated to be 5358 (5285 and 5431 molecules).

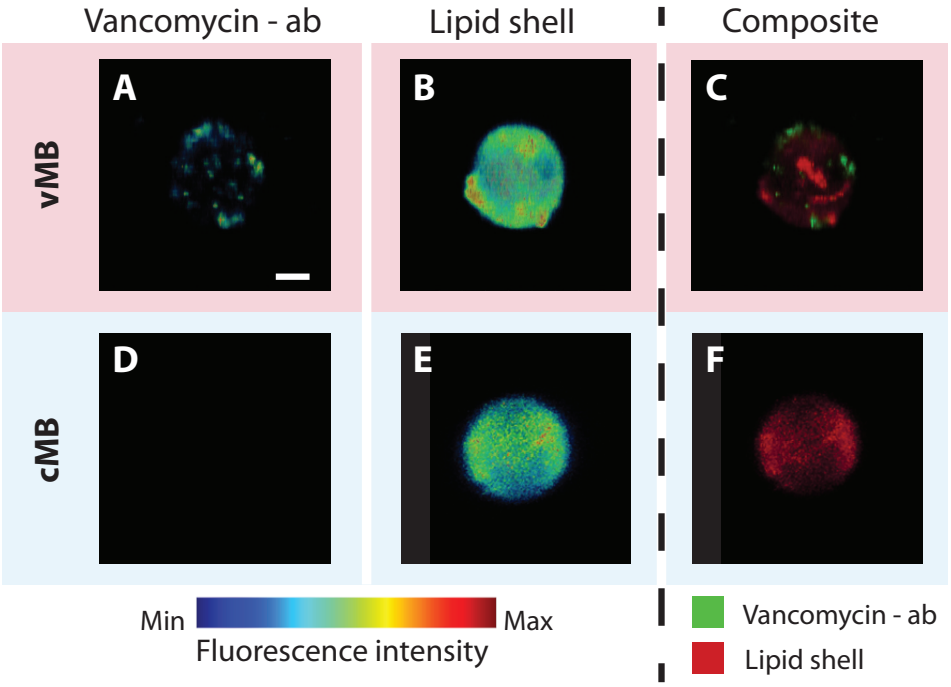

Figure 9.5 Representative 3D reconstructions of high-axial resolution 4Pi confocal microscopy *y*-stacks of (**A-C**) a vancomycin-decorated microbubble (vMB, diameter = 4.2 µm) and (**D-F**) a control microbubble (cMB, diameter = 4.3 µm). (**A, D**) Fluorescence intensity images of the FITC-labeled anti-vancomycin antibody (vancomycin-ab) and (**B, E**) the phospholipid shells with the lipid dye DiD for vMB and DiI for cMB. (**C, F**) The composite image of the fluorescence emitted by the FITC-labeled anti-vancomycin antibody (green) and lipid dye (red). Scale bar is 1 µm and applies to all images.

9.3.2 Binding of targeted microbubbles to bacteria in biofilms

The ability of vMB and cMB to bind to statically grown biofilms was assessed with a competitive microbubble binding assay (Figure 9.6). Significantly more vMB were found at the bacterial biofilms compared to cMB, regardless of the concentration of free vancomycin present. For vMB, increasing the concentration of free vancomycin up to 20 µg/mL prior to the incubation with vMB did not result in a significant decrease in the amount of bound vMB. Only the preincubation of biofilms with a free vancomycin concentration greatly exceeding the maximal clinical dose of 20 µg/mL, namely 100 and 1,000 µg/mL, reduced the number of bound vMB (respectively, $p = 0.02$ and $p < 0.001$). No significant difference ($p = 0.74$) was found between the binding of vMB produced with either the USA or EU lipid conjugate batch. There was no significant difference ($p = 0.065$) between the number of cMB after preincubating without or with 1,000 µg/mL of vancomycin. Furthermore, using the same data as in Figure 9.6 the number of vMB and cMB was found to be unaffected by the location within the µ-Slides (Supplemental Figure 9.2). At most a moderate negative correlation (*i.e.* number of microbubbles moderately decreases

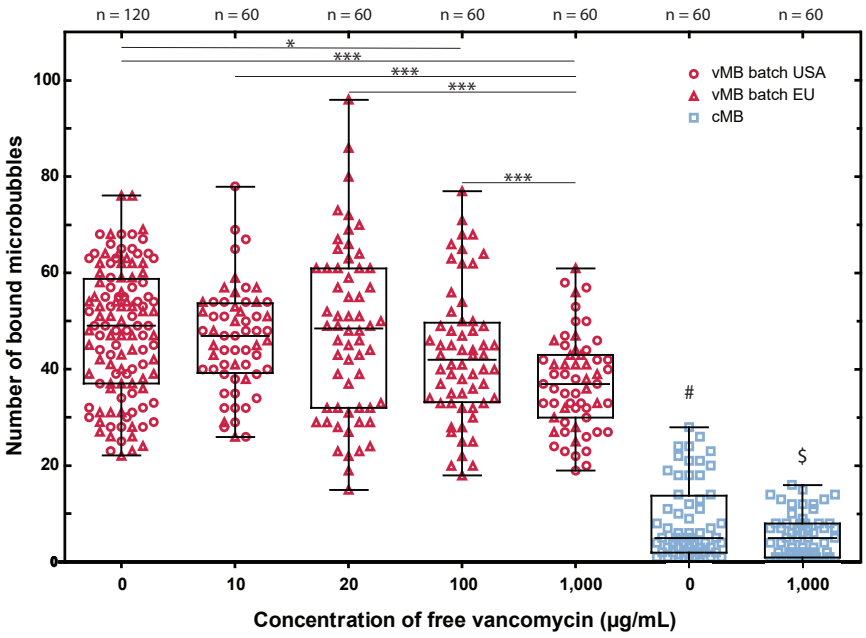

Figure 9.6 The number of bound vancomycin-decorated (vMB, red symbols) and control (cMB, blue squares) for varying concentrations of free vancomycin with statically grown biofilms. The vMB were produced with either lipid conjugate batch USA (red circles) or batch EU (red triangles). Each symbol represents the number of microbubbles counted in one field-of-view. The overlaid boxplots show the median, interquartile range, and the minimum to maximum values. Statistical significance for vMB is indicated with *$p < 0.05$, and ***$p < 0.001$ when comparing different free vancomycin concentrations, #($p < 0.001$) when comparing cMB without free vancomycin to all vMB conditions, and $($p < 0.001$) when comparing cMB with 1,000 µg/mL free vancomycin to all vMB conditions.

as the distance from the inlet increases) was observed for two conditions, both with vMB, with a free vancomycin concentration of 10 µg/mL (r = −0.53, p < 0.001) and 1,000 µg/mL (r = −0.54, p < 0.001). All other conditions had coefficient values less than 0.4 (r values ranging from -0.33 to 0.13), which indicate little to no relationship between the two variables. The stability of the vMB did not decrease during the three-day period the microbubbles were used for experiments (Supplemental Figure 9.3). On day 3 there was even a slight but significant increase in the number of bound vMB (p <0.05).

cMB showed negligible non-specific binding to the µ-Slides without biofilm. Figure 9.7 shows that the percentage of vMB bound to the µ-Slide without biofilm was approximately two-thirds of the percentage of vMB bound to biofilms. When 0.1% BSA was added, the percentage of vMB bound to the µ-Slide without biofilm significantly (p < 0.05) dropped while no significant changes (p = 0.51) were observed for the vMB bound to biofilms. When the BSA concentration was increased to 1%, the same trend was visible; a significant decrease of the percentage of vMB bound to the µ-Slide without biofilm (p < 0.05) and no significant differences (p = 0.13) for the percentage of vMB bound to the biofilm. Similar results were obtained when BSA was substituted for casein (Supplemental Figure 9.4).

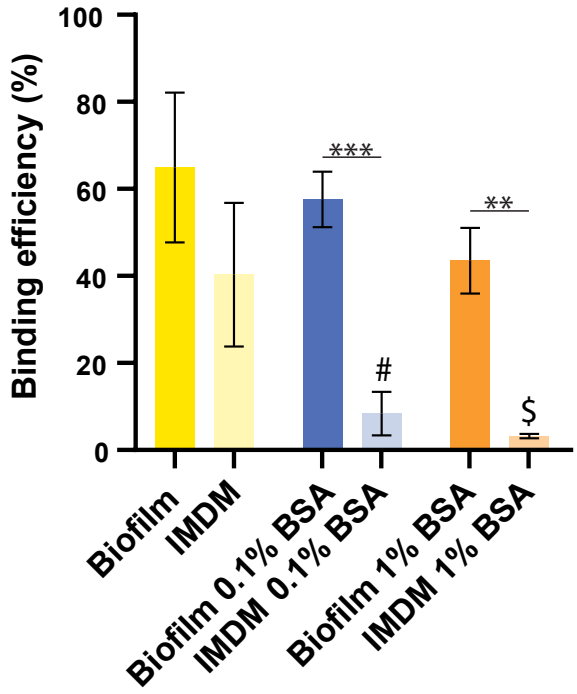

Figure 9.7 Non-specific binding of vancomycin-decorated microbubbles. Ibidi µ-Slides with and without statically grown biofilms in IMDM were incubated with either 0 %, 0.1 % or 1% bovine serum albumin (BSA) to bind to non-specific binding sites. Each bar represents the mean binding efficiency percentage with standard deviation overlaid of N = 3. Statistical significance is indicated with **p < 0.01, ***p < 0.001, #(p < 0.05) between IMDM 0.1% BSA and all other conditions except for IMDM 1% BSA, and \$(p < 0.05) between IMDM 1% BSA and all other conditions except for IMDM 0.1% BSA.

To determine the number of microbubbles that remained bound under flow, the vMB and cMB were distinguished by the different lipid dyes incorporated into their coating as shown in Figure 9.8B, E and C, F, respectively. The average number of vMB present before flow was 51 ± 37 and for cMB 61 ± 44 (mean ± SD; *N* = 8) per field-of-view, and the ratio of vMB/cMB was 0.87 ± 0.16. Time-lapse imaging while flow shear stress increased from 1.5 to 12 dyn/cm^2 was performed to distinguish bound from unbound microbubbles and revealed that vMB had a significantly higher binding percentage in comparison to cMB at all shear stress values, except from 7 to 9 dyn/cm^2 (Figure 9.8G). The biofilm remained attached to the microchannel throughout the duration of flow binding experiments (Figure 9.8A,D).

9.3.3 Sonobactericide with vancomycin-decorated microbubbles

Biofilms grown under flow had a field-of-view coverage of 89.7 ± 10.7% (mean ± SD) (*N* = 22 fields-of-view in 11 different µ-Slides). A typical example of a biofilm treated with sonobactericide using vMB is shown in Figure 9.9, where five vMB (diameter ranging from 2.0 to 4.5 µm) remained attached to the biofilm under flow (5 dyn/cm^2) before ultrasound treatment (Figure 9.9A). Upon ultrasound insonification using 5,000 cycles, all vMB displaced from the field-of-view resulting in a 24.0% reduction in biofilm area localized along the microbubble displacement trajectories (Figure 9.9B). The corresponding confocal microscopy recording is shown in Video 9.3. Overall, biofilms (*N* = 7) treated with vMB and a single ultrasound burst of 5,000 cycles resulted in a median reduction of 19.6% (interquartile range 11.5%; Figure 9.9C). When

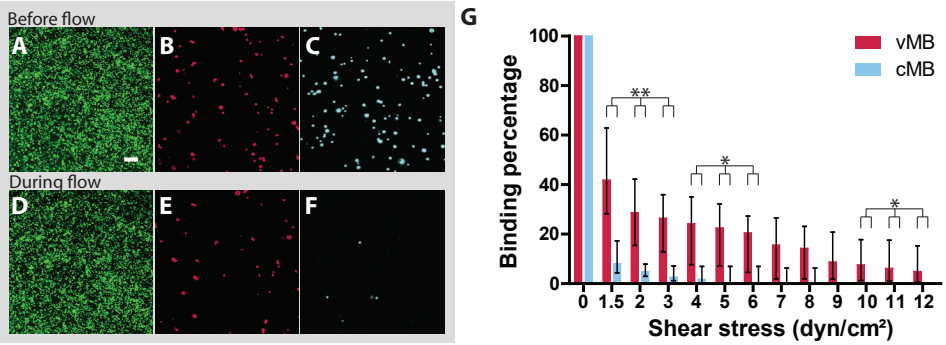

Figure 9.8 Percentage of microbubbles that remained bound upon increasing shear stress with flow grown biofilms. Confocal microscopy images of (**A-C**) the initial state before flow and (**D-F**) after 60 s of 1.5 dyn/cm^2 shear stress flow. Both sets of images are the same biofilm with (**A, D**) bacteria stained with SYTO 9 (green), (**B, E**) vancomycin-decorated microbubbles (vMB) stained with DiD (red), and (**C, F**) control microbubbles (cMB) stained with DiI (blue). Scale bar is 20 µm and applies to all confocal images. (**G**) Bars represent median percentage with interquartile range of microbubbles in the field-of-view remaining bound to the bacterial biofilm during increasing shear stress (*N* = 8). Statistical significance between bound vMB percentage and bound cMB percentage is indicated with *p < 0.05 or **p < 0.01.

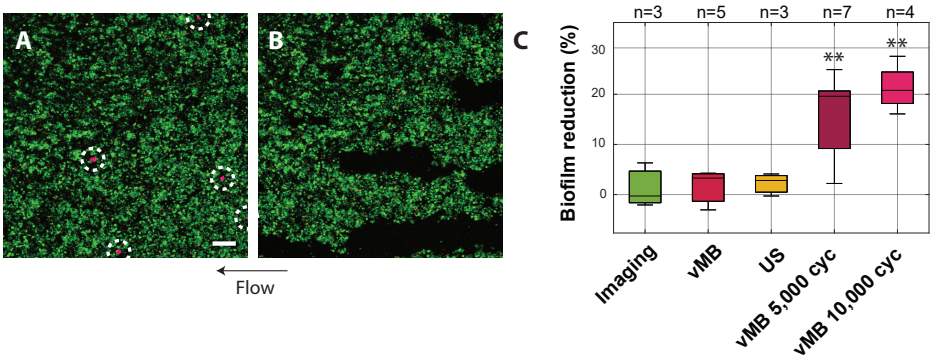

Figure 9.9 Biofilms treated under flow at 5 dyn/cm^2 with vancomycin-decorated microbubbles (vMB) and ultrasound. Confocal microscopy images of (**A**) before and (**B**) after sonobactericide treatment (2 MHz, 250 kPa, 5,000 cycles. Live bacteria were stained with SYTO 9 (green), dead bacteria with propidium iodide (orange), and vMB with DiD (red; indicated by white dashed circles). Scale bar is 20 µm and applies to all confocal images. (**C**) Percentage of biofilm reduction upon treatment. Boxplots show the median, interquartile range, and the minimum to maximum values. The ultrasound (US) setting of 2 MHz, 250 kPa, 10,000 cycles was used for US alone. Statistical significances between vMB in combination with US and the control treatment groups are indicated with $^{**}p < 0.01$; cyc = cycles.

vMB were exposed to 10,000 cycles, a more consistent biofilm reduction amount was observed, with the highest being 27.6% and a median of 20.8% (interquartile range 6.3%; $N = 4$; Figure 9.9C), albeit not significantly different from 5,000 cycles. No noticeable increase in PI positive cells was observed following all treatments. Both ultrasound settings in combination with vMB resulted in significantly higher biofilm area reduction than any of the control treatments (imaging under flow only, vMB only, and ultrasound only). Similar low percentages (< 6.3%) of biofilm area reduction were obtained for all control treatments partly due to focus drift during the confocal microscopy recordings and biofilm erosion.

To visualize the effect of the sonobactericide treatment on a microsecond time scale, Brandaris 128 ultra-high-speed camera recording was combined with time-lapse confocal microscopy. Figure 9.10A shows an example of a selected confocal microscopy frame of a biofilm with two vMB (diameter 6.3 µm and 4.3 µm) attached under flow before ultrasound insonification. During continuous flow, the vMB were simultaneously insonified (5,000 cycles) and the largest vMB in the middle of the field-of-view recorded at an ultra-high-speed for the first 14 cycles, where selected frames of this recording are shown in Figure 9.10B. Throughout the Brandaris 128 recording (Figure 9.10E), the vMB remained bound to the bacterial biofilm and the microbubble oscillation amplitude was determined in each frame, resulting in a diameter range from 4.7 µm to 7.8 µm during ultrasound exposure. The corresponding Brandaris 128 recording is shown in Video 9.4. After ultrasound insonification, the effect of the oscillating vMB on the biofilm was clearly visible (Figure 9.10C), where approximately 606.1 µm^2 was removed, corresponding to a

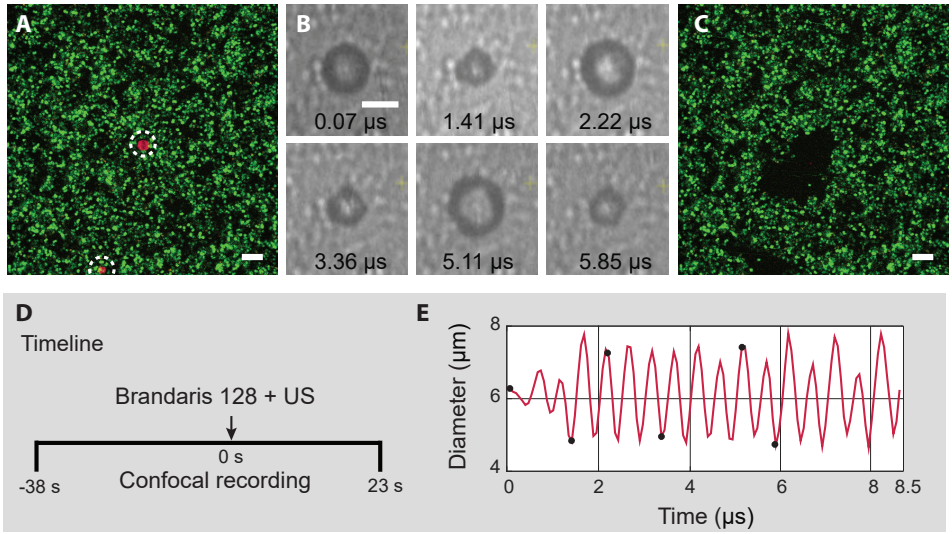

Figure 9.10 Theranostic potential of vancomycin-decorated microbubble (vMB) upon ultrasound under flow (5 dyn/cm^2). (**A**) Initial state confocal microscopy image of vMB (red, DiD stained; indicated by white dashed circles) bound to bacteria (green, SYTO 9 stained) ~1 s before ultrasound exposure. Dead bacteria were stained with propidium iodide (orange). Scale bar is 10 µm and also applies to C. (**B**) Selected frames of Brandaris 128 ultra-high-speed camera recording showing the vMB in the center of A oscillating in response to a single burst of ultrasound (US; 2 MHz, 250 kPa, 5,000 cycles). Scale bar is 5 µm. (**C**) Corresponding confocal image ~3 s after ultrasound exposure showing biofilm disruption. (**D**) Imaging timeline during recordings. (**E**) Microbubble diameter as a function of time visualizing the oscillation behavior of the microbubble during ultrasound insonification. The black dots correspond to the selected images in B.

3.7% total reduction in the field-of-view. This reduction is within the range observed for this insonification as shown in Figure 9.9C, even though the magnification was higher.

9.3.4 Ultrasound molecular imaging

B-mode images of µ-Slides without biofilm showed minimal ultrasonic signal compared to µ-Slides containing biofilms (Supplemental Figure 9.5). Non-linear contrast mode imaging showed only minimal signal for µ-Slides without biofilm (Figure 9.11A). When a biofilm grown under flow was imaged in non-linear contrast mode, thicker parts of the biofilm could be detected in the microchannel before the introduction of vMB (Figure 9.11B). After incubation with vMB (Figure 9.11C), the contrast-to-tissue ratio increased dramatically by 20.2 dB. The ultrasound molecular signal, with an 18.1 dB contrast-to-tissue ratio, only slightly decreased after washing away unbound vMB (Figure 9.11D). To confirm that the non-linear signal was generated by the vMB, bursts were applied on three different places resulting in three individual lines across the 3D rendered image (Figure 9.11E) where the vMB were destroyed.

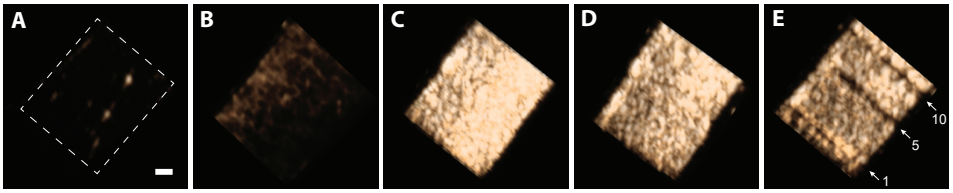

Figure 9.11 Ultrasound molecular imaging of biofilm. 3D rendered non-linear contrast image of the microchannel of a µ-Slide (**A**) without biofilm (microchannel delineated by the white dashed rectangle), (**B**) with biofilm before addition of vancomycin-decorated microbubbles (vMB), (**C**) with biofilm after incubation with vMB, (**D**) with biofilm after incubation and washing away unbound vMB, and (**E**) after applying 1, 5 or 10 flash bursts (white arrows followed by 1, 5 and 10). Scale bar is 1 mm and applies to all images.

9.4 Discussion

In this study, a novel targeted microbubble was successfully developed based on the NHS ester chemical reaction that resulted in the coupling of the antibiotic vancomycin to the microbubble coating. Furthermore, using bacteria-associated biofilms, ultrasound, and flow, the theranostic proof-of-principle was demonstrated for the first time using a vMB and ultra-high-speed recording of the microbubble oscillation behavior. Targeting microbubbles directly to biofilms has the potential to further enhance therapy and provide a diagnostic component at the same time, both of which are desperately needed.

9.4.1 Successful conjugation of vancomycin to phospholipid and incorporation in the microbubble shell

The coupling of vancomycin to the microbubble phospholipid component DSPE-PEG(3400) was done via the NHS ester functional group of the lipid and primary amine of the vancomycin, a method also used by others for coupling vancomycin to a fluorescent dye [565]. MALDI-TOF mass spectrometry confirmed successful conjugation, where the starting material only shows a peak at around ~4,260 Da and all conjugated samples had a second peak at ~5,700 Da indicating the conjugate (Figure 9.3). However, due to the chloride isotopes of vancomycin and multiplicity of the lipid's PEG-tail, it was not possible to determine the exact ratio between starting materials and final conjugate. The 4Pi microscopy data shows that the vancomycin was heterogeneously distributed over the microbubble coating after production (Figure 9.5). This heterogeneous ligand distribution might play a role in binding given that not every part of the microbubble coating can bind to bacteria. Although heterogeneous ligand distributions have previously been reported for DSPC-based microbubbles [389, 392], a more homogeneous distribution could increase the probability of the vMB to bind to the bacteria. Lipid handling prior to microbubble production [427] or different heating-cooling protocols after

microbubble production [389] have been shown to alter ligand distribution to become homogeneous in DSPC-based microbubbles, but these require organic solvents or high temperatures which may compromise vancomycin functionality. One of the possibilities to improve the binding profile of the vMB is to expand the purification process of the lipid conjugate after dialysis.

The antimicrobial property of vancomycin coupled to a microbubble coating should still be present since the binding site used to inhibit cell wall synthesis remains intact after conjugation. The overall therapeutic effect of the conjugated vancomycin alone is then only limited by the amount that is coupled and how many bacteria can bind to each microbubble. By determining the vancomycin concentration on the vMB, the amount of vancomycin in a clinical dose of 1×10^9 vMB [24] was calculated to be 0.78 µg. This is extremely low when considering the clinical target serum concentration of vancomycin is 15-20 µg/ml [568, 569]. On the other hand, the calculated average number of 5358 vancomycin molecules per μm^2 of microbubble shell is in the similar range as the previously reported ~2500 antibody molecules for P-selectin targeted lipid coated microbubbles [49]. Although microbubble coating coverage is crucial when considering it may increase chances of microbubble binding *in vivo*, the therapeutic enhancement effects that vMB can provide lies more on the ultrasound-mediated microbubble behavior. This includes the potential to decrease the current dosage of vancomycin necessary for patients, which could lower the incidence of antibiotic-induced nephrotoxicity.

9.4.2 Successful binding of targeted microbubbles to bacteria in biofilms

Almost all sonobactericide studies use static biofilm cultivation [382]. For some research questions and target diseases, static biofilms are adequate. However, to also include flow-related biofilm-mediated diseases, the addition of multiple flow shear stresses to the biofilm model was pivotal. This addition, in combination with the human plasma coating, resulted in differently grown biofilms which often had a more three-dimensional structure to it than statically grown biofilms. Our vMB successfully bound to bacteria and remained bound through increasing shear stresses of up to 12 dyn/cm^2 (Figure 9.8). Although the maximal shear stress used in this *in vitro* model is on the lower spectrum in healthy human arteries (10-70 dyn/cm^2), it is above the shear stress found in healthy veins (1-6 dyn/cm^2) [574]. Binding of targeted microbubbles under high shear stress conditions can be challenging. To bypass this problem, one could make use of primary acoustic radiation forces. Dayton et al. [120] and Rychak et al. [570, 575] showed that this phenomenon increases microbubble binding in flow conditions by displacing microbubbles towards the desired binding area *in vitro* and *in vivo*, while also significantly reducing the flow

speed of these microbubbles. Theoretically, this approach can increase the number of targeted microbubbles binding to biofilms. Another consideration is that the circulatory system experiences pulsatile flow with each heartbeat. The lull between each cyclical increase and decrease in flow and the forwards and backwards motion of fluid, both due to pulsatile flow, could provide enough time for vMB to bind compared to a continuous flow state. It therefore is of interest for future studies to investigate binding under flow using ultrasound and pulsatile flow, potentially providing an even better binding profile of vMB.

A factor that could affect vMB binding success is that patients are started on antibiotic therapy the moment infection is suspected, which means that the available binding sites could already be occupied before vMB are administered. Therefore, competition was assessed using free vancomycin concentrations ranging from 0 to 1,000 μg/ml (Figure 9.6), and no significant differences were observed between 0 and 20 μg/ml, which is the clinical dose. This lends support that vMB can still be used as a theranostic whether or not the patient is already on high-concentration vancomycin therapy. Another factor which can also affect vMB efficiency is plasma protein binding. For free vancomycin, this has been reported as approximately 26% [576], which could also be the case for vMB. It is also possible that if vancomycin is administered to the patient before vMB are infused, it could minimize the off-target binding to plasma proteins and other potential non-desired attachment. Nonetheless, experiments need to be performed in order to make this determination.

Variability was seen in the number of bound vMB (Figure 9.6), which partly could be explained by the heterogenous nature of biofilms, such as differences in the amount and accessibility of the D-Ala-D-Ala moiety of the bacteria in the biofilm. This relation between binding of targeted microbubbles and the density of the biomarker is clearly demonstrated by Takalkar et al. [49] in their *in vitro* study using anti P-selectin antibody microbubbles and P-selectin as biomarker. Likely, this variability can also partly be explained by the fluctuation in the number of microbubbles entering the microchannel of the Ibidi μ-Slide. Regardless, the number of bound vMB for each condition was all significantly higher than the cMB groups. cMB did exhibit some non-specific binding to the biofilm (Figure 9.6), however this was minor and known to also occur with non-targeted microbubbles for mammalian cells [502, 577, 578]. Under flow conditions the cMB adherence to biofilms, for example at 1.5 dyn/cm^2 (Figure 9.8G), could in fact be due to the natural rough, irregular surface of biofilms preventing microbubbles from moving away and requiring a certain level of flow to overcome this. cMB binding results were significantly different than vMB, both in number of microbubbles bound statically and in their ability to withstand flow, except for 7 to 9 dyn/cm^2 which could also be explained by microbubbles getting

stuck in the biofilm's irregular surface (e.g., protuberances) without binding. Higher flow shear stresses remove the residual unbound control microbubbles from the irregular surface while vMB remained bound. To minimize the effect heterogenous biofilms could have on the binding percentage, both vMB and cMB were tested together in the flow experiments at a 1:1 ratio. However, the ratio in the fields-of-view was found to be 0.87:1, and therefore the percentage in the microbubble binding under increasing shear stress represents a smaller number of vMB compared to cMB. It is possible that vMB could have bound to bacteria potentially growing within the tubing set or inlet, and/or planktonic bacteria in the media before reaching the field-of-view within the µ-Slides resulting in the lower amount of vMB in comparison to cMB.

The non-specific binding of vMB found in µ-Slides only containing IMDM, *i.e.* without biofilm, (Figure 9.7) was likely due to electrostatic non-specific binding to the microchannel of the µ-Slide. When 0.1% or 1% BSA was added to the vMB solution, this non-specific binding was significantly decreased while maintaining the specific binding to the bacterial biofilm. No similar non-specific binding is expected *in vivo*, since human serum albumin is abundantly present in the bloodstream, *i.e.* up to 5.5% [579].

9.4.3 Theranostic proof-of-principle of vancomycin-decorated microbubbles

This study provides diagnostic and therapeutic proof-of-principle by showing vMB response upon ultrasound insonification. The ability of bound vMB to biofilms to generate an echogenic signal in non-linear contrast mode (Figure 9.11) shows vMB could be used to detect early biofilm development via ultrasound molecular imaging, for which up till now no single suitable detection method is available. Using the Brandaris 128 ultra-high-speed camera, a vMB under flow was shown to exhibit oscillations upon insonification while staying bound to the biofilm (Figure 9.10). Concerning therapeutic potential, vMB bound to bacteria were able to significantly disrupt biofilms when exposed to ultrasound (Figure 9.8). This conforms to other reports from sonobactericide papers where non-targeted microbubbles combined with ultrasound can have a therapeutic effect on *in vitro* and *in vivo* biofilms [382]. However, this study revealed some different biofilm reduction effects which might be contributed to targeted microbubbles and flow. Specifically, the streak pattern and large amount of reduction caused by individual microbubbles and one burst of ultrasound versus the craters and holes that others report by concentrated non-targeted microbubbles and different insonification schemes. Biofilm reduction was most likely caused by the microbubble oscillatory mechanical effects (Figure 9.10), such as microstreaming in combination with flow. Regardless of the mechanism,

damaged biofilms become more sensitive to antibiotics [580], which could translate to shorter duration and lower dosage of antibiotics needed to achieve biofilm eradication.

Direct bacterial killing could also occur and in a manner of two avenues. Firstly, the vancomycin on vMB bound to bacteria still has the ability to kill via the same mechanisms as free vancomycin. Secondly, ultrasound-induced microbubble behavior could enhance membrane permeabilization ultimately leading to cell death, as observed in mammalian cells [169]. The PI fluorescence stain is commonly used as a marker of cell death, as used in this study to assess the initial state of bacteria within biofilms, but also as a permeabilization marker since it is cell impermeable to intact membranes. However, direct PI uptake after sonobactericide treatment was not observed in this study. This could be due to bacterial cells requiring more time to die following membrane damage and dispersed cells not being trackable outside of the field-of-view, since other studies report higher PI positive cell numbers but only seen by optical imaging minutes to days after insonification [382]. The therapeutic impact of one bound vMB is probably multifaceted, with direct and indirect consequences on both the bacteria and biofilm structure.

While this new approach shows promise to improve biofilm infection patient outcomes, it needs to be certain that vMB do not contribute to bacterial dispersal and or the release of biofilm fragments into the circulation. Bacteria that are dispersed or dislodged from biofilms due to vMB should be characterized to understand and be able to address the potential risks to be viable as a therapeutic [580, 581]. For vMB as a diagnostic, less risk is envisioned since the ultrasound settings used would remain within a few cycles and on the lower acoustic pressure spectrum not intended to induce major bioeffects. It is expected that the vMB itself will not contribute to adverse effects. The main compound, DSPC, is also the main component of SonoVue microbubbles which are already safely used in the clinic for several decades [582]. PEG-40 stearate is widely used as an emulsifier in microbubble formulations [25, 583, 584]. The gas used to produce the vMB, C_4F_{10}, is a component of Sonazoid, another clinically approved microbubble [585]. Although in this study DSPE-PEG(3400) was used to couple vancomycin, the comparable DSPE-PEG(2000) is a component of the BR55 microbubble, which has shown safety in clinical trials [386]. Vancomycin as an antibiotic is used in the clinic with minimal side-effects [586].

9.5 Conclusion

In this study, to the best of our knowledge for the first time, vMB were produced and characterized which showed successful incorporation of the antibiotic vancomycin to the microbubble's lipid shell. Confocal microscopy revealed that vMB were able to bind to *S. aureus* biofilms and remained attached under increasing physiological flow conditions. Significant biofilm reduction was seen upon ultrasound-activation of vMB. vMB oscillation under flow was visualized on a microsecond time-scale using the Brandaris 128 ultra-high-speed camera. Bound vMB to the biofilm evidently enhanced the ultrasound signal during ultrasound molecular imaging. The ability of vMB to bind to biofilms combined with the mechanical effects induced upon ultrasound insonification have promising potential to both enhance treatment through sonobactericide and provide early diagnosis by ultrasound molecular imaging of biofilm-mediated diseases.

Acknowledgments—This project has received funding from the European Research Council (ERC) under the European Union's Horizon 2020 research and innovation program [grant agreement 805308)]. Gaëtan Mislin acknowledges the Interdisciplinary Thematic Institute (ITI) InnoVec (Innovative Vectorization of Biomolecules, IdEx, ANR-10-IDEX-0002) and SFRI (ANR-20-SFRI-0012). The authors would like to thank Robert Beurskens, Frits Mastik and Reza Pakdaman Zangabad from the Department of Biomedical Engineering, Michiel Manten from the Department of Experimental Medical Instrumentation, Andi R. Sultan from the Department of Medical Microbiology and Infectious Diseases and Ruud Huisman from the Department of Hospital Pharmacy, all from the Erasmus University Medical Center Rotterdam, for their skillful technical assistance. The authors thank the Optical Imaging Centre of Erasmus MC for the use of their facilities and Gert van Cappellen and Alex Nigg for their help. The authors also thank the members of the Therapeutic Ultrasound Contrast Agent group (Biomedical Engineering Dept.) and the *S. aureus* working group (Medical Microbiology and Infectious Diseases Dept.) from Erasmus University Medical Center Rotterdam for their useful discussions.

Supporting information

The Supporting Information is available free of charge at
https://doi.org/10.1016/j.ijpharm.2021.121154

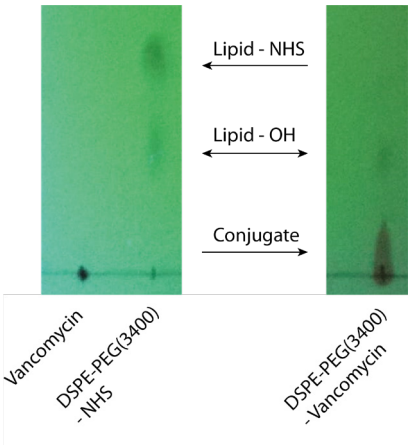

Supplementary Figure 9.1 Vancomycin coupling to the DSPE-PEG(3400)-NHS lipid. Thin-layer chromatography (TLC) visualized the main components of the conjugation before the chemical reaction (left). Vancomycin did not migrate, while DSPE-PEG(3400)-NHS did migrate and separated into two components: an unreacted part (Lipid-NHS) and a hydrolyzed part (Lipid-OH). After the conjugation, TLC reveals the chemically coupled end product after dialysis and freeze-drying (right). The hydrolyzed unreacted Lipid-OH remains visible while the Lipid-NHS has reacted with the vancomycin and is not present anymore. Lipid-NHS is DSPE-PEG(3400)-NHS; Lipid-OH is hydrolyzed DSPE-PEG(3400); conjugate is DSPE-PEG(3400)-vancomycin.

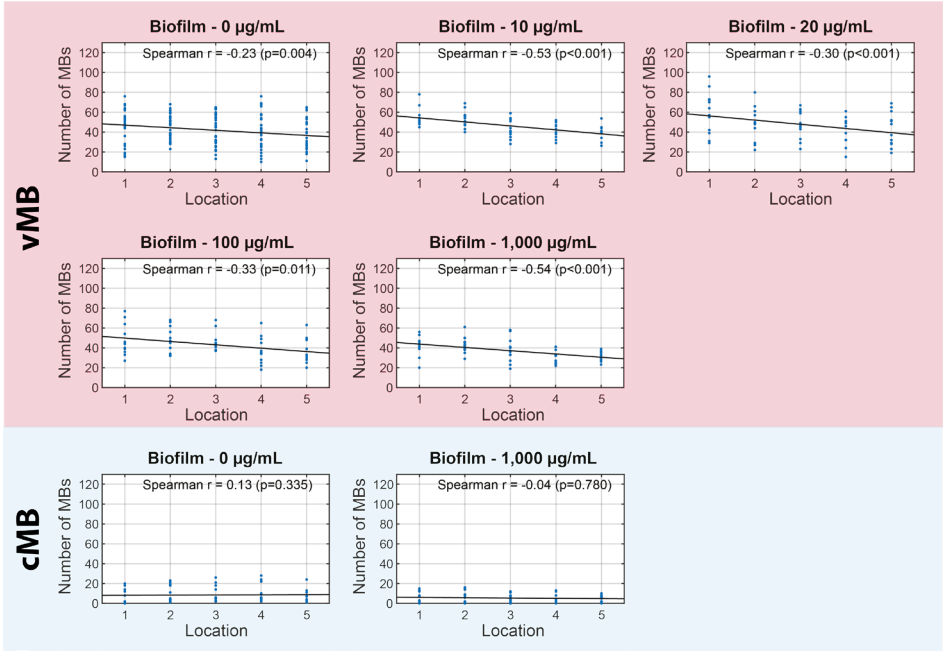

Supplemental Figure 9.2 Scatter plots visualizing the relationship between the number of bound microbubbles (MBs) for vancomycin-decorated microbubbles (vMB) or control microbubbles (cMB) and their location within µ-Slides with statically grown biofilms and free vancomycin (0 – 1,000 µg/mL). The blue circles are the experimental data points, and the lines represent the best fit, with correlation assessed using the Spearman's correlation coefficient (*r*). Location 1 to 5 were equally spaced, with 1 representing the field-of view nearest to the inlet and 5 nearest to the outlet.

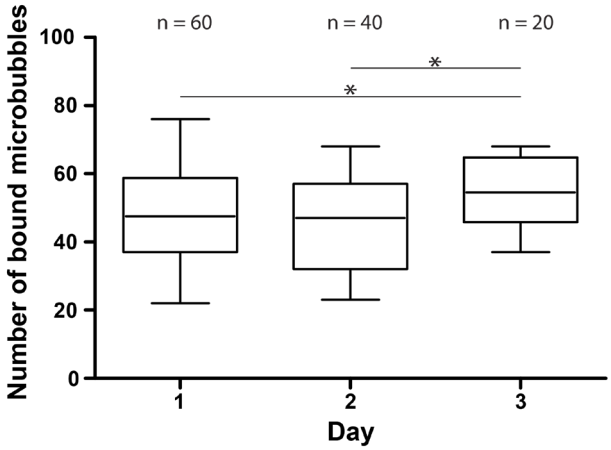

Supplemental Figure 9.3 The number of bound vancomycin-decorated microbubbles (vMB) in µ-Slides with statically grown biofilms over the three-day period the vMB were used for experiments. The boxplots show the median, interquartile range, and the minimum to maximum values. Statistical significance between the number of bound vMB on different days is indicated with *$p < 0.05$.

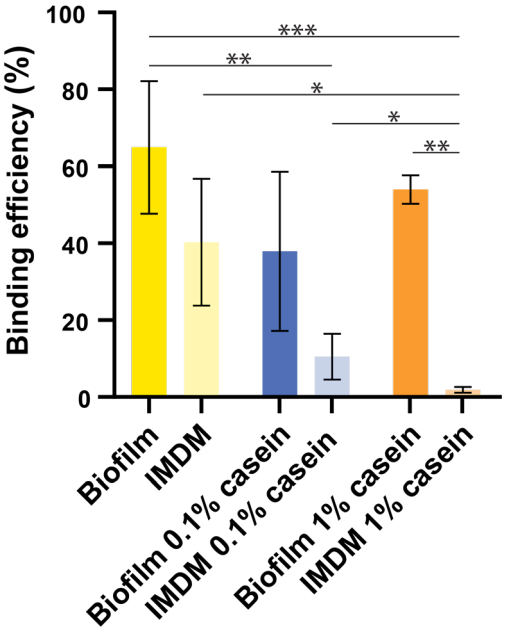

Supplemental Figure 9.4 Non-specific binding of vancomycin-decorated microbubbles. µ-Slides with and without statically grown biofilms in IMDM were incubated with either 0, 0.1 % or 1% casein to bind to non-specific binding sites. Each bar represents the mean binding efficiency percentage with standard deviation overlaid of $N = 3$. Statistical significance is indicated with *$p < 0.05$, **$p < 0.01$ or ***$p < 0.001$.

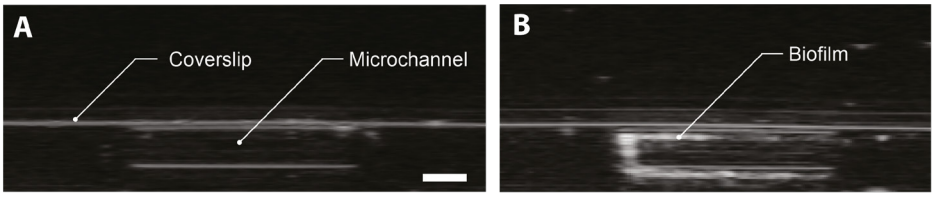

Supplemental Figure 9.5 B-mode imaging of an µ-Slide. Cross-section of a µ-Slide (**A**) without biofilm, and (**B**) with biofilm grown under flow. Scale bar is 1 mm and applies to both images.

10

Phospholipid-coated targeted microbubbles for ultrasound molecular imaging and therapy

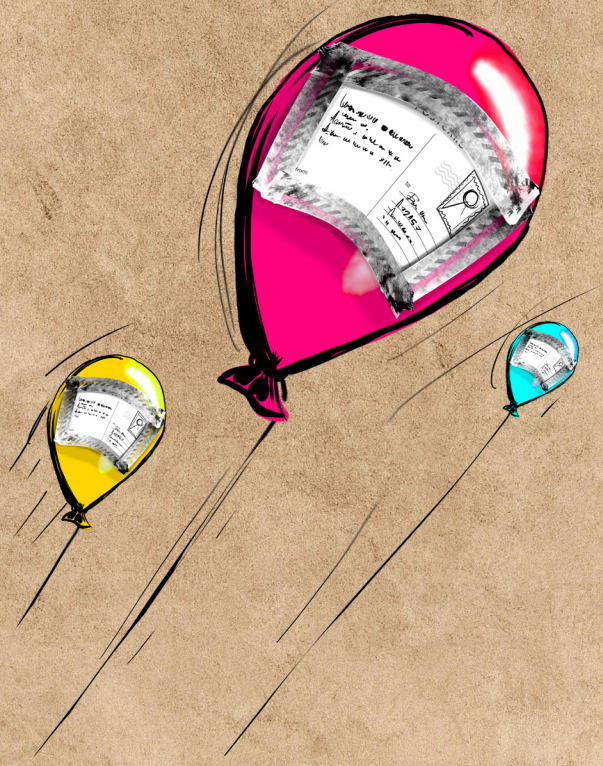

Simone A.G. Langeveld, Bram Meijlink, Klazina Kooiman

Based on:
Current Opinion in Chemical Biology, Vol. 63, pp. 171-179, 2021 [487].

Abstract

Phospholipid-coated microbubbles are ultrasound contrast agents that, when functionalized, adhere to specific biomarkers on cells. In this concise review, we highlight recent developments in strategies for targeting the microbubbles and their use for ultrasound molecular imaging (UMI) and therapy. Recently developed novel targeting strategies include magnetic functionalization, triple targeting, and the use of several new ligands. UMI is a powerful technique for studying disease progression, diagnostic imaging, and monitoring of therapeutic responses. Targeted microbubbles (tMBs) have been used for treatment of cardiovascular diseases and cancer, with therapeutics either co-administered or loaded onto the tMBs. Regardless of which disease was treated, the use of tMBs always resulted in better therapeutic outcome than non-tMBs when compared *in vitro* or *in vivo*.

Keywords—Targeted microbubble; Ultrasound molecular imaging; Targeted drug delivery; Ultrasound; Biomarker; Ligand

10.1 Introduction

Microbubbles (MBs) with sizes of ~1-10 µm are clinically used as ultrasound contrast agent (UCA) for perfusion imaging [587]. The MB coating can be functionalized with a ligand thereby creating targeted microbubbles (tMBs) that can bind to biomarkers expressed during disease. Biomarkers expressed by endothelial cells are excellent targets for ultrasound molecular imaging (UMI) since microbubbles are confined to the vasculature due to their size. Ultrasound imaging of adhered tMBs allows UMI [50], which has recently been used successfully in clinical studies with tMBs targeted to VEGFR2 in prostate [51], breast, and ovarian tumors [386]. Although non-targeted microbubbles (non-tMBs) are known to enhance drug delivery since 1997 [64], for example by creating a pore in the membrane called sonoporation [425], it was not until 2011 that tMBs were reported to also induce sonoporation in an *in vitro* study using endothelial cells [442]. For both UMI and therapy, it is the response of the tMB to ultrasound, *i.e.* by expanding and compressing, that provides the acoustic signal and stimulates drug uptake.

Since the field of tMBs is relatively new in comparison to non-tMBs, it is still in full development regarding 1) targeting strategies, 2) UMI, and 3) therapy. This review focuses on the latest developments of phospholipid-coated tMBs in these three areas. Articles were excluded if they used nanosized agents (<1 µm), for example nanobubbles, for which the reader is referred to an excellent other review [588]. Articles that mentioned ultrasound targeted MB destruction (UTMD) or ultrasound and MB targeted drug delivery (UMTD) and used non-tMBs were also excluded.

These terms relate to the ultrasound signal targeting a tissue or organ, but have become confusing since the development of tMBs. In total 55 articles were selected for this review.

10.2 Microbubble targeting strategies

Besides the conventional way of targeting with an antibody or small peptide, several new strategies were recently reported. Magnetically responsive MBs were produced by incorporating lipid-coated magnetic nanoparticles in the MB coating by sonication [589]. Iron oxide nanoparticles (IONPs) can be loaded on the outside surface of MBs, within the coating, or within an oil layer underneath the coating, with surface loading yielding the highest number of retained MBs in a magnetic field [590]. IONPs can be coated with different phospholipids or dendrons, affecting the size and stability of the MBs that incorporate them [591]. Magnetic functionalization of MBs requires specialized hardware for optimal use: the use of a combined magnetic-acoustic device, when compared to the use of two separate devices, increased drug delivery *in vitro* in an agar phantom and improved tumor response in vivo in a xenograft pancreatic cancer murine model [592].

Conventional targeting of MBs was improved by conjugating two or more ligands to the same tMB. The difference in signal intensity in hepatocellular carcinoma tumors in mice was significantly higher for dual-targeted MBs labeled with anti-VEGFR2 and an RGD peptide, compared to those labeled with only anti-VEGFR2 or only an RGD peptide [593]. Triple-targeted MBs were developed to mimic leukocytes by conjugating anti-VCAM-1, anti-ICAM-1, and synthetic polymeric sialyl Lewis X to custom-made 1,2-distearoyl-*sn*-glycero-3-phosphocholine (DSPC)-based MBs [594]. These tMBs adhered more efficiently than single-targeted MBs to activated murine bEnd.3 cells *in vitro*, and were used *in vivo* to monitor atherosclerosis development and atorvastatin treatment in ApoE-deficient mice with atherosclerosis.

With the ever-increasing number of known biomarkers, new ligands and therefore newly developed tMBs follow. For example, for diagnostic UMI, a Thy1-binding single-chain antibody was used as ligand on tMBs for the detection of pancreatic ductal adenocarcinoma [506] and anti-netrin-1 for breast cancer [505], both in tumor bearing mice. An affibody, a ligand smaller than a full-sized antibody, was used to produce breast cancer-marker B7-H3-tMB for UMI in an orthotopic human breast cancer and a transgenic breast cancer mouse model [595]. Furthermore, tMBs functionalized with anti-MMP-1 were used for early diagnosis of laryngeal squamous cell carcinoma in mice [596], anti-Type IV collagen functionalized tMBs were used to monitor endothelial injury after carotid balloon angioplasty in rats [597], and anti-GPC3 functionalized tMBs were used for targeted sonophotodynamic therapy

in mice with hepatocellular carcinoma [598]. One study used DSPC-based MBs first conjugated with anti-CD4, then coupled to CD4 positive lymphocytes, to monitor lymphocyte-endothelium adhesion during acute rejection of cardiac allografts in rats [599]. All of these studies used streptavidin-biotin bridging to couple the new ligand to the commercially available Target-Ready Micromarker [505, 506, 595] or custom-made DSPC-based MBs [596-599].

To bridge the gap between pre-clinical tMBs and those suitable for clinical use, an alternative to biotin-streptavidin coupling must be used to avoid immune responses [471]. To produce a UMI agent targeting P- and E-selectin, one study used a recombinant protein based on TIM-1 for covalent conjugation with a thioether bond in a canine model of myocardial ischemia-reperfusion [600]. Another strategy involved chemical coupling of the ligand to a maleimide group incorporated in the MB coating, which can be done either prior to [433], or after MB formation [601]. These tMBs were evaluated *in vitro* using a parallel plate flow system and *in vivo* in mice with colon adenocarcinoma [433] and atherosclerotic mice [601]. Newly developed strain-promoted [3+2] azide-alkyne cycloaddition (SPAAC) click chemistry was used in a sterile process of ligand conjugation after MB formation which was used in a canine tolerability study [602]. Finally, Sonazoid was functionalized with lactadherin in a top-down approach [499, 603], in which the use of an already approved UCA may speed up translation to the clinic. These tMBs were evaluated *in vitro* using activated platelets and human blood clots [603], and *in vivo* using mice with human ovarian adenocarcinoma [499]. Many of the studies mentioned in this review use their own custom-made MBs without reporting a thorough characterization of the

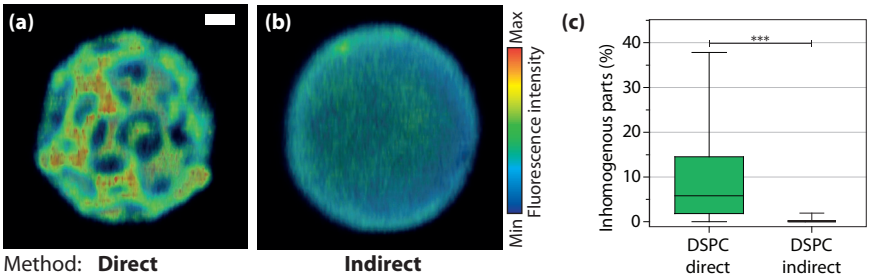

Figure 10.1 Lipid handling prior to MB production affects ligand distribution. (**A,B**) 3D reconstructions of 4Pi confocal microscopy images showing the ligand distribution (Streptavidin-Oregon Green 488) of MBs coated with DSPC/PEG40-stearate/DSPE-PEG2000/DSPE-PEG2000-biotin (molar ratio 84.8/8.2/5.9/1.1) with C_4F_{10} gas core, produced by (**A**) the direct method, *i.e.* lipids directly dispersed in aqueous solution, or (**B**) the indirect method, *i.e.* lipids first dissolved in organic solvent, then dried and dispersed in aqueous solution. Scale bar is 1 µm and applies to both images. (**C**) Quantification of ligand distribution showing inhomogeneous parts (%) of direct DSPC (N = 47) and indirect DSPC (N = 46) MBs. Boxplots show the median, interquartile range and have whiskers from minimum to maximum. Statistical significance was indicated with ***p < 0.001. Reprinted (adapted) with permission from Langmuir 2020, 36, 12, 3221-3233. https://pubs.acs.org/doi/full/10.1021/acs.langmuir.9b03912 Copyright (2020) American Chemical Society.

tMB's response to ultrasound, thereby hindering systematic comparison of their performance. Seemingly minor differences in the production method, such as the lipid handling prior to MB production, already result in significant differences in ligand distribution (Figure 10.1) [427].

10.3 Ultrasound molecular imaging

UMI can be employed for three main goals (Figure 10.2A): studying disease progression, diagnostic imaging, and monitoring of response to therapy, for example for cardiovascular disease, inflammation, and cancer. To study disease progression, the targets P-selectin, VCAM-1, VWF or SDF-1 were used to track the inflammatory response after myocardial infarction in atherosclerotic mice [508] and swine with acute myocardial infarction [509]. Dual-P and E-selectin-tMBs have been established for longitudinal monitoring of anti-inflammatory treatment in swine with acute ileitis [604], however, inflammation could not be detected when the same tMBs were applied in newly developed chronic colitis mouse models [605]. As for diagnostic imaging, P-selectin-tMBs were used to assess thrombotic risk in atrial fibrillation in rats [606] and, together with leukocyte- and CD4-lymphocyte-tMBs, ventricular fibrosis and remodeling could be predicted in an autoimmune myocarditis mouse model [399]. Netrin-1-tMBs were used to detect Netrin-1 positive breast cancer in mice (Figure 10.2B, C), a vital diagnostic before starting Netrin-1 interference therapy [505]. UMI with B7-H3-tMBs allowed differentiation between metastatic and reactive sentinel lymph nodes in a breast cancer mouse model [607], while dual-targeted MBs – with P-selectin and $\alpha_V\beta_3$-integrin as targets – resulted in significantly higher signal intensity in metastatic lymph nodes than in benign lymph nodes in swine with melanoma tumors [608].

UMI is well-suited to monitor the effect of antiangiogenic therapy. The inhibitory effect of sunitinib and bevacizumab on the expression of VEGFR can be directly monitored with VEGFR1- or VEGFR2-tMBs. Commercially available VEGFR2-tMBs, for example BR55, were used to track disease progression and therapy response in different models, including a colon cancer mouse model [511], a rat mammary tumor model [609], and a clear-cell renal cell carcinoma (ccRCC) mouse model [52], with therapeutic effects being detected by UMI before changes in tumor volume could be observed, as also demonstrated previously [510]. VEGFR1- and FSHR-tMBs were used to evaluate the response to sunitinib in a ccRCC mouse model, with a significant difference in signal between the placebo and sunitinib-treated groups and between responders and non-responders [512]. When antioxidant therapy in mice with atherosclerosis was assessed by UMI, three types of tMBs were used, namely P-selectin-, VWF-, or platelet GP1ba-targeted [610]. The reduced signal

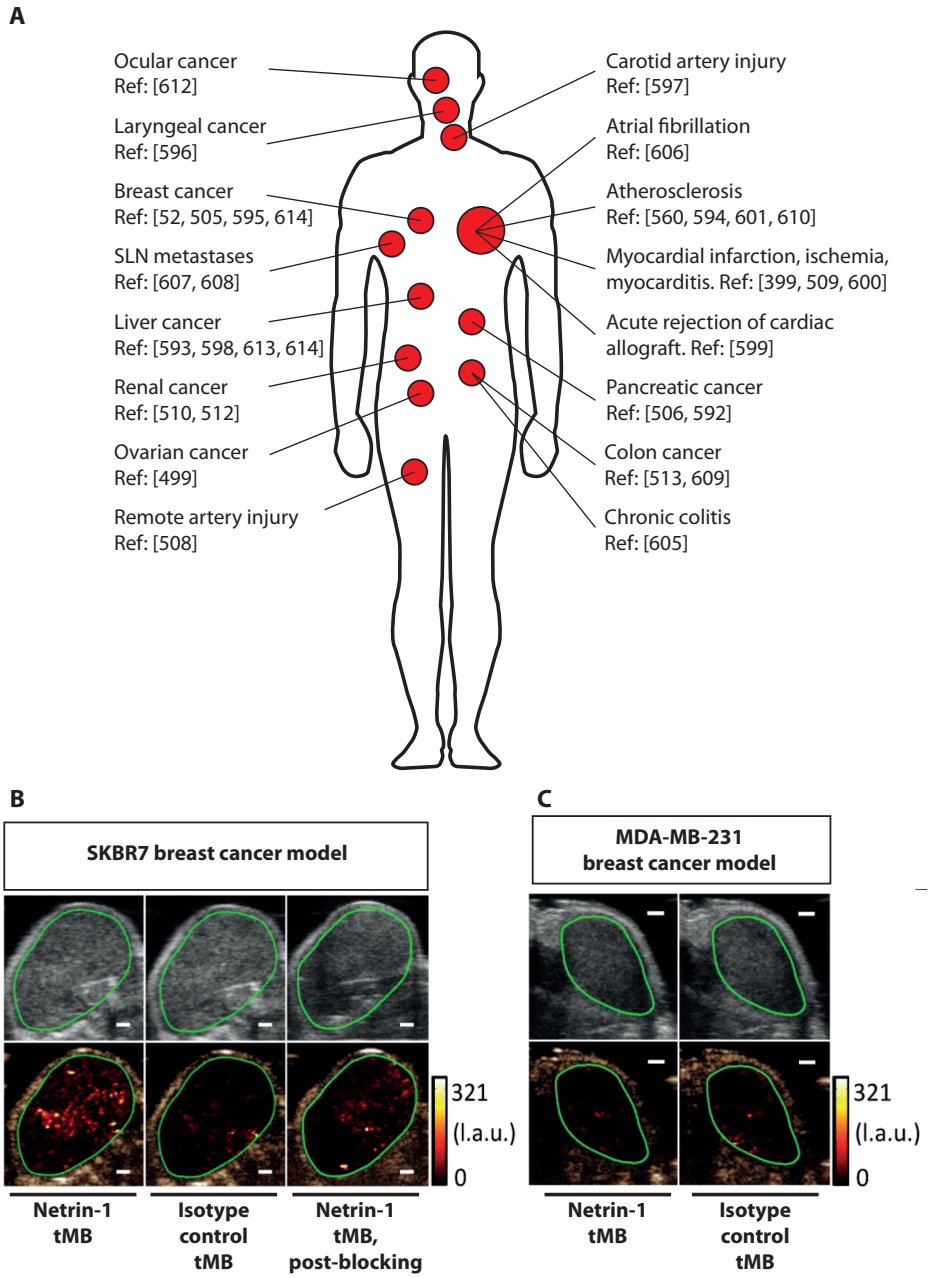

Figure 10.2 (**A**) UMI applications in vivo (preclinically) as described in the review. (**B,C**) UMI with netrin-1-tMBs and isotype control tMBs in (**B**) netrin-1-positive human subcutaneous SKBR7 breast tumor in nude mice prior to and post-blocking with NET1-H-antibody, and (**C**) weakly netrin-1 expressing human subcutaneous MDA-MB-231 breast tumors in nude mice. Top rows: B-mode ultrasound image; bottom rows: UMI signal; region of interest outlined in green. (**B,C**) Reprinted (adapted) from Theranostics 2018, 8, 18, 5126-5142. Copyright (2018) Ivyspring International Publisher. SLN, sentinel lymph node.

intensities found after therapy correlated well with therapeutic effects found in the *ex vivo* plaque histology.

Before UMI can be translated, the clinical relevance of each molecular target has to be demonstrated. Biomarkers for high-risk carotid plaques in atherosclerosis, such as VCAM-1, LOX-1, P-selectin, and VWF, were identified using *ex vivo* high- and low-risk human carotid plaques [611]. After development of clinically translatable small peptide-bearing tMBs with ligands to these four targets [560], the VCAM-1-tMB bound best *in vitro* using human aortic endothelial grown under flow [611]. VEGFR1 was validated as biomarker for vascular mimicry in an ocular melanoma mouse model, where vascular networks formed by tumor cells could be quantitatively monitored with UMI of VEGFR1-tMBs [612].

Ultrasound settings and post-processing for UMI is constantly advancing, alike the tMBs used as active agents. Short-lag spatial coherence (SLSC) beamforming was compared to conventional delay-and-sum beamforming and proved to be particularly useful for detecting low concentrations of tMBs [613]. New ways to distinguish adhered from circulating tMBs without using a destructive ultrasound pulse – which is the conventional method – include the use of a 4-layer convolutional neural network [614] and the use of normalized singular spectrum area instead of differential targeted enhancement during post-processing [513].

10.4 Therapy

To enhance local drug delivery, tMBs can be used in multiple ways and for a wide variety of therapeutic applications (Figure 10.3A). The mechanism behind these therapeutic effects is not fully understood but multiple drug delivery pathways have been described, like sonoporation, endocytosis, and cell-cell contact opening [425]. Recently, it was reported that *in vitro* endothelial cell-cell contact opening only occurred upon sonoporation (Figure 10.3b) [58]. Furthermore, irreversible calcium influx into an endothelial cell upon sonoporation could predict cell-cell contact opening *in vitro* [59].

Targeted MBs show significantly better therapeutic outcomes than non-tMBs both *in vitro* [500, 515, 516, 615] and *in vivo* in mice [500, 616, 617] and rats [369, 618, 619]. The therapeutic outcome was improved regardless of whether tumors [500, 515, 516, 518, 616, 617, 619] or cardiovascular diseases [355, 369, 514, 615, 618, 620] were treated, or whether the therapeutic was co-administered [518, 615, 617, 618] or coupled to the tMB [355, 369, 500, 514-517, 616, 619, 620]. For *in vivo* studies on cardiovascular diseases, the intravenously injected tMBs were retained with a magnetic field [618] or targeted to ICAM-1 [514, 517] or P-selectin [369]. For *in vivo*

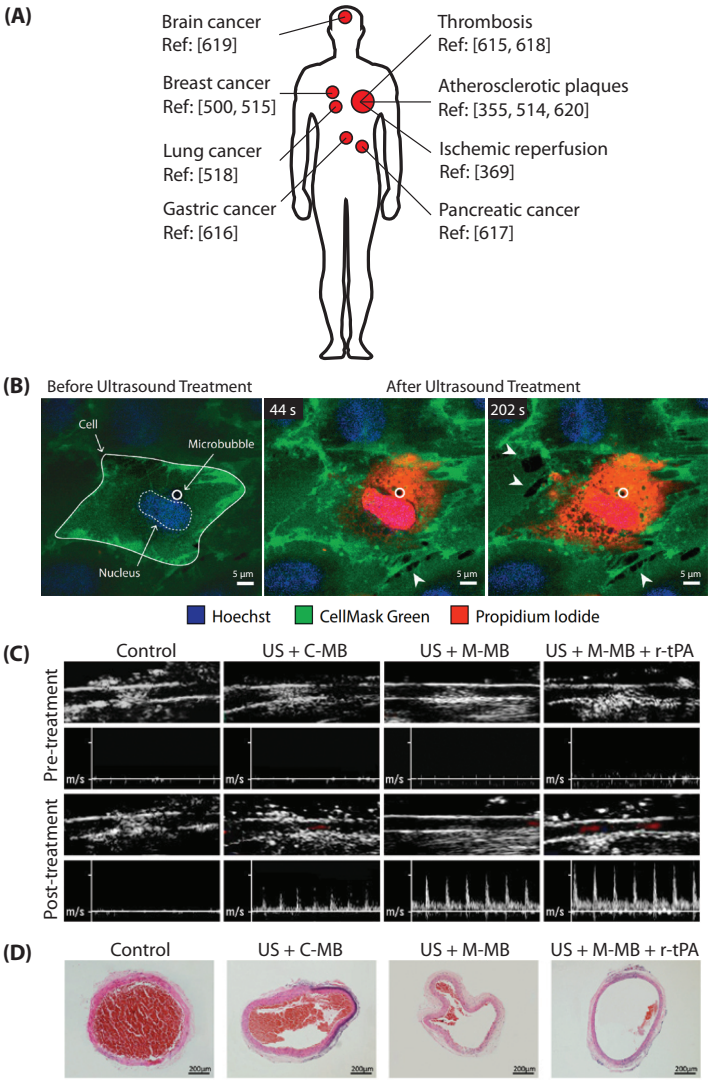

Figure 10.3 (**A**) Therapeutic applications of tMBs *in vivo* (preclinically) as described in this review. (**B**) Endothelial cell before (left) and after (middle and right) 2 MHz ultrasound treatment (10 cycles, 200 kPa peak negative pressure) *in vitro* with nuclei stained with Hoechst and cell membrane with CellMask Green. The tMB induced sonoporation, indicated by the infiltration of Propidium Iodide (red) into the cell, which resulted in cell-cell contact opening indicated with the white arrowheads. Reprinted (adapted) from Journal of Controlled Release 2020, 322, 426-438. Copyright (2020) Elsevier. (**C-D**) Magnetically responsive MBs to treat red thrombi *in vivo* in rats; the four treatment groups consisted of control (sham), ultrasound and control MB (US+C-MB), ultrasound and magnetically responsive MB (US+M-MB), and ultrasound and magnetically responsive MB in combination with the co-administered fibrinolytic agent r-tPA (US+M-MB+r-tPA). Magnetic field was applied in all groups, US therapy parameters: frequency of 2 MHz and a mechanical index of 1.9. (**C**) Ultrasound longitudinal images (top) and Doppler blood flow velocity maps (bottom) of thrombi *in vivo* pre and post treatment. (**D**) Cross-section HE staining of the middle of a thrombus after treatment. Reprinted (adapted) from Thrombosis and Haemostasis 2019, 119, 11, 1752-1766. Copyright (2019) Georg Thieme Verlag KG Stuttgart, New York.

studies on tumors, the intravenously injected tMBs were targeted to VEGFR-2 [617], $\alpha_V\beta_3$ [500], CD13 [619] or DLL4 [616]. The intratumorally injected tMBs had CD326 as target [518]. Ultrasound treatment *in vivo* varied from single treatment between 1-20 min [369, 514, 518, 617-619] up to multiple treatments ranging from 2 to 18 days for 10 s-2 min [355, 500, 616, 620]. Most *in vivo* studies applied an ultrasound frequency of 1 MHz [355, 369, 500, 514, 616, 618-620], but some studies used a lower or higher frequency, namely 0.25 [518] or 4 MHz [617]. Besides this, magnetically responsive tMBs with co-administrated r-tPA were used to increase thrombolytic effects and enhance cavitation energy near the clot in an *in vivo* rat thrombus model (Figure 10.3C, D) [618].

Therapeutics can be loaded onto the tMB by incorporating drugs, like 5-fluorouracil and paclitaxel, in the lipid coating during MB production [515, 516], cationic binding of DNA to the coating [369, 517], or linked to the coating by streptavidin-biotin bridging of antibodies [514, 616, 620], liposomes [500, 619], or biotinylated drugs like Endostar [355]. Ultrasound-mediated destruction of anti-DLL4-loaded tMBs resulted in pro-apoptotic effects on gastric tumors in mice [616] and anti-IL-8-loaded tMBs stabilized atherosclerotic plaques in an atherosclerotic rabbit model [620]. Antibodies were also used to couple MBs to stem cells, using a dual-targeted MB with a CD90 antibody, binding to the stem cell, and a ICAM-1 antibody that targets endothelial cells in atherosclerotic plaques [514]. This so called 'Stembell' reduced inflammation and stabilized plaques in an *in vivo* atherosclerotic mouse model. For tMBs with liposomes attached, the ligand is incorporated in the liposome coating [500, 619]. An example is a MB with a CD13-targeted liposome containing short hairpin RNA (shRNA) to open the blood brain barrier (BBB) and enhance delivery of shRNA, which inhibited tumor growth and prolonged survival in an *in vivo* glioma rat model [619].

10.5 Outlook and conclusion

This overview underlines the diverse use and potential of phospholipid-coated tMBs for ultrasound molecular imaging and therapy and the advantage of using tMBs over non-tMBs for therapy. The tMBs could even be used as theranostics, a combination of diagnostic imaging and therapy. At the same time, the complex biological mechanism and tMB-cell-drug interaction need further elucidation to maximize the therapeutic efficacy of tMB treatment. With new UCAs being constantly developed [100], these could also be tailored towards UMI and therapy. To advance development of phospholipid-coated tMBs or other UCAs and accelerate their translation to clinical use, it is imperative that investigators report the method of MB production in sufficient detail, including not only the different components with

molar ratio, but also what solvents were used since this can have significant effects. The variety of ligands on the tMB complicates the path to the clinic because approval is likely needed for each individual tMB. Consensus on good manufacturing practice and a gold standard for tMB production are also needed to facilitate widespread use of tMBs.

Acknowledgments—The authors thank the members of the Therapeutic UCA group at the Biomedical Engineering Department of Erasmus MC University Medical Center in Rotterdam for their useful discussions.

Funding

This work was supported by the Phospholipid Research Center [KKO-2017-057/1-1], Heidelberg, Germany; the Thoraxcenter of Erasmus MC; and Applied and Engineering Sciences TTW [Vidi-project 17543], part of NWO.

11

Discussion

Phospholipid-coated microbubbles have been around since the 90s [15] with new diagnostic and therapeutic applications being discovered constantly, for example to image and kill bacterial infections, *i.e.* sonobactericide [8]. While several formulations of non-targeted microbubbles have been approved for diagnostic ultrasound imaging in the clinic [23, 24], targeted microbubbles for ultrasound molecular imaging and locally enhanced drug delivery are still under evaluation [51]. This thesis focused on the current status of theranostic microbubbles by looking at microstructures in the coating and how to tailor new formulations to specific applications. The relation between microstructures in the microbubble coating and the acoustic response to ultrasound was investigated and the microbubble-cell interaction and binding dynamics of targeted microbubbles were evaluated. Finally, a new theranostic microbubble formulation was developed for sonobactericide and an overview of recent literature on targeted microbubbles was provided. This concluding chapter will touch on the new findings presented in this thesis and the implications for future research and development of theranostic phospholipid-coated microbubbles.

11.1 Microstructures

The first step towards tailored microbubble formulations was to characterize the existing or conventional formulations. The two most commonly used formulations that are clinically approved, Definity (called Luminity in Europe) [23] and SonoVue (called Lumason in the United States) [24], are based on DPPC and DSPC as main lipid component. These phospholipids have proven to be favorable as main lipid component and are also widely used in custom-made microbubble formulations (*Chapter 2*). The microbubble formulations characterized in *Chapter 3* were based on the same main lipid components, however, with a different gas core as perfluorobutane was used instead of octafluoropropane (gas core of Definity microbubbles) or sulfur hexafluoride (gas core of SonoVue microbubbles). Perfluorobutane was selected because this gas has a lower solubility in water than octafluoropropane and sulfur hexafluoride [621], resulting in more stable microbubbles. Fluorinated gases have significant impact on the phospholipid phase behavior, both in the context of flat monolayers and microbubbles [421, 422]. The compression isotherms of pure DPPC [421] and a binary mixture of DPPC with 5 mol% DSPE-PEG2000 [422] indicate that the surface tension was decreased in the presence of perfluorohexane (C_6F_{14}). Furthermore, microbubbles with a C_4F_{10} gas core had a longer lifetime with lower coefficient of diffusivity than microbubbles with a C_3F_{10} gas core [422]. Based on these reports, it is possible that the liquid condensed (LC) area in Definity and SonoVue microbubbles is smaller than in the custom-made microbubbles investigated in

Chapter 3. Besides the main lipid component, Definity and SonoVue both contain emulsifying components, being DPPA and DPPE-PEG5000 for Definity [23] and DPPG-Na for SonoVue [24]. As these components affect the lipid phase behavior in a complex manner, future studies on the lipid phase distribution in commercially available microbubble formulations remain of interest.

After characterization of existing microbubble formulations and confirming the presence of microstructures in the coating, the next step was to manipulate the lipid phase behavior in order to eliminate the microstructures. Two new formulations were developed as described in *Chapter 4* and *6*. In *Chapter 4*, the main lipid component of the formulations studied in Chapter 3 was replaced by DSPE. This resulted in microbubbles with a homogeneous lipid phase distribution lacking microstructures, although the concentration and size decreased considerably within one hour after production and after dilution of the microbubbles in PBS. In *Chapter 6*, the lipid phase distribution was altered by adding different concentrations of cholesterol to the DSPC-based formulation studied in *Chapter 3*. This resulted in a more homogeneous lipid phase distribution, depending on the cholesterol concentration. However, the amount of buckles on the outside of the microbubbles increased with an increasing amount of cholesterol and after diluting the cholesterol-containing microbubbles in PBS. Hence, while the microstructures could be eliminated, the microbubble population was not homogeneous. Previous studies on the effect of microstructures on the gas permeability of the microbubble coating reported that the amount of gas exchange was negatively correlated with the LC area, and proposed that the gas from the microbubble core mainly diffuses through the LE interdomain region as opposed to the LC domains [468]. Together, these findings demonstrate the importance of phase separation for stability of the microbubble coating, inspiring the concept that the presence of microstructures in the coating is a requirement for sufficient stability of microbubbles for *in vivo* use as theranostic agents.

In order to study the relation between microstructures and the acoustic response of microbubbles, an advanced system was needed that could image the lipid phase distribution in micrometer resolution and the microbubble oscillation in microsecond resolution. *Chapter 5* describes the development and use of the combined confocal microscope and Brandaris 128 ultra-high-speed camera. This unparalleled innovation created the opportunity to study the lipid phase distribution and acoustic behavior of individual microbubbles simultaneously, whereas previously it was only possible to study the lipid phase distribution and acoustic behavior separately, so on different bubbles, making it impossible to relate a particular acoustic response directly to the lipid phase distribution.

The microstructures and acoustic response of individual microbubbles were studied in *Chapter 6*, comparing DSPC-based microbubbles produced by the direct method, that is directly dispersing the coating components in PBS, or produced by the indirect method, where the coating components were first dissolved in organic solvent to obtain a lipid film, which was dried and then dispersed in PBS (Figure 11.1) to DSPC-based microbubbles containing 12 mol% cholesterol. Initially the aim of this study was to compare variability in response to ultrasound of microbubbles with heterogeneous lipid distribution, *i.e.* microstructures, to those with a homogeneous lipid distribution without microstructures. Yet it became apparent that the stability of the coating was significantly reduced after dilution of the DSPC-cholesterol microbubbles in PBS, which resulted in more than twice the amount of buckles than for microbubbles without cholesterol. While this increased occurrence of buckles was reflected in the variability of the oscillation amplitudes with the maximum variability found for the DSPC-cholesterol microbubbles, the direct DSPC microbubbles had the highest median variability. The lipid handling prior to microbubble production had just as much influence on the variability of response as the addition of cholesterol, since the indirect DSPC microbubbles had the lowest variability in oscillation amplitudes. Furthermore, for the direct and indirect DSPC microbubble types, the microbubbles with only large LC domains had significantly lower maximum oscillation amplitudes than microbubbles with both small and large LC domains. While it has been demonstrated nearly two decades ago that lipid domain size and distribution in microbubble coatings affect the coating material properties including elasticity [388], the fact that lipid handling prior to microbubble production can significantly influence the acoustic properties of microbubbles with exactly the same components is an entirely new concept.

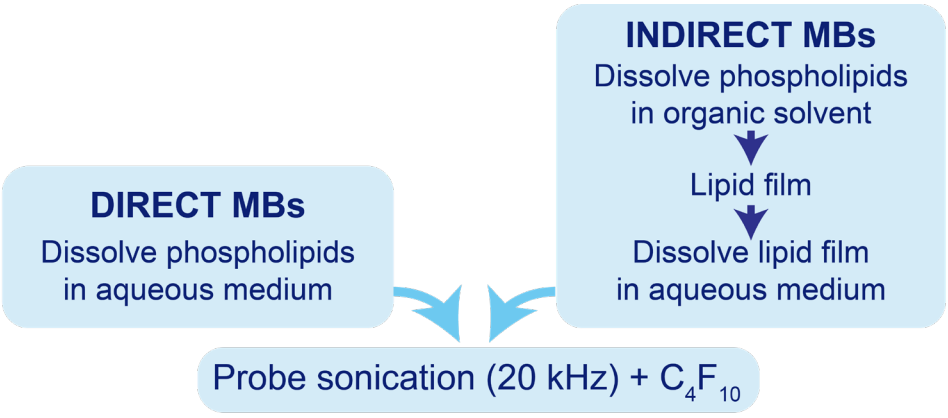

Figure 11.1 Scheme detailing the direct and indirect production methods for phospholipid-coated microbubbles as used in *Chapter 3, 6, 7,* and *8*.

Based on the results presented in *Chapter 6*, the hypothesis that microstructures in the microbubble coating contribute to an unpredictable response to ultrasound can be accepted. At the same time, microstructures may also form the solution to the problem of a non-uniform response to ultrasound. The first half of this thesis centered around developing a new microbubble formulation with all coating components miscible and in the same phase. After achieving this goal and performing preliminary acoustic characterization on DSPE-based microbubbles in *Chapter 4* and extensive acoustic characterization on DSPC-cholesterol microbubbles in *Chapter 6*, it became clear that a coating with all components miscible and in the same phase will inherently lead to an unstable microbubble formulation that is unsuitable for *in vivo* use. Thus, microstructures are needed to create a stable microbubble, and as the results from *Chapter 6* have shown, the LC domain size affects the maximum oscillation amplitude. In order to understand this, the microbubble must be viewed as a heterogeneous object and can be imagined as a planet with landmasses, *i.e.* LC domains, floating in a viscous lava, *i.e.* the LE interdomain region. There is a difference in elasticity between the LC domains and LE interdomain region, with the LC domain size and shape affecting not only the permeability of the microbubble coating before ultrasound insonification, but also the magnitude of expansion during microbubble oscillation. This sparked the notion that a microbubble with microstructures in the coating and all LC domains in the same size and shape may have a uniform response to ultrasound and be stable enough for *in vivo* use.

11.2 Targeted microbubbles

In the second half of this thesis, the focus was shifted from microstructures in the microbubble coating to the therapeutic and theranostic application of microbubbles. Phospholipid-coated microbubbles can be functionalized with a ligand targeting a specific biomarker. A common method to achieve this in pre-clinical research is through streptavidin-biotin bridging [48], as used in *Chapter 7* and *8*. A consequence of this method is that the ligand is only attached to the biotinylated component of the microbubble coating, in this case DSPE-PEG2000-biotin. Therefore, the DSPE-PEG2000-biotin or ligand distribution was studied in DPPC-based and DSPC-based microbubbles in *Chapter 3*. The effect of lipid handling prior to microbubble production was also investigated by comparing DSPC-based microbubbles produced either by the direct or indirect method (Figure 11.1). The production method had a remarkable effect on the ligand distribution as the indirect method resulted in a homogeneous ligand distribution while the direct method resulted in a heterogeneous ligand distribution. Hence, the indirect method was selected for production of targeted microbubbles in *Chapter 7*.

For therapeutic applications, the bioeffects induced by the microbubbles' response to ultrasound are harnessed to achieve safe and effective drug delivery. Hence, the drug delivery outcome is the result of a complex interaction between the microbubbles and endothelial cells. *Chapter 7* addressed the microbubble-endothelial cell morphology in 3D, including the internalization of microbubbles by endothelial cells and the influence on drug delivery outcome. To the best of our knowledge, this is the first study looking into microbubble-endothelial cell interaction prior to ultrasound insonification by comparing the internalization of non-targeted microbubbles, $\alpha_V\beta_3$-targeted, CD31-targeted, and isotype control microbubbles by endothelial cells. The internalized depth of $\alpha_V\beta_3$-targeted microbubbles was significantly higher that of CD31-targeted microbubbles, while non-targeted microbubbles were not internalized by the endothelial cells. Moreover, the internalization depth also affected the microbubbles' acoustic response and drug delivery outcome, as the oscillation of internalized microbubbles was damped and endothelial cells with internalized microbubbles were more susceptible to sonoporation. This highlights an important consideration in the design of theranostic microbubbles: not all ligands available may result in the same level of internalization. A step further would be that targeting certain receptors, such as $\alpha_V\beta_3$, may result in activation of cellular pathways and for example increased platelet adhesion [492]. While platelet adhesion is vital to maintain homeostasis, it has been suggested that platelet adhesion may induce an inflammatory cascade leading to thrombosis [622]. Therefore, the activation of cellular pathways by targeting $\alpha_V\beta_3$ should be examined to give insight on the possible development of thrombosis as adverse effect.

Currently there are several ligands available for ultrasound molecular imaging of angiogenesis and targeted delivery of anti-tumor therapeutics. The anti-$\alpha_V\beta_3$ antibody [608] as used in this thesis, lactadherin [499], and cyclic RGD peptide [500, 593] have all been used as ligand to target microbubbles to $\alpha_V\beta_3$ integrin, which is a marker for angiogenesis [523], atherosclerosis [524], and different types of tumors [525]. Anti-VEGFR1 [612], anti-VEGFR2 [512, 593], and a heterodimer peptide [511, 609] have all been used as ligand to target microbubbles to VEGFR1 and VEGFR2, both receptors that are expressed in different types of tumors [623, 624] and other diseases such as diabetes [625]. When both VEGF receptors were recently evaluated as biomarker to discriminate between benign and malignant breast cancer in humans, VEGFR2 proved to be a better vascular target for microbubbles while $\alpha_V\beta_3$ was more suitable as target for smaller agents, for example droplets or PET and SPECT probes, that are able to extravasate and reach tumor cells outside the vasculature [626]. Both VEGFR2 and $\alpha_V\beta_3$ are excellent candidate targets for theranostic agents, since both receptors can be used to obtain diagnostic information, track disease progression and are located at the site where therapeutics must be delivered. However, as the results

presented in *Chapter 7* demonstrated, the complex microbubble-cell interaction must be taken into consideration before a certain ligand can be selected for a diagnostic, therapeutic, or theranostic application. The internalization of VEGFR2-targeted microbubbles by endothelial cells remains to be investigated, as well as the influence on internalization of different ligands targeting the same receptor. Furthermore, when the cellular pathways that are activated by microbubbles binding to $\alpha_V\beta_3$ or VEGFR2 are identified this will aid in the design and establishment of theranostic microbubbles.

The difference in ligand distribution found in *Chapter 3* was expected to influence the binding efficacy of the microbubbles, although this had not been investigated previously. Therefore, the aim of *Chapter 8* was to compare direct and indirect targeted microbubbles to evaluate the influence of ligand distribution on binding efficacy. While the difference in binding efficacy between the microbubbles was smaller *in vivo* than *in vitro*, there was still a 25% increase in bound microbubbles with homogeneous ligand distribution compared to those with heterogeneous ligand distribution. As the signal of individual microbubbles can be detected with ultrasound molecular imaging [397], this increase in bound microbubbles could mean a 25% improvement of ultrasound molecular signal. A recent review on ultrasound molecular imaging mentioned that while targeted microbubbles are already applied in pre-clinical research and the first clinical trials had promising results, the field could benefit from more standardized protocols on microbubble production, targeting, and ultrasound imaging [50]. The results presented in *Chapter 8* will hopefully contribute to a consensus and standardization of targeted microbubble production, with the indirect method being preferable over the direct method.

In *Chapter 9*, the development of a novel theranostic agent for *S. aureus* biofilms is described: the conjugation of vancomycin to one of the microbubble coating components, *in vitro* validation of the targeted microbubbles binding to *S. aureus* biofilms, and performing ultrasound molecular imaging and sonobactericide therapy using the vancomycin-decorated microbubbles. As a proof-of-principle study, the results on ultrasound molecular imaging and sonobactericide therapy were promising. Nonetheless, the binding efficacy of the targeted microbubbles under flow was lower compared to the $\alpha_V\beta_3$-targeted microbubbles studied in *Chapter 7* and *8*. Both the direct and indirect DSPC-based microbubbles studied in *Chapter 3* had a larger area covered with ligand on the outside of the coating, than the vancomycin-decorated microbubbles studied in *Chapter 9*. This indicates that the amount of ligand on the vancomycin-decorated microbubbles was lower than on the $\alpha_V\beta_3$-targeted microbubbles. Another explanation for the lower binding efficacy could be the difference in dissociation constant [627], as the $\alpha_V\beta_3$ antibody

has a dissociation constant (K_D) of 0.1 nM whereas vancomycin has a dissociation constant in the range of 1-3 μM [628]. Several challenges can be identified in the development of microbubbles targeted to *S. aureus* biofilms. Firstly, since vancomycin is insoluble in organic solvent, the indirect method could not be used for production of vancomycin-decorated microbubbles and instead the direct method was used resulting in a heterogeneous distribution of vancomycin in the coating. Secondly, the vancomycin loading efficiency was only 0.71%, which may be improved by using a different or optimized method for the production of targeted microbubbles. In a study using amalgamation to produce targeted microbubbles, the ligand was conjugated to a lipid in a similar fashion as the vancomycin-lipid conjugate used in *Chapter 9*. The ligand loading efficiency was then optimized by changing the lipid concentration during amalgamation and the concentration of co-surfactant propylene glycol [433]. Furthermore, a dual-targeted approach may result in a microbubble formulation with higher binding efficiency. Dual-targeted microbubbles have shown promising results in ultrasound molecular imaging of angiogenesis [593] and as theranostic agent for breast cancer [209]. *S. aureus* biofilms produce a variety of proteins and fibrin [629], which could be a potential target for a second ligand incorporated into the vancomycin-decorated microbubbles.

A concise overview of recent developments (2018-2020) in phospholipid-coated targeted microbubbles for ultrasound molecular imaging and therapy is provided in *Chapter 10*. Targeted microbubbles have a bright future with new targeting strategies being developed, such as magnetic targeting, and new biological targets being discovered. In fact, targeted microbubbles had significantly better therapeutic outcomes than non-targeted microbubbles in all *in vitro* and *in vivo* studies comparing the two, emphasizing the great potential of targeted microbubbles as theranostic agents.

11.3 Future perspectives

The field of microbubble research can be imagined as a concert piano. Without an expert piano tuner, it does not matter how well the pianist plays the keys of the piano, if it is out of tune the sounds from the strings will fail to enchant the audience. In a similar way, when the wrong type of microbubble is used for a certain application, wrong either because of the coating composition or because of the production method, it does not matter how advanced the ultrasound pulse and data processing methods are, the microbubble oscillation will fail to achieve the intended goal. It is concerning that the microbubble background is often disregarded when researchers focus on testing a new type of insonification scheme or signal processing, and there are numerous papers published that failed to mention the exact composition or

detailed production method of the microbubbles that were used [47, 49, 324, 399, 437, 508, 513, 610]. To help advance the field of microbubbles, it must become standard practice that all researchers using microbubbles invest their time in learning and understanding the background and considerations of microbubble composition and manufacturing. Moreover, there should be a golden standard for which details on microbubble composition and production are necessary to report, such as the molar ratio of different coating components and the use of organic solvent, to ensure that experiments can be reproduced by others.

Targeted microbubbles hold great promise as ultrasound molecular imaging or therapeutic agents, and when imaging and therapy can be combined as theranostic agents. In pre-clinical research, targeted microbubbles are already starting to live up to this expectation as they have been used to study disease progression [508, 509] and monitor response to treatment [610]. Ultrasound molecular imaging is also an excellent imaging modality for longitudinal studies; since the technique is non-invasive and non-toxic it can help reduce the numbers of animals needed for experiments. Better standardization of microbubble production and reporting of detailed production protocols will aid in the comparison of results between groups and help in standardization of the ultrasound imaging protocols, which are highly dependent on the microbubble characteristics such as size and resonance frequency.

Translation of targeted microbubbles to clinical use is ongoing and several clinical trials have reported exciting results on ultrasound molecular imaging with a VEGFR2-targeted microbubble formulation in patients with prostate cancer [51] and breast and ovarian lesions [386]. As the literature overview in *Chapter 10* showed, targeted microbubbles are the future for therapeutic applications. However, the step from pre-clinical proof-of-principle studies to approved clinical use in humans is immense and for novel ligands and microbubble formulations it will take tremendous time and effort to perform all the safety studies needed to commence clinical trials. In this regard, clinical research involving targeted microbubbles is lagging behind as the first formulations were developed over two decades ago [48]. A recent study used Sonazoid, a commercially available formulation of phosphatidylserine-containing microbubbles [630], for molecular imaging of myocardial ischemia in humans [631]. Although Sonazoid does not contain a specific ligand, phosphatidylserine-containing microbubbles have been shown to attach to leukocytes which can be used to image inflammation [632]. With this innovative strategy, ultrasound molecular imaging could be done in humans using an already approved microbubble formulation. Clinical trials using non-targeted microbubbles for therapeutic applications show promising results, for example on enhanced delivery of trastuzumab to treat Her2-positive brain metastases in human patients [6]. Clinical approval of the first targeted

microbubble formulation will pave the way for more clinical research focused on the therapeutic use and ultimately theranostic use of targeted microbubbles.

This thesis has focused on different aspects of theranostic microbubbles, from the microstructures in the coating to the ligand distribution and binding efficacy *in vitro* and *in vivo*. The findings presented here contribute to advancement towards the "perfect microbubble". Admittedly, there is no one perfect microbubble, as each application requires specific characteristics. Therefore, the perfect microbubble is one where all features are designed with the ultimate goal in mind: a specific gas core is needed for delivery of a therapeutic gas such as oxygen, a specific ligand is needed for molecular imaging of certain biomarkers, and a balanced or symmetrical microstructure is needed for a uniform response to ultrasound. Besides these choices that can be controlled during the design of a theranostic agent, one must keep in mind that microbubbles can be like people. Often the response of an individual person is tainted by their history, whether they had a negative or positive experience in the past will influence how they react to certain situations. Each individual microbubble is influenced by their history as well, for example changes in temperature and dilution may result in deflation and formation of buckles in the coating. This will influence the microbubbles' acoustic response to ultrasound, making it non-uniform by nature. The perfect microbubble would therefore be stable enough not to be disturbed by its history, to an extent that all microbubbles in a bulk will respond within a limited range of oscillation amplitudes and can be trusted to achieve the desired effect without causing irreversible damage.

References

[1] L. Rayleigh. "On the pressure developed in a liquid during the collapse of a spherical cavity", Philosophical Magazine, 34, pp. 94-98, (1917).

[2] M. S. Plesset. "The Dynamics of Cavitation Bubbles", Journal of Applied Mechanics, 16, pp. 277-282, (1949).

[3] B. Helfield. "A Review of Phospholipid Encapsulated Ultrasound Contrast Agent Microbubble Physics", Ultrasound Med Biol, 45, pp. 282-300, (2019).

[4] R. Gramiak and P. M. Shah. "Echocardiography of the aortic root", Invest Radiol, 3, pp. 356-366, (1968).

[5] R. G. Barr. "Use of lumason/sonovue in contrast-enhanced ultrasound of the kidney for characterization of renal masses-a meta-analysis", Abdom Radiol (NY), (2021).

[6] Y. Meng, R. M. Reilly, R. C. Pezo, M. Trudeau, A. Sahgal, A. Singnurkar, J. Perry, S. Myrehaug, C. B. Pople, B. Davidson, M. Llinas, C. Hyen, Y. Huang, C. Hamani, S. Suppiah, K. Hynynen, and N. Lipsman. "MR-guided focused ultrasound enhances delivery of trastuzumab to Her2-positive brain metastases", Sci Transl Med, 13, p. eabj4011, (2021).

[7] R. T. Kleven, K. B. Karani, N. Hilvert, S. M. Ford, K. P. Mercado-Shekhar, J. M. Racadio, M. B. Rao, T. A. Abruzzo, and C. K. Holland. "Accelerated sonothrombolysis with Definity in a xenographic porcine cerebral thromboembolism model", Sci Rep, 11, p. 3987, (2021).

[8] K. R. Lattwein, H. Shekhar, W. J. B. van Wamel, T. Gonzalez, A. B. Herr, C. K. Holland, and K. Kooiman. "An in vitro proof-of-principle study of sonobactericide", Scientific reports, 8, pp. 3411-3411, (2018).

[9] Q. Wen, S. Wan, Z. Liu, S. Xu, H. Wang, and B. Yang. "Ultrasound contrast agents and ultrasound molecular imaging", J Nanosci Nanotechnol, 14, pp. 190-209, (2014).

[10] C. Edsall, Z. M. Khan, L. Mancia, S. Hall, W. Mustafa, E. Johnsen, A. L. Klibanov, Y. Y. Durmaz, and E. Vlaisavljevich. "Bubble Cloud Behavior and Ablation Capacity for Histotripsy Generated from Intrinsic or Artificial Cavitation Nuclei", Ultrasound Med Biol, 47, pp. 620-639, (2021).

[11] A. L. Klibanov, "Ultrasound Contrast Agents: Development of the Field and Current Status," in Contrast Agents II: Optical, Ultrasound, X-Ray and Radiopharmaceutical Imaging, W. Krause, Ed., ed Berlin, Heidelberg: Springer Berlin Heidelberg, 2002, pp. 73-106.

[12] C. Greis. "Ultrasound contrast agents as markers of vascularity and microcirculation", Clin Hemorheol Microcirc, 43, pp. 1-9, (2009).

[13] M. W. Grinstaff and K. S. Suslick. "Air-filled proteinaceous microbubbles: synthesis of an echo-contrast agent", Proceedings of the National Academy of Sciences, 88, pp. 7708-7710, (1991).

[14] J. A. Straub, D. E. Chickering, C. C. Church, B. Shah, T. Hanlon, and H. Bernstein. "Porous PLGA microparticles: AI-700, an intravenously administered ultrasound contrast agent for use in echocardiography", J Control Release, 108, pp. 21-32, (2005).

[15] E. Unger, D. Shen, T. Fritz, B. Kulik, P. Lund, G. L. Wu, D. Yellowhair, R. Ramaswami, and T. Matsunaga. "Gas-filled lipid bilayers as ultrasound contrast agents", Invest Radiol, 29 Suppl 2, pp. S134-136, (1994).

[16] K. Engelhardt, A. Rumpel, J. Walter, J. Dombrowski, U. Kulozik, B. Braunschweig, and W. Peukert. "Protein Adsorption at the Electrified Air–Water Interface: Implications on Foam Stability", Langmuir, 28, pp. 7780-7787, (2012).

[17] A. H. Khan and S. V. Dalvi. "Kinetics of albumin microbubble dissolution in aqueous media", Soft Matter, 16, pp. 2149-2163, (2020).

[18] S. H. Bloch, M. Wan, P. A. Dayton, and K. W. Ferrara. "Optical observation of lipid- and polymer-shelled ultrasound microbubble contrast agents", Applied Physics Letters, 84, pp. 631-633, (2004).

[19] P. van Hoogevest and A. Wendel. "The use of natural and synthetic phospholipids as pharmaceutical excipients", Eur J Lipid Sci Technol, 116, pp. 1088-1107, (2014).

[20] A. D. Bangham, M. M. Standish, and J. C. Watkins. "Diffusion of univalent ions across the lamellae of swollen phospholipids", Journal of Molecular Biology, 13, pp. 238-IN227, (1965).

[21] K. W. Ferrara, M. A. Borden, and H. Zhang. "Lipid-shelled vehicles: engineering for ultrasound molecular imaging and drug delivery", Acc. Chem. Res., 42, pp. 881-892, (2009).

[22] S. Sirsi and M. Borden. "Microbubble Compositions, Properties and Biomedical Applications", Bubble Sci. Eng. Technol., 1, pp. 3-17, (2009).

[23] FDA. (06/11/2019). Definity label. Available: https://www.accessdata.fda.gov/drugsatfda_docs/label/2011/021064s011lbl.pdf

[24] FDA. (11/2/2021). Lumason label. Available: https://www.accessdata.fda.gov/drugsatfda_docs/label/2016/203684s002lbl.pdf

[25] J. Owen, S. Kamila, S. Shrivastava, D. Carugo, J. Bernardino de la Serna, C. Mannaris, V. Pereno, R. Browning, E. Beguin, A. P. McHale, J. F. Callan, and E. Stride. "The Role of PEG-40-stearate in the Production, Morphology, and Stability of Microbubbles", Langmuir, (2018).

[26] J. F. Nagle. "Theory of lipid monolayer and bilayer phase transitions: Effect of headgroup interactions", The Journal of Membrane Biology, 27, pp. 233-250, (1976).

[27] S. Kilic and E. S. Bolukcu. "Phase behavior of DSPC/PEG40St mixtures at higher emulsifier contents", Colloids Surf., B, 171, pp. 368-376, (2018).

[28] C. W. McConlogue and T. K. Vanderlick. "A Close Look at Domain Formation in DPPC Monolayers", Langmuir, 13, pp. 7158-7164, (1997).

[29] M. M. Lozano and M. L. Longo. "Complex formation and other phase transformations mapped in saturated phosphatidylcholine/DSPE-PEG2000 monolayers", Soft Matter, 5, p. 1822, (2009).

[30] M. A. Borden, G. Pu, G. J. Runner, and M. L. Longo. "Surface phase behavior and microstructure of lipid/PEG-emulsifier monolayer-coated microbubbles", Colloids Surf., B, 35, pp. 209-223, (2004).

[31] D. Marsh, R. Bartucci, and L. Sportelli. "Lipid membranes with grafted polymers: physicochemical aspects", Biochim. Biophys. Acta, Biomembr., 1615, pp. 33-59, (2003).

[32] R. H. Abou-Saleh, M. Swain, S. D. Evans, and N. H. Thomson. "Poly(ethylene glycol) Lipid-Shelled Microbubbles: Abundance, Stability, and Mechanical Properties", Langmuir, 30, pp. 5557-5563, (2014).

[33] C. C. Chen and M. A. Borden. "The role of poly(ethylene glycol) brush architecture in complement activation on targeted microbubble surfaces", Biomaterials, 32, pp. 6579-6587, (2011).

[34] S. Campbell, D. Griffin, D. Little, and L. Allan. "Use of ultrasound in the prenatal diagnosis of congenital disorders", Methods Cell Biol, 26, pp. 181-227, (1982).

[35] H. M. Frost, "3 - Electromagnetic–Ultrasound Transducers: Principles, Practice, and Applications," in Physical Acoustics. vol. 14, W. P. Mason and R. N. Thurston, Eds., ed: Academic Press, 1979, pp. 179-275.

[36] H. A. Ahmad, H. J. Yu, and C. G. Miller, "Medical Imaging Modalities," in Medical Imaging in Clinical Trials, C. G. Miller, J. Krasnow, and L. H. Schwartz, Eds., ed London: Springer London, 2014, pp. 3-26.

[37] W. K. Chong, V. Papadopoulou, and P. A. Dayton. "Imaging with ultrasound contrast agents: current status and future", Abdom Radiol (NY), 43, pp. 762-772, (2018).

[38] N. de Jong, L. Hoff, T. Skotland, and N. Bom. "Absorption and scatter of encapsulated gas filled microspheres: Theoretical considerations and some measurements", Ultrasonics, 30, pp. 95-103, (1992).

[39] J. M. Correas, L. Bridal, A. Lesavre, A. Mejean, M. Claudon, and O. Helenon. "Ultrasound contrast agents: properties, principles of action, tolerance, and artifacts", Eur. Radiol., 11, pp. 1316-1328, (2001).

[40] M. Emmer, A. van Wamel, D. E. Goertz, and N. de Jong. "The Onset of Microbubble Vibration", Ultrasound in Medicine & Biology, 33, pp. 941-949, (2007).

[41] W. T. Shi, F. Forsberg, A. Tornes, J. Østensen, and B. B. Goldberg. "Destruction of contrast microbubbles and the association with inertial cavitation", Ultrasound in Medicine & Biology, 26, pp. 1009-1019, (2000).

[42] J. Collis, R. Manasseh, P. Liovic, P. Tho, A. Ooi, K. Petkovic-Duran, and Y. Zhu. "Cavitation microstreaming and stress fields created by microbubbles", Ultrasonics, 50, pp. 273-279, (2010).

[43] P. Marmottant, S. Meer, M. Emmer, M. Versluis, N. Jong, S. Hilgenfeldt, and D. Lohse. "A model for large amplitude oscillations of coated bubbles accounting for buckling and rupture", J Acoust Soc Am, 118, pp. 3499-3505, (2005).

[44] S. M. van der Meer, B. Dollet, M. M. Voormolen, C. T. Chin, A. Bouakaz, N. de Jong, M. Versluis, and D. Lohse. "Microbubble spectroscopy of ultrasound contrast agents", J Acoust Soc Am, 121, pp. 648-656, (2007).

[45] T. van Rooij, Y. Luan, G. Renaud, A. F. van der Steen, M. Versluis, N. de Jong, and K. Kooiman. "Non-linear response and viscoelastic properties of lipid-coated microbubbles: DSPC versus DPPC", Ultrasound Med. Biol., 41, pp. 1432-1445, (2015).

[46] M. Emmer, H. J. Vos, M. Versluis, and N. de Jong. "Radial modulation of single microbubbles", IEEE Trans. Ultrason. Ferroelectr. Freq. Control, 56, pp. 2370-2379, (2009).

[47] J. R. Lindner, J. Song, J. Christiansen, A. L. Klibanov, F. Xu, and K. Ley. "Ultrasound Assessment of Inflammation and Renal Tissue Injury With Microbubbles Targeted to P-Selectin", Circulation, 104, pp. 2107-2112, (2001).

[48] A. L. Klibanov, M. S. Hughes, J. N. Marsh, C. S. Hall, J. G. Miller, J. H. Wible, and G. H. Brandenburger. "Targeting of ultrasound contrast material. An in vitro feasibility study", Acta Radiol Suppl, 412, pp. 113-120, (1997).

[49] A. M. Takalkar, A. L. Klibanov, J. J. Rychak, J. R. Lindner, and K. Ley. "Binding and detachment dynamics of microbubbles targeted to P-selectin under controlled shear flow", J Control Release, 96, pp. 473-482, (2004).

[50] A. Kosareva, L. Abou-Elkacem, S. Chowdhury, J. R. Lindner, and B. A. Kaufmann. "Seeing the Invisible-Ultrasound Molecular Imaging", Ultrasound Med Biol, 46, pp. 479-497, (2020).

[51] M. Smeenge, F. Tranquart, C. K. Mannaerts, T. M. de Reijke, M. J. van de Vijver, M. P. Laguna, S. Pochon, J. de la Rosette, and H. Wijkstra. "First-in-Human Ultrasound Molecular Imaging With a VEGFR2-Specific Ultrasound Molecular Contrast Agent (BR55) in Prostate Cancer: A Safety and Feasibility Pilot Study", Invest. Radiol., 52, pp. 419-427, (2017).

[52] J. D. Rojas, F. L. Lin, Y. C. Chiang, A. Chytil, D. C. Chong, V. L. Bautch, W. K. Rathmell, and P. A. Dayton. "Ultrasound Molecular Imaging of VEGFR-2 in Clear-Cell Renal Cell Carcinoma Tracks Disease Response to Antiangiogenic and Notch-Inhibition Therapy", Theranostics, 8, pp. 141-155, (2018).

[53] S. Roovers, T. Segers, G. Lajoinie, J. Deprez, M. Versluis, S. C. De Smedt, and I. Lentacker. "The Role of Ultrasound-Driven Microbubble Dynamics in Drug Delivery: From Microbubble Fundamentals to Clinical Translation", Langmuir, 35, pp. 10173-10191, (2019).

[54] K. Hynynen, N. McDannold, N. Vykhodtseva, and F. A. Jolesz. "Noninvasive MR imaging-guided focal opening of the blood-brain barrier in rabbits", Radiology, 220, pp. 640-646, (2001).

[55] J. D. Martin, H. Cabral, T. Stylianopoulos, and R. K. Jain. "Improving cancer immunotherapy using nanomedicines: progress, opportunities and challenges", Nature Reviews Clinical Oncology, 17, pp. 251-266, (2020).

[56] J. J. Kwan, M. Kaya, M. A. Borden, and P. A. Dayton. "Theranostic oxygen delivery using ultrasound and microbubbles", Theranostics, 2, pp. 1174-1184, (2012).

[57] X. Wang, Y. Gkanatsas, J. Palasubramaniam, J. D. Hohmann, Y. C. Chen, B. Lim, C. E. Hagemeyer, and K. Peter. "Thrombus-Targeted Theranostic Microbubbles: A New Technology towards Concurrent Rapid Ultrasound Diagnosis and Bleeding-free Fibrinolytic Treatment of Thrombosis", Theranostics, 6, pp. 726-738, (2016).

[58] I. Beekers, M. Vegter, K. R. Lattwein, F. Mastik, R. Beurskens, A. F. W. van der Steen, N. de Jong, M. D. Verweij, and K. Kooiman. "Opening of endothelial cell–cell contacts due to sonoporation", J Control Release, 322, pp. 426-438, (2020).

[59] I. Beekers, F. Mastik, R. Beurskens, P. Y. Tang, M. Vegter, A. F. W. van der Steen, N. de Jong, M. D. Verweij, and K. Kooiman. "High-resolution imaging of intracellular calcium fluctuations caused by oscillating microbubbles", Ultrasound Med Biol, 46, pp. 2017-2029, (2020).

[60] Z. I. Kovacs, S. Kim, N. Jikaria, F. Qureshi, B. Milo, B. K. Lewis, M. Bresler, S. R. Burks, and J. A. Frank. "Disrupting the blood–brain barrier by focused ultrasound induces sterile inflammation", Proceedings of the National Academy of Sciences, 114, pp. E75-E84, (2017).

[61] D. McMahon and K. Hynynen. "Acute Inflammatory Response Following Increased Blood-Brain Barrier Permeability Induced by Focused Ultrasound is Dependent on Microbubble Dose", Theranostics, 7, pp. 3989-4000, (2017).

[62] C. T. Chin, C. Lancée, J. Borsboom, F. Mastik, M. E. Frijlink, N. de Jong, M. Versluis, and D. Lohse. "Brandaris 128: A digital 25 million frames per second camera with 128 highly sensitive frames", Rev Sci Instrum, 74, pp. 5026-5034, (2003).

[63] K. Tachibana and S. Tachibana. "Albumin microbubble echo-contrast material as an enhancer for ultrasound accelerated thrombolysis", Circulation, 92, pp. 1148-1150, (1995).

[64] S. Bao, B. D. Thrall, and D. L. Miller. "Transfection of a reporter plasmid into cultured cells by sonoporation in vitro", Ultrasound Med Biol, 23, pp. 953-959, (1997).

[65] I. Lentacker, S. C. De Smedt, and N. N. Sanders. "Drug loaded microbubble design for ultrasound triggered delivery ", Soft Matter, 5, pp. 2161-2170, (2009).

[66] K. Kooiman, H. J. Vos, M. Versluis, and N. de Jong. "Acoustic behavior of microbubbles and implications for drug delivery", Adv. Drug. Deliv. Rev., 72, pp. 28-48, (2014).

[67] J. T. Sutton, K. J. Haworth, G. Pyne-Geithman, and C. K. Holland. "Ultrasound-mediated drug delivery for cardiovascular disease", Expert Opin Drug Deliv, 10, pp. 573-592, (2013).

[68] V. Paefgen, D. Doleschel, and F. Kiessling. "Evolution of contrast agents for ultrasound imaging and ultrasound-mediated drug delivery", Front Pharmacol, 6, p. 197, (2015).

[69] A. N. Nowbar, M. Gitto, J. P. Howard, D. P. Francis, and R. Al-Lamee. "Mortality From Ischemic Heart Disease Analysis of Data From the World Health Organization and Coronary Artery Disease Risk Factors From NCD Risk Factor Collaboration", Circ-Cardiovasc Qual, 12, (2019).

[70] C. P. Nolsøe and T. Lorentzen. "International guidelines for contrast-enhanced ultrasonography: ultrasound imaging in the new millennium", Ultrasonography, 35, pp. 89-103, (2016).

[71] L. Xing, Q. Shi, K. Zheng, M. Shen, J. Ma, F. Li, Y. Liu, L. Lin, W. Tu, Y. Duan, and L. Du. "Ultrasound-Mediated Microbubble Destruction (UMMD) Facilitates the Delivery of CA19-9 Targeted and Paclitaxel Loaded mPEG-PLGA-PLL Nanoparticles in Pancreatic Cancer", Theranostics, 6, pp. 10-10, (2016).

[72] S. Goutal, M. Gerstenmayer, S. Auvity, F. Caillé, S. Mériaux, I. Buvat, B. Larrat, and N. Tournier. "Physical blood-brain barrier disruption induced by focused ultrasound does not overcome the transporter-mediated efflux of erlotinib", Journal of Controlled Release, 292, pp. 210-220, (2018).

[73] J. Hu, N. Zhang, Jr., L. Li, N. Zhang, Sr., Y. Ma, C. Zhao, Q. Wu, Y. Li, N. He, and X. Wang. "The synergistic bactericidal effect of vancomycin on UTMD treated biofilm involves damage to bacterial cells and enhancement of metabolic activities", Scientific reports, 8, pp. 192-192, (2018).

[74] M. Schneider, B. Anantharam, M. Arditi, D. Bokor, A. Broillet, P. Bussat, X. Fouillet, P. Frinking, I. Tardy, J. Terrettaz, R. Senior, and F. Tranquart. "BR38, a new ultrasound blood pool agent", Investigative radiology, 46, pp. 486-494, (2011).

[75] T. Y. Wang, J. W. Choe, K. Pu, R. Devulapally, S. Bachawal, S. Machtaler, S. M. Chowdhury, R. Luong, L. Tian, B. Khuri-Yakub, J. Rao, R. Paulmurugan, and J. K. Willmann. "Ultrasound-guided delivery of microRNA loaded nanoparticles into cancer", J Control Release, 203, pp. 99-108, (2015).

[76] VisualSonics, PN11691 - Vevo MicroMarkerTM Non-Targeted Contrast Agent Kit: Protocol and Information Booklet Rev 1.4, 2016.

[77] B. Theek, M. Baues, T. Ojha, D. Mockel, S. K. Veettil, J. Steitz, L. van Bloois, G. Storm, F. Kiessling, and T. Lammers. "Sonoporation enhances liposome accumulation and penetration in tumors with low EPR", J Control Release, 231, pp. 77-85, (2016).

[78] S. Eggen, S.-M. Fagerland, Ý. Mørch, R. Hansen, K. Søvik, S. Berg, H. Furu, A. D. Bøhn, M. B. Lilledahl, A. Angelsen, B. Angelsen, and C. de Lange Davies. "Ultrasound-enhanced drug delivery in prostate cancer xenografts by nanoparticles stabilizing microbubbles", Journal of Controlled Release, 187, pp. 39-49, (2014).

[79] A. J. Dixon, J. Li, J. M. R. Rickel, A. L. Klibanov, Z. Y. Zuo, and J. A. Hossack. "Efficacy of Sonothrombolysis Using Microbubbles Produced by a Catheter-Based Microfluidic Device in a Rat Model of Ischemic Stroke", Ann Biomed Eng, 47, pp. 1012-1022, (2019).

[80] S. M. Fix, V. Papadopoulou, H. Velds, S. K. Kasoji, J. N. Rivera, M. A. Borden, S. Chang, and P. A. Dayton. "Oxygen microbubbles improve radiotherapy tumor control in a rat fibrosarcoma model - A preliminary study", Plos One, 13, (2018).

[81] R. Pandit, G. Leinenga, and J. Götz. "Repeated ultrasound treatment of tau transgenic mice clears neuronal tau by autophagy and improves behavioral functions", Theranostics, 9, pp. 3754-3767, (2019).

[82] H. Dewitte, K. Vanderperren, H. Haers, E. Stock, L. Duchateau, M. Hesta, J. H. Saunders, S. C. De Smedt, I. Lentacker, and S. C. De. "Theranostic mRNA-loaded Microbubbles in the Lymphatics of Dogs: Implications for Drug Delivery", Theranostics, 5, pp. 97-109, (2015).

[83] H. Horsley, J. Owen, R. Browning, D. Carugo, J. Malone-Lee, E. Stride, and J. L. Rohn. "Ultrasound-activated microbubbles as a novel intracellular drug delivery system for urinary tract infection", Journal of Controlled Release, 301, pp. 166-175, (2019).

[84] Y. J. Bae, Y. I. Yoon, T. J. Yoon, and H. J. Lee. "Ultrasound-Guided Delivery of siRNA and a Chemotherapeutic Drug by Using Microbubble Complexes: In Vitro and In Vivo Evaluations in a Prostate Cancer Model", Korean J Radiol, 17, pp. 497-508, (2016).

[85] J. T. Sutton, J. L. Raymond, M. C. Verleye, G. J. Pyne-Geithman, and C. K. Holland. "Pulsed ultrasound enhances the delivery of nitric oxide from bubble liposomes to ex vivo porcine carotid tissue", International Journal of Nanomedicine, 9, pp. 4671-4683, (2014).

[86] C. McEwan, J. Owen, E. Stride, C. Fowley, H. Nesbitt, D. Cochrane, C. C. Coussios, M. Borden, N. Nomikou, A. P. McHale, and J. F. Callan. "Oxygen carrying microbubbles for enhanced sonodynamic therapy of hypoxic tumours", Journal of Controlled Release, 203, pp. 51-56, (2015).

[87] S. Rossi, C. Szíjjártó, F. Gerber, G. Waton, and M. P. Krafft. "Fluorous materials in microbubble engineering science and technology—Design and development of new bubble preparation and sizing technologies", Journal of Fluorine Chemistry, 132, pp. 1102-1109, (2011).

[88] H. Nesbitt, Y. Sheng, S. Kamila, K. Logan, K. Thomas, B. Callan, M. A. Taylor, M. Love, D. O'Rourke, P. Kelly, E. Beguin, E. Stride, A. P. McHale, and J. F. Callan. "Gemcitabine loaded microbubbles for targeted chemo-sonodynamic therapy of pancreatic cancer", Journal of Controlled Release, 279, pp. 8-16, (2018).

[89] H. Kim, G. L. Britton, T. Peng, C. K. Holland, D. D. McPherson, and S. L. Huang. "Nitric oxide-loaded echogenic liposomes for treatment of vasospasm following subarachnoid hemorrhage", Int J Nanomedicine, 9, pp. 155-165, (2014).

[90] Y. He, B. Zhang, Y. Chen, Q. Jin, J. Wu, F. Yan, and H. Zheng. "Image-Guided Hydrogen Gas Delivery for Protection from Myocardial Ischemia-Reperfusion Injury via Microbubbles", ACS Applied Materials and Interfaces, 9, pp. 21190-21199, (2017).

[91] S. Chen, J. Chen, X. L. Meng, J. S. Shen, J. Huang, P. Huang, Z. Pu, N. H. McNeill, and P. A. Grayburn. "ANGPTL8 reverses established adriamycin cardiomyopathy by stimulating adult cardiac progenitor cells", Oncotarget, 7, pp. 80391-80403, (2016).

[92] Y. Y. Fu, L. Zhang, Y. Yang, C. W. Liu, Y. N. He, P. Li, and X. Yu. "Synergistic antibacterial effect of ultrasound microbubbles combined with chitosan-modified polymyxin B-loaded liposomes on biofilm-producing Acinetobacter baumannii", Int J Nanomedicine, 14, pp. 1805-1815, (2019).

[93] J. P. Kilroy, A. L. Klibanov, B. R. Wamhoff, D. K. Bowles, and J. A. Hossack. "Localized in vivo model drug delivery with intravascular ultrasound and microbubbles", Ultrasound in Medicine and Biology, 40, pp. 2458-2467, (2014).

[94] G. Bioley, A. Lassus, J. Terrettaz, F. Tranquart, and B. Corthesy. "Long-term persistence of immunity induced by OVA-coupled gas-filled microbubble vaccination partially protects mice against infection by OVA-expressing Listeria", Biomaterials, 57, pp. 153-160, (2015).

[95] Y. Dong, Y. Xu, P. Li, C. Wang, Y. Cao, and J. Yu. "Antibiofilm effect of ultrasound combined with microbubbles against Staphylococcus epidermidis biofilm", International Journal of Medical Microbiology, 307, pp. 321-328, (2017).

[96] A. Goyal, F. T. H. Yu, M. G. Tenwalde, X. C. Chen, A. Althouse, F. S. Villanueva, and J. J. Pacella. "Inertial Cavitation Ultrasound with Microbubbles Improves Reperfusion Efficacy When Combined with Tissue Plasminogen Activator in an in Vitro Model of Microvascular Obstruction", Ultrasound Med Biol, 43, pp. 1391-1400, (2017).

[97] J. T. Belcik, B. P. Davidson, A. Xie, M. D. Wu, M. Yadava, Y. Qi, S. Liang, C. R. Chon, A. Y. Ammi, J. Field, L. Harmann, W. M. Chilian, J. Linden, and J. R. Lindner. "Augmentation of Muscle Blood Flow by Ultrasound Cavitation Is Mediated by ATP and Purinergic Signaling", Circulation, 135, pp. 1240-1252, (2017).

[98] Y. J. Ho, T. C. Wang, C. H. Fan, and C. K. Yeh. "Spatially Uniform Tumor Treatment and Drug Penetration by Regulating Ultrasound with Microbubbles", ACS Applied Materials and Interfaces, 10, pp. 17784-17791, (2018).

[99] J. T. Belcik, B. H. Mott, A. Xie, Y. Zhao, S. Kim, N. J. Lindner, A. Ammi, J. M. Linden, and J. R. Lindner. "Augmentation of limb perfusion and reversal of tissue ischemia produced by ultrasound-mediated microbubble cavitation", Circulation: Cardiovascular Imaging, 8, pp. 1-9, (2015).

[100] E. Stride, T. Segers, G. Lajoinie, S. Cherkaoui, T. Bettinger, M. Versluis, and M. Borden. "Microbubble Agents: New Directions", Ultrasound Med Biol, 46, pp. 1326-1343, (2020).

[101] S. Snipstad, S. Berg, Y. Morch, A. Bjorkoy, E. Sulheim, R. Hansen, I. Grimstad, A. van Wamel, A. F. Maaland, S. H. Torp, and C. de Lange Davies. "Ultrasound Improves the Delivery and Therapeutic Effect of Nanoparticle-Stabilized Microbubbles in Breast Cancer Xenografts", Ultrasound Med Biol, 43, pp. 2651-2669, (2017).

[102] C. McEwan, S. Kamila, J. Owen, H. Nesbitt, B. Callan, M. Borden, N. Nomikou, R. A. Hamoudi, M. A. Taylor, E. Stride, A. P. McHale, and J. F. Callan. "Combined sonodynamic and antimetabolite therapy for the improved treatment of pancreatic cancer using oxygen loaded microbubbles as a delivery vehicle", Biomaterials, 80, pp. 20-32, (2016).

[103] J. J. Choi, R. C. Carlisle, C. Coviello, L. Seymour, and C.-C. Coussios. "Non-invasive and real-time passive acoustic mapping of ultrasound-mediated drug delivery", Physics in Medicine and Biology, 59, pp. 4861-4877, (2014).

[104] H. Shekhar, K. B. Bader, S. W. Huang, T. Peng, S. L. Huang, D. D. McPherson, and C. K. Holland. "In vitro thrombolytic efficacy of echogenic liposomes loaded with tissue plasminogen activator and octafluoropropane gas", Phys Med Biol, 62, pp. 517-538, (2017).

[105] S. Kotopoulis, E. Stigen, M. Popa, M. M. Safont, A. Healey, S. Kvåle, P. Sontum, B. T. Gjertsen, O. H. Gilja, and E. McCormack. "Sonoporation with Acoustic Cluster Therapy (ACT®) induces transient tumour volume reduction in a subcutaneous xenograft model of pancreatic ductal adenocarcinoma", Journal of Controlled Release, 245, pp. 70-80, (2017).

[106] (!!! INVALID CITATION !!! [106]).

[107] OptisonTM. US Food and Drug Administration, (2012).

[108] N. Xiao, J. Liu, L. Liao, J. Sun, W. Jin, and X. Shu. "Ultrasound Combined With Microbubbles Increase the Delivery of Doxorubicin by Reducing the Interstitial Fluid Pressure", Ultrasound Quarterly, 35, pp. 103-109, (2019).

[109] A. H. Payne, G. W. Hawryluk, Y. Anzai, H. Odéen, M. A. Ostlie, E. C. Reichert, A. J. Stump, S. Minoshima, and D. J. Cross. "Magnetic resonance imaging-guided focused ultrasound to increase localized blood-spinal cord barrier permeability", Neural Regeneration Research, 12, pp. 2045-2049, (2017).

[110] N. S. S. Maria, S. R. Barnes, M. R. Weist, D. Colcher, A. A. Raubitschek, and R. E. Jacobs. "Low dose focused ultrasound induces enhanced tumor accumulation of natural killer cells", PLoS ONE, 10, (2015).

[111] Y. Cao, Y. Chen, T. Yu, Y. Guo, F. Liu, Y. Yao, P. Li, D. Wang, Z. Wang, Y. Chen, and H. Ran. "Drug Release from Phase-Changeable Nanodroplets Triggered by Low-Intensity Focused Ultrasound", Theranostics, 8, pp. 1327-1339, (2018).

[112] R. Myers, C. Coviello, P. Erbs, J. Foloppe, C. Rowe, J. Kwan, C. Crake, S. Finn, E. Jackson, J.-M. Balloul, C. Story, C. Coussios, and R. Carlisle. "Polymeric Cups for Cavitation-mediated Delivery of Oncolytic Vaccinia Virus", Molecular therapy : the journal of the American Society of Gene Therapy, 24, pp. 1627-1633, (2016).

[113] S. Y. Wu, S. M. Fix, C. B. Arena, C. C. Chen, W. Zheng, O. O. Olumolade, V. Papadopoulou, A. Novell, P. A. Dayton, and E. E. Konofagou. "Focused ultrasound-facilitated brain drug delivery using optimized nanodroplets: vaporization efficiency dictates large molecular delivery", Phys Med Biol, 63, p. 035002, (2018).

[114] H. Guo, Z. Wang, Q. Du, P. Li, Z. Wang, and A. Wang. "Stimulated phase-shift acoustic nanodroplets enhance vancomycin efficacy against methicillin-resistant Staphylococcus aureus biofilms", International Journal of Nanomedicine, 12, pp. 4679-4690, (2017).

[115] H. G. Flynn. "Cavitation Dynamics: I. Mathematical Formulation", J Acoust Soc Am, 57, pp. 1379-1396, (1975).

[116] H. G. Flynn. "Cavitation Dynamics: II. Free pulsations and models for cavitation bubbles", J Acoust Soc Am, 58, pp. 1160-1170, (1975).

[117] A. van Wamel, K. Kooiman, M. Harteveld, M. Emmer, F. J. ten Cate, M. Versluis, and N. de Jong. "Vibrating microbubbles poking individual cells: Drug transfer into cells via sonoporation", J Control Release, 112, pp. 149-155, (2006).

[118] N. Kudo. "High-Speed In Situ Observation System for Sonoporation of Cells With Size- and Position-Controlled Microbubbles", IEEE Trans Ultrason Ferroelectr Freq Control, 64, pp. 273-280, (2017).

[119] H. Chen, A. A. Brayman, W. Kreider, M. R. Bailey, and T. J. Matula. "Observations of translation and jetting of ultrasound-activated microbubbles in mesenteric microvessels", Ultrasound Med Biol, 37, pp. 2139-2148, (2011).

[120] P. Dayton, A. Klibanov, G. Brandenburger, and K. Ferrara. "Acoustic radiation force in vivo: a mechanism to assist targeting of microbubbles", Ultrasound Med Biol, 25, pp. 1195-1201, (1999).

[121] C. N. Acconcia, B. Y. Leung, and D. E. Goertz. "The microscale evolution of the erosion front of blood clots exposed to ultrasound stimulated microbubbles", J Acoust Soc Am, 139, p. EL135, (2016).

[122] K. B. Bader, M. J. Gruber, and C. K. Holland. "Shaken and Stirred: Mechanisms of Ultrasound-Enhanced Thrombolysis", Ultrasound in Medicine and Biology, 41, pp. 187-196, (2015).

[123] C. F. Caskey, S. Qin, P. A. Dayton, and K. W. Ferrara. "Microbubble tunneling in gel phantoms", J Acoust Soc Am, 125, pp. EL183-189, (2009).

[124] J. Kolb and W. L. Nyborg. "Small-Scale Acoustic Streaming in Liquids", J Acoust Soc Am, 28, pp. 1237-1242, (1956).

[125] V. C. Pereno and E. Stride. "Cavitation induced intracellular streaming", (under review), (2018).

[126] W. L. Nyborg. "Acoustic Streaming near a Boundary", J Acoust Soc Am, 30, pp. 329-339, (1958).

[127] P. Marmottant and S. Hilgenfeldt. "Controlled vesicle deformation and lysis by single oscillating bubbles", Nature, 423, pp. 153-156, (2003).

[128] C. F. Naudé and A. T. Ellis. "On the Mechanism of Cavitation Damage by Nonhemispherical Cavities Collapsing in Contact With a Solid Boundary", J Basic Eng, 83, pp. 648-656, (1961).

[129] T. B. Benjamin and A. T. Ellis. "The Collapse of Cavitation Bubbles and the Pressures thereby Produced against Solid Boundaries", Phil Trans R Soc A, 260, pp. 221-240, (1966).

[130] N. Kudo and Y. Kinoshita. "Effects of cell culture scaffold stiffness on cell membrane damage induced by sonoporation", J Med Ultrason, 41, pp. 411-420, (2014).

[131] S. Hilgenfeldt, D. Lohse, and M. Zomack. "Sound scattering and localized heat deposition of pulse-driven microbubbles", J Acoust Soc Am, 107, pp. 3530-3539, (2000).

[132] R. G. Holt and R. A. Roy. "Measurements of bubble-enhanced heating from focused, MHz-frequency ultrasound in a tissue-mimicking material", Ultrasound Med Biol, 27, pp. 1399-1412, (2001).

[133] A. Prosperetti. "Thermal Effects and Damping Mechanisms in Forced Radial Oscillations of Gas-Bubbles in Liquids", J Acoust Soc Am, 61, pp. 17-27, (1977).

[134] E. B. Flint and K. S. Suslick. "The temperature of cavitation", Science, 253, pp. 1397-1399, (1991).

[135] C. C. Winterbourn. "Reconciling the chemistry and biology of reactive oxygen species", Nat Chem Biol, 4, pp. 278-286, (2008).

[136] D. Trachootham, J. Alexandre, and P. Huang. "Targeting cancer cells by ROS-mediated mechanisms: a radical therapeutic approach?", Nat Rev Drug Discov, 8, pp. 579-591, (2009).

[137] I. Rosenthal, J. Z. Sostaric, and P. Riesz. "Sonodynamic therapy--a review of the synergistic effects of drugs and ultrasound", Ultrason Sonochem, 11, pp. 349-363, (2004).

[138] E. Beguin, S. Shrivastava, N. V. Dezhkunov, A. P. McHale, J. F. Callan, and E. Stride. "Direct Evidence of Multibubble Sonoluminescence Using Therapeutic Ultrasound and Microbubbles", ACS Appl Mater Interfaces, 11, pp. 19913-19919, (2019).

[139] O. D. Kripfgans, J. B. Fowlkes, D. L. Miller, O. P. Eldevik, and P. L. Carson. "Acoustic droplet vaporization for therapeutic and diagnostic applications", Ultrasound Med Biol, 26, pp. 1177-1189, (2000).

[140] G. P. Biro and P. Blais. "Perfluorocarbon blood substitutes", Crit Rev Oncol Hematol, 6, pp. 311-374, (1987).

[141] P. S. Sheeran and P. A. Dayton. "Phase-change contrast agents for imaging and therapy", Curr Pharm Des, 18, pp. 2152-2165, (2012).

[142] H. Lea-Banks, M. A. O'Reilly, and K. Hynynen. "Ultrasound-responsive droplets for therapy: A review", J Control Release, 293, pp. 144-154, (2019).

[143] T. Lammers, F. Kiessling, W. E. Hennink, and G. Storm. "Drug targeting to tumors: Principles, pitfalls and (pre-) clinical progress", J Control Release, 161, pp. 175-187, (2012).

[144] H. Maeda. "Macromolecular therapeutics in cancer treatment: The EPR effect and beyond", J Control Release, 164, pp. 138-144, (2012).

[145] D. M. Long, F. K. Multer, A. G. Greenburg, G. W. Peskin, E. C. Lasser, W. G. Wickham, and C. M. Sharts. "Tumor imaging with x-rays using macrophage uptake of radiopaque fluorocarbon emulsions", Surgery, 84, pp. 104-112, (1978).

[146] J. A. Kopechek, E. Park, C. S. Mei, N. J. McDannold, and T. M. Porter. "Accumulation of phase-shift nanoemulsions to enhance MR-guided ultrasound-mediated tumor ablation in vivo", J Healthc Eng, 4, pp. 109-126, (2013).

[147] N. Y. Rapoport, A. M. Kennedy, J. E. Shea, C. L. Scaife, and K. H. Nam. "Controlled and targeted tumor chemotherapy by ultrasound-activated nanoemulsions/microbubbles", J Control Release, 138, pp. 268-276, (2009).

[148] K. Radhakrishnan, C. K. Holland, and K. J. Haworth. "Scavenging dissolved oxygen via acoustic droplet vaporization", Ultrason Sonochem, 31, pp. 394-403, (2016).

[149] O. Shpak, M. Verweij, H. J. Vos, N. de Jong, D. Lohse, and M. Versluis. "Acoustic droplet vaporization is initiated by superharmonic focusing", Proc Natl Acad Sci U S A, 111, pp. 1697-1702, (2014).

[150] O. Shpak, M. Verweij, N. de Jong, and M. Versluis. "Droplets, Bubbles and Ultrasound Interactions", Adv Exp Med Biol, 880, pp. 157-174, (2016).

[151] M. F. Hamilton and D. T. Blackstock, Nonlinear acoustics. Melville: Acoustical Society of America, 2008.

[152] M. T. Burgess and T. M. Porter. "Control of Acoustic Cavitation for Efficient Sonoporation with Phase-Shift Nanoemulsions", Ultrasound Med Biol, 45, pp. 846-858, (2019).

[153] I. Lentacker, I. De Cock, R. Deckers, S. C. De Smedt, and C. T. Moonen. "Understanding ultrasound induced sonoporation: definitions and underlying mechanisms", Adv Drug Deliv Rev, 72, pp. 49-64, (2014).

[154] P. Qin, T. Han, A. C. H. Yu, and L. Xu. "Mechanistic understanding the bioeffects of ultrasound-driven microbubbles to enhance macromolecule delivery", J Control Release, 272, pp. 169-181, (2018).

[155] R. S. Leow, J. M. Wan, and A. C. Yu. "Membrane blebbing as a recovery manoeuvre in site-specific sonoporation mediated by targeted microbubbles", J R Soc Interface, 12, (2015).

[156] D. Qin, L. Zhang, N. Chang, P. Ni, Y. Zong, A. Bouakaz, M. Wan, and Y. Feng. "In situ observation of single cell response to acoustic droplet vaporization: Membrane deformation, permeabilization, and blebbing", Ultrason Sonochem, 47, pp. 141-150, (2018).

[157] Y. Yuana, L. Jiang, B. H. A. Lammertink, P. Vader, R. Deckers, C. Bos, R. M. Schiffelers, and C. T. Moonen. "Microbubbles-Assisted Ultrasound Triggers the Release of Extracellular Vesicles", Int J Mol Sci, 18, (2017).

[158] H. Cho, H. Y. Lee, M. Han, J. R. Choi, S. Ahn, T. Lee, Y. Chang, and J. Park. "Localized Down-regulation of P-glycoprotein by Focused Ultrasound and Microbubbles induced Blood-Brain Barrier Disruption in Rat Brain", Sci Rep, 6, p. 31201, (2016).

[159] M. Aryal, K. Fischer, C. Gentile, S. Gitto, Y. Z. Zhang, and N. McDannold. "Effects on P-Glycoprotein Expression after Blood-Brain Barrier Disruption Using Focused Ultrasound and Microbubbles", PLoS One, 12, p. e0166061, (2017).

[160] D. McMahon, E. Mah, and K. Hynynen. "Angiogenic response of rat hippocampal vasculature to focused ultrasound-mediated increases in blood-brain barrier permeability", Scientific RePoRTS, 8, pp. 12178-12178, (2018).

[161] Y. Hu, J. M. Wan, and A. C. Yu. "Membrane perforation and recovery dynamics in microbubble-mediated sonoporation", Ultrasound Med Biol, 39, pp. 2393-2405, (2013).

[162] X. Chen, R. S. Leow, Y. Hu, J. M. Wan, and A. C. Yu. "Single-site sonoporation disrupts actin cytoskeleton organization", J R Soc Interface, 11, p. 20140071, (2014).

[163] C. Jia, L. Xu, T. Han, P. Cai, A. C. H. Yu, and P. Qin. "Generation of Reactive Oxygen Species in Heterogeneously Sonoporated Cells by Microbubbles with Single-Pulse Ultrasound", Ultrasound Med Biol, 44, pp. 1074-1085, (2018).

[164] B. Helfield, X. Chen, S. C. Watkins, and F. S. Villanueva. "Biophysical insight into mechanisms of sonoporation", Proc Natl Acad Sci U S A, 113, pp. 9983-9988, (2016).

[165] I. De Cock, E. Zagato, K. Braeckmans, Y. Luan, N. de Jong, S. C. De Smedt, and I. Lentacker. "Ultrasound and microbubble mediated drug delivery: acoustic pressure as determinant for uptake via membrane pores or endocytosis", J Control Release, 197, pp. 20-28, (2015).

[166] A. Zeghimi, J. M. Escoffre, and A. Bouakaz. "Role of endocytosis in sonoporation-mediated membrane permeabilization and uptake of small molecules: a electron microscopy study", Phys Biol, 12, p. 066007, (2015).

[167] F. Fekri, R. C. Delos Santos, R. Karshafian, and C. N. Antonescu. "Ultrasound Microbubble Treatment Enhances Clathrin-Mediated Endocytosis and Fluid-Phase Uptake through Distinct Mechanisms", PLoS One, 11, p. e0156754, (2016).

[168] F. T. H. Yu, X. Chen, A. C. Straub, and J. J. Pacella. "The Role of Nitric Oxide during Sonoreperfusion of Microvascular Obstruction", Theranostics, 7, pp. 3527-3538, (2017).

[169] T. van Rooij, I. Skachkov, I. Beekers, K. R. Lattwein, J. D. Voorneveld, T. J. Kokhuis, D. Bera, Y. Luan, A. F. van der Steen, N. de Jong, and K. Kooiman. "Viability of endothelial cells after ultrasound-mediated sonoporation: Influence of targeting, oscillation, and displacement of microbubbles", J Control Release, 238, pp. 197-211, (2016).

[170] Y. W. Han, A. Ikegami, P. Chung, L. Zhang, and C. X. Deng. "Sonoporation is an efficient tool for intracellular fluorescent dextran delivery and one-step double-crossover mutant construction in Fusobacterium nucleatum", Appl Environ Microbiol, 73, pp. 3677-3683, (2007).

[171] S. Li, C. Zhu, S. Fang, W. Zhang, N. He, W. Xu, R. Kong, and X. Shang. "Ultrasound microbubbles enhance human beta-defensin 3 against biofilms", J Surg Res, 199, pp. 458-469, (2015).

[172] Z. Zhou, D. I. Tai, Y. L. Wan, J. H. Tseng, Y. R. Lin, S. Wu, K. C. Yang, Y. Y. Liao, C. K. Yeh, and P. H. Tsui. "Hepatic Steatosis Assessment with Ultrasound Small-Window Entropy Imaging", Ultrasound Med Biol, 44, pp. 1327-1340, (2018).

[173] B. Dollet, P. Marmottant, and V. Garbin. "Bubble dynamics in soft and biological matter", Annu Rev Fluid Mech, 51, pp. 331-355, (2019).

[174] T. Faez, M. Emmer, K. Kooiman, M. Versluis, A. F. van der Steen, and N. de Jong. "20 years of ultrasound contrast agent modeling", IEEE Trans Ultrason Ferroelectr Freq Control, 60, pp. 7-20, (2013).

[175] X. Guo, C. Cai, G. Xu, Y. Yang, J. Tu, P. Huang, and D. Zhang. "Interaction between cavitation microbubble and cell: A simulation of sonoporation using boundary element method (BEM)", Ultrason Sonochem, 39, pp. 863-871, (2017).

[176] A. A. Doinikov and A. Bouakaz. "Theoretical investigation of shear stress generated by a contrast microbubble on the cell membrane as a mechanism for sonoporation", J Acoust Soc Am, 128, pp. 11-19, (2010).

[177] J. Cowley and S. McGinty. "A mathematical model of sonoporation using a liquid-crystalline shelled microbubble", Ultrasonics, 96, pp. 214-219, (2019).

[178] H. Yu and S. Chen. "A model to calculate microstreaming-shear stress generated by oscillating microbubbles on the cell membrane in sonoporation", Biomed Mater Eng, 24, pp. 861-868, (2014).

[179] M. M. Forbes and W. D. O'Brien, Jr. "Development of a theoretical model describing sonoporation activity of cells exposed to ultrasound in the presence of contrast agents", J Acoust Soc Am, 131, pp. 2723-2729, (2012).

[180] J. Wu. "Theoretical study on shear stress generated by microstreaming surrounding contrast agents attached to living cells", Ultrasound Med Biol, 28, pp. 125-129, (2002).

[181] W. Li, T. Yuan, G. Xia-Sheng, X. Di, and Z. Dong. "Microstreaming velocity field and shear stress created by an oscillating encapsulated microbubble near a cell membrane", Chin Phys B, 23, p. 124302, (2014).

[182] C. F. Rowlatt and S. J. Lind. "Bubble collapse near a fluid-fluid interface using the spectral element marker particle method with applications in bioengineering", Int J Multiphas Flow, 90, pp. 118-143, (2017).

[183] H. Yu, Z. Lin, L. Xu, D. Liu, and Y. Shen. "Theoretical study of microbubble dynamics in sonoporation", Ultrasonics, 61, pp. 136-144, (2015).

[184] V. H. Man, P. M. Truong, M. S. Li, J. Wang, N. T. Van-Oanh, P. Derreumaux, and P. H. Nguyen. "Molecular Mechanism of the Cell Membrane Pore Formation Induced by Bubble Stable Cavitation", J Phys Chem B, 123, pp. 71-78, (2019).

[185] K. Koshiyama and S. Wada. "Molecular dynamics simulations of pore formation dynamics during the rupture process of a phospholipid bilayer caused by high-speed equibiaxial stretching", J Biomech, 44, pp. 2053-2058, (2011).

[186] L. L. Zhang, Z. S. Zhang, M. Negahban, and A. Jerusalem. "Molecular dynamics simulation of cell membrane pore sealing", Extreme Mech Lett, 27, pp. 83-93, (2019).

[187] Z. Fan, H. Liu, M. Mayer, and C. X. Deng. "Spatiotemporally controlled single cell sonoporation", Proc Natl Acad Sci U S A, 109, pp. 16486-16491, (2012).

[188] Z. Fan, D. Chen, and C. X. Deng. "Improving ultrasound gene transfection efficiency by controlling ultrasound excitation of microbubbles", J Control Release, 170, pp. 401-413, (2013).

[189] N. Hosseinkhah, D. E. Goertz, and K. Hynynen. "Microbubbles and blood-brain barrier opening: a numerical study on acoustic emissions and wall stress predictions", IEEE Trans Biomed Eng, 62, pp. 1293-1304, (2015).

[190] W. Wiedemair, Z. Tukovic, H. Jasak, D. Poulikakos, and V. Kurtcuoglu. "The breakup of intravascular microbubbles and its impact on the endothelium", Biomech Model Mechanobiol, 16, pp. 611-624, (2017).

[191] M. R. Junttila and F. J. de Sauvage. "Influence of tumour micro-environment heterogeneity on therapeutic response", Nature, 501, pp. 346-354, (2013).

[192] Y. Barenholz. "Doxil (R) - The first FDA-approved nano-drug: Lessons learned", J Control Release, 160, pp. 117-134, (2012).

[193] G. Mehta, A. Y. Hsiao, M. Ingram, G. D. Luker, and S. Takayama. "Opportunities and challenges for use of tumor spheroids as models to test drug delivery and efficacy", J Control Release, 164, pp. 192-204, (2012).

[194] L. Zhang, T. H. Yin, B. Li, R. Q. Zheng, C. Qiu, K. S. Lam, Q. Zhang, and X. T. Shuai. "Size-Modulable Nanoprobe for High-Performance Ultrasound Imaging and Drug Delivery against Cancer", Acs Nano, 12, pp. 3449-3460, (2018).

[195] J. A. Kopechek, A. R. Carson, C. F. McTiernan, X. Chen, B. Hasjim, L. Lavery, M. Sen, J. R. Grandis, and F. S. Villanueva. "Ultrasound Targeted Microbubble Destruction-Mediated Delivery of a Transcription Factor Decoy Inhibits STAT3 Signaling and Tumor Growth", Theranostics, 5, pp. 1378-1387, (2015).

[196] Y. Zhou, H. Gu, Y. Xu, F. Li, S. Kuang, Z. Wang, X. Zhou, H. Ma, P. Li, Y. Zheng, H. Ran, J. Jian, Y. Zhao, W. Song, Q. Wang, and D. Wang. "Targeted antiangiogenesis gene therapy using targeted cationic microbubbles conjugated with CD105 antibody compared with untargeted cationic and neutral microbubbles", Theranostics, 5, pp. 399-417, (2015).

[197] Y. L. Wei, N. Shang, H. Jin, Y. He, Y. W. Pan, N. N. Xiao, J. L. Wei, S. Y. Xiao, L. P. Chen, and J. H. Liu. "Penetration of different molecule sizes upon ultrasound combined with microbubbles in a superficial tumour model", J Drug Target, (2019).

[198] C. P. Keravnou, I. De Cock, I. Lentacker, M. L. Izamis, and M. A. Averkiou. "Microvascular Injury and Perfusion Changes Induced by Ultrasound and Microbubbles in a Machine-Perfused Pig Liver", Ultrasound in Medicine and Biology, 42, pp. 2676-2686, (2016).

[199] D. E. Goertz. "An overview of the influence of therapeutic ultrasound exposures on the vasculature: High intensity ultrasound and microbubble-mediated bioeffects", International Journal of Hyperthermia, 31, pp. 134-144, (2015).

[200] P. T. Yemane, A. Aslund, K. G. Saeterbo, A. Bjorkoy, S. Snipstad, A. Van Wamel, S. Berg, Y. Morch, R. Hansen, B. Angelsen, and C. D. Davies, "The effect of sonication on extravasation and distribution of nanoparticles and dextrans in tumor tissue imaged by multiphoton microscopy," in IEEE International Ultrasonics Symposium, Japan, 2018.

[201] X. Hu, A. Kheirolomoom, L. M. Mahakian, J. R. Beegle, D. E. Kruse, K. S. Lam, and K. W. Ferrara. "Insonation of targeted microbubbles produces regions of reduced blood flow within tumor vasculature", Invest Radiol, 47, pp. 398-405, (2012).

[202] J. Yang, X. J. Zhang, H. J. Cai, Z. K. Chen, Q. F. Qian, E. S. Xue, and L. W. Lin. "Ultrasound-targeted microbubble destruction improved the antiangiogenic effect of Endostar in triple-negative breast carcinoma xenografts", J Cancer Res Clin, 145, pp. 1191-1200, (2019).

[203] J. F. Wang, Z. L. Zhao, S. X. Shen, C. X. Zhang, S. C. Guo, Y. K. Lu, Y. M. Chen, W. J. Liao, Y. L. Liao, and J. P. Bin. "Selective depletion of tumor neovasculature by microbubble destruction with appropriate ultrasound pressure", Int J Cancer, 137, pp. 2478-2491, (2015).

[204] A. Daecher, M. Stanczak, J. B. Liu, J. Zhang, S. S. Du, F. Forsberg, D. B. Leeper, and J. R. Eisenbrey. "Localized microbubble cavitation-based antivascular therapy for improving HCC treatment response to radiotherapy", Cancer Letters, 411, pp. 100-105, (2017).

[205] P. Lai, C. Tarapacki, W. T. Tran, A. El Kaffas, J. Lee, C. Hupple, S. Iradji, A. Giles, A. Al-Mahrouki, and G. J. Czarnota. "Breast tumor response to ultrasound mediated excitation of microbubbles and radiation therapy in vivo", Oncoscience, 3, pp. 98-108, (2016).

[206] H. Lea-Banks, B. Teo, E. Stride, and C. C. Coussios. "The effect of particle density on ultrasound-mediated transport of nanoparticles", Phys Med Biol, 61, pp. 7906-7918, (2016).

[207] F. Yan, L. Li, Z. T. Deng, Q. F. Jin, J. J. Chen, W. Yang, C. K. Yeh, J. R. Wu, R. Shandas, X. Liu, and H. R. Zheng. "Paclitaxel-liposome-microbubble complexes as ultrasound-triggered therapeutic drug delivery carriers", J Control Release, 166, pp. 246-255, (2013).

[208] C. W. Burke, E. Alexander, K. Timbie, A. L. Kilbanov, and R. J. Price. "Ultrasound-activated agents comprised of 5FU-bearing nanoparticles bonded to microbubbles inhibit solid tumor growth and improve survival", Molecular Therapy, 22, pp. 321-328, (2014).

[209] W. X. Luo, G. Wen, L. Yang, J. Tang, J. G. Wang, J. H. Wang, S. Y. Zhang, L. Zhang, F. Ma, L. L. Xiao, Y. Wang, and Y. J. Li. "Dual-targeted and pH-sensitive Doxorubicin Prodrug-Microbubble Complex with Ultrasound for Tumor Treatment", Theranostics, 7, pp. 452-465, (2017).

[210] J. X. Liu, F. F. Xu, J. Huang, J. S. Xu, Y. Liu, Y. Z. Yao, M. Ao, A. Li, L. Hao, Y. Cao, Z. Q. Hu, H. T. Ran, Z. G. Wang, and P. Li. "Low-intensity focused ultrasound (LIFU)-activated nanodroplets as a theranostic agent for noninvasive cancer molecular imaging and drug delivery", Biomater Sci, 6, (2018).

[211] Y. F. Zhou. "Application of acoustic droplet vaporization in ultrasound therapy", J Ther Ultrasound, 3, (2015).

[212] A. van Wamel, P. C. Sontum, A. Healey, S. Kvale, N. Bush, J. Bamber, and C. D. Davies. "Acoustic Cluster Therapy (ACT) enhances the therapeutic efficacy of paclitaxel and Abraxane (R) for treatment of human prostate adenocarcinoma in mice", J Control Release, 236, pp. 15-21, (2016).

[213] R. Gupta, J. Shea, C. Scafe, A. Shurlygina, and N. Rapoport. "Polymeric micelles and nanoemulsions as drug carriers: Therapeutic efficacy, toxicity, and drug resistance", J Control Release, 212, pp. 70-77, (2015).

[214] H. S. Min, S. Son, D. G. You, T. W. Lee, J. Lee, S. Lee, J. Y. Yhee, J. Lee, M. H. Han, J. H. Park, S. H. Kim, K. Choi, K. Park, K. Kim, and I. C. Kwon. "Chemical gas-generating nanoparticles for tumor-targeted ultrasound imaging and ultrasound-triggered drug delivery", Biomaterials, 108, pp. 57-70, (2016).

[215] P. Sontum, S. Kvale, A. J. Healey, R. Skurtveit, R. Watanabe, M. Matsumura, and J. Ostensen. "Acoustic Cluster Therapy (ACT)--A novel concept for ultrasound mediated, targeted drug delivery", Int J Pharm, 495, pp. 1019-1027, (2015).

[216] J. A. Kopechek, E. J. Park, Y. Z. Zhang, N. I. Vykhodtseva, N. J. McDannold, and T. M. Porter. "Cavitation-enhanced MR-guided focused ultrasound ablation of rabbit tumors in vivo using phase shift nanoemulsions", Phys Med Biol, 59, pp. 3465-3481, (2014).

[217] S. Roovers, G. Lajoinie, I. De Cock, T. Brans, H. Dewitte, K. Braeckmans, M. Versuis, S. C. De Smedt, and I. Lentacker. "Sonoprinting of nanoparticle-loaded microbubbles: Unraveling the multi-timescale mechanism", Biomaterials, 217, pp. 119250-119250, (2019).

[218] Y. C. Park, C. Zhang, S. Kim, G. Mohamedi, C. Beigie, J. O. Nagy, R. G. Holt, R. O. Cleveland, N. L. Jeon, and J. Y. Wong. "Microvessels-on-a-chip to assess targeted ultrasound-assisted drug delivery", ACS Applied Materials and Interfaces, 8, pp. 31541-31549, (2016).

[219] I. Beekers, T. van Rooij, M. D. Verweij, M. Versluis, N. de Jong, S. J. Trietsch, and K. Kooiman. "Acoustic Characterization of a Vessel-on-a-Chip Microfluidic System for Ultrasound-Mediated Drug Delivery", IEEE Trans Ultrason Ferroelectr Freq Control, 65, pp. 570-581, (2018).

[220] S. Roovers, G. Lajoinie, J. Prakash, M. Versluis, S. C. De Smedt, and I. Lentacker. "Liposome-loaded microbubbles and ultrasound enhance drug delivery in a 3D tumor spheroid", Abstract book 24th Eur Symp Ultrasound Contrast Imaging, (2019).

[221] S. M. Graham, R. Carlisle, J. J. Choi, M. Stevenson, A. R. Shah, R. S. Myers, K. Fisher, M. B. Peregrino, L. Seymour, and C. C. Coussios. "Inertial cavitation to non-invasively trigger and monitor intratumoral release of drug from intravenously delivered liposomes", J Control Release, 178, pp. 101-107, (2014).

[222] K. J. Haworth, K. B. Bader, K. T. Rich, C. K. Holland, and T. D. Mast. "Quantitative Frequency-Domain Passive Cavitation Imaging", IEEE Trans Ultrason Ferroelectr Freq Control, 64, pp. 177-191, (2017).

[223] J. M. Escoffre, C. Mannaris, B. Geers, A. Novell, I. Lentacker, M. Averkiou, and A. Bouakaz. "Doxorubicin liposome-loaded microbubbles for contrast imaging and ultrasound-triggered drug delivery", IEEE Trans Ultrason Ferroelectr Freq Control, 60, pp. 78-87, (2013).

[224] J. L. Paris, C. Mannaris, M. V. Cabanas, R. Carlisle, M. Manzano, M. Vallet-Regi, and C. C. Coussios. "Ultrasound-mediated cavitation-enhanced extravasation of mesoporous silica nanoparticles for controlled-release drug delivery", Chem Eng J, 340, pp. 2-8, (2018).

[225] S. Y. Wang, C. Y. Wang, S. Unnikrishnan, A. L. Klibanov, J. A. Hossack, and F. W. Mauldin. "Optical Verification of Microbubble Response to Acoustic Radiation Force in Large Vessels With In Vivo Results", Invest Radiol, 50, pp. 772-784, (2015).

[226] S. Kotopoulis, G. Dimcevski, O. H. Gilja, D. Hoem, and M. Postema. "Treatment of human pancreatic cancer using combined ultrasound, microbubbles, and gemcitabine: a clinical case study", Med Phys, 40, p. 072902, (2013).

[227] G. Dimcevski, S. Kotopoulis, T. Bjanes, D. Hoem, J. Schjott, B. T. Gjertsen, M. Biermann, A. Molven, H. Sorbye, E. McCormack, M. Postema, and O. H. Gilja. "A human clinical trial using ultrasound and microbubbles to enhance gemcitabine treatment of inoperable pancreatic cancer", J Control Release, 243, pp. 172-181, (2016).

[228] Y. Wang, Y. Li, K. Yan, L. Shen, W. Yang, J. Gong, and K. Ding. "Clinical study of ultrasound and microbubbles for enhancing chemotherapeutic sensitivity of malignant tumors in digestive system", Chin J Cancer Res, 30, pp. 553-563, (2018).

[229] R. M. Steinman, G. Kaplan, M. D. Witmer, and Z. A. Cohn. "Identification of a novel cell type in peripheral lymphoid organs of mice. V. Purification of spleen dendritic cells, new surface markers, and maintenance in vitro", J Exp Med, 149, pp. 1-16, (1979).

[230] P. M. Santos and L. H. Butterfield. "Dendritic Cell-Based Cancer Vaccines", J Immunol, 200, pp. 443-449, (2018).

[231] H. Dewitte, S. Van Lint, C. Heirman, K. Thielemans, S. C. De Smedt, K. Breckpot, and I. Lentacker. "The potential of antigen and TriMix sonoporation using mRNA-loaded microbubbles for ultrasound-triggered cancer immunotherapy", Journal of Controlled Release, 194, pp. 28-36, (2014).

[232] A. R. Sever, P. Mills, J. Weeks, S. E. Jones, D. Fish, P. A. Jones, and W. Mali. "Preoperative needle biopsy of sentinel lymph nodes using intradermal microbubbles and contrast-enhanced ultrasound in patients with breast cancer", AJR Am J Roentgenol, 199, pp. 465-470, (2012).

[233] A. R. Sever, P. Mills, S. E. Jones, W. Mali, and P. A. Jones. "Sentinel node identification using microbubbles and contrast-enhanced ultrasonography", Clinical radiology, 67, pp. 687-694, (2012).

[234] W. Hu, G. Wang, D. Huang, M. Sui, and Y. Xu. "Cancer Immunotherapy Based on Natural Killer Cells: Current Progress and New Opportunities", Front Immunol, 10, p. 1205, (2019).

[235] C. Yee. "Adoptive T cell therapy: points to consider", Curr Opin Immunol, 51, pp. 197-203, (2018).

[236] D. N. Khalil, E. L. Smith, R. J. Brentjens, and J. D. Wolchok. "The future of cancer treatment: immunomodulation, CARs and combination immunotherapy", Nat Rev Clin Oncol, 13, p. 394, (2016).

[237] A. Gras Navarro, A. T. Bjorklund, and M. Chekenya. "Therapeutic potential and challenges of natural killer cells in treatment of solid tumors", Front Immunol, 6, p. 202, (2015).

[238] R. W. Childs and M. Carlsten. "Therapeutic approaches to enhance natural killer cell cytotoxicity against cancer: the force awakens", Nat Rev Drug Discov, 14, pp. 487-498, (2015).

[239] R. Alkins, A. Burgess, M. Ganguly, G. Francia, R. Kerbel, W. S. Wels, and K. Hynynen. "Focused ultrasound delivers targeted immune cells to metastatic brain tumors", Cancer Res, 73, pp. 1892-1899, (2013).

[240] R. Alkins, A. Burgess, R. Kerbel, W. S. Wels, and K. Hynynen. "Early treatment of HER2-amplified brain tumors with targeted NK-92 cells and focused ultrasound improves survival", Neuro-Oncology, 18, pp. 974-981, (2016).

[241] B. Marty, B. Larrat, M. Van Landeghem, C. Robic, P. Robert, M. Port, D. Le Bihan, M. Pernot, M. Tanter, F. Lethimonnier, and S. Meriaux. "Dynamic study of blood-brain barrier closure after its disruption using ultrasound: a quantitative analysis", J Cereb Blood Flow Metab, 32, pp. 1948-1958, (2012).

[242] N. S. Sta Maria, S. R. Barnes, M. R. Weist, D. Colcher, A. A. Raubitschek, and R. E. Jacobs. "Low Dose Focused Ultrasound Induces Enhanced Tumor Accumulation of Natural Killer Cells", PloS One, 10, p. e0142767, (2015).

[243] C. Yang, M. Du, F. Yan, and Z. Chen. "Focused ultrasound improves NK-92MI cells infiltration into tumors", Frontiers in Pharmacology, 10, (2019).

[244] H. L. Liu, H. Y. Hsieh, L. A. Lu, C. W. Kang, M. F. Wu, and C. Y. Lin. "Low-pressure pulsed focused ultrasound with microbubbles promotes an anticancer immunological response", J Transl Med, 10, p. 221, (2012).

[245] S. J. Hunt, T. Gade, M. C. Soulen, S. Pickup, and C. M. Sehgal. "Antivascular ultrasound therapy: Magnetic resonance imaging validation and activation of the immune response in murine melanoma", Journal of Ultrasound in Medicine, 34, pp. 275-287, (2015).

[246] J. Unga and M. Hashida. "Ultrasound induced cancer immunotherapy", Adv Drug Deliv Rev, 72, pp. 144-153, (2014).

[247] M. T. Silvestrini, E. S. Ingham, L. M. Mahakian, A. Kheirolomoom, Y. Liu, B. Z. Fite, S. M. Tam, S. T. Tucci, K. D. Watson, A. W. Wong, A. M. Monjazeb, N. E. Hubbard, W. J. Murphy, A. D. Borowsky, and K. W. Ferrara. "Priming is key to effective incorporation of image-guided thermal ablation into immunotherapy protocols", JCI Insight, 2, (2017).

[248] J. S. Weber. "Biomarkers for Checkpoint Inhibition", American Society of Clinical Oncology educational book. American Society of Clinical Oncology. Annual Meeting, 37, pp. 205-209, (2017).

[249] S. Bulner, A. Prodeus, J. Gariepy, K. Hynynen, and D. E. Goertz. "Enhancing Checkpoint Inhibitor Therapy with Ultrasound Stimulated Microbubbles", Ultrasound Med Biol, 45, pp. 500-512, (2019).

[250] W. M. Pardridge. "The blood-brain barrier: bottleneck in brain drug development", NeuroRx, 2, pp. 3-14, (2005).

[251] N. Sheikov, N. McDannold, N. Vykhodtseva, F. Jolesz, and K. Hynynen. "Cellular mechanisms of the blood-brain barrier opening induced by ultrasound in presence of microbubbles", Ultrasound Med Biol, 30, pp. 979-989, (2004).

[252] N. Sheikov, N. McDannold, F. Jolesz, Y. Z. Zhang, K. Tam, and K. Hynynen. "Brain arterioles show more active vesicular transport of blood-borne tracer molecules than capillaries and venules after focused ultrasound-evoked opening of the blood-brain barrier", Ultrasound Med Biol, 32, pp. 1399-1409, (2006).

[253] N. Sheikov, N. McDannold, S. Sharma, and K. Hynynen. "Effect of focused ultrasound applied with an ultrasound contrast agent on the tight junctional integrity of the brain microvascular endothelium", Ultrasound Med Biol, 34, pp. 1093-1104, (2008).

[254] J. Deng, Q. Huang, F. Wang, Y. Liu, Z. Wang, Q. Zhang, B. Lei, and Y. Cheng. "The role of caveolin-1 in blood-brain barrier disruption induced by focused ultrasound combined with microbubbles", J Mol Neurosci, 46, pp. 677-687, (2012).

[255] P. Y. Chen, H. L. Liu, M. Y. Hua, H. W. Yang, C. Y. Huang, P. C. Chu, L. A. Lyu, I. C. Tseng, L. Y. Feng, H. C. Tsai, S. M. Chen, Y. J. Lu, J. J. Wang, T. C. Yen, Y. H. Ma, T. Wu, J. P. Chen, J. I. Chuang, J. W. Shin, C. Hsueh, and K. C. Wei. "Novel magnetic/ultrasound focusing system enhances nanoparticle drug delivery for glioma treatment", Neuro Oncol, 12, pp. 1050-1060, (2010).

[256] M. Aryal, N. Vykhodtseva, Y. Z. Zhang, J. Park, and N. McDannold. "Multiple treatments with liposomal doxorubicin and ultrasound-induced disruption of blood-tumor and blood-brain barriers improve outcomes in a rat glioma model", J Control Release, 169, pp. 103-111, (2013).

[257] E. J. Park, Y. Z. Zhang, N. Vykhodtseva, and N. McDannold. "Ultrasound-mediated blood-brain/blood-tumor barrier disruption improves outcomes with trastuzumab in a breast cancer brain metastasis model", J Control Release, 163, pp. 277-284, (2012).

[258] J. F. Jordão, E. Thévenot, K. Markham-Coultes, T. Scarcelli, Y. Q. Weng, K. Xhima, M. O'Reilly, Y. Huang, J. McLaurin, K. Hynynen, and I. Aubert. "Amyloid-β plaque reduction, endogenous antibody delivery and glial activation by brain-targeted, transcranial focused ultrasound", Exp Neurol, 248, pp. 16-29, (2013).

[259] A. Burgess, S. Dubey, S. Yeung, O. Hough, N. Eterman, I. Aubert, and K. Hynynen. "Alzheimer disease in a mouse model: Mr imaging-guided focused ultrasound targeted to the hippocampus opens the blood-brain barrier and improves pathologic abnormalities and behavior", Radiology, 273, pp. 736-745, (2014).

[260] G. Leinenga and J. Götz. "Scanning ultrasound removes amyloid-β and restores memory in an Alzheimer's disease mouse model", Sci Transl Med, 7, p. 278ra233, (2015).

[261] C. T. Poon, K. Shah, C. Lin, R. Tse, K. K. Kim, S. Mooney, I. Aubert, B. Stefanovic, and K. Hynynen. "Time course of focused ultrasound effects on β-amyloid plaque pathology in the TgCRND8 mouse model of Alzheimer's disease", Scientific Reports, 8, (2018).

[262] T. Scarcelli, J. F. Jordão, M. A. O'Reilly, N. Ellens, K. Hynynen, and I. Aubert. "Stimulation of hippocampal neurogenesis by transcranial focused ultrasound and microbubbles in adult mice", Brain Stimulation, 7, pp. 304-307, (2014).

[263] S. J. Mooney, K. Shah, S. Yeung, A. Burgess, I. Aubert, and K. Hynynen. "Focused ultrasound-induced neurogenesis requires an increase in blood-brain barrier permeability", PLoS ONE, 11, (2016).

[264] S. Wang, O. O. Olumolade, T. Sun, G. Samiotaki, and E. E. Konofagou. "Noninvasive, neuron-specific gene therapy can be facilitated by focused ultrasound and recombinant adeno-associated virus", Gene therapy, 22, pp. 104-110, (2015).

[265] A. Alonso, E. Reinz, B. Leuchs, J. Kleinschmidt, M. Fatar, B. Geers, I. Lentacker, M. G. Hennerici, S. C. de Smedt, and S. Meairs. "Focal Delivery of AAV2/1-transgenes Into the Rat Brain by Localized Ultrasound-induced BBB Opening", Mol Ther Nucleic Acids, 2, p. e73, (2013).

[266] B. P. Mead, P. Mastorakos, J. S. Suk, A. L. Klibanov, J. Hanes, and R. J. Price. "Targeted gene transfer to the brain via the delivery of brain-penetrating DNA nanoparticles with focused ultrasound", Journal of controlled release : official journal of the Controlled Release Society, 223, pp. 109-117, (2016).

[267] E. Thevenot, J. F. Jordao, M. A. O'Reilly, K. Markham, Y. Q. Weng, K. D. Foust, B. K. Kaspar, K. Hynynen, and I. Aubert. "Targeted delivery of self-complementary adeno-associated virus serotype 9 to the brain, using magnetic resonance imaging-guided focused ultrasound", Hum Gene Ther, 23, pp. 1144-1155, (2012).

[268] B. P. Mead, N. Kim, G. W. Miller, D. Hodges, P. Mastorakos, A. L. Klibanov, J. W. Mandell, J. Hirsh, J. S. Suk, J. Hanes, and R. J. Price. "Novel Focused Ultrasound Gene Therapy Approach Noninvasively Restores Dopaminergic Neuron Function in a Rat Parkinson's Disease Model", Nano letters, 17, pp. 3533-3542, (2017).

[269] K. Xhima, F. Nabbouh, K. Hynynen, I. Aubert, and A. Tandon. "Noninvasive delivery of an α-synuclein gene silencing vector with magnetic resonance-guided focused ultrasound", Mov Disord, 33, pp. 1567-1579, (2018).

[270] N. McDannold, C. D. Arvanitis, N. Vykhodtseva, and M. S. Livingstone. "Temporary disruption of the blood-brain barrier by use of ultrasound and microbubbles: safety and efficacy evaluation in rhesus macaques", Cancer Res, 72, pp. 3652-3663, (2012).

[271] M. E. Downs, A. Buch, C. Sierra, M. E. Karakatsani, T. Teichert, S. Chen, E. E. Konofagou, and V. P. Ferrera. "Long-Term Safety of Repeated Blood-Brain Barrier Opening via Focused Ultrasound with Microbubbles in Non-Human Primates Performing a Cognitive Task", PLoS One, 10, p. e0125911, (2015).

[272] J. Silburt, N. Lipsman, and I. Aubert. "Disrupting the blood-brain barrier with focused ultrasound: Perspectives on inflammation and regeneration", Proc Natl Acad Sci U S A, (2017).

[273] Z. I. Kovacs, S. R. Burks, and J. A. Frank. "Reply to Silburt et al.: Concerning sterile inflammation following focused ultrasound and microbubbles in the brain", Proceedings of the National Academy of Sciences, 114, pp. E6737-E6738, (2017).

[274] N. McDannold, N. Vykhodtseva, and K. Hynynen. "Targeted disruption of the blood-brain barrier with focused ultrasound: association with cavitation activity", Phys Med Biol, 51, pp. 793-807, (2006).

[275] Y. S. Tung, F. Vlachos, J. J. Choi, T. Deffieux, K. Selert, and E. E. Konofagou. "In vivo transcranial cavitation threshold detection during ultrasound-induced blood-brain barrier opening in mice", Phys Med Biol, 55, pp. 6141-6155, (2010).

[276] M. A. O'Reilly and K. Hynynen. "Blood-brain barrier: real-time feedback-controlled focused ultrasound disruption by using an acoustic emissions-based controller", Radiology, 263, pp. 96-106, (2012).

[277] C. H. Tsai, J. W. Zhang, Y. Y. Liao, and H. L. Liu. "Real-time monitoring of focused ultrasound blood-brain barrier opening via subharmonic acoustic emission detection: implementation of confocal dual-frequency piezoelectric transducers", Phys Med Biol, 61, pp. 2926-2946, (2016).

[278] C. Bing, Y. Hong, C. Hernandez, M. Rich, B. Cheng, I. Munaweera, D. Szczepanski, Y. Xi, M. Bolding, A. Exner, and R. Chopra. "Characterization of different bubble formulations for blood-brain barrier opening using a focused ultrasound system with acoustic feedback control", Sci Rep, 8, p. 7986, (2018).

[279] C. D. Arvanitis, M. S. Livingstone, N. Vykhodtseva, and N. McDannold. "Controlled ultrasound-induced blood-brain barrier disruption using passive acoustic emissions monitoring", PLoS One, 7, p. e45783, (2012).

[280] T. Sun, Y. Zhang, C. Power, P. M. Alexander, J. T. Sutton, M. Aryal, N. Vykhodtseva, E. L. Miller, and N. J. McDannold. "Closed-loop control of targeted ultrasound drug delivery across the blood-brain/tumor barriers in a rat glioma model", Proc Natl Acad Sci U S A, 114, pp. E10281-E10290, (2017).

[281] H. A. Kamimura, J. Flament, J. Valette, A. Cafarelli, R. Aron Badin, P. Hantraye, and B. Larrat. "Feedback control of microbubble cavitation for ultrasound-mediated blood-brain barrier disruption in non-human primates under magnetic resonance guidance", J Cereb Blood Flow Metab, 39, pp. 1191-1203, (2019).

[282] T. Mainprize, N. Lipsman, Y. Huang, Y. Meng, A. Bethune, S. Ironside, C. Heyn, R. Alkins, M. Trudeau, A. Sahgal, J. Perry, and K. Hynynen. "Blood-Brain Barrier Opening in Primary Brain Tumors with Non-invasive MR-Guided Focused Ultrasound: A Clinical Safety and Feasibility Study", Sci Rep, 9, p. 321, (2019).

[283] N. Lipsman, Y. Meng, A. J. Bethune, Y. Huang, B. Lam, M. Masellis, N. Herrmann, C. Heyn, I. Aubert, A. Boutet, G. S. Smith, K. Hynynen, and S. E. Black. "Blood-brain barrier opening in Alzheimer's disease using MR-guided focused ultrasound", Nat Commun, 9, p. 2336, (2018).

[284] R. M. Jones, M. A. O'Reilly, and K. Hynynen. "Transcranial passive acoustic mapping with hemispherical sparse arrays using CT-based skull-specific aberration corrections: a simulation study", Phys Med Biol, 58, pp. 4981-5005, (2013).

[285] R. M. Jones, M. A. O'Reilly, and K. Hynynen. "Experimental demonstration of passive acoustic imaging in the human skull cavity using CT-based aberration corrections", Med Phys, 42, pp. 4385-4400, (2015).

[286] C. D. Arvanitis, M. S. Livingstone, and N. McDannold. "Combined ultrasound and MR imaging to guide focused ultrasound therapies in the brain", Phys Med Biol, 58, pp. 4749-4761, (2013).

[287] Y. Yang, X. Zhang, D. Ye, R. Laforest, J. Williamson, Y. Liu, and H. Chen. "Cavitation dose painting for focused ultrasound-induced blood-brain barrier disruption", Sci Rep, 9, p. 2840, (2019).

[288] L. Deng, M. A. O'Reilly, R. M. Jones, R. An, and K. Hynynen. "A multi-frequency sparse hemispherical ultrasound phased array for microbubble-mediated transcranial therapy and simultaneous cavitation mapping", Phys Med Biol, 61, pp. 8476-8501, (2016).

[289] R. M. Jones, L. Deng, K. Leung, D. McMahon, M. A. O'Reilly, and K. Hynynen. "Three-dimensional transcranial microbubble imaging for guiding volumetric ultrasound-mediated blood-brain barrier opening", Theranostics, 8, pp. 2909-2926, (2018).

[290] M. A. O'Reilly, R. M. Jones, and K. Hynynen. "Three-dimensional transcranial ultrasound imaging of microbubble clouds using a sparse hemispherical array", IEEE Trans Biomed Eng, 61, pp. 1285-1294, (2014).

[291] C. Crake, S. T. Brinker, C. M. Coviello, M. S. Livingstone, and N. J. McDannold. "A dual-mode hemispherical sparse array for 3D passive acoustic mapping and skull localization within a clinical MRI guided focused ultrasound device", Phys Med Biol, 63, p. 065008, (2018).

[292] H.-L. Liu, C.-K. Jan, C.-H. Tsai, S.-M. Huang, M.-L. Li, W. Qui, and H. Zheng, "Design and Implementation of a Dual-Transmit/Receive-Mode Therapeutic Ultrasound Phased Array System for Brain Therapy," in IEEE Ultrasonics Symposium Proceedings, Japan, 2018.

[293] J. Wachsmuth, R. Chopr, and K. Hynynen, "Feasibility of transient image-guided blood-spinal cord barrier disruption," in AIP Conference Proceedings, 2009, pp. 256-259.

[294] D. Weber-Adrian, E. Thévenot, M. A. O'Reilly, W. Oakden, M. K. Akens, N. Ellens, K. Markham-Coultes, A. Burgess, J. Finkelstein, A. J. Yee, C. M. Whyne, K. D. Foust, B. K. Kaspar, G. J. Stanisz, R. Chopra, K. Hynynen, and I. Aubert. "Gene delivery to the spinal cord using MRI-guided focused ultrasound", Gene Ther, 22, pp. 568-577, (2015).

[295] M. A. O'Reilly, T. Chinnery, M. L. Yee, S. K. Wu, K. Hynynen, R. S. Kerbel, G. J. Czarnota, K. I. Pritchard, and A. Sahgal. "Preliminary Investigation of Focused Ultrasound-Facilitated Drug Delivery for the Treatment of Leptomeningeal Metastases", Scientific Reports, 8, (2018).

[296] A. S. Montero, F. Bielle, L. Goldwirt, A. Lalot, G. Bouchoux, M. Canney, F. Belin, K. Beccaria, P. F. Pradat, F. Salachas, S. Boillee, C. Lobsiger, C. Lafon, J. Y. Chapelon, and A. Carpentier. "Ultrasound-Induced Blood-Spinal Cord Barrier Opening in Rabbits", Ultrasound Med Biol, 45, pp. 2417-2426, (2019).

[297] S. P. Fletcher and M. A. O'Reilly. "Analysis of Multifrequency and Phase Keying Strategies for Focusing Ultrasound to the Human Vertebral Canal", IEEE Trans Ultrason Ferroelectr Freq Control, 65, pp. 2322-2331, (2018).

[298] R. Xu and M. A. O'Reilly. "A Spine-Specific Phased Array for Transvertebral Ultrasound Therapy: Design & Simulation", IEEE Trans Biomed Eng, (2019).

[299] A. Carpentier, M. Canney, A. Vignot, V. Reina, K. Beccaria, C. Horodyckid, C. Karachi, D. Leclercq, C. Lafon, J. Y. Chapelon, L. Capelle, P. Cornu, M. Sanson, K. Hoang-Xuan, J. Y. Delattre, and A. Idbaih. "Clinical trial of blood-brain barrier disruption by pulsed ultrasound", Sci Transl Med, 8, p. 343re342, (2016).

[300] A. Idbaih, M. Canney, L. Belin, C. Desseaux, A. Vignot, G. Bouchoux, N. Asquier, B. Law-Ye, D. Leclercq, A. Bissery, Y. De Rycke, C. Trosch, L. Capelle, M. Sanson, K. Hoang-Xuan, C. Dehais, C. Houillier, F. Laigle-Donadey, B. Mathon, A. Andre, C. Lafon, J. Y. Chapelon, J. Y. Delattre, and A. Carpentier. "Safety and Feasibility of Repeated and Transient Blood-Brain Barrier Disruption by Pulsed Ultrasound in Patients with Recurrent Glioblastoma", Clin Cancer Res, 25, pp. 3793-3801, (2019).

[301] A. Abrahao, Y. Meng, M. Llinas, Y. Huang, C. Hamani, T. Mainprize, I. Aubert, C. Heyn, S. E. Black, K. Hynynen, N. Lipsman, and L. Zinman. "Motor Cortex Blood-Brain Barrier Opening in Amyotrophic Lateral Sclerosis using MR-Guided Focused Ultrasound: A First-in-Human Trial", Nat Commun, 10, p. 4373, (2019).

[302] K. B. Bader, K. J. Haworth, H. Shekhar, A. D. Maxwell, T. Peng, D. D. McPherson, and C. K. Holland. "Efficacy of histotripsy combined with rt-PA in vitro", Physics in Medicine and Biology, 61, pp. 5253-5274, (2016).

[303] A. V. Alexandrov, A. W. Wojner, J. C. Grotta, and C. Investigators. "CLOTBUST: design of a randomized trial of ultrasound-enhanced thrombolysis for acute ischemic stroke", J Neuroimaging, 14, pp. 108-112, (2004).

[304] A. V. Alexandrov, A. M. Demchuk, W. S. Burgin, D. J. Robinson, J. C. Grotta, and C. Investigators. "Ultrasound-enhanced thrombolysis for acute ischemic stroke: phase I. Findings of the CLOTBUST trial", J Neuroimaging, 14, pp. 113-117, (2004).

[305] C. A. Molina, M. Ribo, M. Rubiera, J. Montaner, E. Santamarina, R. Delgado-Mederos, J. F. Arenillas, R. Huertas, F. Purroy, P. Delgado, and J. Alvarez-Sabin. "Microbubble administration accelerates clot lysis during continuous 2-MHz ultrasound monitoring in stroke patients treated with intravenous tissue plasminogen activator", Stroke, 37, pp. 425-429, (2006).

[306] Z. Q. Chen, T. Xue, H. C. Huang, J. Y. Xu, S. Shankar, H. Yu, and Z. Wang. "Efficacy and safety of sonothombolysis versus non-sonothombolysis in patients with acute ischemic stroke: A meta-analysis of randomized controlled trials", Plos One, 14, (2019).

[307] W. Mathias, J. M. Tsutsui, B. G. Tavares, F. Xie, M. O. D. Aguiar, D. R. Garcia, M. T. Oliveira, A. Soeiro, J. C. Nicolau, P. A. L. Neto, C. E. Rochitte, J. A. F. Ramires, R. Kalil, and T. R. Porter. "Diagnostic Ultrasound Impulses Improve Microvascular Flow in Patients With STEMI Receiving Intravenous Microbubbles", J Am Coll Cardiol, 67, pp. 2506-2515, (2016).

[308] W. Mathias, J. M. Tsutsui, B. G. Tavares, A. M. Fava, M. O. D. Aguiar, B. C. Borges, M. T. Oliveira, A. Soeiro, J. C. Nicolau, H. B. Ribeiro, H. P. Chiang, J. C. N. Sbano, A. Morad, A. Goldsweig, C. E. Rochitte, B. B. C. Lopes, J. A. F. Ramirez, R. Kalil, T. R. Porter, and M. Investigators. "Sonothrombolysis in ST-Segment Elevation Myocardial Infarction Treated With Primary Percutaneous Coronary Intervention", J Am Coll Cardiol, 73, pp. 2832-2842, (2019).

[309] J. Slikkerveer, L. J. M. Juffermans, N. van Royen, Y. Appelman, T. R. Porter, and O. Kamp. "Therapeutic application of contrast ultrasound in ST elevation myocardial infarction: Role in coronary thrombosis and microvascular obstruction", Eur Heart J Acute Cardiovasc Care, 8, pp. 45-53, (2019).

[310] H. P. Ebben, J. H. Nederhoed, R. J. Lely, W. Wisselink, K. Yeung, and M. Collaborators. "Microbubbles and UltraSound-accelerated Thrombolysis (MUST) for peripheral arterial occlusions: protocol for a phase II single-arm trial", Bmj Open, 7, (2017).

[311] Y. D. Shi, W. Y. Shi, L. Chen, and J. P. Gu. "A systematic review of ultrasound-accelerated catheter-directed thrombolysis in the treatment of deep vein thrombosis", J Thromb Thrombolysis, 45, pp. 440-451, (2018).

[312] R. P. Engelberger and N. Kucher. "Ultrasound-assisted thrombolysis for acute pulmonary embolism: a systematic review", Eur Heart J, 35, pp. 758-764, (2014).

[313] M. Dumantepe, I. Uyar, B. Teymen, O. Ugur, and Y. Enc. "Improvements in pulmonary artery pressure and right ventricular function after ultrasound-accelerated catheter-directed thrombolysis for the treatment of pulmonary embolism", Journal of Cardiac Surgery, 29, pp. 455-463, (2014).

[314] K. A. Lee, A. Cha, M. H. Kumar, C. Rezayat, and C. M. Sales. "Catheter-directed, ultrasound-assisted thrombolysis is a safe and effective treatment for pulmonary embolism, even in high-risk patients", J Vasc Surg-Venous L, 5, pp. 165-170, (2017).

[315] S. Datta, C. C. Coussios, L. E. McAdory, J. Tan, T. Porter, G. De Courten-Myers, and C. K. Holland. "Correlation of cavitation with ultrasound enhancement of thrombolysis", Ultrasound Med Biol, 32, pp. 1257-1267, (2006).

[316] A. F. Prokop, A. Soltani, and R. A. Roy. "Cavitational mechanisms in ultrasound-accelerated fibrinolysis", Ultrasound Med Biol, 33, pp. 924-933, (2007).

[317] B. Petit, Y. Bohren, E. Gaud, P. Bussat, M. Arditi, F. Yan, F. Tranquart, and E. Allemann. "Sonothrombolysis: the contribution of stable and inertial cavitation to clot lysis", Ultrasound Med Biol, 41, pp. 1402-1410, (2015).

[318] S. A. Elder. "Cavitation microstreaming", J Acoust Soc Am, 31, pp. 54-64, (1958).

[319] H. G. Flynn, "Physics of acoustic cavitation in liquids," in Physical Acoustics, W. P. Mason, Ed., ed New York: Academic Press, 1964, pp. 58-172.

[320] A. D. Phelps and T. G. Leighton. "The subharmonic oscillations and combination-frequency subharmonic emissions from a resonant bubble: Their properties and generation mechanisms", Acustica, 83, pp. 59-66, (1997).

[321] K. B. Bader and C. K. Holland. "Gauging the likelihood of stable cavitation from ultrasound contrast agents", Phys Med Biol, 58, pp. 127-144, (2013).

[322] E. L. Carstensen and H. G. Flynn. "The Potential for Transient Cavitation with Microsecond Pulses of Ultrasound", Ultrasound Med Biol, 8, pp. L720-L724, (1982).

[323] H. G. Flynn. "Generation of transient cavities in liquids by microsecond pulses of ultrasound", J Acoust Soc Am, 72, pp. 1926-1932, (1982).

[324] G. E. R. Weller, F. S. Villanueva, A. L. Klibanov, and W. R. Wagner. "Modulating targeted adhesion of an ultrasound contrast agent to dysfunctional endothelium", Ann Biomed Eng, 30, pp. 1012-1019, (2002).

[325] R. T. Kleven, K. B. Karani, N. G. Salido, H. Shekhar, K. J. Haworth, T. D. Mast, D. G. Tadesse, and C. K. Holland. "The effect of 220 kHz insonation scheme on rt-PA thrombolytic efficacy in vitro", Phys Med Biol, 64, p. 165015, (2019).

[326] H. Shekhar, R. T. Kleven, T. Peng, A. Palaniappan, K. B. Karani, S. L. Huang, D. D. McPherson, and C. K. Holland. "In vitro characterization of sonothrombolysis and echocontrast agents to treat ischemic stroke", Sci Rep, 9, (2019).

[327] J. Brüssler, B. Strehlow, A. Becker, R. Schubert, J. Schummelfeder, C. Nimsky, and U. Bakowsky. "Nanoscaled ultrasound contrast agents for enhanced sonothrombolysis", Colloid Surface B, 172, pp. 728-733, (2018).

[328] M. D. De Saint Victor, L. C. Barnsley, D. Carugo, J. Owen, C. C. Coussios, and E. Stride. "Sonothrombolysis with Magnetically Targeted Microbubbles", Ultrasound Med Biol, 45, pp. 1151-1163, (2019).

[329] A. Burgess, Y. X. Huang, A. C. Waspe, M. Ganguly, D. E. Goertz, and K. Hynynen. "High-Intensity Focused Ultrasound (HIFU) for Dissolution of Clots in a Rabbit Model of Embolic Stroke", Plos One, 7, (2012).

[330] S. Monteith, J. Sheehan, R. Medel, M. Wintermark, M. Eames, J. Snell, N. F. Kassell, and W. J. Elias. "Potential intracranial applications of magnetic resonance-guided focused ultrasound surgery", J Neurosurg, 118, pp. 215-221, (2013).

[331] A. Zafar, S. A. Quadri, M. Farooqui, S. Ortega-Gutierrez, O. R. Hariri, M. Zulfiqar, A. Ikram, M. A. Khan, S. S. Suriya, J. R. Nunez-Gonzalez, S. Posse, M. M. Mortazavi, and H. Yonas. "MRI-Guided High-Intensity Focused Ultrasound as an Emerging Therapy for Stroke: A Review", J Neuroimaging, 29, pp. 5-13, (2019).

[332] A. D. Maxwell, C. A. Cain, A. P. Duryea, L. Q. Yuan, H. S. Gurm, and Z. Xu. "Noninvasive Thrombolysis Using Pulsed Ultrasound Cavitation Therapy - Histotripsy", Ultrasound Med Biol, 35, pp. 1982-1994, (2009).

[333] X. Zhang, G. E. Owens, C. A. Cain, H. S. Gurm, J. Macoskey, and Z. Xu. "Histotripsy Thrombolysis on Retracted Clots", Ultrasound in Medicine and Biology, 42, pp. 1903-1918, (2016).

[334] K. B. Bader, E. Vlaisavljevich, and A. D. Maxwell. "For Whom the Bubble Grows: Physical Principles of Bubble Nucleation and Dynamics in Histotripsy Ultrasound Therapy", Ultrasound Med Biol, 45, pp. 1056-1080, (2019).

[335] M. J. Garcia. "Endovascular Management of Acute Pulmonary Embolism Using the Ultrasound-Enhanced EkoSonic System", Semin Intervent Rad, 32, pp. 384-387, (2015).

[336] H. L. Weiss, P. Selvaraj, K. Okita, Y. Matsumoto, A. Voie, T. Hoelscher, and A. J. Szeri. "Mechanical clot damage from cavitation during sonothrombolysis", J Acoust Soc Am, 133, pp. 3159-3175, (2013).

[337] E. C. Everbach and C. W. Francis. "Cavitational mechanisms in ultrasound-accelerated thrombolysis at 1 MHz", Ultrasound Med Biol, 26, pp. 1153-1160, (2000).

[338] K. E. Hitchcock, N. M. Ivancevich, K. J. Haworth, D. N. C. Stamper, D. C. Vela, J. T. Sutton, G. J. Pyne-Geithman, and C. K. Holland. "Ultrasound-enhanced rt-PA thrombolysis in an ex vivo porcine carotid artery model", Ultrasound Med Biol, 37, pp. 1240-1251, (2011).

[339] R. A. Roy, S. I. Madanshetty, and R. E. Apfel. "An Acoustic Backscattering Technique for the Detection of Transient Cavitation Produced by Microsecond Pulses of Ultrasound", J Acoust Soc Am, 87, pp. 2451-2458, (1990).

[340] S. I. Madanshetty, R. A. Roy, and R. E. Apfel. "Acoustic Microcavitation - Its Active and Passive Acoustic Detection", J Acoust Soc Am, 90, pp. 1515-1526, (1991).

[341] V. A. Salgaonkar, S. Datta, C. K. Holland, and T. D. Mast. "Passive cavitation imaging with ultrasound arrays", J Acoust Soc Am, 126, pp. 3071-3083, (2009).

[342] M. Gyöngy and C. C. Coussios. "Passive cavitation mapping for localization and tracking of bubble dynamics", J Acoust Soc Am 128, pp. EL175-180, (2010).

[343] F. Vignon, W. T. Shi, J. E. Powers, E. C. Everbach, J. J. Liu, S. J. Gao, F. Xie, and T. R. Porter. "Microbubble Cavitation Imaging", IEEE Trans Ultrason Ferroelectr Freq Control, 60, pp. 661-670, (2013).

[344] A. N. Pouliopoulos and J. J. Choi. "Superharmonic microbubble Doppler effect in ultrasound therapy", Phys Med Biol, 61, pp. 6154-6171, (2016).

[345] C. Arvanitis and N. McDannold. "Transcranial spatial and temporal assessment of microbubble dynamics for brain therapies", Proc Meet Acoust, 19, p. e075021, (2013).

[346] C. D. Arvanitis and N. McDannold. "Integrated ultrasound and magnetic resonance imaging for simultaneous temperature and cavitation monitoring during focused ultrasound therapies", Med Phys, 40, p. 112901, (2013).

[347] C. N. Acconcia, R. M. Jones, D. E. Goertz, M. A. O'Reilly, and K. Hynynen. "Megahertz rate, volumetric imaging of bubble clouds in sonothrombolysis using a sparse hemispherical receiver array", Phys Med Biol, 62, pp. L31-L40, (2017).

[348] S. M. Flight, P. P. Masci, M. F. Lavin, and P. J. Gaffney. "Resistance of porcine blood clots to lysis relates to poor activation of porcine plasminogen by tissue plasminogen activator", Blood Coagul Fibrin, 17, pp. 417-420, (2006).

[349] D. A. Gabriel, K. Muga, and E. M. Boothroyd. "The Effect of Fibrin Structure on Fibrinolysis", J Biol Chem, 267, pp. 24259-24263, (1992).

[350] S. W. Huang, H. Shekhar, and C. K. Holland. "Comparative lytic efficacy of rt-PA and ultrasound in porcine versus human clots", Plos One, 12, (2017).

[351] L. Auboire, C. A. Sennoga, J. M. Hyvelin, F. Ossant, J. M. Escoffre, F. Tranquart, and A. Bouakaz. "Microbubbles combined with ultrasound therapy in ischemic stroke: A systematic review of in-vivo preclinical studies", Plos One, 13, (2018).

[352] B. C. V. Campbell, P. J. Mitchell, L. Churilov, N. Yassi, T. J. Kleinig, R. J. Dowling, B. Yan, S. J. Bush, H. M. Dewey, V. Thijs, R. Scroop, M. Simpson, M. Brooks, H. Asadi, T. Y. Wu, D. G. Shah, T. Wijeratne, T. Ang, F. Miteff, C. R. Levi, E. Rodrigues, H. Zhao, P. Salvaris, C. Garcia-Esperon, P. Bailey, H. Rice, L. de Villiers, H. Brown, K. Redmond, D. Leggett, J. N. Fink, W. Collecutt, A. A. Wong, C. Muller, A. Coulthard, K. Mitchell, J. Clouston, K. Mahady, D. Field, H. Ma, T. G. Phan, W. Chong, R. V. Chandra, L. A. Slater, M. Krause, T. J. Harrington, K. C. Faulder, B. S. Steinfort, C. F. Bladin, G. Sharma, P. M. Desmond, M. W. Parsons, G. A. Donnan, S. M. Davis, and E.-I. T. Investigators. "Tenecteplase versus Alteplase before Thrombectomy for Ischemic Stroke", New Engl J Med, 378, pp. 1573-1582, (2018).

[353] M. Gauberti. "Reperfusion in acute ischaemic stroke by sonothrombolysis", Lancet Neurol, 18, pp. 320-321, (2019).

[354] A. J. Schissler, R. J. Gylnn, P. S. Sobieszczyk, and A. B. Waxman. "Ultrasound-assisted catheter-directed thrombolysis compared with anticoagulation alone for treatment of intermediate-risk pulmonary embolism", Pulm Circ, 8, (2018).

[355] H. Yuan, H. Hu, J. Sun, M. Shi, H. Yu, C. Li, Y. U. Sun, Z. Yang, and R. M. Hoffman. "Ultrasound Microbubble Delivery Targeting Intraplaque Neovascularization Inhibits Atherosclerotic Plaque in an APOE-deficient Mouse Model", In Vivo, 32, pp. 1025-1032, (2018).

[356] Q. Su, L. Li, Y. Liu, Y. Zhou, J. Wang, and W. Wen. "Ultrasound-targeted microbubble destruction-mediated microRNA-21 transfection regulated PDCD4/NF-kappaB/TNF-alpha pathway to prevent coronary microembolization-induced cardiac dysfunction", Gene Ther, 22, pp. 1000-1006, (2015).

[357] Y. Liu, L. Li, Q. Su, T. Liu, Z. Ma, and H. Yang. "Ultrasound-targeted microbubble destruction enhances gene expression of microRNA-21 in swine heart via intracoronary delivery", Echocardiography, 32, pp. 1407-1416, (2015).

[358] J. P. Kilroy, A. H. Dhanaliwala, A. L. Klibanov, D. K. Bowles, B. R. Wamhoff, and J. A. Hossack. "Reducing Neointima Formation in a Swine Model with IVUS and Sirolimus Microbubbles", Annals of Biomedical Engineering, 43, pp. 2642-2651, (2015).

[359] X. Zhu, J. Guo, C. He, H. Geng, G. Yu, J. Li, H. Zheng, X. Ji, and F. Yan. "Ultrasound triggered image-guided drug delivery to inhibit vascular reconstruction via paclitaxel-loaded microbubbles", Scientific Reports, 6, pp. 1-12, (2016).

[360] Y. Z. Zhao, M. Zhang, H. L. Wong, X. Q. Tian, L. Zheng, X. C. Yu, F. R. Tian, K. L. Mao, Z. L. Fan, P. P. Chen, X. K. Li, and C. T. Lu. "Prevent diabetic cardiomyopathy in diabetic rats by combined therapy of aFGF-loaded nanoparticles and ultrasound-targeted microbubble destruction technique", Journal of Controlled Release, 223, pp. 11-21, (2016).

[361] Y. Z. Zhao, X. Q. Tian, M. Zhang, L. Cai, A. Ru, X. T. Shen, X. Jiang, R. R. Jin, L. Zheng, K. Hawkins, S. Charkrabarti, X. K. Li, Q. Lin, W. Z. Yu, S. Ge, C. T. Lu, and H. L. Wong. "Functional and pathological improvements of the hearts in diabetes model by the combined therapy of bFGF-loaded nanoparticles with ultrasound-targeted microbubble destruction", Journal of Controlled Release, 186, pp. 22-31, (2014).

[362] M. Zhang, W. Z. Yu, X. T. Shen, Q. Xiang, J. Xu, J. J. Yang, P. P. Chen, Z. L. Fan, J. Xiao, Y. Z. Zhao, and C. T. Lu. "Advanced Interfere Treatment of Diabetic Cardiomyopathy Rats by aFGF-Loaded Heparin-Modified Microbubbles and UTMD Technique", Cardiovascular Drugs and Therapy, 30, pp. 247-261, (2016).

[363] X. Q. Tian, X. W. Ni, H. L. Xu, L. Zheng, D. L. ZhuGe, B. Chen, C. T. Lu, J. J. Yuan, and Y. Z. Zhao. "Prevention of doxorubicin-induced cardiomyopathy using targeted MaFGF mediated by nanoparticles combined with ultrasound-targeted MB destruction", International Journal of Nanomedicine, 12, pp. 7103-7119, (2017).

[364] P. J. Lee, D. Rudenko, M. A. Kuliszewski, C. Liao, M. G. Kabir, K. A. Connelly, and H. Leong-Poi. "Survivin gene therapy attenuates left ventricular systolic dysfunction in doxorubicin cardiomyopathy by reducing apoptosis and fibrosis", Cardiovasc Res, 101, pp. 423-433, (2014).

[365] S. Chen, J. Chen, P. Huang, X. L. Meng, S. Clayton, J. S. Shen, and P. A. Grayburn. "Myocardial regeneration in adriamycin cardiomyopathy by nuclear expression of GLP1 using ultrasound targeted microbubble destruction", Biochemical and Biophysical Research Communications, 458, pp. 823-829, (2015).

[366] L. Qian, B. Thapa, J. Hong, Y. Zhang, M. Zhu, M. Chu, J. Yao, and D. Xu. "The present and future role of ultrasound targeted microbubble destruction in preclinical studies of cardiac gene therapy", J Thorac Dis, 10, pp. 1099-1111, (2018).

[367] P. Yan, K. J. Chen, J. Wu, L. Sun, H. W. Sung, R. D. Weisel, J. Xie, and R. K. Li. "The use of MMP2 antibody-conjugated cationic microbubble to target the ischemic myocardium, enhance Timp3 gene transfection and improve cardiac function", Biomaterials, 35, pp. 1063-1073, (2014).

[368] Q. Deng, B. Hu, S. Cao, H. N. Song, J. L. Chen, and Q. Zhou. "Improving the efficacy of therapeutic angiogenesis by UTMD-mediated Ang-1 gene delivery to the infarcted myocardium", International Journal of Molecular Medicine, 36, pp. 335-344, (2015).

[369] W. h. Shentu, C. x. Yan, C. m. Liu, R. x. Qi, Y. Wang, Z. x. Huang, L. m. Zhou, and X. d. You. "Use of cationic microbubbles targeted to P-selectin to improve ultrasound-mediated gene transfection of hVEGF 165 to the ischemic myocardium", J Zheijang Univ Sci B, 19, pp. 699-707, (2018).

[370] W. J. Cao, J. D. Rosenblat, N. C. Roth, M. A. Kuliszewski, P. N. Matkar, D. Rudenko, C. Liao, P. J. Lee, and H. Leong-Poi. "Therapeutic Angiogenesis by Ultrasound-Mediated MicroRNA-126-3p Delivery", Arterioscler Thromb Vasc Biol, 35, pp. 2401-2411, (2015).

[371] J. S. Babischkin, G. W. Aberdeen, J. R. Lindner, T. W. Bonagura, G. J. Pepe, and E. D. Albrecht. "Vascular endothelial growth factor delivery to placental basal plate promotes uterine artery remodeling in the primate", Endocrinology, 160, pp. 1492-1505, (2019).

[372] F. E. Shamout, A. N. Pouliopoulos, P. Lee, S. Bonaccorsi, L. Towhidi, R. Krams, and J. J. Choi. "Enhancement of Non-Invasive Trans-Membrane Drug Delivery Using Ultrasound and Microbubbles During Physiologically Relevant Flow", Ultrasound in Medicine and Biology, 41, pp. 2435-2448, (2015).

[373] E. K. Juang, I. De Cock, C. Keravnou, M. K. Gallagher, S. B. Keller, Y. Zheng, and M. Averkiou. "Engineered 3D Microvascular Networks for the Study of Ultrasound-Microbubble-Mediated Drug Delivery", Langmuir, 35, pp. 10128-10138, (2019).

[374] Y. Dong, J. Li, P. Li, and J. Yu. "Ultrasound Microbubbles Enhance the Activity of Vancomycin Against Staphylococcus epidermidis Biofilms In Vivo", J Ultrasound Med, 37, pp. 1379-1387, (2018).

[375] E. Ronan, N. Edjiu, O. Kroukamp, G. Wolfaardt, and R. Karshafian. "USMB-induced synergistic enhancement of aminoglycoside antibiotics in biofilms", Ultrasonics, 69, pp. 182-190, (2016).

[376] A. H. Liao, C. R. Hung, C. F. Lin, Y. C. Lin, and H. K. Chen. "Treatment effects of lysozyme-shelled microbubbles and ultrasound in inflammatory skin disease", Sci Rep, 7, p. 41325, (2017).

[377] S. Yi, G. Han, Y. Shang, C. Liu, D. Cui, S. Yu, B. Liao, X. Ao, G. Li, and L. Li. "Microbubble-mediated ultrasound promotes accumulation of bone marrow mesenchymal stem cell to the prostate for treating chronic bacterial prostatitis in rats", Scientific reports, 6, pp. 19745-19745, (2016).

[378] M. G. Sugiyama, V. Mintsopoulos, H. Raheel, N. M. Goldenberg, J. E. Batt, L. Brochard, W. M. Kuebler, H. Leong-Poi, R. Karshafian, and W. L. Lee. "Lung Ultrasound and Microbubbles Enhance Aminoglycoside Efficacy and Delivery to the Lung in Escherichia coli-induced Pneumonia and Acute Respiratory Distress Syndrome", Am J Respir Crit Care Med, 198, pp. 404-408, (2018).

[379] T. Lin, X. Z. Cai, M. M. Shi, Z. M. Ying, B. Hu, C. H. Zhou, W. Wang, Z. L. Shi, and S. G. Yan. "In vitro and in vivo evaluation of vancomycin-loaded PMMA cement in combination with ultrasound and microbubbles-mediated ultrasound", Biomed Res Int, 2015, p. 309739, (2015).

[380] H. X. Zhu, X. Z. Cai, Z. L. Shi, B. Hu, and S. G. Yan. "Microbubble-mediated ultrasound enhances the lethal effect of gentamicin on planktonic Escherichia coli", Biomed Res Int, 2014, p. 142168, (2014).

[381] B. H. T. Goh, M. Conneely, H. Kneupner, T. Palmer, E. Klaseboer, B. C. Khoo, and P. Campbell, "High-speed imaging of ultrasound-mediated bacterial biofilm disruption," in 6th European Conference of the International Federation for Medical and Biological Engineering, 2015, pp. 533-536.

[382] A. Agarwal, W. Jern Ng, and Y. Liu. "Removal of biofilms by intermittent low-intensity ultrasonication triggered bursting of microbubbles", Biofouling, 30, pp. 359-365, (2014).

[383] K. R. Lattwein, H. Shekhar, J. J. P. Kouijzer, W. J. B. van Wamel, C. K. Holland, and K. Kooiman. "Sonobactericide: An Emerging Treatment Strategy for Bacterial Infections", Ultrasound Med Biol, 46, pp. 193-215, (2020).

[384] T. Deffieux, G. Montaldo, M. Tanter, and M. Fink. "Shear wave spectroscopy for in vivo quantification of human soft tissues visco-elasticity", IEEE Trans Med Imaging, 28, pp. 313-322, (2009).

[385] S. B. Feinstein, J. Cheirif, F. J. Ten Cate, P. R. Silverman, P. A. Heidenreich, C. Dick, R. M. Desir, W. F. Armstrong, M. A. Quinones, and P. M. Shah. "Safety and efficacy of a new transpulmonary ultrasound contrast agent: initial multicenter clinical results", J. Am. Coll. Cardiol., 16, pp. 316-324, (1990).

[386] T. van Rooij, V. Daeichin, I. Skachkov, N. de Jong, and K. Kooiman. "Targeted ultrasound contrast agents for ultrasound molecular imaging and therapy", Int. J. Hyperthermia, 31, pp. 90-106, (2015).

[387] J. K. Willmann, L. Bonomo, A. C. Testa, P. Rinaldi, G. Rindi, K. S. Valluru, G. Petrone, M. Martini, A. M. Lutz, and S. S. Gambhir. "Ultrasound Molecular Imaging With BR55 in Patients With Breast and Ovarian Lesions: First-in-Human Results", J. Clin. Oncol., 35, pp. 2133-2140, (2017).

[388] M. Schneider, M. Arditi, M. B. Barrau, J. Brochot, A. Broillet, R. Ventrone, and F. Yan. "BR1: a new ultrasonographic contrast agent based on sulfur hexafluoride-filled microbubbles", Invest. Radiol., 30, pp. 451-457, (1995).

[389] D. H. Kim, M. J. Costello, P. B. Duncan, and D. Needham. "Mechanical Properties and Microstructure of Polycrystalline Phospholipid Monolayer Shells: Novel Solid Microparticles", Langmuir, 19, pp. 8455-8466, (2003).

[390] M. A. Borden, G. V. Martinez, J. Ricker, N. Tsvetkova, M. Longo, R. J. Gillies, P. A. Dayton, and K. W. Ferrara. "Lateral phase separation in lipid-coated microbubbles", Langmuir, 22, pp. 4291-4297, (2006).

[391] M. M. Lozano and M. L. Longo. "Microbubbles coated with disaturated lipids and DSPE-PEG2000: phase behavior, collapse transitions, and permeability", Langmuir, 25, pp. 3705-3712, (2009).

[392] A. S. Shaw. "Lipid rafts: now you see them, now you don't", Nat. Immunol., 7, pp. 1139-1142, (2006).

[393] K. Kooiman, T. J. A. Kokhuis, T. van Rooij, I. Skachkov, A. Nigg, J. G. Bosch, A. F. W. van der Steen, W. A. van Cappellen, and N. de Jong. "DSPC or DPPC as main shell component influences ligand distribution and binding area of lipid-coated targeted microbubbles", Eur. J. Lipid Sci. Tech., 116, pp. 1217-1227, (2014).

[394] L. M. Kornmann, K. D. Reesink, R. S. Reneman, and A. P. G. Hoeks. "Critical Appraisal of Targeted Ultrasound Contrast Agents for Molecular Imaging in Large Arteries", Ultrasound Med. Biol., 36, pp. 181-191, (2010).

[395] T. van Rooij, I. Beekers, K. R. Lattwein, A. F. W. van der Steen, N. de Jong, and K. Kooiman. "Vibrational Responses of Bound and Nonbound Targeted Lipid-Coated Single Microbubbles", IEEE Trans. Ultrason. Ferroelectr. Freq. Control, 64, pp. 785-797, (2017).

[396] O. Albrecht, H. Gruler, and E. Sackmann. "Polymorphism of phospholipid monolayers", J. Phys. France, 39, pp. 301-313, (1978).

[397] B. L. Helfield, E. Cherin, F. S. Foster, and D. E. Goertz. "Investigating the subharmonic response of individual phospholipid encapsulated microbubbles at high frequencies: a comparative study of five agents", Ultrasound Med. Biol., 38, pp. 846-863, (2012).

[398] A. L. Klibanov, P. T. Rasche, M. S. Hughes, J. K. Wojdyla, K. P. Galen, J. H. Wible, and G. H. Brandenburger. "Detection of Individual Microbubbles of Ultrasound Contrast Agents", Invest. Radiol., 39, pp. 187-195, (2004).

[399] G. Chen, L. Yang, L. Zhong, S. Kutty, Y. Wang, K. Cui, J. Xiu, S. Cao, Q. Huang, W. Liao, Y. Liao, J. Wu, W. Zhang, and J. Bin. "Delivery of Hydrogen Sulfide by Ultrasound Targeted Microbubble Destruction Attenuates Myocardial Ischemia-reperfusion Injury", Sci. Rep., 6, p. 30643, (2016).

[400] D. C. Steinl, L. Xu, A. Ochoa-Espinosa, M. Punjabi, and B. A. Kaufmann. "Non-invasive contrast enhanced ultrasound molecular imaging of inflammation in autoimmune myocarditis for prediction of left ventricular fibrosis and remodeling", PloS one, 14, pp. e0224377-e0224377, (2019).

[401] V. Daeichin, T. van Rooij, I. Skachkov, B. Ergin, P. A. Specht, A. Lima, C. Ince, J. G. Bosch, A. F. van der Steen, N. de Jong, and K. Kooiman. "Microbubble Composition and Preparation for High-Frequency Contrast-Enhanced Ultrasound Imaging: In Vitro and In Vivo Evaluation", IEEE Trans. Ultrason. Ferroelectr. Freq. Control, 64, pp. 555-567, (2017).

[402] A. Blume. "Lipids at the air–water interface", ChemTexts, 4, p. 3, (2018).

[403] E. Hosgor, T. Kucuk, I. N. Oksal, and D. B. Kaymak. "Design and control of distillation processes for methanol–chloroform separation", Comput. Chem. Eng., 67, pp. 166-177, (2014).

[404] T. Baumgart, G. Hunt, E. R. Farkas, W. W. Webb, and G. W. Feigenson. "Fluorescence probe partitioning between Lo/Ld phases in lipid membranes", Biochim. Biophys. Acta, 1768, pp. 2182-2194, (2007).

[405] S. Wold, K. Esbensen, and P. Geladi. "Principal component analysis", Chemom. Intell. Lab. Syst., 2, pp. 37-52, (1987).

[406] R. L. Tatusov, D. A. Natale, I. V. Garkavtsev, T. A. Tatusova, U. T. Shankavaram, B. S. Rao, B. Kiryutin, M. Y. Galperin, N. D. Fedorova, and E. V. Koonin. "The COG database: new developments in phylogenetic classification of proteins from complete genomes", Nucleic Acids Res., 29, pp. 22-28, (2001).

[407] S. Hell and E. H. K. Stelzer. "Fundamental improvement of resolution with a 4Pi-confocal fluorescence microscope using two-photon excitation", Opt. Commun., 93, pp. 277-282, (1992).

[408] T. R. Baekmark, G. Elender, D. D. Lasic, and E. Sackmann. "Conformational Transitions of Mixed Monolayers of Phospholipids and Polyethylene Oxide Lipopolymers and Interaction Forces with Solid Surfaces", Langmuir, 11, pp. 3975-3987, (1995).

[409] H. Hussain, A. Kerth, A. Blume, and J. Kressler. "Amphiphilic Block Copolymers of Poly(ethylene oxide) and Poly(perfluorohexylethyl methacrylate) at the Water Surface and Their Penetration into the Lipid Monolayer", The Journal of Physical Chemistry B, 108, pp. 9962-9969, (2004).

[410] T. R. Baekmark, T. Wiesenthal, P. Kuhn, A. Albersdorfer, O. Nuyken, and R. Merkel. "A systematic infrared reflection-absorption spectroscopy and film balance study of the phase behavior of lipopolymer monolayers at the air-water interface", Langmuir, 15, pp. 3616-3626, (1999).

[411] C. Theiss and U. Holzgrabe. "Characterization of polydisperse macrogols and macrogol-based excipients via HPLC and charged aerosol detection", J. Pharm. Biomed. Anal., 160, pp. 212-221, (2018).

[412] R. H. Abou-Saleh, J. R. McLaughlan, R. J. Bushby, B. R. Johnson, S. Freear, S. D. Evans, and N. H. Thomson. "Molecular Effects of Glycerol on Lipid Monolayers at the Gas–Liquid Interface: Impact on Microbubble Physical and Mechanical Properties", Langmuir, 35, pp. 10097-10105, (2019).

[413] H. M. McConnell. "Structures and Transitions in Lipid Monolayers at the Air-Water Interface", Annu. Rev. Phys. Chem., 42, pp. 171-195, (1991).

[414] P. Scholtysek, Z. Li, J. Kressler, and A. Blume. "Interactions of DPPC with semitelechelic poly(glycerol methacrylate)s with perfluoroalkyl endgroups.", Langmuir, 28, p. 15651–15662, (2012).

[415] G. W. Feigenson. "Phase behavior of lipid mixtures", Nat. Chem. Biol., 2, pp. 560-563, (2006).

[416] E. Rufeil-Fiori, N. Wilke, and A. J. Banchio. "Dipolar interactions between domains in lipid monolayers at the air–water interface", Soft Matter, 12, pp. 4769-4777, (2016).

[417] D. Andelman, F. Broçhard, and J. F. Joanny. "Phase transitions in Langmuir monolayers of polar molecules", J. Chem. Phys., 86, pp. 3673-3681, (1987).

[418] K. Tanwir and V. Tsoukanova. "Lateral Distribution of a Poly(ethylene glycol)-Grafted Phospholipid in Phosphocholine Monolayers Studied by Epifluorescence Microscopy", Langmuir, 24, pp. 14078-14087, (2008).

[419] M. L. Mitchell and R. A. Dluhy. "In situ FT-IR investigation of phospholipid monolayer phase transitions at the air water interface", J. Am. Chem. Soc., 110, pp. 712-718, (1988).

[420] R. D. Hunt, M. L. Mitchell, and R. A. Dluhy. "The interfacial structure of phospholipid monolayer films: an infrared reflectance study", J. Mol. Struct., 214, pp. 93-109, (1989).

[421] A. Blume and A. Kerth. "Peptide and protein binding to lipid monolayers studied by FT-IRRA spectroscopy", Biochim. Biophys. Acta, 1828, pp. 2294-2305, (2013).

[422] D. Shi, X. Liu, C. Counil, and M. P. Krafft. "Fluorocarbon Exposure Mode Markedly Affects Phospholipid Monolayer Behavior at the Gas/Liquid Interface: Impact on Size and Stability of Microbubbles", Langmuir, 35, pp. 10025-10033, (2019).

[423] R. H. Abou-Saleh, S. A. Peyman, B. R. G. Johnson, G. Marston, N. Ingram, R. Bushby, P. L. Coletta, A. F. Markham, and S. D. Evans. "The influence of intercalating perfluorohexane into lipid shells on nano and microbubble stability", Soft Matter, 12, pp. 7223-7230, (2016).

[424] J. H. Crowe, M. A. Whittam, D. Chapman, and L. M. Crowe. "Interactions of phospholipid monolayers with carbohydrates", Biochim. Biophys. Acta, Biomembr., 769, pp. 151-159, (1984).

[425] S. Lee, D. H. Kim, and D. Needham. "Equilibrium and Dynamic Interfacial Tension Measurements at Microscopic Interfaces Using a Micropipet Technique. 1. A New Method for Determination of Interfacial Tension", Langmuir, 17, pp. 5537-5543, (2001).

[426] K. Kooiman, S. Roovers, S. A. G. Langeveld, R. T. Kleven, H. Dewitte, M. A. O'Reilly, J. M. Escoffre, A. Bouakaz, M. D. Verweij, K. Hynynen, I. Lentacker, E. Stride, and C. K. Holland. "Ultrasound-Responsive Cavitation Nuclei for Therapy and Drug Delivery", Ultrasound Med Biol, pp. 1296-1325, (2020).

[427] S. A. G. Langeveld, I. Beekers, G. Collado-Lara, A. F. W. van der Steen, N. de Jong, and K. Kooiman. "The Impact of Lipid Handling and Phase Distribution on the Acoustic Behavior of Microbubbles", Pharmaceutics, 13, p. 119, (2021).

[428] S. A. G. Langeveld, C. Schwieger, I. Beekers, J. Blaffert, T. van Rooij, A. Blume, and K. Kooiman. "Ligand Distribution and Lipid Phase Behavior in Phospholipid-Coated Microbubbles and Monolayers", Langmuir, pp. 3221-3233, (2020).

[429] M. Overvelde, V. Garbin, J. Sijl, B. Dollet, N. de Jong, D. Lohse, and M. Versluis. "Nonlinear shell behavior of phospholipid-coated microbubbles", Ultrasound Med Biol, 36, pp. 2080-2092, (2010).

[430] H. M. Mansour and G. Zografi. "Relationships between Equilibrium Spreading Pressure and Phase Equilibria of Phospholipid Bilayers and Monolayers at the Air–Water Interface", Langmuir, 23, pp. 3809-3819, (2007).

[431] V. Daeichin, T. van Rooij, I. Skachkov, B. Ergin, P. A. C. Specht, A. Lima, C. Ince, J. G. Bosch, A. F. W. van der Steen, N. de Jong, and K. Kooiman. "Corrections to "Microbubble Composition and Preparation for High-Frequency Contrast-Enhanced Ultrasound Imaging: In Vitro and In Vivo Evaluation"", IEEE Trans Ultrason Ferroelectr Freq Control, 68, p. 2321, (2021).

[432] I. Beekers, K. R. Lattwein, J. J. P. Kouijzer, S. A. G. Langeveld, M. Vegter, R. Beurskens, F. Mastik, R. Verduyn Lunel, E. Verver, A. F. W. van der Steen, N. de Jong, and K. Kooiman. "Combined Confocal Microscope and Brandaris 128 Ultra-High-Speed Camera", Ultrasound Med Biol, 45, pp. 2575-2582, (2019).

[433] N. de Jong, R. Cornet, and C. T. Lancée. "Higher harmonics of vibrating gas-filled microspheres. Part two: measurements", Ultrasonics, 32, pp. 455-459, (1994).

[434] S. Unnikrishnan, Z. M. Du, G. B. Diakova, and A. L. Klibanov. "Formation of Microbubbles for Targeted Ultrasound Contrast Imaging: Practical Translation Considerations", Langmuir, 35, pp. 10034-10041, (2019).

[435] C. J. Malajczuk, Z. E. Hughes, and R. L. Mancera. "Molecular dynamics simulations of the interactions of DMSO, mono- and polyhydroxylated cryosolvents with a hydrated phospholipid bilayer", Biochimica et Biophysica Acta (BBA) - Biomembranes, 1828, pp. 2041-2055, (2013).

[436] L. P. Cavalcanti, I. Tho, O. Konovalov, S. Fossheim, and M. Brandl. "Compressibility study of quaternary phospholipid blend monolayers", Colloids and Surfaces B: Biointerfaces, 85, pp. 153-160, (2011).

[437] K. Sarkar, W. T. Shi, D. Chatterjee, and F. Forsberg. "Characterization of ultrasound contrast microbubbles using in vitro experiments and viscous and viscoelastic interface models for encapsulation", J Acoust Soc Am, 118, pp. 539-550, (2005).

[438] L. Wei, G. Wahyulaksana, B. Meijlink, A. Ramalli, E. Noothout, M. Verweij, E. Boni, K. Kooiman, A. F. W. Van der Steen, P. Tortoli, N. De Jong, and H. J. Vos. "High Frame Rate Volumetric Imaging of Microbubbles Using a Sparse Array and Spatial Coherence Beamforming", IEEE Trans Ultrason Ferroelectr Freq Control, Pp, (2021).

[439] Z. M. Binsalamah, A. Paul, S. Prakash, and D. Shum-Tim. "Nanomedicine in cardiovascular therapy: recent advancements", Expert Rev Cardiovasc Ther, 10, pp. 805-815, (2012).

[440] E. Westein, U. Flierl, C. E. Hagemeyer, and K. Peter. "Destination Known: Targeted Drug Delivery in Atherosclerosis and Thrombosis", Drug Development Research, 74, pp. 460-471, (2013).

[441] X. Chen, J. Wang, M. Versluis, N. d. Jong, and F. S. Villanueva. "Ultra-fast bright field and fluorescence imaging of the dynamics of micrometer-sized objects", Review of Scientific Instruments, 84, p. 063701, (2013).

[442] B. L. Helfield, X. Chen, B. Qin, S. C. Watkins, and F. S. Villanueva. "Mechanistic Insight into Sonoporation with Ultrasound-Stimulated Polymer Microbubbles", Ultrasound Med Biol, 43, pp. 2678-2689, (2017).

[443] K. Kooiman, M. Foppen-Harteveld, A. F. van der Steen, and N. de Jong. "Sonoporation of endothelial cells by vibrating targeted microbubbles", J Control Release, 154, pp. 35-41, (2011).

[444] I. Lentacker, N. Wang, R. E. Vandenbroucke, J. Demeester, S. C. De Smedt, and N. N. Sanders. "Ultrasound Exposure of Lipoplex Loaded Microbubbles Facilitates Direct Cytoplasmic Entry of the Lipoplexes", Molecular Pharmaceutics, 6, pp. 457-467, (2009).

[445] I. Lentacker, B. Geers, J. Demeester, S. C. De Smedt, and N. N. Sanders. "Design and Evaluation of Doxorubicin-containing Microbubbles for Ultrasound-triggered Doxorubicin Delivery: Cytotoxicity and Mechanisms Involved", Molecular Therapy, 18, pp. 101-108, (2010).

[446] I. De Cock, G. Lajoinie, M. Versluis, S. C. De Smedt, and I. Lentacker. "Sonoprinting and the importance of microbubble loading for the ultrasound mediated cellular delivery of nanoparticles", Biomaterials, 83, pp. 294-307, (2016).

[447] B. H. A. Lammertink, R. Deckers, M. Derieppe, I. De Cock, I. Lentacker, G. Storm, C. T. W. Moonen, and C. Bos. "Dynamic Fluorescence Microscopy of Cellular Uptake of Intercalating Model Drugs by Ultrasound-Activated Microbubbles", Molecular Imaging and Biology, 19, pp. 683-693, (2017).

[448] D. Maresca, M. Emmer, P. L. M. J. van Neer, H. J. Vos, M. Versluis, M. Muller, N. de Jong, and A. F. W. van der Steen. "Acoustic Sizing of an Ultrasound Contrast Agent", Ultrasound in Medicine & Biology, 36, pp. 1713-1721, (2010).

[449] J. J. Kwan and M. A. Borden. "Lipid monolayer collapse and microbubble stability", Adv Colloid Interface Sci, 183-184, pp. 82-99, (2012).

[450] E. C. Gelderblom, H. J. Vos, F. Mastik, T. Faez, Y. Luan, T. J. A. Kokhuis, A. F. W. v. d. Steen, D. Lohse, N. d. Jong, and M. Versluis. "Brandaris 128 ultra-high-speed imaging facility: 10 years of operation, updates, and enhanced features", Review of Scientific Instruments, 83, p. 103706, (2012).

[451] Y. Luan, G. Lajoinie, E. Gelderblom, I. Skachkov, A. F. van der Steen, H. J. Vos, M. Versluis, and N. De Jong. "Lipid shedding from single oscillating microbubbles", Ultrasound Med Biol, 40, pp. 1834-1846, (2014).

[452] K. Kooiman, T. van Rooij, B. Qin, F. Mastik, H. J. Vos, M. Versluis, A. L. Klibanov, N. de Jong, F. S. Villanueva, and X. Chen. "Focal areas of increased lipid concentration on the coating of microbubbles during short tone-burst ultrasound insonification", PLoS One, 12, p. e0180747, (2017).

[453] M. Versluis, E. Stride, G. Lajoinie, B. Dollet, and T. Segers. "Ultrasound Contrast Agent Modeling: A Review", Ultrasound Med Biol, 46, pp. 2117-2144, (2020).

[454] S. Garg, A. A. Thomas, and M. A. Borden. "The effect of lipid monolayer in-plane rigidity on in vivo microbubble circulation persistence", Biomaterials, 34, pp. 6862-6870, (2013).

[455] J. S. Lum, J. D. Dove, T. W. Murray, and M. A. Borden. "Single Microbubble Measurements of Lipid Monolayer Viscoelastic Properties for Small-Amplitude Oscillations", Langmuir, 32, pp. 9410-9417, (2016).

[456] J. S. Lum, D. M. Stobbe, M. A. Borden, and T. W. Murray. "Photoacoustic technique to measure temperature effects on microbubble viscoelastic properties", Appl Phys Lett, 112, pp. 111905-111905, (2018).

[457] C. Yuan and L. J. Johnston. "Phase evolution in cholesterol/DPPC monolayers: atomic force microscopy and near field scanning optical microscopy studies", J Microsc, 205, pp. 136-146, (2002).

[458] T. Miyoshi and S. Kato. "Detailed Analysis of the Surface Area and Elasticity in the Saturated 1,2-Diacylphosphatidylcholine/Cholesterol Binary Monolayer System", Langmuir, 31, pp. 9086-9096, (2015).

[459] S. L. Veatch and S. L. Keller. "Separation of liquid phases in giant vesicles of ternary mixtures of phospholipids and cholesterol", Biophys J, 85, pp. 3074-3083, (2003).

[460] R. Kaur, R. Morris, M. Bencsik, A. Vangala, T. Rades, and Y. Perrie. "Development of a Novel Magnetic Resonance Imaging Contrast Agent for Pressure Measurements Using Lipid-Coated Microbubbles", J Biomed Nanotechnol, 5, pp. 707-715, (2009).

[461] H. J. Lee, T. J. Yoon, and Y. I. Yoon. "Synthesis of ultrasound contrast agents: characteristics and size distribution analysis (secondary publication)", Ultrasonography, 36, pp. 378-384, (2017).

[462] D. Chapman. "Handbook of Lipid Research, Volume 4: The Physical Chemistry of Lipids", Biochem Soc Trans, 15, pp. 184-185, (1987).

[463] I. Beekers, T. van Rooij, A. van der Steen, N. Jong, M. Verweij, and K. Kooiman. "Acoustic Characterization of the CLINIcell for Ultrasound Contrast Agent Studies", IEEE Trans Ultrason Ferroelectr Freq Control, PP, pp. 244-246, (2018).

[464] R. A. Demel and B. De Kruyff. "The function of sterols in membranes", Biochim Biophys Acta, 457, pp. 109-132, (1976).

[465] Y. K. Lee, E.-S. Yu, D. J. Ahn, and Y.-S. Ryu. "Elasticity-Driven Membrane Budding through Cholesterol Concentration on Supported Lipid Monolayer–Bilayer Junction", Advanced Materials Interfaces, 7, p. 2000937, (2020).

[466] J. R. Silvius, "Thermotropic Phase Transitions of Pure Lipids in Model Membranes and Their Modifications by Membrane Proteins," in Lipid-Protein Interactions, ed New York: John Wiley & Sons, Inc, 1982.

[467] L. Redondo-Morata, M. I. Giannotti, and F. Sanz. "Influence of Cholesterol on the Phase Transition of Lipid Bilayers: A Temperature-Controlled Force Spectroscopy Study", Langmuir, 28, pp. 12851-12860, (2012).

[468] M. A. Borden, D. E. Kruse, C. F. Caskey, Z. Shukui, P. A. Dayton, and K. W. Ferrara. "Influence of lipid shell physicochemical properties on ultrasound-induced microbubble destruction", IEEE Trans Ultrason Ferroelectr Freq Control, 52, pp. 1992-2002, (2005).

[469] G. Pu, M. L. Longo, and M. A. Borden. "Effect of Microstructure on Molecular Oxygen Permeation through Condensed Phospholipid Monolayers", J Am Chem Soc, 127, pp. 6524-6525, (2005).

[470] G. Pu, M. A. Borden, and M. L. Longo. "Collapse and Shedding Transitions in Binary Lipid Monolayers Coating Microbubbles", Langmuir, 22, pp. 2993-2999, (2006).

[471] R. J. Browning, M. Aron, A. Booth, P. Rademeyer, S. Wing, V. Brans, S. Shrivastava, D. Carugo, and E. Stride. "Spectral Imaging for Microbubble Characterization", Langmuir, 36, pp. 609-617, (2020).

[472] G. Paganelli, C. Belloni, P. Magnani, F. Zito, A. Pasini, I. Sassi, M. Meroni, M. Mariani, M. Vignali, A. G. Siccardi, and et al. "Two-step tumour targetting in ovarian cancer patients using biotinylated monoclonal antibodies and radioactive streptavidin", Eur J Nucl Med, 19, pp. 322-329, (1992).

[473] X. Duan, Q. Zhou, J. M. F. Wan, and A. C. H. Yu. "Sonoporation generates downstream cellular impact after membrane resealing", Sci Rep, 11, p. 5161, (2021).

[474] B. Helfield, X. Chen, S. C. Watkins, and F. S. Villanueva. "Transendothelial Perforations and the Sphere of Influence of Single-Site Sonoporation", Ultrasound Med Biol, 46, pp. 1686-1697, (2020).

[475] P. Hauff, T. Fritzsch, M. Reinhardt, W. Weitschies, F. Lüders, V. Uhlendorf, and D. Heldmann. "Delineation of experimental liver tumors in rabbits by a new ultrasound contrast agent and stimulated acoustic emission", Invest Radiol, 32, pp. 94-99, (1997).

[476] F. Forsberg, B. B. Goldberg, J. B. Liu, D. A. Merton, N. M. Rawool, and W. T. Shi. "Tissue-specific US contrast agent for evaluation of hepatic and splenic parenchyma", Radiology, 210, pp. 125-132, (1999).

[477] M. J. Blomley, T. Albrecht, D. O. Cosgrove, R. J. Eckersley, J. Butler-Barnes, V. Jayaram, N. Patel, R. A. Heckemann, A. Bauer, and R. Schlief. "Stimulated acoustic emission to image a late liver and spleen-specific phase of Levovist in normal volunteers and patients with and without liver disease", Ultrasound Med Biol, 25, pp. 1341-1352, (1999).

[478] E. Quaia, M. J. K. Blomley, S. Patel, C. J. Harvey, A. Padhani, P. Price, and D. O. Cosgrove. "Initial observations on the effect of irradiation on the liver-specific uptake of Levovist", European Journal of Radiology, 41, pp. 192-199, (2002).

[479] K. Yanagisawa, F. Moriyasu, T. Miyahara, M. Yuki, and H. Iijima. "Phagocytosis of ultrasound contrast agent microbubbles by Kupffer cells", Ultrasound Med Biol, 33, pp. 318-325, (2007).

[480] M. Schneider, A. Broillet, P. Bussat, N. Giessinger, J. Puginier, R. Ventrone, and F. Yan. "Gray-scale liver enhancement in VX2 tumor-bearing rabbits using BR14, a new ultrasonographic contrast agent", Invest Radiol, 32, pp. 410-417, (1997).

[481] K. V. Ramnarine, K. Kyriakopoulou, P. Gordon, N. W. McDicken, C. S. McArdle, and E. Leen. "Improved characterisation of focal liver tumours: dynamic power Doppler imaging using NC100100 echo-enhancer", Eur J Ultrasound, 11, pp. 95-104, (2000).

[482] A. K. Lim, N. Patel, R. J. Eckersley, S. D. Taylor-Robinson, D. O. Cosgrove, and M. J. Blomley. "Evidence for spleen-specific uptake of a microbubble contrast agent: a quantitative study in healthy volunteers", Radiology, 231, pp. 785-788, (2004).

[483] N. G. Fisher, J. P. Christiansen, A. Klibanov, R. P. Taylor, S. Kaul, and J. R. Lindner. "Influence of microbubble surface charge on capillary transit and myocardial contrast enhancement", J Am Coll Cardiol, 40, pp. 811-819, (2002).

[484] J. Aksnes, T. J. Eide, and K. Nordstrand. "Lipid entrapment and cellular changes in the rat myocard, lung and liver after long-term parenteral nutrition with lipid emulsion. A light microscopic and ultrastructural study", Apmis, 104, pp. 515-522, (1996).

[485] M. Rengarajan, A. Hayer, and J. A. Theriot. "Endothelial Cells Use a Formin-Dependent Phagocytosis-Like Process to Internalize the Bacterium Listeria monocytogenes", PLoS Pathog, 12, p. e1005603, (2016).

[486] J. Thomas, D. Jones, L. Moldovan, M. Anghelina, K. J. Gooch, and N. I. Moldovan. "Labeling of endothelial cells with magnetic microbeads by angiophagy", Biotechnol Lett, 40, pp. 1189-1200, (2018).

[487] S. A. G. Langeveld, B. Meijlink, and K. Kooiman. "Phospholipid-coated targeted microbubbles for ultrasound molecular imaging and therapy", Curr Opin Chem Biol, 63, pp. 171-179, (2021).

[488] K. W. Dunn and E. Wang. "Optical aberrations and objective choice in multicolor confocal microscopy", Biotechniques, 28, pp. 542-544, 546, 548-550, (2000).

[489] L. Schermelleh, R. Heintzmann, and H. Leonhardt. "A guide to super-resolution fluorescence microscopy", Journal of Cell Biology, 190, pp. 165-175, (2010).

[490] J. R. Lindner, P. A. Dayton, M. P. Coggins, K. Ley, J. Song, K. Ferrara, and S. Kaul. "Noninvasive Imaging of Inflammation by Ultrasound Detection of Phagocytosed Microbubbles", Circulation, 102, pp. 531-538, (2000).

[491] R. E. Serda, S. Ferrati, B. Godin, E. Tasciotti, X. Liu, and M. Ferrari. "Mitotic trafficking of silicon microparticles", Nanoscale, 1, pp. 250-259, (2009).

[492] M. Ahmed, B. Cerroni, A. Razuvaev, J. Härmark, G. Paradossi, K. Caidahl, and B. Gustafsson. "Cellular Uptake of Plain and SPION-Modified Microbubbles for Potential Use in Molecular Imaging", Cell Mol Bioeng, 10, pp. 537-548, (2017).

[493] A. D. Terrisse, N. Puech, S. Allart, P. Gourdy, J. M. Xuereb, B. Payrastre, and P. Sié. "Internalization of microparticles by endothelial cells promotes platelet/endothelial cell interaction under flow", J Thromb Haemost, 8, pp. 2810-2819, (2010).

[494] C. J. Treutiger, A. Heddini, V. Fernandez, W. A. Muller, and M. Wahlgren. "PECAM-1/CDS31, an endothelial receptor for binding Plasmodium falciparum-infected erythrocytes", Nature Medicine, 3, pp. 1405-1408, (1997).

[495] S. Muro, R. Wiewrodt, A. Thomas, L. Koniaris, S. M. Albelda, V. R. Muzykantov, and M. Koval. "A novel endocytic pathway induced by clustering endothelial ICAM-1 or PECAM-1", Journal of Cell Science, 116, pp. 1599-1609, (2003).

[496] P. A. Dayton, J. E. Chomas, A. F. Lum, J. S. Allen, J. R. Lindner, S. I. Simon, and K. W. Ferrara. "Optical and acoustical dynamics of microbubble contrast agents inside neutrophils", Biophys J, 80, pp. 1547-1556, (2001).

[497] D. C. Walker, A. MacKenzie, and S. Hosford. "The structure of the tricellular region of endothelial tight junctions of pulmonary capillaries analyzed by freeze-fracture", Microvasc Res, 48, pp. 259-281, (1994).

[498] A. R. Burns, D. C. Walker, E. S. Brown, L. T. Thurmon, R. A. Bowden, C. R. Keese, S. I. Simon, M. L. Entman, and C. W. Smith. "Neutrophil transendothelial migration is independent of tight junctions and occurs preferentially at tricellular corners", J Immunol, 159, pp. 2893-2903, (1997).

[499] J. Park, Z. Fan, and C. Deng. "Effects of shear stress cultivation on cell membrane disruption and intracellular calcium concentration in sonoporation of endothelial cells", J Biomech, 44, pp. 164-169, (2011).

[500] K. Otani, H. Nishimura, A. Kamiya, and M. Harada-Shiba. "Simplified Preparation of alphavbeta3 Integrin-Targeted Microbubbles Based on a Clinically Available Ultrasound Contrast Agent: Validation in a Tumor-Bearing Mouse Model", Ultrasound Med Biol, 44, pp. 1063-1073, (2018).

[501] J. Zhang, S. Wang, Z. Deng, L. Li, and G. Tan. "Ultrasound-Triggered Drug Delivery for Breast Tumor Therapy Through iRGD-Targeted Paclitaxel-Loaded Liposome-Microbubble Complexes", J Biomed Nanotechnol, 14, pp. 1384-1395, (2018).

[502] H. Leong-Poi, J. Christiansen, A. L. Klibanov, S. Kaul, and J. R. Lindner. "Noninvasive assessment of angiogenesis by ultrasound and microbubbles targeted to alpha(v)-integrins", Circulation, 107, pp. 455-460, (2003).

[503] V. Daeichin, K. Kooiman, I. Skachkov, J. G. Bosch, T. L. Theelen, K. Steiger, A. Needles, B. J. Janssen, M. J. Daemen, A. F. van der Steen, N. de Jong, and J. C. Sluimer. "Quantification of Endothelial αvβ3 Expression with High-Frequency Ultrasound and Targeted Microbubbles: In Vitro and In Vivo Studies", Ultrasound Med Biol, 42, pp. 2283-2293, (2016).

[504] M. Azmin, C. Harfield, Z. Ahmad, M. Edirisinghe, and E. Stride. "How do microbubbles and ultrasound interact? Basic physical, dynamic and engineering principles", Curr Pharm Des, 18, pp. 2118-2134, (2012).

[505] A. L. Klibanov, M. S. Hughes, F. S. Villanueva, R. J. Jankowski, W. R. Wagner, J. K. Wojdyla, J. H. Wible, and G. H. Brandenburger. "Targeting and ultrasound imaging of microbubble-based contrast agents", Magma, 8, pp. 177-184, (1999).

[506] J. Wischhusen, K. E. Wilson, J. G. Delcros, R. Molina-Peña, B. Gibert, S. Jiang, J. Ngo, D. Goldschneider, P. Mehlen, J. K. Willmann, and F. Padilla. "Ultrasound molecular imaging as a non-invasive companion diagnostic for netrin-1 interference therapy in breast cancer", Theranostics, 8, pp. 5126-5142, (2018).

[507] L. Abou-Elkacem, H. Wang, S. M. Chowdhury, R. H. Kimura, S. V. Bachawal, S. S. Gambhir, L. Tian, and J. K. Willmann. "Thy1-Targeted Microbubbles for Ultrasound Molecular Imaging of Pancreatic Ductal Adenocarcinoma", Clin Cancer Res, 24, pp. 1574-1585, (2018).

[508] J. J. P. Kouijzer, K. R. Lattwein, I. Beekers, S. A. G. Langeveld, M. Leon-Grooters, J.-M. Strub, E. Oliva, G. L. A. Mislin, N. de Jong, A. F. W. van der Steen, A. L. Klibanov, W. J. B. van Wamel, and K. Kooiman. "Vancomycin-decorated microbubbles as a theranostic agent for Staphylococcus aureus biofilms", Int J Pharm, p. 121154, (2021).

[509] F. Moccetti, E. Brown, A. Xie, W. Packwood, Y. Qi, Z. Ruggeri, W. Shentu, J. Chen, J. A. López, and J. R. Lindner. "Myocardial Infarction Produces Sustained Proinflammatory Endothelial Activation in Remote Arteries", J Am Coll Cardiol, 72, pp. 1015-1026, (2018).

[510] M. Wang, R. Hu, Y. Yang, L. Xiang, and Y. Mu. "In Vivo Ultrasound Molecular Imaging of SDF-1 Expression in a Swine Model of Acute Myocardial Infarction", Front Pharmacol, 10, p. 899, (2019).

[511] J. E. Streeter, S. G. Herrera-Loeza, N. F. Neel, J. J. Yeh, and P. A. Dayton. "A comparative evaluation of ultrasound molecular imaging, perfusion imaging, and volume measurements in evaluating response to therapy in patient-derived xenografts", Technol Cancer Res Treat, 12, pp. 311-321, (2013).

[512] S. Turco, A. El Kaffas, J. Zhou, A. M. Lutz, H. Wijkstra, J. K. Willmann, and M. Mischi. "Pharmacokinetic Modeling of Targeted Ultrasound Contrast Agents for Quantitative Assessment of Anti-Angiogenic Therapy: a Longitudinal Case-Control Study in Colon Cancer", Mol Imaging Biol, 21, pp. 633-643, (2019).

[513] A. Ingels, I. Leguerney, P. H. Cournède, J. Irani, S. Ferlicot, C. Sébrié, B. Benatsou, L. Jourdain, S. Pitre-Champagnat, J. J. Patard, and N. Lassau. "Ultrasound Molecular Imaging of Renal Cell Carcinoma: VEGFR targeted therapy monitored with VEGFR1 and FSHR targeted microbubbles", Sci Rep, 10, p. 7308, (2020).

[514] E. B. Herbst, S. Unnikrishnan, A. L. Klibanov, F. W. Mauldin, Jr., and J. A. Hossack. "Validation of Normalized Singular Spectrum Area as a Classifier for Molecularly Targeted Microbubble Adherence", Ultrasound Med Biol, 45, pp. 2493-2501, (2019).

[515] L. Woudstra, E. Meinster, L. V. Haren, A. M. Kay, M. Koopman, J. A. M. Belien, M. C. Morrison, A. C. V. Rossum, M. N. Helder, L. J. M. Juffermans, H. W. M. Niessen, and P. A. J. Krijnen. "StemBell therapy stabilizes atherosclerotic plaques after myocardial infarction", Cytotherapy, pp. 1-12, (2018).

[516] J. Su, J. Wang, J. Luo, and H. Li. "Ultrasound-mediated destruction of vascular endothelial growth factor (VEGF) targeted and paclitaxel loaded microbubbles for inhibition of human breast cancer cell MCF-7 proliferation", Mol Cell Probes, 46, pp. 1-9, (2019).

[517] Y. He, Y. Zhang, H. Y. Qin, D. Y. Gu, X. Lu, J. X. Hu, W. L. Ye, and G. B. He. "Inhibitory effect of 5-FU loaded ultrasound microbubbles on tumor growth and angiogenesis", Bioorg Med Chem Lett, 30, p. 127534, (2020).

[518] Y. Wang, X. Li, L. Liu, B. Liu, F. Wang, and C. Chen. "Tissue Targeting and Ultrasound-Targeted Microbubble Destruction Delivery of Plasmid DNA and Transfection In Vitro", Cell Mol Bioeng, 13, pp. 99-112, (2020).

[519] T. Ilovitsh, Y. Feng, J. Foiret, A. Kheirolomoom, H. Zhang, E. S. Ingham, A. Ilovitsh, S. K. Tumbale, B. Z. Fite, B. Wu, M. N. Raie, N. Zhang, A. J. Kare, M. Chavez, L. S. Qi, G. Pelled, D. Gazit, O. Vermesh, I. Steinberg, S. S. Gambhir, and K. W. Ferrara. "Low-frequency ultrasound-mediated cytokine transfection enhances T cell recruitment at local and distant tumor sites", Proc Natl Acad Sci U S A, 117, pp. 12674-12685, (2020).

[520] I. Skachkov, Y. Luan, A. F. van der Steen, N. de Jong, and K. Kooiman. "Targeted microbubble mediated sonoporation of endothelial cells in vivo", IEEE Trans Ultrason Ferroelectr Freq Control, 61, pp. 1661-1667, (2014).

[521] B. Meijlink, I. Skachkov, A. F. W. van der Steen, N. de Jong, and K. Kooiman. "The Preparation of Chicken Ex Ovo Embryos and Chorioallantoic Membrane Vessels as In Vivo Model for Contrast-Enhanced Ultrasound Imaging and Microbubble-Mediated Drug Delivery Studies", JoVE, p. e62076, (2021).

[522] J. A. Feshitan, C. C. Chen, J. J. Kwan, and M. A. Borden. "Microbubble size isolation by differential centrifugation", J Colloid Interface Sci, 329, pp. 316-324, (2009).

[523] T. Papaioannou and C. Stefanadis. "Vascular Wall Shear Stress: Basic Principles and Methods", Hellenic J Cardiol, 46, pp. 9-15, (2005).

[524] C. Brooks Peter, A. F. Clark Richard, and A. Cheresh David. "Requirement of Vascular Integrin αvβ3 for Angiogenesis", Science, 264, pp. 569-571, (1994).

[525] W. S. Jenkins, A. T. Vesey, A. Vickers, A. Neale, C. Moles, M. Connell, N. V. Joshi, C. Lucatelli, A. M. Fletcher, J. C. Spratt, S. Mirsadraee, E. J. van Beek, J. H. Rudd, D. E. Newby, and M. R. Dweck. "In vivo alpha-V beta-3 integrin expression in human aortic atherosclerosis", Heart, 105, pp. 1868-1875, (2019).

[526] V. Pathak, T. Nolte, E. Rama, A. Rix, S. M. Dadfar, V. Paefgen, S. Banala, E. M. Buhl, M. Weiler, V. Schulz, T. Lammers, and F. Kiessling. "Molecular magnetic resonance imaging of Alpha-v-Beta-3 integrin expression in tumors with ultrasound microbubbles", Biomaterials, 275, p. 120896, (2021).

[527] Y. Cao, J. Arbiser, R. J. D'Amato, P. A. D'Amore, D. E. Ingber, R. Kerbel, M. Klagsbrun, S. Lim, M. A. Moses, B. Zetter, H. Dvorak, and R. Langer. "Forty-Year Journey of Angiogenesis Translational Research", Sci Transl Med, 3, pp. 114rv113-114rv113, (2011).

[528] J. M. Tarbell and Z.-D. Shi. "Effect of the glycocalyx layer on transmission of interstitial flow shear stress to embedded cells", Biomech Model Mechanobiol, 12, pp. 111-121, (2013).

[529] J. A. Pedersen, F. Boschetti, and M. A. Swartz. "Effects of extracellular fiber architecture on cell membrane shear stress in a 3D fibrous matrix", J Biomech, 40, pp. 1484-1492, (2007).

[530] S. Jalali, M. A. del Pozo, K. Chen, H. Miao, Y. Li, M. A. Schwartz, J. Y. Shyy, and S. Chien. "Integrin-mediated mechanotransduction requires its dynamic interaction with specific extracellular matrix (ECM) ligands", Proc Natl Acad Sci U S A, 98, pp. 1042-1046, (2001).

[531] E. Tzima, M. A. del Pozo, S. J. Shattil, S. Chien, and M. A. Schwartz. "Activation of integrins in endothelial cells by fluid shear stress mediates Rho-dependent cytoskeletal alignment", EMBO J, 20, pp. 4639-4647, (2001).

[532] I. Gupta, J. Eisenbrey, M. Stanczak, A. Sridharan, J. K. Dave, J. B. Liu, C. Hazard, X. Wang, P. Wang, H. Li, K. Wallace, and F. Forsberg. "Effect of Pulse Shaping on Subharmonic Aided Pressure Estimation In Vitro and In Vivo", J Ultrasound Med, 36, pp. 3-11, (2017).

[533] H. Shekhar, N. J. Smith, J. L. Raymond, and C. K. Holland. "Effect of Temperature on the Size Distribution, Shell Properties, and Stability of Definity((R))", Ultrasound Med Biol, 44, pp. 434-446, (2018).

[534] C. Sun, I. Panagakou, V. Sboros, M. B. Butler, D. Kenwright, A. J. Thomson, and C. M. Moran. "Influence of temperature, needle gauge and injection rate on the size distribution, concentration and acoustic responses of ultrasound contrast agents at high frequency", Ultrasonics, 70, pp. 84-91, (2016).

[535] H. Mulvana, E. Stride, J. V. Hajnal, and R. J. Eckersley. "Temperature dependent behavior of ultrasound contrast agents", Ultrasound Med Biol, 36, pp. 925-934, (2010).

[536] C. Guiot, G. Pastore, M. Napoleone, P. Gabriele, M. Trotta, and R. Cavalli. "Thermal response of contrast agent microbubbles: preliminary results from physico-chemical and US-imaging characterization", Ultrasonics, 44 Suppl 1, pp. e127-130, (2006).

[537] W. Wang, G. J. Liu, X. Y. Xie, Z. F. Xu, L. D. Chen, G. L. Huang, L. Y. Zhou, and M. D. Lu. "Development and evaluation of lipid microbubbles targeted to alpha(v)beta(3)-integrin via biotin-avidin bridge", J Microencapsul, 29, pp. 177-184, (2012).

[538] H. Yang, X. Y. Xiong, L. Zhang, C. H. Wu, and Y. Y. Liu. "Adhesion of bio-functionalized ultrasound microbubbles to endothelial cells by targeting to vascular cell adhesion molecule-1 under shear flow", Int J Nanomed, 6, pp. 2043-2051, (2011).

[539] T. Maul, D. Dudgeon, M. Beste, D. Hammer, J. Lazo, F. Villanueva, and W. Wagner. "Optimization of Ultrasound Contrast Agents with Computational Models to Improve Selection of Ligands and Binding Strength", Biotechnol Bioeng, 107, pp. 854-864, (2010).

[540] P. Charoenphol, R. B. Huang, and O. Eniola-Adefeso. "Potential role of size and hemodynamics in the efficacy of vascular-targeted spherical drug carriers", Biomaterials, 31, pp. 1392-1402, (2010).

[541] M. Schneider, A. Broillet, I. Tardy, S. Pochon, P. Bussat, T. Bettinger, A. Helbert, M. Costa, and F. Tranquart. "Use of intravital microscopy to study the microvascular behavior of microbubble-based ultrasound contrast agents", Microcirculation, 19, pp. 245-259, (2012).

[542] R. E. Serda, J. Gu, R. C. Bhavane, X. Liu, C. Chiappini, P. Decuzzi, and M. Ferrari. "The association of silicon microparticles with endothelial cells in drug delivery to the vasculature", Biomaterials, 30, pp. 2440-2448, (2009).

[543] N. I. o. Health. "Research on Microbial Biofilms. Report No. PA-03-047", (2002).

[544] T. F. Mah and G. A. O'Toole. "Mechanisms of biofilm resistance to antimicrobial agents", Trends Microbiol, 9, pp. 34-39, (2001).

[545] E. M. Waters, S. E. Rowe, J. P. O'Gara, and B. P. Conlon. "Convergence of Staphylococcus aureus Persister and Biofilm Research: Can Biofilms Be Defined as Communities of Adherent Persister Cells?", PLoS Pathog, 12, p. e1006012, (2016).

[546] P. S. Stewart and J. W. Costerton. "Antibiotic resistance of bacteria in biofilms", Lancet, 358, pp. 135-138, (2001).

[547] A. Ito, A. Taniuchi, T. May, K. Kawata, and S. Okabe. "Increased antibiotic resistance of Escherichia coli in mature biofilms", Appl Environ Microbiol, 75, pp. 4093-4100, (2009).

[548] K. Lewis. "Persister cells and the riddle of biofilm survival", Biochemistry (Mosc), 70, pp. 267-274, (2005).

[549] A. Cassini, L. D. Hogberg, D. Plachouras, A. Quattrocchi, A. Hoxha, G. S. Simonsen, M. Colomb-Cotinat, M. E. Kretzschmar, B. Devleesschauwer, M. Cecchini, D. A. Ouakrim, T. C. Oliveira, M. J. Struelens, C. Suetens, D. L. Monnet, and A. M. R. C. G. Burden of. "Attributable deaths and disability-adjusted life-years caused by infections with antibiotic-resistant bacteria in the EU and the European Economic Area in 2015: a population-level modelling analysis", Lancet Infect Dis, 19, pp. 56-66, (2019).

[550] S. W. Lee, K. S. Phillips, H. Gu, M. Kazemzadeh-Narbat, and D. Ren. "How microbes read the map: Effects of implant topography on bacterial adhesion and biofilm formation", Biomaterials, 268, p. 120595, (2021).

[551] C. Chirouze, C. H. Cabell, V. G. Fowler, Jr., N. Khayat, L. Olaison, J. M. Miro, G. Habib, E. Abrutyn, S. Eykyn, G. R. Corey, C. Selton-Suty, B. Hoen, and G. International Collaboration on Endocarditis Study. "Prognostic factors in 61 cases of Staphylococcus aureus prosthetic valve infective endocarditis from the International Collaboration on Endocarditis merged database", Clin Infect Dis, 38, pp. 1323-1327, (2004).

[552] D. R. Murdoch, G. R. Corey, B. Hoen, J. M. Miro, V. G. Fowler, Jr., A. S. Bayer, A. W. Karchmer, L. Olaison, P. A. Pappas, P. Moreillon, S. T. Chambers, V. H. Chu, V. Falco, D. J. Holland, P. Jones, J. L. Klein, N. J. Raymond, K. M. Read, M. F. Tripodi, R. Utili, A. Wang, C. W. Woods, C. H. Cabell, and I. International Collaboration on Endocarditis-Prospective Cohort Study. "Clinical presentation, etiology, and outcome of infective endocarditis in the 21st century: the International Collaboration on Endocarditis-Prospective Cohort Study", Arch Intern Med, 169, pp. 463-473, (2009).

[553] M. Mirabel, R. Sonneville, D. Hajage, E. Novy, F. Tubach, P. Vignon, P. Perez, S. Lavoue, A. Kouatchet, O. Pajot, A. Mekontso-Dessap, J. M. Tonnelier, P. E. Bollaert, J. P. Frat, J. C. Navellou, H. Hyvernat, A. A. Hssain, J. F. Timsit, B. Megarbane, M. Wolff, J. L. Trouillet, and E. S. Group. "Long-term outcomes and cardiac surgery in critically ill patients with infective endocarditis", Eur Heart J, 35, pp. 1195-1204, (2014).

[554] A. Bannay, B. Hoen, X. Duval, J. F. Obadia, C. Selton-Suty, V. Le Moing, P. Tattevin, B. Iung, F. Delahaye, F. Alla, and A. S. Group. "The impact of valve surgery on short- and long-term mortality in left-sided infective endocarditis: do differences in methodological approaches explain previous conflicting results?", Eur Heart J, 32, pp. 2003-2015, (2011).

[555] A. A. Bin Abdulhak, L. M. Baddour, P. J. Erwin, B. Hoen, V. H. Chu, G. A. Mensah, and I. M. Tleyjeh. "Global and regional burden of infective endocarditis, 1990-2010: a systematic review of the literature", Glob Heart, 9, pp. 131-143, (2014).

[556] J. Tahon, P.-J. Geselle, B. Vandenberk, E. E. Hill, W. E. Peetermans, P. Herijgers, S. Janssens, and M.-C. Herregods. "Long-term follow-up of patients with infective endocarditis in a tertiary referral center", International Journal of Cardiology, 331, pp. 176-182, (2021).

[557] D. C. DeSimone and M. R. Sohail. "Management of bacteremia in patients living with cardiovascular implantable electronic devices", Heart Rhythm, 13, pp. 2247-2252, (2016).

[558] L. Kreitmann, D. Montaigne, D. Launay, S. Morell-Dubois, H. Maillard, M. Lambert, E. Hachulla, and V. Sobanski. "Clinical Characteristics and Outcome of Patients with Infective Endocarditis Diagnosed in a Department of Internal Medicine", J Clin Med, 9, (2020).

[559] C. A. Sennoga, E. Kanbar, L. Auboire, P. A. Dujardin, D. Fouan, J. M. Escoffre, and A. Bouakaz. "Microbubble-mediated ultrasound drug-delivery and therapeutic monitoring", Expert Opin Drug Deliv, 14, pp. 1031-1043, (2017).

[560] A. F. L. Schinkel, J. G. Bosch, D. Staub, D. Adam, and S. B. Feinstein. "Contrast-Enhanced Ultrasound to Assess Carotid Intraplaque Neovascularization", Ultrasound Med Biol, 46, pp. 466-478, (2020).

[561] F. Moccetti, C. C. Weinkauf, B. P. Davidson, J. T. Belcik, E. R. Marinelli, E. Unger, and J. R. Lindner. "Ultrasound Molecular Imaging of Atherosclerosis Using Small-Peptide Targeting Ligands Against Endothelial Markers of Inflammation and Oxidative Stress", Ultrasound Med Biol, 44, pp. 1155-1163, (2018).

[562] P. Anastasiadis, K. D. Mojica, J. S. Allen, and M. L. Matter. "Detection and quantification of bacterial biofilms combining high-frequency acoustic microscopy and targeted lipid microparticles", J Nanobiotechnology, 12, p. 24, (2014).

[563] N. Gilboa-Garber and D. Sudakevitz. "The hemagglutinating activities of Pseudomonas aeruginosa lectins PA-IL and PA-IIL exhibit opposite temperature profiles due to different receptor types", FEMS Immunol Med Microbiol, 25, pp. 365-369, (1999).

[564] B. M. Broker, S. Holtfreter, and I. Bekeredjian-Ding. "Immune control of Staphylococcus aureus - regulation and counter-regulation of the adaptive immune response", Int J Med Microbiol, 304, pp. 204-214, (2014).

[565] F. Wang, H. Zhou, O. P. Olademehin, S. J. Kim, and P. Tao. "Insights into Key Interactions between Vancomycin and Bacterial Cell Wall Structures", ACS Omega, 3, pp. 37-45, (2018).

[566] M. van Oosten, T. Schafer, J. A. Gazendam, K. Ohlsen, E. Tsompanidou, M. C. de Goffau, H. J. Harmsen, L. M. Crane, E. Lim, K. P. Francis, L. Cheung, M. Olive, V. Ntziachristos, J. M. van Dijl, and G. M. van Dam. "Real-time in vivo imaging of invasive- and biomaterial-associated bacterial infections using fluorescently labelled vancomycin", Nat Commun, 4, p. 2584, (2013).

[567] C. C. McComas, B. M. Crowley, and D. L. Boger. "Partitioning the loss in vancomycin binding affinity for D-Ala-D-Lac into lost H-bond and repulsive lone pair contributions", Journal of the American Chemical Society, 125, pp. 9314-9315, (2003).

[568] E. Dauty, J. S. Remy, G. Zuber, and J. P. Behr. "Intracellular delivery of nanometric DNA particles via the folate receptor", Bioconjug Chem, 13, pp. 831-839, (2002).

[569] L. Pritchard, C. Baker, J. Leggett, P. Sehdev, A. Brown, and K. B. Bayley. "Increasing vancomycin serum trough concentrations and incidence of nephrotoxicity", Am J Med, 123, pp. 1143-1149, (2010).

[570] S. Tongsai and P. Koomanachai. "The safety and efficacy of high versus low vancomycin trough levels in the treatment of patients with infections caused by methicillin-resistant Staphylococcus aureus: a meta-analysis", BMC Res Notes, 9, p. 455, (2016).

[571] J. J. Rychak, A. L. Klibanov, and J. A. Hossack. "Acoustic radiation force enhances targeted delivery of ultrasound contrast microbubbles: in vitro verification", IEEE Trans Ultrason Ferroelectr Freq Control, 52, pp. 421-433, (2005).

[572] F. W. Kremkau, General principles of echocardiography, 2015.

[573] C. R. Merritt, F. W. Kremkau, and J. C. Hobbins. "Diagnostic ultrasound: bioeffects and safety", Ultrasound Obstet Gynecol, 2, pp. 366-374, (1992).

[574] L. E. Kinsler, A. R. Frey, A. B. Coppens, and J. V. Sanders, Fundamentals of acoustics: John wiley & sons, 2000.

[575] A. M. Malek, S. L. Alper, and S. Izumo. "Hemodynamic shear stress and its role in atherosclerosis", JAMA, 282, pp. 2035-2042, (1999).

[576] J. J. Rychak, A. L. Klibanov, K. F. Ley, and J. A. Hossack. "Enhanced targeting of ultrasound contrast agents using acoustic radiation force", Ultrasound Med Biol, 33, pp. 1132-1139, (2007).

[577] V. Stove, L. Coene, M. Carlier, J. J. De Waele, T. Fiers, and A. G. Verstraete. "Measuring Unbound Versus Total Vancomycin Concentrations in Serum and Plasma: Methodological Issues and Relevance", Therapeutic Drug Monitoring, 37, (2015).

[578] T. Bettinger, P. Bussat, I. Tardy, S. Pochon, J. M. Hyvelin, P. Emmel, S. Henrioud, N. Biolluz, J. K. Willmann, M. Schneider, and F. Tranquart. "Ultrasound molecular imaging contrast agent binding to both E- and P-selectin in different species", Invest Radiol, 47, pp. 516-523, (2012).

[579] S. Wang, E. B. Herbst, F. W. Mauldin, Jr., G. B. Diakova, A. L. Klibanov, and J. A. Hossack. "Ultra-Low-Dose Ultrasound Molecular Imaging for the Detection of Angiogenesis in a Mouse Murine Tumor Model: How Little Can We See?", Invest Radiol, 51, pp. 758-766, (2016).

[580] C. A. Burtis and D. E. Bruns, Tietz fundamentals of clinical chemistry and molecular diagnostics-e-book: Elsevier Health Sciences, 2014.

[581] J. Wille and T. Coenye. "Biofilm dispersion: The key to biofilm eradication or opening Pandora's box?", Biofilm, 2, p. 100027, (2020).

[582] A. Franca, V. Carvalhais, M. Vilanova, G. B. Pier, and N. Cerca. "Characterization of an in vitro fed-batch model to obtain cells released from S. epidermidis biofilms", AMB Express, 6, p. 23, (2016).

[583] K. Lv, H. Zhai, Y. Jiang, P. Liang, H.-X. Xu, L. Du, Y.-H. Chou, X. Xie, Y. Luo, and Y. J. Lee. "Prospective assessment of diagnostic efficacy and safety of SonazoidTM and SonoVue® ultrasound contrast agents in patients with focal liver lesions", Abdominal Radiology, pp. 1-13, (2021).

[584] Z. Xing, H. Ke, J. Wang, B. Zhao, X. Yue, Z. Dai, and J. Liu. "Novel ultrasound contrast agent based on microbubbles generated from surfactant mixtures of Span 60 and polyoxyethylene 40 stearate", Acta biomaterialia, 6, pp. 3542-3549, (2010).

[585] A. J. Dixon, A. H. Dhanaliwala, J. L. Chen, and J. A. Hossack. "Enhanced intracellular delivery of a model drug using microbubbles produced by a microfluidic device", Ultrasound in medicine & biology, 39, pp. 1267-1276, (2013).

[586] Y. H. Chou, J. D. Liang, S. Y. Wang, S. J. Hsu, J. T. Hu, S. S. Yang, H. K. Wang, T. Y. Lee, and C. M. Tiu. "Safety of Perfluorobutane (Sonazoid) in Characterizing Focal Liver Lesions", J Med Ultrasound, 27, pp. 81-85, (2019).

[587] E. Rubinstein and Y. Keynan. "Vancomycin revisited - 60 years later", Front Public Health, 2, p. 217, (2014).

[588] P. Frinking, T. Segers, Y. Luan, and F. Tranquart. "Three Decades of Ultrasound Contrast Agents: A Review of the Past, Present and Future Improvements", Ultrasound Med Biol, 46, pp. 892-908, (2020).

[589] A. Zlitni and S. S. Gambhir. "Molecular imaging agents for ultrasound", Curr Opin Chem Biol, 45, pp. 113-120, (2018).

[590] J. Owen, C. Crake, J. Y. Lee, D. Carugo, E. Beguin, A. A. Khrapitchev, R. J. Browning, N. Sibson, and E. Stride. "A versatile method for the preparation of particle-loaded microbubbles for multimodality imaging and targeted drug delivery", Drug Deliv Transl Res, 8, pp. 342-356, (2018).

[591] E. Beguin, L. Bau, S. Shrivastava, and E. Stride. "Comparing Strategies for Magnetic Functionalization of Microbubbles", ACS Appl Mater Interfaces, 11, pp. 1829-1840, (2019).

[592] D. Shi, J. Wallyn, D. V. Nguyen, F. Perton, D. Felder-Flesch, S. Bégin-Colin, M. Maaloum, and M. P. Krafft. "Microbubbles decorated with dendronized magnetic nanoparticles for biomedical imaging: effective stabilization via fluorous interactions", Beilstein J Nanotechnol, 10, pp. 2103-2115, (2019).

[593] E. Beguin, M. D. Gray, K. A. Logan, H. Nesbitt, Y. Sheng, S. Kamila, L. C. Barnsley, L. Bau, A. P. McHale, J. F. Callan, and E. Stride. "Magnetic microbubble mediated chemo-sonodynamic therapy using a combined magnetic-acoustic device", J Control Release, 317, pp. 23-33, (2020).

[594] H. X. Yuan, W. P. Wang, J. X. Wen, L. W. Lin, A. A. Exner, P. S. Guan, and X. J. Chen. "Dual-Targeted Microbubbles Specific to Integrin alphaVbeta3 and Vascular Endothelial Growth Factor Receptor 2 for Ultrasonography Evaluation of Tumor Angiogenesis", Ultrasound Med Biol, 44, pp. 1460-1467, (2018).

[595] F. Yan, Y. Sun, Y. Mao, M. Wu, Z. Deng, S. Li, X. Liu, L. Xue, and H. Zheng. "Ultrasound Molecular Imaging of Atherosclerosis for Early Diagnosis and Therapeutic Evaluation through Leucocyte-like Multiple Targeted Microbubbles", Theranostics, 8, pp. 1879-1891, (2018).

[596] R. Bam, P. S. Lown, L. A. Stern, K. Sharma, K. E. Wilson, G. R. Bean, A. M. Lutz, R. Paulmurugan, B. J. Hackel, J. Dahl, and L. Abou-Elkacem. "Efficacy of Affibody-Based Ultrasound Molecular Imaging of Vascular B7-H3 for Breast Cancer Detection", Clin Cancer Res, 26, pp. 2140-2150, (2020).

[597] Y. Zhou, Z. Song, Q. Hu, X. Ji, H. Zheng, X. Wang, and Z. Li. "Evaluation of the Expression of Matrix Metalloproteinase-1 of Laryngeal Squamous Cell Carcinoma by Ultrasound Molecular Imaging", Front Pharmacol, 10, p. 655, (2019).

[598] X. Mo, F. Yan, and B. Zhang. "Molecular Ultrasound Monitoring of Early Artery Injury After Carotid Balloon Angioplasty", Front Pharmacol, 9, p. 1569, (2018).

[599] J. Zhu, Y. Wang, P. Yang, Q. Liu, J. Hu, W. Yang, P. Liu, F. He, Y. Bai, S. Gai, R. Xie, and C. Li. "GPC3-targeted and curcumin-loaded phospholipid microbubbles for sono-photodynamic therapy in liver cancer cells", Colloids Surf B, 197, p. 111358, (2020).

[600] Y. Xie, Y. Chen, L. Zhang, M. Wu, Z. Deng, Y. Yang, J. Wang, Q. Lv, H. Zheng, M. Xie, and F. Yan. "Ultrasound Molecular Imaging of Lymphocyte-endothelium Adhesion Cascade in Acute Cellular Rejection of Cardiac Allografts", Transplantation, 103, pp. 1603-1611, (2019).

[601] A. Luong, D. Smith, C.-H. Tai, B. Cotter, C. Luo, M. Strachan, A. DeMaria, and J. J. Rychak. "Development of a Translatable Ultrasound Molecular Imaging Agent for Inflammation", Ultrasound Med Biol, 46, pp. 690-702, (2020).

[602] M. Punjabi, L. Xu, A. Ochoa-Espinosa, A. Kosareva, T. Wolff, A. Murtaja, A. Broisat, N. Devoogdt, and B. A. Kaufmann. "Ultrasound Molecular Imaging of Atherosclerosis With Nanobodies: Translatable Microbubble Targeting Murine and Human VCAM (Vascular Cell Adhesion Molecule) 1", Arterioscler Thromb Vasc Biol, 39, pp. 2520-2530, (2019).

[603] C. J. Slagle, D. H. Thamm, E. K. Randall, and M. A. Borden. "Click Conjugation of Cloaked Peptide Ligands to Microbubbles", Bioconjug Chem, 29, pp. 1534-1543, (2018).

[604] K. Otani, A. Kamiya, T. Miyazaki, A. Koga, A. Inatomi, and M. Harada-Shiba. "Surface Modification with Lactadherin Augments the Attachment of Sonazoid Microbubbles to Glycoprotein IIb/IIIa", Ultrasound Med Biol, 45, pp. 1455-1465, (2019).

[605] H. Wang, J.-M. Hyvelin, S. A. Felt, I. Guracar, J. G. Vilches-Moure, S. Cherkaoui, T. Bettinger, L. Tian, A. M. Lutz, and J. K. Willmann. "US Molecular Imaging of Acute Ileitis: Anti-Inflammatory Treatment Response Monitored with Targeted Microbubbles in a Preclinical Model", Radiology, 289, pp. 90-100, (2018).

[606] H. Wang, J. G. Vilches-Moure, S. Cherkaoui, I. Tardy, C. Alleaume, T. Bettinger, A. Lutz, and R. Paulmurugan. "Chronic Model of Inflammatory Bowel Disease in IL-10(-/-) Transgenic Mice: Evaluation with Ultrasound Molecular Imaging", Theranostics, 9, pp. 6031-6046, (2019).

[607] Y. Jing, Y. Hu, H. Li, J. Wang, X. Si, H. Zheng, J. Liu, W. Liao, Y. Liao, and J. Bin. "Assessment of Thrombotic Risk in Atrial Fibrillation with Ultrasound Molecular Imaging of P-Selectin", Thromb Haemost, 118, pp. 388-400, (2018).

[608] F. Zheng, P. Li, S. V. Bachawal, H. Wang, C. Li, W. Yuan, B. Huang, and R. Paulmurugan. "Assessment of Metastatic and Reactive Sentinel Lymph Nodes with B7-H3-Targeted Ultrasound Molecular Imaging: A Longitudinal Study in Mouse Models", Mol Imaging Biol, 22, pp. 1003-1011, (2020).

[609] K. Nam, M. Stanczak, F. Forsberg, J. B. Liu, J. R. Eisenbrey, C. C. Solomides, and A. Lyshchik. "Sentinel Lymph Node Characterization with a Dual-Targeted Molecular Ultrasound Contrast Agent", Mol Imaging Biol, 20, pp. 221-229, (2018).

[610] A. Helbert, M. Von Wronski, D. Colevret, C. Botteron, F. Padilla, T. Bettinger, I. Tardy, and J. M. Hyvelin. "Ultrasound Molecular Imaging With BR55, a Predictive Tool of Antiangiogenic Treatment Efficacy in a Chemo-Induced Mammary Tumor Model", Invest Radiol, 55, pp. 657-665, (2020).

[611] T. Atkinson, W. Packwood, A. Xie, S. Liang, Y. Qi, Z. Ruggeri, J. Lopez, B. P. Davidson, and J. R. Lindner. "Assessment of Novel Antioxidant Therapy in Atherosclerosis by Contrast Ultrasound Molecular Imaging", J Am Soc Echocardiogr, 31, pp. 1252-1259.e1251, (2018).

[612] C. C. Weinkauf, K. Concha-Moore, J. R. Lindner, E. R. Marinelli, K. P. Hadinger, S. Bhattacharjee, S. S. Berman, K. Goshima, L. R. Leon, Jr., T. O. Matsunaga, and E. Unger. "Endothelial vascular cell adhesion molecule 1 is a marker for high-risk carotid plaques and target for ultrasound molecular imaging", J Vasc Surg, 68, pp. 105s-113s, (2018).

[613] H. Liu, M. Gao, J. Gu, X. Wan, H. Wang, Q. Gu, Y. Zhou, and X. Sun. "VEGFR1-Targeted Contrast-Enhanced Ultrasound Imaging Quantification of Vasculogenic Mimicry Microcirculation in a Mouse Model of Choroidal Melanoma", Transl Vis Sci Technol, 9, p. 4, (2020).

[614] D. Hyun, L. Abou-Elkacem, V. A. Perez, S. M. Chowdhury, J. K. Willmann, and J. J. Dahl. "Improved Sensitivity in Ultrasound Molecular Imaging With Coherence-Based Beamforming", IEEE Trans Med Imaging, 37, pp. 241-250, (2018).

[615] D. Hyun, L. Abou-Elkacem, R. Bam, L. L. Brickson, C. D. Herickhoff, and J. J. Dahl. "Nondestructive Detection of Targeted Microbubbles Using Dual-Mode Data and Deep Learning for Real-Time Ultrasound Molecular Imaging", IEEE Trans Med Imaging, 39, pp. 3079-3088, (2020).

[616] m. d. s. Victor, L. C. Barnsley, D. Carugo, J. Owen, C. C. Coussios, and E. Stride. "Sonothrombolysis with magnetically targeted microbubbles", Ultrasound Med Biol, 45, pp. 1151-1163, (2019).

[617] M. Kang, Y. Zhang, X. Jin, G. Chen, Y. Huang, D. Wu, G. Li, J. Shan, P. Huang, and J. Chen. "Concurrent Treatment with Anti-DLL4 Enhances Antitumor and Proapoptotic Efficacy of a γ -Secretase Inhibitor in Gastric", Transl Oncol, 11, pp. 599-608, (2018).

[618] N. Shimamoto, M. Ito, M. Chiba, S. Honma, H. Imazu, and K. Sumiyama. "Antitumor effect of VEGFR2-targeted microbubble destruction with gemcitabine using an endoscopic ultrasound probe: In vivo mouse pancreatic ductal adenocarcinoma model", Hepatobiliary Pancreat Dis Int, 19, pp. 478-485, (2020).

[619] X. Chen, W. Wu, S. Wang, J. Zhong, N. M. Djama, G. Wei, Y. Lai, X. Si, S. Cao, W. Liao, Y. Liao, H. Li, and J. Bin. "Magnetic Targeting Improves the Therapeutic Efficacy of Microbubble-Mediated Obstructive Thrombus Sonothrombolysis", in J Thromb Heamost vol. 119, ed, 2019, pp. 1752-1766.

[620] G. Zhao, Q. Huang, F. Wang, X. Zhang, J. Hu, Y. Tan, N. Huang, Z. Wang, Z. Wang, and Y. Cheng. "Targeted shRNA-loaded liposome complex combined with focused ultrasound for blood brain barrier disruption and suppressing glioma growth", Cancer Lett, 418, pp. 147-158, (2018).

[621] H. Yang, Y. Sun, J. Wei, L. Xu, Y. Tang, L. Yang, X. Zhang, and Y. Lu. "The effects of ultrasound-targeted microbubble destruction (UTMD) carrying IL-8 monoclonal antibody on the inflammatory responses and stability of atherosclerotic plaques", Biomed Pharmacother, 118, p. 109161, (2019).

[622] E. Wilhelm, R. Battino, and R. J. Wilcock. "Low-pressure solubility of gases in liquid water", Chemical Reviews, 77, pp. 219-262, (1977).

[623] B. Nieswandt, I. Pleines, and M. Bender. "Platelet adhesion and activation mechanisms in arterial thrombosis and ischaemic stroke", Journal of Thrombosis and Haemostasis, 9, pp. 92-104, (2011).

[624] J.-D. Yan, Y. Liu, Z.-Y. Zhang, G.-Y. Liu, J.-H. Xu, L.-Y. Liu, and Y.-M. Hu. "Expression and prognostic significance of VEGFR-2 in breast cancer", Pathology - Research and Practice, 211, pp. 539-543, (2015).

[625] B. Jenny, J. Harrison, D. Baetens, J.-C. Tille, K. Burkhardt, H. Mottaz, J. Kiss, P.-Y. Dietrich, N. De Tribolet, G. Pizzolato, and M. Pepper. "Expression and localization of VEGF-C and VEGFR-3 in glioblastomas and haemangioblastomas", The Journal of Pathology, 209, pp. 34-43, (2006).

[626] M. E. Cooper, D. Vranes, S. Youssef, S. A. Stacker, A. J. Cox, B. Rizkalla, D. J. Casley, L. A. Bach, D. J. Kelly, and R. E. Gilbert. "Increased renal expression of vascular endothelial growth factor (VEGF) and its receptor VEGFR-2 in experimental diabetes", Diabetes, 48, pp. 2229-2239, (1999).

[627] J. Ehling, M. Misiewicz, S. von Stillfried, D. Möckel, J. Bzyl, S. Pochon, W. Lederle, R. Knuechel, T. Lammers, M. Palmowski, and F. Kiessling. "In situ validation of VEGFR-2 and α v ß 3 integrin as targets for breast lesion characterization", Angiogenesis, 19, pp. 245-254, (2016).

[628] M. Swiatkowska, J. Szymański, G. Padula, and C. S. Cierniewski. "Interaction and functional association of protein disulfide isomerase with alphaVbeta3 integrin on endothelial cells", Febs j, 275, pp. 1813-1823, (2008).

[629] C. S. Hughes, E. Longo, M. K. Phillips-Jones, and R. Hussain. "Characterisation of the selective binding of antibiotics vancomycin and teicoplanin by the VanS receptor regulating type A vancomycin resistance in the enterococci", Biochimica et biophysica acta. General subjects, 1861, pp. 1951-1959, (2017).

[630] T. Vanassche, A. Kauskot, J. Verhaegen, W. E. Peetermans, J. van Ryn, O. Schneewind, M. F. Hoylaerts, and P. Verhamme. "Fibrin formation by staphylothrombin facilitates Staphylococcus aureus-induced platelet aggregation", Thromb Haemost, 107, pp. 1107-1121, (2012).

[631] P. C. Sontum. "Physicochemical characteristics of Sonazoid, a new contrast agent for ultrasound imaging", Ultrasound Med Biol, 34, pp. 824-833, (2008).

[632] B. P. Davidson, J. Hodovan, M. E. Layoun, H. Golwala, F. Zahr, and J. R. Lindner. "Echocardiographic Ischemic Memory Molecular Imaging for Point-of-Care Detection of Myocardial Ischemia", J Am Coll Cardiol, 78, pp. 1990-2000, (2021).

[633] J. R. Lindner, J. Song, F. Xu, A. L. Klibanov, K. Singbartl, K. Ley, and S. Kaul. "Noninvasive Ultrasound Imaging of Inflammation Using Microbubbles Targeted to Activated Leukocytes", Circulation, 102, pp. 2745-2750, (2000).

Summary

Microbubbles are small particles, 1 to 10 µm in diameter, that consist of a gas core coated with phospholipids, proteins, or polymers. When exposed to an ultrasound wave, microbubbles respond by compressing and expanding, known as oscillation. This acoustic response is used in contrast enhanced ultrasound imaging and can have various cellular effects on the endothelial cell layer lining the vasculature. **Chapter 1** introduces how phospholipid molecules in the microbubble's coating are organized in microstructures which affect the acoustic response of microbubbles. By incorporating a ligand targeting a specific biomarker on the cell, microbubbles can also be functionalized for ultrasound molecular imaging and targeted therapeutic applications. For these purposes it is of essence that microbubbles respond uniformly to ultrasound, as each individual microbubble's response is needed to detect the imaging signal and must be controlled for safe drug delivery to the endothelial cell layer and beyond. The aim of this thesis was to develop a novel microbubble formulation with all coating components in the same phase, *i.e.* without microstructures, and to study the contribution of microstructures to an unpredictable microbubble response to ultrasound.

Chapter 2 provides an overview of microbubbles and other ultrasound-responsive cavitation nuclei, such as nanodroplets, used for therapy and drug delivery. The different available cavitation nuclei are summarized as well as the microbubble-cell interactions. Developments in different therapeutic areas are described, including treatment of tumors, immunotherapy, opening of the blood-brain and blood-spinal cord barriers, sonothrombolysis, cardiovascular drug delivery, and sonobactericide.

Two microbubble formulations based on the widely used main lipids DPPC and DSPC were characterized in **Chapter 3**. The lipid phase behavior of both formulations was evaluated using a Langmuir trough to study the phospholipid monolayers at the air/water interface. Both the DPPC- and DSPC-based formulations had a transition plateau due to a change in conformation of the PEGylated components, from mushroom to brush. While the domain morphology of both monolayers was different, the microstructures in DPPC- and DSPC-based microbubbles had a similar appearance. DSPC-based microbubbles were produced by probe sonication using the direct method, *i.e.* by directly dispersing the coating components in aqueous medium, or the indirect method, *i.e.* by dissolving the coating components in organic solvent, drying to form a lipid film, and finally dispersing the lipid film in aqueous medium. This lipid handling prior to microbubble production significantly

affected the ligand distribution on the outside of the microbubble coating, with the direct method resulting in a heterogeneous ligand distribution and the indirect method resulting in a homogeneous ligand distribution.

A new microbubble formulation with DSPE as main lipid was developed and characterized in **Chapter 4**. Microbubbles were produced by probe sonication or amalgamation and the stability, lipid phase distribution, and acoustic attenuation were investigated. Microbubbles produced by probe sonication and microbubbles produced by amalgamation with 30% propylene glycol both had a homogeneous lipid phase distribution, with all coating components miscible and in the same lipid phase. Microbubbles produced by amalgamation with 10% propylene glycol had circular condensed phase domains in the coating. Furthermore, all microbubble formulations had a short shelf-life stability as they decreased in size within one hour post-production. Although this limits the use of DSPE-based microbubbles *in vivo*, the formulations with homogeneous lipid phase distribution remain of interest for further studies on the relation between lipid phase distribution and the acoustic behavior of microbubbles.

To study the lipid phase distribution and acoustic response of individual microbubbles simultaneously, a unique optical imaging system was developed as described in **Chapter 5**. A custom-built confocal microscope was coupled to the Brandaris 128 ultra-high-speed camera, which was used in **Chapter 6 to 9**. In **Chapter 6**, the effect of cholesterol on the lipid phase distribution of DSPC-based microbubbles was investigated. Increasing concentrations of cholesterol resulted in decreased phase separation and microbubbles with 12 mol% cholesterol had a coating with all lipids miscible and in the same phase. However, the occurrence of buckles in the coating also increased with the addition of cholesterol. The combined confocal and Brandaris 128 system was used to study the relation between lipid handling and phase distribution to the acoustic behavior of individual microbubbles. Indirect method DSPC-based microbubbles had a more uniform response to ultrasound than direct method DSPC-based microbubbles and indirect method DSPC-based microbubbles containing 12 mol% cholesterol. Thus, the lipid handling and phase distribution significantly affected the acoustic behavior and indirect method DSPC-based microbubbles were the most promising formulation for ultrasound molecular imaging and therapeutic applications.

After the development and characterization of the new DSPE-based and cholesterol-containing microbubble formulations, the focus was shifted to the microbubble-cell morphology and interaction with indirect DSPC-based microbubbles in **Chapter 7**. Microbubbles targeted to $\alpha_V\beta_3$ or CD31 were compared to non-targeted and isotype control microbubbles. The internalization of microbubbles and effect on microbubble

oscillation and sonoporation were evaluated using the combined confocal microscope and Brandaris 128 system, with 3D confocal microscope imaging before and after exposure to ultrasound. Internalization of targeted microbubbles was found to be receptor-mediated, as non-targeted and isotype-control microbubbles were not internalized. Additionally, internalization of microbubbles had a damping effect on the oscillation and increased the cellular susceptibility to sonoporation. Finally, different cellular responses were observed, including pore formation resulting in intracellular drug delivery and tunnel formation, *i.e.* transcellular perforation, which may lead to transcellular drug delivery.

The influence of ligand distribution on binding efficacy was investigated in **Chapter 8**, by comparing the binding of $\alpha_V\beta_3$-targeted DSPC-based microbubbles produced by the direct and indirect method *in vitro* to a HUVEC monolayer under static conditions and under flow, and *in vivo* to the endothelial cells in chicken embryos. A homogeneous ligand distribution resulted in higher binding efficacy in all three experimental models. Finally, the internalization of $\alpha_V\beta_3$-targeted microbubbles was evaluated and found to be independent of ligand distribution.

In **Chapter 9**, the ultrasound molecular imaging and therapeutic potential of vancomycin-decorated microbubbles is described. This novel theranostic agent was targeted to bacterial biofilms and able to bind under flow. Moreover, the biofilm area could be reduced by ultrasound insonification and subsequent oscillation of the bound vancomycin-decorated microbubbles.

An overview of recent literature on phospholipid-coated targeted microbubbles for ultrasound molecular imaging and therapy is provided in **Chapter 10**. Different targeting strategies are discussed, as well as the use of ultrasound molecular imaging for studying disease progression, diagnostic imaging, and monitoring of therapeutic responses. In addition, studies on treatment of cardiovascular diseases and cancer with targeted microbubbles are summarized and it was concluded that targeted microbubbles always resulted in improved therapeutic outcome when compared to non-targeted microbubbles, both *in vitro* and *in vivo*.

Finally, the scientific contributions presented in this thesis are discussed in the context of microstructures in the microbubble coating and in the context of targeted microbubbles as theranostic agents in Chapter 11, including a future outlook on the continuing development of theranostic microbubbles.

Samenvatting

Microbellen zijn kleine gasbelletjes, 1 tot 10 µm in diameter, die bestaan uit een kern van gas ingekapseld in een dun laagje van lipiden, eiwitten, of polymeren. Wanneer ze blootgesteld worden aan ultrageluidsgolven reageren microbellen door kleiner en groter te worden, ook wel oscilleren genoemd. Dit acoustische gedrag wordt gebruikt voor ultrageluid beeldvorming met contrast en kunnen verschillende cellulaire effecten op de endotheellaag van de vaatwand hebben. **Hoofdstuk 1** introduceert hoe fosfolipiden zijn georganiseerd in microstructuren die de acoustische respons van microbellen beïnvloeden. Door de toevoeging van een ligand dat aan een specifieke biomarker op de cel kan binden, kunnen microbellen gefunctionaliseerd worden voor moleculaire beeldvorming met ultrageluid en voor doelgerichte therapeutische toepassingen. Om dit te bereiken is het belangrijk dat microbellen uniform reageren op ultrageluid, omdat elke individuele bel belangrijk is voor het beeldvormend signaal en voor veilige geneesmiddelafgifte aan de endotheel cellaag en onderliggend weefsel. Het doel van deze thesis was om een nieuwe microbel formulering te ontwikkelen waarin alle componenten van de schil in dezelfde fase zijn, dat wil zeggen zonder microstructuren in de schil, en om te bepalen hoe microstructuren in de schil bijdragen aan de onvoorspelbare respons van microbellen op ultrageluid.

Hoofdstuk 2 geeft een overzicht van de microbellen en andere deeltjes die op ultrageluid reageren, zoals nanodruppels, die gebruikt worden voor therapie en geneesmiddelafgifte. De verschillende beschikbare deeltjes worden samengevat net als de microbel-cel interacties. Ontwikkelingen op verschillende therapeutische gebieden worden beschreven, met name de behandeling van tumoren, immunotherapie, opening van de bloed-hersen- en bloed-ruggengraat-barrière, sonothrombolyse, cardiovasculaire geneesmiddelafgifte en sonobactericide.

Twee microbel formuleringen, gebaseerd op de veelgebruikte hoofdbestanddelen DPPC en DSPC, werden gekarakteriseerd in **Hoofdstuk 3**. Het fase gedrag van de lipiden in beide formuleringen werd bekeken met een Langmuir trog om de fosfolipide monolaag op het lucht/water oppervlak te bestuderen. Zowel de DPPC- als de DSPC-gebaseerde formulering had een transitie plateau door de verandering in conformatie van de gePEGyleerde componenten van de zogenaamde ´paddestoel´ naar ´borstel´ configuratie. Hoewel de domein morfologie verschilde in beide soorten monolagen, hadden de DPPC- en DSPC-gebaseerde microbellen vergelijkbare microstructuren in de schil. DSPC-gebaseerde microbellen werden geproduceerd door tip-sonicatie met de directe methode, dat wil zeggen door de schil componenten direct op te lossen in een waterige oplossing, of met de indirecte

methode, dat wil zeggen door de schil componenten eerst op te lossen in organisch oplosmiddel, te drogen tot een filmlaag is gevormd, en daarna de filmlaag op te lossen in een waterige oplossing. Deze lipide behandeling voorafgaand aan de productie van microbellen had een significant effect op de ligand distributie aan de buitenkant van de schil, waarbij de directe methode resulteerde in een heterogene ligand distributie en de indirecte methode resulteerde in een homogene ligand distributie.

Een nieuwe microbel formulering met DSPE als hoofdbestanddeel werd ontwikkeld en gekarakteriseerd in **Hoofdstuk 4**. Microbellen werden geproduceerd door tip sonicatie of amalgamatie en de stabiliteit, lipide fase distributie en acoustische attenuatie werden onderzocht. Microbellen geproduceerd door tip-sonicatie en microbellen geproduceerd door amalgamatie met 30% propyleen glycol hadden beide een homogene lipide fase distributie, met alle schil ocmponenten gemengd en in dezelfde fase. Microbellen geproduceerd door amalgamtie met 10% propyleen glycol hadden ronde gecondenseerde fase domeinen in de schil. Verder hadden alle microbel formuleringen een korte houdbaarheid, aangezien de grootte van de bellen binnen een uur na productie sterk afnam. Hoewel dit de toepassing van DSPE-gebaseerde microbellen *in vivo* beperkt, zijn de formuleringen met homogene lipide fase distributie interessant voor verdere studies naar de relatie tussen de lipide fase distributie en de acoustische respons in microbellen.

Om de lipide fase distributie en acoustische respons van individuele microbellen tegelijkertijd te onderzoeken, werd een uniek optisch systeem ontwikkeld en beschreven in **Hoofdstuk 5**. Een speciaal aangepaste confocale microscoop werd gekoppeld aan de Brandaris 128 ultra-hogesnelheidscamera. Dit systeem werd verder gebruikt voor de studies beschreven in **Hoofdstuk 6** tot en met **9**. In H**oofdstuk 6** werd het effect van cholesterol op de lipide fase distributie van DSPC-gebaseerde microbellen onderzocht. De toevoeging van cholesterol resulteerde in verminderde fase scheiding en microbellen met 12 mol% cholesterol hadden een schil met alle componenten gemengd en in dezelfde fase. Echter, de hoeveelheid uitstulpingen aan de buitenkant van de schil was ook toegenomen. De gecombineerde confocale microscoop en Brandaris 128 ultra-hogesnelheidscamera werden vervolgens gebruikt om de relatie tussen lipide behandeling, fase distributie en het acoustische gedrag van microbellen te bestuderen. Indirecte methode DSPC-gebaseerde bellen hadden een meer uniforme respons op ultrageluid dan directe methode DSPC-gebaseerde bellen en indirecte methode DSPC-gebaseerde bellen met 12 mol% cholesterol. De lipide behandeling en fase distibutie hadden dus signficant effect op het acoustische gedrag en indirecte methode DSPC-gebaseerde microbellen waren de meest veelbelovende kandidaat voor moleculaire beeldvorming met ultrageluid en therapeutische toepassingen.

Na de ontwikkeling en karakterisatie van de nieuwe DSPE-gebasserde en cholesterol-bevattende microbel formuleringen, werd de focus verschoven naar de microbel-cel morfologie en interactie met indirect DSPC-gebaseerde microbellen in **Hoofdstuk 7**. Microbellen die gericht bonden aan $\alpha_V\beta_3$ of CD31 werden vergeleken met niet-gebonden en controle microbellen. Het opnemen van bellen en het effect daarvan op de microbel oscillatie en sonoporatie werden onderzocht met het gecombineerde optische systeem, waarbij 3D opnames werden gemaakt voor en na blootstelling aan ultrageluidsgolven. Het opnemen van gebonden microbellen door endotheel cellen was afhankelijk van de receptoren waaraan de microbellen bonden, aangezien de niet gebonden bellen niet door de endotheel cellen werden opgenomen. Daarnaast had de opname van microbellen een dempend effect op de microbel oscillatie en werden cellen meer ontvankelijk voor sonoporatie na het opnemen van een microbel. Tot slot werden verschillende cellulaire reacties vastgelegd, zoals het ontstaan van poriën in het celmembraan, wat tot intracellulaire geneesmiddelafgifte leidde, en het ontstaan van tunnels, ook wel transcellulaire perforatie genoemd, wat mogelijk leidt tot transcellulaire geneesmiddelafgifte.

De invloed van ligand distributie op de binding van DSPC-gebaseerde microbellen met een ligand gericht op $\alpha_V\beta_3$ integrin was onderzocht in **Hoofdstuk 8**. Dit werd gedaan door de binding van microbellen geproduceerd met de directe en indirecte methode met elkaar te vergelijken *in vitro* met een monolaag van endotheel cellen onder statische condities en met stroming, en *in vivo* met de binding aan endotheel cellen van kippen embryo's. Een homogene ligand distributie leidde tot betere binding in alle drie de experimentele modellen. Tenslotte werd de opname van $\alpha_V\beta_3$-gebonden bellen door endotheel cellen bekeken en dit bleek onafhankelijk te zijn van de ligand distributie.

In **Hoofdstuk 9** wordt het moleculaire beeldvorming en therapeutische potentieel van vancomycin-bevattende microbellen beschreven. Deze nieuwe theranostische microbel bond gericht aan bacteriële biofilms onder stroming. Verder werd het oppervlak van de biofilm kleiner door toepassing van ultrageluid en de daaropvolgende trilling van gebonden vancomycin-bevattende microbellen.

Een overzicht van recente literatuur over microbellen met een fosfolipide schil die gericht binden voor moleculaire beeldvorming met ultrageluid en therapie wordt gegeven in **Hoofdstuk 10**. Er worden verschillende strategiën genoemd om de microbellen gericht aan een biomarker te laten binden en het gebruik van moleculaire beeldvorming met ultrageluid wordt besproken voor het bestuderen van ziekteverloop, diagnostische beeldvorming en het monitoren van de therapeutische respons. Daarnaast worden studies naar de behandeling van cardiovasculaire aandoeningen en kanker met gericht gebonden microbellen samengevat en kon

worden geconcludeerd dat het gebruik van gericht gebonden microbellen altijd resulteerde in significant betere therapeutische respons dan het gebruik van niet-gebonden microbellen, zowel *in vitro* als *in vivo*.

Tenslotte worden de wetenschappelijke vindingen uit deze thesis besproken in de context van microstructuren in de microbel schil en in de context van gericht gebonden microbellen voor theranostische toepassingen in **Hoofdstuk 11**, inclusief een perspectief op de toekomst en ontwikkeling van theranostische microbellen.

Publications

In this thesis

Klazina Kooiman, Silke Roovers, **Simone A.G. Langeveld**, Robert T. Kleven, Heleen Dewitte, Meaghan A. O'Reilly, Jean-Michel Escoffre, Ayache Bouakaz, Martin D. Verweij, Kullervo Hynynen, Ine Lentacker, Eleanor Stride, Christy K. Holland
Ultrasound-responsive cavitation nuclei for therapy and drug delivery
Ultrasound in Medicine & Biology, Vol. 46, No. 6, pp. 1296-1325, 2020

Simone A.G. Langeveld, Christian Schwieger, Inés Beekers, Jacob Blaffert, Tom van Rooij, Alfred Blume, and Klazina Kooiman
Ligand distribution and lipid phase behavior in phospholipid-coated microbubbles and monolayers
Langmuir, Vol. 36, No. 12, pp. 3221-3233, 2020

Simone A.G. Langeveld, Gonzalo Collado-Lara, Gerrit J.W. Wiggers, Antonius F.W. van der Steen, Nico de Jong, Klazina Kooiman
Lipid phase distribution and acoustic response of DSPE-based microbubbles
2021 IEEE International Ultrasonics Symposium (IUS), 2021

Inés Beekers, Kirby R. Lattwein, Joop J.P. Kouijzer, **Simone A.G. Langeveld**, Merel Vegter, Robert Beurskens, Frits Mastik, Rogier Verduyn Lunel, Emma Verver, Antonius F.W. van der Steen, Nico de Jong, Klazina Kooiman
Combined confocal microscope and Brandaris 128 ultra-high-speed camera
Ultrasound in Medicine & Biology, Vol. 45, No. 9, pp. 2575-2582, 2019

Simone A.G. Langeveld, Inés Beekers, Gonzalo Collado-Lara, Antonius F.W. van der Steen, Nico de Jong, Klazina Kooiman
The impact of lipid handling and phase distribution on the acoustic behavior of microbubbles
Pharmaceutics, Vol. 13, No. 1, pp. 119-140, 2021

Simone A.G. Langeveld, Bram Meijlink, Inés Beekers, Mark Olthof, Antonius F.W. van der Steen, Nico de Jong, Klazina Kooiman
Theranostic microbubbles with homogeneous ligand distribution for higher binding efficacy
Pharmaceutics, Vol. 14, No. 2, pp. 311-331, 2022

Joop J.P. Kouijzer, Kirby R. Lattwein, Inés Beekers, **Simone A.G. Langeveld**, Mariël Leon-Grooters, Jean-Marc Strub, Estefania Oliva, Gaëtan L.A. Mislin, Nico de Jong, Antonius F.W. van der Steen, Alexander L. Klibanov, Willem J.B. van Wamel, Klazina Kooiman
Vancomycin-decorated microbubbles as a theranostic agent for Staphylococcus aureus biofilms
International Journal of Pharmaceutics, Vol. 609, 2021

Simone A.G. Langeveld, Bram Meijlink, Klazina Kooiman
Phospholipid-coated targeted microbubbles for ultrasound molecular imaging and therapy
Current Opinion in Chemical Biology, Vol. 63, pp. 171-179, 2021

Submitted for publication

Inés Beekers, **Simone A.G. Langeveld**, Bram Meijlink, Antonius F.W. van der Steen, Nico de Jong, Martin D. Verweij, Klazina Kooiman
The 3D microbubble-endothelial cell dynamics: microbubble internalization and drug delivery by pores and tunnels

Supervised academic reports

Gerrit J.W. Wiggers, "*Theranostic phospholipid-coated microbubbles: The search for the perfect coating*", Bachelor Biology and Medical Laboratory Research internship report, Saxion University of Applied Sciences Deventer, the Netherlands, 2021.

Mark Olthof, "*The in vitro binding behavior of targeted microbubbles with homogeneous versus heterogeneous ligand distribution to endothelial cells under flow*", MSc Infection and Immunity internship report, Erasmus University Medical Center Rotterdam, the Netherlands, 2021.

Publication not in this thesis

Brigitta M. Laksono, Christina Grosserichter-Wagener, Rory D. de Vries, **Simone A.G. Langeveld**, Maarten D. Brem, Jacques J.M. van Dongen, Peter D. Katsikis, Marion P.G. Koopmans, Menno C. van Zelm, Rik L. de Swart.
In vitro measles virus infection of human lymphocyte subsets demonstrates high susceptibility and permissiveness of both naïve and memory B cells
Journal of Virology, Vol. 92, No. 8, 2018

PhD portfolio

Conferences	Year	ECTS
Symposium Phospholipids in Pharmaceutical Research *Phospholipid Research Center*	2017	1.1
NVMU Meeting *University of Twente*	2017	0.4
23rd European Symposium on Ultrasound Contrast Imaging, *Erasmus MC*	2018	0.6
6th SURE Symposium *Student Union of Research Masters of Erasmus MC*	2018	0.3
Researcher's Day *Phospholipid Research Center*	2018	0.3
PhD Day *Erasmus MC, Promeras*	2018	0.3
Leeds Microbubble Symposium *Leeds Microbubble Consortium*	2018	1.1
IEEE IUS - Kobe, Japan *IEEE UFFC*	2018	2.2
ASA - Victoria, Canada *Acoustical Society of America*	2018	2.2
24th European Symposium on Ultrasound Contrast Imaging, *Erasmus MC*	2019	1.1
Symposium Phospholipids in Pharmaceutical Research *Phospholipid Research Center*	2019	1.1
25th European Symposium on Ultrasound Contrast Imaging, *Erasmus MC*	2020	1.1
Innovation for Health	2020	0.3
IEEE IUS Online IEEE UFFC	2020	1.7
26th European Symposium on Ultrasound Contrast Imaging, *Erasmus MC*	2021	1.5
Researcher's Day *Phospholipid Research Center*	2021	1.3
IEEE IUS Online IEEE UFFC	2021	1.7

Courses	**Year**	**ECTS**
Microscopic Image Analysis: From theory to practice *Molecular Medicine Postgraduate School*	2018	0.8
Leeds ThUNDDAR Workshop *Leeds Microbubble Consortium*	2018	0.3
Microbubbles and Nanodroplets for Biomedical Ultrasound Applications, *IEEE IUS - Kobe, Japan*	2018	0.15
ExCOEURsion to General Medical Council *Cardiovascular Research School Erasmus University*	2018	0.2
Workshop Career Development for PhD Candidates *Molecular Medicine Postgraduate School*	2019	0.15
Personal Leadership, Management & Communication *Molecular Medicine Postgraduate School*	2019	1.0
Therapeutic Ultrasound School *École de Physique des Houches*	2019	3.0
Research Integrity *Erasmus MC*	2019	0.3
Summer School on Ultrasound Contrast Agents *IEEE UFFC, University of Colorado*	2019	3.0
Vascular Biology & Pathology *Dutch Heart Foundation*	2019	3.0
Biomedical English Writing Course *Molecular Medicine Postgraduate School*	2019	1.1

Other	**Year**	**ECTS**
Supervision Bachelor HBO internship - Gert-Jan Wiggers *Saxion University of Applied Sciences Deventer*	2021	0.9
Supervision MSc internship - Mark Olthof *Infection & Immunity, Erasmus MC*	2021	0.9
Chair of Young Medical Delta board	2021	1.5
	Total	**37.1**

About the author

Simone Langeveld was born on March 1st, 1993 in Haarlem, the Netherlands. From a young age she has been passionate about two things: drug development and harp. In 2010 she started her Bachelor degree in Bio-Pharmaceutical Sciences at Leiden University and her Bachelor degree in classical harp at the Royal Conservatory in The Hague. After completing both degrees she continued her education in 2015 with a research master in Infection & Immunity at the Erasmus University in Rotterdam. After two research internships within the Erasmus University Medical Center, at the department of Medical Microbiology and Infectious Diseases and the department of Viroscience, she joined the Biomedical Engineering department in 2017 to start her PhD project under supervision of Associate Professor Klazina Kooiman, Professor Ton van der Steen, and Professor Nico de Jong. Her research was focused on the development and characterization of a novel phospholipid-based microbubble coating that can be used for both ultrasound molecular imaging and local drug delivery.

Besides her research project, Simone worked as chair of Young Medical Delta in 2020 to connect students and young professionals with a passion for medical technology as part of Medical Delta. In addition, she toured the Netherlands and Ljubljana, Slovakia, with the Dutch Student Orchestra in 2018, and joined several other orchestra projects, for example with the European Doctors Orchestra. Simone was involved as volunteer with the VoorleesExpress where she spent time helping children learn Dutch by reading and with Stichting Mano where she helped refugees with laboratory expertise find employment in the Netherlands.